



ACADEMIA OAMENILOR DE ȘTIINȚĂ DIN ROMÂNIA

Strada Ilfov, nr. 3, sector 5, 050044, București, România
Tel.+4021/314.74.91; Fax. +4021/314.75.39,
email: secretariat.aosr@gmail.com
<http://www.aosr.ro>

Competiția de proiecte de cercetare a Academiei Oamenilor de Știință din România destinată tinerilor cercetători „AOSR-TEAMS-II” EDIȚIA 2023-2024 – „Transformarea digitală în științe”

Sesiune științifică AOSR tineri cercetători etapa IV – Decembrie 2024

Titlul proiectului:

Digitalizare 3D de precizie în agricultură și silvicultură, utilizând platformele UAV și fuzionarea livrabilelor fotogrammetrice și LiDAR

Domeniul științific propus: Științe agricole și silvice

Membrii echipei de cercetare:

Șef lucrări dr. ing. **Paul Sestraș** (Director Proiect) - Departamentul de Măsurători Terestre și Cadastru, Facultatea de Construcții, Universitatea Tehnică din Cluj-Napoca

Asistent dr. ing. **Irina Todea** - Departamentul de Silvicultură, Facultatea de Silvicultură și Cadastru, Universitatea de Științe Agricole și Medicină Veterinară Cluj-Napoca

Cuvinte cheie

Algoritmi de digitalizare, generarea computerizată, digitalizarea terenurilor, drone, senzori de măsurare, modele 3D, nori de puncte, agricultură și silvicultură de precizie, geomatică, măsurători terestre

Obiective, cu indicarea importanței acestora

Creșterea continuă a populației Globului, schimbările climatice și fenomenele naturale extreme, procesele de eroziune și degradare a solului, pericolul crizelor alimentare și sociale etc. sunt factori extrem de importanți pe care trebuie să-i aibă în vedere factorii de decizie, politici și administrativi, precum și oamenii de știință, pentru a asigura populației resursele alimentare și condițiile de trai necesare pentru generația actuală și pentru cele următoare (López *et al.*, 2021; Radoglou-Grammatikis *et al.*, 2020). În acest scop, agricultura trebuie să-și recâștige poziția și rolul primordial, ancestral, în societatea actuală, numită ‘modernă’, respectiv de activitate de bază care asigură hrana celor opt miliarde de oameni de pe Terra, în condițiile în care prin această activitate să fie protejată natura și totodată să se desfășoare pe baza principiilor de sustenabilitate, care să asigure perpetuarea resurselor de viață și a biodiversității pentru generațiile viitoare. Evoluția cunoașterii, a științei și tehnologiei, odată cu evoluția societății și a omului modern, oferă posibilitatea realizării acestor deziderate. Însă agricultura și silvicultura pot genera resursele necesare pentru a asigura hrana și standardele de viață dorite de societatea umană actuală și viitoare doar în condițiile unor remodelări ale concepțiilor, metodologiilor și tehnicilor de utilizare și valorificare ale terenurilor agricole, pădurilor și biodiversității acestora (Gómez-Candón *et al.*, 2014). În acest scop, monitorizarea suprafețelor agricole și forestiere, a fenomenelor de eroziune și degradare a solurilor, alunecări de teren și alte fenomene naturale cu consecințe nefavorabile asupra producțiilor agricole și mediului înconjurător, reprezintă o primă condiție în cunoașterea situațiilor existente pe teren (Comba *et al.*, 2018). Doar prin identificarea și cunoașterea exhaustivă a condițiilor și posibilităților de elaborare de noi strategii și aplicare a unor tehnologii adecvate de cultură se pot asigura ulterior producții sustenabile, o calitate adecvată a producțiilor agricole și se poate proteja mediul ambiant și înfrumuseța condițiile de viață (Aslan *et al.*, 2022).

Utilizarea tehnologiilor moderne în agricultură pentru a îndeplini toate aceste deziderate servește scopului agriculturii și silviculturii de precizie. Întrucât cu ajutorul vehiculelor aeriene fără pilot (UAV) se pot obține cu ușurință date în timp real, acestea au un potențial mare de abordare și optimizare a soluțiilor la problemele cu care se confruntă agricultura, horticultura și silvicultura. În ciuda unor limitări datorită echipamentelor actuale (acumulatori, sarcina etc.), sau condițiilor meteorologice uneori nefavorabile zborurilor, se preconizează că UAV-urile vor fi tot mai mult utilizate în agricultură în viitor, datorită utilității excepționale a informațiilor pe care le furnizează și multiplelor aplicații ale acestora (Delavarpour *et al.*, 2021). Pentru sporirea eficienței oferită de UAV-uri, este necesară o gestionare și o organizare adecvată a datelor, bazată pe sisteme de poziționare globală (GPS) și analiză spațială folosind sisteme de informații geografice (GIS). Agricultura de precizie (AP) este un concept agricol modern, bazat pe noi tehnologii, instrumente și dispozitive informatice, care vizează îmbunătățirea și optimizarea proceselor de producție agricolă prin monitorizarea culturilor, calibrarea inputurilor și a operațiunilor. Beneficiile provin din creșterea calitativă și cantitativă a producției agricole și din reducerea impactului asupra mediului. Necesarul tot mai mare de alimente la nivel mondial, necesită dezvoltarea unor sisteme de înaltă performanță, promovarea unei agriculturi de înaltă productivitate și durabilă, ceea ce implică introducerea de noi tehnologii în activitățile de monitorizare legate de control și de luare a deciziilor.

Tehnologiile emergente pot oferi un potențial semnificativ în aplicațiile de agricultură și silvicultură inteligentă și de precizie, permițând achiziționarea de date de mediu în timp real. Dispozitivele UAV pot fi exploatate într-o varietate de aplicații legate de gestionarea culturilor, prin captarea de imagini cu rezoluție spațială și temporală ridicată. Se așteaptă ca aceste tehnologii să

revoluționeze agricultura, permițând luarea deciziilor în timp scurt (ex., uneori zile în loc de săptămâni), asigurând o reducere semnificativă a costurilor de producție și totodată creșterea randamentului. Aceste tehnologii oferă eficiență și inputuri agricole semnificative, susținând cei patru piloni ai agriculturii de precizie, respectiv aplicarea practicilor potrivite, la locul potrivit, la momentul potrivit și în cantitatea potrivită.

Silvicultura de precizie reprezintă o nouă direcție pentru o mai bună gestionare a pădurilor. Silvicultura de precizie utilizează tehnologia informației și instrumente analitice pentru a sprijini deciziile economice, de mediu și durabile; utilizarea instrumentelor informaționale geospațiale permite efectuarea de măsurători, acțiuni și procese pentru gestionarea eficientă a suprafețelor forestiere și recoltarea producției lemnoase din arborete, permițând în același timp crearea de legături informaționale între producție și lanțul de aprovizionare cu lemn, inclusiv între administratorii de resurse și comunitățile din mediile de interes (Hassaan *et al.*, 2016). Măsurătorile privind înălțimea arborilor reprezintă un atribut important al arborilor în scopul calculării creșterilor, volumului și biomasei arborilor, care, la rândul lor, furnizează informații ecologice și economice importante pentru factorii de decizie (Krause *et al.*, 2019). Înălțimea arborilor a fost măsurată în mod tradițional, individual, pe teren, prin metode clasice și bine cunoscute. Odată cu progresele recente în tehnologiile de teledetecție cu vehicule aeriene fără pilot (UAV), posibilitatea de a înregistra înălțimea exactă a arborilor în mod semiautomat a devenit o realitate. Măsurătorile fotogrammetrice UAV ale înălțimii arborilor și cantitatea de biomasă reprezintă o opțiune viabilă pentru parcelele de monitorizare intensivă a pădurilor (Puliti *et al.*, 2020). Caracteristicile geometrice ale arborilor și arboretelor, cum sunt suprafața superioară a coronamentului, înălțimea arborilor și volumul coroanei, oferă informații utile pentru a elucida starea arboretelor și pentru elaborarea și aplicarea unui management sustenabil al pădurilor. Aceste aspecte sunt aplicabile și în cadrul plantațiilor agricole, particularitățile livezilor, pomilor fructiferi, arbuștilor fructiferi, viță de vie etc. și monitorizarea acestora oferind informații deosebit de utile referitoare la creșterea plantelor și capacității lor productive, la starea lor de vegetație și la cea fitosanitară.

Încorporarea de tehnologii avansate în platformele vehiculelor aeriene fără pilot (UAV) a permis numeroase aplicații practice în agricultura de precizie (AP) a ultimului deceniu (Chang *et al.*, 2017). Aceste instrumente de AP oferă capacități care sporesc productivitatea agricolă și eficiența inputurilor și minimizează simultan costurile operaționale. Tehnicile de teledetecție sunt utilizate ca parte a practicilor AP pentru monitorizarea culturilor și a solului. Aceste tehnici au fost îmbunătățite recent prin reducerea prețului senzorilor (RGB, multispectrali, hiperspectrali, termici). Dezvoltarea și modernizarea vehiculelor aeriene fără pilot (UAV) joacă, de asemenea, un rol esențial în monitorizarea AP (Popescu *et al.*, 2020). Rezultatul calculului bazat pe mai multe surse de informații se concretizează frecvent în realizarea hărților ortomosaice, indici de vegetație sau nori de puncte. Informații suplimentare privind culturile pot fi furnizate de modelarea recentă a norului de puncte tridimensional (3D). Norul de puncte este un set mare de date de puncte, denumit sistem de coordonate 3D, care reprezintă puncte de pe suprafața exterioară a obiectelor vizibile, unde se reflectă lumina. Datele pentru modelarea 3D a culturilor pot fi furnizate direct de către scanerile cu laser (cum sunt sistemele de detectare a luminii și de măsurare a distanței - LiDAR) sau derivate din imaginile multispectrale și termice prin fotogrammetrie și algoritmi de viziune computerizată, de exemplu Structure from Motion (SfM). O precizie mare a informațiilor va contribui la o bună susținere a rezultatelor care se vor putea obține în agricultură și silvicultură, prin: (1) monitorizarea terenurilor în vederea depistării eroziunii solurilor și alunecărilor de teren, în vederea implementării de soluții privind îmbunătățirile funciare; (2) cartografierea precisă a terenurilor și generarea de modele 3D care vor contribui la buna gestionare și bonitare a terenurilor; (3) cartografierea de precizie a vegetației și a biomasei arboretelor, cu aplicații diverse în silvicultura de precizie; (4) topografia și cadastrul agricol/silvic.

Cercetările anterioare ale directorului de proiect (DP) s-au axat pe dezvoltarea unor analize spațiale GIS și a unor hărți de risc în vederea identificării zonelor și a punctelor sensibile la eroziune și alunecări de teren. Cercetările efectuate, inclusiv investigațiile bibliografice și acumularea unui fond

bibliografic adecvat, pe baza altor studii legate de apariția alunecărilor de teren în zona Dealurilor Clujului (Kerekes *et al.* 2018, 2020), au făcut parte dintr-un deziderat amplu de monitorizare a anumitor hotspot-uri de mare importanță pentru zona Clujului și municipalitate, de mare interes social, datorită posibilelor riscuri cu un potențial impact economic și chiar decese. Astfel, mai multe hotspot-uri alese au fost monitorizate prin intermediul măsurătorilor geodezice și topografice cu instrumente precum sistemele GNSS și stațiile totale, însoțite de ridicări în zbor cu UAV-uri și tehnici geomatice pentru a evalua areale susceptibile la eroziuni și alunecări de teren. Prin combinarea celor două metode, rezultatele obținute au fost cuprinzătoare și au oferit o mai bună înțelegere a mișcărilor și deplasărilor complexe prezente în eroziunea și alunecările de teren monitorizate, fiind valorificate prin publicații de impact (Sestras *et al.*, 2021). Cu toate acestea, metodologiile propuse de către DP au prezentat anumite constrângeri și limitări, astfel încât soluțiile inovatoare sunt imperative pentru îmbunătățirea unor măsurători complexe și obținerea unor informații extrem de relevante și utile.

Eroziunea solului are consecințe deosebit de negative pentru agricultură, fiind un procesul natural cauzat de activitatea dinamică a agenților de eroziune, respectiv apa, gheața (ghețarii), zăpada, aerul (vântul), plantele și animalele, la care se adaugă factorul antropic. Alunecările de teren reprezintă un risc la nivel mondial care reprezintă 9% din dezastrele mondiale (Galli *et al.* 2008), acestea fiind definite ca mișcări ale solului, resturi și roci sub influența gravitației, care au cea mai mare incidență în zonele de deal și de munte (Cruden *et al.*, 1996). Măsurătorile precise ale deplasărilor verticale și orizontale ale pământului îmbunătățesc înțelegerea mecanismelor de alunecări de teren responsabile de dinamica alunecărilor și sunt cruciale pentru predicția mișcărilor viitoare precum și pentru elaborarea și aplicarea unor măsuri de prevenire eficiente. Există numeroase cercetări și metodologii privind instrumentele și tehnologiile utilizate în monitorizarea alunecărilor de teren, de la aparatura geodezico-topografică tradițională (stații totale, sisteme GNSS, scanere laser terestre), până la soluții moderne: fotogrammetrie UAV (vehicule aeriene fără pilot), sau LiDAR ('light detection and ranging'), InSAR, senzori și aplicații geomatice (Peduto *et al.*, 2021). Soluțiile terestre, cum sunt instrumentele geodezico-topografice menționate, au o acuratețe precisă și pot produce observații precise cu privire la posibile deplasări și mișcări de suprafață. Dezavantajul preciziei milimetrice care poate rezulta pe baza reperelor topografice, constă într-o muncă manuală intensă și consumatoare de timp, cu o acoperire spațială redusă, care oferă cu precizie anumite deplasări, în detrimentul unei reprezentări limitate a suprafeței Pământului (Sestras *et al.*, 2021). O tehnologie emergentă importantă o reprezintă UAV-urile, numite în mod obișnuit drone, care oferă un ajutor indispensabil, eficiență în ceea ce privește viteza și precizia, precum și economii de costuri în locații inaccesibile sau greu de navigat. UAV-urile sunt în ascensiune în rândul multor industrii și au devenit foarte populare. În topografie și inginerie se consideră că acestea reprezintă un mare salt calitativ în tehnologie (Devoto *et al.*, 2020). În ultimul deceniu, există numeroase studii referitoare la monitorizarea alunecărilor de teren cu ajutorul UAV-urilor, acestea folosindu-se pentru a colecta imagini de înaltă rezoluție, utilizate în tehnici complexe de fotogrammetrie și geomatică (Solazzo *et al.*, 2018). Mai multe studii au demonstrat utilitatea și fiabilitatea software-ului Structure from Motion (SfM), care este o tehnică de procesare a imaginilor bazată pe calcul care permite reconstrucția unei suprafețe fotografiate. Incorporate cu plasarea unor puncte de control la sol (GCP) cu coordonate cunoscute sau măsurate, rezultatele obținute, georeferențiate, permit monitorizarea caracteristicilor de suprafață și analiza deplasărilor. Dezavantajele fotogrammetriei sunt dependența de o lumină optimă și de o textură suficientă, împreună cu imposibilitatea de a capta sau de a penetra structuri și vegetație (Glira *et al.*, 2019). Reconstrucția fotogrammetrică dobândește punctele de la suprafața cea mai de sus, iar în cazul monitorizării alunecărilor de teren și a ridicării terenurilor, în general, vegetația este prezentă în aproape toate scenariile, astfel că limitează sau exclude utilizarea unei astfel de tehnici.

LiDAR este o tehnologie dezvoltată în ultimele decenii, dar abia recent disponibilă la o dimensiune și o putere fezabilă pentru a fi transportată pe drone mari, precum și la prețuri accesibile (Bandini *et al.*, 2020). Trimițând impulsuri de lumină laser și măsurând timpul exact necesar pentru ca aceste impulsuri să se întoarcă pe măsură ce ricoșează de pe sol, senzorul LiDAR este considerat de mulți

ca fiind următorul pas în ceea ce privește ridicarea eficiență și precisă a terenurilor, cu multe avantaje în raport cu tehnicile clasice bazate pe teren. Există numeroase studii legate de modelele digitale ale terenului (DTM), modelele digitale de suprafață (DSM) sau modelele digitale de elevație (DEM) derivate din LiDAR, care au permis evaluarea comportamentului evolutiv al instabilității versanților, interpretări geomorfice și monitorizarea alunecărilor de teren (Pirasteh și Li, 2017), precum și încorporări în diferite domenii, cum sunt: inginerie civilă, geomorfologie, patrimoniu cultural, ecologie, mediu etc. Având în vedere toate progresele tehnologice, împreună cu nevoia imperativă de noi abordări privind dezvoltarea unor studii și monitorizări moderne ale terenurilor, proiectul își propune să genereze cunoștințe esențiale în domeniu, precum și să stabilească o abordare nouă în ceea ce privește fuziunea datelor UAV LiDAR și fotogrammetrice, care să completeze avantajele și să compenseze dezavantajele fiecăruia.

Noutatea proiectului propus constă în interdisciplinaritatea datelor și cunoștințelor, precum și în combinarea pragmatică și armonioasă a unor abordări din diferite domenii cu scopul de a asigura generarea unui nor de puncte de mare precizie, cu ramificații și implementări ulterioare. Atât datele LiDAR, cât și datele fotogrammetrice au fost utilizate pe scară largă în ultimii ani pentru a obține reconstrucția 3D a suprafeței Pământului, a obiectelor naturale sau a infrastructurii (Carey *et al.*, 2019). Deși ambele tehnici se bazează pe principii de reconstrucție diferite (măsurare polară *vs.* triangulație de raze), ambele au furnizat rezultate excepționale (Glira *et al.*, 2019; Cramer *et al.*, 2018). Având în vedere avantajele, dezavantajele și limitările fiecărui senzor și ale fiecărei tehnici, au existat mai multe încercări de a fuziona cele două seturi de date, pentru a obține o soluție completă și o fuziune a norilor de puncte. Proiectul prezentat are ca scop fuziunea dintre norii de puncte LiDAR și fotogrammetrie pe baza diferitelor caracteristici prezente pe teren. Inițierea acestei metodologii s-a bazat pe aplicațiile LiDAR specifice arheologiei, dezvoltate de Ștular *et al.* (2021) și Pingel *et al.* (2015). În toate domeniile legate de geostiință, datele derivate din LiDAR și fotogrammetrie sunt utilizate pentru a genera DSM-uri, DTM-uri și DEM-uri, care sunt utilizate ulterior în fiecare domeniu specific în diverse analize spațiale. Fiecare metodă a dezvoltat instrumente hardware și software pentru generarea norilor de puncte din LiDAR și pentru potrivirea imaginilor, iar până de curând ambele abordări au fost considerate ca fiind tehnici concurente, eforturile de cercetare concentrându-se pe îmbunătățirea individuală a senzorilor și a algoritmilor (Glira *et al.*, 2019). Senzorii LiDAR utilizează principiul de măsurare polară și sunt avantajoși ori de câte ori aspectul obiectului se modifică rapid atunci când este văzut din poziții diferite. Procesul de reconstrucție fotogrammetrică oferă informații 3D pentru fiecare pixel al imaginii la o calitate considerabilă dacă există o suprapunere suficientă a imaginii și o textură suficientă, cu o scădere a acurateței în zonele cu textură scăzută sau în zonele umbrite. Principalele diferențe geometrice dintre cei doi senzori provin din capacitatea fasciculului lidar de a penetra stratul de vegetație. Fotogrammetria poate capta doar suprafața tuturor structurilor de pe teren, astfel că datele derivate pot obține DSM-uri. Datele LiDAR, cu capacitatea de a penetra stratul de vegetație, pot genera atât DSM-uri (caracteristicile naturale și construite ale mediului), cât și DTM-uri (terenul natural) pe parcursul clasificării. În aplicațiile LiDAR în arheologie, termenul DFM (*'Digital feature model'*) a fost adoptat pentru a se referi la terenul natural cu elementele semnificative construite de om, care sunt șterse în mod intenționat de alte tehnici de procesare LiDAR. Prin urmare, considerăm DFM ca fiind un subtip de DEM, care încorporează caracteristici de microrelief și structuri antropice. Noutatea metodologică propusă în acest proiect constă în dezvoltarea DFM-urilor bazate pe achiziția de date hibride, însă în loc de crearea unui pachet de nori de puncte între cele două seturi de date, se propune selectarea anumitor elemente din fiecare senzor. Astfel, DTM va fi obținut din LiDAR în zonele naturale cu vegetație, cu o precizie verticală preconizată (în funcție de marca senzorului, IMU etc.), de aproximativ 5-10 cm. DSM-ul elementelor de vegetație mare sau antropice va fi obținut din procesul SfM. În zonele cu o textură bună și o distanță mică de eșantionare GSD, precizia verticală preconizată poate fi mai mare decât cea a LiDAR, respectiv <5 cm (Westoby *et al.*, 2012; Fonstad *et al.*, 2013).

Metodologie, cu indicarea gradului de originalitate

Pe baza ipotezelor menționate în secțiunea anterioară, prezentul proiect își propune să exploreze, să evalueze și să inoveze achiziția de date și să consolideze nevoia de studii calitative, eficiente și precise ale modelării 3D a terenurilor în vederea monitorizării eroziunilor și riscurilor de alunecare de teren, precum și să sprijine procesul de modelare a norilor de puncte în agricultura și silvicultura de precizie. Având în vedere că agricultura este una dintre cele mai mari ramuri ale economiei, care trebuie susținută peremptoriu pentru că asigură resursele necesare omenirii, și măsurătorile topografice trebuie să evolueze pentru a o putea susține. Modelul DFM propus poate fi adaptat cu ușurință pentru a genera produse livrabile, cum ar fi curbe de nivel, profilele de teren și altitudinile detaliilor topografice. Deoarece o gestionare a terenurilor nu poate fi realizată fără planuri topografice actualizate, implementarea proiectului ar asigura și o conexiune benefică între topografi și inginerii agricoli și silvici.

Proiectul este alcătuit din patru pachete de lucru (PL), fiecare fiind considerat un obiectiv intermediar cheie (Figura 1). Acestea sunt descrise în detaliu în Tabelul 1, inclusiv metodele de cercetare în raport cu cele mai noi abordări din domeniu, precum și planul de lucru (Tabelele 3, 4 și 5 din secțiunea nr. 5). Obiectivele specifice, cuplate cu cunoștințele actuale, și elementele corespunzătoare de originalitate și inovații sunt prezentate în Tabelul 1.

Tabelul 1. Cunoștințe generale vs. elemente de originalitate și inovare

Obiectiv specific I. Realizarea DFM cu achiziția hibridă de date și fuziunea norilor de puncte cu caracteristici și avantaje diferite

Cunoștințe generale. După cum s-a menționat, ingineria topografică se ocupă cu reprezentarea suprafeței Pământului, folosind diferite metode și instrumente în funcție de preciziile impuse în proiect, tipul de topografie, configurația terenului etc. În acest prim obiectiv, potențialul datelor hibride obținute prin LiDAR UAV și fotogrammetrie este explorat prin dezvoltarea unei noi abordări și metodologii de fuziune a caracteristicilor selectate între norii de puncte derivați din senzori. Până în prezent, au fost realizate diferite studii privind posibilitatea fuzionării acestor tehnologii (ex. Glira *et al.*, 2019), fiind dezvoltată o orientare hibridă a norilor de puncte LiDAR și a imaginilor aeriene pentru a optimiza discrepanțele mari, de până la câțiva decimetri, dintre alinierea benzii LiDAR și triangulația aeriană. Rezultatele obținute de Cramer *et al.* (2018) au evidențiat precizia ultra-înaltă a potrivirii combinate a LiDAR pe bază de UAV și a imaginilor dense. Fuziunea lor de date atinge acuratețea impusă la nivel de centimetru în spațiul obiectului, ceea ce până acum doar geodezia inginerească putea îndeplini sarcina aspirată. Algoritmul Iterative Closest Point (ICP) și metodele de viziune computerizată pentru fuzionarea a doi nori de puncte, au oferit rezultate care au demonstrat că golurile din norii de puncte fotogrammetrice pot fi completate cu date LiDAR după procesul de fuziune a datelor (Doumit, 2020).

Elemente de originalitate și inovare. Deși au existat și alte încercări de fuziune a datelor, originalitatea proiectului și obiectivului specific propus, constau în implementarea modelului DFM din anumite aplicații LiDAR arheologice. Pingel *et al.* (2015) și Ștular *et al.* (2021) au prezentat funcționalitatea DFM ca un subtip de DEM, datorită importanței reprezentării atât a terenului, cât și a structurilor antropice. Aceste solicitări exacte sunt obligatorii și în cazul monitorizării studiilor și construcțiilor. Ca urmare, prin adaptarea modelului DFM și a caracteristicii selectate (pe baza avantajelor/dezavantajelor fiecărui senzor) din cei doi nori de puncte, care reprezintă scopul nostru final, considerăm că se pot face pași importanți în direcția unei maturități și noutăți metodologice în domeniu.

Obiectivul specific II. Analiza preciziei norului de puncte și a DFM-ului general

Cunostinte generale. Din punct de vedere al preciziei, nu toate studiile cu drona sunt egale în ceea ce privește acuratețea; cu toate acestea, dacă se folosește o dronă profesională echipată cu senzori specializați, rezultatele pot fi spectaculoase. În ultimul deceniu, au fost realizate mai multe studii privind precizia metodelor de topografie cu drone. Kršák *et al.* (2016) au analizat acuratețea DEM-urilor derivate din UAV SfM și au obținut criteriile de acuratețe dorite și un interval ΔH de 5-10 cm (studiu de caz real; mediu necontrolat/optimal). Oniga *et al.* (2020) au obținut rezultate similare, concluzionând asupra numeroaselor aspecte care influențează acuratețea DEM-urilor. Cercetări LiDAR privind precizia verticală a modelului reconstruit au fost efectuate în ultimii ani (You și Lee, 2020). Luo *et al.* (2019) au prezentat rezultate de 3-5 cm de precizie a elevației în medii controlate și optime, în timp ce Akturk și Altunel (2020) au obținut o precizie a elevației de ≈ 10 cm în implementări pe terenuri autentice.

Elemente de originalitate și inovare. Originalitatea obiectivului propus constă într-o nouă abordare DFM și a metodologiei preconizată de fuziune a datelor cu caracteristici selectate, după cum s-a precizat anterior. Evaluarea acurateții modelului DFM va fi testată pe baza principiilor și metodologiilor prezentate de Pinton *et al.* (2020) pentru datele LiDAR și Oniga *et al.* (2020) pentru datele SfM. Pe baza rezultatelor și cunoștințelor științifice actuale, precum și pe baza instrumentarului logistic dorit (prezentat în continuare în secțiunea C3), rezultatele așteptate vor consta într-o precizie verticală de 5-10 cm pentru datele LiDAR (în funcție de parametrii de zbor, de software-ul de postprocesare, de senzorul și de configurația terenului). În cazul SfM, distanța de eșantionare spațială la sol (GSD) preconizată va fi < 1 cm, pe baza camerei dorite (DJI P1), a obiectivelor de 35 mm și a unei înălțimi de zbor de 50 m. Astfel, deși este imposibil de prezis cu exactitate precizia verticală care poate fi obținută din cauza numărului mare de variabile în fotogrammetrie, estimăm o valoare cuprinsă între 2-5 cm. După cum au concluzionat Westoby *et al.* (2012) și Fonstad *et al.* (2013), SfM în condiții optime este mai precisă decât datele LiDAR.

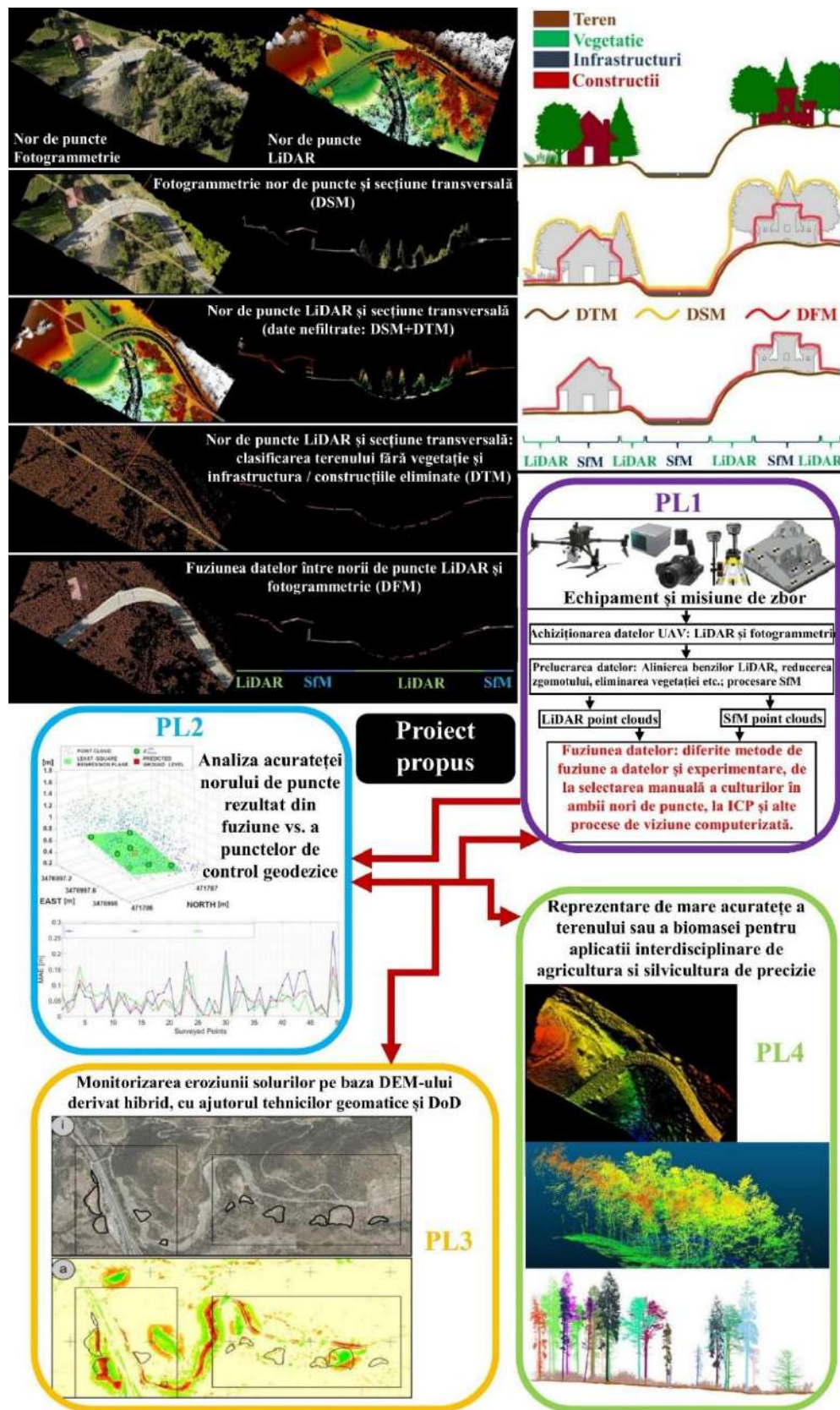


Figura 1. Cadrul conceptual al fuziunii LiDAR și SfM; conceptul DFM; cele patru pachete de lucru corelate (concept original, nepublicat)

Tabelul 3. Cele 4 pachetul de lucru ale proiectului propus cu descrierea activitatilor

PL1	Obiectivul I. Realizarea DFM cu achiziția hibridă de date și fuziunea norilor de puncte cu caracteristici diferite	
Descrierea activităților	Începutul - Sfârșitul lunii	L1 – L5
<p>A.I.1 Testarea sistemului UAV, a senzorilor și a software-ului; activități complementare ad interim L1 – L3</p>		
<p>Proceduri pentru testarea echipamentelor, analiza suplimentară a literaturii de specialitate, pagina web a proiectului etc.</p>		
<p>A.I.2 Zboruri de testare cu sistemul UAV, planificarea misiunii și achiziția de date LiDAR/SfM într-un mediu controlat. L3</p>		
<p>Odată ce echipamentul necesar a fost verificat și testat, primii pași pentru dezvoltarea și testarea DFM-ului preconizat vor fi făcuți în curtea și terenul de testare al Facultății de Construcții, Clădirea Observatorului, UTCN. Mediul controlat pentru testele inițiale oferă un spațiu de manevră adecvat și condiții de siguranță. De asemenea, acesta conține un amestec de diferite tipuri de teren, niveluri de vegetație și o mulțime de structuri solide cu texturi diferite. Vor fi testate mai multe softuri de planificare a misiunilor în funcție de sistemul de drone (de la DJI Pilot, la DroneDeploy, UgCS, Pix4D) pentru a selecta cea mai bună soluție compatibilă și eficientă. Terenul va fi pregătit cu markeri specifici, GCP pentru procedee SfM și puncte de control pentru verificarea datelor LiDAR/SfM, coordonatele markerilor fiind determinate cu ajutorul instrumentelor și metodelor topografice-geodezice. Numărul optim de GCP-uri și amplasarea lor se va face în conformitate cu concluziile lui Oniga <i>et al.</i> (2020).</p>		
<p>A.I.3 Prelucrarea datelor LiDAR și fotogrammetrice L4</p>		
<p>Datele LiDAR vor consta în procesarea traiectoriei senzorului și a punctelor brute, pentru a obține un nor de puncte inițial. Următoarea etapă va consta în alinierea benzilor LiDAR, reducerea zgomotului, colorarea norului de puncte, clasificarea și eliminarea vegetației. Softurile utilizate sunt TOPOLiDAR Post Processing, Global Mapper și LiDAR360. De asemenea, această etapă va include transformarea din WGS în Stereografic 1970.</p>		
<p>Datele fotogrammetrice vor fi prelucrate cu ajutorul softului specializat Agisoft Metashape Professional Edition. Fluxul de lucru va consta în metodologii stabilite (Sestras <i>et al.</i>, 2020), cu o atenție deosebită acordată proceselor de georeferențiere pentru a obține cea mai bună precizie. Etapele vor consta în alinierea fotografiilor, construirea punctelor de legătură, GCP de referință, construirea norului dens, plasă, textură, DEM, ortomosaic. Ulterior, datele vor fi exportate în diferite formate de fișier, .jpg/.png pentru ortofotografie, .tif pentru analiza spațială GIS și în format .las pentru procesarea ulterioară a norului de puncte.</p>		
<p>A.I.4 Fuziunea optimă de date a caracteristicilor selectate, DFM L5</p>		
<p>Ambii nori de puncte derivați de senzori vor fi analizați și experimentați în continuare în cadrul acestei activități. Deși studiile LiDAR și SfM se bazează pe același datum (sistemul de coordonate stereografice 1970), se va acorda o atenție deosebită fuziunii dintre cele două seturi de date și evaluării eventualelor discrepante dintre blocul LiDAR și blocul de imagini. Pe baza cunoștințelor noastre de specialitate, diferențele nu ar trebui să depășească câțiva centimetri. Software-ul utilizat în aceste etape de fuziune a datelor selectate va fi LiDAR 360 și CloudCompare, pentru a obține DFM-ul preconizat. În cazul în care situația o impune, se vor utiliza algoritmi de viziune computerizată, cum ar fi ICP, pentru a minimiza diferența dintre doi nori de puncte, așa cum este descris de Doumit (2020).</p>		

Tabelul 4. Descrierea rezultatelor obținute asociate cu activitățile proiectului

No.	Rezultate	Nr. activitate	Data de livrare
R1	Revizuirea literaturii cu privire la datele disponibile privind scopul proiectului, verificarea sistemului UAV, galeria foto a site-ului proiectului	A.I.1	L3
R2	Zboruri de testare, test de calibrare a camerei, achiziție de date	A.I.2	L3
R3	Prelucrarea datelor LiDAR și fotogrammetrice	A.I.3	L4

Tabelul 5. Planul de lucru eșalonat în timp

WP	Act.	Numărul lunii																			
		1	2	3	4	5	6	7	8	9	10	11	12	13	14	15	16	17	18	19	20
I	A.I.1	█	█	█																	
	A.I.2			█																	
	A.I.3				█																
	A.I.4					█															
II	A.II.1					█	█														
	A.II.2						█	█													
	A.II.3								█												
III	A.III.1			█	█	█															
	A.III.2						█	█	█	█	█	█	█	█	█	█	█	█	█	█	█
	A.III.3																	█	█	█	█
IV	A.IV.1												█	█							
	A.IV.2													█	█	█	█	█	█	█	█
	A.IV.3																	█	█	█	█
Mgmt.	Raport final																				█
Management		█	█	█	█	█	█	█	█	█	█	█	█	█	█	█	█	█	█	█	█

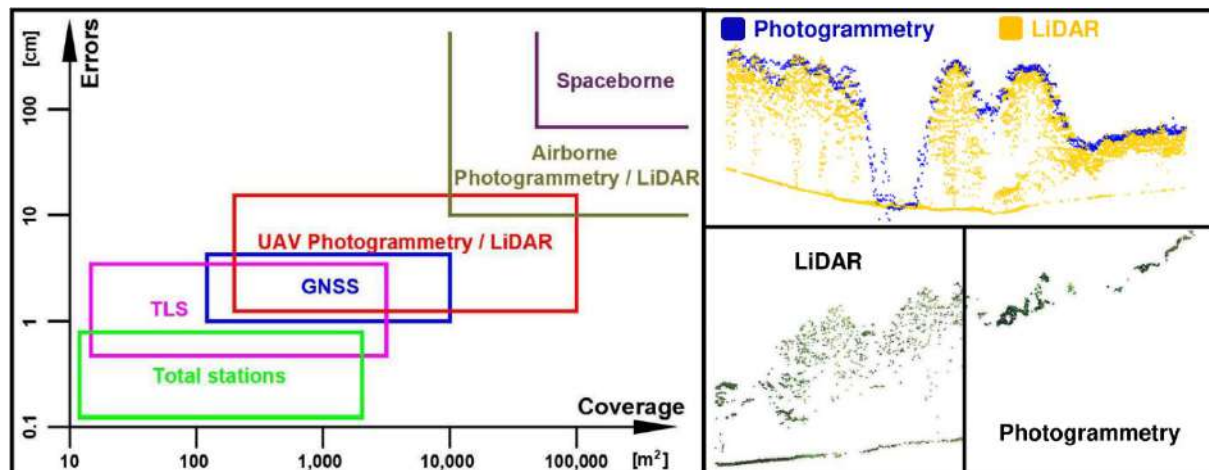


Sistemul DJI M300 RTK cu camera P1 si LiDAR L1

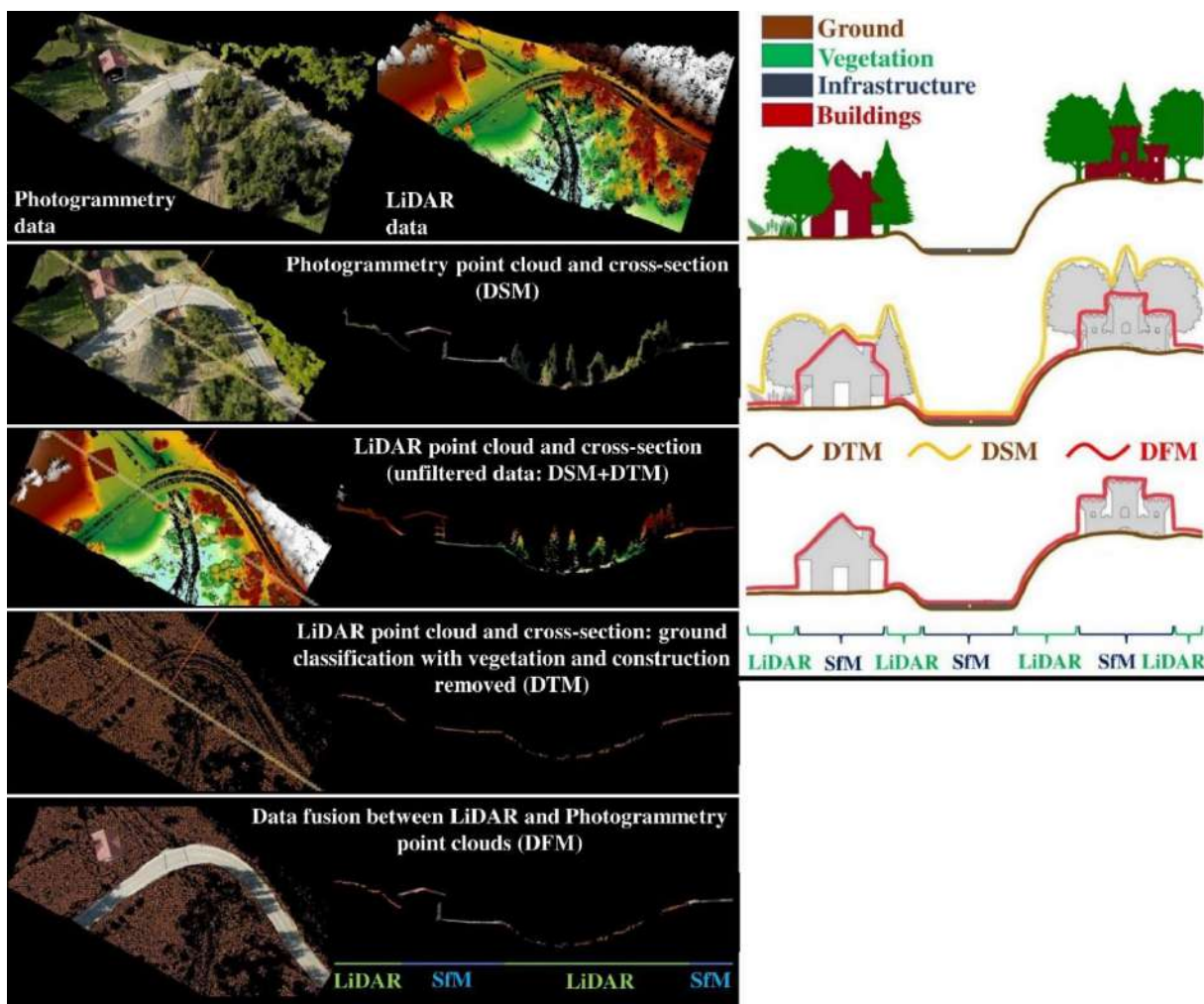
Implementarea conceptului DFM într-o monitorizare de alunecări de teren (în curs de publicare)

Implementarea de DFM propus ca inovatie metodologica într-o lucrare de monitorizare de alunecări de teren/eroziune a solului – grad de realizare 100%

Alunecările de teren sunt pericole la nivel mondial care reprezintă părți semnificative din catastrofele globale. Deoarece alunecările de teren includ decese și daune materiale, este important să înțelegem modelele de mișcare a suprafeței pentru a atenua riscurile sau posibilele reactivări. Modelarea cinematică a pantei poate fi realizată utilizând topografie geodezică sau alte observații directe, deși vehiculele aeriene fără pilot cu tehnologii fotogrammetrice sau de scanare laser au fost utilizate pe scară largă în ultimele decenii. Această cercetare prezintă o strategie nouă pentru monitorizarea alunecărilor de teren folosind fotogrammetrie UAV și date LiDAR. Pentru a oferi o integrare completă, imaginile raster derivate din LiDAR și fotogrammetrie au fost îmbinate pe baza caracteristicilor peisajului care includ zone cu vegetație sau structuri antropice. Această fuziune își propune să valorifice punctele forte ale fiecărei tehnologii și să minimizeze limitele acestora, deoarece fotogrammetria excelează în precizie pe suprafețe cu textură bună, în timp ce LiDAR pe suprafețe acoperite cu vegetație. Noua metodă, concepută ca Digital Feature Model (DFM), a demonstrat o precizie superioară în comparație cu modelele convenționale de elevație. Pentru a evalua robustețea metodologiei propuse, 496 de puncte au fost măsurate folosind instrumente topo-geodezice în interiorul unei alunecări de teren active, fiecare punct reprezentând caracteristici ale terenului, inclusiv terenul gol, diferite grade de vegetație sau elemente antropice. Această analiză a evidențiat combinația de date de succes de la ambii senzori, rezultând rezultate cuprinzătoare care au descris cu acuratețe suprafața solului folosind cea mai potrivită tehnologie. Valorile RMSE obținute pentru diferențele verticale dintre adevărul de la sol și DFM propus au fost de 0,060 metri, ceea ce este semnificativ mai mic decât valoarea RMSE de 0,206 metri pentru Modelul digital de teren (DTM) obținută din fotogrammetrie și valoarea RMSE de 0,441 metri. pentru cel obținut din LiDAR. Această metodă nouă are potențialul de a contribui la o evaluare mai profundă a dinamicii complicate și a mișcărilor alunecărilor de teren, deoarece cercetările ulterioare care utilizează această abordare permit rezultate mai precise ale diferențelor dintre epoci.



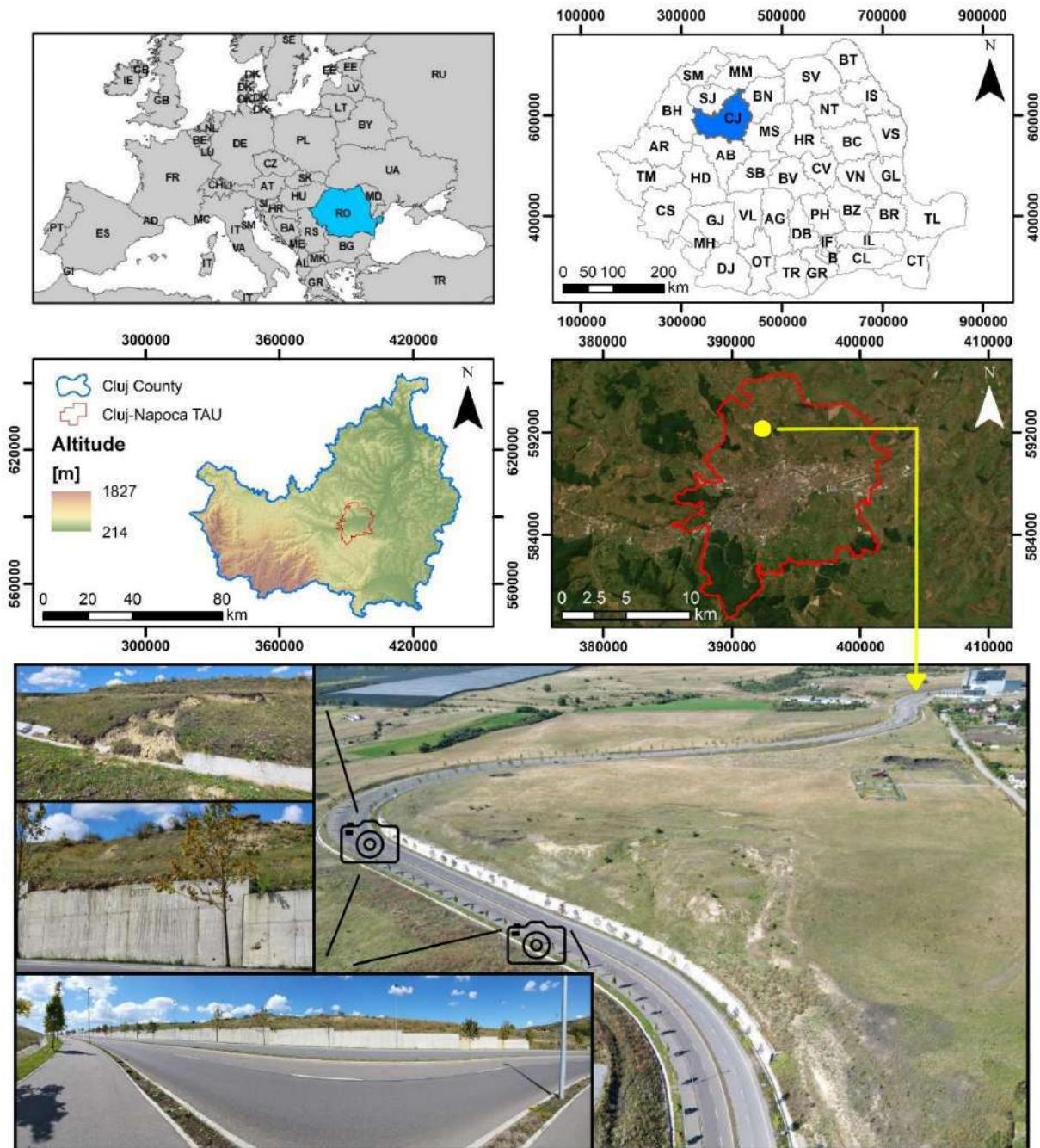
Acoperirea cartografierii UAV în comparație cu alte echipamente (stânga); Fotogrammetrie față de punctele forte ale cartografierii LiDAR (dreapta)



Cadru conceptual de fuziune LiDAR și SfM; principiul DFM

Schimbările de utilizare a terenurilor și creșterea construcției sunt o problemă majoră în Cluj-Napoca, România, o metropolă în creștere rapidă. Planificarea ingineriei și cartografierea pericolelor necesită studii de înaltă calitate, fiabile, eficiente și rentabile. Afacerea construcțiilor este în creștere din cauza constrângerilor de teren cauzate de urbanizare și extinderea orașului, care are avantaje și dezavantaje. Au fost construite dealurile din jurul regiunii, iar satele din apropiere din Cluj-Napoca au fost transformate în suburbii nepregătite din cauza dezvoltării urbane. Terenul abrupt și geomorfologia fac posibile alunecările de teren și eroziunea. O mare parte din zonă este stabilă, dar infrastructura excesivă de construcție și transport poate pune presiune pe versanți, provocând alunecări de teren și impact semnificativ asupra populației și asupra mediului. Astfel, studiul pe această temă este legitim și necesar datorită caracterului dificil al regiunii și a necesității unor modalități și proceduri noi pentru a produce sondaje eficiente și amănunțite.

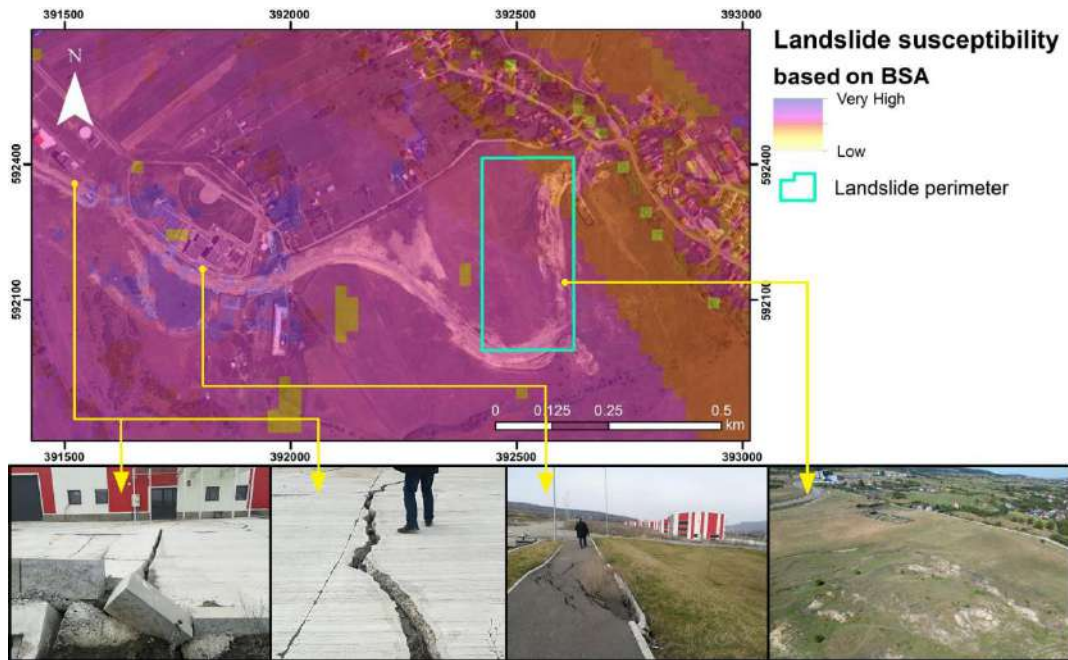
Ancheta de cercetare a început în orașul Cluj-Napoca, județul Cluj. Județul Cluj este în inima Transilvaniei, România. Județul Cluj este în centrul-vestul României și acoperă 3% din suprafața țării. Regiunea este în mare parte abruptă și muntoasă, cu platouri ocazionale. Cea mai mare parte din Cluj-Napoca se află în „Dealurile Clujului”, un teren abrupt predispus la inundații, eroziune a solului și alunecări de teren. Datorită condițiilor dificile ale regiunii, prevenirea alunecărilor de teren și cercetarea locală pentru reducerea riscurilor sunt bine întemeiate și necesare.



Localizarea geografică a zonei de studiu; fotografii aeriene și de la sol

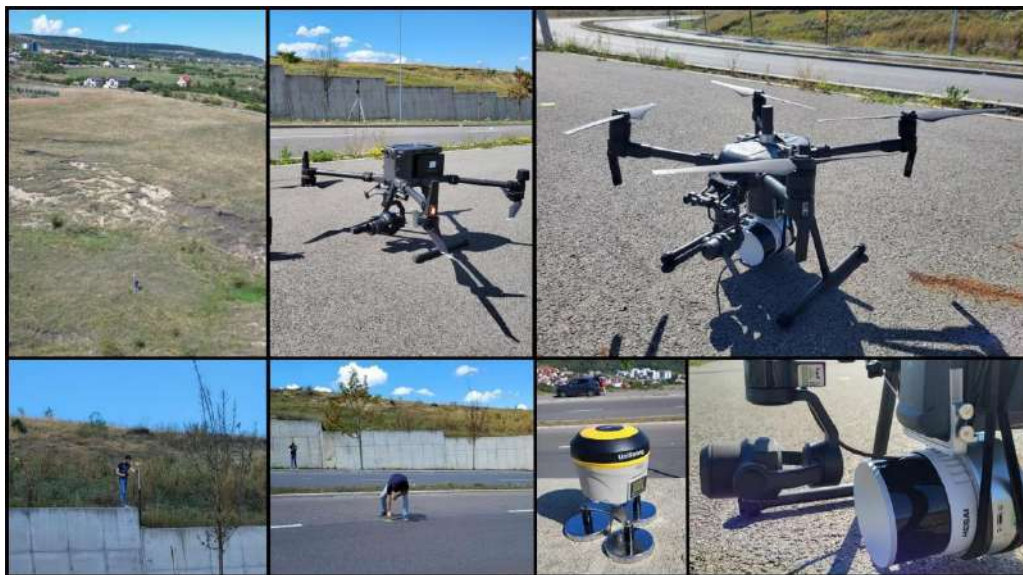
Figura următoare arată o zonă mică a regiunii în care parcurile industriale și infrastructura s-au extins în ultimul deceniu. Ortofotografie pe harta de bază din Figura 4 arată construcția în plină desfășurare. Se suprapune ortofotografiei zonei de cercetare un strat raster al hărții de susceptibilitate la alunecări de teren care arată scenarii cu risc ridicat și foarte ridicat. Vulnerabilitatea zonei la alunecarea de teren a fost examinată folosind analiza statistică bivariată (BSA). Conform Sestras et al. În 2019, modelul BSA a folosit douăsprezece elemente pentru a crea o hartă de susceptibilitate la alunecări de teren la cinci niveluri: scăzut, moderat, moderat ridicat, ridicat și extrem de ridicat. Modelarea a indicat multe puncte fierbinți importante în regiunea vitală a orașului, inclusiv zona de implementare a DFM. Figurile 3 și 4 prezintă fotografiile învecinate ale structurilor și

pavajelor deteriorate, alunecării de teren activă și a numeroaselor defecțiuni de pantă de-a lungul zidului de sprijin de lângă carosabil.



Susceptibilitatea la alunecare de teren a zonelor studiate; fotografii de pe site cu daune vizibile

Pentru regiunile mari care necesită cartografiere complicată și detaliată, topografia terenurilor pentru cartografierea pericolelor necesită timp. Astfel, astfel de eforturi cresc adesea costurile de operare și cerințele de muncă. În ultimii ani, sondajele UAV au devenit mai populare din cauza topografiei neregulate, care impune personalului să urce și să coboare dealuri separat pentru a ajunge la locație. UAV-urile au fost populare în multe industrii în ultimul deceniu. UAV-urile reprezintă o revoluție tehnologică în ingineria sondajelor și în domeniile conexe. Sondajele UAV cu măsurători fotogrammetrice, LiDAR și GNSS topo-geodezice oferă o referință de adevăr la sol, precum și GCP-uri și ICP-uri pentru fotogrammetrie.

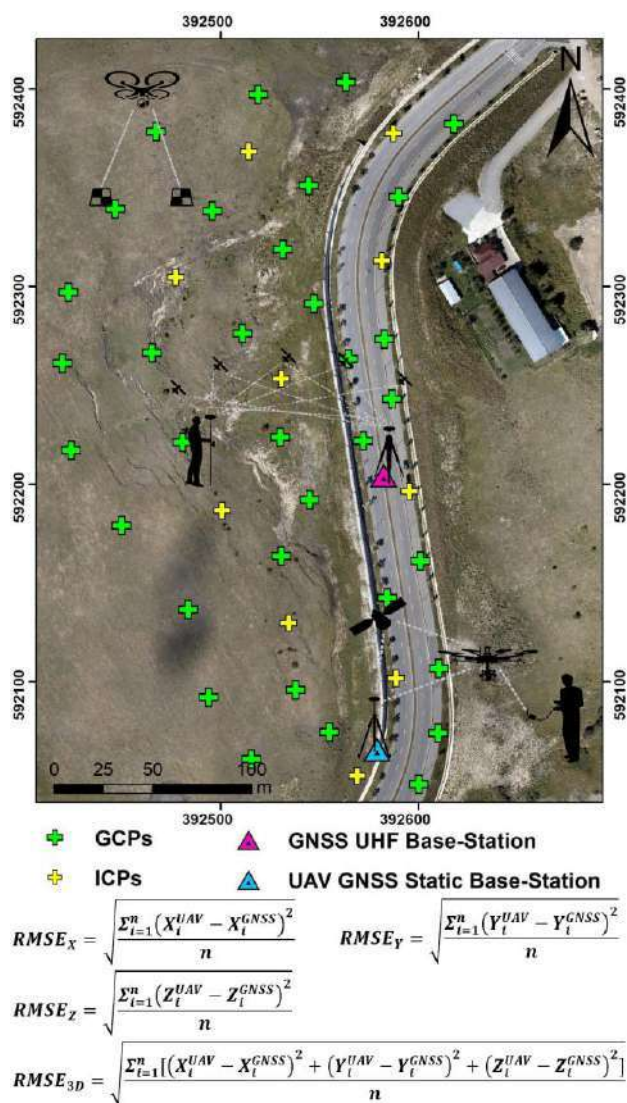


Fotografii cu instrumentele GNSS, platformele UAV și senzorii

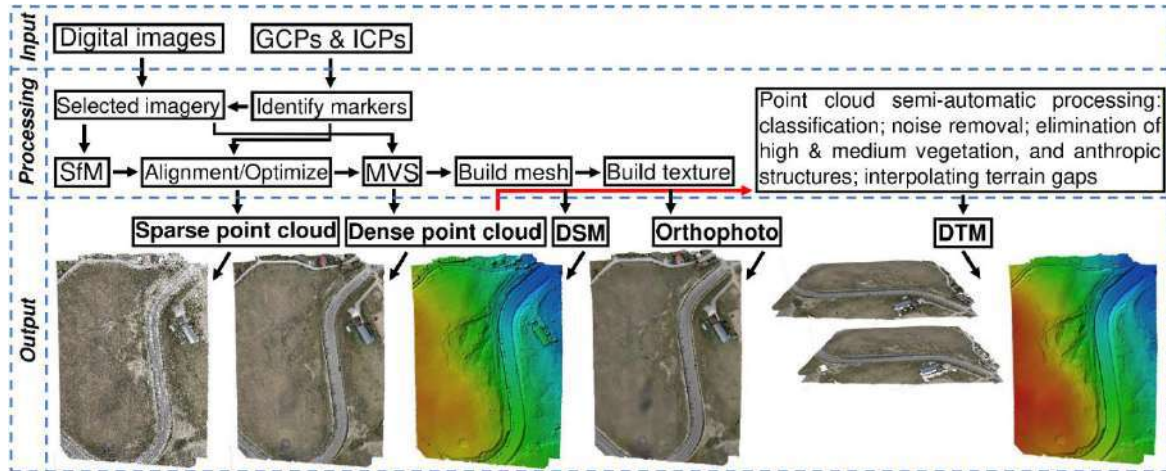
Pentru fotogrammetrie a fost folosită drona DJI Matrice 300 RTK cu o sarcină utilă fotografică ancorată pe cardanul stabilizat cu trei axe. Camera profesională DJI Zenmuse P1 a fost folosită ca senzor fotogrammetric pentru aplicații la scară largă. Fotogrammetria produce modele tridimensionale prin triangularea fotografiilor bidimensionale de la camere de înaltă rezoluție. Camera P1 a arătat rezultate impresionante de la lansare. Valorile RMSE, caracteristicile de configurare și parametrii de zbor sunt prezentate în tabel.

Flight plan properties	
Aircraft	DJI Matrice 300 RTK
Flight Date	September 2023
Mapping Flight Speed	5 m/s
Sensor	Zenmuse P1; 45MP; Focal Length 35mm; Resolution 8192 x 5460
Fly height ground level (m)	85 m
Image Forward Overlap (%)	80%
Image Side Overlap (%)	70%
Image Overlap	>9
Number of Images Captured	358
Number of GCPs and ICPs	44 (placed inside/surrounding the area of interest)
Ground Resolution	0.98 cm/px
RMSE _{x,y,z}	0.028 m X, 0.027 m Y and 0.016 m Z

Procesarea SfM și georeferențierea s-au făcut folosind sistemul de drone DJI M300 RTK și evaluând acuratețea planimetrică și altimetrică. Planificarea misiunii a fost realizată folosind programul proprietar DJI Enterprise Pilot 2 de trei ori, cu setări de conectivitate variate: Poziționare RTK, Stație mobilă DJI D-RTK2 sau fără poziționare RTK. Metoda de poziționare RTK este cea mai eficientă soluție de georeferențiere directă deoarece sistemul UAV este conectat la sateliți și la stația GNSS permanentă prin internet pentru corecții, permițând UAV-ului să mențină o locație fixă și să atribuie coordonate corecte tuturor fotografiilor. Stația mobilă DJI D-RTK2 poate fi cuplată cu drona DJI M300 RTK și fixată pe un punct de coordonate cunoscut pentru ajustările de zbor de referință. După procesarea ieșirilor fotogrammetrice ale acestor două abordări, poziționarea planimetrică a fost bună, cu câțiva milimetri pe direcțiile XY, dar diferențele altimetrice dintre modelele de elevație și adevărul la sol au fost mari. Poziționarea RTK a avut diferențe verticale între modelul 3D și punctele măsurate la sol de 30-40 cm, în timp ce D-RTK2 a avut variații de 10 cm. Cu toate acestea, topografia de precizie pentru monitorizarea alunecărilor de teren sau alte proiecte de inginerie nu poate detecta schimbările într-o alunecare de teren de mică adâncime, făcând imposibilă o astfel de distincție. Pentru a oferi cea mai mare acuratețe a produselor fotogrammetrice, au fost folosite o serie de GCP și ICP-uri pentru a georeferenția manual pachetul de fotografii.

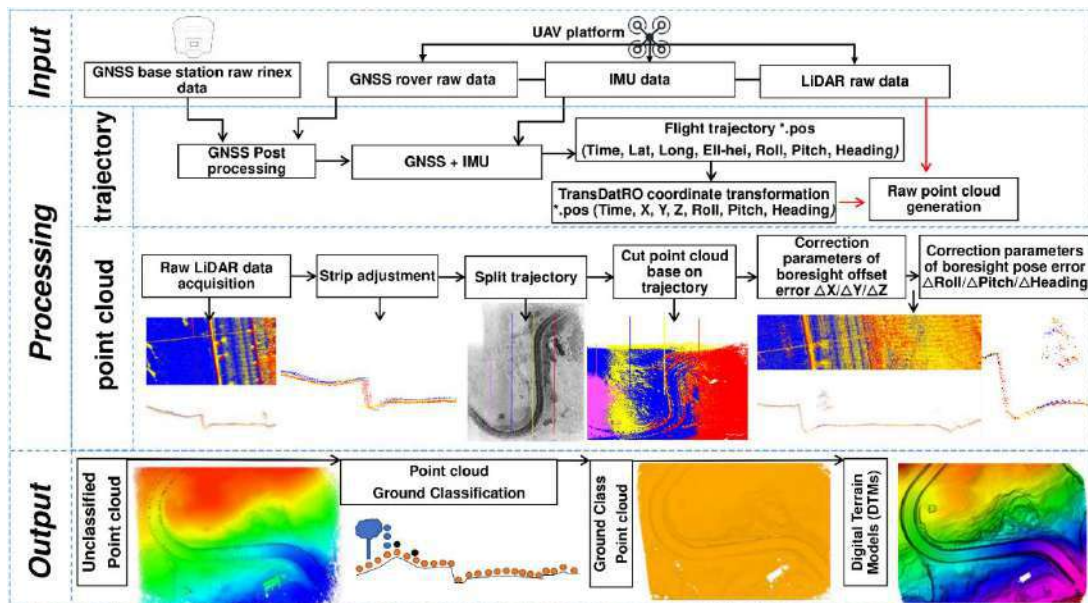


După obținerea unei orientări adecvate a fotografiilor, devine posibil să se urmeze pașii convenționali de aliniere a imaginii, construirea de nor dens, plasă și textură, pentru a dezvolta principalele produse fotogrammetrice, inclusiv modele digitale de suprafață (DSM), modele digitale de teren (DTM-uri), și ortofoto. Reconstrucția 3D a fost efectuată folosind software-ul de fotogrammetrie Agisoft Metashape, cu fluxul de lucru general ilustrat în figura următoare.



Flux de lucru fotogrammetric cu livrabilele generate

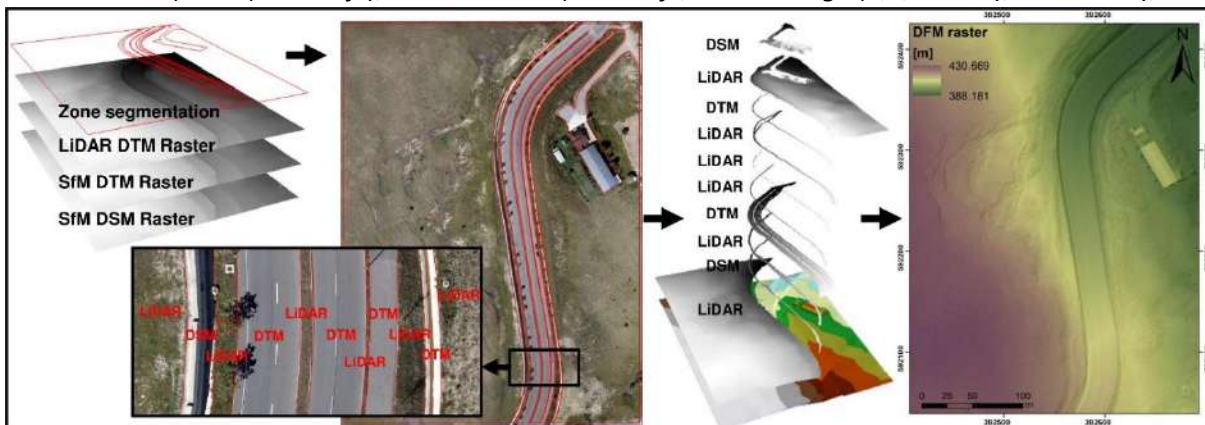
LiDAR folosește multe tehnologii cu ecou laser pentru a tăia vegetația în orice lumină. Folosind o metodă de filtrare, ea clasifică cu precizie caracteristicile solului și oferă date de cotă a solului. LiDAR poate identifica poziția alunecării de teren, viteza și alte caracteristici. Circumstanțele meteorologice pot împrăștia fasciculul laser și pot reduce puterea, făcând LiDAR-ul aeropurtat dificil de utilizat pentru datele țintă. LiDAR pentru monitorizarea alunecărilor de teren a fost îngreunată de costul ridicat al acestor instrumente foarte precise până de curând. Funcția clasifică sistemele LiDAR ca scanare laser aeropurtată sau terestră. LiDAR aerian poate produce rapid și precis date fără restricții terestre. Figura următoare prezintă procedura stabilită pentru misiunea de zbor LiDAR, inclusiv colectarea și post-procesarea datelor.



Flux de lucru LiDAR cu livrabilele generate

Fuziunea în prezenta metodologie între seturile de date raster a fost realizată astfel: (1) O segmentare a zonei bazată pe stratul ortofoto de înaltă rezoluție în GIS a întregii zone de studiu pentru a obține zonele (poligoane) diferitelor caracteristici prezente în câmpul (de exemplu, teren cu vegetație, structuri din beton, fâșii de vegetație de-a lungul carosabilului, carosabil asfaltat, trotuar și piste pentru biciclete etc.). (2) Importarea celor trei imagini raster de elevație obținute din sondajele UAV, respectiv DTM-ul LiDAR, DTM-ul SfM și DSM-ul SfM. Atât produsele fotogrammetrice DTM, cât și DSM au fost utilizate în mozaic, din cauza anumitor inadvertențe în software-ul de procesare disponibil la extragerea sau clasificarea solului față de structura de reținere. (3) Identificarea celui mai bun raster adecvat pentru fiecare zonă, în conformitate cu fiecare avantaj al sensorului și considerentul menționat anterior (de exemplu, zonele cu teren natural cu vegetație scăzută până la înaltă, sau fâșiile de vegetație de-a lungul drumului sunt cartografiate mai precis din LiDAR). sensor, astfel se selectează DTM-ul LiDAR, zonele cu structuri antropice (de exemplu, zid de sprijin și construcție adiacentă) sunt mapate mai precis cu senzor fotogrammetric și fără o clasificare a solului, astfel încât rasterul SfM DSM este selectat (de exemplu, drum, trotuar). și banda pentru biciclete) sunt mapate mai precis cu senzorul fotogrammetric, astfel încât rasterul SfM DTM este selectat (4) Setul de instrumente „Extract by Mask” de analist spațial GIS pentru a extrage celelele unui raster care corespund zonelor definite de. zone stabilite Astfel, cele zece segmente de zone au fost extrase în conformitate cu imaginea raster corespunzătoare, așa cum a fost stabilită în etapa anterioară. caracteristică zonă. (5) Fuziunea celor zece modele digitale de elevație interblocate mai mici, pentru a obține un mozaic al întregii zone de studiu, folosind instrumentul GIS Mosaic to New Raster. (6) Umplerea golurilor foarte mici de-a lungul poligoanelor de zonare, care a avut ca rezultat tăierea inițială a imaginilor raster și fuziunea ulterioară între imaginile raster, utilizând comanda ecuației ArcMap de mai jos:

`Con(IsNull("DFM.tif"), FocalStatistics("DFM.tif", NbrRectangle(9,9, "CELL"), "MEDIAN"), "DFM.tif")`

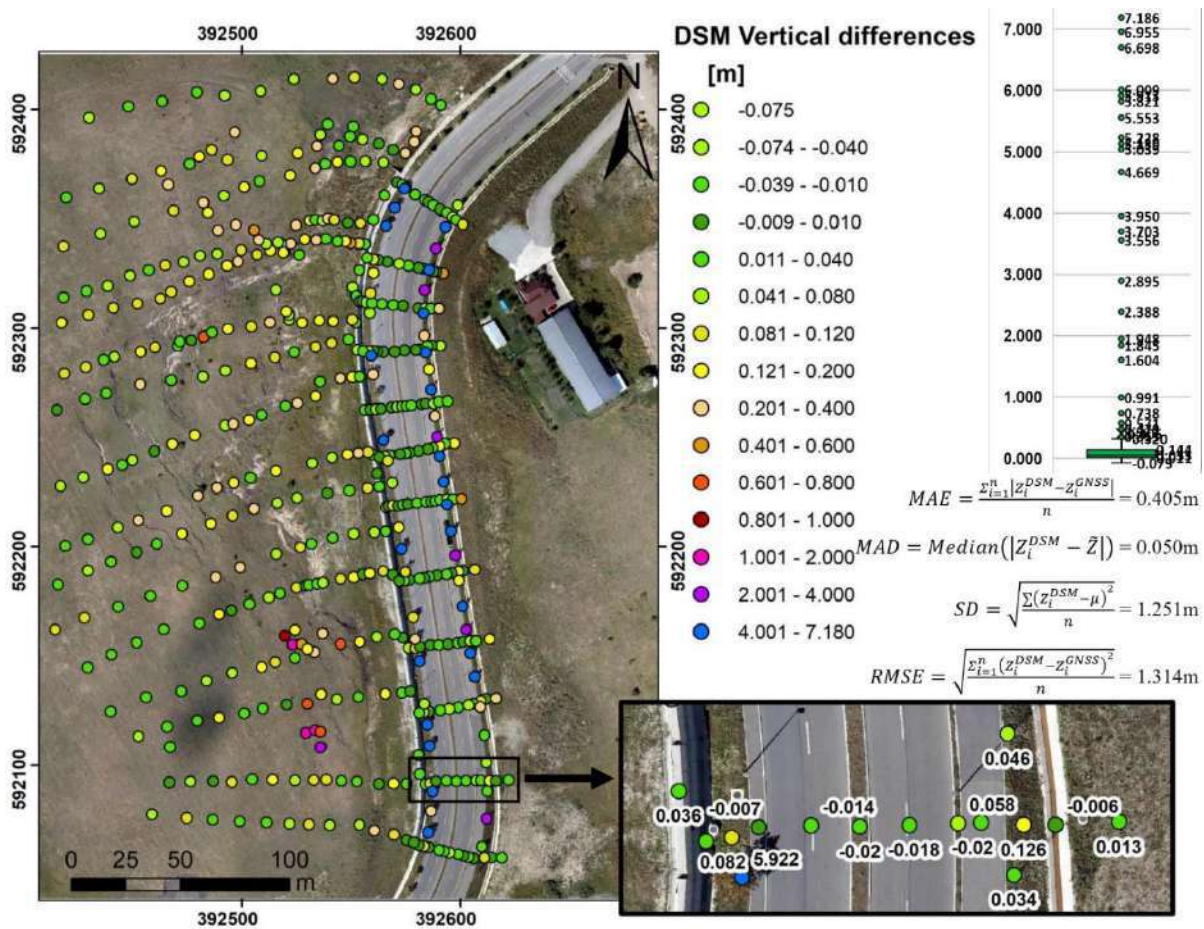


Segmentarea zonei a rasterului cu trei cote utilizate pentru a crea rasterul mozaic DFM

Cele patru modele de altitudine au fost comparate cu cele 494 de puncte măsurate pentru a determina diferențele verticale pentru testarea statistică. Astfel, patru indicatori statistici au evaluat acuratețea fiecărui model de altitudine: Eroarea medie absolută (MAE) măsoară acuratețea predicției prin calculul mediei diferențelor absolute dintre valorile așteptate și cele reale, cu valori mai mici MAE indicând predicții mai precise; Deviația absolută mediană (MAD) estimează în mod constant răspândirea unui set de date calculând mediana abaterilor absolute de la mediana acestuia; Deviația standard (SD) măsoară dispersia punctului de date față de medie, dezvăluind variabilitatea setului de date; Rădăcina pătrată a mediei disparităților pătrate dintre valorile așteptate și cele reale este eroarea pătrată medie (RMSE), care măsoară eroarea de predicție.

Primul model de elevație evaluat, DSM din fotogrammetrie SfM, este prezentat în figura următoare. Capacitatea LiDAR de a pătrunde în vegetație provoacă principalele diferențe geometrice între cei doi senzori. Fotogrammetria surprinde exclusiv exteriorul obiectelor de la sol. Datele din această metodă pot fi utilizate

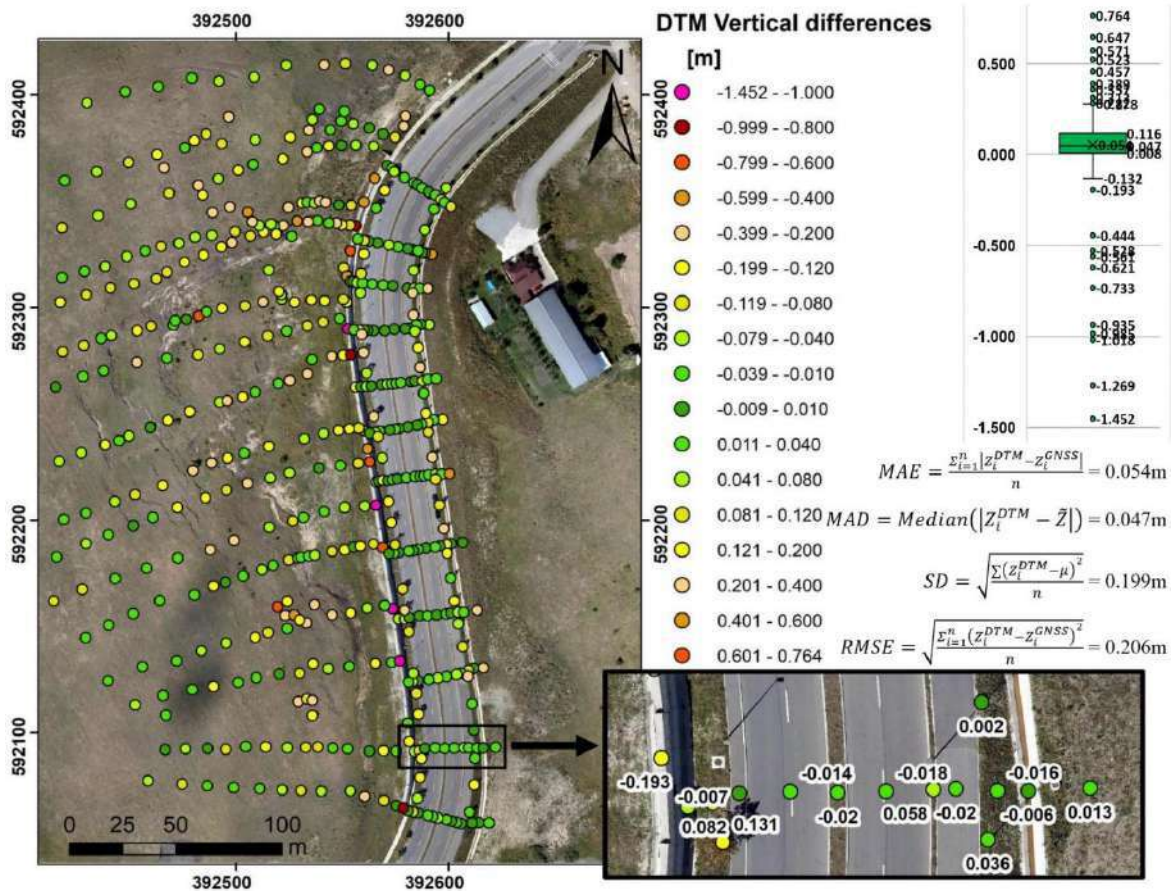
pentru a construi DSM-uri și DTM-uri în timpul categorizării și procesării. În monitorizarea alunecărilor de teren și a studiilor de teren, vegetația blochează adesea reconstrucția fotogrammetrică, care colectează date de pe suprafața superioară. Partea stângă a graficului arată cele 494 de puncte măsurate sub formă de puncte cu o simbolică de culoare care arată diferența de înălțime incrementală dintre adevărul terenului și modelul de elevație. Astfel, verdele mai închis denotă cea mai mică diferență verticală de la -1 la +1 cm, urmată de verde mai deschis, galben și roșu. Magenta, violetul și albastrul reprezintă diferențe verticale anormale. Jumătatea centrală a graficului arată aceste valori de interval plus un diagramă cu casete cu mediana, quartilele și valorile aberante ale setului de date. Modelul DSM a prezis variații verticale substanțiale pe punctele cu vegetație medie și înaltă, așa cum se vede de simbolul culorii figurilor și punctelor față de terenul respectat. Astfel, tufișurile și arbuștii sunt evidențiate cu disparități verticale de la câțiva decimetri la câțiva metri, cel mai înalt sub arborii traseului. Sondajul fotogrammetric a funcționat bine pe asfalt, beton, teren gol și vegetație joasă. Cu toate acestea, pe baza tuturor celor 494 de diferențe verticale, modelul DSM a avut cele mai slabe rezultate anticipate, cu valori MAE de 0,405 m, valori MAD de 0,050 m, valori SD de 1,251 m și valori RMSE de 1,314 m.



Diferențele verticale între valorile de bază și SfM DSM

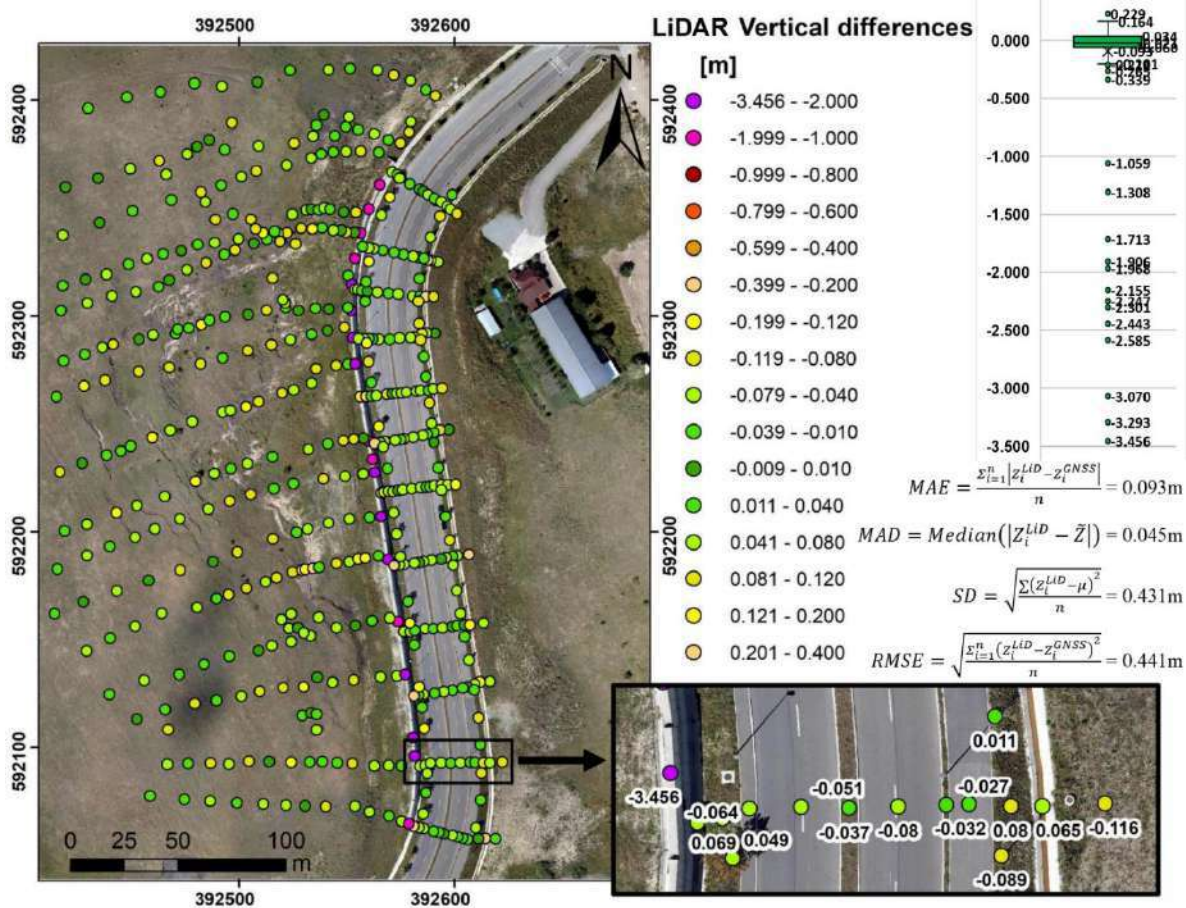
Figura următoare prezintă cel de-al doilea model de elevație evaluat, DTM de fotogrammetrie SfM. Tehnica de fotogrammetrie inițială poate înregistra doar suprafața superioară a lucrurilor de pe sol, iar modelul de elevație implicit este un DSM, dar un DTM poate fi generat prin clasificarea norului de puncte și excluzând vegetația medie și înaltă sau alte componente. Analizând simbolul culorii figurii și punctelor în raport cu peisajul respectat, arată că DTM-ul generat are variații verticale minore până la semnificative în golurile interpolate de vegetație. Micul medalion (dreapta jos) din figură arată că UAV-urile cu camere digitale de ultimă generație și o procesare adecvată pot cartografi asfaltul și terenul gol cu diferențe verticale foarte mici. Suprafața betonului

peretelui de sprijin are cele mai mari variații verticale. Algoritmii au tăiat părți mari ale peretelui de sprijin în timpul clasificării și producției DTM. Modelul de altitudine DTM SfM are un MAE de 0,054 m, MAD de 0,047 m, SD de 0,199 m și RMSE de 0,206 m.



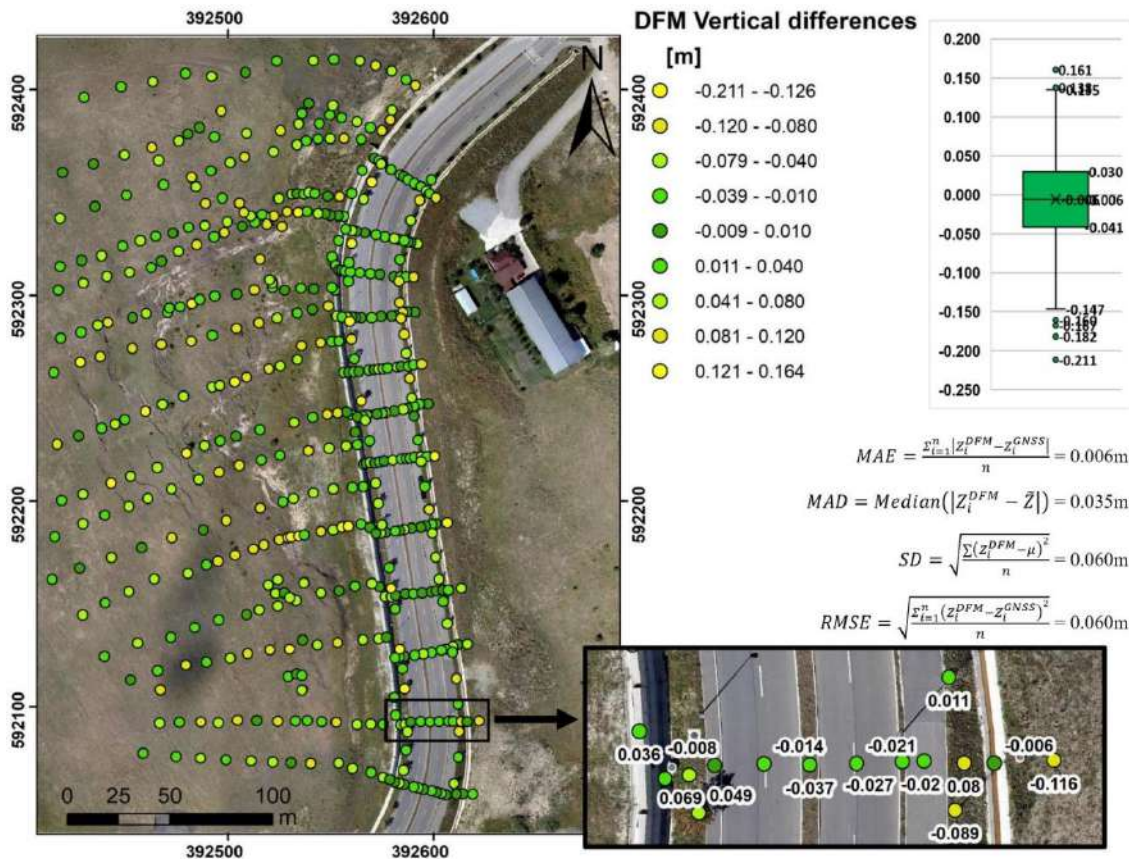
Diferențele verticale între valorile de bază și SfM DTM

Figura următoare prezintă al treilea model de elevație evaluat, DTM derivat din LiDAR. Senzorii LiDAR sunt ideali pentru mediile cu vegetație medie spre înaltă, deoarece pot pătrunde în stratul de vegetație. LiDAR poate pătrunde parțial în vegetație pentru a aduna date de suprafață, ceea ce îl face ideal pentru zonele acoperite cu vegetație. Datele norilor de puncte LiDAR pot fi clasificate pentru a elimina vegetația și a crea un DTM precis. Symbolismul figurilor și culorii punctelor în raport cu topografia arată că DTM-ul generat de LiDAR a redus foarte mult disparitățile verticale în zonele cu vegetație, atât medie, cât și înaltă, și vegetație joasă. După cum se arată în micul medalion (dreapta jos) din interiorul imaginii, asfaltul și terenul gol au diferențe verticale relativ mici, dar valorile sunt mai mari decât în DTM-ul SfM. Variațiile verticale au fost cele mai mari pe betonul zidului de sprijin. Algoritmii utilizați pentru clasificarea și generarea DTM au tăiat porțiuni mari ale peretelui de sprijin. Modelul de altitudine LiDAR DTM are un MAE de 0,093 m, MAD de 0,045 m, SD de 0,431 m și RMSE de 0,441 m. Senzorul LiDAR a determinat cu precizie suprafața solului pe regiunile de vegetație cu cele mai mici diferențe verticale, dar regiunile antropice de beton și asfalt au dezechilibrat modelul de elevație, producând indicatori inferiori decât DTM-ul SfM.



Diferențele verticale între valorile de bază și LiDAR DTM

Figura următoare prezintă cel de-al patrulea model de elevație, DFM inovator derivat din fotogrammetrie SfM și date LiDAR. DFM propune integrarea datelor UAV LiDAR și fotogrammetrie pentru a maximiza beneficiile și a minimiza dezavantajele fiecărui senzor și tehnologie. Metoda propusă a fuzionat LiDAR și fotogrammetria ca un colaj de imagini raster în funcție de atributele topografice. Astfel, zonele de vegetație au folosit DTM-ul derivat din LiDAR, zonele de asfalt de carosabil au folosit DTM-ul derivat din SfM, iar zonele de ziduri de reținere din beton au folosit DSM-ul derivat din SfM. Prin cartografierea fiecărei zone utilizând cei mai buni senzori și tehnologie de topografie, modelul de elevație a fost cât de precis posibil pentru a le baza adevărului. Privind imaginea și simbolismul de culoare al punctelor în raport cu terenul arată că noul DFM a redus considerabil discrepanțele verticale în toate locațiile. După cum se arată în medalionul mic (dreapta jos) din interiorul figurii, asfaltul, betonul și vegetația au cele mai mici diferențe verticale față de modelele de elevație anterioare, dar terenul gol are o diferență verticală de 11 centimetri, ceea ce indică faptul că fotogrammetria este mai bună la reprezentarea terenului gol. Pentru a valida robustețea DFM dezvoltat, indicatorii statistici sunt MAE 0,006 m, MAD 0,035 m, SD 0,060 m și RMSE 0,060 m.

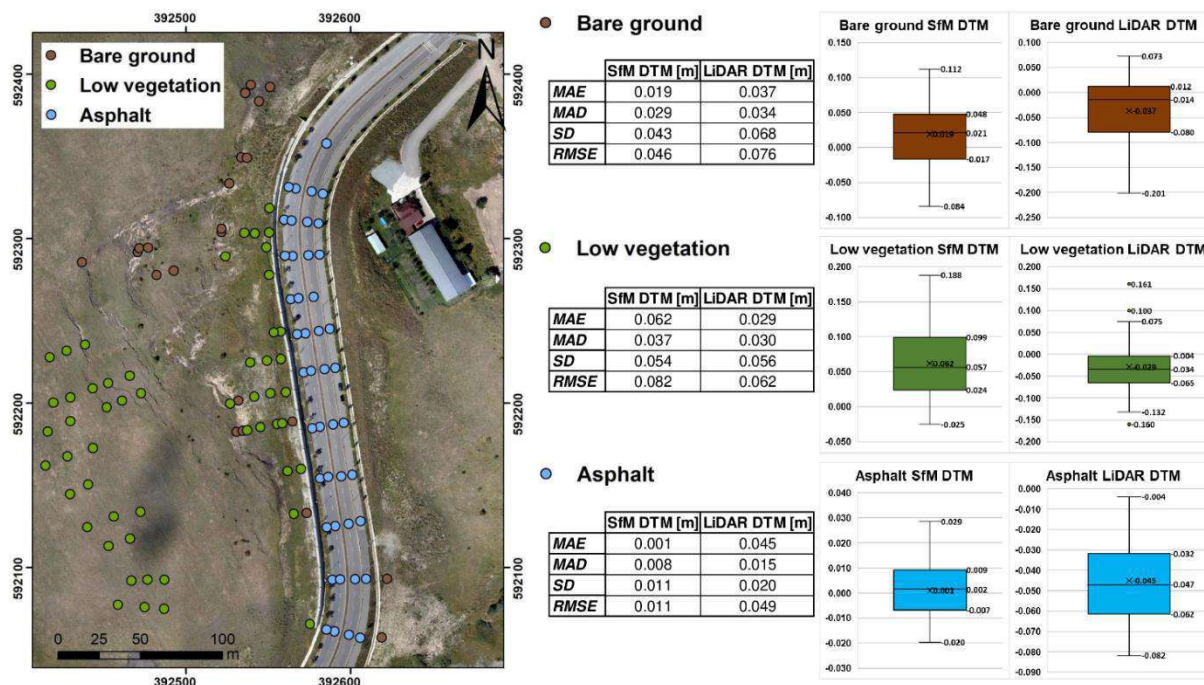


Diferențele verticale între valorile de bază și DFM

Fiecare senzor și abordare are avantaje, dezavantaje și limitări, astfel încât seturile de date au fost combinate pentru a oferi o soluție și o integrare cuprinzătoare. Metodologia propusă combină imagini raster LiDAR și fotogrammetrie bazate pe caracteristicile terenului. Această fuziune a valorificat punctele forte ale fiecărei metode și a compensat defectele acestora. Astfel, tehnica inovatoare DFM a avut cei mai buni indicatori statistici, cu un RMSE de 0,060 metri, mult mai mic decât celelalte modele de cota. Integrarea datelor de la ambii senzori și portretizarea suprafeței solului cu cea mai bună tehnologie a îmbunătățit înțelegerea mișcărilor și deplasărilor complexe ale alunecării de teren.

Cercetările actuale și-au propus să dobândească cunoștințe fundamentale în domeniu și să combine datele UAV LiDAR și fotogrammetrie pentru a crea un model DFM prin integrarea diferitelor suprafețe din regiunea de studiu, care au fost reprezentate geospațial folosind cel mai bun senzor și imagine raster. RMSE al DFM a fost mult mai mic decât celelalte modele, ceea ce demonstrează rezistența livrabilului noutății, totuși ar trebui luați în considerare unii factori pentru implementări și îmbunătățiri viitoare. Figura 14 arată doar o parte din cele 496 de locuri evaluate cu teren gol, vegetație mică și coduri de asfalt. Senzorul LiDAR ar trebui să funcționeze mai bine sub vegetație medie și grea, totuși cele trei suprafețe enumerate ar trebui examinate mai atent. Indicatorii statistici și box plot pentru cele trei suprafețe arată că senzorul fotogrammetric poate reprezenta mai bine asfaltul, cu o diferență verticală RMSE de 0,011 metri față de 0,049 metri pentru LiDAR. Acest lucru întărește superioritatea fotogrammetriei în locuri cu textură bună, circumstanțe adecvate și flux de lucru adecvat. Zonele mari ale pantei cu iarbă sub 15 cm înălțime au fost mapate mai bine cu senzorul LiDAR, care avea o valoare rezonabilă a diferenței verticale RMSE de 0,062 metri și o valoare fotogrammetrică de 0,082 metri. Suprafața intrigantă era pământul gol, care avea o diferență verticală acceptabilă RMSE de 0,046 metri cu senzorul fotogrammetric și 0,076 metri cu LiDAR. Acest lucru arată că fotogrammetria este mai bună decât

scanarea laser pentru reprezentări de teren gol, precum și suprafețe antropice cu textura bună. Rețineți că toate punctele „teren gol” se aflau în interiorul corpului alunecării de teren cu segmentarea zonei de vegetație, prin urmare au fost reprezentate de imaginea raster derivată din LiDAR în colajul DFM. Astfel, segmentarea regiunilor de teren gol din SfM DTM ar îmbunătăți acuratețea DFM și ar minimiza diferența verticală RMSE.



Diferențele verticale între tipul de suprafață și senzorul utilizat

Această cercetare prezintă o metodă inovatoare de fuzionare a fotogrammetriei UAV și a datelor LiDAR pentru a monitoriza alunecările de teren. Tehnica propusă depinde de un flux de lucru adecvat de achiziție de date din teren cu cei doi senzori, fuziunea ulterioară bazată pe avantajul fiecărui senzor în ceea ce privește caracteristica terenului. Fotogrammetria UAV nu poate dezvălui suprafața de sub frunzișul dens, în timp ce LiDAR poate pătrunde parțial în vegetație și poate captura date de suprafață, făcându-l ideal pentru zonele acoperite de vegetație. Pentru a oferi o soluție și o integrare cuprinzătoare, imaginile raster LiDAR și fotogrammetrie au fost combinate pe baza caracteristicilor de teren constând din regiuni de vegetație sau elemente antropice. Această fuziune a merit să valorifice punctele forte ale fiecărei metode și să-și atenueze defectele, deoarece fotogrammetria este mai precisă pe suprafețe cu textură bună, în timp ce LiDAR este mai precis pe suprafețele de vegetație. Noutatea propusă Digital Feature Model a avut cei mai puternici indicatori statistici din celelalte modele convenționale de altitudine. Acest lucru a demonstrat că integrarea datelor de la ambii senzori a produs rezultate complete prin reprezentarea suprafeței solului folosind cea mai adecvată tehnologie, ajutând la o mai bună înțelegere a evoluțiilor complexe și a cinematicii alunecărilor de teren. În timp ce metoda propusă s-a dovedit a fi foarte robustă și benefică, rezultatele au evidențiat neajunsurile în ceea ce privește procesul manual de zonare, cu necesitatea unei automatizări viitoare și, de asemenea, necesitatea separării suprafețelor de pământ gol de zonele de vegetație. Lucrările viitoare vor îmbunătăți în continuare metodologia propusă, împreună cu o monitorizare multianuală continuă a zonei de studiu și alte implementări în domeniile de cercetare dependente de tehnici de topografie precise și inovatoare.

Bibliografie

1. Akturk, E., & Altunel, A. O. (2019). Accuracy assessment of a low-cost UAV derived digital elevation model (DEM) in a highly broken and vegetated terrain. *Measurement*, 136, 382-386.
2. Aslan, M. F., Durdu, A., Sabanci, K., Ropelewska, E., & Gültekin, S. S. (2022). A comprehensive survey of the recent studies with UAV for precision agriculture in open fields and greenhouses. *Applied Sciences*, 12(3), 1047.
3. Bandini, F., Sunding, T. P., Linde, J., Smith, O., Jensen, I. K., Köppl, C. J., ... & Bauer-Gottwein, P. (2020). Unmanned Aerial System (UAS) observations of water surface elevation in a small stream: Comparison of radar altimetry, LIDAR and photogrammetry techniques. *Remote Sensing of Environment*, 237, 111487.
4. Carey, J. A., Pinter, N., Pickering, A. J., Prentice, C. S., & Delong, S. B. (2019). Analysis of Landslide Kinematics Using Multi-temporal Unmanned Aerial Vehicle Imagery, La Honda, California. *Environmental and Engineering Geoscience*, 25(4), 301-317.
5. Chang, A., Jung, J., Maeda, M. M., & Landivar, J. (2017). Crop height monitoring with digital imagery from Unmanned Aerial System (UAS). *Computers and Electronics in Agriculture*, 141, 232-237.
6. Chebrolu, N., Läbe, T., & Stachniss, C. (2018). Robust long-term registration of UAV images of crop fields for precision agriculture. *IEEE Robotics and Automation Letters*, 3(4), 3097-3104.
7. Comba, L., Biglia, A., Aimonino, D. R., & Gay, P. (2018). Unsupervised detection of vineyards by 3D point-cloud UAV photogrammetry for precision agriculture. *Computers and electronics in agriculture*, 155, 84-95.
8. Conforti, M., Mercuri, M., & Borrelli, L. (2021). Morphological Changes Detection of a Large Earthflow Using Archived Images, LiDAR-Derived DTM, and UAV-Based Remote Sensing. *Remote Sensing*, 13(1), 120.
9. Cramer, M., Haala, N., Laupheimer, D., Mandlbürger, G., & Havel, P. (2018). ULTRA-HIGH PRECISION UAV-BASED LIDAR AND DENSE IMAGE MATCHING. *International Archives of the Photogrammetry, Remote Sensing & Spatial Information Sciences*.
10. Cruden, D. M., & Varnes, D. J. (1996). *Landslides: Investigation and Mitigation*. Chapter 3—Landslides Types and Processes. Transportation Research Board: Washington, DC, USA, 2019.
11. De Souza, C. H. W., Lamparelli, R. A. C., Rocha, J. V., & Magalhães, P. S. G. (2017). Height estimation of sugarcane using an unmanned aerial system (UAS) based on structure from motion (SfM) point clouds. *International journal of remote sensing*, 38(8-10), 2218-2230.
12. Delavarpour, N., Koparan, C., Nowatzki, J., Bajwa, S., & Sun, X. (2021). A technical study on UAV characteristics for precision agriculture applications and associated practical challenges. *Remote Sensing*, 13(6), 1204.
13. Devoto, S., Macovaz, V., Mantovani, M., Soldati, M., & Furlani, S. (2020). Advantages of using UAV digital photogrammetry in the study of slow-moving coastal landslides. *Remote Sensing*, 12(21), 3566.
14. Fernández, T., Pérez, J. L., Colomo, C., Cardenal, J., Delgado, J., Palenzuela, J. A., ... & Chacón, J. (2017). Assessment of the evolution of a landslide using digital photogrammetry and LiDAR techniques in the Alpujarras region (Granada, southeastern Spain). *Geosciences*, 7(2), 32.
15. Fernández, T., Pérez-García, J. L., Gómez-López, J. M., Cardenal, J., Moya, F., & Delgado, J. (2021). Multitemporal Landslide Inventory and Activity Analysis by Means of Aerial Photogrammetry and LiDAR Techniques in an Area of Southern Spain. *Remote Sensing*, 13(11), 2110.

16. Fonstad, M. A., Dietrich, J. T., Courville, B. C., Jensen, J. L., & Carbonneau, P. E. (2013). Topographic structure from motion: a new development in photogrammetric measurement. *Earth surface processes and Landforms*, 38(4), 421-430.
17. Galli, M., Ardizzone, F., Cardinali, M., Guzzetti, F., & Reichenbach, P. (2008). Comparing landslide inventory maps. *Geomorphology*, 94(3-4), 268-289.
18. Glira, P., Pfeifer, N., & Mandlbürger, G. (2019). HYBRID ORIENTATION OF AIRBORNE LIDAR POINT CLOUDS AND AERIAL IMAGES. *ISPRS Annals of Photogrammetry, Remote Sensing & Spatial Information Sciences*, 4.
19. Gómez-Candón, D., De Castro, A. I., & López-Granados, F. (2014). Assessing the accuracy of mosaics from unmanned aerial vehicle (UAV) imagery for precision agriculture purposes in wheat. *Precision Agriculture*, 15, 44-56.
20. Hassaan, O., Nasir, A. K., Roth, H., & Khan, M. F. (2016). Precision forestry: trees counting in urban areas using visible imagery based on an unmanned aerial vehicle. *IFAC-PapersOnLine*, 49(16), 16-21.
21. Kerekes, A. H., Poszet, S. L., & Andrea, G. Á. L. (2018). Landslide susceptibility assessment using the maximum entropy model in a sector of the Cluj–Napoca Municipality, Romania. *Revista de Geomorfologie*, 20(1), 130-146.
22. Kerekes, Anna Hajnalka, Szilárd Lehel Poszet, And Laurențiu Călin Baci. Investigating land surface deformation using InSAR and GIS techniques in Cluj-Napoca city's most affected sector by urban sprawl (Romania). *Revista de Geomorfologie* 22.1 (2020): 43-59.
23. Krause, S., Sanders, T. G., Mund, J. P., & Greve, K. (2019). UAV-based photogrammetric tree height measurement for intensive forest monitoring. *Remote sensing*, 11(7), 758.
24. Kršák, B., Blišťan, P., Pauliková, A., Puškárová, P., Kovanič, Ľ., Palková, J., & Zelizňaková, V. (2016). Use of low-cost UAV photogrammetry to analyze the accuracy of a digital elevation model in a case study. *Measurement*, 91, 276-287.
25. López, A., Jurado, J. M., Ogayar, C. J., & Feito, F. R. (2021). A framework for registering UAV-based imagery for crop-tracking in Precision Agriculture. *International Journal of Applied Earth Observation and Geoinformation*, 97, 102274.
26. Luo, Q., Hu, M., Zhao, Z., Li, J., & Zeng, Z. (2020). Design and experiments of X-type artificial control targets for a UAV-LiDAR system. *International Journal of Remote Sensing*, 41(9), 3307-3321.
27. Nguyen, Q. L., Goyal, R., Bui, K. L., Van Canh, L., Cao, X. C., Pham, V. C., ... & Bui, X. N. (2020). Influence of Flight Height on The Accuracy of UAV Derived Digital Elevation Model at Complex Terrain. *Inżynieria Mineralna*.
28. Oniga, V. E., Breaban, A. I., Pfeifer, N., & Chirila, C. (2020). Determining the suitable number of ground control points for UAS images georeferencing by varying number and spatial distribution. *Remote Sensing*, 12(5), 876.
29. Oniga, V. E., Pfeifer, N., & Loghin, A. M. (2018). 3D calibration test-field for digital cameras mounted on unmanned aerial systems (UAS). *Remote Sensing*, 10(12), 2017.
30. Peduto, D., Oricchio, L., Nicodemo, G., Crosetto, M., Ripoll, J., Buxó, P., & Janeras, M. (2021). Investigating the kinematics of the unstable slope of Barbera de la Conca (Catalonia, Spain) and the effects on the exposed facilities by GBSAR and multi-source conventional monitoring. *Landslides*, 18(1), 457-469.
31. Pellicani, R., Argentiero, I., Manzari, P., Spilotro, G., Marzo, C., Ermini, R., & Apollonio, C. (2019). UAV and airborne LiDAR data for interpreting kinematic evolution of landslide

- movements: the case study of the Montescaglioso landslide (Southern Italy). *Geosciences*, 9(6), 248.
32. Pingel, T. J., Clarke, K., & Ford, A. (2015). Bonemapping: A LiDAR processing and visualization technique in support of archaeology under the canopy. *Cartography and Geographic Information Science*, 42(sup1), 18-26.
 33. Pinton, D., Canestrelli, A., Wilkinson, B., Ifju, P., & Ortega, A. (2020). A new algorithm for estimating ground elevation and vegetation characteristics in coastal salt marshes from high-resolution UAV-based LiDAR point clouds. *Earth Surface Processes and Landforms*, 45(14), 3687-3701.
 34. Pirasteh, S., & Li, J. (2017). Landslides investigations from geoinformatics perspective: quality, challenges, and recommendations. *Geomatics, Natural Hazards and Risk*, 8(2), 448-465.
 35. Popescu, D., Stoican, F., Stamatescu, G., Ichim, L., & Dragana, C. (2020). Advanced UAV–WSN system for intelligent monitoring in precision agriculture. *Sensors*, 20(3), 817.
 36. Puliti, S., Dash, J. P., Watt, M. S., Breidenbach, J., & Pearse, G. D. (2020). A comparison of UAV laser scanning, photogrammetry and airborne laser scanning for precision inventory of small-forest properties. *Forestry: An International Journal of Forest Research*, 93(1), 150-162.
 37. Radoglou-Grammatikis, P., Sarigiannidis, P., Lagkas, T., & Moscholios, I. (2020). A compilation of UAV applications for precision agriculture. *Computer Networks*, 172, 107148.
 38. Sestras, P., Bilaşco, Ş., Roşca, S., Dudic, B., Hysa, A., & Spalević, V. (2021). Geodetic and UAV Monitoring in the Sustainable Management of Shallow Landslides and Erosion of a Susceptible Urban Environment. *Remote Sensing*, 13(3), 385.
 39. Solazzo, D., Sankey, J. B., Sankey, T. T., & Munson, S. M. (2018). Mapping and measuring aeolian sand dunes with photogrammetry and LiDAR from unmanned aerial vehicles (UAV) and multispectral satellite imagery on the Paria Plateau, AZ, USA. *Geomorphology*, 319, 174-185.
 40. Štular, B., Lozić, E., & Eichert, S. (2021). Airborne LiDAR-Derived Digital Elevation Model for Archaeology. *Remote Sensing*, 13(9), 1855.
 41. Torres-Sanchez, J., de Castro, A. I., Pena, J. M., Jimenez-Brenes, F. M., Arquero, O., Lovera, M., & Lopez-Granados, F. (2018). Mapping the 3D structure of almond trees using UAV acquired photogrammetric point clouds and object-based image analysis. *Biosystems engineering*, 176, 172-184.
 42. Westoby, M. J., Brasington, J., Glasser, N. F., Hambrey, M. J., & Reynolds, J. M. (2012). ‘Structure-from-Motion’ photogrammetry: A low-cost, effective tool for geoscience applications. *Geomorphology*, 179, 300-314.
 43. You, R. J., & Lee, C. L. (2020). Accuracy Improvement of Airborne Lidar Strip Adjustment by Using Height Data and Surface Feature Strength Information Derived from the Tensor Voting Algorithm. *ISPRS International Journal of Geo-Information*, 9(1), 50.

Obiective si diseminarea rezultatelor

Articole din tema proiectului (autor principal):

- **Monitorizare alunecari de teren prin fuziunea datelor fotogrammetrice si LiDAR (finalizat, in peer-review, 2 runde de Major revisions)**
- **Modelarea eroziunii solului la nivelul Judetului Cluj prin modelul USLE (publicat; prim autor)**
- **Ridicari topografice de precizie intr-o zona urbana prin fuziunea datelor fotogrammetrice si LiDAR (finalizat, in peer-review)**
- **Analiza influenței provenienței geografice asupra creșterii și rezistenței la stres mecanic în faza tânără a arborilor de salcâm (Robinia pseudoacacia) (finalizat, in peer-review)**

Articole adiacente temei abordate (autor principal sau coautor):

- **Proiectare peisagistica in vederea valorificarii terapeutice a spatiilor verzi din cadrul clinicilor universitare din Cluj-Napoca (publicat; autor corespondent)**
- **2 articole publicate in jurnale din grupul MDPI**
- **1 articol publicat in jurnal din grupul Cell Press**
- **1 articol publicat in jurnal din grupul Frontiers**
- **3 articole publicate in jurnale din grupul Elsevier**
- **4 articole publicate in jurnale din grupul Springer**
- **+ alte articole in faze avansate**

ARTICOLE PUBLICATE:

1. Sestras, P., Mircea, S., ROȘCA, S., Bilașco, Ș., SĂLĂGEAN, T., Dragomir, L. O., ... & Kader, S. (2023). GIS based soil erosion assessment using the USLE model for efficient land management: A case study in an area with diverse pedo-geomorphological and bioclimatic characteristics. *Notulae Botanicae Horti Agrobotanici Cluj-Napoca*, 51(3), 13263-13263. **Q3 WoS**
2. Dinu Roman Szabo, M., Dumitras, A., Mircea, D. M., Doroftei, D., Sestras, P., Boscaiu, M., ... & Sestras, A. F. (2023). Touch, feel, heal. The use of hospital green spaces and landscape as sensory-therapeutic gardens: a case study in a university clinic. *Frontiers in Psychology*, 14, 1201030. **Q2 WoS**
3. Oniga, V. E., Loghin, A. M., Macovei, M., Lazar, A. A., Boroianu, B., & Sestras, P. (2023). Enhancing LiDAR-UAS Derived Digital Terrain Models with Hierarchic Robust and Volume-Based Filtering Approaches for Precision Topographic Mapping. *Remote Sensing*, 16(1), 78. **Q1 WoS**
4. Ștefan, B., Horeczki, R., Rácz, S., Sanda, R., Vasile, D., Iuliu, V., ... & Sestras, P. (2024). Spatial Analysis of Creative Industries for Urban Functional Zones: A GIS-Based Comparative Study in Eastern European Regional Centres: Cluj-Napoca (Romania) and Pécs (Hungary). *Applied Sciences*, 14(3), 1088. **Q1 WoS**
5. Morar, I. M., Stefan, R., Dan, C., Sestras, R. E., Truta, P., Medeleanu, M., ... & Sestras, A. F. (2024). FT-IR and HPLC analysis of silver fir (*Abies alba* Mill.) bark compounds from different geographical provenances. *Heliyon*, 10(5). **Q1 WoS**
6. Sadkaoui, D., Brahim, B., Kader, S., Agharroud, K., Mihraje, A. I., Aluni, K., ... & Sestras, P. (2024). Evaluation of tectonic activity using morphometric indices: Study of the case of Taïliloute ridge (middle-Atlas region, Morocco). *Journal of African Earth Sciences*, 213, 105219. **Q2 WoS**
7. Bammou, Y., Benzougagh, B., Abdessalam, O., Brahim, I., Kader, S., Spalevic, V., ... & Ercişli, S. (2024). Machine learning models for gully erosion susceptibility assessment in the Tensift catchment, Haouz plain, Morocco for sustainable development. *Journal of African Earth Sciences*, 213, 105229. **Q2 WoS**
8. Bammou, Y., Benzougagh, B., Igmoullan, B., Ouallali, A., Kader, S., Spalevic, V., ... & Marković, S. B. (2024). Optimizing flood susceptibility assessment in semi-arid regions using ensemble algorithms: a case study of Moroccan High Atlas. *Natural Hazards*, 120(8), 7787-7816. **Q2 WoS**
9. Bashir, O., Bangroo, S. A., Shafai, S. S., Shah, T. I., Kader, S., Jaufer, L., ... & Hysa, A. (2024). Mathematical vs. machine learning models for particle size distribution in fragile soils of North-Western Himalayas. *Journal of Soils and Sediments*, 1-15. **Q2 WoS**
10. Bammou, Y., Benzougagh, B., Igmoullan, B., Kader, S., Ouallali, A., Spalevic, V., ... & Kuriqi, A. (2024). Spatial mapping for multi-hazard land management in sparsely vegetated watersheds using machine learning algorithms. *Environmental Earth Sciences*, 83(15), 447. **Q2 WoS**
11. Sbihi, A., Mastere, M., Benzougagh, B., Spalevic, V., Sestras, P., Radovic, M., ... & Kader, S. (2024). Assessing landslide susceptibility in northern Morocco: A geostatistical mapping approach in Al Hoceima-Ajdir. *Journal of African Earth Sciences*, 218, 105361. **Q2 WoS**
12. Herbei, M. V., Bădăluță-Minda, C., Popescu, C. A., Horablaga, A., Dragomir, L. O., Popescu, G., ... & Sestras, P. (2024). Rainfall-runoff modeling based on HEC-HMS model: a case study in an area with increased groundwater discharge potential. *Frontiers in Water*, 6, 1474990. **Q2 WoS**
13. Ouallali, A., Bouhsane, N., Bouhlassa, S., Spalevic, V., Kader, S., Michael, R., & Sestras, P. (2024). Exploring soil pedogenesis through frequency-dependent magnetic susceptibility in varied lithological environments. *Euro-Mediterranean Journal for Environmental Integration*, 1-14. **Q3 WoS**

Peer review status

[2nd revision] A novel method for landslide deformation monitoring by fusing UAV photogrammetry and LiDAR data based on each sensor's mapping advantage in regards to terrain feature

- Reviews completed: 0
- Review invitations accepted: 1
- Review invitations sent: 1

2nd revision

Under Review

Last review activity: 2nd
December 2024 ⓘ

Watch to learn what we're doing behind
the scenes ↗

Journal:

Engineering Geology

Corresponding author:

Shuraik Kader

First author:

Paul Sestras

Date of submission:

11th August 2024

Manuscript number:

ENGEO-D-24-
01897R2

ENGINEERING GEOLOGY

Publisher name: ELSEVIER

Journal Impact Factor™

6.9

2023

7.6

Five Year

JCR Category	Category Rank	Category Quartile
ENGINEERING, GEOLOGICAL <i>in SCIE edition</i>	3/63	Q1
GEOSCIENCES, MULTIDISCIPLINARY <i>in SCIE edition</i>	16/254	Q1

Innovative Land Surveying with UAV Photogrammetry and LiDAR for Optimal Building Planning

- Reviews completed: 1
- Review invitations accepted: 2
- Review invitations sent: 2+

Under Review

Last review activity: 25th
November 2024 ⓘ

Watch to learn what we're doing behind
the scenes ↗

Journal:

Automation in Construction

Corresponding author:

Shuraik Kader

First author:

Paul Sestras

Date of submission:

24th September 2024

Manuscript number:

AUTCON-D-24-
03136

Need more help?

AUTOMATION IN CONSTRUCTION

Publisher name: ELSEVIER

Journal Impact Factor™

9.6

2023

10.6

Five Year

JCR Category	Category Rank	Category Quartile
CONSTRUCTION & BUILDING TECHNOLOGY <i>in SCIE edition</i>	4/92	Q1
ENGINEERING, CIVIL <i>in SCIE edition</i>	1/182	Q1

Growth and resistance to mechanical stress in the young phase of black locust (*Robinia pseudoacacia* L.) trees based on geographical provenances

- Reviews completed: 0
- Review invitations accepted: 1
- Review invitations sent: 2+

Under Review
Last review activity: 29th November 2024 ⓘ

Watch to learn what we're doing behind the scenes ↗

Journal:
Science of the Total Environment

Corresponding author:
Shuraik Kader

First author:
Paul Sestras

Date of submission:
14th November 2024

Manuscript number:
STOTEN-D-24-45972

[Need more help?](#)

SCIENCE OF THE TOTAL ENVIRONMENT

Publisher name: ELSEVIER

Journal Impact Factor™

8.2
2023

8.6
Five Year

JCR Category	Category Rank	Category Quartile
ENVIRONMENTAL SCIENCES <i>in SCIE edition</i>	31/358	Q1

GIS based soil erosion assessment using the USLE model for efficient land management: A case study in an area with diverse pedo-geomorphological and bioclimatic characteristics

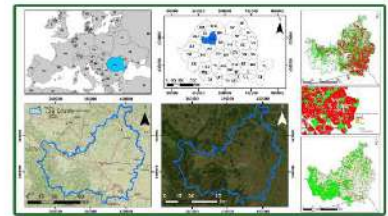
Paul SESTRAS

Technical University of Cluj-Napoca, Faculty of Civil Engineering, 400020 Cluj-Napoca
 Academy of Romanian Scientists, Ilfov 3, 050044 Bucharest (RO)

<https://orcid.org/0000-0002-8554-0924>

Sevastel MIRCEA

University of Agronomic Sciences and Veterinary Medicine Bucharest, Faculty of Land Reclamation and Environmental Engineering, 011464 Bucharest (RO)



 **MANUSCRIPT (PDF)**

NOTULAE BOTANICAE HORTI AGROBOTANICI CLUJ-NAPOCA

Publisher name: UNIV AGR SCI & VETERINARY MED CLUJ-NAPOCA

Journal Impact Factor™

1.4

2023

1.6

Five Year

JCR Category	Category Rank	Category Quartile
PLANT SCIENCES <i>in SCIE edition</i>	161/265	Q3

Source: Journal Citation Reports 2023. [Learn more](#)

Journal Citation Indicator™

0.39

2023

0.4

2022

JCI Category	Category Rank	Category Quartile
PLANT SCIENCES <i>in SCIE edition</i>	162/265	Q3

GIS based soil erosion assessment using the USLE model for efficient land management: A case study in an area with diverse pedo-geomorphological and bioclimatic characteristics

Paul SESTRAS^{1,2}, Sevastel MIRCEA³, Sanda ROȘCA^{2,4*}, Ștefan BILAȘCO^{4,5}, Tudor SĂLĂGEAN⁶, Lucian O. DRAGOMIR^{7*}, Mihai V. HERBEI⁷, Simion BRUMA⁸, Catalin SABOU⁸, Rastko MARKOVIĆ⁹, Shuraik KADER^{10,11}

¹Technical University of Cluj-Napoca, Faculty of Civil Engineering, 400020 Cluj-Napoca, Romania; psestras@mail.utcluj.ro

²Academy of Romanian Scientists, Ilfov 3, 050044 Bucharest, Romania

³University of Agronomic Sciences and Veterinary Medicine Bucharest, Faculty of Land Reclamation and Environmental Engineering, 011464 Bucharest, Romania; smircea@usamv.ro

⁴Babes-Bolyai University, Faculty of Geography, 400006 Cluj-Napoca, Romania; sanda.rosca@ubbcluj.ro (*corresponding author); stefan.bilasco@ubbcluj.ro

⁵Cluj-Napoca Subsidiary Geography Section, Romanian Academy, 400015 Cluj-Napoca, Romania

⁶University of Agricultural Sciences and Veterinary Medicine, Faculty of Forestry and Cadastre, Department of Land Measurements and Exact Sciences, 400372 Cluj-Napoca, Romania; tudor.salagean@usamvcluj.ro

⁷University of Life Sciences "King Mihai I", Department of Sustainable Development and Environmental Engineering, 300645 Timișoara, Romania; luciandragomir@usvt.ro (*corresponding author); mihai_herbei@yahoo.com

⁸Technical University of Civil Engineering, Faculty of Geodesy, 020396 Bucharest, Romania; brumasimion@gmail.com; sabou_cata@yahoo.com

⁹University of Niš, Faculty of Science, Department of Geography, Višegradska 11, 18000 Niš, Serbia; rastko.markovic@pmf.edu.rs

¹⁰Griffith University, School of Engineering and Built Environment, Nathan, QLD 4111; Australia shuraik.mohamedabdulkader@griffithuni.edu.au

¹¹Griffith University, Cities Research Institute, Green Infrastructure Research Labs (GIRLS), Gold Coast, QLD 4215, Australia

Abstract

The complex environmental process of soil erosion is crucial to sustainable land management and conservation. This study uses the Universal Soil Loss Equation (USLE) model to understand the intricate interactions that cause soil erosion in Cluj County, Romania, a region susceptible to complex erosion and landslide phenomenon. The established analysis depicts erosion patterns from localised hotspots to regions of relative stability, providing valuable insights into this critical issue. Spatial distribution maps with color-coded gradients show soil erosion risk and identify vulnerable regions, with temporal investigations depicting how environmental changes affect soil erosion, making it relevant to soil conservation and land management. A careful analysis of the USLE model's parameters (Ls, Cs, C, S, K) shows their soil erosion contributions. The erosion rates were graded in five classes in accordance to general practices of USLE modelling, which range from very-low, low, moderate, high and very-high susceptibility to soil erosion. While a significant majority of the county's surface is represented by very-low and low erosion risk, several hotspots were identified with intense erosion processes that highlights the critical need to implement soil conservation measures in the area.

Received: 26 Jun 2023. Received in revised form: 24 Sep 2023. Accepted: 26 Sep 2023. Published online: 26 Sep 2023.

From Volume 49, Issue 1, 2021, Notulae Botanicae Horti Agrobotanici Cluj-Napoca journal uses article numbers in place of the traditional method of continuous pagination through the volume. The journal will continue to appear quarterly, as before, with four annual numbers.

Identifying erosion hotspots and conservation solutions encourages stakeholders to protect soils, and can provide policymakers with useful information for developing improved guidelines for soil and water conservation.

Keywords: database; GIS analysis; land management; soil erosion; USLE

Introduction

Soil erosion poses a significant environmental concern on a global scale, since it leads to the depletion of fertile topsoil and consequent reduction in agricultural productivity (Spalevic *et al.*, 2020). Due to the increasing focus on advancing soil erosion models for more accurate estimation of soil loss at watershed and basin scales, the issues of soil loss and sediment supply have emerged as significant global difficulties in contemporary times. Direct measures of erosion in a watershed can be obtained by quantifying the mobility of solid particles within the downstream portion over an extended period of time (Gocić *et al.*, 2020; Mohammadi *et al.*, 2021). In cases where hydrometric and discharge data for a certain watershed are insufficient, the utilisation of modelling techniques emerges as a viable and established method for assessing the extent of erosion and discharge within said watershed. Mathematical erosion models were developed to predict the extent of erosion and the quantity of silt generated, owing to these causes. A multitude of soil erosion models have been developed globally with the aim of assessing the extent of soil erosion and the maximum discharge capacity at the regional or basin scale (Greiner *et al.*, 2017; Sestras *et al.*, 2023). The Universal Soil Loss Equation (USLE) developed by the United States Department of Agriculture (USDA) has played a significant role in the realm of soil erosion research and land management for an extended period of time (Roşca *et al.*, 2014). Since its establishment in the late 1960s, this empirical model has offered significant insights into the intricate mechanisms that regulate soil erosion. It has proven to be a pragmatic instrument for evaluating the hazards associated with soil loss and directing conservation endeavours in various geographical settings (Devatha *et al.*, 2015; Girmay *et al.*, 2020; Mazigh *et al.*, 2022). Given the escalating complexities associated with alterations in land use, fluctuations in climatic patterns, and growing global environmental apprehensions, the USLE model has acquired heightened importance in the realm of current soil conservation and land management.

Erosion is an intrinsic natural phenomenon that can provide significant ramifications for the overall well-being of soil, the quality of water, and the integrity of ecosystems (Mancino *et al.*, 2016; Kruk *et al.*, 2020). The repercussions of this phenomenon have wide-ranging implications that transcend beyond the agriculture sector, exerting influence on the sustainability of urban developments, infrastructure, and the broader environment (Bagherzadeh, 2014; Alewell *et al.*, 2019; Youssef *et al.*, 2023). In light of the ongoing expansion of the world population, it has become increasingly crucial to comprehend and address the hazards associated with soil erosion. This urgency arises from the need to safeguard food security, preserve water resources, and effectively administer our landscapes in a sustainable manner (Ahmad and Verma, 2019).

This research study aims to comprehensively explore the USLE erosion model, encompassing its historical evolution, theoretical foundations, and practical implementations. The objective of this study is to provide a comprehensive analysis of the model's inherent advantages and drawbacks, examine current developments and alterations, and evaluate its applicability in light of changing environmental circumstances. In undertaking this endeavour, our aim is to offer a thorough examination of the present condition of the USLE model and its prospects for future advancements in the realm of soil erosion forecasting.

The primary objective of this article is to provide researchers, land managers, and policymakers with a comprehensive understanding of the USLE model. By doing so, it aims to enhance their ability to make well-informed decisions and implement targeted conservation initiatives. In the context of contemporary soil erosion prediction, the USLE model continues to serve as a helpful instrument, aiding us in the pursuit of

sustainable land management strategies and the promotion of environmental stewardship (Dragicevic *et al.*, 2018; Ghosh *et al.*, 2022). The objective of acquiring a comprehensive map encompassing all areas of degraded terrain is to emphasise their spatial arrangement, particularly the regions exhibiting the highest concentration of soil erosion. This facilitates the consideration of both structural and non-structural approaches to mitigate erosion-induced deterioration (Costea *et al.*, 2022).

The phenomenon of soil erosion is a multifaceted environmental concern that has wide-ranging implications, underscoring the necessity of employing rigorous approaches for both forecasting and mitigating its effects (Verheijen *et al.*, 2009; Sabzevari and Talebi, 2009). This section provides a description of the materials and methods employed in our research, whereby it was employed the Universal Soil Loss Equation (USLE) model to evaluate the potential for soil erosion in the selected study region.

Materials and Methods

Study area

The study region, which plays a crucial role in providing context for our findings, was meticulously delineated. The geographical locations, dimensions, and significant environmental factors, including historical context related to soil erosion in the region, were taken into consideration. Cluj County, encompassing an area of 6674 square kilometres, is situated in the northwestern region of Romania, positioned between the latitudinal parallels of 46°24'47" and 47°28'44" north, and the longitudinal meridians of 23°39'22" and 24°13'46" east. This county has a total of 81 Territorial Administrative Units (TAUs). Cluj County is situated in the central region of Transylvania, where it intersects with three significant physical-geographical regions: the Transylvania Plain, the Someşan Plateau (including the Cluj and Dej Hills), and the Apuseni mountain area (Figure 1). The presence of diverse geomorphological, lithological, bioclimatic, and pedological characteristics contributes to a significant range of vegetation components within this particular region (Bilasco *et al.*, 2009).

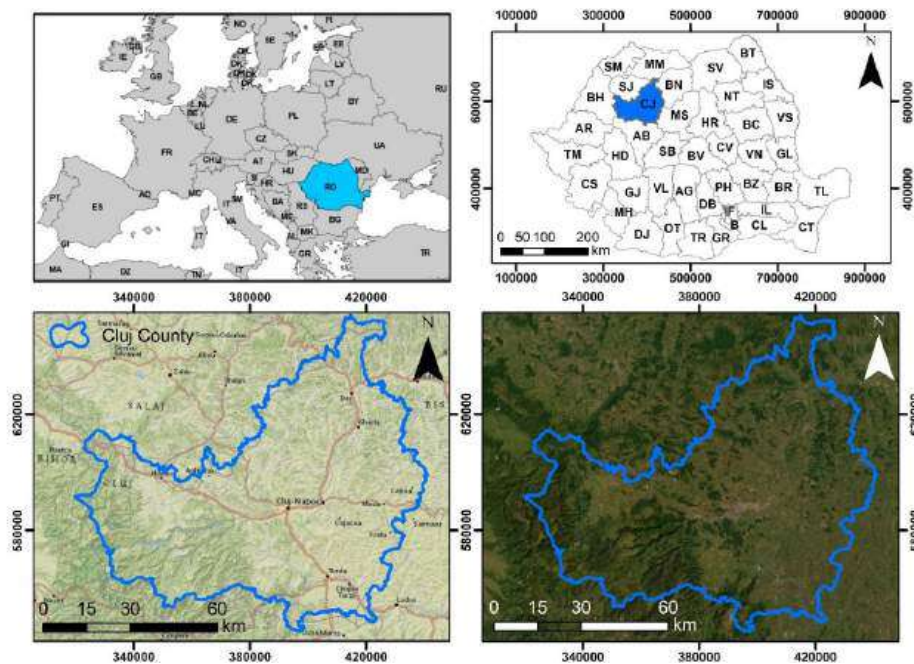


Figure 1. The geographical location of the study area

A breakdown of the county's land usage reveals that agricultural land accounts for 63.8% of the total area, while forest land occupies 25.1%. Constructions occupy 2.9% of the land, roads cover 1.8%, and degraded and unproductive land make up 5% of the county's territory. The topographically elevated region inside Cluj County is considered a constituent component of the broader Transylvanian Depression from a geographical standpoint. This region is characterised as the most extensive negative morphological area within the Carpathian Mountain range. It was formed as a result of alpine tectonic activity, exhibiting a predominantly hilly and plateau-like topography. The area is divided into distinct sequences of geomorphological zones, which are arranged in a nearly concentric manner. These zones progressively decrease in elevation from the outermost to the innermost regions. Notably, there are significant variations in both structural composition and relief characteristics observed across different areas within this region (Sestras *et al.*, 2023).

Methodological approach and database

The present study utilised an extensive dataset including soil characteristics, precipitation patterns, and land utilisation information to foster a full comprehension of the dynamics of soil erosion. The USLE model is dependent on a number of crucial characteristics, all of which are necessary in order to provide precise soil erosion prediction. The methodologies employed for determining these characteristics were delineated. The process of soil erosion is governed by several geomorphological elements, such as slope length and steepness, as well as climatic and soil properties (Desmet and Govers, 1996; Jiang *et al.*, 2023). Additionally, land cover management practises also play a role in this process. This work presents a geographic information system (GIS) based model that aims to calculate and visualise the regions that are susceptible to soil erosion in Cluj County. During the implementation phase of the USLE model, a vector and raster GIS database were developed to encompass the geographic unit under research (Figure 2). This was achieved by the utilisation of spatial analysis methodologies and database queries, which facilitated the quantitative assessment of the soil volume eroded within the designated study region.

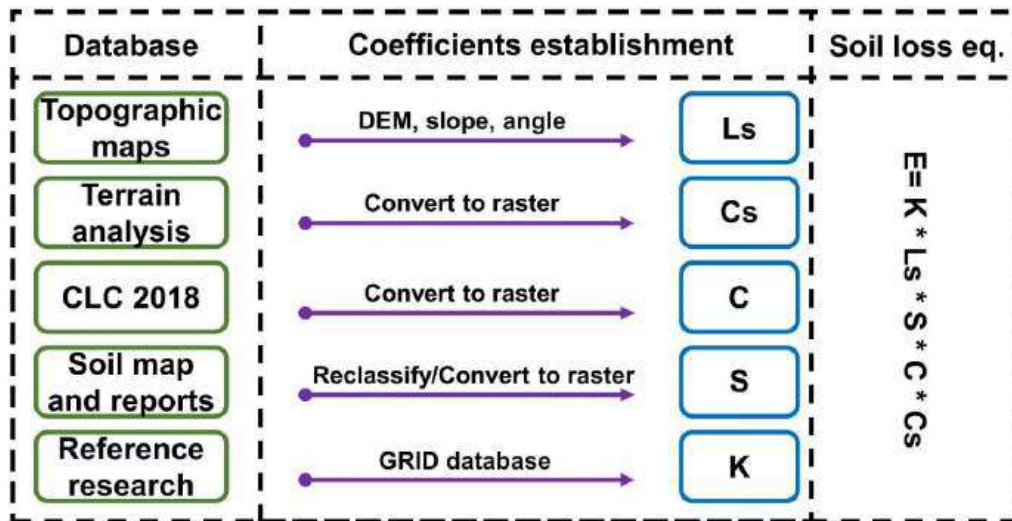


Figure 2. Methods for calculating soil erosion using the USLE model

The calculation of the erosion rate was determined using the widely recognised Universal Soil Loss Equation (USLE), as modified by Moțoc *et al.* in 1975 based on the work of Wischmeier and Smith in 1965. The computational framework of the model incorporates five primary components in the estimation of soil

erosion within a certain geographical region. Each element represents a quantitative evaluation of a distinct situation that has an impact on the severity of soil erosion within a certain geographical area. The erosion values exhibit a concurrent relationship with climatic fluctuations, so rendering the values derived from the Universal Soil Loss Equation (USLE) more accurate by employing long-term average values (Costea *et al.*, 2022). The formula can be expressed as follows:

$$E = K * Ls * S * C * Cs \quad (1)$$

The variable **E** represents the mean annual rate of surface erosion, measured in tonnes per hectare per year. The correction coefficient, denoted as **K**, is a measure of climatic aggressivity, specifically in relation to rainfall. It serves as an indicator of the erodibility index associated with precipitation. In its initial form, the USLE was the cumulative annual product of the erosive rainfalls' energy (**E**) and their greatest intensities during a 30-minute period (**I30**). Indirect estimation approaches have been developed to address the challenge of directly calculating rainfall erodibility, given meteorological stations do not currently record rainfall intensity. These methods rely on statistical relationships between erodibility and other quantifiable factors. The slope length coefficient **Ls** and slope degree are topographic factors that serve as coefficients in the analysis of a researched region. These factors are determined by considering both the slope and length of the area under investigation (Kinnell, 2005). As the length of the slope increases, there is a corresponding increase in the quantity of cumulative runoff. Moreover, it should be noted that there exists a positive correlation between the steepness of a terrain's slope and the velocity of the runoff, which in turn leads to an increased contribution to the process of erosion. The correction coefficient for soil erodibility **S** denotes the capacity of soil or rock to withstand the erosive forces exerted by rainfall and the micro currents induced by the movement of meteorologically derived water. The correction coefficient, denoted as **C**, pertains to the cover-management factor and plant features. It quantifies the ratio between soil loss from land with a certain vegetation type and the soil loss from an equivalent area of continuous barren land. The values of erosion are contingent upon factors such as vegetation cover, management practises, as well as the growth stage and degree of cover during periods of high rainfall-induced erosion. The correction coefficient, denoted as **Cs**, is utilised to account for the impact of erosion control measures. The aforementioned factor pertains to the practise of conservation. Values are derived from empirical observations in the field pertaining to tables on soil conservation practises. These tables provide information on the ratio of soil loss in areas where contouring and contour strip-cropping techniques are implemented compared to areas where these techniques are not employed. The final erosion map encompasses the five previously established coefficients, as depicted in Figure 3.

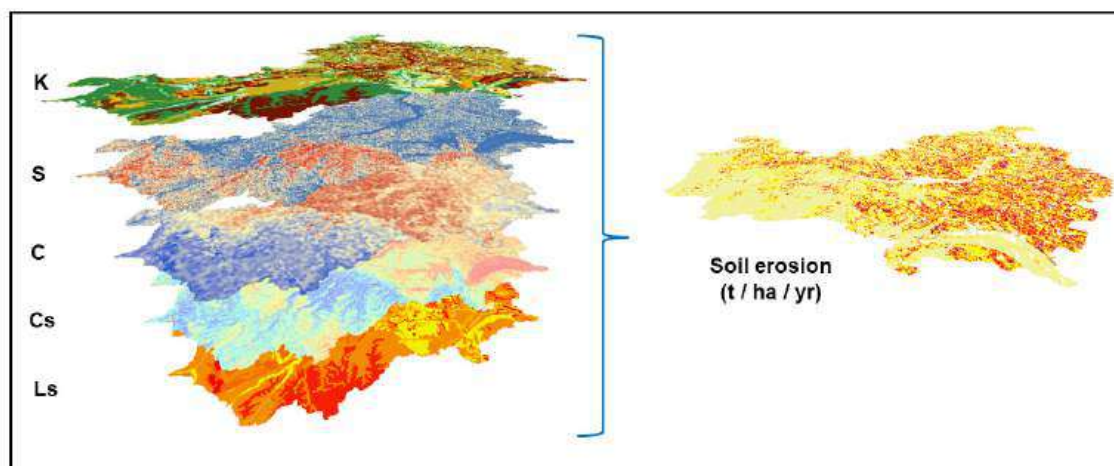


Figure 3. The five coefficients used in the USLE model

The calibration and validation of the Universal Soil Loss Equation (USLE) model were important stages in the research endeavour. The calibration method was explicated, providing a comprehensive account of the criteria employed for evaluating the performance of the model, by comparing the areas highlighted by high erosion with field and Google Earth investigations. Additionally, we provided a thorough explanation of our validation process, which encompasses the datasets and statistical methodologies utilised to assess the accuracy of our model (Rizeei *et al.*, 2016; Serbaji *et al.*, 2023). In order to provide a thorough viewpoint, a comparative study was undertaken, when appropriate, to compare the results of the USLE model with those of other soil erosion models or historical data, such as the Intensity of Erosion and Outflow (IntErO) model. This analysis aimed to evaluate the effectiveness of the USLE model in predicting soil erosion (Sestras *et al.*, 2023).

Regarding software and tools, we have delineated the specific software and Geographic Information System (GIS) tools employed for the purpose of data processing, model implementation, and statistical analysis (Hysa *et al.*, 2021; Hyka *et al.*, 2022). Thus, the software ArcMap 10.8 was employed for the USLE modelling, along with open source data such as the Shuttle Radar Topography Mission Digital Elevation Model (SRTM DEM), Corine Land Cover 2018 (CLC 2018) dataset that provided information on land cover and land use, average annual precipitation datasets regarding the rainfall were used from meteorological stations inside of Cluj County, and the soil database constructed by digitizing 1:200,000 scale maps with the SRCS ICPA-1980 (Romanian Soil Classification System). This meticulous approach has been adopted to guarantee transparency and repeatability in our research methodology. The utilisation of specific materials and methodologies in our study established the groundwork for a thorough evaluation of the potential hazards associated with soil erosion, hence facilitating a more profound comprehension of this significant ecological concern.

Results and Discussion

Our study focuses on soil erosion, an environmental issue of great significance that has far-reaching implications for land management and sustainability. Using the Universal Soil Loss Equation (USLE) model, our objective was to analyse the complex soil erosion patterns within our selected research area. The investigation was initiated by taking a comprehensive perspective on the patterns of soil erosion. The USLE model facilitated the identification of a diverse array of erosion risks distributed throughout the landscape. The complex interaction among variables such as topography, land cover, and soil properties resulted in diverse levels of susceptibility to soil erosion. The aforementioned viewpoint provided the fundamental basis from which we proceeded to explore the intricacies in greater detail.

Spatial distribution maps played a prominent role in depicting the spatial patterns of soil erosion risk. The maps shown in this study utilise color-coded gradients to visually depict the vulnerability of the study area to erosion, so providing a narrative representation. The model's ability to reflect localised dynamics was demonstrated by the emergence of several variants, ranging from low-risk zones to erosion hotspots. When applicable, temporal analysis sheds light on the temporal evolution of soil erosion risk. Graphs and charts provide a visual representation of temporal patterns, illustrating trends, variations, and the influence of altering environmental factors on the dynamics of soil erosion. The inclusion of the temporal dimension has contributed to a more comprehensive display of the erosion process. By examining the inner workings of the model, it was conducted an analysis on the impact of its individual components (Ls, Cs, C, S, K) on the process of soil erosion, thus shedding light on the relative significance of each parameter in influencing erosion patterns.

Focusing on the practical ramifications of our research outcomes, we have identified specific areas of erosion concentration known as hotspots, as well as determined the priority for conservation efforts. These regions with a high-risk factor necessitate concentrated attention and well-informed methods for conservation. The research conducted in this context provided practical insights that can be utilised by land managers, policymakers, and conservationists.

The calculation of the modelled erosion rate was determined using the USLE model as modified by Moțoc *et al.* in 1975. The soil erosion map for Cluj County is displayed in Figure 4. The computational framework of the model incorporates five primary factors to estimate soil loss within a certain geographical region. Thus, the modelled erosion based on five classes incorporates the following: very-low (tolerable) rate of below 3 tonnes per hectare per year ($t\ ha^{-1}\ yr^{-1}$); low rate which is between the interval of 3.1 to 10 $t\ ha^{-1}\ yr^{-1}$; moderate rate which is between the interval of 10.1 to 20 $t\ ha^{-1}\ yr^{-1}$; high rate which is between the interval of 20.1 to 40 $t\ ha^{-1}\ yr^{-1}$; very-high rate of over 40.1 $t\ ha^{-1}\ yr^{-1}$. Highlighted inside of Figure 4 is the percentage chart of each of the five erosion susceptibility classes, in regards to the occupied surface from Cluj County total area. Thus, it was established that almost half of the surface of Cluj County, namely 49.63%, belongs to the low class of soil erosion. The highlighted regions belonging to the very-low class of erosion are predominantly situated in the West and South-West part of Cluj County, which belong to the Apuseni Mountain area, a geographical unit well constituted in terms of forests and appropriate land use. The low and moderate rates represent 32.40%, respectively 14.16% of the total area, and are distributed across all the county's surface. The high and very-high rates of soil erosion represent 3.56%, respectively 0.24% of the total area, and are considered hotspots of significant land degradation. The aforementioned discovery denote that the highlighted hotspots are undergoing substantial degradation, underscoring the imperative requirement for the implementation of soil conservation measures in those regions. The main regions subjected to high and very-high rates of soil erosion belong to the Transylvanian Plain, located in the Eastern part of Cluj County, a geographical region with significant agricultural use. Moțoc *et al.* (1975) established that the acceptable limit for soil erosion in the Romanian region varies between 2 and 8 tonnes per hectare annually, thus more than three quarters of Cluj County fall in an expected and manageable threshold (Moțoc, 1983; Moțoc and Mircea, 2002).

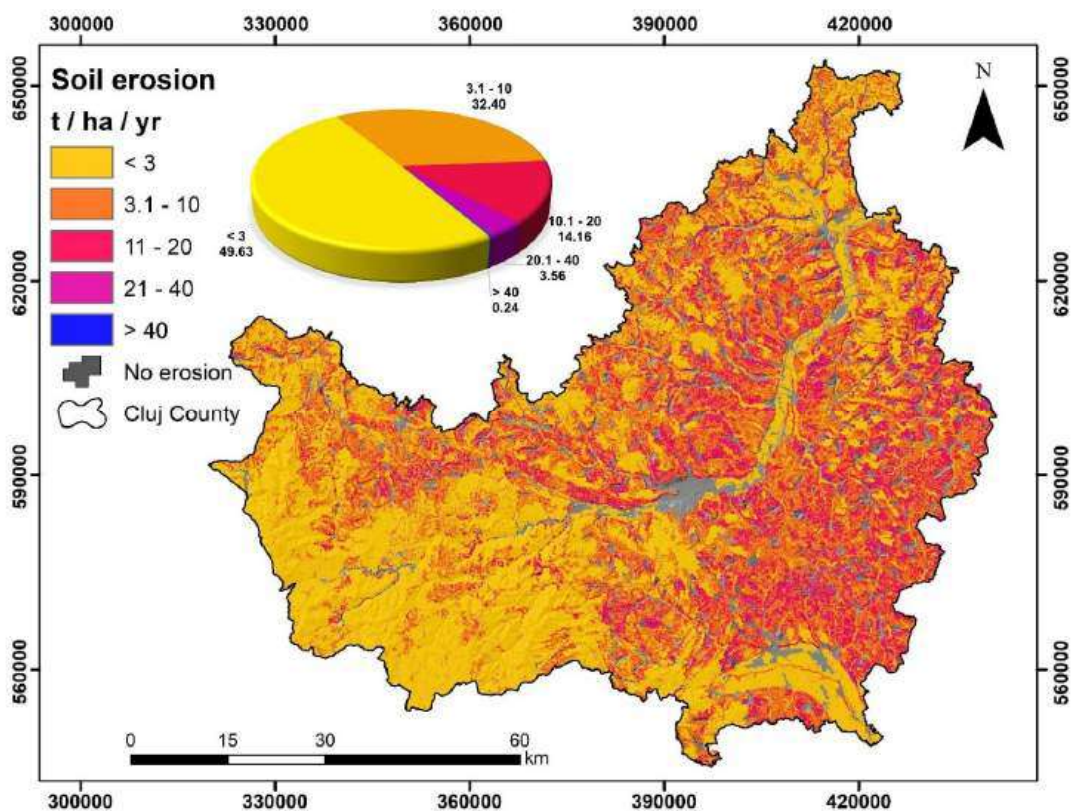


Figure 4. Soil erosion map for Cluj County

The utilisation of GIS technology and geospatial databases enables the modelling and querying of soil erosion classes, which we find highly advantageous. In order to provide landowners with an initial assessment of the susceptibility to soil erosion in plots used for agricultural and non-agricultural purposes, it is necessary to ensure that they have a comprehensive understanding of the situation. Consequently, determinations can be formulated pertaining to the strategies aimed at mitigating the hazards associated with soil erosion, encompassing both the broader context of the TAU and the specific scope of individual plots. The examination focused on the plots exhibiting the most significant erosion rates, with particular attention given to the geographical locations in which they are situated. Figure 5 illustrates the average annual erosion rate for agricultural and non-agricultural plots, based on the parcels obtained from *Agenția de Plăți și Intervenție pentru Agricultură* APIA (Payments and Intervention Agency for Agriculture).

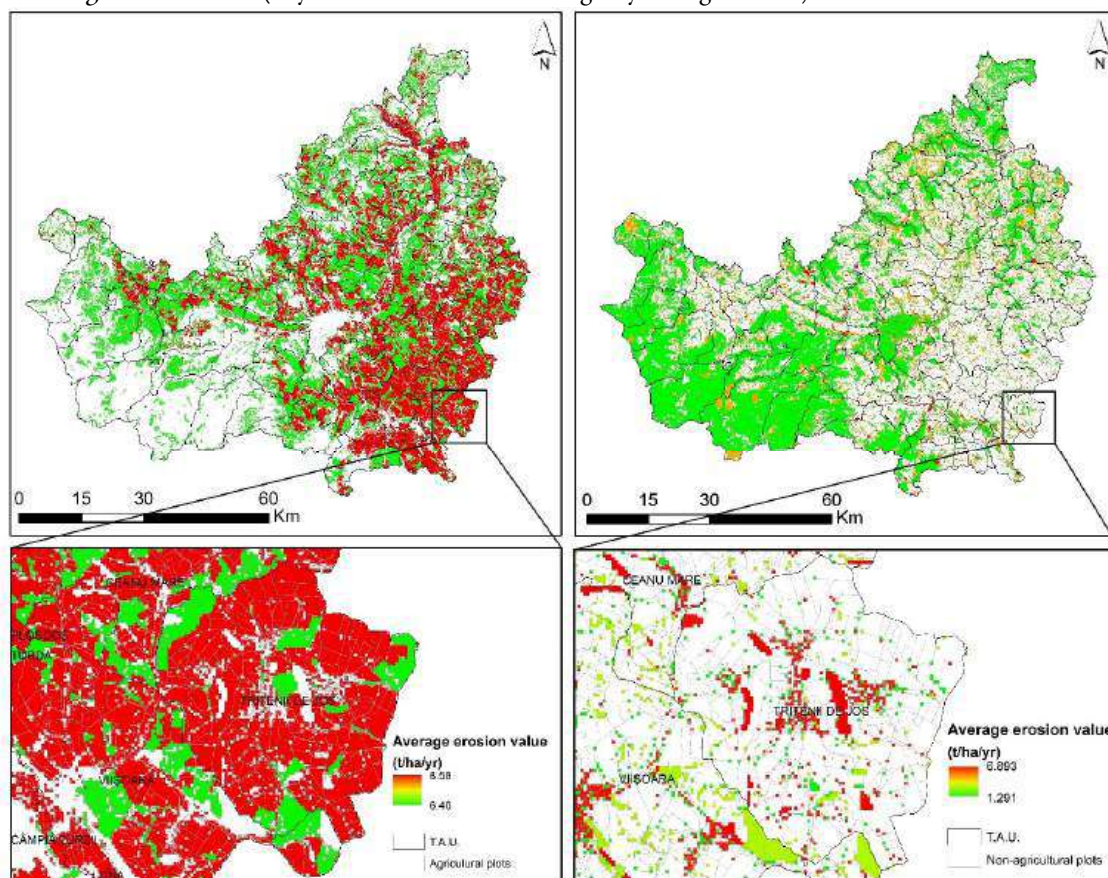


Figure 5. The average annual erosion rate for agricultural (left) and non-agricultural (right) plots

By utilising the modelled values of soil erosion acquired at the Cluj County level, it was derived the average soil erosion value for each parcel within the study region, considering both agricultural and non-agricultural land use. Based on the APIA obtained parcels, six large distinct classes were identified, respectively: 1. Permanent crops other than vineyards, orchards, hops; 2. Non-productive land; 3. Permanent pasture; 4. Arable land including greenhouses, solariums; 5. Gravel, sands, rocks, tailings ponds, rubbish pits; 6. Forest vegetation, shrubs, bushes. In the case of plots designated for non-agricultural purposes, the average rate of erosion ranges from $6.40 \text{ t ha}^{-1} \text{ yr}^{-1}$ to $8.58 \text{ t ha}^{-1} \text{ yr}^{-1}$. It is worth noting that the higher erosion values are typically observed in isolated plots that are utilised for non-agricultural activities, such as the class identified by gravel, sands, rocks, tailings ponds, rubbish pits. The individual analysis of agricultural plots focused on identifying

permanent crops, in addition to arable land that includes greenhouses and solariums. These land uses account for 28.26% and 36.43% respectively, falling within the categories of moderate erosion.

Regarding non-agricultural plots, it is identified that a significant majority, specifically 79.08% (449 plots), exhibit a low average erosion value ranging from 3 to 10 t ha⁻¹ yr⁻¹. Conversely, the remaining 21.91% (126 plots) demonstrate an even lower average erosion rate, thereby enhancing their economic worth. In 2022, there were a total of 281 parcels categorised for agricultural use. These parcels, on average, exhibit moderate erosion levels. However, it is important to note that there are localised instances of rapid erosion within these parcels. Figure 6 illustrates the five degrees of erosion intensity (very-low, low, moderate, high, very-high) based on the USLE modelling, together with the six APIA distinct classes of land use.

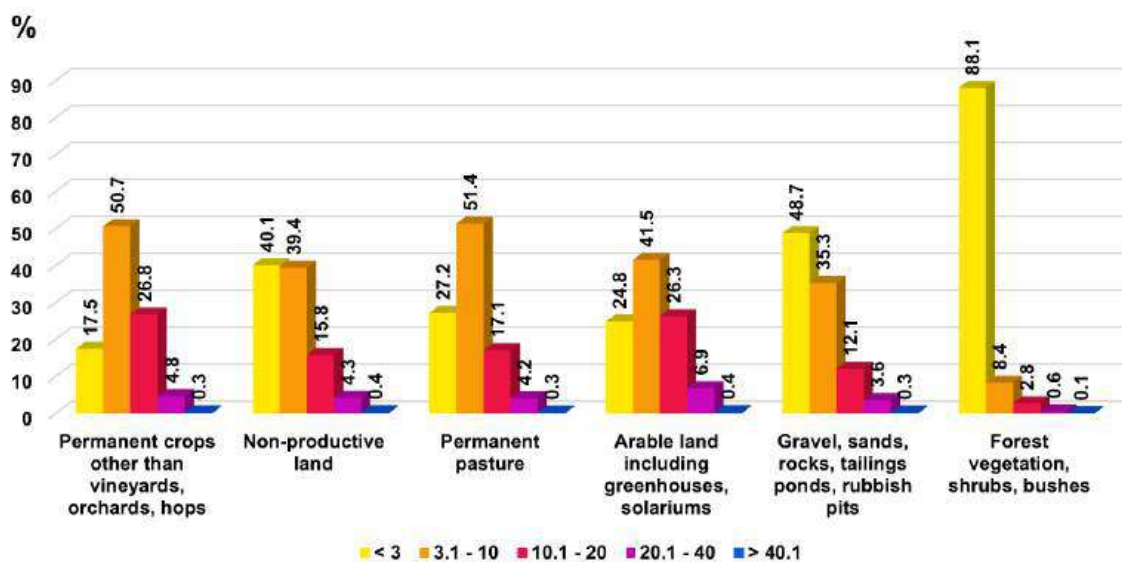


Figure 6. The distribution of soil erosion rates based on the APIA land parcel classes

Within regions characterised by forest vegetation, the soil erosion rate is seen to be at its minimum level, encompassing around 88.1% of the total area. This phenomenon can be attributed to the well-established understanding that forest vegetation plays a crucial role in water retention, particularly during periods of excessive precipitation, thereby effectively mitigating the occurrence of floods (Curovic *et al.*, 2020; Bilaşco *et al.*, 2022). The regions characterised by continuous agriculture exhibit a notable rate of soil erosion, ranging from 20 to 40 t ha⁻¹ yr⁻¹. This phenomenon can be attributed to the elevated erosivity resulting from the expansion of non-vegetated land areas. The present study aimed to analyse unproductive areas with the objective of accurately classifying them in future agricultural circuit classifications.

The regions designated as "Gravel, sands, rocks, tailings ponds, rubbish pits" are primarily situated alongside the primary watercourses, which do not possess agricultural significance. However, these regions were incorporated into the analysis to ensure comprehensive territorial representation at the county level. The statistical examination of agricultural and non-agricultural parcels in Cluj County reveals that a majority of these parcels (41.5%) are categorised as having low erosion. However, a small portion of the land (0.4% of the total area) falls into the high erosion class, with erosion rates reaching up to 40 t ha⁻¹ yr⁻¹. This necessitates the implementation of both structural and non-structural measures to mitigate erosion, such as agrotechnical implementations, afforestation, crop rotation, and the cultivation of crops with high soil coverage. In addition to the aforementioned, the implementation of the works is carried out in accordance with the overall alignment of the contour lines, while incorporating the establishment of strip crops designed to serve as a protective measure against erosion, with due consideration given to the permissible yearly erosion rate, which according

to Moțoc *et al.* 1975 the permissible threshold for soil erosion in the Romanian area ranges from 2 to 8 tonnes per hectare per year. The areas exhibiting soil erosion under the category of permanent pastures are primarily situated in the hilly and premontane regions of Cluj County. This circumstance contributes to the deterioration of the unique pasture ecosystem and the reduction in the diversity of plant and animal species.

The primary goal of obtaining a complete map that encompasses all degraded terrains is to highlight their spatial distribution, with a specific emphasis on places exhibiting the greatest concentration of soil erosion. This enables the examination of both structural and non-structural measures intended to alleviate the degradation caused by erosion. The research was augmented by incorporating a comparative analysis utilising several soil erosion models or datasets. The analysis indicated above not only accomplished the purpose of validating the USLE model, but also drew attention to its notable strengths and revealed areas that may require further improvement. Figure 7 illustrates the hotspots and coldspots identified in terms of soil erosion at the TAU level in Cluj County.

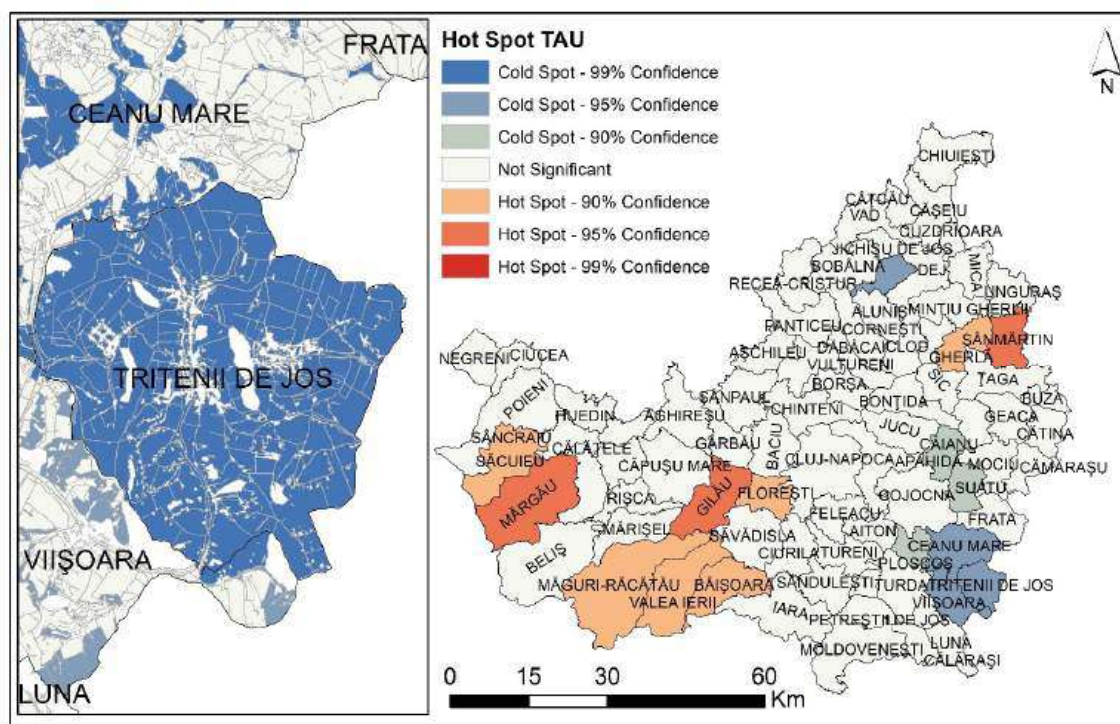


Figure 7. The identified erosion hotspots and coldspots at TAU level in Cluj County

To identify agricultural plots with a high susceptibility to soil erosion, we employed GIS statistical analysis tools. These tools facilitated the extraction of average erosion values for each individual agricultural plot and enabled the implementation of the HotSpot model within the studied area. The plots exhibiting a significant level of confidence in relation to soil erosion were consequently emphasised. A hotspot can be described as a geographic location characterised by a significantly higher concentration of events in relation to the expected number of events that would occur if they were randomly distributed. The concept of hotspot identification has undergone development through the examination of point distributions or spatial configurations of points inside a given location.

The territorial administrative units located in the mountainous region of the Apuseni mountains (Mărgău, Săcuieni, Măguri-Răcățau, Valea Ierii, and Băișoara) are susceptible to accelerated soil erosion. This vulnerability is primarily attributed to the topographical characteristics, including steep slopes and increased torrentiality. Additionally, the expansion of deforested areas (Hartel *et al.*, 2017; Dragan *et al.*, 2019) further

exacerbates the erosion process until new forest vegetation is established. In these regions, there is a noticeable rise in the density of access roads leading to the properties, indicating that the area is at the forefront in terms of constructing vacation residences.

The urban areas of Gherla, Sânmărtin, and Gilău are classified as hotspots due to the significant expansion of agricultural land, specifically permanent crop cultivation, which mostly caters to the nearby urban communities. An elevated rate of soil erosion was documented in both regional investigations, such as the one conducted by PATJ Cluj (Cluj County Territorial Development Plan), as well as in studies conducted at the level of hydrographic sub-basins.

Despite the increase of the built environment (Dolean *et al.*, 2020), TAU Florești remains a significant hotspot. The proliferation of concrete surfaces has resulted in a decrease in the rate of water infiltration into the soil inside urbanised areas, while simultaneously causing an excessive discharge of water in neighbouring regions. TAU Triteni, situated in the Transylvania Plain, is totally within the 99% confidence interval of the coldspot category, indicating a higher level of clustering of low values. In this particular scenario, the implementation of agrotechnical measures and the appropriate utilisation of agricultural plots have a beneficial impact on soil erosion. The recorded average soil erosion rates at the plot level range from 1.3 to 6.9 t ha⁻¹ yr⁻¹, which are within the acceptable threshold for the Romanian territory.

Conclusions

Soil erosion is significantly impacted by global climate change, including the intensity and magnitude of climatic risk events such as heavy rainfall, uneven precipitation patterns throughout the year, and the inadequate management of agricultural land, characterised by non-compliance with recommended agrotechnical practises. Additionally, human activities such as deforestation, alterations in land use, and the expansion of transportation networks also contribute to soil erosion. The implications of our findings extend beyond the scope of this study. These concepts resonate within the domains of land-use planning, erosion control strategies, and sustainable land management techniques. The practical implications of the research highlight the need for well-informed decision-making and the conservation of the existing valuable soil resources. The future presents prospects for the advancement of soil erosion modelling, with continuous progress in data gathering, technological advancements, and modelling methodologies, thus establishing an opportunity of enhancing the comprehension of this crucial environmental issue.

Authors' Contributions

All authors have contributed equally to the work. All authors have read and agreed to the published version of the manuscript.

Ethical approval (for researches involving animals or humans)

Not applicable.

Acknowledgements

This work of Paul Sestras was supported by the project “PROINVENT”, Contract no. 62487/03.06.2022 POCU/993/6/13–cod SMIS: 153299 financed by The Human Capital Operational Programme 2014–2020 (POCU), Romania.

Conflict of Interests

The authors declare that there are no conflicts of interest related to this article.

References

- Ahmad I, Verma MK (2013). Application of USLE model & GIS in estimation of soil erosion for Tandula reservoir. *International Journal of Emerging Technology and Advanced Engineering*, 3(4):570-576.
- Alewell C, Borrelli P, Meusburger K, Panagos P (2019). Using the USLE: Chances, challenges and limitations of soil erosion modelling. *International Soil and Water Conservation Research* 7(3):203-225. <https://doi.org/10.1016/j.iswcr.2019.05.004>
- Bagherzadeh A (2014). Estimation of soil losses by USLE model using GIS at Mashhad plain, Northeast of Iran. *Arabian Journal of Geosciences* 7:211-220. <https://doi.org/10.1007/s12517-012-0730-3>
- Bilaşco Ş, Hognogi GG, Roşca S, Pop AM, Iuliu V, Fodorean I, ... Sestras P (2022). Flash flood risk assessment and mitigation in digital-era governance using unmanned aerial vehicle and GIS spatial analyses case study: Small river basins. *Remote Sensing* 14(10):2481. <https://doi.org/10.3390/rs14102481>
- Bilaşco Ş, Horvath C, Cocean P, Sorocovschi V, Oncu M (2009). Implementation of the USLE model using GIS techniques. Case study the Someşean Plateau. *Carpathian Journal of Earth and Environmental Sciences* 4(2):123-132.
- Costea A, Bilasco S, Irimus IA, Rosca S, Vescan I, Fodorean I, Sestras P (2022). Evaluation of the risk induced by soil erosion on land use. Case study: Guruslău depression. *Sustainability* 14(2):652. <https://doi.org/10.3390/su14020652>
- Curovic M, Spalevic V, Sestras P, Motta R, Dan C, Garbarino M, ... Urbinati C (2020). Structural and ecological characteristics of mixed broadleaved old-growth forest (Biogradska Gora-Montenegro). *Turkish Journal of Agriculture and Forestry* 44(4):428-438. <https://doi.org/10.3906/tar-2003-103>
- Desmet PJJ, Govers G (1996). A GIS procedure for automatically calculating the USLE LS factor on topographically complex landscape units. *Journal of Soil and Water Conservation* 51(5):427-433.
- Devatha CP, Deshpande V, Renukaprasad MS (2015). Estimation of soil loss using USLE model for Kulhan Watershed, Chattisgarh-A case study. *Aquatic Procedia* 4:1429-1436. <https://doi.org/10.1016/j.aqpro.2015.02.185>
- Dolean BE, Bilaşco Ş, Petrea D, Moldovan C, Vescan I, Roşca S, Fodorean I (2020). Evaluation of the built-up area dynamics in the first ring of Cluj-Napoca metropolitan area, Romania by semi-automatic GIS analysis of Landsat satellite images. *Applied Sciences* 10(21):7722. <https://doi.org/10.3390/app10217722>
- Drăgan M, Mureşan GA, Benedek J (2019). Mountain wood-pastures and forest cover loss in Romania. *Journal of Land Use Science* 14(4-6):397-409. <https://doi.org/10.1080/1747423X.2020.1719224>
- Dragicevic N, Karleusa B, Ozanic N (2018). Modification of erosion potential method using climate and land cover parameters. *Geomatics, Natural Hazards and Risk* 9:1085-1105. <https://doi.org/10.1080/19475705.2018.1496483>
- Ghosh A, Rakshit S, Tikle S, Das S, Chatterjee U, Pande CB, ... Mattar MA (2022). Integration of GIS and remote sensing with RUSLE model for estimation of soil erosion. *Land* 12(1):116. <https://doi.org/10.3390/land12010116>
- Girmay G, Moges A, Mulunch A (2020). Estimation of soil loss rate using the USLE model for Agewmariayam Watershed, northern Ethiopia. *Agriculture and Food Security* 9(1):1-12. <https://doi.org/10.1186/s40066-020-00262-w>

- Gocić M, Dragičević S, Radivojević A, Martić Bursać N, Stričević L, Đorđević M (2020). Changes in soil erosion intensity caused by land use and demographic changes in the Jablanica River Basin, Serbia. *Agriculture* 10(8):345. <https://doi.org/10.3390/agriculture10080345>
- Greiner L, Keller A, Grêt-Regamey A, Papritz A (2017). Soil function assessment: review of methods for quantifying the contributions of soils to ecosystem services. *Land Use Policy* 69:224-237. <https://doi.org/10.1016/j.landusepol.2017.06.025>
- Hartel T, Réti KO, Craioveanu C (2017). Valuing scattered trees from wood-pastures by farmers in a traditional rural region of Eastern Europe. *Agriculture, Ecosystems and Environment* 236:304-311. <https://doi.org/10.1016/j.agee.2016.11.019>
- Hyka I, Hysa A, Dervishi S, Solomun MK, Kuriqi A, Vishwakarma DK, Sestras P (2022). Spatiotemporal dynamics of landscape transformation in Western Balkans' metropolitan areas. *Land* 11(11):1892. <https://doi.org/10.3390/land11111892>
- Hysa A, Spalevic V, Dudic B, Roșca S, Kuriqi A, Bilașco Ș, Sestras P (2021). Utilizing the available open-source remotely sensed data in assessing the wildfire ignition and spread capacities of vegetated surfaces in Romania. *Remote Sensing* 13(14):2737. <https://doi.org/10.3390/rs13142737>
- Jiang N, Yao F, Liu T, Chen Z, Hu C, Geng X (2023). Estimating the soil erosion response to land-use change using GIS-Based RUSLE and remote sensing: A case study of Heilongjiang province, China. *Sustainability* 15(10):8004. <https://doi.org/10.3390/su15108004>
- Kinnell PI (2005). Alternative approaches for determining the USLE-M slope length factor for grid cells. *Soil Science Society of America Journal* 69(3):674-680. <https://doi.org/10.2136/sssaj2004.0047>
- Kruk E, Klapa P, Ryzek M, Ostrowski K (2020). Influence of DEM elaboration methods on the USLE model topographical factor parameter on steep slopes. *Remote Sensing* 12(21):3540.
- Mancino G, Nolè A, Salvati L, Ferrara A (2016). In-between forest expansion and cropland decline: A revised USLE model for soil erosion risk under land-use change in a Mediterranean region. *Ecological Indicators* 71:544-550. <https://doi.org/10.1016/j.ecolind.2016.07.040>
- Mazigh N, Taleb A, El Bilali A, Ballah A (2022). The effect of erosion control practices on the vulnerability of soil degradation in Oued EL Malleh catchment using the USLE model integrated into GIS, Morocco. *Trends in Sciences* 19(2):2059-2059. <https://doi.org/10.48048/tis.2022.2059>
- Mohammadi M, Khaleli Darvishan A, Spalevic V, Dudic B, Billi P (2021). Analysis of the impact of land use changes on soil erosion intensity and sediment yield using the IntErO model in the Talar watershed of Iran. *Water* 13(6):881. <https://doi.org/10.3390/w13060881>
- Moșoc M (1983). Ritmul mediu de degradare erozională a solului în RS România. *Bul. Inf. ASAS Bucuresti*, 12.
- Moșoc MD, Băloiu V (1975). *Eroziunea solului și metodele de combatere*. Ed Ceres, Bucuresti.
- Moșoc M, Mircea S (2002). *Evaluarea factorilor care determina riscul eroziunii hidrice in suprafata*. Ed Bren, Bucuresti.
- Rizeei HM, Saharkhiz MA, Pradhan B, Ahmad N (2016). Soil erosion prediction based on land cover dynamics at the Semenyih watershed in Malaysia using LTM and USLE models. *Geocarto International* 31(10):1158-1177. <https://doi.org/10.1080/10106049.2015.1120354>
- Roșca S, Bilașco Ș, Petrea D, Vescan I, Fodorean I, Filip S (2014). Application of soil loss scenarios using the ROMSEM model depending on maximum land use pretability classes. A case study. *Studia UBB Geographia* 59:101-116.
- Sabzevari T, Talebi A (2019). Effect of hillslope topography on soil erosion and sediment yield using USLE model. *Acta Geophysica* 67(6):1587-1597. <https://doi.org/10.1007/s11600-019-00361-8>
- Serbaji MM, Bouaziz M, Weslati O (2023). Soil water erosion modeling in Tunisia using RUSLE and GIS integrated approaches and Geospatial Data. *Land* 12(3):548. <https://doi.org/10.3390/land12030548>
- Sestras P, Mircea S, Cîmpeanu SM, Teodorescu R, Roșca S, Bilașco Ș, ... Spalevic V (2023). Soil erosion assessment using the intensity of erosion and outflow model by estimating sediment yield: Case study in river basins with different characteristics from Cluj County, Romania. *Applied Sciences* 13(16):9481. <https://doi.org/10.3390/app13169481>
- Spalevic V, Barovic G, Vujacic D, Curovic M, Behzadfar M, Djurovic N, ... Billi P (2020). The impact of land use changes on soil erosion in the river basin of Miocki Potok, Montenegro. *Water* 12(11):2973. <https://doi.org/10.3390/w12112973>
- Verheijen FG, Jones RJ, Rickson RJ, Smith CJ (2009). Tolerable versus actual soil erosion rates in Europe. *Earth-Science Reviews* 94(1-4):23-38. <https://doi.org/10.1016/j.earscirev.2009.02.003>

Wischmeier WH, Smith DD (1965). Predicting rainfall-erosion losses from cropland east of the Rocky Mountains: Guide for selection of practices for soil and water conservation (No. 282). Agricultural Research Service, US Department of Agriculture.

Youssef B, Bouskri I, Brahim B, Kader S, Brahim I, Abdelkrim B, Spalević V (2023). The contribution of the frequency ratio model and the prediction rate for the analysis of landslide risk in the Tizi N'tichka area on the national road (RN9) linking Marrakech and Ouarzazate. *Catena* 232:107464. <https://doi.org/10.1016/j.catena.2023.107464>



The journal offers free, immediate, and unrestricted access to peer-reviewed research and scholarly work. Users are allowed to read, download, copy, distribute, print, search, or link to the full texts of the articles, or use them for any other lawful purpose, without asking prior permission from the publisher or the author.



License - Articles published in *Norulae Botanicae Horti Agrobotanici Cluj-Napoca* are Open-Access, distributed under the terms and conditions of the Creative Commons Attribution (CC BY 4.0) License.

© Articles by the authors; Licensee UASVM and SHST, Cluj-Napoca, Romania. The journal allows the author(s) to hold the copyright/to retain publishing rights without restriction.

Notes:

- **Material disclaimer:** The authors are fully responsible for their work and they hold sole responsibility for the articles published in the journal.
- **Maps and affiliations:** The publisher stay neutral with regard to jurisdictional claims in published maps and institutional affiliations.
- **Responsibilities:** The editors, editorial board and publisher do not assume any responsibility for the article's contents and for the authors' views expressed in their contributions. The statements and opinions published represent the views of the authors or persons to whom they are credited. Publication of research information does not constitute a recommendation or endorsement of products involved.

ORIGINAL RESEARCH article

Front. Psychol., 24 November 2023

Sec. Environmental Psychology

Volume 14 - 2023 | <https://doi.org/10.3389/fpsyg.2023.1201030>

Download Article

Touch, feel, heal. The use of hospital green spaces and landscape as sensory-therapeutic gardens: a case study in a university clinic

Mihaela Dinu Roman Szabo¹ Adelina Dumitras¹ Diana-Maria Mircea^{1,2} Dana Doroftei³ Paul Sestras^{4,5*} Monica Boscaiu⁶ Robert F. Brzuszek⁷ Adriana F. Sestras¹

¹ Faculty of Forestry and Cadastre, University of Agricultural Sciences and Veterinary Medicine, Cluj-Napoca, Romania² Institute for Conservation and Improvement of Valencian Agrobiodiversity (COMAV), Universitat Politècnica de València, Valencia, Spain³ Pharmacy Science and Technology, University of Medicine, Târgu Mureș, Romania⁴ Faculty of Civil Engineering, Technical University of Cluj-Napoca, Cluj-Napoca, Romania⁵ Academy of Romanian Scientists, Bucharest, Romania⁶ Mediterranean Agroforestry Institute (IAM), Universitat Politècnica de València, Valencia, Spain⁷ Department of Landscape Architecture, Mississippi State University (MSU), Mississippi State, MS, United States461
Total views17
Downloads[View article impact >](#)[View altmetric score >](#)

SHARE ON



Edited by



Franco L. Souza

Federal University of Mato Grosso do Sul, Brazil

FRONTIERS IN PSYCHOLOGY

Publisher name: FRONTIERS MEDIA SA

Journal Impact Factor™

2.6

2023

3.3

Five Year

JCR Category	Category Rank	Category Quartile
PSYCHOLOGY, MULTIDISCIPLINARY <i>in SSCI edition</i>	56/218	Q2

Source: Journal Citation Reports 2023. [Learn more](#)

Journal Citation Indicator™

0.97

2023

1.04

2022

JCI Category	Category Rank	Category Quartile
PSYCHOLOGY, MULTIDISCIPLINARY <i>in SSCI edition</i>	62/218	Q2



OPEN ACCESS

EDITED BY

Franco Leandro de Souza,
Federal University of Mato Grosso do Sul, Brazil

REVIEWED BY

Florin Ioras,
Buckinghamshire New University,
United Kingdom
Konstantinos Bertsoyklis,
Agricultural University of Athens, Greece

*CORRESPONDENCE

Paul Sestras
✉ psestras@mail.utcluj.ro

RECEIVED 05 April 2023

ACCEPTED 27 October 2023

PUBLISHED 24 November 2023

CITATION

Dinu Roman Szabo M, Dumitras A,
Mircea D-M, Doroftei D, Sestras P, Boscaiu M,
Brzuszek RF and Sestras AF (2023) Touch, feel,
heal. The use of hospital green spaces
and landscape as sensory-therapeutic
gardens: a case study in a university clinic.
Front. Psychol. 14:1201030.
doi: 10.3389/fpsyg.2023.1201030

COPYRIGHT

© 2023 Dinu Roman Szabo, Dumitras, Mircea,
Doroftei, Sestras, Boscaiu, Brzuszek and
Sestras. This is an open-access article
distributed under the terms of the [Creative
Commons Attribution License \(CC BY\)](#). The
use, distribution or reproduction in other
forums is permitted, provided the original
author(s) and the copyright owner(s) are
credited and that the original publication in this
journal is cited, in accordance with accepted
academic practice. No use, distribution or
reproduction is permitted which does not
comply with these terms.

Touch, feel, heal. The use of hospital green spaces and landscape as sensory-therapeutic gardens: a case study in a university clinic

Mihaela Dinu Roman Szabo¹, Adelina Dumitras¹,
Diana-Maria Mircea^{1,2}, Dana Doroftei³, Paul Sestras^{4,5*},
Monica Boscaiu⁶, Robert F. Brzuszek⁷ and Adriana F. Sestras¹

¹Faculty of Forestry and Cadastre, University of Agricultural Sciences and Veterinary Medicine, Cluj-Napoca, Romania, ²Institute for Conservation and Improvement of Valencian Agrodiversity (COMAV), Universitat Politècnica de València, Valencia, Spain, ³Pharmacy Science and Technology, University of Medicine, Târgu Mureș, Romania, ⁴Faculty of Civil Engineering, Technical University of Cluj-Napoca, Cluj-Napoca, Romania, ⁵Academy of Romanian Scientists, Bucharest, Romania, ⁶Mediterranean Agroforestry Institute (IAM), Universitat Politècnica de València, Valencia, Spain, ⁷Department of Landscape Architecture, Mississippi State University (MSU), Mississippi State, MS, United States

It has been documented that patients with mental or physical disabilities can benefit from being placed within the setting of a natural environment. Consequently, the concept of creating spaces that can enhance health preservation or patient recovery, while also augmenting environmental and aesthetic value, has merged as a contemporary discourse. Green areas around hospitals can offer a great opportunity to incorporate healing gardens to benefit their patients and not only. The aim of this paper is to propose a design for a sensory-therapeutic garden based on key principles derived from selected academic literature, focusing on the application of these principles in a healthcare setting in Cluj-Napoca, Romania. The design was informed also by onsite data collection and analysis, and it aims to create a healing landscape that addresses the needs of patients, healthcare providers, and visitors. This study seeks to augment the discourse in the field by demonstrating the practical application of key therapeutic garden design principles in a specific context and how these principles impacted the design process.

KEYWORDS

garden design, healing, hospital green space, sensory garden, therapeutic

1 Introduction

Research has shown that human wellbeing and health improves with the ability to spend time outdoors and to have access to green spaces and other forms of Nature (Gidlöf-Gunnarsson and Öhrström, 2007; Bush and Doyon, 2019; Jennings and Bamkole, 2019; de Bell et al., 2020). Our connection to Nature is strongly rooted in our evolutionary process and is an integral part of our regional identity. As humans, we engage with our environment and the natural world on both a physical and psychological level. The physical level refers

to the direct interaction between humans and landscape, as a part of a complex, self-regulating system that includes biotic and abiotic elements that work together to maintain and perpetuate the conditions for life on Earth. The psychological level goes beyond what is tangible and delves into the underlying connection existent between humans and their environment (Born et al., 2001; Roös, 2021). This psychological connection is explored in the concept of "biophilia," which was introduced by Fromm (1973) and later developed by Wilson (1984). The term biophilia refers to the innate attraction humans have toward nature and natural elements and is exemplified in the fields of architecture and urban planning by Kellert and Wilson (1995). The impact of biophilia can be traced to two different origins: first, being in the proximity of nature and visually interacting with natural elements (plants, animals, other people) and second, the response to biomimetic environments, which are designs that incorporate elements inspired by nature (Fromm, 1973; Wilson, 1984; Kellert and Wilson, 1995; Berto and Barbiero, 2017; Salingeros, 2019; Zhong et al., 2022). The mechanisms underlying these responses to the natural environment, as indicated by Philipp (2012), are similar to those of many other complementary and alternative medicine (CAM) therapies. External sensory stimuli releases natural opiates, such as endorphins and enkephalins, in specific regions of the brain. Thus, biophilic environmental stimuli can reduce depressive symptoms, speed up the healing process after stressful situations, and enhance cognitive function (Beute and de Kort, 2018; Gianfredi et al., 2021; Meuwese et al., 2021; Syrbe et al., 2021; Bressane et al., 2022; Szabo et al., 2022; Jin et al., 2023). These scientific insights bring a greater depth to our understanding of the strategies for incorporating biophilia in outdoor spaces design, including in urban design, cities presenting challenges in meeting environmental and societal wellbeing needs. The profound effects of biophilia demonstrate the importance of intentionally designing these spaces with a strong focus on nature, with strategies like integrating natural elements and processes, large variety of plants for a rich sensory experience and biodiversity, create habitats for wildlife, inclusion of water bodies that can add aesthetic value while providing calming sounds, generally use natural materials and mimic natural forms and patterns. A successful biophilic design encourages interaction with the natural world by integrating areas for gardening and sensory experiences, edible landscape, walking trails that incite and create curiosity, while learning about environmental systems, this leading to a stronger connection between man and nature, reinforcing the vital role of biophilia in communities, underscoring the potential for created green spaces to contribute to the environmental, physical and mental health (Soderlund and Newman, 2015; Lin et al., 2018; Xue et al., 2019; Totaforti, 2020; Russo and Andreucci, 2023). These principles find exceptional significance and their potential could be explored especially in spaces used by people that need recovery and care, in the context of healthcare facilities. Green spaces around the hospitals serve as prime locations for fulfilling the potential of biophilic design, forming a key aspect of the built environment, and also playing a significant role in the health and wellbeing of patients (Zhao et al., 2022). This importance transcends active engagement with nature; studies show that, sometimes, even a passive interaction, something as simple as a view of a natural scene from a hospital bed can have positive effects on patients that had surgical intervention, creating feelings of hope and strength that

may contribute to a more efficient recovery process (Ulrich, 1986). The healing process consists not only in providing medical care, access to treatment, and medical procedures; but also in providing a healing environment for both physical and spiritual rehabilitation (Bratman et al., 2019; Fancourt et al., 2021), since "healing is a psychological and spiritual concept of health" (Özcan, 2006). The Optimal Healing Environment (OHE) framework suggests that the healing process has both inner and outer implications, and healing spaces that incorporate natural elements may be an important factor that still needs further research (Ananth, 2008).

Looking back in history, ever since the Middle Ages, the outdoor spaces of hospitals were designed in order to provide resting places where the ill could enjoy fresh air. As modern medicine advanced and the architectural design of hospitals became increasingly complex, the incorporation of outdoor healing spaces has been varied in use, new ideas and research directions began to develop, having as goals to explore the therapeutic opportunities of healing gardens or restorative landscapes, bringing together fields like architecture, landscape design and medicine, a blend that begins to reintroduce the ancient connections between healing and nature into the contemporary medical environment (Cooper Marcus and Barnes, 1995; van den Berg, 2005). Gardens, being humanity's closest connection to the natural environment, have been and continue to be an important adjuvant in the process of stress rehabilitation being not just spaces for recovery but also for interaction and exploration. Furthermore, green spaces can be a statement to the power or adaptability and resilience, their natural cyclicity and transition through seasons suggest the potential for renewal and growth after periods of dormancy, thus serving as a metaphor for patients on their healing journey, supporting the idea of hope and resilience during challenging times (Nordh et al., 2009; Adevi and Mårtensson, 2013). Current research has shown that gardens can offer sensorial places for autistic children, giving them opportunities to spend time outdoors in a calming environment, or designed to create invigorating landscapes for hyporeactive patients (Barakat et al., 2019; Ghazali et al., 2019). Other conditions, like depression and anxiety are experienced not only by mentally ill patients, but also in cases of convalescence, post-surgery recovery, COVID-19 measures of isolation or prolonged hospital stay. Being involved in outdoor gardening activities can have an ameliorative effect on people suffering from psychological distress by alleviating symptoms (Gerdes et al., 2022; Yang et al., 2022). During the COVID-19 pandemic, the use of green spaces and parks and participating in outdoor activities enhanced young people's mental health and wellbeing, and was linked to lower the levels of emotional distress (Jackson et al., 2021; Larson et al., 2022). Designing areas surrounding hospitals as therapeutic gardens provides spaces for patients, institution staff, and family members to use and enjoy. It is proven that spending time in the garden walking, contemplating, or engaging in gardening activities could result in a decreased dosage of antipsychotics in dementia affected patients, in mood improvement and increased calmness (Rivasseau-Jonveaux et al., 2012; Whear et al., 2014). This pandemic underscored the critical role that well-designed and maintained therapeutic spaces can play in human health, and one way to ensure the effectiveness of these spaces is by conducting Post-occupancy evaluations.

Post-occupancy evaluation (POE) is a process by which the performance of a built environment is evaluated by users that

express the satisfaction level concerning the space. This helps to determine how successful the design intent is and contributes to improving the design of therapeutic spaces (Moore, 1983; Preiser et al., 2015). Even though involving the end-user in the design process helps to create more suitable environments, post-occupancy evaluation is an important tool that offers valuable insight into the newly created space from the perspective of patients, family, and staff (Jiang et al., 2018; Lygum et al., 2019). It might provide information that may not have been considered even during the participatory design process (Buse et al., 2017). The physical environment, even though it has a major influence in a patient's recovery, is not the only focus a design should have but also the social and interaction aspects, psychological or spiritual implications, thus the exploration and comprehension of the necessities that the final user has, are vital in developing an effective outcome (Abbas and Ghazali, 2011; Ghazali and Abbas, 2012a).

The presence of a garden is highly valued, and participating in garden activities can make nursing home residents feel a sense of familiarity and comfort (Eijkelenboom et al., 2017). Gardening activities or even spending time outdoors in a garden have beneficial implications in the patient's state of mind, caring for the plants and enjoying the outcome from that process can have therapeutic effects (Piat et al., 2017). Horticulture therapy, along with other forms of conventional therapy can be an adjuvant factor and make a difference in the treatment of individuals suffering from mental disorders. Being involved in activities like fruit harvesting, planting, weeding, provides patients with a sense of purpose, and a valuable opportunity to spend time outdoors (Vujcic et al., 2017).

This paper provides a unique exploration of the opportunities offered by the green spaces around healthcare facilities, specifically, their development as sensory-therapeutic gardens. While similar research focuses on the physical characteristics of such spaces, the present study delves deeper into the importance of user feedback research for the improvement of design strategies for this type of garden. This research integrates findings from a selection of existing Post-occupancy studies conducted in healthcare facilities, underlining how user experiences can meaningfully inform the design process. The gathered information has led to the identification of a set of key principles which were subsequently applied in the design of a sensory-therapeutic garden in a healthcare setting in Cluj-Napoca, Romania. The study bridges the gap between theory and practice, demonstrating how insights from the field can be transformed into design decisions and its contribution lies the way the principles are applied, integrating user feedback, and situational context to enhance the functionality and relevance of therapeutic gardens. This approach can enhance the quality of user's life while contributing to more sustainable, user-centered healthcare environments.

2 Materials and methods

The research methodology for this study consists in three distinct stages. The first stage, was the consultation of various articles focusing on Post-occupancy evaluations of healthcare facilities, with the goal of identifying key principles in therapeutic landscape design. The second stage involved on site visits for data

collection and the final stage, the application of these principles, informed by the literature and on site data, in the specific context of a sensory-therapeutic garden design in Cluj-Napoca, Romania.

2.1 Literature resources

Although not systematic, a literature exploration was conducted to gather information and better understand the key features of sensory-therapeutic gardens, selecting and examining papers that focus on the results of post-occupancy evaluations of healing spaces. From the examined literature, recurring findings were extracted to form a list of common design principles, emerging from the collective findings of multiple studies and provide a base upon which to construct a therapeutic garden that meets the needs of patients, staff, and visitors. The selected studies, each contributing to these principles, are discussed below.

In the studies by Carnemolla et al. (2021) and Giebel et al. (2022), the primary focus was on the interior design of the building of a residential aged care setting, however, they strongly emphasize the potential role of outdoor environments in enhancing the wellbeing of residents, advocating for the inclusion of natural elements in these facilities, thus providing opportunities for patients, visitors and staff to interact with nature, explore, or simply spend time outdoors. Ryan et al. (2014) and Tekin et al. (2023a,b) note that gardens, as natural healing environments, can offer a welcoming and relaxing space characterized by the presence of vegetation. The type of garden and plants used must be chosen according to the facilities' context; for instance, an abundance of seasonal plants, even appreciated by most patients, may have adverse effects on cancer patients by constantly reminding them of life's transient nature; or even traffic noises that can be disturbing. Among the sensory experiences that a garden could offer are: stimulation of the sense of smell using flower fragrance and can be carried by the wind, filling the entire space; and auditory stimulation through moving leaves, rain, birds, and water features. The tactile sense can be stimulated by vegetation through organic textures, by materials such as wood, which visually stand out, giving the space natural features.

Comments left in a visitor's book in Lady Cilento Children's Hospital (Australia) revealed that even when located in a crowded area, not having much space, there was still room for a recreational oasis to be built. There was recorded appreciation from the visitors for the numerous seating areas (benches or lawn) to admire the view or colorful plants, or outdoor equipment for physical therapy and secluded spaces for staff recovery (Reeve et al., 2017).

Further design considerations are brought to light in the Whitehouse et al. (2001) study, where, it was observed that a design skewed toward hardscape elements, led to suggestions from users for more diverse vegetation, including shade-providing trees. Younger users expressed a desire for more activities within the garden, such as gardening tasks and plant identification opportunities. Existing garden features such as the presence of water and interactive elements, the plants decor, the bright colors, and the opportunity it provides to spend time outdoors were elements mentioned as relevant and helpful in the design. These examples illustrate the complexity of users needs and preferences in the context of sensory-therapeutic garden design, and further inform the evolving list of design principles.

A POE study of a rooftop hospital garden by Davis (2011) concluded that providing easy access and visibility to the garden encourages exploration. The study mentioned that the space should

be organized to avoid ambiguity and help patients get around instead of creating confusion, and long-term maintenance should be another aspect to consider in the design process. Providing



FIGURE 1
Design process.

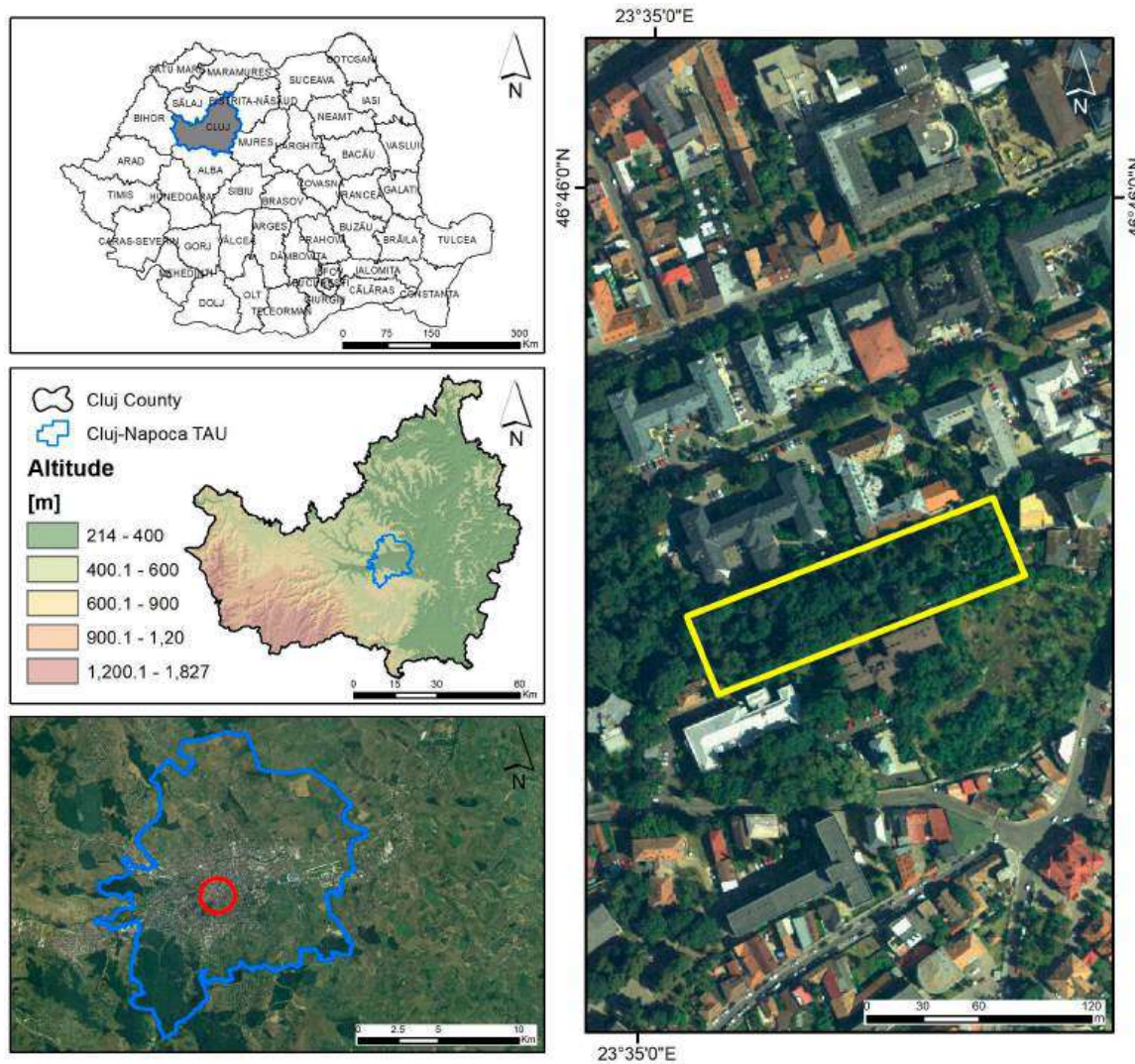


FIGURE 2
Geographic location of the study area; TAU: territorial administrative unit.

comfortable shaded seating is recommended, and also creating secluded spots for individuals who want privacy might contribute to the design's use. This understanding is reinforced by research conducted across various children's hospitals in Texas, where the provision of shade was found to create a desirable ambiance and positively influence visitor decisions to spend time in the garden (Pasha, 2013). The quality and quantity of seating areas also directly impacted the frequency and duration of visits. Children, being

more active, particularly benefited from a diverse range of garden activities. Additionally, staff members were found to value secluded areas where they could take breaks away from patients, walk or socialize. Notably, staff visits to the garden were seldom solitary, indicating a demand for personal space and time (Sherman et al., 2005; Naderi and Shin, 2008).

The role of gardens extends beyond the mere provision of a physical space. The literature points to a profound psychological

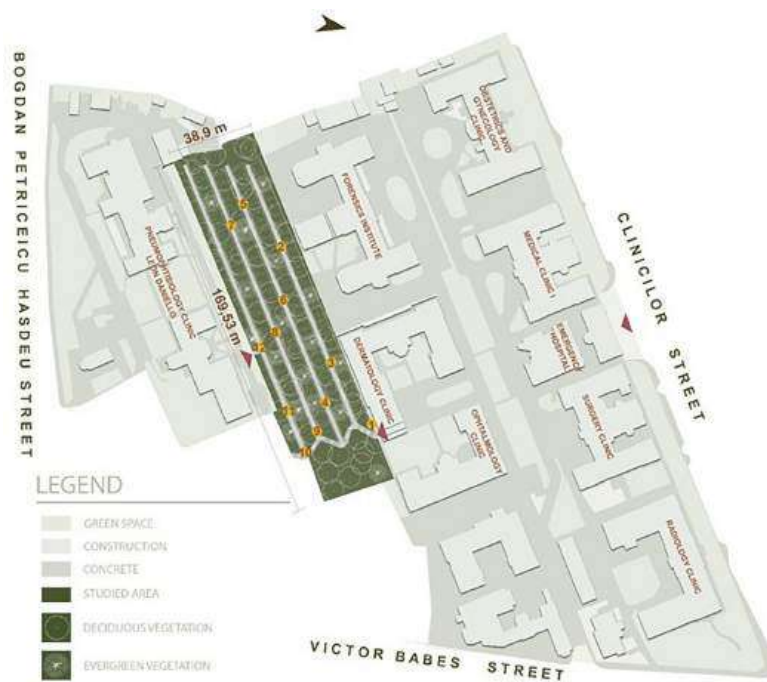


FIGURE 3 Site location.



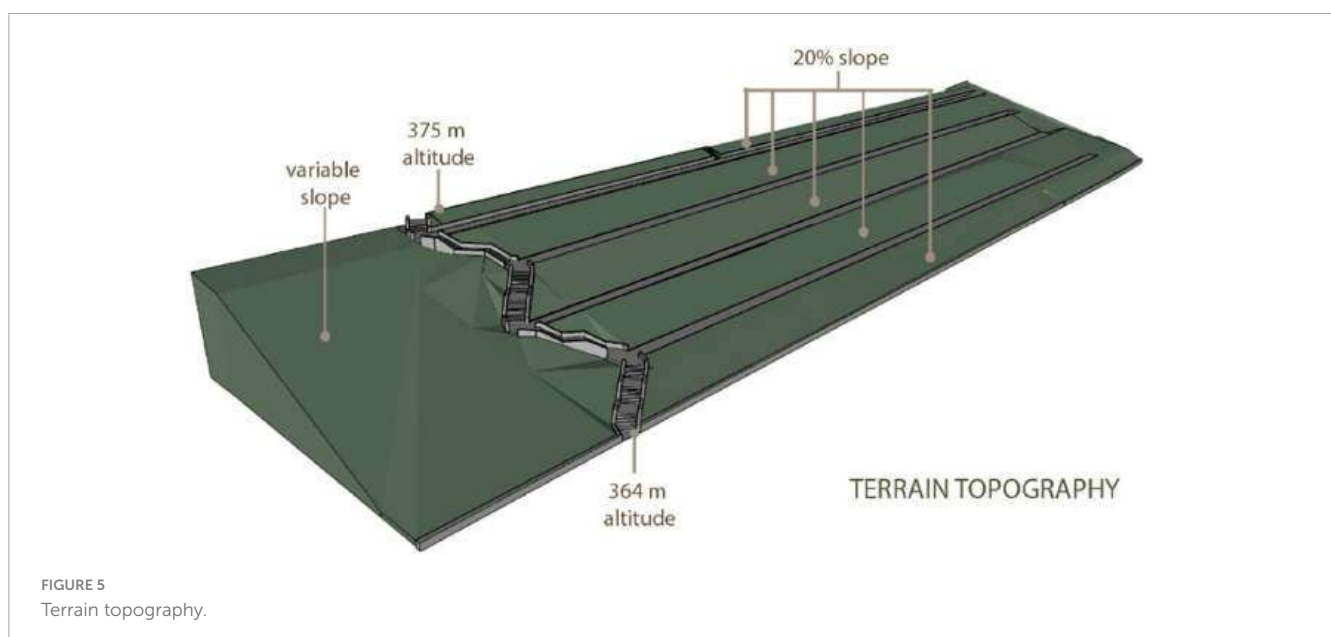
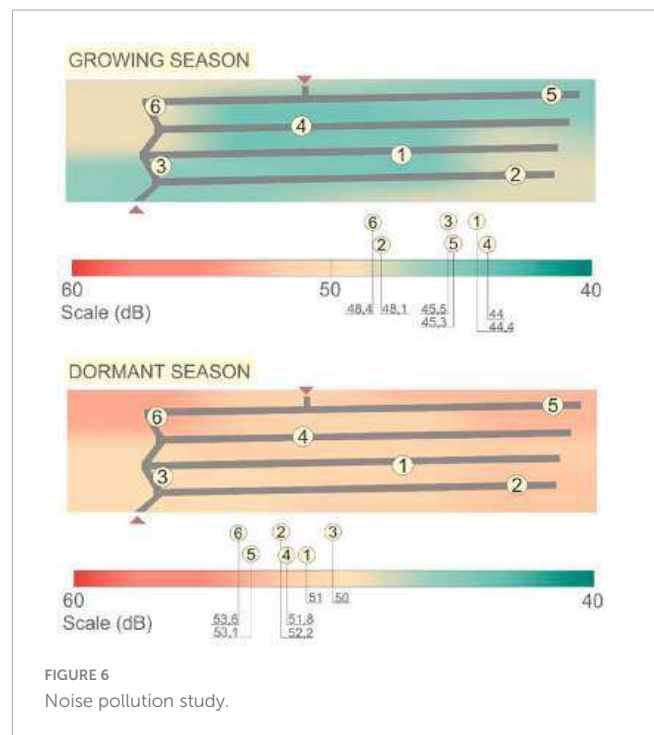
FIGURE 4 Site photographs.

impact resulting from the presence and use of a garden (Boffi et al., 2022). For example, Eijkelenboom et al. (2017) suggests that the simple presence of a garden in nursing homes settings greatly contributes to residents' comfort and familiarity, furthermore, the act of getting involved in gardening activities has been proven to have therapeutic benefits, improving the mental state of patients (Piat et al., 2017). Horticulture therapy, along with other forms of conventional therapy can be an adjuvant factor and make a difference in the treatment of individuals suffering from mental disorders. Being involved in activities like fruit harvesting, planting, weeding, provides patients with a sense of purpose, and a valuable opportunity to spend time outdoors (Davis, 2001; Vujcic et al., 2017). These findings underline the importance of not only incorporating a garden within the healthcare facility but also creating opportunities for users to interact with the garden, further informing the principles for designing sensory-therapeutic gardens.

Based upon the findings in the selected literature, a series of recurring design principles have been identified, supporting the creation of sensory-therapeutic gardens that meets the needs of patients, staff and visitors:

- a. Contextual design: the selected vegetation and the design of the space should fit the specific context of the healthcare facility, factors like climate, native species and specific user demographics should guide design decisions.
- b. Organization: the design should minimize ambiguity and confusion risk, be well organized, facilitating user navigation through the space.
- c. Accessibility and visibility: the garden should be visible and inviting, easily accessible to all users.
- d. Sensory stimulation: the design should leverage vegetation and natural processes for sensory stimulation.
- e. Biodiversity: the presence of wildlife, such as bees, butterflies, squirrels should be encouraged.
- f. Shade and seating: in order to meet users' needs for relaxation and rest, plenty of seating areas and shade should be provided.

- g. Softscape dominance: a dominance of vegetation over the hardscape elements is more appreciated.
- h. Water features: including water elements in the design can improve users' sensory experience and therapeutic qualities of the space.
- i. Staff privacy: private areas for staff are necessary to be included in the design.
- j. User interaction with nature: opportunities for the user to interact with the garden and natural elements directly should be provided through activities (planting, weeding, fruit/medicinal plants harvesting, sensory experiences).



2.2 The design process

The design process began with the identification of design principles in literature exploration, which later guided the design, translating them into the unique context of the site in Cluj-Napoca, Romania.

The second stage consisted in an onsite visit for data collection (sound measurements using Decibel Meter and Recorder eS528L, ennoLogic), developing a comprehensive understanding of the site's topography, and in order to create a visual record of the site's current state, photographic documentation was carried out. These specific site conditions, coupled with the insights from the literature, informed the design decisions, ensuring that the resultant design was both theoretically sound and contextually appropriate. The last stage consisted in applying the insights from the design principles to incorporate them into the sensory-therapeutic garden design concept, in order to create a space for healing and wellbeing. In order to validate the garden design we analyzed how well the key features revealed by the scientific literature were integrated into the design concept (Figure 1).

For the representation of graphical elements such as 2D plans or renderings, CorelDraw Graphics Suite X8, SketchUp Pro 2021 and Photoshop CS5 software were used.

2.3 Design proposal and representation of the graphical elements

2.3.1 Site location and context

The studied site is located in Cluj-Napoca, an academic city in the North-Western part of Romania (Figure 2). The site is close to the city center, being part of the University Clinics Ensemble. It is represented by a terraced green space, having a 6,593 m² surface in the near proximity to the Ophthalmology,

Dermatology, Pneumophysiology, and Forensic Clinics and close to the Emergency, Radiology, Gynecology and Surgery Clinics (Figure 3). In the early plans of the Clinics, this green space was built to provide recreational space for the patients and the medical staff. Nowadays, the area is used only for transit due to its degradation.

2.3.2 The studied area—Current situation

As the photographs taken on the site show (Figure 4), the terrain has abundant natural vegetation invading the space and overshadowing it (*Fraxinus excelsior*, *Acer pseudoplatanus*, *Rosa canina*, *Rubus idaeus*, *Sambucus nigra*, *Fagus sylvatica*, *Phalaris arundinacea*, *Campanula rapunculoides*, *Hedera helix*), sometimes with fallen trees blocking the way. The drainage system is clogged by vegetation and the pathways are also covered with obstruction by plants. The concrete railing, the stairs, and the alleys show significant signs of decay (Figure 4).

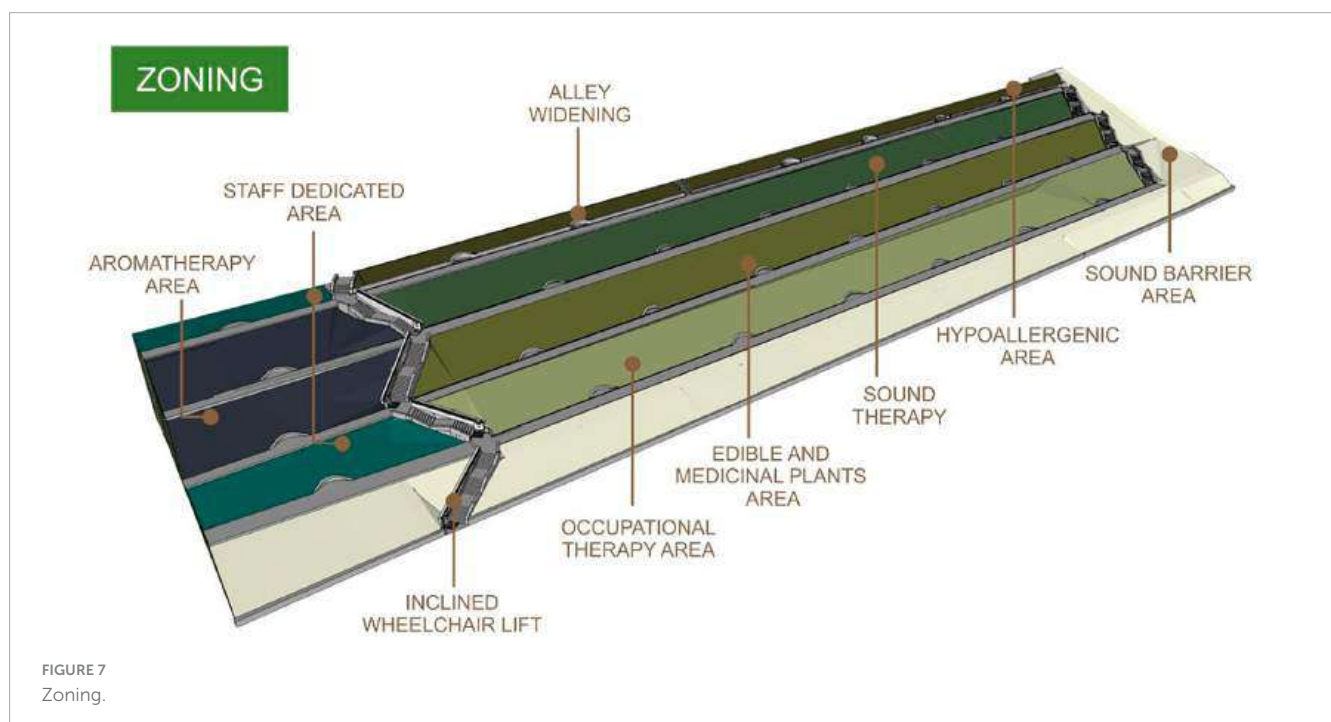
2.3.3 Terrain morphology

The studied site consists of four terraces and five slopes of approximately 20% and the 11 meters difference between the areas is linked by concrete stairs. At the edges of the terraces, the land is unlevel. The terrace in the proximity of the stairs has a variable slope, and one can observe that in the past, that zone was also terraced (Figure 5).

3 Results

3.1 Noise pollution study

Even though the site is located far from the surrounding streets, a noise pollution study was needed to reduce noise levels. The



human ear is comfortable with sounds between 40 and 60 dB, and the site resides in this range both in the growing season and in the dormant period, with higher measured levels of noise during the leafless stage. The central areas are more protected by vegetation during the growing season while the peripheral zones are a bit affected by nearby traffic (Figure 6).

3.2 Design proposal—Zoning and masterplan

A major design recommendation would be for the space to be cleaned of unwanted vegetation, keeping only the healthy trees providing shade—a key feature identified in the literature review. Additionally, it's advisable to trim the overcrowding indigenous bushes so that the sun and light make room inside the space.

Based on the design principles and the results of the site visit, the proposed design has a primary aim to create a recreational space that alleviates the patient's state, acts as adjuvant in the healing process and encourages the visitor's interaction with nature,

by using diverse textured plants or materials, and create activity-engaging opportunities like fruit or flower harvesting, gardening or long walks. This approach addresses the principle for providing opportunities for users to interact with the garden directly. Due to the present configuration of the terrain, it is considered opportune to split the site into seven main areas. Each terrace-slope ensemble would have specific tasks creating platforms with different purposes (occupational therapy, edible and medicinal plants, sound therapy, hypo-allergenic area). The area near the stairs would serve two purposes, the central part would be dedicated to an aromatherapy area. The upper and lower extremities, being isolated, would create spaces for the medical staff to relax, supporting the principle for a more private area for staff. The peripheral areas would act as sound barriers, for the possible much-elevated noise values after the unnecessary vegetation removal (Figure 7).

It is considered that the purposes of the created areas would serve not only the patients with sensory deficiencies (ophthalmological or dermatological) but would also act as comfort zones for post-surgery recovering patients, new mothers, and individuals with respiratory conditions. This fits the clinics' context,

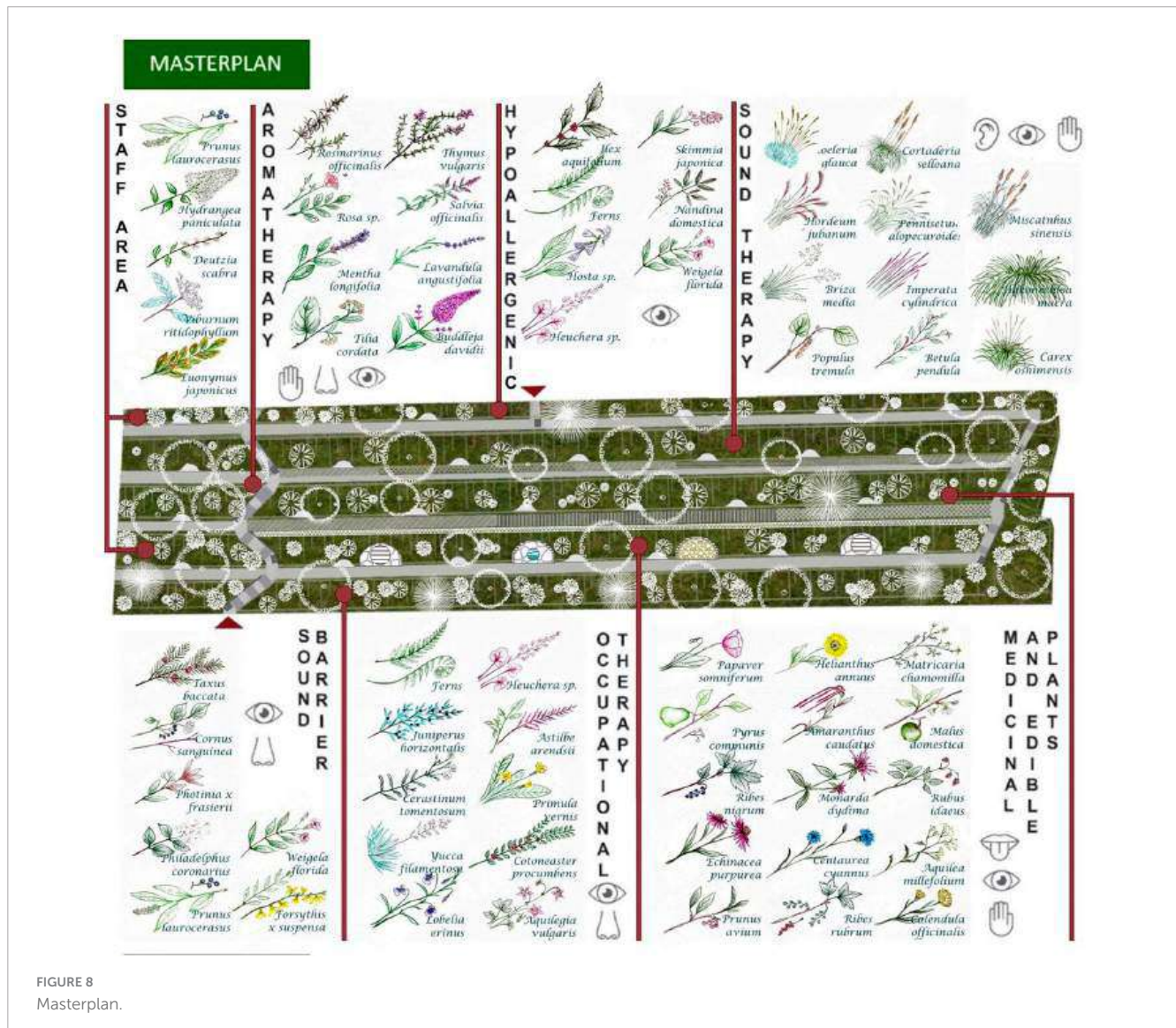


FIGURE 8 Masterplan.

TABLE 1 The proposed plant material that would reflect and enhance the functions of the intended area, along with various features.

Species	Aromatic properties	Therapeutic effects	Decorative elements	Tactile experience	Plant type/growth habit/decorative period
<i>Tilia cordata</i>	Soft pleasant scent; attracts pollinators	Contains volatile organic compounds that released into the air have calming effect; its scent can help promote relaxation and create a peaceful atmosphere (Arcos et al., 2006; Al-Essa et al., 2007; Redzic, 2010)	Heart-shaped vibrant green colored leaves; clusters of cream-colored flowers	Rough mature bark, smoother texture of younger trees or branches; delicate flowers, soft leaves	Perennial/tree/early to mid-summer
<i>Buddleja davidii</i>	Sweet, honey-like fragrance; attracts pollinators	Mood improvement; positive effects on the respiratory and nervous systems (Hikal et al., 2022)	Colorful inflorescences; soft, grayish-green foliage	Rough bark on the stems and branches; smooth fuzzy textured leaves; soft, velvety flowers	Perennial/shrub/summer-early autumn
<i>Lavandula angustifolia</i>	Sweet, floral, herbaceous scent; attracts pollinators	Calming effects of the nervous system; improves sleep quality and alleviates headaches; reduces stress, anxiety, and symptoms of depression (Yaghoobi et al., 2016; de Melo Alves Silva et al., 2023)	Gray-green foliage; dense spikes or purple flowers	Soft textured leaves; it releases a gentle fragrance when the leaves or flowers are rubbed, adding to the sensory experience; soft, delicate flowers with velvet texture	Perennial/shrub/late spring to late summer
<i>Mentha longifolia</i>	Fresh scent, slightly sweet; attracts pollinators	Cooling and invigorating effect on the senses, stimulates the mind and improves concentration (Hanafy et al., 2020)	Small lilac flowers arranged in whorls; bright green colored leaves, grow densely on the stems, creating a lush appearance	Soft slightly velvety textured leaves; square-shaped slightly ridged stems; it releases a gentle fragrance when the leaves are crushed, adding to the sensory experience	Perennial/herbaceous/mid-summer-early autumn
<i>Salvia officinalis</i>	Strong, herbaceous, slightly floral, earthy scent; attracts pollinators	Reduces stress and anxiety, enhances mental clarity, and improves memory (Kennedy et al., 2005)	Gray-green leaves; small tubular purple flowers that grow in whorls along the stems	Leaves and stems with slightly rough texture	Perennial/herbaceous/late spring to early summer
<i>Rosa damascena</i>	Rich, floral scent; attracts pollinators	Mood-enhancing properties; petals can be used in herbal tea blends or as natural air freshener (Vinokur et al., 2006; Baydar and Baydar, 2013)	Abundant pink flowers; pinnate green leaves	Soft, velvety petals	perennial/shrub/late spring to early summer
<i>Rosmarinus officinalis</i>	Strong, woody, refreshing scent; attracts pollinators	Improves mental clarity, focus and memory; has calming effect on the nervous system, helps relieve stress and anxiety; used in aromatherapy to ease respiratory problems such as congestion and coughing (Hamidpour et al., 2017; Rahbardar and Hosseinzadeh, 2020)	Needle-like leaves, dark green and glossy; small, blue-violet flowers	Slightly rough leaves with a waxy surface; It releases a gentle fragrance when the leaves are crushed, adding to the sensory experience	Perennial/shrub/early spring to late summer
<i>Thymus vulgaris</i>	Strong pleasant, herbal aroma with hints of mint and slightly spicy; attracts pollinators	Supports respiratory health; has calming and soothing scent; improves focus and concentration (Rizwan, 2021)	Small narrow leaves with a grayish-green color; small pink flowers	Fuzzy textured leaves; it releases a gentle fragrance when the leaves are crushed, adding to the sensory experience	Perennial/shrub/late spring to early summer

as one of the key features suggested, while also providing outdoor space for visiting family or medical staff. The occupational therapy, aromatherapy, edible and medicinal plants areas are more activity oriented, and the rest of the garden focuses more on nature contemplation and relaxation, bringing balance to the

static/dynamic ratio of the garden. Every zone would have plenty of seating areas regardless of its use, no matter if they would be used by the patients or companions. Given the fact that the stairs are the main and only access in the garden, installing an inclined platform stair lift for disabled people would be crucial.

This will facilitate access as the literature design principles suggest, and additionally create widened spaces in the alleys at 15-meter intervals for the wheelchairs to comfortably pass each other, as the alleys maximum width does not pass 1.70 meters (Figure 7). The area would be accessed through the four long alleys that cross it from one end to the other in order to prevent confusion in perceiving the environment. Also, the entrance in each zone would have signage so that the visitor would have a choice whether to explore that area and create expectations concerning the possible experiences, and provide visibility and clarity to the space, according to the principles (Figure 8). Since the presence of wildlife is a key feature in a healing garden design, animating the spaces and enchanting the viewers, the installation of bird houses and feeders, insect hotels and bat boxes is recommended in each area. Overall, the proposed design primarily seeks to create a recreational space that aids in the healing process, promotes interactions with nature and provides engagement opportunities, meeting the principles of a well-organized space, being aligned with the facility profile, providing direct access and visibility.

3.3 Aromatherapy area

The space near the stairs would be an extension of the existing terraces, thus creating continuity in the design and accessibility. The central area of this space would be dedicated to aromatherapy. Besides the olfactory stimulating vegetation and resting places, bird baths and container ponds would bring movement and sound, by the presence of water elements, encouraging wildlife, offering sensory stimulation and integrating water features being between the found key features. Plant harvesting would be encouraged and have not only a momentary effect, but allow patients to keep near their beds the flowers they have gathered would extend the pleasant olfactory experience they had outdoors. This would offer opportunities for the patients to interact with the garden directly, as the design principles suggest. The proposed plant material that would reflect and enhance the functions of this area, along with various features, are described in Table 1. The profile of the area would be designed accordingly to the facility profile, contributing to the overall organization of the space having a central location and accessibility, and meeting other literature key features like shaded sitting areas and softscape dominance.

3.4 Medicinal and edible plants area

This area contains species with curative role and edible plants, supporting the healthcare function of the facility. The sensory alley has a greater variety of materials (mulch, different types of stone, lawn, pine cones, wood, or wood chips) and it is accompanied by a concrete alley on its entire length to facilitate mobility, overall contributing to the principles of a well-organized and accessible space. Besides the generous pathway, the space can also be explored by the adventurous on the scattered stepping wood logs arranged on the slope (Figure 9). Visitors can recognize and learn about the medicinal plants and their healing properties from information panels. Plant harvesting and

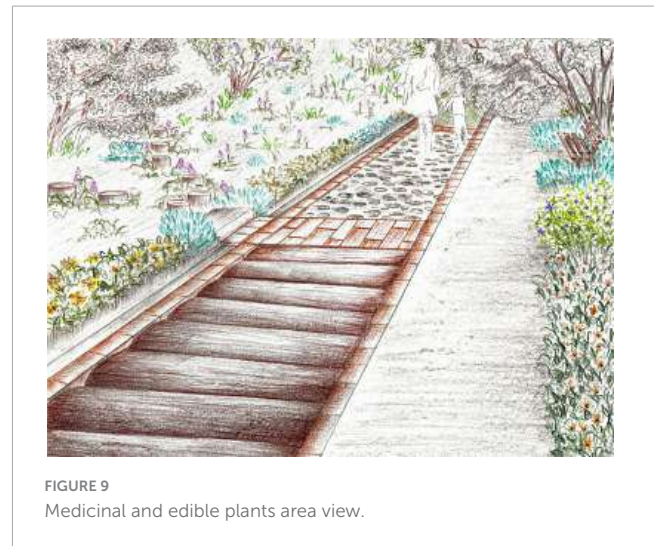


FIGURE 9
Medicinal and edible plants area view.

fruit eating would be suggested activities, encouraging movement and providing gustatory stimulation, being in line with the key findings of providing sensory stimulation and interaction with nature. The proposed plant material that would reflect and enhance the functions of this area, along with various features, are described in Table 2. Various plant species would encourage the presence of wildlife and the dominance of softscape, while the space can be enjoyed also from shaded sitting areas as the literature's findings suggest.

3.5 Occupational therapy area

Since the importance of activity in therapeutic gardens was highlighted, it was considered necessary to create a space where the patients could be directly involved in gardening activities in specifically designed areas, such as U-shaped pockets in the slopes with accessible raised beds (Figure 10). The area also contains a sand play zone and a water fountain. These features would align with the principles of a well-organized space and encourage interaction with the natural environment. The presence of a water feature (recommended in the key features) associated with indigenous vegetation like the ferns give the place a wilderness vibe, and according to the key feature list, plants would offer sensory stimulation and habitat for wildlife, dominating the hardscape. The space can be explored following a pathway divided into three different sensory-stimulating materials (gravel with stepping stones, grass, stone, and wood slices). The proposed plant material that would reflect and enhance the functions of this area, along with various features, are described in Table 3.

3.6 Sound healing area

To complete the idea of a sensory-therapeutic garden it is beneficial for the inclusion of a sound stimulation area. The plants from the *Poaceae* family are representative for the pleasant noises they make when wind blows and are characterized as relaxing.

TABLE 2 Plants proposed for the medicinal and edible plants area and their features.

Species	Medicinal/edible features	Therapeutic effects	Decorative elements	Tactile experience	Plant type/growth habit/decorative period
<i>Papaver somniferum</i>	Edible seeds	Medical use for pain relief; attracts birds and other pollinators (Bao and Zhu, 2022)	Large flowers in shades of red, pink, purple or white	Silky petals, smooth leaves	Annual/herbaceous/late spring to early summer
<i>Helianthus annuus</i>	Edible seeds	Rich in nutrients seeds; attractive to butterflies, birds, and bees (Pal, 2011)	Large, composite inflorescences with prominent yellow ray florets surrounding a brown disk	Hairy stems, rough leaves	Annual/herbaceous/summer to early fall
<i>Matricaria chamomilla</i>	Flowers	Calming, soothing, reduces inflammation; attracts bees and other pollinators (Mao et al., 2016; Amsterdam et al., 2020)	Small, radiate capitula with white ligulate ray florets and yellow tubular disk florets	Feathery leaves, silky flowers	Annual/herbaceous/summer
<i>Pyrus communis</i>	Edible fruits	Provides vitamins and fibers; attractive to butterflies, birds, and bees (Kolniak-Ostek, 2016; Simionca Mărcășan et al., 2023)	White blossoms, aesthetically pleasing foliage	Smooth bark and leaves, glossy fruit surface	Perennial/tree/spring to fall
<i>Amaranthus caudatus</i>	Edible seeds and young leaves	Rich in nutrients; attractive to butterflies, birds, and bees (Gamel et al., 2004)	Pendulous red inflorescences	Rough leaves and stems, soft inflorescences	Annual/herbaceous/summer to early fall
<i>Malus domestica</i>	Edible fruits	Rich in vitamins and fiber; attractive to butterflies, birds, and bees (Patocka et al., 2020; Sestras and Sestras, 2023)	White or pink flowers in spring, colored fruits in autumn	Rough textured bark, smooth leaves, and fruit	Perennial/tree/spring to fall
<i>Ribes nigrum</i>	Edible berries	High in vitamin C, supports immune system health; attractive to butterflies, birds, and bees (Karjalainen et al., 2009)	Racemes of greenish-yellow flowers followed by black berries	Hairy leaves, smooth berries	Perennial/shrub/spring to fall
<i>Monarda didyma</i>	Edible flowers and leaves	Antiseptic, antibacterial, antifungal; attractive to butterflies, birds, and bees (Côté et al., 2021)	Vibrant red flowers that attract pollinators	Slightly rough textured leaves, soft flowers	Perennial/herbaceous/summer
<i>Rubus idaeus</i>	Edible berries	High in vitamin C; attractive to butterflies, birds, and bees (Zhbanova, 2019)	White flowers that develop into red berries	Soft and fuzzy leaves; delicate hairy flowers	Perennial/shrub/spring to fall
<i>Echinacea purpurea</i>	Roots, leaves and flowers	Boosts immune system, reduces inflammation; attractive to butterflies, birds, and bees (Goel et al., 2005)	Large, daisy-like flowers with purple ligules and orange-brown central cones	Soft and smooth petals	Perennial/shrub/summer to fall
<i>Centaurea cyanus</i>	Flowers	Mild anti-inflammatory and soothing properties; attractive to butterflies, and bees (Garbacki et al., 1999)	Blue, purple, pink, or white flowers with involucre bracts	Silky petals, rough leaves	Annual/herbaceous/late spring to early fall
<i>Achillea millefolium</i>	Aerial parts of the plant	Anti-inflammatory, antispasmodic, astringent effects; attracts bees and butterflies (Tadić et al., 2017)	Flat-topped corymbs with white, yellow, pink, or red flowers	Feathery leaves, smooth flowers	Perennial/herbaceous/summer to fall
<i>Prunus avium</i>	Edible fruits	Rich in vitamins and antioxidants; attractive to bees, and other pollinators, birds are attracted to the fruit (Kelebek and Selli, 2011; Nunes et al., 2021)	White or pink blossoms in spring, followed by red berries	Smooth bark and leaves	Perennial/tree/spring to fall
<i>Ribes rubrum</i>	Edible berries	High in vitamin C, supports immune system health; attractive to bees, and other pollinators, birds are attracted to the fruit (Zdunić et al., 2016)	Greenish-yellow flowers followed by red berries	Slightly hairy leaves, smooth berries	Perennial/shrub/spring to fall
<i>Calendula officinalis</i>	Edible flowers	Reduces inflammation, promotes skin health; attractive to bees, and other pollinators (Parente et al., 2012; Silva et al., 2021)	Liguliflorous capitula with bright orange ray florets	Smooth petals, slightly rough leaves	Annual/herbaceous/spring to fall

The feeling of calmness is highlighted also by their diaphanous appearance. Additional species that would complement the planting are *Populus tremula*, *Betula pendula*, *Campanula* sp., and also the placement of garden bells. Even though this zone has a primarily purpose relaxing and the enjoyment of sound is made by vegetation, tactile exploration experience is also encouraged,

since ornamental grasses are known for their captivating texture. The proposed plant material that would reflect and enhance the functions of this area, along with various features, are described in Table 4. The area provides a variety of sensory stimulation through the presence of plants and not only, this providing habitat for wildlife and dominance of the softscape while supporting and



FIGURE 10 Occupation therapy area view.

3.7 The hypo-Allergenic area

Being in the proximity of the Pneumophthiziology Institute, it is necessary to create a safe space for the patients with respiratory diseases, taking in consideration the facility profile, as the key feature suggest. Pollen is considered to be a major allergenic factor and the use of plants with none or few flowers is recommended (such as ferns, *Buxus* sp., *Euonymus* sp.). Non-flowering plants still contribute to the sensory stimulation, especially tactile and visual, and for providing habitat for wildlife. The space has plenty of shaded sitting areas for rest or to enjoy a pleasant conversation in an outdoor space, aligning with the principles. The planned plant material, together with different characteristics, that would reflect and improve the functions of this area are listed in [Table 5](#).

3.8 Sound barrier area

Even though the sound study didn't reveal any concerning results regarding the noise, once the invading vegetation is removed, it is considered necessary to incorporate the abundant

creating opportunities to interact with the materials and relax in shaded sitting area, these components are in alignment with the key features of therapeutic garden design.

TABLE 3 Plants proposed for the occupation therapy area and their features.

Species	Therapeutic effects	Decorative elements	Tactile experience	Plant type/growth habit/decorative period
Ferns	Stress reduction, connection to nature due to its texture; air purification; attracts bees and butterflies (Lee and Shin, 2010)	Delicate, feathery foliage in various nuances of green	Soft, feathery, finely textured fronds offer a delicate tactile experience	Perennial/herbaceous/spring to fall
<i>Heuchera</i> sp.	Raises interest and creates a relaxing environment due to diverse foliage colors (Xu et al., 2023)	Colorful foliage in shade of green, purple, bronze, silver; delicate bell-shaped flowers	Diverse textures from smooth, slightly ruffled, or veined leaves; delicate small flowers	Perennial/herbaceous/spring to fall
<i>Juniperus horizontalis</i>	Calming effects, has evergreen foliage that can create a sense of stability and continuity; provides nesting opportunities for birds (Cantrell et al., 2014)	Attractive blue-green foliage	Needle-like foliage, spiky texture	Perennial/shrub/year-round
<i>Astilbe arendsii</i>	Attracts pollinators, promotes relaxation (Kharchenko et al., 2016)	Plumes of flowers in various colors	Feathery flowers	Perennial/herbaceous/spring to late summer
<i>Cerastium tomentosum</i>	Provides visual contrast and rises interest; attractive to bees and other pollinators (Khalaf and Stace, 2001)	Silvery foliage and masses of small star shaped white flowers	Soft, velvet textured leaves	Perennial/herbaceous/spring to fall
<i>Primula Veris</i>	Colorful flowers can uplift moods and reduce stress stimulating the senses; attracts bees and butterflies (Tarapatsky et al., 2021)	Bright colorful flowers	Smooth flowers with silky texture	Perennial/herbaceous/spring
<i>Yucca filamentosa</i>	Provides visual interest; attracts pollinators (Althoff et al., 2005)	Sword-shaped leaves and creamy-white bell-shaped flowers	Stiff leaves	Perennial/shrub/year-round
<i>Cotoneaster procumbens</i>	Calming effects, has evergreen foliage that can create a sense of stability and continuity provides habitat for wildlife (Dmitruk et al., 2022)	White small flowers, red berries	Smooth, glossy textured leaves	Perennial/shrub/year-round
<i>Lobelia erinus</i>	Colorful flowers can uplift moods and reduce stress stimulating the senses; attractive to butterflies (Folquitto et al., 2019)	Tubular flowers in shades of blue, violet, pink or white	Smooth leaves, delicate flowers	Annual/herbaceous/late spring to early autumn
<i>Aquilegia vulgaris</i>	Graceful nodding flowers that can promote relaxation, offer visual stimulation, and attract pollinators (Hassan et al., 2010)	Various colored flowers	Lacy leaves with soft flowers	Perennial/herbaceous/late spring to early summer

TABLE 4 Plants proposed for the sound healing area and their features.

Species	Sound-generating features	Therapeutic effects (He et al. 2022)	Decorative elements	Tactile experience	Plant type/growth habit/decorative period
<i>Koeleria glauca</i>	Leaf and inflorescence movement	Calming rustling sounds; the seeds can be foods for birds	Silvery-blue foliage	Fine leaves, delicate seed heads	Perennial/herbaceous/late spring to early summer
<i>Cortaderia selloana</i>	Inflorescence and foliage movement	Soothing swaying plumes, rustling leaves; the seeds can be attractive to birds	Tall, elegant inflorescences; green to golden foliage	Feathery texture; slender leaves with sharp edges	Perennial/herbaceous/late summer to early winter
<i>Hordeum jubatum</i>	Leaf and inflorescence movement	Calming rustling sounds; the seeds can be attractive to birds	Slender, arching inflorescences; green to golden foliage	Fine, feathery texture	Perennial/herbaceous/late spring to autumn
<i>Pennisetum alopecuroides</i>	Inflorescence and foliage movement	Relaxing swaying plumes, rustling leaves; the seeds can be attractive to birds	Bottlebrush-like plumes, arching foliage	Fluffy plumes, soft texture	Perennial/herbaceous/summer to fall
<i>Miscanthus sinensis</i>	Foliage interaction and inflorescence movement	Calming rustling sounds, swaying plumes the seeds can be attractive to birds	Arching foliage with silver/pink plumes	Smooth leaves, feathery inflorescences with a silky touch	Perennial/herbaceous/late summer to winter
<i>Briza media</i>	Seed head movement and foliar interaction	Soothing seed head movement; the seeds can be attractive to birds	Delicate seed heads	Fine leaves, delicate seed heads that create a light, airy texture	Perennial/herbaceous/late spring to early summer
<i>Imperata cylindrica</i>	Foliage interaction and inflorescence movement	Gentle rustling sounds	Striking red to crimson foliage	Smooth leaves with sharp edges	Perennial/herbaceous/summer to fall
<i>Hakonechloa macra</i>	Foliage interaction and plant sway	Delicate swaying	Cascading, bright green foliage	Smooth, flowing texture	Perennial/herbaceous/spring to fall
<i>Populus tremula</i>	Foliage interaction and plant sway	Calming rustling leaves, swaying branches; attracts bees, provides cover and nesting opportunities for birds	Fluttering leaves	Smooth leaves with fine veins and rough branches	Perennial/tree/spring to fall
<i>Betula pendula</i>	Foliage interaction and branch movement	Soothing, whispering leaves, swaying branches; attracts bees and other pollinators, provides cover and nesting opportunities for birds	Pendulous, graceful branches; white bark	Smooth leaves, rough textured bark	Perennial/tree/year-round
<i>Carex oshimensis</i>	Foliage movement and plant sway	Gentle rustling sounds	Arching foliage in various shades of green	Smooth, arching leaves	Perennial/herbaceous/year-round

use of trees and bushes with great variety of decorative elements to minimize sounds (i.e., *Photinia × fraseri*, *Weigela florida*, *Cornus sanguinea*, *Prunus laurocerasus*). This area would not only decrease the sound coming from passing cars passing but also add an aesthetic part to the garden by having an animating and refreshing effect. Table 6 describes the suggested plant material that would represent and enhance the functions of this space, as well as various ornamental aspects. The plant material would serve as visual stimulation, but the absorption of sound would contribute to the auditory comfort of the area, minimizing the external noise, thus enhancing other pleasant auditory stimulation, as the key features suggest.

3.9 Dedicated employee area

Taking in account the fact that medical staff need privacy, and considering the site's structure, the most suited zones dedicated to

the healthcare professionals are the ones at the left extremities of the garden. The upper area would serve the personnel from the Pneumophtisiology clinic, while the lower area would serve the specialties in its proximity. The vegetation would not present much diversity in colors nor textures, mostly composed by green shrubs. The suggested benches would have the proper dimensions for users to recline, thus creating a non-triggering, neutral background for relaxation. Table 7 details the suggested features and plant material that would accurately reflect and improve upon the area's many uses, dominating the hardscape, providing habitat for wildlife and privacy as the design principles suggest.

4 Discussion

Green spaces within the proximities of hospitals offer opportunities for patients to break a monotonous daily indoor routine and to spend time in nature. It is also beneficial for

TABLE 5 Plants proposed for the hypo-allergenic area and their features.

Species	Allergenic potential	Therapeutic effects	Decorative elements	Tactile experience	Plant type/growth habit/decorative period
<i>Ilex aquifolium</i>	Low (female cultivar- does not produce pollen)	Calming effects, has evergreen foliage that can create a sense of stability and continuity; attracts birds with their berries (Obeso, 1998)	Glossy, dark green leaves; bright red berries that add color during autumn and winter	Glossy, stiff leaves with spiny edges	Perennial/shrub/year-round
Ferns	Low, they do not produce pollen	Stress reduction, connection to nature due to its texture; air purification (Mannan et al., 2008; Lee and Shin, 2010)	Delicate, feathery foliage in various nuances of green	Soft, feathery, finely textured fronds offer a delicate tactile experience	Perennial/herbaceous/spring to autumn
<i>Nandina domestica</i>	Low, produces minimal pollen, it's not known to cause significant allergy issues	Creates a relaxing environment through visually appealing foliage and wildlife attraction; can attract butterflies and birds	Colorful, lacy foliage that changes color throughout the seasons; produces clusters of white flowers in spring and red berries in autumn	Lacy, compound leaves with slender, smooth leaflets	Perennial/shrub/year-round foliage, white flowers in spring, red berries in autumn
<i>Skimmia japonica</i>	Low, female cultivars do not produce pollen	Relaxing effects due to the evergreen foliage, evokes the idea of continuity; wildlife attraction; attracts bees and butterflies (Brndevska and Rizovska Atanasovska, 2012)	Glossy, dark green leaves provide year-round interest; fragrant pale pink flowers in spring and colorful berries in autumn	Smooth, glossy leaves; smooth textured small flowers	Perennial/shrub/year-round foliage, flowers in spring, colorful berries in autumn
<i>Hosta</i> sp.	Low, produces minimal pollen, is not known to cause allergy issues	Creates a relaxing atmosphere in shading areas due to the bold, visually appealing foliage; attractive to bees and other pollinators (Suzuki et al., 2002)	Large, bold leaves in various nuances of green; spikes of trumpet-shaped flowers	Diverse textured, smooth, veined foliage with slightly wavy or ruffled margins	Perennial/herbaceous/foliage -spring to autumn, flowers in summer
<i>Weigela florida</i>	Low, produces minimal pollen	Suggests calmness and relaxation due to the flexed branches abundant in flowers; attractive to butterflies and bees (Stawiarz and Wróblewska, 2016)	Arching branches with abundant trumpet-shaped flowers	Smooth leaves; delicate flowers	Perennial/shrub/spring to early summer flowering and foliage until autumn
<i>Heuchera</i> sp.	Low, produces minimal pollen	Raises interest and creates a relaxing environment due to diverse foliage colors; attracts pollinators (Andruk, 2017)	Colorful foliage in shade of green, purple, bronze, silver; delicate bell-shaped flowers	Diverse textures from smooth, slightly ruffled, or veined leaves; delicate small flowers	Perennial/herbaceous/spring to autumn foliage, spring to summer flowers

family members and visitors to interact with patients in a comfortable, relaxing environment and for the medical staff to have a peaceful place to retreat during a break. Using program elements like the present study suggests can help to redeem underutilized places in healthcare areas and help to transform them into healing environments (Cordoza et al., 2018; Weerasuriya et al., 2019). This paper adds to this body of knowledge by presenting an integrated approach toward designing sensory-therapeutic gardens. Drawing from a range of literature sources focusing on Post-occupancy Evaluations, rather than conducting a traditional literature review, to gather a set of key principles for therapeutic garden design. However, despite the design principles presented in this study, the design of sensory-therapeutic gardens remains a challenge due to the complexities of users' needs and specific site conditions, underpinning the need for continuous

refinement and adaptation of design principles based on site-specific evaluations (Jiang, 2014; Thaneshwari et al., 2018). Our research included a literature exploration of various articles focusing on Post-occupancy evaluations of healthcare facilities, gathering insights from a spectrum of healthcare contexts, further translating these principles into the specific context of a sensory-therapeutic garden design in Cluj-Napoca, Romania (Polat et al., 2019). Implementation of such initiatives and feedback from the users can bring improvements in the design process and thus lead to better understanding about the requirements of a therapeutic garden (Ivarsson and Grahn, 2010; Uwajeh et al., 2019). Post-occupancy research emphasizes the user's needs, and highlights the positive and negative aspects of the newly created space. This then contributes to the constant improvement of the therapeutic garden design guidelines, aiding specialists in developing enhanced healing environments (Abbas and Ghazali, 2012; Sidenius et al., 2017).

TABLE 6 Plants proposed for the sound barrier area and their features.

Species	Sound barrier features	Therapeutic effects	Decorative elements	Tactile experience	Plant type/growth habit/decorative period
<i>Taxus baccata</i>	Dense, evergreen foliage	Calming effect, creates a sense of privacy; provides nesting opportunities and food for birds (Lavabre and García, 2015)	Dark green foliage; bright red fruits	Needle-like foliage, spiky texture	Perennial/shrub/year-round
<i>Cornus sanguinea</i>	Dense branching structure with thick foliage	Visual interest due to colorful stems in winter, can have positive impact on mood; attracts bees, birds (Krüsi and Debussche, 1988)	Intense red stems	Slightly rough textured stems	Perennial/shrub/year-round
<i>Photinia × frasierii</i>	Evergreen with dense foliage	Provides privacy, attractive red new growth can have good influence on mood; attracts bees and other pollinators	Red new growth	Glossy and slightly leathery leaves	Perennial/shrub/year-round
<i>Philadelphus coronarius</i>	Dense branching structure	Fragrant flowers can have a calming effect; attracts bees and other pollinators (Mach and Potter, 2018)	Dense white flowers	Soft, delicate flowers	Perennial/shrub/spring to fall
<i>Weigela florida</i>	Dense arching branches with abundant foliage	Dense colorful flowers, can have uplifting effect on mood; attracts bees, butterflies (Stawiarz and Wróblewska, 2016)	Dense pink flowers	Slightly waxy -flowers; slightly rough textured leaves	Perennial/shrub/spring to fall
<i>Prunus laurocerasus</i>	Evergreen, dense foliage	Dense foliage creates a sense of closure, privacy; attracts bees and other pollinators, birds might be attracted to the fruits (Mach and Potter, 2017)	Glossy, dark green foliage; small white flowers	Glossy, fine leaves	Perennial/shrub/year-round
<i>Forsythia suspensa</i>	Dense, arching branches with abundant foliage	Bright yellow flowers can have positive impact on mood by providing a vibrant visual display; the flowers can be attractive to bees and other pollinators (Mach and Potter, 2017)	Bright yellow flowers	Soft, delicate flowers; slightly rough branches	Perennial/shrub/spring to fall

Healing gardens with therapeutic properties are spaces that assist the recovery process and have both physical and spiritual implications (Hastuti, 2020; Hastuti and Lorica, 2020). Drawing from the user feedback and design key principles extracted from the literature exploration, the defining design features of therapeutic gardens encompass: (1) creating a well-organized space, (2) taking in account the facility's profile when designing the space, (3) prioritizing softscape over hardscape, (4) supporting human-nature interaction, (5) ensure access and visibility, (6) provide plenty of seating and shaded areas, (7) include water features (8) design secluded areas for staff, (9) use vegetation and natural elements for multi-sensory stimulation, and (10) encourage biodiversity. This comprehensive set of principles provides a blueprint for the sensory-therapeutic garden design, that aligns with the previous findings (Vapaa, 2002; Asano, 2008; Pouya and Demirel, 2015). Furthermore, the design process presented in this study demonstrates how the principles derived from the literature exploration and user feedback were translated into a specific garden design, thus proving their applicability in real-world design scenarios.

The design features of the therapeutic garden should ideally meet the specialization of the hospital and the pathology of the users, as different types of patients have different needs. It is important to emphasize that not all pathologies have been

extensively researched in terms of therapeutic gardens design, thus there still might be cases where in order for the user's needs to be met, the specialists creating the garden need to rely on their professional experience and on a collaboration with the end user in developing the design (Eckerling, 1996). For example, garden design for cancer patients should have different properties than the one designed for children, mentally ill patients, or hospital staff in terms of colors, activities, fragrances, and accessibility; but they all should create a safe space with plenty of vegetation, provide shade, comfortable seating and facilitate independent movement (Fleming and Figueiredo, 2013; Paraskevopoulou and Kamperi, 2018). These are facts that are in concordance with the design proposal, having specific vegetation for lung pathology-related patients, providing medicinal plants and fresh fruits through the medicinal and edible plants area, that enhance the tactile sensory experience for patients with visual impairments.

By design, the aim of sensory-therapeutic gardens is to offer sensory experiences, with a recreational and/or educational outcome, actively engaging its visitors in exploration by stimulating all the senses: tactile, gustatory, olfactory, visual, auditory and movement (Hussein, 2010; Stepansky et al., 2022), the present proposal includes these features by integrating tactile, visual or auditory stimulating vegetation. Such gardens, besides a senses-themed design, should afford activities like fruit harvesting,

TABLE 7 Plants proposed for the staff dedicated area and their features.

Species	Therapeutic effects	Decorative elements	Tactile experience	Plant type/growth habit/decorative period
<i>Prunus laurocerasus</i>	Calming effect, creates a sense of privacy and closure due to the evergreen foliage; attracts bees and other pollinators (Mach and Potter, 2017)	Glossy, dark green foliage; small white flowers	Glossy, fine leaves	Perennial/shrub/year-round
<i>Hydrangea paniculata</i>	Visual appealing flowers, in contrast with the background can have invigorating effects on the mood; attractive to bees, butterflies, and other pollinators (Mach and Potter, 2017)	Large flower clusters that can range in color from white to pink	Rough textured leaves; soft and fluffy leaves	Perennial/shrub/late spring to fall
<i>Deutzia scabra</i>	Visual appealing dense flowers, in contrast with the background can have invigorating effects on the mood; attracts bees and other pollinators (Mach and Potter, 2017)	Dense, white flowers	Coarse leaves	Perennial/shrub/spring to fall
<i>Viburnum davidii</i>	Its textures and color combinations provide visual interest; attractive to bees and other pollinators (Sharifi-Rad et al., 2021)	Textured leaves; Small white flowers	Soft and delicate flowers with silky texture	Perennial/shrub/year-round
<i>Euonymus japonicus</i>	Variiegated leaves rise visual interest, can have invigorating and uplifting effect on mood; can be attractive to bees and other pollinators (Yucedag et al., 2019)	Green variegated foliage	Glossy and smooth leaves with leathery texture	Perennial/shrub/year-round

exploration, interaction with the environment by using species with interesting foliage, incorporating water features, diversifying hardscape materials, stimulating curiosity, being accessible to all visitors, and to encourage social gathering (Hussein et al., 2016; Siu et al., 2020), a requirement sustained by the proposed occupational therapy area.

A very important part of a successful therapeutic design would be the patient's, family members and medical staff involvement and/or opinion in the design process from the beginning, since they will be the final users of the space, and maybe have different expectations, needs or ideas for the garden (Heath, 2004; Senes et al., 2012). This was an aspect that in this study was not considered. Also, staff members are directly involved in the patient's recovery and are as equally important when making design choices about their working environment. Research indicates a significant gap in finding what medical staff needs in order to provide quality services while preserving their own health (Huisman et al., 2012; Smidl et al., 2017), so in the present design proposal it was considered necessary to integrate a secluded area for the medical staff. Besides recommendations from scientific literature or user feedback, another factor that might influence the outcome of a therapeutic garden design is the site's location and surroundings. Aspects like the terrain topography (slopes, flat terrain, or mixed), climate (influences the vegetation palette that can be used in the design), vicinities (can bring the necessity to create sound barriers being located near a noisy area, or some sights might need to be highlighted or, conversely, hidden) can have major implications in the decision making process regarding the zoning, functions

and aesthetics of the garden (Salamy, 1995; Shahrad, 2012). In the present study, the fragmented space led to the partitioning of the functional zoning of the space.

While POE method can provide valuable information on designing healing spaces, more modern evaluation methods can be used, that offer more objective, time efficient and standardized approaches. For instance, in individuals with dementia, the positive impact that the garden exposure had on the mood and reduced medication was reflected in the lower levels of cortisol and blood pressure, offering a more accurate evaluation of the therapeutic effects (Pedrinolla et al., 2019; Murrioni et al., 2021). Electroencephalogram technology is a non-invasive approach that allows the measurement of mood indicators, and in the context of evaluating individuals participating in gardening-related activities, revealed that, in addition to experiencing relaxation, participants also felt a sense of interest and engagement in the activity (Du et al., 2022). Other methods, like wearable sensors can be used to measure physiological responses to outdoor environments, a method that, combined with the use of virtual reality can reveal the potential impact of a proposed design even before it was built (Skulimowski and Badurowicz, 2017; Zhang et al., 2021). Eye tracking technology can reveal insights on what elements of the garden capture visitors' attention and for how long, allowing designers to understand what elements are most engaging and appealing, or aspects that may be less successful in capturing interest, and even more, it can help uncover any discrepancies between what the subjects verbally report as their preferences and what their gaze patterns disclose (Amati et al., 2018; Junker and Nollen, 2018).

The evolution of technology and new findings in medicine provide hospitals with equipment that improves the quality of the medical services. However, studies have shown that often this is not enough, and the quality of the environment around the patient has a major impact on the recovery process and length of hospital stay. There has been a preference for the design of old hospitals as compared to the new ones, and there is a correlation between the time spent in the hospital and the user's satisfaction level concerning the surrounding environment. This shows that over time, designers have lost something of essential value in conceiving healing environments (Ghazali and Abbas, 2012b).

5 Conclusion

Since ancient times man has felt a deep connection with nature and natural environment, always seeking to integrate it in the healing process, and green spaces around hospitals can provide a great opportunity to create sensory-therapeutic gardens. This study has shed light on the importance of these types of spaces showcasing their potential to facilitate interaction not only between people, but also to encourage a human-nature connection, to provide access to all visitors, and to create a recreational space also for staff and family members. Not only does this enrich the aesthetic of a place with great variety in color and texture given by the materials and vegetation used, but also can invite for further investigation, to bring curiosity into the visitor's mind. They can create opportunities for outdoor activities like gardening or sensory exploration of nature, by using intriguing and captivating elements in the design but they can serve also as contemplative spaces where one can just spend time outdoor observing nature in silence. Since there are not any precise guidelines for how sensory-therapeutic garden should look like, the design often reflects the landscape designer's perspective and intuition, but post-occupancy studies often reveal new perspectives, bringing constant improvements. Through an exploration of scientific literature focusing on Post-occupancy evaluations, we have identified key features of healing landscapes that contribute to the effectiveness of these spaces. This paper offers an innovative perspective by translating these general principles into a specific design context, filling a gap in existing guidelines, bringing practical aspects for future sensory-therapeutic garden design, combining literature-derived principles with user feedback and site-specific condition, demonstrating the flexibility and adaptability of these features. However, it is crucial to acknowledge that further research is needed in order to continually refine and improve the design of healing spaces by

integrating emerging technologies, enabling more evidence-based design practices.

Data availability statement

The original contributions presented in the study are included in the article/supplementary material, further inquiries can be directed to the corresponding author.

Author contributions

MD and AS: conceptualization, resources, project administration, and funding acquisition. MD, AD, and PS: methodology and software. PS, MB, RB, and AS: validation. DD, PS, and MB: formal analysis. MD, D-MM, and DD: investigation. MD and DD: writing—original draft preparation. PS, RB, and AS: writing—review and editing. MD, D-MM, and PS: visualization. MB, RB, and AS: supervision. All authors have read and agreed to the published version of the manuscript.

Funding

This research was funded by the University of Agricultural Sciences and Veterinary Medicine of Cluj-Napoca (USAMVCN) and Doctoral School from the UASMVCN, granted to MD.

Conflict of interest

The authors declare that the research was conducted in the absence of any commercial or financial relationships that could be construed as a potential conflict of interest.

Publisher's note

All claims expressed in this article are solely those of the authors and do not necessarily represent those of their affiliated organizations, or those of the publisher, the editors and the reviewers. Any product that may be evaluated in this article, or claim that may be made by its manufacturer, is not guaranteed or endorsed by the publisher.

References

- Abbas, M. Y., and Ghazali, R. (2011). Physical environment: The major determinant towards the creation of a healing environment? *Procedia Soc. Behav. Sci.* 30, 1951–1958.
- Abbas, M. Y., and Ghazali, R. (2012). Healing environment: Paediatric wards – status and design trend. *Procedia Soc. Behav. Sci.* 49, 28–38.
- Adevi, A. A., and Mårtensson, F. (2013). Stress rehabilitation through garden therapy: The garden as a place in the recovery from stress. *Urban For. Urban Green.* 12, 230–237.
- Al-Essa, M. K., Mohammed, F. I., Shafagoj, Y. A., and Afifi, F. U. (2007). Studies on the direct effects of the alcohol extract of *Tilia cordata*. on dispersed intestinal smooth muscle cells of Guinea pig. *Pharm. Biol.* 45, 246–250. doi: 10.1080/13880200701213195
- Althoff, D. M., Segraves, K. A., and Pellmyr, O. (2005). Community context of an obligate mutualism: Pollinator and florivore effects on *Yucca filamentosa*. *Ecology* 86, 905–913. doi: 10.1890/04-1454
- Amati, M., Ghanbari Parmehr, E., McCarthy, C., and Sita, J. (2018). How eye-catching are natural features when walking through a park? Eye-tracking responses to videos of walks. *Urban For. Urban Green.* 31, 67–78.

- Amsterdam, J. D., Li, Q. S., Xie, S. X., and Mao, J. J. (2020). Putative antidepressant effect of chamomile (*Matricaria chamomilla* L.) oral extract in subjects with comorbid generalized anxiety disorder and depression. *J. Altern. Complement. Med.* 26, 815–821. doi: 10.1089/acm.2019.0252
- Ananth, S. (2008). Healing environments: The next natural step. *Explore* 4, 273–274.
- Andruk, N. (2017). Criteria of assessing introduced varieties of the genus *Heuchera* L. *Plant Var. Stud. Prot.* 13, 55–63. doi: 10.21498/2518-1017.13.1.2017.97260
- Arcos, M. L. B., Cremaschi, G., Werner, S., Coussio, J., Ferraro, G., and Anesini, C. (2006). *Tilia cordata* Mill. extracts and scopoletin (isolated compound): Differential cell growth effects on lymphocytes. *Phytother. Res.* 20, 34–40. doi: 10.1002/ptr.1798
- Asano, F. (2008). Healing at a hospital garden: Integration of physical and non-physical aspects. *Acta Horticult.* 775, 13–22.
- Bao, X.-Y., and Zhu, L. (2022). Therapeutic effect and mechanism of *Papaver somniferum* on myopia and complete chloroplast genome analysis. *Sci. Adv. Mat.* 14, 499–504. doi: 10.1166/sam.2022.4228
- Barakat, H. A.-E.-R., Bakr, A., and El-Sayad, Z. (2019). Nature as a healer for autistic children. *Alex. Eng. J.* 58, 353–366.
- Baydar, N. G., and Baydar, H. (2013). Phenolic compounds, antiradical activity and antioxidant capacity of oil-bearing rose (*Rosa damascena* Mill.) extracts. *Ind. Crops Prod.* 41, 375–380. doi: 10.1016/j.indcrop.2012.04.045
- Berto, R., and Barbiero, G. (2017). The biophilic quality index. A tool to improve a building from “green” to restorative. *Vis. Sustainabil.* 8, 38–45.
- Beute, F., and de Kort, Y. A. W. (2018). The natural context of wellbeing: Ecological momentary assessment of the influence of nature and daylight on affect and stress for individuals with depression levels varying from none to clinical. *Health Place* 49, 7–18. doi: 10.1016/j.healthplace.2017.11.005
- Boffi, M., Pola, L. G., Fermani, E., Senes, G., Inghilleri, P., Piga, B. E. A., et al. (2022). Visual post-occupancy evaluation of a restorative garden using virtual reality photography: Restoration, emotions, and behavior in older and younger people. *Front. Psychol.* 13:927688. doi: 10.3389/fpsyg.2022.927688
- Born, R. J. G. V. D., Lenders, R. H. J., Groot, W. T. D., and Huijsman, E. (2001). The new biophilia: An exploration of visions of nature in western countries. *Environ. Conserv.* 28, 65–75.
- Bratman, G. N., Anderson, C. B., Berman, M. G., Cochran, B., De Vries, S., Flanders, J., et al. (2019). Nature and mental health: An ecosystem service perspective. *Sci. Adv.* 5:eax0903.
- Bressane, A., Negri, R. G., De Brito Junior, I., Medeiros, L. C. D. C., Araújo, I. L. L., Silva, M. B., et al. (2022). Association between contact with nature and anxiety, stress and depression symptoms: A primary survey in Brazil. *Sustainability* 14:10506.
- Brdavska, V., and Rizovska Atanasovska, J. (2012). Some shade tolerant plants that can be used in landscape design in the open green spaces in R. Macedonia. *For. Rev.* 43, 51–56.
- Buse, C., Nettleton, S., Martin, D., and Twigg, J. (2017). Imagined bodies: Architects and their constructions of later life. *Ageing Soc.* 37, 1435–1457.
- Bush, J., and Doyon, A. (2019). Building urban resilience with nature-based solutions: How can urban planning contribute? *Cities* 95:102483.
- Cantrell, C. L., Zheljzakov, V. D., Carvalho, C. R., Astatkie, T., Jeliazkova, E. A., and Rosa, L. H. (2014). Dual extraction of essential oil and podophyllotoxin from creeping juniper (*Juniperus horizontalis*). *PLoS One* 9:e106057. doi: 10.1371/journal.pone.0106057
- Carnemolla, P., Debono, D., Hourihan, F., Hor, S., Robertson, H., and Travaglia, J. (2021). The influence of the built environment in enacting a household model of residential aged care for people living with a mental health condition: A qualitative post-occupancy evaluation. *Health Place* 71:102624. doi: 10.1016/j.healthplace.2021.102624
- Cooper Marcus, C., and Barnes, M. (1995). *Gardens in healthcare facilities: Uses, therapeutic benefits, and design recommendations*. Concord, CA: The Center for Health Design, Inc.
- Cordoza, M., Ulrich, R. S., Manulik, B. J., Gardiner, S. K., Fitzpatrick, P. S., Hazen, T. M., et al. (2018). Impact of nurses taking daily work breaks in a hospital garden on burnout. *Am. J. Crit. Care* 27, 508–512. doi: 10.4037/ajcc2018131
- Côté, H., Pichette, A., St-Gelais, A., and Legault, J. (2021). The biological activity of *Monarda didyma* L. essential oil and its effect as a diet supplement in mice and broiler chicken. *Molecules* 26:3368. doi: 10.3390/molecules26113368
- Davis, B. (2001). *Healing the whole person: A post occupancy evaluation of the rooftop therapy park at Fort Sanders Regional Medical Center*. Knoxville, TN: Louisiana State University Libraries. doi: 10.31390/gradschool_theses.4067
- Davis, B. E. (2011). Rooftop hospital gardens for physical therapy: A post-occupancy evaluation. *Health Environ. Res. Design J.* 4, 14–43. doi: 10.1177/193758671100400303
- de Bell, S., White, M., Griffiths, A., Darlow, A., Taylor, T., Wheeler, B., et al. (2020). Spending time in the garden is positively associated with health and wellbeing: Results from a national survey in England. *Landsc. Urban Plan.* 200:103836.
- de Melo Alves Silva, L. C., de Oliveira Mendes, F., de C., de Castro Teixeira, F., de Lima Fernandes, T. E., et al. (2023). Use of *Lavandula angustifolia* essential oil as a complementary therapy in adult health care: A scoping review. *Heliyon* 9:e15446. doi: 10.1016/j.heliyon.2023.e15446
- Dmitruk, M., Strzałkowska-Abramek, M., Bożek, M., and Denisow, B. (2022). Plants enhancing urban pollinators: Nectar rather than pollen attracts pollinators of *Cotoneaster* species. *Urban For. Urban Green.* 74:127651. doi: 10.1016/j.ufug.2022.127651
- Du, J., Yin, J., Chen, X., Hassan, A., Fu, E., and Li, X. (2022). Electroencephalography (EEG)-Based Neural Emotional Response to Flower Arrangements (FAs) on Normal Elderly (NE) and Cognitively Impaired Elderly (CIE). *Int. J. Environ. Res. Public Health* 19:3971. doi: 10.3390/ijerph19073971
- Eckerling, M. (1996). Guidelines for designing healing gardens. *J. Ther. Horticult.* 8, 21–25.
- Eijkelenboom, A., Verbeek, H., Felix, E., and Van Hoof, J. (2017). Architectural factors influencing the sense of home in nursing homes: An operationalization for practice. *Front. Archit. Res.* 6, 111–122. doi: 10.1016/j.foar.2017.02.004
- Fancourt, D., Aughterson, H., Finn, S., Walker, E., and Steptoe, A. (2021). How leisure activities affect health: A narrative review and multi-level theoretical framework of mechanisms of action. *Lancet Psychiatry* 8, 329–339. doi: 10.1016/S2215-0366(20)30384-9
- Fleming, L., and Figueiredo, M. (2013). Healing gardens for cancer populations. *Am. Hortic. Ther. Assoc.* 41, 13–15.
- Folquitto, D. G., Swiech, J. N. D., Pereira, C. B., Bobek, V. B., Halila Possagno, G. C., Farago, P. V., et al. (2019). Biological activity, phytochemistry and traditional uses of genus *Lobelia* (Campanulaceae): A systematic review. *Fitoterapia* 134, 23–38. doi: 10.1016/j.fitote.2018.12.021
- Fromm, E. (1973). *The anatomy of human destructiveness*. New York, NY: Holt, Rinehart and Winston.
- Gamel, T. H., Linssen, J. P., Alink, G. M., Mosallem, A. S., and Shekib, L. A. (2004). Nutritional study of raw and popped seed proteins of *Amaranthus caudatus* L. and *Amaranthus cruentus* L. *J. Sci. Food Agric.* 84, 1153–1158. doi: 10.1002/jsfa.1781
- Garbacki, N., Gloaguen, V., Damas, J., Bodart, P., Tits, M., and Angenot, L. (1999). Anti-inflammatory and immunological effects of *Centaurea cyanus* flower-heads. *J. Ethnopharmacol.* 68, 235–241. doi: 10.1016/s0378-8741(99)00112-9
- Gerdes, M. E., Aistis, L. A., Sachs, N. A., Williams, M., Roberts, J. D., and Rosenburg Goldstein, R. E. (2022). Reducing anxiety with nature and gardening (RANG): Evaluating the impacts of gardening and outdoor activities on anxiety among U.S. adults during the Covid-19 pandemic. *Int. J. Environ. Res. Public Health* 19:5121. doi: 10.3390/ijerph19095121
- Ghazali, R., and Abbas, M. Y. (2012a). Assessment of healing environment in paediatric wards. *Procedia Soc. Behav. Sci.* 38, 149–159. doi: 10.1016/j.procs.2012.09.001
- Ghazali, R., and Abbas, M. Y. (2012b). Newly built public paediatric wards increase length of stay (LOS)? *Procedia Soc. Behav. Sci.* 50, 623–632.
- Ghazali, R., Md Sakip, S. R., and Samsudin, E. (2019). Creating positive environment for autism using sensory design. *Environ. Behav. Proc. J.* 4, 19–26.
- Gianfredi, V., Buffoli, M., Rebecchi, A., Croci, R., Oradini-Alacreu, A., Stirparo, G., et al. (2021). Association between urban greenspace and health: A systematic review of literature. *Int. J. Environ. Res. Public Health* 18:5137. doi: 10.3390/ijerph18105137
- Gidlöf-Gunnarsson, A., and Öhrström, E. (2007). Noise and well-being in urban residential environments: The potential role of perceived availability to nearby green areas. *Landsc. Urban Plan.* 83, 115–126.
- Giebel, C., De Boer, B., Gabbay, M., Watkins, C., Wilson, N., Tetlow, H., et al. (2022). Developing a meaningful garden space in a care home with staff and family members: A qualitative study. *Int. J. Environ. Res. Public Health* 19:7025. doi: 10.3390/ijerph19127025
- Goel, V., Lovlin, R., Chang, C., Slama, J. V., Barton, R., Gahler, R., et al. (2005). A proprietary extract from the echinacea plant (*Echinacea purpurea*) enhances systemic immune response during a common cold. *Phytother. Res.* 19, 689–694. doi: 10.1002/ptr.1733
- Hamidpour, R., Hamidpour, S., and Elias, G. (2017). *Rosmarinus officinalis* (Rosemary): A novel therapeutic agent for antioxidant, antimicrobial, anticancer, antidiabetic, antidepressant, neuroprotective, anti-inflammatory, and anti-obesity treatment. *Biomed. J. Sci. Techn. Res.* 1, 1098–1103. doi: 10.26717/bjstr.2017.01.000371
- Hanafy, D. M., Burrows, G. E., Prenzler, P. D., and Hill, R. A. (2020). Potential role of phenolic extracts of *Mentha* in managing oxidative stress and Alzheimer's Disease. *Antioxidants* 9:631. doi: 10.3390/antiox9070631
- Hassan, A. M., Mohamed, S. R., El-Nekeety, A. A., Hassan, N. S., and Abdel-Wahhab, M. A. (2010). *Aquilegia vulgaris* L. extract counteracts oxidative stress and cytotoxicity of fumonisin in rats. *Toxicol.* 56, 8–18. doi: 10.1016/j.toxicol.2010.03.006
- Hastuti, A. S. O. (2020). “Healing garden therapy: A phenomenology of holistic healing for patients,” in *Proceedings of the 3rd SPUP International Research Conference Journal*. Tuguegarao City: St. Paul University Philippines.
- Hastuti, A. S. O., and Lorica, J. (2020). The effect of healing garden to improve the patients healing: An integrative literature review. *J. Health Caring Sci.* 2, 34–47.

- He, M., Wang, Y., Wang, W. J., and Xie, Z. (2022). Therapeutic plant landscape design of urban forest parks based on the five senses theory: A case study of Stanley Park in Canada. *Int. J. Geoheritage Parks* 10, 97–112. doi: 10.1016/j.ijgeop.2022.02.004
- Heath, Y. (2004). Evaluating the effect of therapeutic gardens. *Am. J. Alzheimers Dis. Other Dement.* 19, 239–242.
- Hikal, W. M., Said-Al Ahl, H. A. H., and Tkachenko, K. G. (2022). Bioactive constituents of *Buddleja* spp., and their therapeutic potentials. *J. Biochem. Int.* 9, 1–11. doi: 10.56557/job/2022/v9i117388
- Huisman, E. R. C. M., Morales, E., Van Hoof, J., and Kort, H. S. M. (2012). Healing environment: A review of the impact of physical environmental factors on users. *Build. Environ.* 58, 70–80.
- Hussein, H. (2010). Sensory gardens: Assessing their design and use. *Intell. Build. Int.* 2, 116–123.
- Hussein, H., Omar, Z., and Ishak, S. A. (2016). Sensory garden for an inclusive society. *Asian J. Behav. Stud.* 1, 33–43.
- Ivarsson, C. T., and Grahn, P. (2010). Patients' experiences and use of a therapeutic garden: From a designer's perspective. *Schweizerische Zeitschr. Forstwesen* 161, 104–113.
- Jackson, S. B., Stevenson, K. T., Larson, L. R., Peterson, M. N., and Seekamp, E. (2021). Outdoor activity participation improves adolescents' mental health and well-being during the COVID-19 pandemic. *Int. J. Environ. Res. Public Health* 18:2506.
- Jennings, V., and Bamkole, O. (2019). The relationship between social cohesion and urban green space: An avenue for health promotion. *Int. J. Environ. Res. Public Health* 16:452. doi: 10.3390/ijerph16030452
- Jiang, S. (2014). Therapeutic landscapes and healing gardens: A review of Chinese literature in relation to the studies in western countries. *Front. Archit. Res.* 3, 141–153. doi: 10.1016/j.foar.2013.12.002
- Jiang, S., Staloch, K., and Kaljevic, S. (2018). Opportunities and barriers to using hospital gardens: Comparative post occupancy evaluations of healthcare landscape environments. *J. Ther. Hortic.* 28, 23–56.
- Jin, Z., Wang, J., Liu, X., Han, X., Qi, J., and Wang, J. (2023). Stress recovery effects of viewing simulated urban parks: Landscape types, depressive symptoms, and gender differences. *Land* 12:22.
- Junker, D., and Nollen, C. (2018). "Mobile eye tracking in landscape architecture: Discovering a new application for research on site," in *Landscape architecture: The sense of places, models and applications*, ed. A. Almusaed (London: IntechOpen).
- Karjalainen, R., Anttonen, M., Saviranta, N., Stewart, D., McDougall, G. J., Hilz, H., et al. (2009). A review on bioactive compounds in black currants (*Ribes nigrum* L.) and their potential health-promoting properties. *Acta Hort.* 839, 301–307. doi: 10.17660/actahortic.2009.839.38
- Kelebek, H., and Selli, S. (2011). Evaluation of chemical constituents and antioxidant activity of sweet cherry (*Prunus avium* L.) cultivars. *Int. J. Food Sci. Techn.* 46, 2530–2537. doi: 10.1111/j.1365-2621.2011.02777.x
- Kellert, S. R., and Wilson, E. O. (1995). *The biophilia hypothesis*. Washington, DC: Island press.
- Kennedy, D. O., Pace, S., Haskell, C., Okello, E. J., Milne, A., and Scholey, A. B. (2005). Effects of cholinesterase inhibiting sage (*Salvia officinalis*) on mood, anxiety and performance on a psychological stressor battery. *Neuropsychopharmacology* 31, 845–852. doi: 10.1038/sj.npp.1300907
- Khalaf, M. K., and Stace, C. A. (2001). The distinction between *Cerastium tomentosum* L. and *C. biebersteinii* DC. (Caryophyllaceae), and their occurrence in the wild in Britain. *Watsonia* 23, 481–491.
- Kharchenko, V. E., Shelekhova, O. M., Barinova, S. S., and Fomenko, E. I. (2016). Morphological peculiarities productive shoots and pollinators of *Astilbe chinensis*. *Hortus Bot.* 11, 172–183. doi: 10.15939/j4.art.2016.3282
- Kolniak-Ostek, J. (2016). Chemical composition and antioxidant capacity of different anatomical parts of pear (*Pyrus communis* L.). *Food Chem.* 203, 491–497. doi: 10.1016/j.foodchem.2016.02.103
- Krüsi, B. O., and Debussche, M. (1988). The fate of flowers and fruits of *Cornus sanguinea* L. in three contrasting Mediterranean habitats. *Oecologia* 74, 592–599. doi: 10.1007/bf00380058
- Larson, L. R., Mullenbach, L. E., Browning, M. H. E. M., Rigolon, A., Thomsen, J., Metcalf, E. C., et al. (2022). Greenspace and park use associated with less emotional distress among college students in the United States during the COVID-19 pandemic. *Environ. Res.* 204, 112367. doi: 10.1016/j.envres.2021.112367
- Lavabre, J. E., and García, D. (2015). Geographic consistency in the seed dispersal patterns of *Taxus baccata* L. in the Iberian Peninsula. *For. Syst.* 24:e040. doi: 10.54244/fs/2015243-07462
- Lee, C. H., and Shin, S. L. (2010). "Functional activities of ferns for human health," in *Working with Ferns*, eds H. Fernández, A. Kumar, and M. Revilla (New York, NY: Springer), 347–359. doi: 10.1007/978-1-4419-7162-3_24
- Lin, B. B., Egerer, M. H., and Ossola, A. (2018). Urban gardens as a space to engender biophilia: Evidence and ways forward. *Front. Built Environ.* 4:79. doi: 10.3389/fbuil.2018.00079
- Lygum, V. L., Poulsen, D. V., Djernis, D., Djernis, H. G., Sidenius, U., and Stigsdotter, U. K. (2019). Post-occupancy evaluation of a crisis shelter garden and application of findings through the use of a participatory design process. *Health Environ. Res. Design J.* 12, 153–167. doi: 10.1177/1937586718812444
- Mach, B. M., and Potter, D. A. (2017). *Woody ornamentals for bee-friendly landscapes (Ohio Valley Region)*. *Entomology Reports*. Available online at: https://uknowledge.uky.edu/entomology_reports/1
- Mach, B. M., and Potter, D. A. (2018). Quantifying bee assemblages and attractiveness of flowering woody landscape plants for urban pollinator conservation. *PLoS One* 13:e0208428. doi: 10.1371/journal.pone.0208428
- Mannan, M. M., Maridass, M., and Victor, B. (2008). A review on the potential uses of ferns. *Ethnobotanical Leaflets* 1:33.
- Mao, J. J., Xie, S. X., Keefe, J. R., Soeller, I., Li, Q. S., and Amsterdam, J. D. (2016). Long-term chamomile (*Matricaria chamomilla* L.) treatment for generalized anxiety disorder: A randomized clinical trial. *Phytomedicine* 23, 1735–1742. doi: 10.1016/j.phymed.2016.10.012
- Meuwese, D., Dijkstra, K., Maas, J., and Koole, S. L. (2021). Beating the blues by viewing Green: Depressive symptoms predict greater restoration from stress and negative affect after viewing a nature video. *J. Environ. Psychol.* 75:101594.
- Moore, G. T. (1983). Teaching design evaluation, with results from case studies of playgrounds, schools, and housing for the elderly. *Des. Stud.* 4, 100–114.
- Murroni, V., Cavalli, R., Basso, A., Borella, E., Meneghetti, C., Melendugno, A., et al. (2021). Effectiveness of therapeutic gardens for people with dementia: A systematic review. *Int. J. Environ. Res. Public Health* 18:9595.
- Naderi, J. R., and Shin, W.-H. (2008). Humane design for hospital landscapes: A case study in landscape architecture of a healing garden for nurses. *Health Environ. Res. Design J.* 2, 82–119. doi: 10.1177/193758670800200112
- Nordh, H., Grahn, P., and Währborg, P. (2009). Meaningful activities in the forest, a way back from exhaustion and long-term sick leave. *Urban For. Urban Green.* 8, 207–219.
- Nunes, A. R., Gonçalves, A. C., Falcão, A., Alves, G., and Silva, L. R. (2021). *Prunus avium* L. (sweet cherry) by-products: A source of phenolic compounds with antioxidant and anti-hyperglycemic properties – A review. *Appl. Sci.* 11:8516. doi: 10.3390/app11188516
- Obeso, J. R. (1998). Patterns of variation in *Ilex aquifolium* fruit traits related to fruit consumption by birds and seed predation by rodents. *Écoscience* 5, 463–469. doi: 10.1080/11956860.1998.11682494
- Özcan, H. (2006). "Healing design: A holistic approach to social interaction in pediatric intensive care units in the United States and Turkey," in *Proceedings of the 1st international CIB endorsed METU postgraduate conference built environment & information technologies*, (Ankara).
- Pal, D. (2011). "Sunflower (*Helianthus annuus* L.) seeds in health and nutrition," in *Nuts and seeds in health and disease prevention*, eds V. R. Preedy, R. R. Watson, and V. B. Patel (Amsterdam: Elsevier), 1097–1105. doi: 10.1016/b978-0-12-375688-6.10130-6
- Paraskevopoulou, A. T., and Kamperi, E. (2018). Design of hospital healing gardens linked to pre- or post-occupancy research findings. *Front. Archit. Res.* 7, 395–414. doi: 10.1016/j.foar.2018.05.004
- Parente, L. M. L., Lino Júnior, R., de, S., Tresvenzol, L. M. F., Vinaud, M. C., de Paula, J. R., et al. (2012). Wound healing and anti-inflammatory effect in animal models of *Calendula officinalis* L. growing in Brazil. *Evid. Based Complement. Alternat. Med.* 2012:375671. doi: 10.1155/2012/375671
- Pasha, S. (2013). Barriers to garden visitation in children's hospitals. *Health Environ. Res. Design J.* 6, 76–96.
- Patocka, J., Bhardwaj, K., Klimova, B., Nepovimova, E., Wu, Q., Landi, M., et al. (2020). *Malus domestica*: A review on nutritional features, chemical composition, traditional and medicinal value. *Plants* 9:1408. doi: 10.3390/plants9111408
- Pedrinolla, A., Tamburin, S., Brasioli, A., Sollima, A., Fonte, C., Muti, E., et al. (2019). An indoor therapeutic garden for behavioral symptoms in Alzheimer's disease: A randomized controlled trial. *J. Alzheimers Dis.* 71, 813–823. doi: 10.3233/JAD-190394
- Philipp, R. (2012). "Fostering the art of well-being: An alternative medicine," in *A compendium of essays on alternative therapy*, ed. A. Bhattacharya (Rijeka: InTech).
- Piat, M., Seida, K., Sabetti, J., and Padgett, D. (2017). (Em)placing recovery: Sites of health and wellness for individuals with serious mental illness in supported housing. *Health Place* 47, 71–79. doi: 10.1016/j.healthplace.2017.07.006
- Polat, A. T., Güngör, S., and Demir, M. (2019). The design principles of therapeutic gardens. *Uluslararası Peyzaj Mimarlığı Araştırmaları Dergisi* 1, 37–42.
- Pouya, S., and Demirel, Ö. (2015). What is a healing garden? *Akdeniz Üniversitesi Ziraat Fakültesi Dergisi* 28, 5–10.
- Preiser, W. F., White, E., and Rabinowitz, H. (2015). *Post-occupancy evaluation (Routledge Revivals)*. Abingdon: Routledge.
- Rahbardar, G. M., and Hosseinzadeh, H. (2020). Therapeutic effects of rosemary (*Rosmarinus officinalis* L.) and its active constituents on nervous system disorders. *Iran. J. Basic Med. Sci.* 23, 1100–1112. doi: 10.22038/ijbms.2020.45269.10541
- Redzic, S. (2010). Wild medicinal plants and their usage in traditional human therapy (Southern Bosnia and Herzegovina, W. Balkan). *J. Med. Plants Res.* 4, 1003–1027. doi: 10.5897/jmpr09254

- Reeve, A., Nieberler-Walker, K., and Desha, C. (2017). Healing gardens in children's hospitals: Reflections on benefits, preferences and design from visitors' books. *Urban For. Urban Green.* 26, 48–56.
- Rivasseau-Jonveaux, T., Pop, A., Fescharek, R., Chuzeville, S., Jacob, C., Demarche, L., et al. (2012). Les jardins thérapeutiques: Recommandations et critères de conception. *Geriatr. Psychol. Neuropsychiatr. Vieil* 10, 245–253.
- Rizwan, B. (2021). Therapeutic potential of *Thymus vulgaris*: A review. *Ann. Res.* 3, 147–161. doi: 10.31219/osf.io/3fzvt
- Roös, P. B. (2021). *Regenerative-adaptive design for sustainable development: A pattern language approach*. Berlin: Springer.
- Russo, A., and Andreucci, M. B. (2023). Raising healthy children: Promoting the multiple benefits of green open spaces through biophilic design. *Sustainability* 15:1982.
- Ryan, C. O., Browning, W. D., Clancy, J. O., Andrews, S. L., and Kallianpurkar, N. (2014). Biophilic design patterns: Emerging nature-based parameters for health and well-being in the built environment. *Int. J. Arch. Res.* 8, 62–76.
- Salamy, V. M. (1995). *Healing gardens: Design guidelines for landscape architects*. Master's thesis. Columbus, OH: The Ohio State University.
- Salingaros, N. A. (2019). The biophilic healing index predicts effects of the built environment on our wellbeing. *J. Biourbanism* 8, 13–34.
- Senes, G., Fumagalli, N., Crippa, R., and Bolchini, F. (2012). Nursing homes: Engaging patients and staff in healing garden design through focus group interviews. *Neuropsychol. Trends* 12, 135–146.
- Sestras, R. E., and Sestras, A. F. (2023). Quantitative traits of interest in apple breeding and their implications for selection. *Plants* 12:903. doi: 10.3390/plants12040903
- Shahrad, A. (2012). *What are the design principles of Healing Gardens*. Master program Urban Landscape Dynamics MSc, SLU. Uppsala: Swedish University of Agricultural Sciences.
- Sharifi-Rad, J., Quispe, C., Vergara, C. V., Kitic, D., Kostic, M., Armstrong, L., et al. (2021). Genus *Viburnum*: Therapeutic potentialities and agro-food-pharma applications. *Oxid. Med. Cell. Longev.* 2021:3095514. doi: 10.1155/2021/3095514
- Sherman, S. A., Varni, J. W., Ulrich, R. S., and Malcarne, V. L. (2005). Post-occupancy evaluation of healing gardens in a pediatric cancer center. *Lands. Urban Plan.* 73, 167–183.
- Sidenius, U., Karlsson Nyed, P., Linn Lygum, V., and Stigsdotter, K. U. (2017). A diagnostic post-occupancy evaluation of the Nacadia® therapy garden. *Int. J. Environ. Res. Public Health* 14:882. doi: 10.3390/ijerph14080882
- Silva, D., Ferreira, M. S., Sousa-Lobo, J. M., Cruz, M. T., and Almeida, I. F. (2021). Anti-inflammatory activity of *Calendula officinalis* L. flower extract. *Cosmetics* 8:31. doi: 10.3390/cosmetics8020031
- Simionca Mărcășan, L. I., Pop, R., Somsai, P. A., Oltean, I., Popa, S., Sestras, A. F., et al. (2023). Comparative evaluation of *Pyrus* species to identify possible resources of interest in pear breeding. *Agronomy* 13:1264. doi: 10.3390/agronomy13051264
- Siu, A. M. H., Kam, M., and Mok, I. (2020). Horticultural therapy program for people with mental illness: A mixed-method evaluation. *Int. J. Environ. Res. Public Health* 17:711. doi: 10.3390/ijerph17030711
- Skulimowski, S., and Badurowicz, M. (2017). "Wearable sensors as feedback method in virtual reality anti-stress therapy," in *Proceedings of the 2017 International Conference on Electromagnetic Devices and Processes in Environment Protection with Seminar Applications of Superconductors (ELMECO & AoS), 3–6 December 2017, (Lublin), 1–4*.
- Smidl, S., Mitchell, D. M., and Creighton, C. L. (2017). Outcomes of a therapeutic gardening program in a mental health recovery center. *Occup. Ther. Ment. Health* 33, 374–385.
- Soderlund, J., and Newman, P. (2015). Biophilic architecture: A review of the rationale and outcomes. *AIMS Environ. Sci.* 2, 950–969. doi: 10.3934/environsci.2015.4.950
- Stawiarz, E., and Wróblewska, A. (2016). Flowering phenology of *Weigela florida* Bunge and the effect of color change in its flowers on the behavior of visiting insects. *Acta Sci. Pol. Hortorum Cultus* 15, 45–57.
- Stepansky, K., Delbert, T., and Bucey, J. C. (2022). Active student engagement within a university's therapeutic sensory garden green space: Pilot study of utilization and student perceived quality of life. *Urban For. Urban Green.* 67:127452.
- Suzuki, K., Dohzono, I., Hiei, K., and Fukuda, Y. (2002). Pollination effectiveness of three bumblebee species on flowers of *Hosta sieboldiana* (Liliaceae) and its relation to floral structure and pollinator sizes. *Plant Spec. Biol.* 17, 139–146. doi: 10.1046/j.1442-1984.2002.00076.x
- Syrbe, R.-U., Neumann, I., Grunewald, K., Brzoska, P., Louda, J., Kochan, B., et al. (2021). The value of urban nature in terms of providing ecosystem services related to health and well-being: An empirical comparative pilot study of cities in Germany and the Czech Republic. *Land* 10:341.
- Szabo, M., Dumitras, A., Mircea, D.-M., Sestras, A. F., and Brzuszek, R. F. (2022). Analysis of compositional lines in natural landscapes. *Nova Geodesia* 2:29. doi: 10.55779/ng2229
- Tadić, V., Arsić, I., Zvezdanović, J., Zugić, A., Cvetković, D., and Pavkov, S. (2017). The estimation of the traditionally used yarrow (*Achillea millefolium* L. Asteraceae) oil extracts with anti-inflammatory potential in topical application. *J. Ethnopharmacol.* 199, 138–148. doi: 10.1016/j.jep.2017.02.002
- Tarapatyky, M., Gumienna, A., Sowa, P., Kapusta, I., and Puchalski, C. (2021). Bioactive phenolic compounds from *Primula veris* L.: Influence of the extraction conditions and purification. *Molecules* 26:997. doi: 10.3390/molecules26040997
- Tekin, B. H., Corcoran, R., and Gutiérrez, R. U. (2023a). The impact of biophilic design in Maggie's Centres: A meta-synthesis analysis. *Front. Archit. Res.* 12, 188–207. doi: 10.1016/j.foar.2022.06.013
- Tekin, B. H., Corcoran, R., and Gutiérrez, R. U. (2023b). A systematic review and conceptual framework of biophilic design parameters in clinical environments. *HERD* 16, 233–250. doi: 10.1177/19375867221118675
- Thaneshwari, P. K., Sharma, R., and Sahare, H. A. (2018). Therapeutic gardens in healthcare: A review. *Ann. Biol.* 34, 162–166.
- Totaforti, S. (2020). Emerging biophilic urbanism: The value of the human–nature relationship in the urban space. *Sustainability* 12:5487.
- Ulrich, R. S. (1986). Human responses to vegetation and landscapes. *Lands. Urban Plan.* 13, 29–44.
- Uwajeh, P. C., Iyendo, T. O., and Polay, M. (2019). Therapeutic gardens as a design approach for optimising the healing environment of patients with Alzheimer's disease and other dementias: A narrative review. *Explore* 15, 352–362. doi: 10.1016/j.explore.2019.05.002
- Vapaa, A. G. (2002). *Healing gardens: Creating places for restoration, meditation, and sanctuary*. Master's Thesis. Blacksburg, VA: Virginia Polytechnic Institute and State University.
- Vinokur, Y., Rodov, V., Reznick, N., Goldman, G., Horev, B., Umiel, N., et al. (2006). Rose petal tea as an antioxidant-rich beverage: Cultivar effects. *J. Food Sci.* 71, S42–S47. doi: 10.1111/j.1365-2621.2006.tb12404.x
- Vujcic, M., Tomicevic-Dubljevic, J., Grbic, M., Lecic-Tosevski, D., Vukovic, O., and Toskovic, O. (2017). Nature based solution for improving mental health and well-being in urban areas. *Environ. Res.* 158, 385–392.
- van den Berg, A. (2005). *Health impacts of healing environments; A review of evidence for benefits of nature, daylight, fresh air, and quiet in healthcare settings*. Groningen: University Hospital Groningen.
- Weerasuriya, R., Henderson-Wilson, C., and Townsend, M. (2019). A systematic review of access to green spaces in healthcare facilities. *Urban For. Urban Green.* 40, 125–132.
- Whear, R., Thompson-Coon, J., Bethel, A., Abbott, R., Stein, K., and Garside, R. (2014). What is the impact of using outdoor spaces such as gardens on the physical and mental well-being of those with dementia? A systematic review of quantitative and qualitative evidence. *J. Am. Med. Dir. Assoc.* 15, 697–705. doi: 10.1016/j.jamda.2014.05.013
- Whitehouse, S., Varni, J. W., Seid, M., Cooper-Marcus, C., Ensberg, M. J., Jacobs, J. R., et al. (2001). Evaluating a children's hospital garden environment: Utilization and consumer satisfaction. *J. Environ. Psychol.* 21, 301–314.
- Wilson, E. O. (1984). *Biophilia*. Cambridge, MA: Harvard University Press.
- Xu, C., Guo, H., Wang, Z., and Chen, Y. (2023). Development and comparative analysis of initiation ability in large-scale *Heuchera* propagation using tissue culture versus cuttings. *Sci. Rep.* 13:14785. doi: 10.1038/s41598-023-42001-8
- Xue, F., Gou, Z., Lau, S. S.-Y., Lau, S.-K., Chung, K.-H., and Zhang, J. (2019). From biophilic design to biophilic urbanism: Stakeholders' perspectives. *J. Clean. Prod.* 211, 1444–1452.
- Yaghoobi, K., Kaka, G. R., Davoodi, S. H., and Ashayeri, H. (2016). Therapeutic effects of *Lavandula angustifolia*. *J. Gorgan Univ. Med. Sci.* 17, 1–9.
- Yang, Y., Ro, E., Lee, T.-J., An, B.-C., Hong, K.-P., Yun, H.-J., et al. (2022). The multi-sites trial on the effects of therapeutic gardening on mental health and well-being. *Int. J. Environ. Res. Public Health* 19:8046. doi: 10.3390/ijerph19138046
- Yucedag, C., Ozel, H. B., Cetin, M., and Sevik, H. (2019). Variability in morphological traits of seedlings from five *Euonymus japonicus* cultivars. *Environ. Monit. Assess.* 191:285. doi: 10.1007/s10661-019-7464-6
- Zdunić, G., Šavikin, K., Pljevljakušić, D., and Djordjević, B. (2016). Black (*Ribes nigrum* L.) and red currant (*Ribes rubrum* L.) cultivars. *Nutr. Composit. Fruit Cultiv.* 101–126. doi: 10.1016/b978-0-12-408117-8.00005-2
- Zhang, Z., Long, Y., Chen, L., and Chen, C. (2021). Assessing personal exposure to urban greenery using wearable cameras and machine learning. *Cities* 109:103006.
- Zhao, Y., Zhan, Q., and Xu, T. (2022). Biophilic design as an important bridge for sustainable interaction between humans and the environment: Based on practice in Chinese healthcare space. *Comput. Math. Methods Med.* 2022:8184534. doi: 10.1155/2022/8184534
- Zhbanova, E. (2019). Fruit of raspberry *Rubus idaeus* L. as a source of functional ingredients (review). *Food Process. Tech. Technol.* 48, 5–14. doi: 10.21603/2074-9414-2018-1-5-14
- Zhong, W., Schröder, T., and Bekkering, J. (2022). Biophilic design in architecture and its contributions to health, well-being, and sustainability: A critical review. *Front. Arch. Res.* 11, 114–141. doi: 10.1016/j.foar.2021.07.006

Submit to this Journal

Review for this Journal

Propose a Special Issue

Article Menu

Academic Editors

- Amr Abd-Elrahman
- Benjamin E. Wilkinson
- H. Andrew Lassiter

Subscribe SciFeed

Get citation

Open Access Article

Enhancing LiDAR-UAS Derived Digital Terrain Models with Hierarchic Robust and Volume-Based Filtering Approaches for Precision Topographic Mapping

by Valeria-Ersilia Oniga ¹, Ana-Maria Loghin ^{2,*}, Mihaela Macovei ¹, Anca-Alina Lazar ¹, Bogdan Boroianu ³ and Paul Sestras ^{4,5}

¹ Department of Terrestrial Measurements and Cadastre, Faculty of Hydrotechnical Engineering, Geodesy and Environmental Engineering, "Gheorghe Asachi" Technical University of Iasi, Professor Dimitrie Mangeron Boulevard 67, 700050 Iasi, Romania

² Department of Remote Sensing, Federal Office of Metrology and Surveying, Schiffamtsgasse 1-3, 1020 Vienna, Austria

³ Geocad Profesional SRL (Smart Imaging and Mapping Services-SIMS), 022683 București, Romania

⁴ Department of Land Measurements and Cadastre, Faculty of Civil Engineering, Technical University of Cluj-Napoca, 400020 Cluj-Napoca, Romania

⁵ Academy of Romanian Scientists, Ilfov 3, 050044 Bucharest, Romania

* Author to whom correspondence should be addressed.

Remote Sens. 2024, 16(1), 78; <https://doi.org/10.3390/rs16010078>

Submission received: 3 November 2023 / Revised: 16 December 2023 / Accepted: 18 December 2023 / Published: 24 December 2023

REMOTE SENSING

Publisher name: MDPI

Journal Impact Factor™

4.2
2023

4.9
Five Year

JCR Category	Category Rank	Category Quartile
ENVIRONMENTAL SCIENCES <i>in SCIE edition</i>	110/358	Q2
GEOSCIENCES, MULTIDISCIPLINARY <i>in SCIE edition</i>	34/253	Q1
IMAGING SCIENCE & PHOTOGRAPHIC TECHNOLOGY <i>in SCIE edition</i>	10/36	Q2
REMOTE SENSING <i>in SCIE edition</i>	16/62	Q2



Article

Enhancing LiDAR-UAS Derived Digital Terrain Models with Hierarchic Robust and Volume-Based Filtering Approaches for Precision Topographic Mapping

Valeria-Ersilia Oniga ¹, Ana-Maria Loghin ^{2,*}, Mihaela Macovei ¹, Anca-Alina Lazar ¹, Bogdan Boroianu ³ and Paul Sestras ^{4,5}

¹ Department of Terrestrial Measurements and Cadastre, Faculty of Hydrotechnical Engineering, Geodesy and Environmental Engineering, "Gheorghe Asachi" Technical University of Iasi, Professor Dimitrie Mangeron Boulevard 67, 700050 Iasi, Romania; valeria-ersilia.oniga@academic.tuiasi.ro (V.-E.O.); mihaela.macovei@academic.tuiasi.ro (M.M.); anca-alina.lazar@academic.tuiasi.ro (A.-A.L.)

² Department of Remote Sensing, Federal Office of Metrology and Surveying, Schiffamtsgasse 1-3, 1020 Vienna, Austria

³ Geocad Profesional SRL (Smart Imaging and Mapping Services-SIMS), 022683 București, Romania; office@sims.ro

⁴ Department of Land Measurements and Cadastre, Faculty of Civil Engineering, Technical University of Cluj-Napoca, 400020 Cluj-Napoca, Romania; psestras@mail.utcluj.ro

⁵ Academy of Romanian Scientists, Ilfov 3, 050044 Bucharest, Romania

* Correspondence: loghin.anamaria@yahoo.com; Tel.: +40-751-893-777

Abstract: Airborne Laser Scanning (ALS) point cloud classification in ground and non-ground points can be accurately performed using various algorithms, which rely on a range of information, including signal analysis, intensity, amplitude, echo width, and return number, often focusing on the last return. With its high point density and the vast majority of points (approximately 99%) measured with the first return, filtering LiDAR-UAS data proves to be a more challenging task when compared to ALS point clouds. Various algorithms have been proposed in the scientific literature to differentiate ground points from non-ground points. Each of these algorithms has advantages and disadvantages, depending on the specific terrain characteristics. The aim of this research is to obtain an enhanced Digital Terrain Model (DTM) based on LiDAR-UAS data and to qualitatively and quantitatively compare three filtering approaches, i.e., hierarchical robust, volume-based, and cloth simulation, on a complex terrain study area. For this purpose, two flights over a residential area of about 7.2 ha were taken at 60 m and 100 m, with a DJI Matrice 300 RTK UAS, equipped with a Geosun GS-130X LiDAR sensor. The vertical and horizontal accuracy of the LiDAR-UAS point cloud, obtained via PPK trajectory processing, was tested using Check Points (ChPs) and manually extracted features. A combined approach for ground point classification is proposed, using the results from a hierarchic robust filter and applying an 80% slope condition for the volume-based filtering result. The proposed method has the advantage of representing with accuracy man-made structures and sudden slope changes, improving the overall accuracy of the DTMs by 40% with respect to the hierarchical robust filtering algorithm in the case of a 60 m flight height and by 28% in the case of a 100 m flight height when validated against 985 ChPs.

Keywords: LiDAR-UAS; PPK; DTM; filtering approaches; proposed method



Citation: Oniga, V.-E.; Loghin, A.-M.; Macovei, M.; Lazar, A.-A.; Boroianu, B.; Sestras, P. Enhancing LiDAR-UAS Derived Digital Terrain Models with Hierarchic Robust and Volume-Based Filtering Approaches for Precision Topographic Mapping. *Remote Sens.* **2024**, *16*, 78. <https://doi.org/10.3390/rs16010078>

Academic Editors: Amr Abd-Elrahman, Benjamin E. Wilkinson and H. Andrew Lassiter

Received: 3 November 2023

Revised: 16 December 2023

Accepted: 18 December 2023

Published: 24 December 2023



Copyright: © 2023 by the authors. Licensee MDPI, Basel, Switzerland. This article is an open access article distributed under the terms and conditions of the Creative Commons Attribution (CC BY) license (<https://creativecommons.org/licenses/by/4.0/>).

1. Introduction

Airborne Laser Scanning (ALS), also known as airborne Light Detection and Ranging (LiDAR), and LiDAR-Unmanned Aerial System (LiDAR-UAS) are two different methods for collecting LiDAR data. LiDAR, an active remote sensing technology, has found applications in various fields, including topography [1], hydrography [2], archaeology [3,4], oil exploration [5], mining [6], and forestry [7,8], and has been in use for more than a decade.

One of the advantages of LiDAR technology compared to aerial photogrammetry or high-resolution optical satellite data is the acquisition of high-precision three-dimensional (3D) data using the polar coordinate method (angles and inclined distances) to capture a terrain's geometry. Moreover, Full-waveform (FWF) ALS systems have been operational for two decades. In addition to waveform digitization, these systems offer supplementary information, including echo width. When combined with amplitude data, this additional information can enhance ground filtering even in areas with dense canopy cover [7]. However, the Structure from Motion (SfM) photogrammetric technique reconstructs three-dimensional information from two-dimensional images, showing promising results for DTM derivation, with the main advantages being RGB color information and, especially, its cost-effectiveness.

Both ALS and LiDAR-UAS play crucial roles in collecting high-resolution and accurate elevation data for various applications. While both methods rely on LiDAR principles, they differ in terms of data acquisition platforms, applications, characteristics, point densities, and scale coverages. Compared with the widespread and well-established method of ALS, typically used for mapping large territories, the LiDAR-UAS technique can be seen as a desirable solution for performing topographic surveys for small- to medium-sized areas, up to a few square kilometers. The choice between ALS and LiDAR-UAS often depends on the specific requirements of a project, considering factors such as area extent, resolution, and environmental conditions. Due to its advantages, such as suitability for small-scale projects, flexibility in capturing data in hard-to-reach areas, cost-effectiveness, and the capability to achieve very high point density and resolution, LiDAR-UASs often present a superior solution for small-scale projects when compared to traditional airborne LiDAR or photogrammetry methods.

LiDAR-UASs consist of LiDAR sensors and UAVs equipped with Global Navigation Satellite Systems (GNSSs) that determine the position of the UAS and Inertial Navigation System (INS) using an Inertial Measurement Unit (IMU) that measures the rotation angles of the UAS with respect to its navigation coordinate system (roll, pitch, and yaw) and acceleration. Alternatively, LiDAR-UASs can be equipped with an RGB digital camera to obtain a textured LiDAR-UAS point cloud [9]. The LiDAR sensor emits laser pulses toward the ground, and the distance between the sensor (emitter) and the measured object that generates the backscatter echo is calculated based on the time it takes for the laser pulse to return to the sensor. Multiple returns, with the first return typically being the reflection from the topmost object (e.g., tree canopy) and the last return being the reflection from the ground, are recorded [10].

There are several manufacturers available on the market, such as Velodyne LiDAR Inc. (San Jose, CA, USA), Routsence Inc. (Edinburgh, UK), LeddarTech Inc. (Quebec City, QC, Canada), RIEGL Laser Measurement System GmbH (Horn, Austria), and Geodetics Inc. (San Diego, CA, USA), that have developed small and fully integrated LiDAR sensors for UAVs, with the various types offering different capabilities and specifications [11].

Modeling topographic surfaces is a very important stage in a wide range of applications, namely: hydrographic studies, engineering projects, telecommunications, geology, geomorphology, and more. A Digital Terrain Model (DTM) represents the bare earth terrain with uniformly spaced Z-values in X (Easting) and Y (Northing) directions, excluding vegetation and artificial objects. DTMs often include not only the elevations of prominent topographic features on the ground but also mass points and breaklines that are unevenly distributed. This uneven distribution is intentional and designed to more accurately represent the actual contour and shape of the bare earth surface [12].

An essential step in data pre-processing for terrain modeling is classifying LiDAR-UAS point clouds into ground and non-ground points. This classification process involves distinguishing points that represent the ground surface from those that represent non-ground objects such as buildings and vegetation. Once the ground points are accurately classified, the creation of the DTM becomes a straightforward process [13]. Often, a combination of automated and manual methods is used to classify LiDAR point clouds

effectively. Automated methods provide initial classifications, which can then be reviewed and corrected manually where necessary. The effectiveness of point cloud classification into ground and non-ground points can be influenced by factors such as point cloud density [14], terrain complexity [15], and the quality of LiDAR-UAS data. Therefore, it is important to select the classification method that best suits the specific characteristics of the study area. As LiDAR-UASs are subject to technological advancements and LiDAR data become more readily accessible, research on LiDAR-UAS-based DTM generation is gaining greater attention [16].

Different ground filtering algorithms have been developed over the past 30 years [17]. Depending on the concept used, the existing methods for point cloud filtering are classified into six categories [16] as follows:

- Morphological-based filters: These algorithms use a structural parameter that describes the height differences within a threshold based on the horizontal distances used. The smaller the distance between a point and its neighbor, the smaller the height difference between them. A variant of this method is described in [15], in which the structural parameter depends on the terrain's shape. Morphology-based filtering may be challenging in terrains with a variety of non-ground objects [16].
- Surface-based filters: These algorithms work iteratively. In the first iteration, the lowest point for each grid cell is used to create an initial surface. Subsequently, residuals, which represent the distances between the measured points and the initial surface, are calculated. Each point is assigned a weight based on its residual value. Points with higher weights have a stronger influence on the surface, attracting the surface toward them, while points with lower weights have a lesser impact on the overall configuration of the surface. This iterative process continues until a stable surface is achieved, or the maximum allowable number of iterations is reached [18–20]. This type of method can present challenges in preserving terrain details, such as sharp ridges and cliffs. Additionally, it may have a tendency to misclassify small non-ground objects within the point cloud data [16].
- Triangulated irregular network (TIN)-based refinement: An initial TIN is created based on the points with the lowest elevation in each grid cell. Gradually, other points are added by establishing reference thresholds [21]. This approach may encounter challenges when it comes to detecting discontinuous terrains, such as sharp ridges, and is time-consuming [16].
- Segmentation and classification: These methods work with segments, which are classified based on height differences in their neighborhoods. In [22], a region growing technique of creating a surface was applied, based on height differences, to obtain segments that were subsequently classified into three categories: ground, buildings, and vegetation. In [23], segmentation compactness and height differences were applied to determine various types of areas, including the ground. Features such as geometry, radiometry, topology, the number of returns, intensity, and echo characteristics are used for better filtering ground points. These methods may encounter difficulties when applied to densely vegetated areas and strongly depend on the accuracy of segmentation [16].
- Statistical analysis: These filters, particularly parameter-free algorithms, help minimize the need for manual parameter tuning, thus reducing uncertainty and enhancing the robustness of applying specific methods to different study sites. Additionally, these methods tend to excel in relatively flat terrains without intricate non-ground objects [16].
- Multi-scale comparison: In general, this type of method operates through two main steps. First, several preliminary trend surfaces are created at different resolutions; second, each point in the point cloud is examined at various scales by comparing the elevation difference between the point and the different trend surfaces. This method is better suited for relatively flat terrains and may exhibit suboptimal performance in rapidly changing or complex landscapes [16].

Filtering high-density point clouds is more challenging than filtering low-density ones because as point density increases, the performance of the filtering algorithm tends to decrease [24].

In the existing literature, most studies have primarily focused on DTMs derived from ALS point clouds. In contrast, a limited number of studies have examined the accuracy of DTMs generated from LiDAR-UAS point clouds. For example, in [25], the vertical error of a DTM, created based on a LiDAR-UAS point cloud acquired with a Velodyne laser sensor VLP-16 at a 50 m height with a density of 180 points/sqm, was evaluated for uncovered and vegetation areas, separately, using 193 checkpoints measured via GNSS-RTK technology. The RMSE_Z values ranged between 10 and 14 cm for the different vegetation height levels. The ground points were filtered using Axelsson's algorithm, and a DTM with a 0.25 m cell size was created using the moving average interpolation method combined with natural neighbor interpolation.

In [26], the DTM accuracy, generated based on AL3 S1000 and AL3-32 LiDAR, was tested for two different terrains (i.e., flat, slope, and overall) for three different heights (i.e., 20 m, 40 m, and 60 m), using 129 reference points measured via different technologies. For the 60 m flight height, the RMSE was 10.5 cm for the flat area, 34.3 cm for the slope area, and 61.6 cm overall. The ground points were filtered using the Axelsson's algorithm.

In [27], a DTM was created for three small (around 1.5 ha) different forest sites, differing in terms of the nature of the forest and the terrain. The data acquisition was carried out with a DJI Zenmuse L1 mounted on a DJI Matrice 300 RTK UAS at a 100 m height under leaf-off conditions. The ground points were obtained using a combination of the structural filtering method CANUPO and a CSF. The vertical accuracy was tested, having as a reference a Terrestrial Laser Scanner (TLS) point cloud. For test site no. 2, which is an old forest with rugged terrain, the error was 5 cm, and for test site no. 3, the error was 6.5 cm. It is important to note that these sites are devoid of low and medium vegetation, making them unsuitable for a direct comparison with the DTM results obtained in our tests. Nevertheless, they can serve as reference points for evaluating the vertical accuracy of LiDAR-UAS point clouds.

Despite the significant advancements in terms of algorithms, the generation of DTMs, particularly in specific and complex terrain situations, continues to pose challenges [28].

Research Scope

The primary objective of this study is to identify the most suitable filtering method for generating a DTM in challenging terrain surfaces, utilizing UAS LiDAR data. Three distinct filtering techniques, namely, a cloth simulation filter, a volume-based filter, and hierarchic robust filtering, were applied to two LiDAR-UAS point clouds, and the resulting DTMs were tested in terms of vertical accuracy using a total of 985 ChPs measured via a total station and GNSS-RTK technology. The LiDAR-UAS point clouds were acquired at different altitudes, specifically at 60 m and 100 m. Furthermore, the accuracy of the georeferencing process of the LiDAR-UAS point cloud data was assessed using 85 ChP elevations, 33 ChP tridimensional coordinates, and 64 ChP tridimensional coordinates measured with the total station on the rooftop's corners and manually digitized polylines on the edges of the rooftops. The georeferencing process was carried out using a GNSS-aided method with Post-Processed Kinematic (PPK) processing, without the use of additional information such as Ground Control Points (GCPs). We propose a workflow to enhance the LiDAR-UAS DTM by combining the results of the hierarchic robust and volume-based filtering approaches for precision topographic mapping.

2. Materials and Methods

2.1. Study Area

The study area covers approximately 7.2 ha and constitutes a residential district situated in Iasi city, which is close to the administrative border of Rediu commune. It encompasses 22 houses and 2 residential apartment buildings, each enclosed by a combination

of natural and artificial fences, along with private roads and a private cemetery (Figure 1). In terms of administrative classification, it falls within the jurisdiction of the inner city of the Municipality of Iasi, according to the Urban General Plan. The characteristics of the study area include those of complex terrains with sudden slope changes, man-made structures such as retaining concrete walls, artificially terraced terrain, and a long concrete pathway with steps.

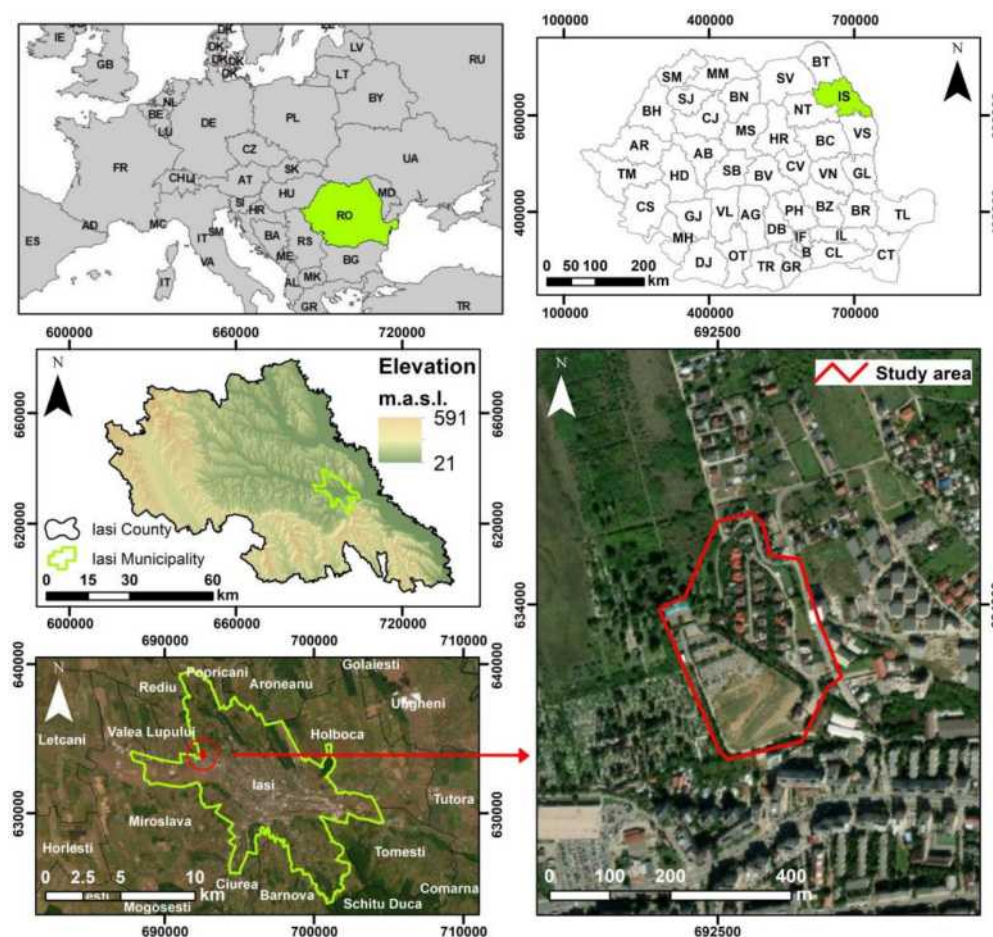


Figure 1. Study area location.

2.2. Research Methodology

The workflow applied for this study area is depicted in Figure 2 and comprises the following processing steps: (1) fieldwork with measurements for determining the coordinates of ChPs using GNSS-RTK technology and total station measurements, (2) planning and execution of the LiDAR-UAS flights, (3) coordinate transformation from ETRS-84 coordinate system to Romanian national coordinate system, (4) processing the LiDAR flight trajectory and processing to obtain the LiDAR-UAS point cloud, (5) accuracy assessment of the LiDAR-UAS point cloud based on ChPs and manually measured features, (6) point cloud filtering to extract the ground and off-ground points for subsequent DTM generation, (7) proposed combined method to obtain an enhanced DTM and accuracy assessment of derived DTMs using different filtering algorithms based on 985 ChPs.

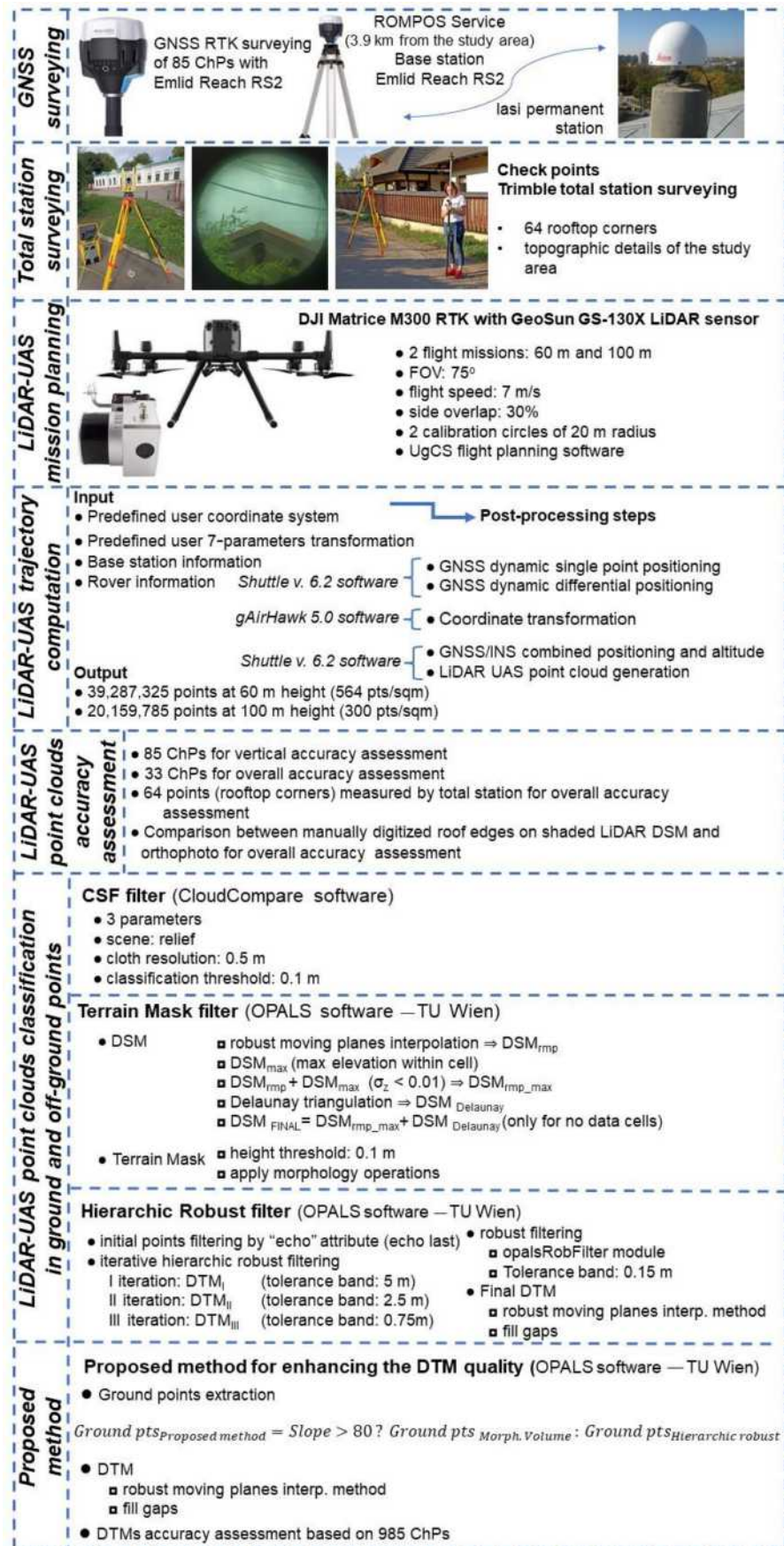


Figure 2. Flow chart of research methodology.

2.3. Check Points (ChPs)

ChPs were systematically positioned across the study area, as shown in Figure 3. Out of the total points that were established, 85 ChPs were specifically selected for assessing the vertical accuracy of the LiDAR-UAS point clouds. These ChPs were strategically positioned in areas devoid of vegetation, such as streets, parking lots, and a cemetery. They were marked on the ground using metallic bolts and wooden sticks, particularly in the cemetery area. To ensure a high degree of precision, the 85 ChPs' locations were surveyed using a multi-band Emlid Reach RS2 GNSS receiver, achieving centimetric accuracy through the use of the Romanian Positioning Determination System (ROMPOS) [29] and GNSS-RTK technology. The planimetric coordinates of the ChPs were determined within the Romanian national coordinate system known as "Stereographic on a unique secant plane-1970" (STEREO-70). Furthermore, the ellipsoidal heights were converted from the ETRS89 European datum to the Black Sea-1975 normal heights, corresponding to the RO Const/NH vertical datum, as outlined in [30]. Also, 33 of these points were marked on the ground by painting two red and two white triangles, using a hand-crafted pattern of 40 cm × 40 cm. Subsequently, the coordinates of 64 specific points, representing the corners of rooftops, were obtained through the reflectorless function of a total station (Figure 3a). The 33 painted ChPs and the 64 roof corners, were used for the overall accuracy assessment of LiDAR-UAS point clouds.

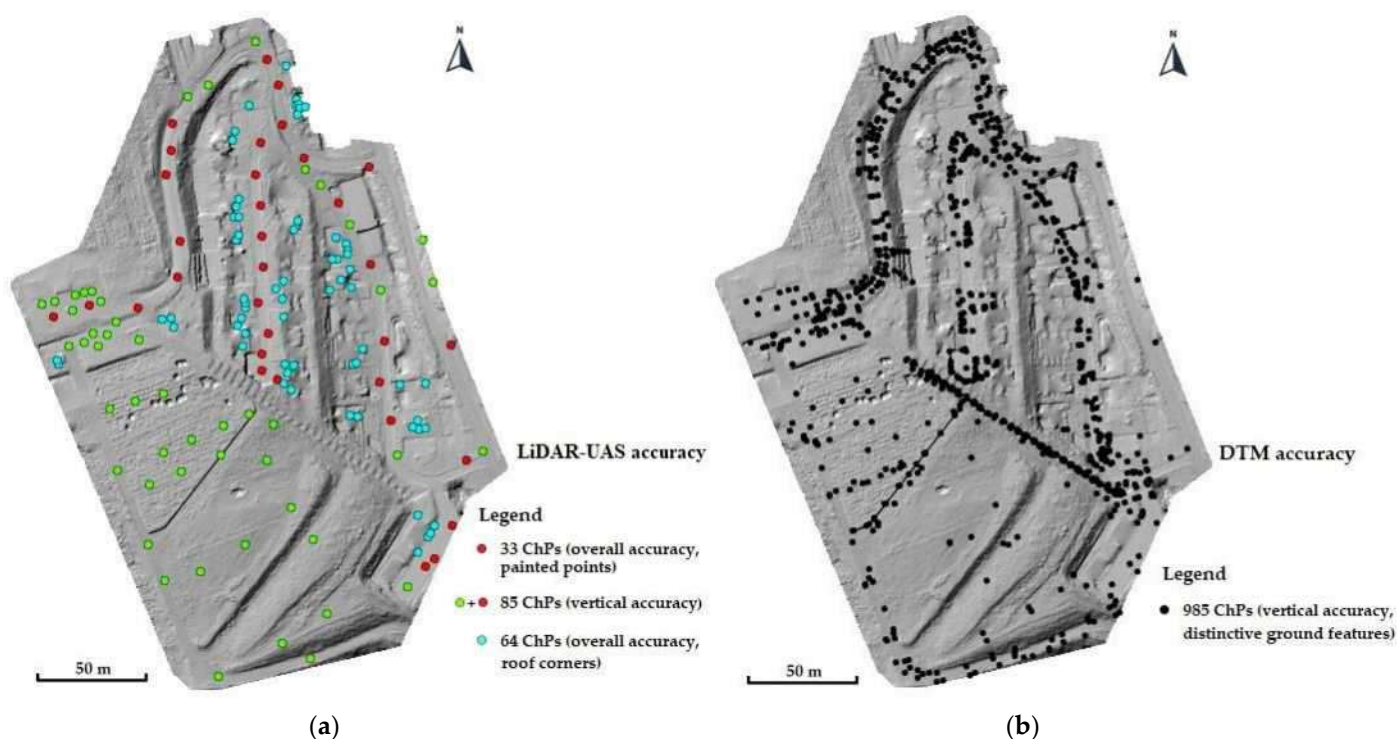


Figure 3. Overview of ChPs distribution for LiDAR-UAS accuracy (a), DTM vertical accuracy assessment (b).

A total of 985 ChPs (Figure 3b) were employed for the DTM accuracy assessment. These points are characteristic points of the surrounding space, such as road edges and fences, as well as man-made structures (Figure 4), and have been measured using a total station. This set of ChPs also encompasses the previously mentioned 85 ChPs to guarantee their distribution across the entire surface of the study area.

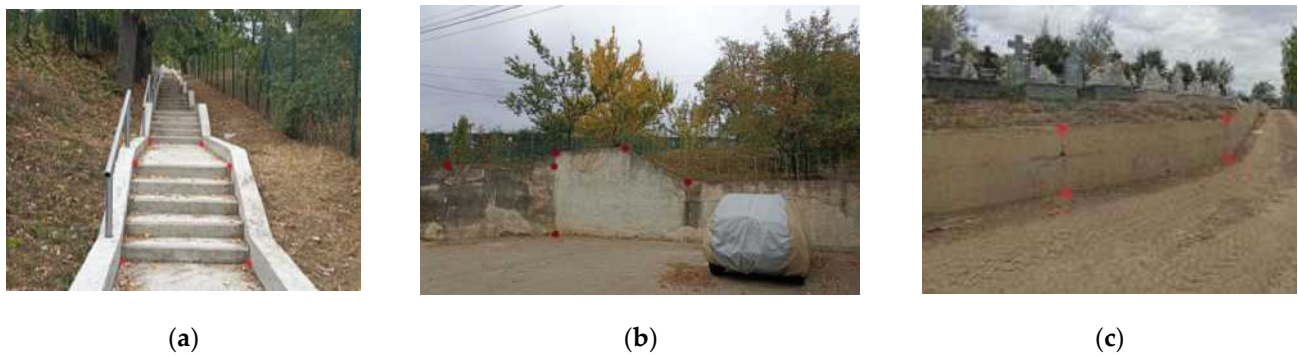


Figure 4. Total station measurements of the ChPs marked with red dots for accuracy assessment of derived DTMs: long concrete pathway with steps (a), retaining concrete walls (b,c).

2.4. GeoSun GS-130X LiDAR Scanner

For this particular case study, a GeoSun GS-130X LiDAR sensor was employed. This sensor is purposefully designed for remote sensing and data collection across a wide spectrum of applications. Its versatility extends to fields such as forestry, agriculture, mining, environmental monitoring, and topographic mapping. Some key features and information about the GeoSun GS-130X can be found in Appendix A. Weighing just 1.26 kg, this system is well suited for seamless integration with small- to medium-sized UASs. It has the capability to scan at a rate of 1,280,000 points per second while maintaining a measurement accuracy of less than 10 cm at a flight height of 120 m.

2.5. LiDAR-UAS Mission Planning

For the LiDAR-UAS mission planning, the Unmanned Ground Control Software (UgCS) Expert v4.17 (2141) was used, which is a software platform developed by SPH Engineering, primarily designed for the planning and execution of autonomous drone missions. Offering a user-friendly interface, the mission plan was created based on a few parameters, with the most important ones being the UAS (DJI Matrice 300 RTK for this case study), LiDAR mission, take-off and landing points, area of interest, field of view (FOV) (75° for these missions), flight height (60 m and 100 m), flight speed (7 m/s), side overlap (30%), and altitude mode (AGL), as well as with avoid obstacle and avoid terrain options selected. For both missions, two calibration circles with a 20 m radius were specified in the first point of the itinerary, as can be seen in Figure 5.

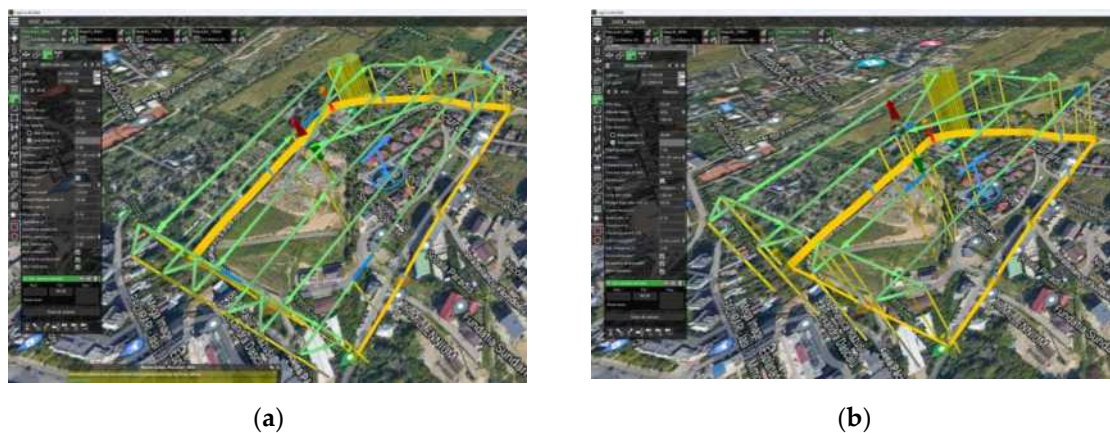


Figure 5. Mission planning for the DJI Matrice 300 RTK equipped with a GeoSun GS-130X LiDAR sensor using UgCS v4.17 (2141) software, parameters, and flight itinerary for the (a) 60 m height and (b) 100 m height.

A GeoSun GS-130X LiDAR-UAS scanner was mounted on the DJI Matrice 300 RTK UAS (Figure 6a). During the flights, an Emlid Reach RS2 GNSS receiver was set as the base station (Figure 6b) to record GNSS observations. The position of the receiver was determined with GNSS-RTK technology in 2 min intervals at 5 Hz (600 measurements) using the corrections through the ROMPOS service from the permanent reference station, namely, the IASI station from the national geodetic network, which was 3.9 km apart from the study area.

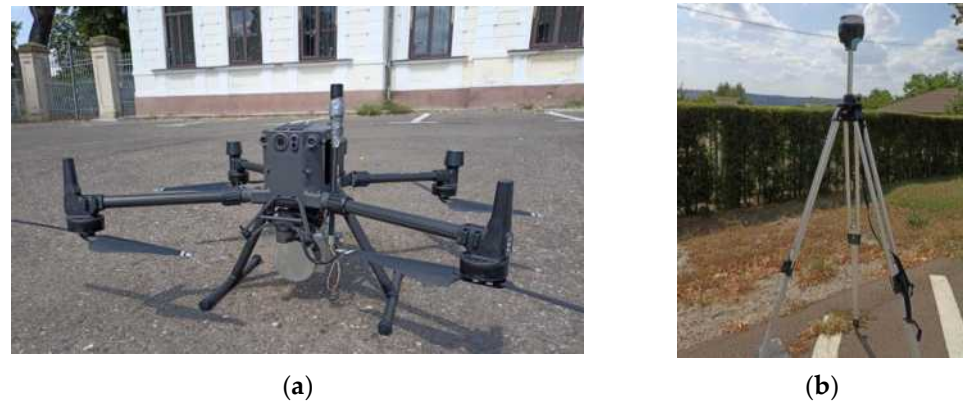


Figure 6. (a) DJI Matrice 300 RTK UAS with GeoSun GS-130X LiDAR scanner. (b) Emlid Reach RS2 GNSS receiver, set as the base station for PPK processing.

2.6. LiDAR-UAS Trajectory Computation

In general, the primary sources of error in UAV-based laser scanning are associated with the estimation of the GNSS/INS trajectory. These errors can be categorized into two main types: position errors and orientation errors. Position errors refer to inaccuracies in determining the exact location of the system or device as it moves. Orientation errors pertain to deviations in the device's spatial orientation or attitude. These errors can be systematic and consistent, which means they occur in a predictable manner, and they tend to propagate into errors in the point cloud data collected by the system. This underscores the importance of accurate trajectory estimation for obtaining precise and reliable geospatial data through UAV-based laser scanning [31].

Developed by Wuhan Geosun Navigation Technology Co., Ltd. (Wuhan, China), Shuttle is a high-precision GNSS/INS positioning and attitude determination post-processing software, which was used for the GeoSun GS-130X LiDAR-UAS trajectory computation. Shuttle employs single-epoch ambiguity algorithms and high-order Kalman filters to maximize the integration of GNSS carrier phase data and information from the inertial navigation component (IMU). Compared to GNSS post-processing alone, the GNSS/INS combination provides a more comprehensive set of carrier dynamics information, thus enhancing resolution accuracy and overall reliability [32].

The processing steps for this case study are presented in Figure 7 and can be summarized as follows: GNSS dynamic (the receiver moves relative to the surface of the Earth) precision single-point positioning (Figure 8a,c), GNSS dynamic differential positioning (Figure 8b,d), coordinate transformation, GNSS/INS combined positioning and attitude measurement, and point cloud generation. Shuttle's GNSS positioning solution is based on the fuzzy degree core algorithm, which combines several single-epoch ambiguity-solving techniques. The observation data of a dual-frequency GNSS receiver, the corresponding precision ephemeris, and the precision clock are used to achieve precise single-point positioning. The GNSS/INS-combined positioning attitude uses a high-order Kalman filter to establish a random error model of up to 24 orders for the system, and performs algorithms such as round-trip filtering, smoothing, and zero-speed updating.

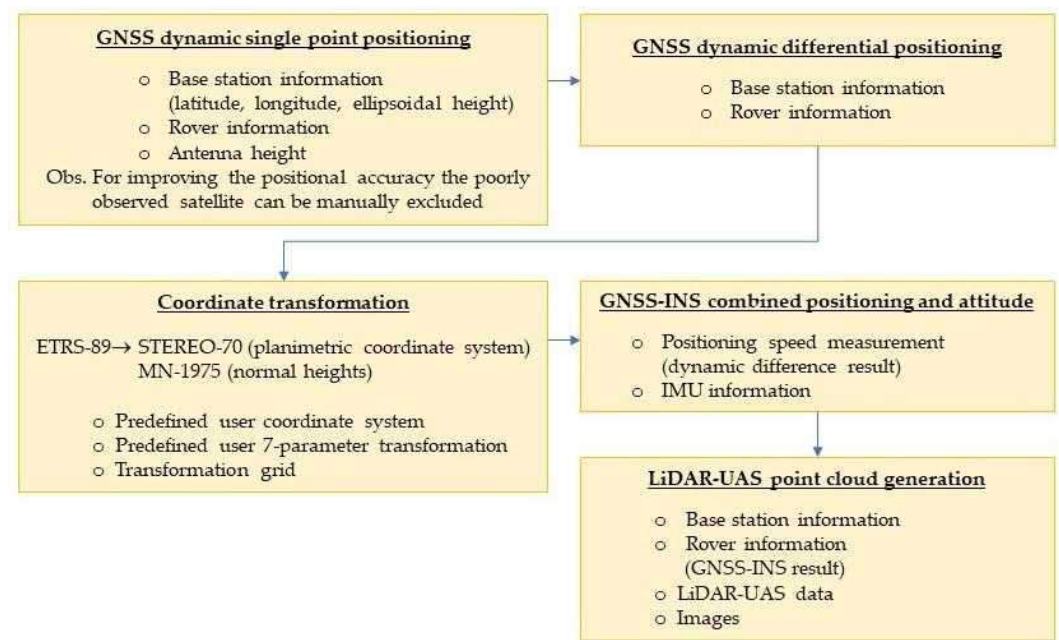


Figure 7. Processing of UAV-based laser scanning data.

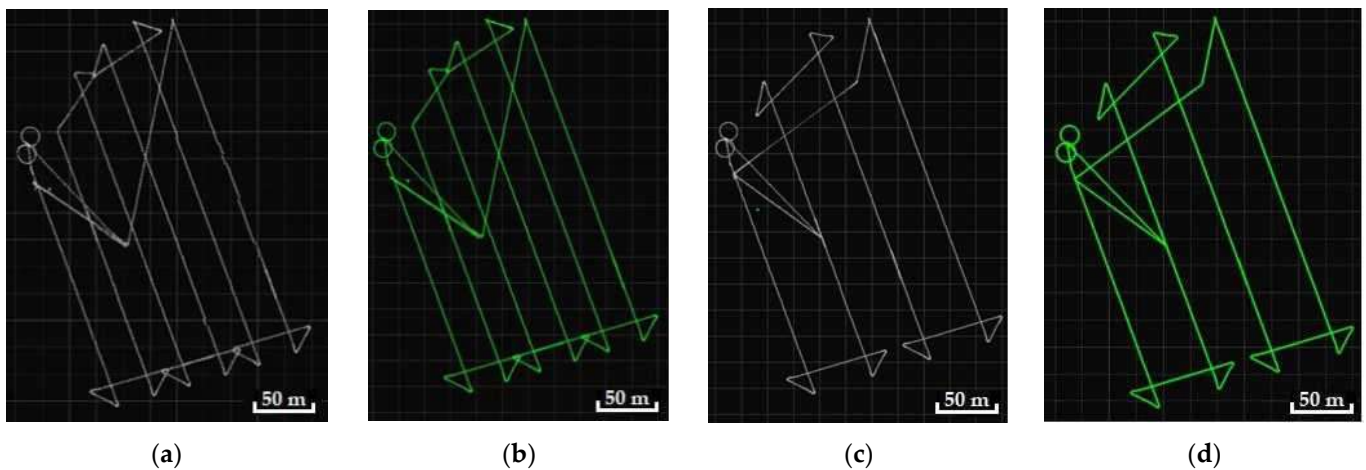


Figure 8. Flight trajectory computation: the GNSS dynamic single-point and differential positioning result for the 60 m height (a,b), the GNSS dynamic single-point and differential positioning result for the 100 m height (c,d).

Following the computation of the LiDAR-UAS trajectory using the GNSS information, the geodetic coordinates, defined within the ETRS-89 coordinate system, were subsequently transformed to the STEREO-70 coordinate system for the horizontal position and the Black Sea-1975 system for normal heights. This transformation was carried out using the coordinate transformation tool integrated into Geosun's self-developed gAirHawk 5.0 software. For 2D coordinate transformation, a predefined 7-parameter method specific to the Romanian territory was employed. As for the vertical position, the transformation grid, also accessible through TransDatRO v4.07 software [33] provided by the National Agency for Cadaster and Land Registry (NACLRO), was utilized.

At a flight height of 60 m, a total of 6 strips were acquired with a side overlap of 30%, as shown in Figure 9a, and at a flight height of 100 m, 4 strips were acquired, as depicted in Figure 9b.

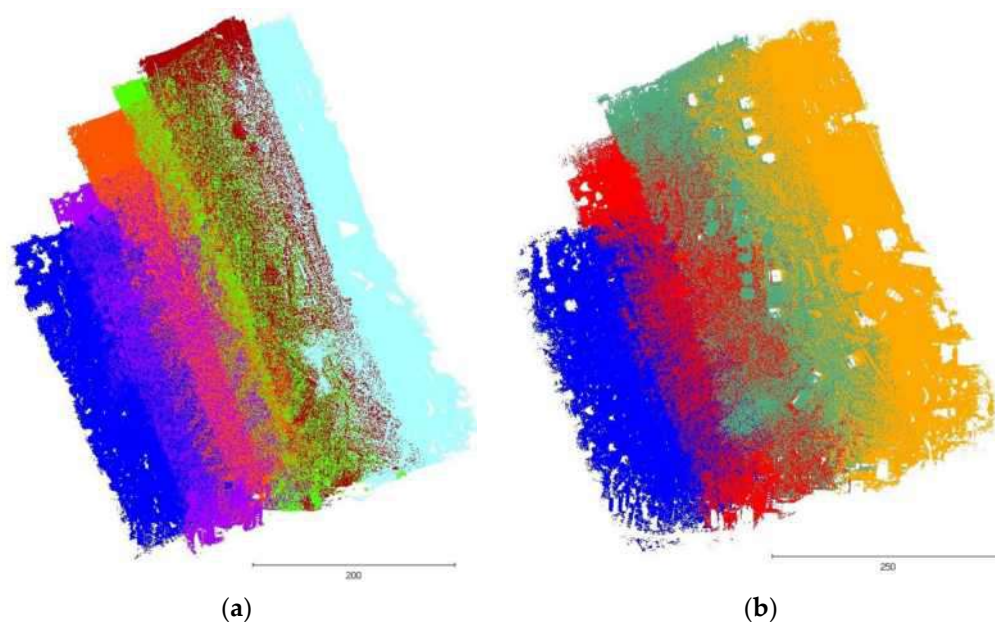


Figure 9. LiDAR-UAS point cloud strips acquired at (a) 60 m height (6 strips colored with different colors); (b) 100 m height (4 strips colored with different colors).

The point density of the LiDAR-UAS data was determined for both flights using the “opalsCell” module of Orientation and Processing of Airborne Laser Scanning data (OPALS) v2.5.0 software, developed by the Department of Geodesy and Geoinformation from Technical University of Vienna [34,35]. The analysis revealed varying point densities. For the 100 m flight, the point density ranged from 0 to a maximum of 1209 points/sqm, while for the 60 m flight, it varied between 0 and 2585 points/sqm. To estimate point density more effectively, histograms and color-coded visualizations were calculated (refer to Appendix B). From these, the Root-Mean-Square (RMS) value was considered as a reliable approximation of the point density per square meter. For the 100 m flight, the RMS value was found to be approximately 300 points/sqm, and for the 60 m flight, it was about 564 points/sqm. A visual representation of the point clouds from both flights is shown in Figure 10. Additionally, a summary of the LiDAR-UAS point clouds is provided in Table 1.

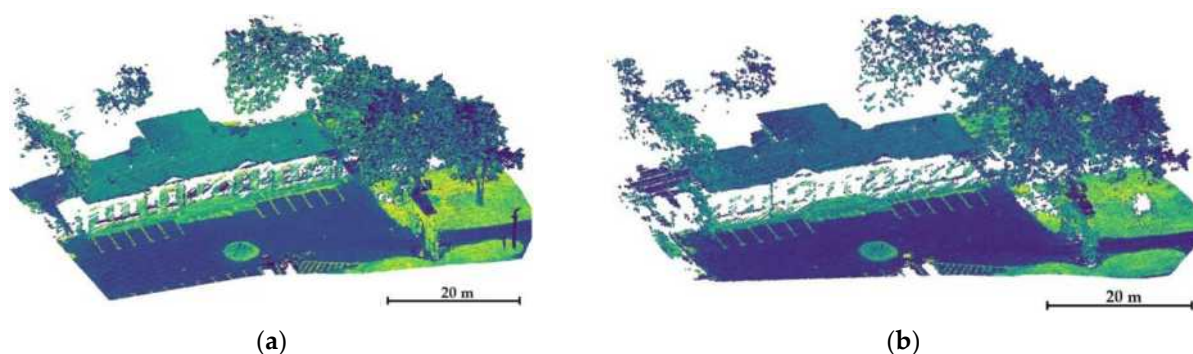


Figure 10. Details of the (a) 60 m height and (b) 100 m LiDAR-UAS point cloud colored by intensity.

Table 1. Summary of the LiDAR-UAS point clouds.

LiDAR-UAS Point Cloud	No. of Points	Density Points/sqm
60 m height	39,287,325	564
100 m height	20,159,785	300

3. Results

3.1. Quality Assessment of the LiDAR-UAS Point Clouds

Assessing the accuracy of LiDAR data collected from a UAS involves several steps and considerations. First, the standard deviation was computed to assess the disparity between LiDAR-derived elevation data and Ground Control Point (GCP) elevations, employing 85 ChPs, as detailed above (Figure 11a). Next, the coordinates of the 64 corners of rooftops were compared with the coordinates of the same points manually extracted directly from LiDAR-UAS point clouds. In Figure 11b, a close-up view is provided, highlighting certain points denoting the corners of rooftops. These specific points are distinguished by their red coloring and are superimposed onto the shaded Digital Surface Model (DSM). This presentation aims to enhance the clarity and understanding of the data.

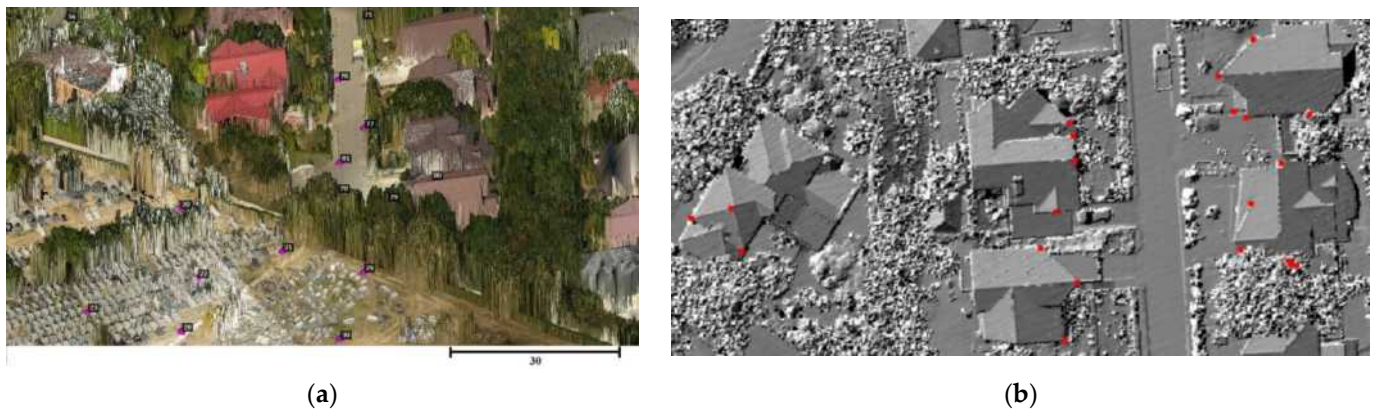


Figure 11. Quality assessment of LiDAR-UAS point cloud: (a) detail with some ChPs (markers with purple dots and their corresponding assigned numbers) superimposed on the LiDAR-UAS mesh surface; (b) points measured with a total station (red color) superimposed on a shaded DSM.

Subsequently, the coordinates of 33 painted points were manually measured directly on the mesh surface by visually approximating the center to assess the planimetric, vertical, and overall accuracy of the LiDAR-UAS point cloud. This step is not simple but is of high importance, as reported in [36], where the global accuracy was measured using high-intensity targets. The point cloud was colored by intensity attribute using the “viridis” color palette from CloudCompare v2.12.4 software [37], and an RGB point cloud was created by choosing a 0–40 range for saturation. The solution to creating the mesh surface for the ChPs arises due to point cloud density, as no LiDAR point is measured in the ChP center (Figure 12a–c). The coordinates were compared with those measured via GNSS-RTK technology.

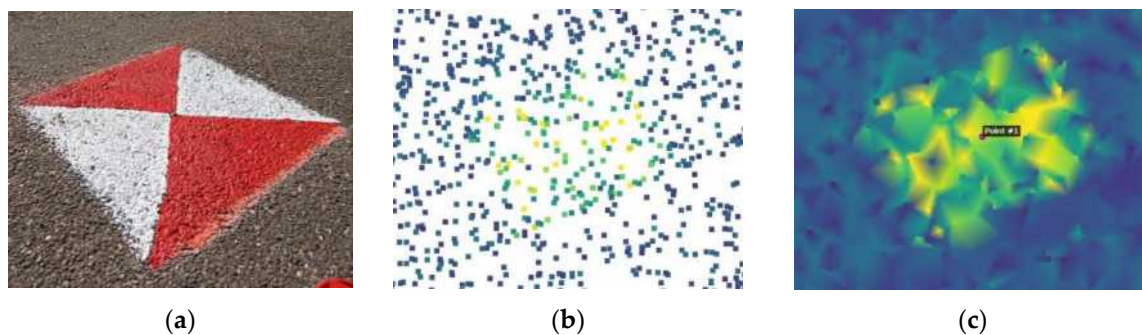


Figure 12. Quality assessment of LiDAR-UAS point cloud: (a) ChP ground marked with paint; (b) LiDAR-UAS point cloud colored by intensity for a ChP; (c) mesh surface created for a ChP point cloud.

Finally, a manual digitization process was applied on shaded Digital Surface Models (DSMs) (Section 3) to delineate the edges of building roofs. These manually digitized roof edges were then compared with edges manually digitized from orthophotos generated from a 60 m oblique UAS flight, as reported in [30] (Figure 13).

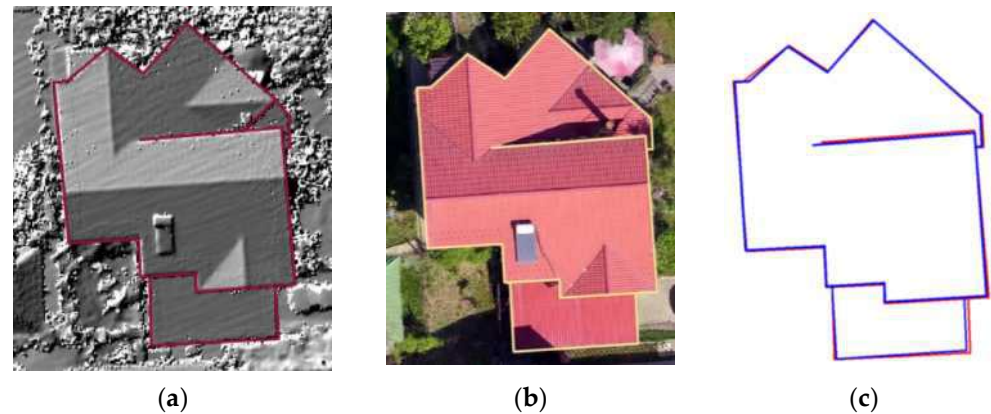


Figure 13. Quality assessment of LiDAR-UAS point cloud: (a) manually digitized rooftop edges based on the 60 m shaded DSM; (b) manually digitized rooftop edges based on 60 m UAS orthophoto; (c) superimposed digitized rooftop edges.

To evaluate the disparities between the LiDAR-derived elevation data and the elevations provided by ChPs, a mesh surface was generated based on the LiDAR-UAS point clouds using CloudCompare software. The Hausdorff distances between each ChP point and the mesh surface were measured, and a histogram representing the distribution of the Hausdorff distances was then computed, as shown in Figure 14. The values of the Root-Mean-Square Error were computed using the average difference (Hausdorff distances) between reference ChP elevations (as actual values) and the mesh surface created based on LiDAR-UAS points. The analysis indicates that for the 60 m flight, approximately 39% of the ChPs exhibit calculated distances falling within a range of 1 to 2 cm, with an RMSE value of 2 cm. For the 100 m flight, about 35% of the ChPs have calculated distances ranging from 2 to 3 cm, with an RMSE value of 4 cm, as reported in [27]. The 4 cm error was also obtained in [27], but after rasterization of LiDAR-UAS point cloud averaging the data within a 0.1 m cell, providing significant smoothing. These data suggest the degree of agreement between LiDAR-derived elevations and the ChPs at different flight heights.

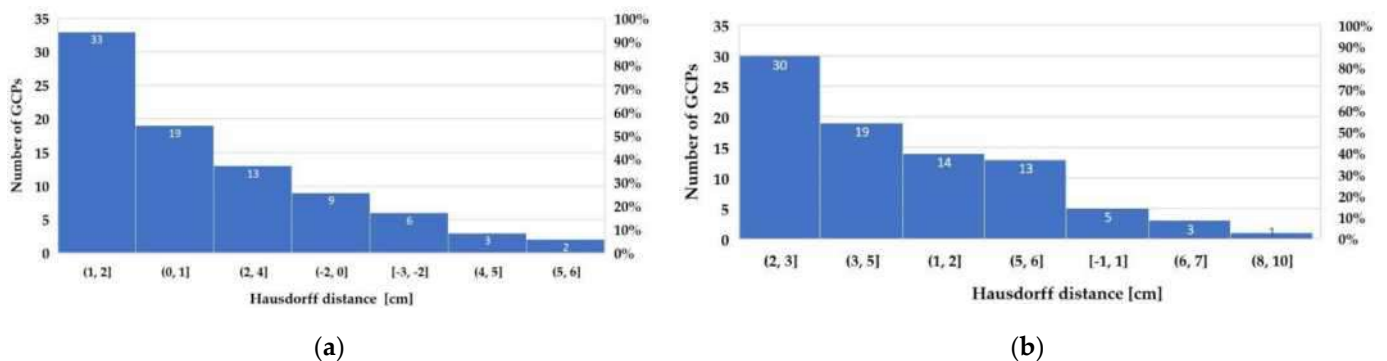


Figure 14. Histogram of Hausdorff distances between ChP altitude and mesh-DSM based on LiDAR-UAS point cloud acquired at (a) 60 m flight height and (b) 100 m flight height.

By comparing the coordinates of the 33 ChPs measured via GNSS-RTK with the coordinates of the same points manually measured directly on the mesh surface, errors along each axis were computed. These errors include the $RMSE_X$, $RMSE_Y$, and $RMSE_Z$, as well as the planimetric error $RMSE_{X,Y}$ and the total error $RMSE_T$. Additionally, the standard deviation was calculated, and the results are presented in Table 2.

Table 2. The residuals of the 33 ChPs marked with paint along the roads.

LiDAR-UAS Point Cloud	RMSE _X σ (cm)	RMSE _Y σ (cm)	RMSE _Z σ (cm)	RMSE _{X,Y} σ (cm)	RMSE _{TOT} σ (cm)
60 m height	3.3	3.5	2.2	4.8	5.3
	3.3	2.9	1.4	2.0	2.0
100 m height	5.0	4.2	3.7	6.5	7.5
	4.9	3.7	2.2	3.0	2.8

Upon analyzing the results, it can be seen that the planimetric error for the 60 m flight is 4.8 cm and 6.5 cm for the 100 m height. Furthermore, the total errors are 5.3 cm for the 60 m height and 7.5 cm for the 100 m height, which is in accordance with the values reported in [36]. However, the total errors found in [36] were approx. 3.8 cm at the 50 m flight altitude and approx. 4.8 cm at the 70 m flight altitude after the removal of the georeferencing global error using 3D transformation of the entire point cloud.

Subsequently, by comparing the coordinates of the roof corners measured via the total station with the coordinates of the same points manually extracted directly from LiDAR-UAS point clouds, the errors along each axis were computed; the results are summarized in Table 3.

Table 3. The residuals of the 64 points representing rooftop corners.

LiDAR-UAS Point Cloud	RMSE _X (cm)	RMSE _Y (cm)	RMSE _Z (cm)	RMSE _{X,Y} (cm)	RMSE _{TOT} (cm)
60 m height	6	8	7.6	10	12.6
100 m height	8.2	11.4	11	14.1	17.9

It is essential to note that the accuracy of corner measurements in a laser-scanned point cloud depends on various factors, including the point cloud density, the laser scanner characteristics, scan angle, vegetation, noise, and environmental conditions. The density of laser points in the point cloud plays a significant role in the identification of corners and edges. Higher point densities provide more information, making it easier to detect sharp transitions in elevation or slope, which are indicative of corners or edges. Low-density point clouds may not capture subtle features effectively. The type of laser scanner used for data acquisition affects the point cloud's quality. Scanners with different laser wavelengths, pulse repetition rates, and scanning patterns can influence the quality and accuracy of the data. Thus, the planimetric accuracy for the 60 m height was found to be 10 cm, and for the 100 m height, it was found to be 14.1 cm. The total errors are 12.6 cm for the 60 m flight height and 17.9 cm for the 100 m flight height.

In order to automatically compare the extracted roof edges based on shaded DSM and 60 m flight orthophotos, we relied on comparing two polylines (the sequences of connected line segments) to obtain the standard deviation of the distances between them. ArcGIS Pro v10.8.2 software was used for this particular task, obtaining a standard deviation of 10.4 cm for the 60 m flight and a standard deviation of 15.5 cm for the 100 m flight.

3.2. LiDAR-UAS Point Cloud Classification in Ground and Off-Ground Points

To classify the LiDAR-UAS point cloud into ground and off-ground points, three methods were applied: a Cloth Simulation Filter (CSF) [38] implemented in CloudCompare software, a volume-based algorithm [39], and a hierarchic robust filter algorithm [40] implemented into Opals v2.5.0 software.

3.2.1. Cloth Simulation Filtering Approach

The CSF algorithm is very easy to apply and requires three parameters, i.e., the type of terrain surface (steep slope, relief, or flat), the cloth resolution (grid size), and the threshold

for the off-ground point classification. However, for obtaining optimal results, an important aspect is to carefully choose the values for the parameters, as also emphasized in [41]. The significance of the cloth resolution parameter when conducting ground filtering within the CSF was demonstrated in [42]. This study concluded that increasing the cloth resolution makes the DTM coarser in quality. Additionally, it is essential to note that various data types require distinct parameter settings. For the present study, the “relief” option was chosen since the terrain level difference is about 30 m, the cloth resolution was set to 0.5 m, and the threshold for the off-ground points was 0.1 m.

For DTM generation, the “opalsGrid” module was utilized, opting for the robust moving interpolation method, and the following parameter configurations were selected: 0.3 m search radius, 20 neighbors, and 0.1 m grid size for the 60 m height; 0.6 m search radius, 20 neighbors, and 0.2 m grid size for the 100 m height. As anticipated, gaps in information (void pixels) persisted in the resulting data. To address this and create a final DTM without these information gaps, the “opalsFillGaps” module, designed to identify gaps in raster models, was employed. The adaptive interpolation method was applied to calculate values for the void pixels, ensuring a complete DTM (Appendix C).

Visually analyzing the ground and non-ground points, it can be seen that some points belonging to the bare earth surface (for example, a part of the parking lot and some points on the street), and also the points measured on the concrete retaining walls, were falsely classified as off-ground points (Appendix C, Figure A2, profiles P1–P5). Conversely, points that are not associated with bare earth are categorized as ground points, which include features like graves (Appendix C, Figure A2, profile P2), medium vegetation, or even construction rooftops, as highlighted on the shaded DTM (Appendix C, Figure A2). If the cloth resolution is set to 0.2 m, the points belonging to the building roofs are classified as ground points.

The effect of planar areas such as building roofs, which were misclassified as ground points by the CSF, was also reported in [43]. One of the conclusions of this study was that in order to precisely evaluate the performance of the CSF, a more extensive and statistically rigorous accuracy assessment is necessary. This assessment should encompass a variety of landscapes, including urban, rural, and forested areas.

3.2.2. Volume-Based Filtering Approach DSM Generation

When using the volume-based filtering approach, the basic input is the Digital Surface Model (DSM) of the study area in raster format. For the DSM derivation, first, all LiDAR-UAS points were interpolated using the “robust moving plane” interpolation method, implemented into “opalsGrid” module. The DSM_{rmp} corresponding to the 60 m height resulted in a regular grid structure with a grid cell dimension of 10 cm. The height for each grid cell was estimated by finding the best-fitting tilted plane of the 20 nearest points of the grid point (x, y) within the 30 cm search radius ($3 \times$ cell size) with quadrant-oriented data selection, without taking into consideration the points detected as outliers. For each neighbor point, the individual weight was calculated by applying a weight function defined as the inverse of the squared distance. For the 100 m height, the grid cell dimension was set as 20 cm, and the search radius was set to 60 cm.

Details of the shaded DSM_{rmp} for the 60 m height are shown in Figure 15a, where the averaging effect of the moving least squares method is evident along building edges, as noted by [44]. While the DSM_{rmp} effectively represents smooth surfaces, its application along building edges and within forested areas can result in either an overestimation or underestimation of surface heights. In addition to the elevation, moving least squares interpolation enables the extraction of additional attributes for each grid point. These attributes encompass the standard error of the estimated grid point elevation (σ_z , indicating roughness), excentricity (distance between the grid point and the center of gravity of input points), point count, point density, slope, and exposure. These attributes have demonstrated their significance in subsequent data processing stages, particularly in identifying concealed

and vegetated areas [44]. Hence, by employing the “opalsCell” module of Opals, the DSM_{max} was computed based on the highest elevation within a 0.1 m grid cell for the 60 m height and 0.2 m for the 100 m height. Although the method accurately represents building edges, it does introduce artificial roughness on building roofs and streets (Figure 15b).

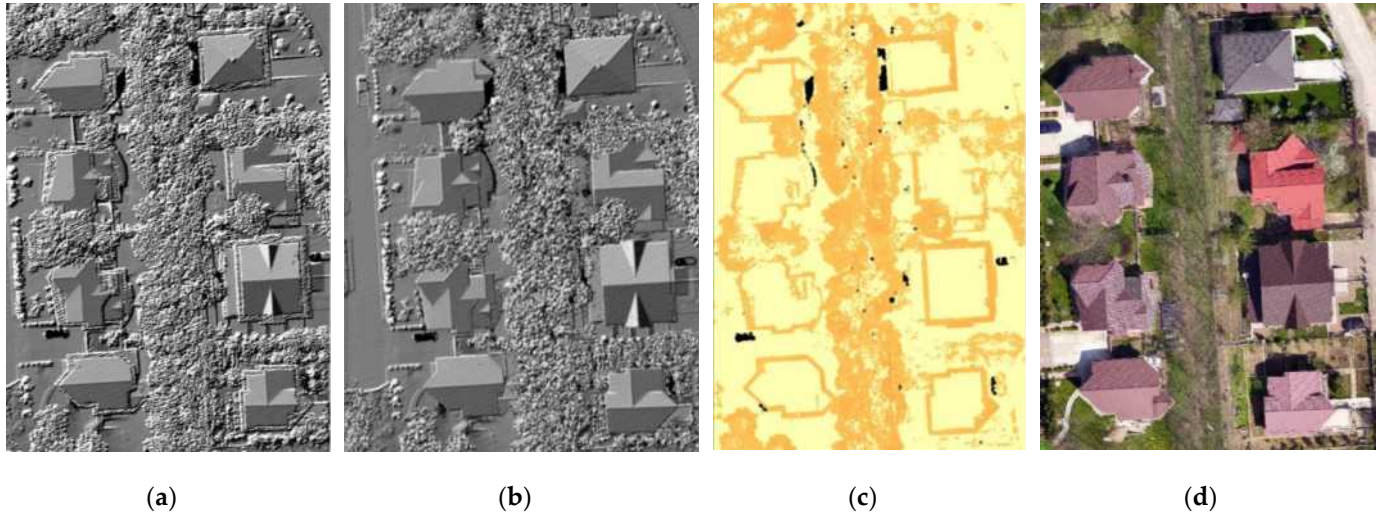


Figure 15. (a) Shading of the DSM_{rmp} , (b) shading of the DSM_{max} , (c) σz raster (0.1 m cell size), (d) UAS orthophoto.

Using the σz values (as shown in Figure 15c), a combination of rasters was utilized through the “opalsAlgebra” module, calculated using pseudocode (1) with a set threshold value of 0.01 m. When the σz values are lower than the threshold, the DSM height is derived from the DSM_{rmp} ; otherwise, it is obtained from the DSM_{max} :

$$z [DSM_{rmp_max}] = z[\sigma z] < 0.01 \text{ or not } z[DSM_{max}]? z [DSM_{rmp}] : z [DSM_{max}] \quad (1)$$

To address the gaps (void pixels due to the acquisition angle, grid size, number of neighbors, point density, or interpolation method) in the obtained DSM_{rmp_max} , another interpolation technique, Delaunay triangulation (OPALS-“delaunayTriangulation”), was applied. To create a complete DSM (DSM_{final}) without information gaps, the two rasters, DSM_{rmp_max} and $DSM_{Delaunay}$, were merged using pseudocode (2), performed in the “opalsAlgebra” module of Opals software. Specifically, cells from DSM_{rmp_max} were retained, and cells from $DSM_{Delaunay}$ were incorporated only in cases where information gaps existed in the first DSM.

$$z [DSM_{final}] = z[DSM_{rmp_max}]? z [DSM_{rmp_max}] : z [DSM_{Delaunay}] \quad (2)$$

The shading of the final DSM for the 60 m height is shown in Appendix C1, Figure A3a. By using the two attributes, σz and eccentricity, a mask for the terrain and planar surfaces can be calculated setting a threshold value of 0.1 for the σz attribute and 0.8 for the eccentricity attribute, as shown in Appendix C, Figure A3b. The vegetated areas are highlighted very well as well as the roof’s edges.

Ground Point Filtering

The volume-based filtering approach by [39] identifies open terrain parts of a DSM input raster. Two key parameters are needed to apply this approach, i.e., the minimum height for the off-ground point classification and the maximum size of an elevated object, specifically the maximum length or width, and are typically used to limit the consideration of very large objects, such as buildings. The algorithm runs the classification separately for all four directions: N–S, E–W, NW–SE, and SW–NE. To obtain the final terrain mask,

a straightforward voting scheme is employed, which combines the outcomes of all four directional masks. Therefore, the parameter “minConsensus” specifies the minimum number of directional masks that must classify a particular pixel as elevated for it to be considered as such. Taking as input the DSM_{final} raster, setting the minimum height at 0.1 m and the maximum length at 40 m (building situated in the N-V part of the study area), and considering all four directions for voting a pixel, the terrain mask is calculated. By analyzing the result, it can be seen that some elevated points remain. The adopted solution was to apply morphological operations on the terrain mask using the “opalsMorph” module.

Dilation and erosion are fundamental operations in mathematical morphology, initially developed for binary images and later extended to grayscale images. Opening implies erosion and dilation in this order, while closing consists of dilation and erosion applied in this order.

The structural element, a small mask (a matrix with “0” and “1” values), typically of an odd size, often 3×3 pixels, is placed over the binary image and moved to all possible positions, being compared to all corresponding pixels in the image being analyzed. In the case of dilation, it tests whether the structural element intersects with the corresponding pixels in the image, while in the case of erosion, it tests whether the structural element matches with all the pixels under the mask (each pixel with a “1” value within the structural element corresponds to a pixel with a “1” value in the image segment under the mask). The new image created through a morphological operation is still a binary image, where pixels have a non-zero value only if they correspond to the binarization mode in that location. Dilation and erosion have opposite effects: dilation creates the background of an object, while erosion operates inversely. The size of the matrix defines the size of the structural element, and the positions of the “0” and “1” values define the shape of the structural element. The origin of the structural element is usually one of its pixels, typically located at its center, but it can also be situated outside the structural element. The structural element can have any shape: cross, square, diamond, etc. For this particular case study, the closing morphological operation was applied to the “terrain mask” binary raster image, using a square-shaped structural element, with a size of 3. The binary terrain mask before applying the morphological operation is shown in Appendix D, Figure A4a, and after applying the morphological operation in Figure A4b in Appendix D.

For DTM generation, the robust moving interpolation method, with the same parameter configurations as described above (Section 3.2.1), was applied, in addition to the adaptive interpolation method, to calculate values for the void pixels (Appendix D, Figure A5a,b). The effect of the “close” morphological operation on the final DTM can be observed in Figure 16. The isolated points that remain in areas of high vegetation cause artifacts in the generated DTM (Figure 16b) that are removed in the DTM obtained via volume-based morphological filtering (Figure 16c).

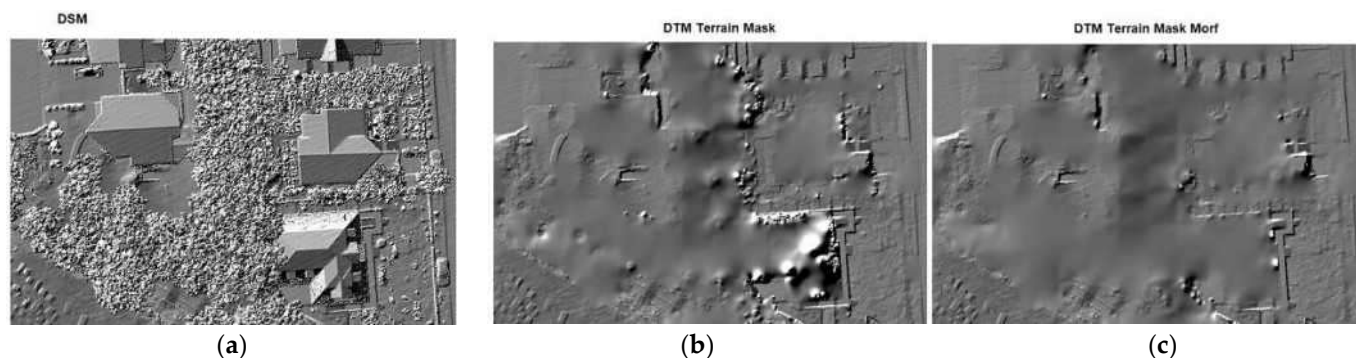


Figure 16. DSM of the study area in raster format with 0.1 m cell size (60 m height) (a), DTM after applying volume-based filtering algorithm (b), DTM after applying volume-based filtering algorithm and morphological operation on the terrain mask (c).

The details of non-ground points identified via volume-based morphological filtering superimposed on the DSM are shown in Figure 17. Natural elements, such as high, medium, and low vegetation, and artificial elements, such as graves, cars, and buildings, were correctly classified as non-ground points (Figure 17a). However, some omission errors can be seen on the edges of the study area, where a part of the street and the slanting terrain surface are wrongly classified as non-ground points (Figure 17b).

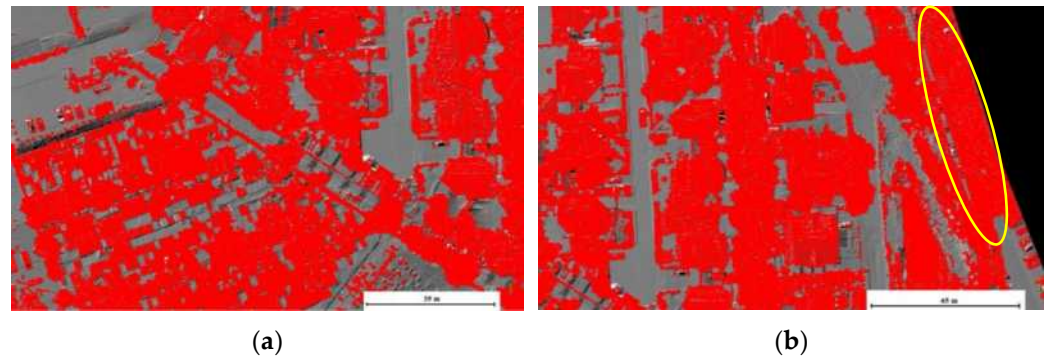


Figure 17. Details of non-ground points identified via volume-based morphological filter. Correctly identified elements: low, medium, and high vegetation; buildings; graves; and cars (a). Omission errors that involve the exclusion of part of a street and a sloping terrain surface (yellow ellipse) (b).

3.2.3. Hierarchic Robust Filtering Approach

To filter the LiDAR-UAS point cloud in order to automatically classify the ground and off-ground points, the point clouds obtained at 60 m and 100 m heights were filtered using the hierarchic robust filtering algorithm implemented into Opals software with four iterations, establishing threshold strips for elevation for noise filtering. For this purpose, the “opalsRobFilter” module was employed. First, the point cloud was filtered via the last return, a total of 657,466 points measured with the second return, representing only 1.7% of the total number of points for the 60 m height and 58,509 representing only 0.3% of the total number of points, were eliminated. The same percentage of first and second return points was reported by [25]. A HESAI Pandar XT laser sensor attached to a LiDAR-UAS scanner can only measure two returns, with the number of points measured using one return being significantly higher than the points measured using the second return. The process continues with an initial approximation of the surface, considering all points within the dataset, which may include elements such as vegetation, powerlines, buildings, and ground. Subsequently, the residuals, representing the distances between the measured points and the initial surface approximation are calculated and stored as attribute “normalizedZ”. Each point is assigned a weight based on its distance from the surface, prioritizing points located below the surface over those situated above it. Consequently, the surface is drawn toward the points located at lower elevations, typically representing the ground. For this case study, the initial surface was created using three iterations, considering the minimum height of two points for the first iteration and one point for the next iterations, in grid cell sizes of 5 m, 3 m, and 1 m. To calculate the DTM surface, the “moving average” interpolation method was used, setting the grid sizes at 2.5 m, 1.5 m, and 0.5 m for each iteration. The threshold strips for elevation considering the normalizedZ values were $[-3 \text{ m} \div +2 \text{ m}]$ for the first iteration, $[-1.5 \text{ m} \div +1 \text{ m}]$ for the second iteration, and $[-0.25 \text{ m} \div +0.5 \text{ m}]$ for the third iteration. Therefore, a point is classified as a ground point if the normalized value is within the range interval.

After obtaining the ground points in the third iteration, the “opalsRobFilter” module was used next. The result was an XYZ file containing all points classified as ground. The parameter settings for the module are described in (3):

```

opalsRobfilter -Infile: ground_points.odm;
               -Interpolation: plane;
               -Number of Threads: 1;
               -Sigma a priori: 0.1;
               -Penetration: 20;
               -Outfile: filter_ground_points.xyz
    
```

(3)

The processing sequence in this module follows a grid-oriented approach, starting with the creation of an internal grid with a grid size equivalent to the specified search radius (parameter `searchRadius = 3` by default). A local surface is estimated for each grid node, using the “moving plane” interpolation method with a titled plane (parameter `interpolation = plane`), from the three available interpolation methods, taking into consideration all the points situated within the defined search radius. The point classification into ground and non-ground points is given by a threshold (parameter `maxSigma = 0.5` m by default), i.e., the standard deviation of the surface interpolation. As not all laser pulses are able to reach the ground, in the context of robust interpolation, the penetration rate (parameter `penetration = 20`) given in percentages is utilized as an estimate to establish an initial course for the local surfaces, which occurs prior to the detailed interpolation process. The robust interpolation process is carried out through iterations; during each iteration, the individual point weights are adjusted according to the residuals. This process of surface interpolation and re-weighting is reiterated until either the changes in the surface are within a defined threshold or the maximum number of iterations has been reached. By default, the maximum number of iterations is 100. For the ground points found by hierarchic robust interpolation, a surface was created using the “nearest point” interpolation method, with a grid size of 0.5 m and a 15 m search radius. Defining a range interval of $-0.1 \text{ m} \div 0.05 \text{ m}$ for the `normalizedZ` attribute calculated for each ground point with respect to this surface, the final classification of ground points is made.

The details of the mesh surface created based on ground points identified via hierarchic robust filtering are displayed in Figure 18. It can be observed that even though the upper surface of the graves was filtered via the algorithm, some points at the bottom part, which were identified as ground points, led to irregularities. This same effect was observed in areas with medium vegetation.

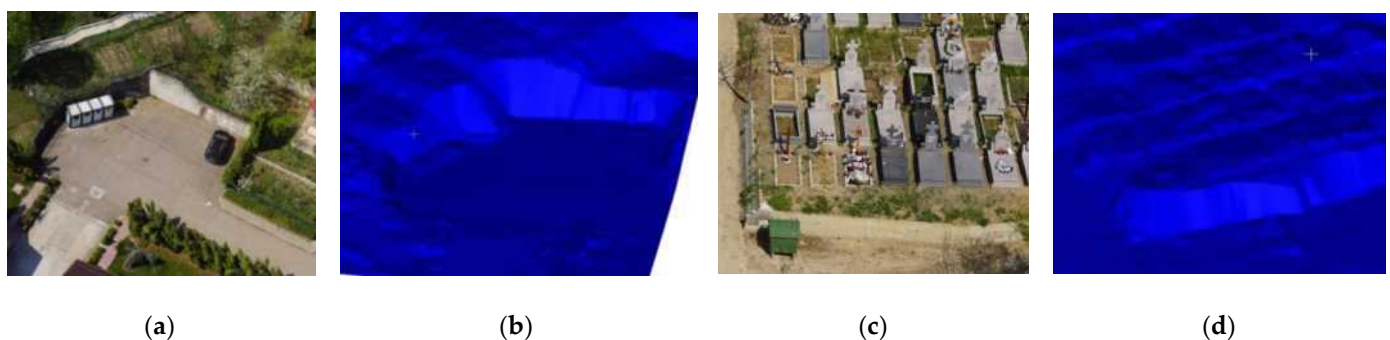


Figure 18. Details of the mesh surface created based on ground points identified via hierarchic robust filtering and UAS images for two specific areas: a parking lot with a ~4 m high wall (a,c) and a ~1 m high wall and graves (b,d).

For DTM generation, the robust moving interpolation method with the same parameter configurations as described above (Section 3.2.1) was applied, in addition to the adaptive interpolation method, to calculate values for the void pixels (Appendix E).

3.2.4. Proposed Method for Enhancing DTM Quality by Combining Robust Filtering and Volume-Based Filtering Approaches for Ground Points

By analyzing and comparing the DTMs resulting from the CSF, volume-based filtering, and hierarchic robust filtering methods, advantages and disadvantages could be identified for each. As observed, the estimated models at 60 m and 100 m heights obtained via hierarchic robust filtering approximate the ground topography with the highest fidelity. However, a significant drawback arises with steep slopes, where the algorithm is not able to capture ground points in close proximity to terrain edges. Consequently, the applied interpolation introduces smoothing effects in the DTM, deviating from the precise shape of the actual terrain. However, the volume-based filtering approach eliminates all areas under the corresponding ground mask but keeps the points at very steep slopes (e.g., retaining walls). Among the three algorithms analyzed, the CSF algorithm demonstrated the poorest performance, as it failed to identify large terrain areas as ground. It did not identify points on concrete retaining walls, artificial terraces, or sudden terrain slopes as ground points, erroneously classifying points on graves, building roofs, and medium vegetation as the “ground” class. Therefore, to obtain a final DTM with higher quality, we proposed a combined approach based on the strengths of the two methods, namely, hierarchical robust and volume-based filtering. In this way, the void areas at steep slopes with missing ground points in the hierarchic robust filter algorithm are filled with the corresponding ground points identified through the volume-based filtering approach.

The proposed solution is described with pseudocode (4), where, in the case of steep slopes of more than 80%, the ground points identified via the morphological-based filtering approach are considered; otherwise, the ground points extracted via the hierarchic robust filter are taken in the final combined approach. In this manner, the difficulties in identifying the ground points at steep edges encountered by robust filters are compensated for via the volume-based filtering approach.

For this, in the first step, a slope map of the entire area of interest (for both 60 m and 100 m flights) was computed using the “OpalsGrid” module with the feature “slope” implemented in Opals software. Secondly, with the “OpalsAlgebra” module, only the regions with a slope greater than 80% were selected and saved in a corresponding mask. A detailed view of the slope and the corresponding mask, which includes two retaining walls and an artificially terraced terrain, is illustrated in Figure 19.

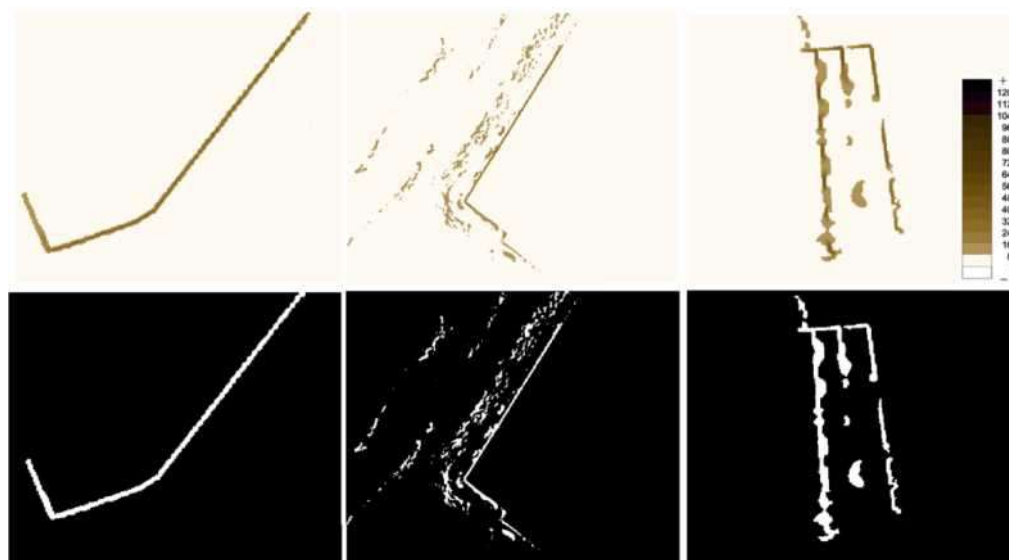


Figure 19. Detailed views of slope map (first row) with corresponding mask of identified regions with slopes greater than 80% (second row).

The computed mask was then further employed to select and extract the corresponding areas from the ground points identified with the volume-based filtering method. The purpose of this was to merge the points extracted via hierarchic robust filtering with the ground points identified via the volume-based filtering approach for areas with very steep slopes. Hence, the number of ground points increased by 1% and 0.8% for the 60 m and 100 m heights, respectively (Table 4).

$$\text{Ground pts}_{\text{Proposed method}} = \text{Slope} > 80 ? \text{Ground pts}_{\text{Morph. Volume}} : \text{Ground pts}_{\text{Hierarchic robust}} \quad (4)$$

where:

- $\text{Ground pts}_{\text{Proposed method}}$ —ground points identified via the proposed approach;
- $\text{Ground pts}_{\text{Hierarchic robust}}$ —ground points extracted via the hierarchic robust filtering approach;
- $\text{Ground pts}_{\text{Morph. Volume}}$ —ground points extracted via the morphological volume-based approach;
- $\text{Slope} > 80$ —condition for ground point selection only in steep terrain areas with slopes > 80%.

Table 4. Number of LiDAR-UAS ground points for the enhanced DTM.

No. of LiDAR-UAS Ground Points	60 m Heigh	100 m Height
Hierarchic robust	17,814,702	11,092,862
Morphological volume-based (steep slopes only)	175,641	88,681
Total (combined)	17,990,343	11,181,543

Finally, a new interpolation was performed on the combined point cloud with only ground points using the robust moving interpolation method, keeping the same configuration parameters as presented in Section 3.2.1. Additionally, void areas were filled via the adaptive interpolation method. As expected, the newly obtained DTM is improved compared to hierarchical robust DTM, especially in areas with very steep slopes. Detailed views of the enhancements at a retaining wall and terraces are visible in Figure 20 in the last column. Compared to the robust filtering-based DTM with missing information in these specific areas containing sudden slope changes, the final combined model added the corresponding ground points from the volume-based DTM, thus increasing ground point completeness and improving the quality of the final result.

A summary of the number of ground points obtained by applying different filtering approaches on LiDAR-UAS point clouds acquired at 60 m and 100 m heights is presented in Table 5.

Table 5. Summary of the LiDAR-UAS ground points identified via different filtering approaches.

No. of Ground Points	CSF	Volume-Based Filter	Volume-Based Morphological Filter	Hierarchic Robust Filter	Proposed Method
60 m height	19,844,316	16,611,900	15,300,117	17,990,702	17,990,343
100 m height	11,713,850	10,016,332	9,071,908	11,092,862	11,181,543

Using QGIS v3.28.13 software, the elevations of the 985 ChPs were interpolated in the derived DTMs, applying different filtering approaches. The resulting statistics, including mean, median, standard deviation, and Root-Mean-Square error for the differences between the initial elevations and the interpolated ones, are presented in Table 6.

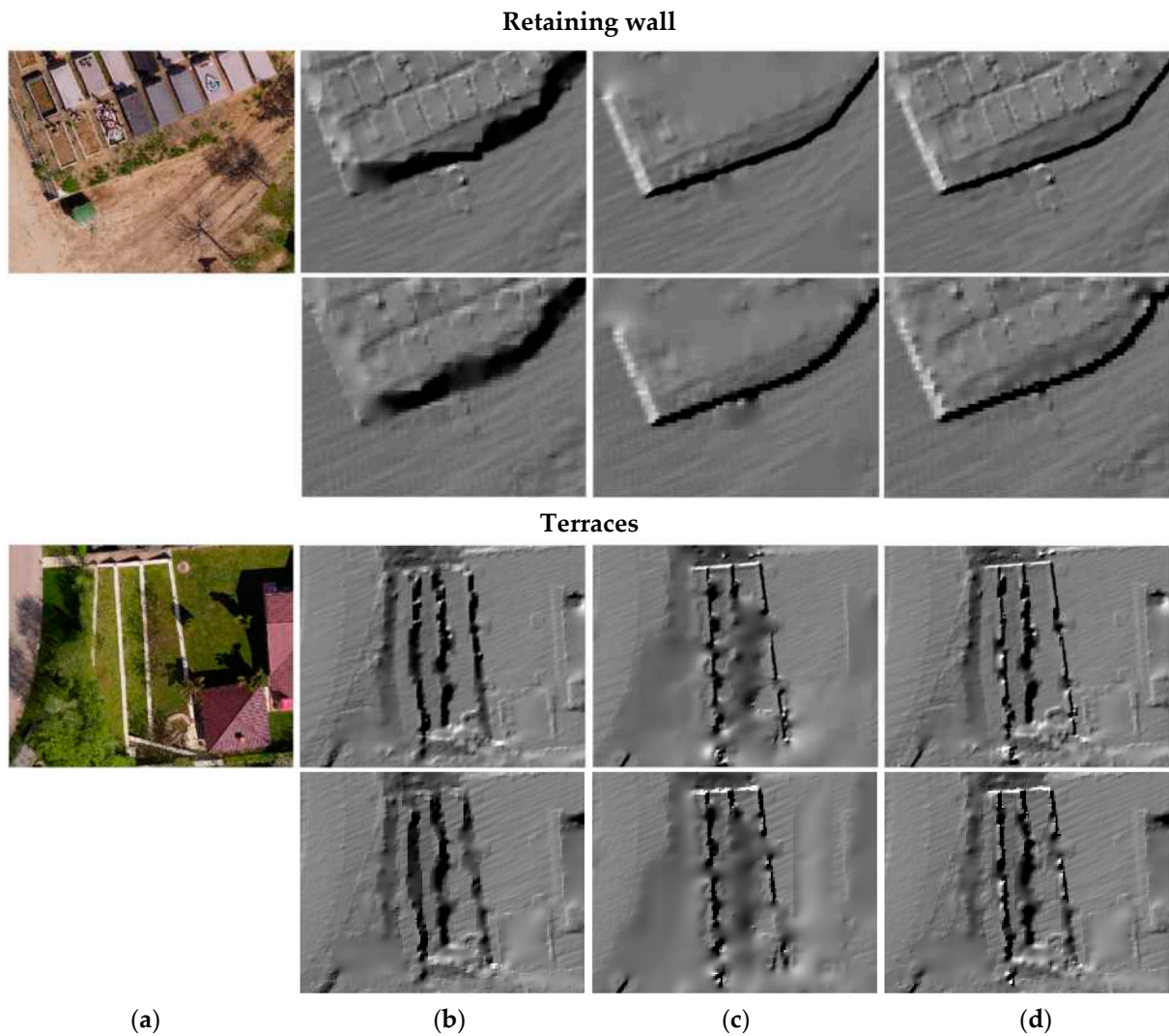


Figure 20. Detailed view of the shaded DTMs for a retaining wall and terraces with 0.1 m cell size (60 m flight: first rows) and DTMs with 0.2 m cell size (100 m flight: second rows): (a) orthophoto; (b) DTM hierarchic robust filtering; (c) DTM terrain mask; and (d) DTM combined approach.

Table 6. Vertical accuracy of derived DTMs based on 985 ChPs.

Filtering Method	Accuracy Metrics (m)			
	μ	Median	σ	RMSE
CSF				
60 m	−0.04	0.01	0.29	0.29
100 m	−0.05	−0.01	0.28	0.29
Volume-based morphological filter				
60 m	0.01	0.00	0.28	0.28
100 m	−0.01	−0.02	0.29	0.29
Hierarchic robust filter				
60 m	−0.02	0.01	0.25	0.25
100 m	−0.04	−0.01	0.25	0.25
Proposed method				
60 m	−0.00	0.01	0.16	0.15
100 m	−0.02	−0.01	0.18	0.18

The statistical values were calculated after filtering the outliers. Upon analyzing the histogram of the distribution of vertical errors for the 60 m flight height when using the hierarchic robust filtering method, it was observed that the calculated errors fell within a range of -1.86 m to $+2.20$ m, with a standard deviation of 0.25 m. In contrast, when the proposed method was applied in the DTM generation process based on LiDAR-UAS point clouds, the error range was notably reduced to -1.05 m to $+0.76$ m, with a standard deviation of 0.15 m. This means that the proposed method significantly decreases the error range, with the maximum error being approximately three times smaller compared to the hierarchic robust filtering method. For the 100 m flight height, the errors ranged from -2.05 m to $+2.00$ m, which was then reduced to -2.05 m to $+0.66$ m when employing the proposed method. Again, the maximum error was approximately three times smaller with the proposed method. Overall, the proposed method enhances DTM quality compared to the hierarchic robust filter, resulting in a 40% improvement for the 60 m flight height and a 28% improvement for the 100 m flight height.

4. Discussion

Through the examination of the three considered strategies for UAS point cloud filtering (CSF, volume-based morphological, and hierarchic robust filtering algorithms), the strengths and weaknesses associated with each approach were identified. While CSF shows the weakest performance, by eliminating a significant number of ground points, the volume-based morphological filter has a better efficiency, as it identifies ground points at very steep slopes. However, hierarchic robust filtering shows the best behavior overall but faces challenges in identifying ground points on steep slopes and in close proximity to terrain edges. Therefore, our proposed algorithm makes use of the strengths of the two most effective methods, namely: hierarchical robust filtering and volume-based morphological filter.

Figure 21 shows detailed profiles of “ground” points classified via the analyzed filtering approaches, along with the corresponding DTMs created based on these points. These profiles focus on specific areas, particularly those with steep slopes where the proposed methodology has notably increased the number of identified ground points. By looking at all profiles, the CSF performed worst overall. The retaining walls were successfully identified using the volume-based filtering approach. In addition, the hierarchic robust and CSF were effective in identifying the points located beneath trees. In the P2 profile, it is evident that there are graves with points identified as “ground” via the CSF, but they were correctly classified via the hierarchic robust and volume-based filters. In the P3 profile, tree branches cover the upper part of the wall, resulting in no points being identified as ground points via the volume-based filter. This effect can also be seen in profile P5, where an anthropic terraced terrain is illustrated. In the P4 profile, all points on the wall are correctly identified via the volume-based filter, but when generating the DTM, the points are located in the same cell (vertical wall), so the values are averaged, leading to a point in the middle of the wall.

The most significant advantages and disadvantages for each considered ground filtering approach and for the final combined proposed method, as identified in this paper, are summarized in Table 7.

Our present results form the basis for further detailed analyses and represent the beginning of future research directions, such as the application of the proposed method in other test areas with different topographic characteristics (mountainous, urban, and land areas), on datasets with different acquisition times (leaf-on vs. leaf-off conditions), and acquisitions with different LiDAR-UAS sensors.

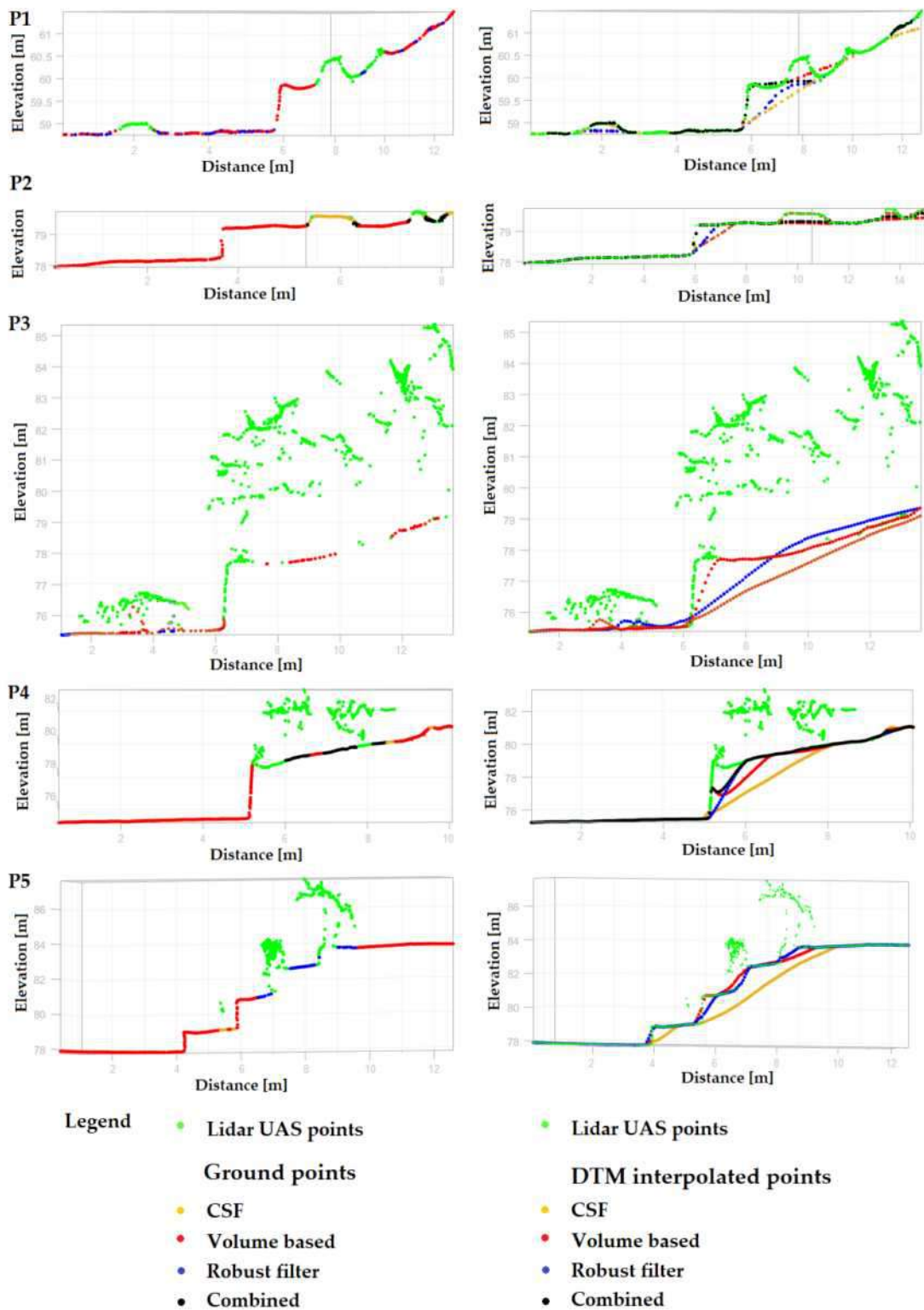


Figure 21. Detailed profiles (P1, P2, P3, P4, and P5) of LiDAR-UAS acquisition with corresponding extracted ground points (left column) and with DTM interpolated points (right column) for different retaining concrete walls. Here, on the vertical walls, the CSF algorithm does not identify any ground points. In profile P2, the grave contains points identified as “ground”. The location of the detailed profiles in the test area is shown in Figure A2 (Appendix C).

Table 7. Advantages and disadvantages of the CSF, volume-based morphological, hierarchic robust filtering, and proposed methods (advantages are indicated with a tick, while disadvantages are indicated with a circle).

CSF		Volume-Based Morphological Filter		Hierarchic Robust Filter		Proposed Method	
✓	Free of charge	○	Paid license	○	Paid license	○	Paid license
✓	Fast processing	○	Longer computation time	○	Similar computation time to volume-based filter	○	Longer computation time (requires processing of both volume-based and hierarchic robust methods)
○	Sudden slope changes are not depicted	✓	Sudden slope changes are depicted	○	Sudden slope changes are not depicted	✓	Sudden slope changes are depicted
○	Points belonging to bare earth are misclassified as non-ground points	✓	Points belonging to bare earth are correctly classified as non-ground points	✓	Correctly identifies ground points, except for areas of steep slopes	✓	Correctly identifies ground points
○	Reduced number of identified ground points	○	Reduced number of identified ground points because only points under the “terrain” mask are extracted (points under the tree canopy are not extracted)	✓	Increased number of extracted ground points	✓	Increased number of extracted ground points (more than hierarchic-robust-filter-identified points)
○	Missing ground points at steep slopes	✓	Ground points close to the edges of very steep slopes are well identified	○	Ground points close to the edges of very steep slopes are not identified	✓	Extracts ground points at steep slopes
✓	Needs only 3 parameters	○	Requires more parameters	○	Requires more parameters	○	Requires more parameters
○	Multiple tests to find the suitable parameters	✓	Fewer number of tests to find the suitable parameters	✓	Fewer number of tests to find the suitable parameters	✓	Fewer number of tests to find the suitable parameters
○	Objects with a low height compared to the ground (such as graves with a height of approximately 40 cm) are added to the Digital Terrain Model (commission errors)	○	Objects with a low height compared to the ground are correctly classified				
✓	Effective on many types of terrain						
○	Points situated in the middle of roofs are misclassified as ground points	✓	Correctly eliminates points belonging to buildings and roofs	✓	Correctly eliminates points belonging to buildings and roofs	✓	Correctly eliminates points belonging to buildings and roofs
○	DTM affected by interpolation effects due to large gaps	○	When generating the DTM, the interpolation method causes a smoothing effect of the terrain surface, thus not reflecting the real terrain	✓	Resulting DTM characterized by smoothing effects at steep slopes, due to interpolation	✓	DTM with improved quality

5. Conclusions

The filtering of ground points represents an essential step in LiDAR data pre-processing, particularly for terrain modeling and the derivation of Digital Terrain Models. Over the last three decades, various ground filtering algorithms have been developed, with a primary focus on Airborne Laser Scanning (ALS) point clouds. Even though LiDAR-UAS and ALS methods both rely on LiDAR principles, they differ in terms of data acquisition platforms, applications, and characteristics. While LiDAR-UASs provide the advantage of a high point density, they also have the drawback of typically having a smaller number of returns in comparison to ALS systems, with the first return often representing about 99% of the entire point cloud. The high point density in LiDAR-UAS data may result in the reduced performance of filtering algorithms, rendering the task of filtering LiDAR-UAS point clouds more challenging compared to ALS point clouds.

In this study, the focus falls on obtaining a highly accurate DTM that faithfully reflects the actual ground features of a complex landscape, using as input data LiDAR-UAS point clouds. For this, different filtering approaches (i.e., hierarchical robust, volume-based, and cloth simulation) were tested, and their results were qualitatively and quantitatively compared.

For assessing the vertical, planimetric, and overall accuracy of the LiDAR-UAS point clouds, a total of 85 ChPs placed in open areas (measured via GNSS-RTK technology) were employed, together with 64 points representing roof corners (measured via a total station) and manually drawn polylines for roof edges. The vertical accuracy of the derived DTMs was assessed using 985 ChPs, including the 85 ChPs and topographical details measured via the total station, i.e., man-made structures, roads, and fences.

Ground points are “approximately” well identified by all three tested filtering methods, but the quality of the final obtained DTMs is affected by the adopted interpolation and void area filling strategies. Therefore, while the volume-based algorithm effectively identifies ground points, the subsequent application of the interpolation method produces a continuous surface that may not accurately represent the actual shape of the terrain. The main advantage of this algorithm is its capability to accurately classify points measured on steep or sudden slopes as ground points. From all three analyzed filters, the CSF performed worst overall, while the hierarchic robust filter performed the best in classifying ground points, except for areas with steep slopes and rapid changes in elevation, such as vertical walls. Therefore, to obtain an enhanced DTM that represents the real terrain shape with higher confidence, we proposed a new method that makes use of the strengths of the two filtering approaches, namely, hierarchical robust and volume-based filtering approaches. The results of the two techniques have been combined, applying an 80% slope condition for the volume-based filtering approach, thereby obtaining an increased number of ground points. Finally, the newly interpolated DTM shows improvements of 40% and 28% for the LiDAR-UAS flights at 60 m and 100 m, respectively. Furthermore, in comparison to the terrain models generated via the individual filtering methods, the final combined DTM shows the best overall quality and accuracy metrics. The obtained enhanced DTM represents a valuable dataset for further precision topographic mapping applications, such as urban planning, infrastructure development, and environmental monitoring, where having an accurate and detailed representation of the Earth’s surface is essential.

Author Contributions: Conceptualization, V.-E.O. and A.-M.L.; data curation, V.-E.O., A.-M.L., M.M., A.-A.L., B.B. and P.S.; formal analysis, V.-E.O., A.-M.L. and B.B.; funding acquisition, V.-E.O. and P.S.; investigation, V.-E.O., A.-M.L., M.M. and B.B.; methodology, V.-E.O., A.-M.L., B.B. and P.S.; project administration, V.-E.O.; resources, V.-E.O., A.-M.L., M.M., A.-A.L., B.B. and P.S.; software, V.-E.O., A.-M.L. and B.B.; supervision, V.-E.O. and A.-M.L.; validation, V.-E.O., A.-M.L. and B.B.; visualization, V.-E.O., A.-M.L., M.M., A.-A.L., B.B. and P.S.; writing—original draft, V.-E.O., A.-M.L. and P.S.; writing—review and editing, V.-E.O. and A.-M.L. All authors have read and agreed to the published version of the manuscript.

Funding: The work was supported by a grant from the Ministry of Research, Innovation and Digitization, CNCS-UEFISCDI (project number: PN-III-P1-1.1-TE-2021-1185), within PNCDI III.

Data Availability Statement: The data that support the findings of this study are available from the first author upon reasonable request. The data are not publicly available due to privacy restriction.

Acknowledgments: The grant from the Ministry of Research, Innovation and Digitization, CNCS-UEFISCDI (project number: PN-III-P1-1.1-TE-2021-1185), within PNCDI III, is gratefully acknowledged. The authors would like to thank the Department of Geodesy and Geoinformation from Technische Universität Wien, for the “OPALS” software license.

Conflicts of Interest: Author B.B was employed by the company Geocad Profesional SRL (Smart Imaging and Mapping Services-SIMS). The remaining authors declare that the research was conducted in the absence of any commercial or financial relationships that could be construed as a potential conflict of interest.

Appendix A

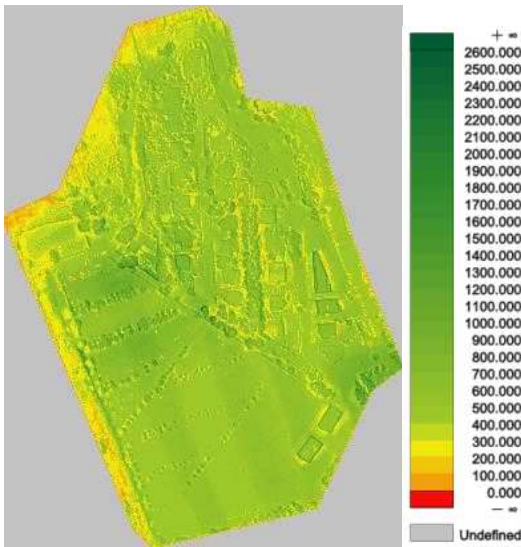
Table A1. Specification of GS-130X UAS LiDAR Scanning System.

Component Name	System Parameters		
GS-130X	Weight	1.26 kg	
	Measuring accuracy	Less than 0.1 m @120 m	
	Working temperature	−20 °C~+65 °C	
	Power range	12 V–24 V	
	Consumption	10 W	
	Carrying platform	GS-800 Multi Rotor and other brand	
	Storage	64 GB storage, maximum support 128 GB TF card	
	LiDAR Unit	Measuring range	0.3 m–120 m@10% reflectivity
Laser class		905 nm Class 1 (IEC 60825-1:2014)	
Channel		32 channels	
Range accuracy		±1 cm (typical value)	
Scanning frequency		10 HZ, 20 HZ	
Data		Double echo 1,280,000 points/sec	
FOV		360°, adjustable	
Laser sensor		HESAI Pandar XT	
POS unit		Update frequency	200 HZ
		Heading accuracy	0.017°
	Pitch accuracy	0.005°	
	Rolling accuracy	0.005°	
	Position accuracy	≤0.05 m	
Pre-processing software	GNSS signal type	GPSL1/L2/L5 GLONASSL1/L2 BDS B1/B2/B3 GAL E1/E5a/5b	
	POS software	Output information: position, speed, attitude	
Camera (built-in)	Point cloud software	Output point cloud data format: LAS format, custom TXT format	
	FOV	83 degrees	
	Effective pixel	26 megapixels	
	Focal length(mm)	16	

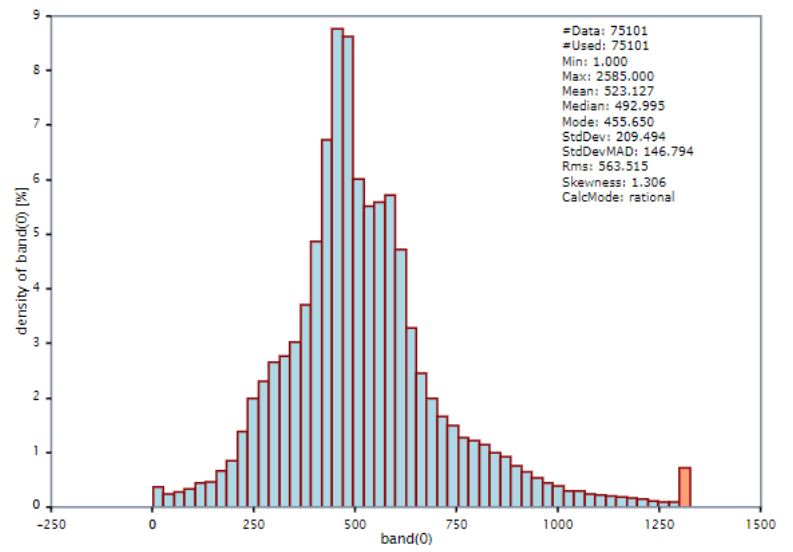


Appendix B

60 m

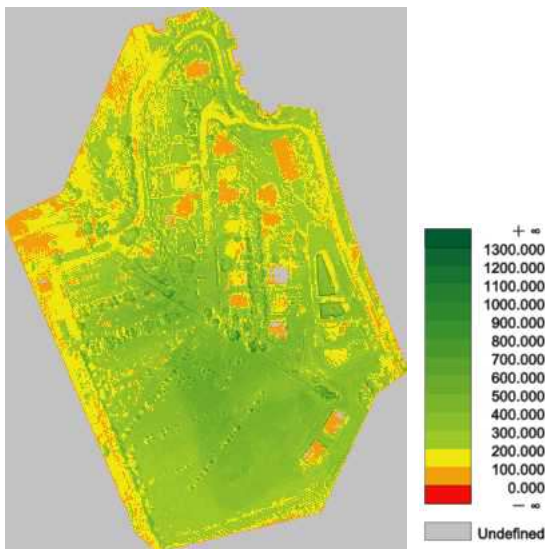


(a)

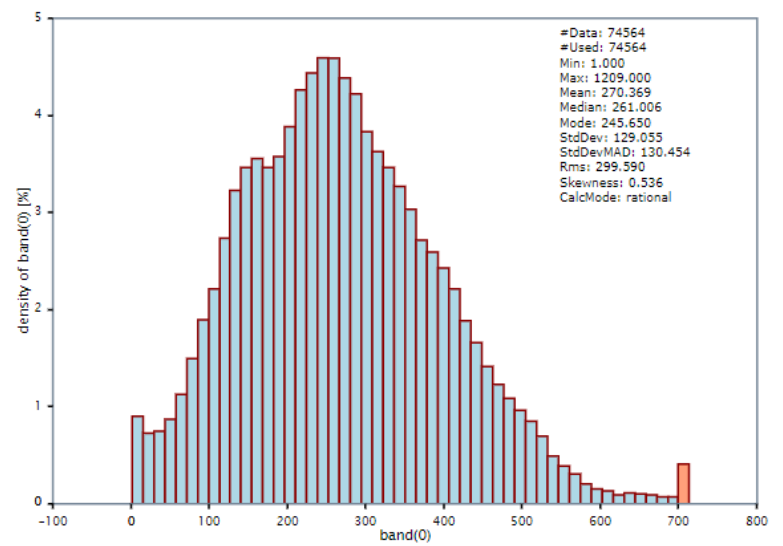


(b)

100 m



(c)



(d)

Figure A1. LiDAR-UAS point clouds colored by density (first column) and corresponding histograms (second column) for (a,b) 60 m flight height; (c,d) 100 m flight height.

Appendix C

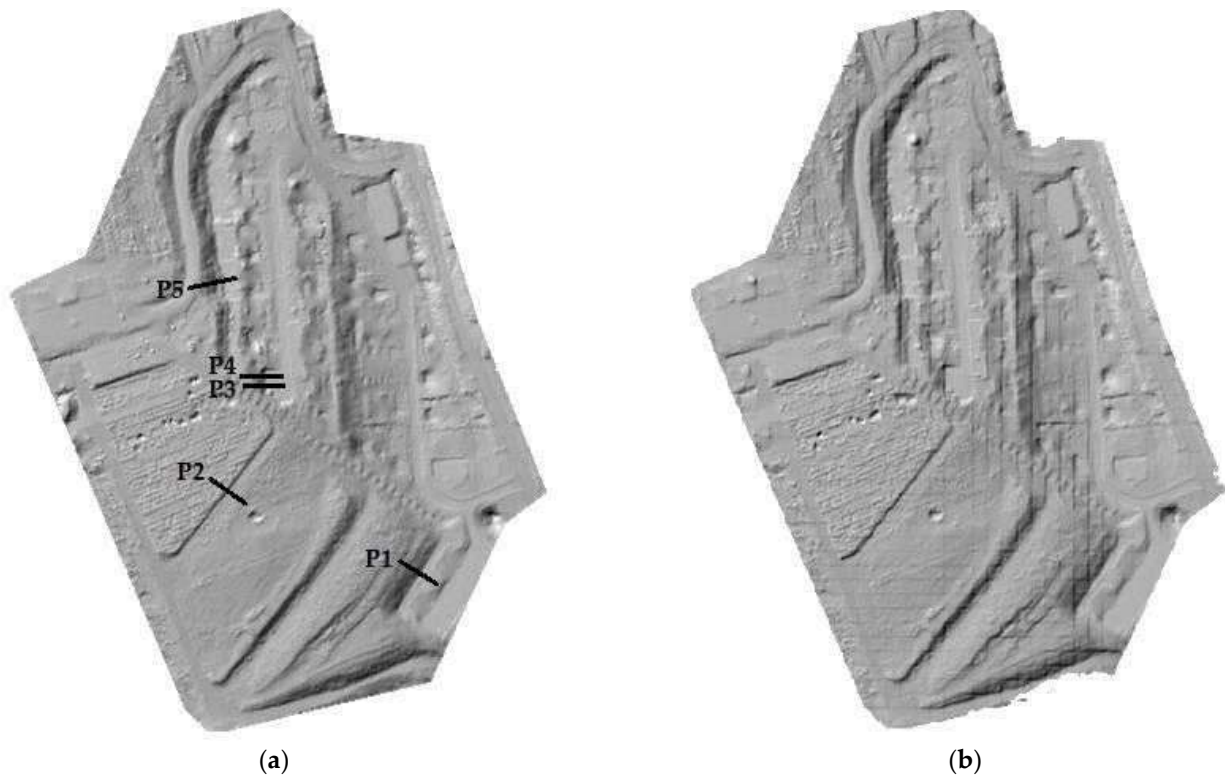


Figure A2. Shaded DTM based on ground points obtained via CSF algorithm for (a) 60 m flight height (0.1 m cell size); (b) 100 m flight height (0.2 m cell size).

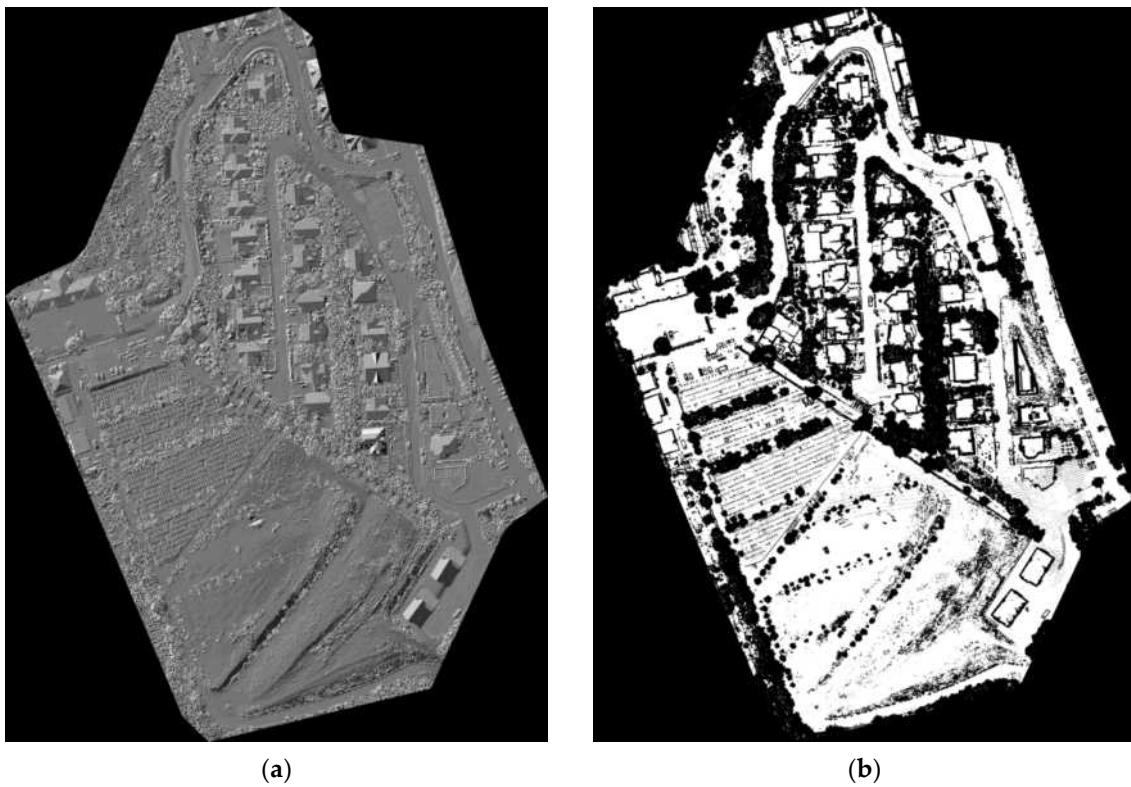


Figure A3. (a) DSM of the study area in raster format with 0.1 m cell size (60 m height), (b) mask with $\sigma < 0.1$ and eccentricity < 0.8 .

Appendix D

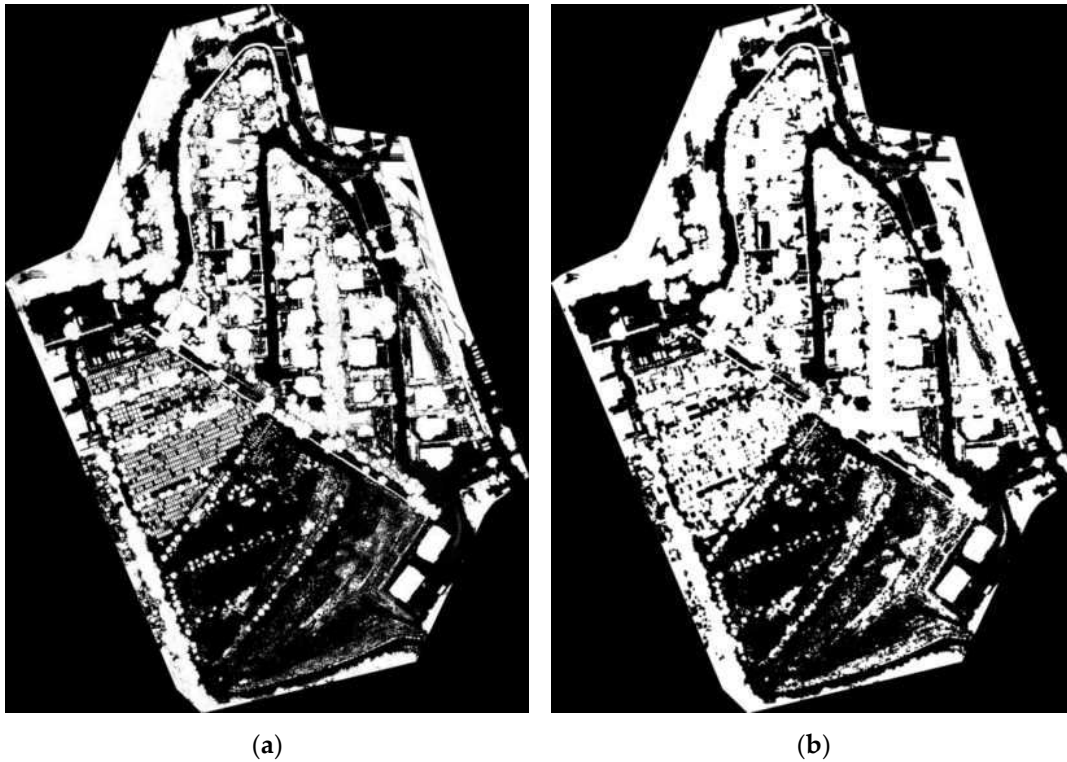


Figure A4. (a) Terrain mask obtained with volume-based filter algorithm in raster format with 0.1 m cell size (60 m height), (b) terrain mask obtained with volume-based filter algorithm in raster format after applying the “close” morphological operation.

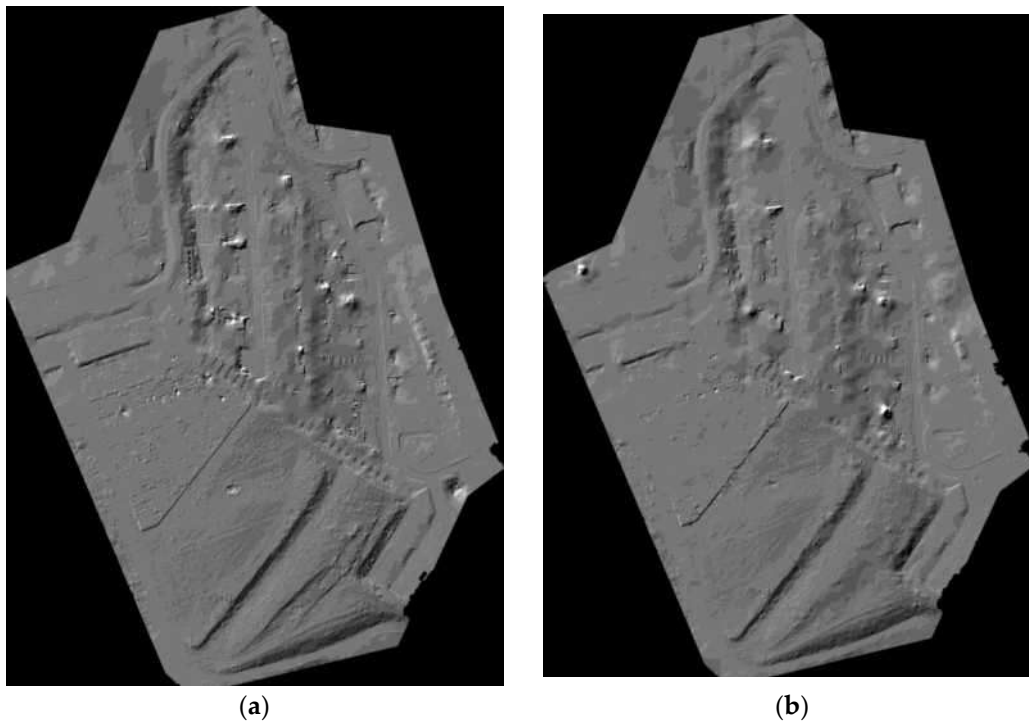


Figure A5. Digital Terrain Model obtained via volume-based filter algorithm in raster format for the (a) 60 m flight height with 0.1 m cell size, (b) 100 m flight height with 0.2 m cell size.

Appendix E

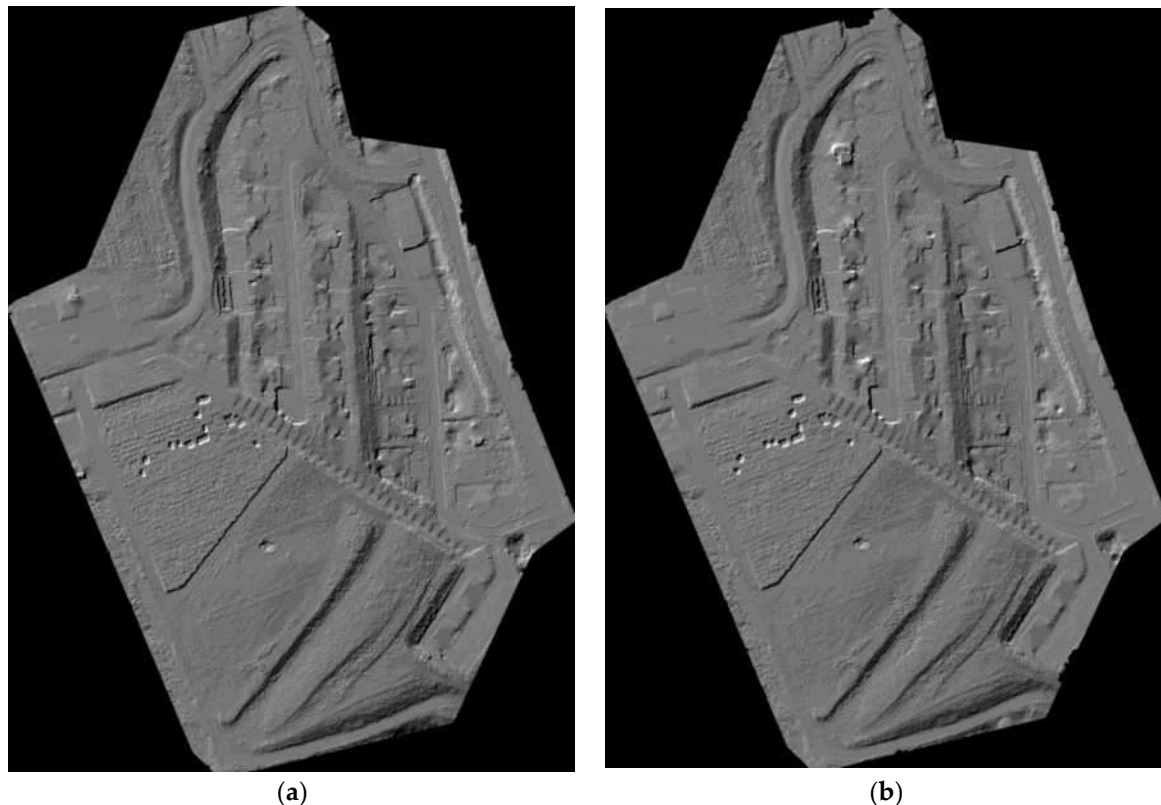


Figure A6. Digital Terrain Model obtained via hierarchic robust filtering algorithm in raster format for the (a) 60 m flight height with 0.1 m cell size, (b) 100 m flight height with 0.2 m cell size.

References

1. Kucharczyk, M.; Hugenholtz, C.H.; Zou, X. UAV–LiDAR accuracy in vegetated terrain. *J. Unmanned Veh. Syst.* **2018**, *6*, 212–234. [[CrossRef](#)]
2. Mandlbürger, G.; Pfennigbauer, M.; Haring, A.; Wieser, M.; Glira, P.; Winiwarter, L. Complementing airborne laser bathymetry with UAV-based lidar for capturing alluvial landscapes. In Proceedings of the SPIE Remote Sensing, Toulouse, France, 14 October 2015.
3. Seitsonen, O.; Ikäheimo, J. Detecting Archaeological Features with Airborne Laser Scanning in the Alpine Tundra of Sápmi, Northern Finland. *Remote Sens.* **2021**, *13*, 1599. [[CrossRef](#)]
4. Herrault, P.-A.; Poterek, Q.; Keller, B.; Schwartz, D.; Ertlen, D. Automated detection of former field systems from airborne laser scanning data: A new approach for Historical Ecology. *Int. J. Appl. Earth Obs. Geoinf.* **2021**, *104*, 102563. [[CrossRef](#)]
5. Hodgetts, D. Laser scanning and digital outcrop geology in the petroleum industry: A review. *Mar. Pet. Geol.* **2013**, *46*, 335–354. [[CrossRef](#)]
6. Wajs, J.; Trybała, P.; Górniak-Zimroz, J.; Krupa-Kurzynowska, J.; Kasza, D. Modern Solution for Fast and Accurate Inventorization of Open-Pit Mines by the Active Remote Sensing Technique—Case Study of Mikoszków Granite Mine (Lower Silesia, SW Poland). *Energies* **2021**, *14*, 6853. [[CrossRef](#)]
7. Hollaus, M.; Mücke, W.; Roncat, A.; Pfeifer, N.; Briese, C. Full-Waveform Airborne Laser Scanning Systems and Their Possibilities in Forest Applications. In *Forestry Applications of Airborne Laser Scanning: Concepts and Case Studies*; Maltamo, M., Næsset, E., Vauhkonen, J., Eds.; Managing Forest Ecosystems; Springer: Dordrecht, The Netherlands, 2014; pp. 43–61, ISBN 978-94-017-8663-8.
8. Appiah Mensah, A.; Jonzén, J.; Nyström, K.; Wallerman, J.; Nilsson, M. Mapping site index in coniferous forests using bi-temporal airborne laser scanning data and field data from the Swedish national forest inventory. *For. Ecol. Manag.* **2023**, *547*, 121395. [[CrossRef](#)]
9. Elamin, A.; Abdelaziz, N.; El-Rabbany, A. A GNSS/INS/LiDAR Integration Scheme for UAV-Based Navigation in GNSS-Challenging Environments. *Sensors* **2022**, *22*, 9908. [[CrossRef](#)]
10. Loghin, A.; Oniga, E.; Wieser, M. Analysing and Modelling Terrain Surface Changes using Airborne Laser Scanning Data. *World J. Eng. Res. Technol.* **2016**, *2*, 87–95.
11. Torresan, C.; Berton, A.; Carotenuto, F.; Chiavetta, U.; Miglietta, F.; Zaldei, A.; Gioli, B. Development and Performance Assessment of a Low-Cost UAV Laser Scanner System (LasUAV). *Remote Sens.* **2018**, *10*, 1094. [[CrossRef](#)]

12. Maune, D.F.; Kopp, S.M.; Crawford, C.A.; Zervas, C.E. Introduction. In *Digital Elevation Model Technologies and Applications: The DEM Users Manual*, 2nd ed.; Maune, D.F., Ed.; American Society for Photogrammetry and Remote Sensing; Bethesda: Rockville, MD, USA, 2007; pp. 9–16.
13. Wagner, W.; Ullrich, A.; Ducic, V.; Melzer, T.; Studnicka, N. Gaussian Decomposition and Calibration of a Novel Small-Footprint Full-Waveform Digitising Airborne Laser Scanner. *ISPRS J. Photogramm. Remote Sens.* **2006**, *60*, 100–112. [[CrossRef](#)]
14. Ruiz, L.A.; Hermosilla, T.; Mauro, F.; Godino, M. Analysis of the Influence of Plot Size and LiDAR Density on Forest Structure Attribute Estimates. *Forests* **2014**, *5*, 936–951. [[CrossRef](#)]
15. Sithole, G.; Vosselman, G. Experimental comparison of filter algorithms for bare-Earth extraction from airborne laser scanning point clouds. *ISPRS J. Photogramm. Remote Sens.* **2004**, *59*, 85–101. [[CrossRef](#)]
16. Chen, Z.; Gao, B.; Devereux, B. State-of-the-Art: DTM Generation Using Airborne LIDAR Data. *Sensors* **2017**, *17*, 150. [[CrossRef](#)] [[PubMed](#)]
17. Yilmaz, V. Automated ground filtering of LiDAR and UAS point clouds with metaheuristics. *Opt. Laser Technol.* **2021**, *138*, 106890. [[CrossRef](#)]
18. Kraus, K.; Pfeifer, N. Determination of terrain models in wooded areas with airborne laser scanner data. *ISPRS J. Photogramm. Remote Sens.* **1998**, *53*, 193–203. [[CrossRef](#)]
19. Kraus, K.; Pfeifer, N. Advanced DTM generation from LIDAR data. *Int. Arch. Photogramm. Remote Sens.* **2001**, *34*, 23–30.
20. Pfeifer, N.; Stadler, P.; Briese, C. Derivation of Digital Terrain Models in the SCOP ++ Environment. In Proceedings of the OEEPE Workshop on Airborne Laser Scanning and Interferometric SAR for Detailed Digital Elevation Models, Stockholm, Sweden, 1–3 March 2001.
21. Axelsson, P. DEM generation from laser scanner data using adaptive TIN models. *Int. Arch. Photogramm. Remote Sens.* **2000**, *4*, 110–118.
22. Nardinocchi, C.; Forlani, G.; Zingaretti, P. Classification and filtering of laser data. *Int. Arch. Photogramm. Remote Sens.* **2003**, *34*. Available online: https://www.isprs.org/proceedings/XXXIV/3-W13/papers/Nardinocchi_ALSDD2003.PDF (accessed on 20 October 2023).
23. Jacobsen, K.; Lohmann, P. Segmented filtering of laser scanner DSMs. *Int. Arch. Photogramm. Remote Sens.* **2003**, *34*. Available online: https://www.isprs.org/proceedings/XXXIV/3-W13/papers/Jacobsen_ALSDD2003.pdf (accessed on 10 October 2023).
24. Serifoglu, Y.C.; Gungor, O. Comparison of the performances of ground filtering algorithms and DTM generation from a UAV-based point cloud. *Geocarto Int.* **2018**, *33*, 522–537. [[CrossRef](#)]
25. Salach, A.; Bakula, K.; Pilarska, M.; Ostrowski, W.; Górski, K.; Kurczyński, Z. Accuracy Assessment of Point Clouds from LiDAR and Dense Image Matching Acquired Using the UAV Platform for DTM Creation. *ISPRS Int. J. Geo-Inf.* **2018**, *7*, 342. [[CrossRef](#)]
26. Fuad, N.A.; Ismail, Z.; Majid, Z.; Darwin, N.; Ariff, M.F.M.; Idris, K.M.; Yusoff, A.R. Accuracy evaluation of digital terrain model based on different flying altitudes and conditional of terrain using UAV LiDAR technology. In Proceedings of the IOP Conference Series: Earth and Environmental Science, Kuala Lumpur, Malaysia, 24–25 April 2018; IOP Publishing: Bristol, UK, 2018; Volume 169, p. 012100.
27. Štroner, M.; Urban, R.; Křemen, T.; Braun, J. UAV DTM acquisition in a forested area—comparison of low-cost photogrammetry (DJI Zenmuse P1) and LiDAR solutions (DJI Zenmuse L1). *Eur. J. Remote Sens.* **2023**, *56*, 2179942. [[CrossRef](#)]
28. Chen, C.; Guo, J.; Wu, H.; Li, Y.; Shi, B. Performance Comparison of Filtering Algorithms for High-Density Airborne LiDAR Point Clouds over Complex LandScapes. *Remote Sens.* **2021**, *13*, 2663. [[CrossRef](#)]
29. Romanian Position Determination System: Real Time Products. Available online: <https://www.unoosa.org/documents/pdf/psa/activities/2010/moldova/presentations/3-3.pdf> (accessed on 20 October 2023).
30. Oniga, V.E.; Morelli, L.; Macovei, M.; Chirila, C.; Breaban, A.I.; Remondino, F.; Sestras, P. PPK Processing to Boost Accuracy in Cadastral Mapping. *Int. Arch. Photogramm. Remote Sens. Spat. Inf. Sci.* **2023**, *48*, 345–352. [[CrossRef](#)]
31. Dreier, A.; Janßen, J.; Kuhlmann, H.; Klingbeil, L. Quality Analysis of Direct Georeferencing in Aspects of Absolute Accuracy and Precision for a UAV-Based Laser Scanning System. *Remote Sens.* **2021**, *13*, 3564. [[CrossRef](#)]
32. Shuttle V5.7 User Guide. Available online: <https://fshop.oss-accelerate.aliyuncs.com/20200611113453747081734.pdf> (accessed on 1 November 2023).
33. *Help TransDatRO: User Guide; National Agency for Cadastre and Land Registration; National Center for Cartography*: Bucharest, Romania, 2022. Available online: <https://cngcft.ro/index.php/ro/> (accessed on 20 October 2023).
34. OPALS Orientation and Processing of Airborne Laser Scanning Data. Available online: <http://geo.tuwien.ac.at/opals/html/ModuleGrid.html> (accessed on 1 November 2023).
35. Pfeifer, N.; Mandlbürger, G.; Otepka, J.; Karel, W. OPALS—A framework for Airborne Laser Scanning data analysis. *Comput. Environ. Urban Syst.* **2014**, *45*, 125–136. [[CrossRef](#)]
36. Štroner, M.; Urban, R.; Linková, L. A New Method for UAV Lidar Precision Testing Used for the Evaluation of an Affordable DJI ZENMUSE L1 Scanner. *Remote Sens.* **2021**, *13*, 4811. [[CrossRef](#)]
37. CloudCompare Official Web Site. Available online: <http://www.danielgm.net/cc/> (accessed on 1 November 2023).
38. Zhang, W.; Qi, J.; Wan, P.; Wang, H.; Xie, D.; Wang, X.; Yan, G. An Easy-to-Use Airborne LiDAR Data Filtering Method Based on Cloth Simulation. *Remote Sens.* **2016**, *8*, 501. [[CrossRef](#)]
39. Piltz, B.; Bayer, S.; Poznanska, A.M. Volume based DTM generation from very high resolution photogrammetric DSMs. *Int. Arch. Photogramm. Remote Sens. Spatial Inf. Sci.* **2016**, *41*, 83–90. [[CrossRef](#)]

40. Pfeifer, N.; Mandlbürger, G. Filtering and DTM Generation. In *Topographic Laser Ranging and Scanning: Principles and Processing*; Shan, J., Toth, C., Eds.; CRC Press: Boca Raton, FL, USA, 2008; pp. 307–333, ISBN 9781420051421.
41. Štroner, M.; Urban, R.; Lidmila, M.; Kolár, V.; Kremen, T. Vegetation Filtering of a Steep Rugged Terrain: The Performance of Standard Algorithms and a Newly Proposed Workflow on an Example of a Railway Ledge. *Remote Sens.* **2021**, *13*, 3050. [[CrossRef](#)]
42. Kuçak, R.A.; Büyüksalih, İ. Comparison of CSF Ground Filtering Method by Using Airborne LiDAR Data. *Adv. LiDAR* **2023**, *3*, 47–52.
43. Sarıtaş, B.; Kaplan, G. Enhancing Ground Point Extraction in Airborne LiDAR Point Cloud Data Using the CSF Filter Algorithm. *Adv. LiDAR* **2023**, *3*, 53–61.
44. Hollaus, M.; Mandlbürger, G.; Pfeifer, N.; Mücke, W. Land Cover Dependent Derivation of Digital Surface models from Airborne Laser Scanning Data. *IAPRS* **2010**, *38*, 221–226.

Disclaimer/Publisher’s Note: The statements, opinions and data contained in all publications are solely those of the individual author(s) and contributor(s) and not of MDPI and/or the editor(s). MDPI and/or the editor(s) disclaim responsibility for any injury to people or property resulting from any ideas, methods, instructions or products referred to in the content.

Submit to this Journal

Review for this Journal

Propose a Special Issue

Article Menu

Academic Editor

 Jianbo Gao

Subscribe SciFeed

Recommended Articles

Related Info Link

IK

Order Article Reprints



Open Access Article

Spatial Analysis of Creative Industries for Urban Functional Zones: A GIS-Based Comparative Study in Eastern European Regional Centres: Cluj-Napoca (Romania) and Pécs (Hungary)

by Bilaşco Ştefan ^{1,2,*} , Réka Horeczki ³ , Szilárd Rác ³ , Roşca Sanda ^{1,4} , Dohotar Vasile ¹ , Vescan Iuliu ¹ , Fodorean Ioan ¹  and Paul Sestras ^{4,5} 

¹ Faculty of Geography, Babes-Bolyai University, Clinicilor Street 5-7, 400006 Cluj-Napoca, Romania

² Cluj-Napoca Subsidiary Geography Section, Romanian Academy, 400015 Cluj-Napoca, Romania

³ Centre for Economic and Regional Studies, Institute for Regional Studies, 22. Papnövelde Street, 7621 Pécs, Hungary

⁴ Academy of Romanian Scientists, Ilfov 3, 050044 Bucharest, Romania

⁵ Faculty of Civil Engineering, Technical University of Cluj-Napoca, 400020 Cluj-Napoca, Romania

* Author to whom correspondence should be addressed.

Appl. Sci. **2024**, *14*(3), 1088; <https://doi.org/10.3390/app14031088>

Submission received: 28 December 2023 / Revised: 25 January 2024 / Accepted: 25 January 2024 /

Published: 27 January 2024

APPLIED SCIENCES-BASEL

Publisher name: MDPI

Journal Impact Factor™

2.5

2023

2.7

Five Year

JCR Category	Category Rank	Category Quartile
CHEMISTRY, MULTIDISCIPLINARY <i>in SCIE edition</i>	114/230	Q2
ENGINEERING, MULTIDISCIPLINARY <i>in SCIE edition</i>	44/179	Q1
MATERIALS SCIENCE, MULTIDISCIPLINARY <i>in SCIE edition</i>	257/438	Q3
PHYSICS, APPLIED <i>in SCIE edition</i>	87/179	Q2

Article

Spatial Analysis of Creative Industries for Urban Functional Zones: A GIS-Based Comparative Study in Eastern European Regional Centres: Cluj-Napoca (Romania) and Pécs (Hungary)

Bilaşco Ştefan ^{1,2,*}, Réka Horeczki ³, Szilárd Rác ³, Roşca Sanda ^{1,4}, Dohotar Vasile ¹, Vescan Iuliu ¹, Fodorean Ioan ¹ and Paul Sestras ^{4,5}

¹ Faculty of Geography, Babes-Bolyai University, Clinicilor Street 5-7, 400006 Cluj-Napoca, Romania; sanda.rosca@ubbcluj.ro (R.S.); vasile.dohotar@ubbcluj.ro (D.V.); iuliu.vescan@ubbcluj.ro (V.I.); ioan.fodorean@ubbcluj.ro (F.I.)

² Cluj-Napoca Subsidiary Geography Section, Romanian Academy, 400015 Cluj-Napoca, Romania

³ Centre for Economic and Regional Studies, Institute for Regional Studies, 22. Papnövelde Street, 7621 Pécs, Hungary; horeczki.reka@krtk.hun-ren.hu (R.H.); racz.szilard@krtk.hun-ren.hu (S.R.)

⁴ Academy of Romanian Scientists, Ilfov 3, 050044 Bucharest, Romania; psestras@mail.utcluj.ro

⁵ Faculty of Civil Engineering, Technical University of Cluj-Napoca, 400020 Cluj-Napoca, Romania

* Correspondence: stefan.bilasco@ubbcluj.ro

Abstract: Creative industries, by their nature of innovation through creativity, add value to any territory by giving it spatial functionality, and at the same time, they favour sustainable development through the sustainability of the urban centres in which they operate. This paper develops a GIS methodology based on the implementation of a spatial analysis model that captures, in a comparative way, the spatial functionality of two different urban centres—(Cluj-Napoca (Romania) and Pécs (Hungary))—in terms of spatial extent based on the impact of the spatial distribution of creative industries. The spatial analysis model is based on the management of alpha-numeric databases representing the addresses of the creative industries, based on geolocation, for the development of spatial analyses of pedestrian accessibility. The main aim is to identify the specific areas of 15 and 5 min model cities. The comparative analysis was carried out by implementing a deterministic methodology through which the areas with certain degrees of accessibility were analysed in relation to the total analysed area, with the main aim of standardising the scale of analysis due to the difference between the two urban centres, thus facilitating the use of qualitative boning in the final comparison process. The results obtained highlight the local behaviour, at the same time making it possible to conduct a realistic deterministic comparative analysis of the two urban centres, which are also identifiable from the point of view of local territorial functionality, thereby validating the GIS model implemented in the present study.

Keywords: cultural and creative industry; accessibility; GIS spatial analysis; comparative assessment



Citation: Ştefan, B.; Horeczki, R.; Rác, S.; Sanda, R.; Vasile, D.; Iuliu, V.; Ioan, F.; Sestras, P. Spatial Analysis of Creative Industries for Urban Functional Zones: A GIS-Based Comparative Study in Eastern European Regional Centres: Cluj-Napoca (Romania) and Pécs (Hungary). *Appl. Sci.* **2024**, *14*, 1088. <https://doi.org/10.3390/app14031088>

Academic Editor: Jianbo Gao

Received: 28 December 2023

Revised: 25 January 2024

Accepted: 25 January 2024

Published: 27 January 2024



Copyright: © 2024 by the authors. Licensee MDPI, Basel, Switzerland. This article is an open access article distributed under the terms and conditions of the Creative Commons Attribution (CC BY) license (<https://creativecommons.org/licenses/by/4.0/>).

1. Introduction

Knowledge, innovation and creativity are key themes to be explored in the areas related to urban and regional development. In addition to the social and economic environment of cities, the cultural milieu is increasingly becoming an installation factor. Since the 1990s and mostly after the millennium, the development of knowledge-based economic sectors has become a key topic in national, regional, and international economic strategies. The creative industry uses culture as a source material, although the result it produces is rather functional [1]. Culture and creative industries (CCIs) play a major role in the European economy, accounting for 4.5% of total European GDP (Gross Domestic Product) in 2019 [2]. Their contribution is higher than that of the telecommunications sector or agriculture. Their growing role is also demonstrated by the 17% growth in economic output in

the last eight years and the 12% increase in household cultural expenditure (between 2010 and 2015). The role of CCIs is outstanding in terms of employment, with 7.6 million people in the European Union. The overwhelming majority of people employed in the sector are young people with tertiary education (43% under 39 years). Spatial differences in creative and knowledge-intensive sectors within the urban network show a significant pattern. The urban network of Eastern Europe is characterised by capital-centricity. Metropolitan spaces dominate the innovative workforce and concentrate on advanced economic sectors, high-quality institutions, and services [3]. Transport options are also mostly capital-centric. There have been several attempts to introduce a polycentric development model, with successes mainly in countries with a larger territory. The development and consolidation of counterpoint cities have favoured regional centres. Different roles have been defined for regional centres, so decentralisation has led not only to the availability of public services but also to a rethinking of the economic structure. Functional urban area-based development can help to resolve the historically defined system of inequalities between the centrum and periphery [4]. Network development, whether in terms of public services or physical infrastructure, can also improve the quality of life of the population and the availability of institutions.

Creativity is an essential factor for economic development in post-industrial societies. The share of the CCI sector in a city or FUA (Functional Urban Area) is an indicator of how fast the economy of that area can grow. It can also be seen as a measure of development [5]. The two regional centres subject to our interest have many similarities and a number of unique features in terms of their function scope and agglomeration. Their comparative analyses, resource base, local circumstances and processes may result in interesting results. In order to meet the great global challenges that the two cities have to face, more attention needs to be paid to resource efficiency in the creative sector. Establishing a resource-efficient economy is a major environmental and development challenge today and requires political actions at all (international, national and local) levels. Improving resource efficiency by better understanding the available amount, value, structure, ownership, use, etc. of resources within a given locality is crucial to planning and implementing good resource-based spatial policies. For the adaptive and sustainable development of a territory, the decision-makers need exact information about the potential and consumption (new working places, culture-based economy, innovation ecosystem, etc.) of resources related to the development processes of a given place.

Geographic information systems (GISs), through the large analysis capacity of spatial databases, offer multiple possibilities for evaluating a territory, taking into account the main components that generate dysfunction or that impose functionality in the territory [5–15].

An integrated analysis of the components, as spatially referenced databases, through the integrated applications and analysis models developed, produces notable results that support analysis and decision-making [16–19].

Analyses based on the point distribution of territorial infrastructures [20,21], here including industrial locations such as creative industries within large urban centres, lend themselves very well to the development of simple GIS spatial analysis models that are implemented mainly through spatial proximity analysis [22,23], spatial interpolation [24,25], or spatial geostatistics [26,27].

The development of these types of GIS spatial analysis models has a number of limitations that derive from the fact that only point location and distance are considered in the spatial analysis process.

The development of GIS spatial analysis models for identifying areas with certain degrees of functionality requires the integrated analysis of several factors that contribute to determining the type of territorial functionality. This requires the development of integrated spatial analysis models that do not rely solely on the facilities offered by geoinformation software—models that include in their structure the correlative analysis of spatial databases of different types, in terms of structure and geometry [28].

Integrating into this modern trend of GIS spatial analysis, a series of models have been developed to assess territorial dysfunctions using network analysis as a method to study the relationships between the components of a network and the locations of industrial centres that generate different types of territorial functionality [29–31].

The present study is outlined as a GIS model of spatial analysis that takes into account only the locations of the creative industries chosen as test elements, excluding the population component, focusing on the quantitative analysis of the impact of accessibility within territorial structures with different geometries and surfaces.

The main aim of the present investigation is to propose a GIS model for spatial analysis that allows for the comparative analysis of two urban centres that are different in terms of the spatial extension, shape, and placement of analysed infrastructures, namely Cluj-Napoca, Romania, and Pécs, Hungary. The focus of the study is the spatial distribution of creative industries (as territorially arranged test infrastructures), using network analysis as the main methodological approach to identify their cumulative impact in terms of accessibility. In order to achieve the proposed main objective, an integrated geographic information system (GIS) model for spatial analysis has been developed, focusing on pedestrian accessibility in view of the role of the recently developed and implemented 15 min cities concept in large urban centres.

The accomplishment of the primary goal entails the accomplishment of the following secondary goals: locating the creative industries; acquiring the spatial extension of intervals with varying temporal accessibility in minutes; integrating databases that represent accessibility uniformly for the analysis of the territorial impact of creative industry components; and integrating the analysis of spatial databases for the identification of cumulative accessibility. All of these integrations are based on a specific methodology that is proposed and implemented both vertically and horizontally within the main stages of the model.

2. Study Area

The economic space of Eastern Europe is dominated by urban areas, leading to a top-down diffusion of modernisation and innovation from the highest levels of the settlement hierarchy [32]. The geographical focus of the study is two regional centres of Romania and Hungary (Cluj-Napoca and Pécs) (Figure 1), which can be defined as having a high priority for changes in the settlement network: the establishment of new states and new capitals, positive changes in the cross-border mobility of states, and new neighbourhoods [33].



Figure 1. Geographical position of the study area.

Hungarian and Romanian urbanisation processes have progressed along similar lines since 1990. The main differences can be observed in their population size and the dynamics before the regime change. In the countries of Central and Eastern Europe, the demarcation of regions and their centres became increasingly important in the run-up to EU membership. These delimitations have been accompanied by a lively discussion, partly for historical reasons and partly because of political positioning. In many places (e.g., Romania and Bulgaria), the leading role of centres has been questioned [34]. There are many specific aspects concerning the development of regional centres in the countries, but in most cases, it is clear that in most regions the largest city is at the centre—the location of concentrated interventions. Cities are the power centres of economic life due to their population density and heterogeneous employment build-up, and because their morphologic image and standards are different from those of villages.

By the end of the socialist period in Romania, a network of large cities had been created, providing a relatively modern industrial base, with 7 relatively evenly spaced cities of 300,000 people, in addition to the capital of 2 million. The urban hierarchy at the end of the socialist era can be seen in the work of Ioan Ianoş (1987) [35], who used a number of indicators (demographic, economic, administrative, political, social, cultural and spatial) to construct an eight-level functional hierarchy. Cities reacted differently to radical socio-economic changes, depending on their endowments and their capacity to adapt and innovate. A more pronounced differentiation of the urban hierarchy was initiated, and the big cities were in a more advantageous position [36,37]. Bucharest was the clear winner of the territorial processes, while Banat and Central Transylvania were able to preserve their relative historical development. Foreign capital investment was concentrated in the large cities in the west and some industrial centres in the south, with the capital city as the primary location. The winners of the transition include large cities with advanced or fast-growing service sectors, cities with high value-added productive sectors, and Black Sea and western border regions. In general, the losers were the small and medium-sized towns, the declining industrial centres, and the inflated county centres alienated from local resources [32,36,38].

The settlement network has developed in an unbalanced way, with dense urban networks developing in some areas, while larger urban deprivation zones have been preserved [36,37]. The number and scope of regional centres have been unchanged in the last four censuses; only their order has changed. As in the countries of the region, the transformation of the urban network is essentially characterised by increasing economic fragmentation and the dominance of the capital, with the rise in the value of cities in certain areas. The most important centres on the country's periphery are the selected regional centres: the major city in Transylvania is Cluj-Napoca, and in South Transdanubia, the major city is Pécs.

3. Methodology and Database

The comparative analysis of two regional centres, with relatively identical characteristics in terms of the development of functional areas but differences in terms of geographical characteristics and the spatial extension of the research area, based on the influence of the spatial arrangement of creative industries, involves the development of a methodology of research to capture the conditional relations between the location of the industry and its impact in the territory as well as the impact they have on the human component as a direct beneficiary of the harmonious development of the urban territory.

Taking into account these defining requirements, a proprietary research methodology was developed and implemented in the GIS environment on numeric, vector, and raster database structures. This methodology, which takes shape as a GIS of complex spatial analysis, allows for the integration of the principles of development and regional planning in functional systems of response-process type for the analysis of specificity and territorial development.

The developed methodology has at its centre the evaluation of the territorial specificity based on the analysis of pedestrian accessibility to the infrastructure of the creative industry, considering that the infrastructure of the creative industries generates additional territorial value through economic growth and a small negative impact on the environment due to the specificity of economic productivity and non-polluting matters. Thus, the analysis of urban centres from the point of view of pedestrian accessibility of the population emerges as a defining factor in the establishment of functional urban areas due to the fact that easy pedestrian access will lead to the development of the spatial component, which takes into account the reduction of transport infrastructures necessary for transporting the human component to the workplace and implicitly significantly reducing the intense traffic generating territorial dysfunction.

Having in its centre the assessment of pedestrian accessibility, the spatial analysis methodology is structured in three distinct stages (the acquisition of numerical database and spatial databases; the implementation of the proposed GIS spatial analysis; and the analysis of the intermediate results and presentation and analysis of the final results to identify areas with dysfunctions in order to issue their remedial solutions). These stages, when viewed as a whole, take shape as a complex system of spatial analyses that cannot function without referring to, within the research approach, the spatial databases and the results obtained in the previous stages and sub-stages (Figure 2).

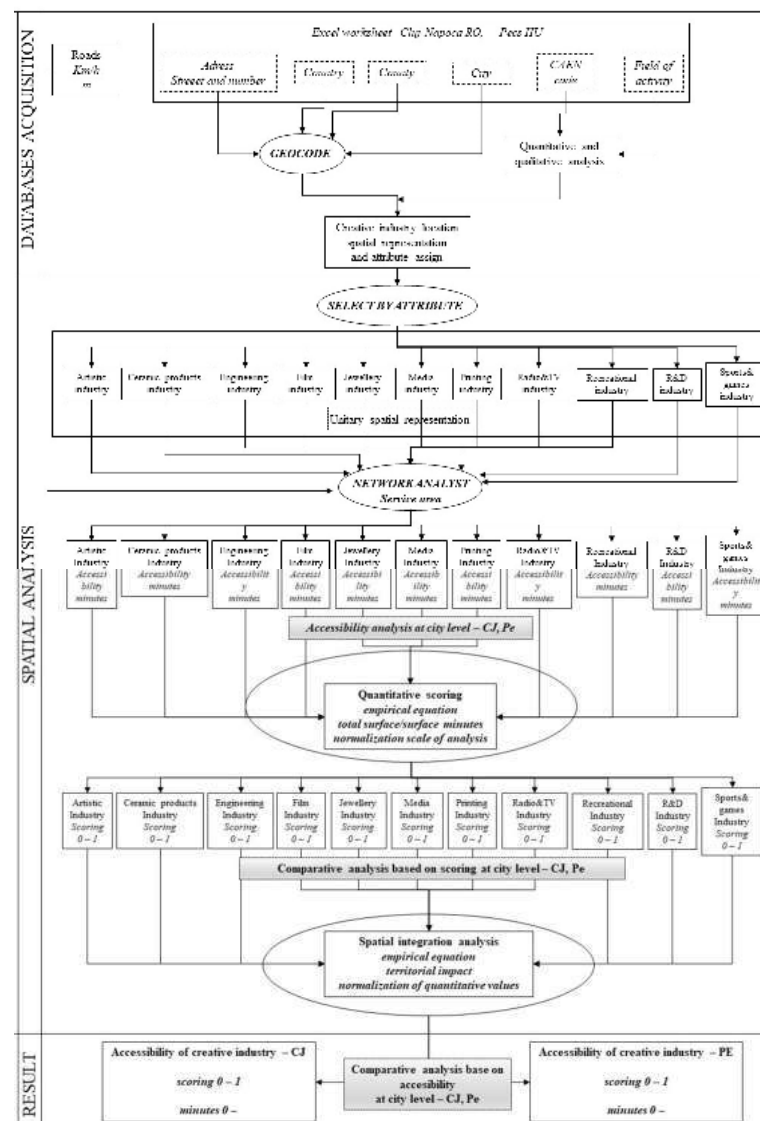


Figure 2. The scheme of the methodological workflow.

The first step within the spatial analysis process is the acquisition and creation of a GIS spatial database on which the entire research process is based. The databases used in the spatial analysis process are divided into two different structures: vector databases representing the network of communication paths obtained on the basis of direct acquisition from OSM, and alpha-numeric databases representing the spatial localisation elements of each unit entity that represent a certain type of creative industry. Considering the fact that the entire research approach is based on pedestrian accessibility, the vector databases representing the communication paths were subjected to the process of spatial analysis on the attribute table to obtain the time in minutes required for the movement of a person on road segments—times that together highlight the areal access to the locations of the creative industries. The preparation of the vector database representing the communication paths involves the use of the average travel speed of 5 km/hour, related to metric distances.

The alpha-numeric database obtained in the form of an .xls file from listafirme.ro for Cluj-Napoca, and the KRTK Databank for Pécs, provide, on the one hand, information related to the spatial location of creative industries (street and number, county, country, and city) and information used in the geolocation process, and, on the other hand, information related to the CAEN/NACE code and field of activity for each individual location. The first part of the information was used to geolocate the creative industries and obtain point vector databases using the geolocation services provided by ESRI for each individual record. The second part of the information is constituted as an attribute database used in the qualitative spatial analysis of grouping creative industries according to their specifics.

The spatial analysis stage foregrounds the management and integration of spatial databases (communication paths and spatial location of creative industries) on a logical basis, using mathematical integration formulas for the spatial representation of the main categories of creative industries and using time analysis and modelling of access related to the location of the creative industries. This is in order to highlight the areas with high and low accessibility, which can later be analysed comparatively for the two territorial administrative units taken into account. The first part of the spatial analysis is dedicated to obtaining the main categories of creative industries, starting from the grouping of unitary creative industries according to the specifics of the activity, taking into account the CAEN/NACE code and their field of activity. The study uses the NACE code delimitation for cultural and creative industries [39]. Thus, using the geocoded vector database and the spatial analysis on the attribute table, from a total of 4839 companies for the city of Cluj-Napoca and 1308 companies for Pécs, 11 classes with unique characteristics were used in the process of spatial accessibility modelling and the comparison of the two main urban centres.

The identification of the territorial accessibility related to the locations of the classes representing creative industries for the two main urban centres is carried out on the basis of the network analysis, considering the service area module made available by the ArcGis 10.8 geoinformational software. Accessibility analysed in terms of the time needed to access the creative industries is based on the identification of standard time intervals. As part of the analysis, five temporal intervals were chosen to meet the urban planning requirements in force. Thus, the time intervals 0–5 min, 5–15 min, 15–30 min, 30–60 min and more than 60 min on foot were chosen. Considering the fact that the concept of the 15 min city (developed by Arthur Clarence in 1920) [40], which is still relevant today, was proposed for implementation at the Climate Change Conference (COP 21) in Paris, 2015 [41–43], the 5–15 min interval was used in the analysis. The 0–5 min analysis is based on the 5 min city concept being implemented in Copenhagen to highlight the socially, architecturally and sustainably designed developed city, a city with ideal urban development.

The other two intervals—30–60 and more than 60 min—were implemented in the accessibility analysis due to the large spatial extension of the two cities and the concentration of the creative industries (for the most part) in the central areas, thus highlighting the areas with accessibility reduced from the periphery of the main functional areas.

The analysis of accessibility obtained for the five categories can be carried out in the current stage of unitary spatial analysis for each class of creative industry and at the level of each administrative unit analysed, but it is not possible to make a direct comparison between the two urban centres analysed due to the spatial scale of different representation. The comparative analysis is based on the standardisation of the spatial analysis scale, involving comparing the spatial extension of each accessibility interval with the entire analysis surface of the analysed urban centre, based on the qualitative scoring technique. Thus, it was decided to credit each accessibility interval with values between 0 and 1 according to Table 1.

Table 1. Rating classes/accessibility intervals.

Industry Type	Accessibility in Minutes									
	0–5		5–15		15–30		30–60		>60	
	Scoring									
	0–0.20		0.20–0.40		0.40–0.60		0.60–0.80		0.80–1	
	Cluj	Pécs	Cluj	Pécs	Cluj	Pécs	Cluj	Pécs	Cluj	Pécs
Artistic	sv	sv	sv	sv	sv	sv	sv	sv	sv	sv
Ceramic	sv	sv	sv	sv	sv	sv	sv	sv	sv	sv
etc	sv	sv	sv	sv	sv	sv	sv	sv	sv	sv

The qualitative assessment used to standardise the scale of spatial analysis has as its main concept the fact that a larger area occupied by a certain accessibility interval compared to the entire study area has a greater impact on the territory. It takes values between the same limits of the interval for both urban centres analysed, thus allowing us to make real comparisons between the two. The calculation of the credit rating within the range, specific to each accessibility class, is performed using the formula proposed by Petrea et al., 2017 [44].

$$(x \times y)/100 = z \tag{1}$$

$$x = S_{max} - S_{min} \tag{2}$$

where

- x—the value of the scoring interval;
- y—the interval area of spatial extension, as percentage;
- z—the value of the accessibility scoring depending on the area;
- S_{max}, S_{min}—the maximal value of the scoring interval, the minimal value of the scoring interval.

$$sv = a + z \tag{3}$$

where

- sv—the scoring value;
- a—the basic value of the scoring interval;
- z—the value of the accessibility scoring depending on the area.

The unitary comparative analysis of each class of creative industry can be conducted taking into account the variation of the results in the rating range specific to the accessibility class. The higher the rated value is in the range, the greater the influence of the range-specific accessibility class in the territory, thus having a significant spatial impact. Obtaining credit values for each accessibility interval and class of creative industry offers the possibility of integrating them to identify the general accessibility of the territory influenced by the 11 classes.

The identification of general accessibility is based on the concept of the importance of the class in terms of the creative industry it represents. Due to the fact that, together

with the qualitative rating, the working scale was standardised and the characteristic rating intervals were established for each accessibility class at the same time, the integration of the obtained databases is performed on the basis of the empirical equation that provides the normalisation of the scoring values (formula 4) [10,44–46], so they fall within the general scoring interval (0–1) and can be comparatively analysed later using the scoring intervals employed (Table 1).

$$\text{ACCES} = \sqrt{\frac{\text{R\&D} \times \text{ENG}}{9}} \times (\text{ART} + \text{CER} + \text{FLM} + \text{JEL} + \text{MED} + \text{PRN} + \text{RTV} + \text{REC} + \text{SPT})$$

Terms:

R&D—Research and development industry.

ENG—Engineering industry.

ART—Artistic industry.

CER—Ceramic products industry.

FLM—Film industry.

JEL—Jewellery industry.

MED—Media industry.

PRN—Printing industry.

RTV—Radio TV industry.

REC—Recreational industry.

SPT—Sports and games industry.

The final stage of the proposed model is represented by the result based on spatial integration, obtained by using the proposed equation, adapted from [10,44–46].

This highlights the cumulative accessibility and, thanks to the unit values obtained for each urban centre separately, it makes possible the final comparison of accessibility for the two urban centres analysed and at the same time the identification of the functional areas and those with spatial coverage problems with access to creative industries.

4. Results and Discussion

The results obtained as a consequence of the implementation of the proposed model and methodology are based on the quantitative analysis of the results obtained following the implementation of the spatial analysis stage, both for obtaining databases representing the locations of creative industries and for their management and spatial integration, in order to finally compare the two cities in terms of accessibility to creative industries.

The spatial arrangement of creative industries within cities reveals two different patterns in terms of their clustering—patterns that directly influence the spatial arrangement of accessibility ranges. The analysis of hot-spot clusters brings to the fore the clustering in a single hot-spot identified near the centre of Pécs. Instead, three main hot-spots can be identified in the city of Cluj-Napoca: a very well-connected hot-spot in the centre of the city; a hot-spot in the eastern part of the city spatially identified with the largest block of flats (Mănăstur district) in Cluj-Napoca—thus, in one postal code, several creative industries are identified, but they are on different floors; and a hot-spot in the making (the Grigorescu neighbourhood)—an expanding neighbourhood where many commercial companies have their headquarters but operate in other locations (Figure 3). From the point of view of the spatial arrangement of the cold hot-spots, the city of Cluj-Napoca stands out with such a hot-spot in the northern part; a hot-spot developed due to the expansion over large areas of neighbourhoods with individual homes; and a cold hot-spot in the immediate vicinity of the airport, where more storage spaces and less creative industries are identified. Approximately the same directional distribution is identified in the NE/SW direction imprinted by the inner-city development of the two cities, around the main transport axes that serve them.

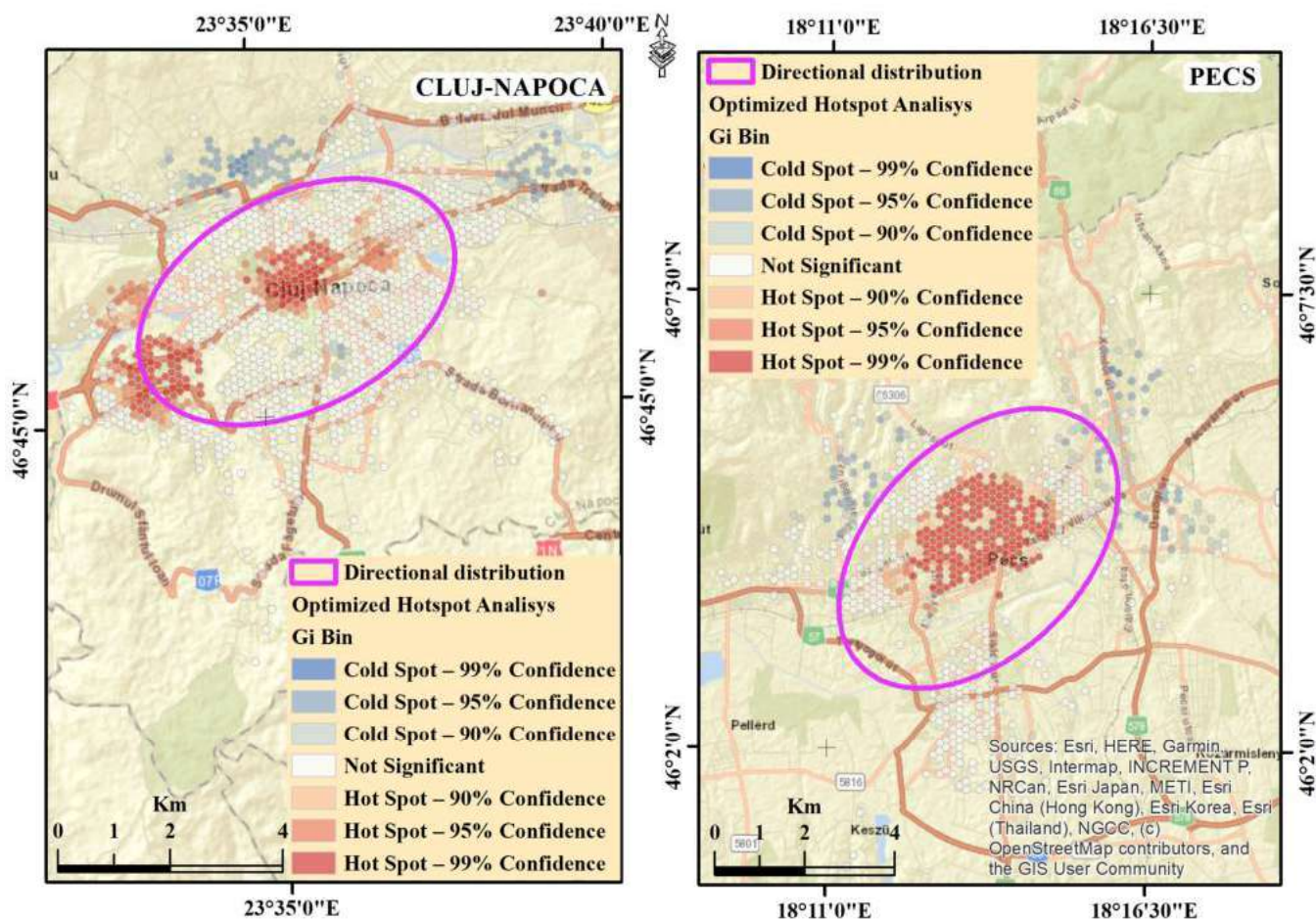


Figure 3. Hot-spot of creative industry distribution.

The activities of the cultural economy are not evenly distributed [47]. In some spaces, they are organised in clusters, especially in larger cities, where there is a complex system of specialised services and a specialised workforce. In regional centres, productive activities are co-located or linked to larger economic sectors such as high-tech and financial services, which depend on cultural and design-based industries as input sources. As we have seen in the business registers, most of the CCI sector is made up of micro and small enterprises and is therefore characterised by both fragmentation and economic networking, specialisation, and flexibility. Spatial proximity provides agglomeration benefits through cost reduction and access to knowledge [48].

These effects can be well exploited in the CCI sector, and a conscious intervention of urban policy can help. In the case of Pécs, the preparation for the European Capital of Culture title has provided a huge opportunity for the renewal of the city's creative industries and their locations [49].

The hot-spots in Pécs show the extent to which economic policy can have an impact on businesses in the CCI sector. The renovation of the Zsolnay district has extended the city centre, creating a new creative quarter within the city.

Due to the large number of creative industries (36 depending on the field of activity and their CAEN code), it was decided, within the accessibility comparison analysis, to classify them into 11 classes to highlight their specificity (Table 2).

Table 2. Creative industries classes.

No. Crt.	Class	Code	Creative Industries	Number of Industries			
				Cluj-Napoca		Pécs	
				Number	%	Number	%
1	Ceramic products industry	2341	Manufacture of ceramic household and ornamental articles	27	0.55	14	1.07
		2349	Manufacture of other ceramic products n.e.c.				
2	Jewellery industry and repair	3212	Manufacture of jewellery and related articles of precious metals and precious stones	60	1.23	26	1.98
		3213	Manufacture of imitation jewellery and related articles				
		9525	Repair of watches and jewellery				
3	Arts industry	3220	Manufacture of musical instruments	461	9.52	219	16.74
		9001	Artistic interpretation activities (performances)				
		9002	Support activities for artistic interpretation (performances)				
		9003	Artistic creation activities				
4	Sports and games industry	3230	Manufacture of sports goods	126	2.60	27	2.06
		3240	Manufacture of games and toys				
		3299	Manufacture of other manufactured products				
5	Printing industry	5811	Book publishing activities	191	3.94	40	3.05
		5813	Newspaper publishing activities				
		5814	Publishing activities of magazines and periodicals				
		5819	Other editing activities				
6	Media industry	5821	Computer game editing activities	1004	20.74	172	13.14
		7311	Activities of advertising agencies				
		7312	Media representation services				
		7420	Photographic activities				
7	Film industry	5911	Motion picture, video and television programme production activities	194	4	39	2.98
		5912	Film, video and television post-production activities				
		5913	Motion picture, video and television distribution activities				
		5914	Screening of cinema films				
		5920	Audio recording and music editing activities				
8	Radio and TV industry	6010	Radio broadcasting activities	24	0.49	10	0.76
		6020	Television broadcasting activities				
9	Engineering industry	7111	Architectural activities	2152	44.47	569	43.50
		7112	Engineering activities and related technical consultancy				
		7410	Specialised design activities				
		8130	Landscape maintenance activities				
10	Research and development industry	7220	Research and development in social sciences and humanities	263	5.43	153	11.69
		7320	Market research and public opinion polling activities				
		7430	Written and oral translation activities (interpreters)				
11	Recreational industry	9321	Amusement parks and amusement parks	337	6.96	39	2.98
		9329	Other recreational and fun activities				

A direct comparative analysis of the number of companies whose main activity is in the creative industry highlights the large numerical difference between the two urban centres analysed. The large number of creative industries identified in Cluj-Napoca (4839) highlights its character as a polarising centre, not only on the neighbouring localities that are part of the metropolitan area but also on the whole north-west region due to its role as a centre of influence and attractor due to the facilities and business opportunities it offers to potential investors. Compared to the area of territorial influence, the city of Pécs has the same spatial influence and investment attraction behaviour from the periphery to the centre; thus, we were able to identify 1308 companies whose main activity is in the creative industry. The small spatial influence, location and administrative division mean that the number of creative industries is low due to their dispersion within other urban centres, which act as a secondary pole of influence. Analysed comparatively, the two cities have similar behaviour in terms of their development based on the creative industries, showing a major influence in the territory and attracting investments in the creative industries due to their role as a pole of development and growth in the territory or as a result of, on the one hand, the influence and facilities offered, and on the other hand, the existence of consumers/demand for such industries.

The comparative analysis at the level of the type of creative industry highlights the high weight of the engineering industry and the research and development industry, which have relatively close weights—over 50%—in both urban centres. This highlights the role of the centre of innovation and application of practical technologies in the complex process of sustainable development of the urban centres analysed. The sustainability of the polarising urban centres is also highlighted by the offer, materialised in leisure and entertainment activities addressed to residents and commuters. The two urban centres have a varied and relatively similar offer, materialised in the media industry with a plus for the city of Cluj-Napoca—a plus that emerges from the character of its information hub, the arts industry (with a higher share in the city of Pécs, mainly related to the European Capital of Culture investments projects (Zsolnay District, Kodály Centre, Knowledge Centre and Library)), and the recreational industry.

The territorial impact of the creative industry types places the accessibility of the workplace to the population at the forefront as the main factor in the analysis of mobility aimed at the 15 min city goal. The spatial distribution of the types of creative industry within the two urban centres analysed reveals similarities and differences, each of which has its own specific reasons for the type of industry it is located in. The analysis of the creative industries with the most locations in the territory reveals a different spatial distribution for the engineering industry (Figure 4).

As far as the city of Cluj-Napoca is concerned, there is an agglomeration of locations in the central area and in the large housing districts, which is due to the configuration of the housing network (where most of the companies have their headquarters) imposed by the specific relief of the city, which imposes a compact development of the housing districts with a gravity towards the central axis (E-V axis of the Someşul Mic river) of the city's development. In the case of Pécs, a more fragmented picture can be seen, indicating the growth of the city, with villages administratively annexed from 1950 (in the north and north-east) and built-up residential areas (in the south) [33].

These spatial differences have a direct impact on the accessibility of the territory. It can be noticed that the territorially extended areas, with accessibility in the range 0–15 min, are compact in the centre and close to the city centre. Within the city of Pécs some areas of discontinuity are identified, generated by administrative annexes and the construction of districts linked to coal and uranium mines. Discontinuity and location of industry types throughout the administrative territory adds value to territorial accessibility, which was identified in the city of Pécs where the maximum accessibility is in the range of up to 30 min, while for the city of Cluj-Napoca access times of more than 60 min were calculated for large areas, thus inducing territorial dysfunction in terms of engineering industry.

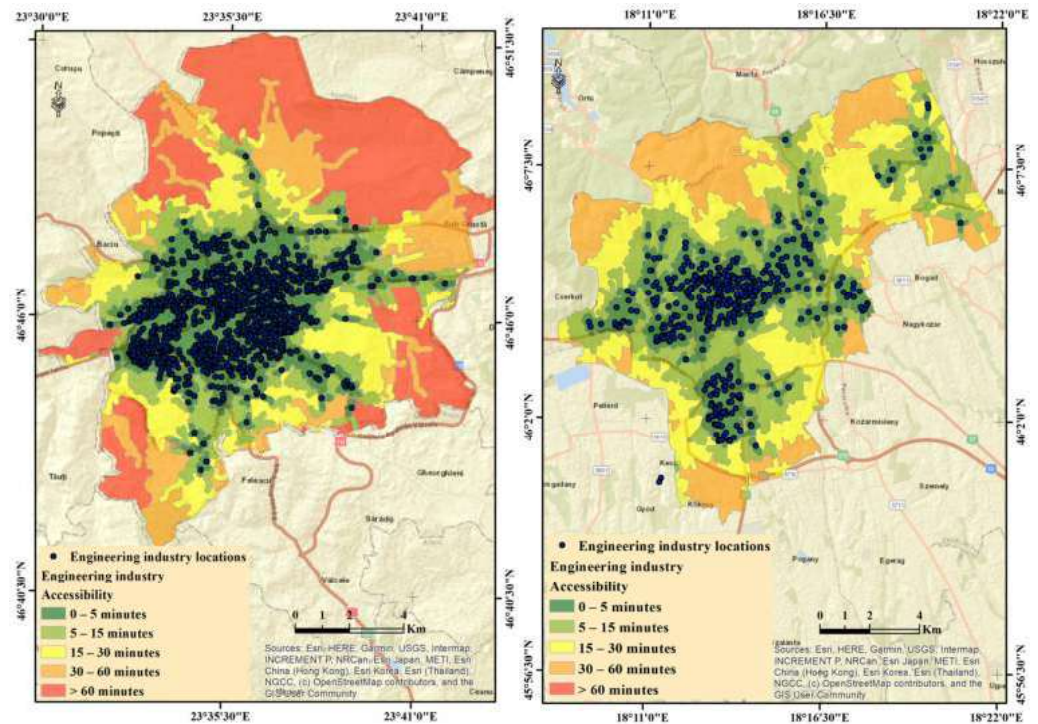


Figure 4. Maps of accessibility.

The other types of creative industries have a similar spatial distribution within the cities, being mainly located near the centres, giving them good accessibility, within the range 0–15 min. For the city of Pécs, the distribution of creative industries is divided into three main clusters: a cluster in the central area of the city, a cluster in the eastern area and a cluster in the south of the city, which does not affect accessibility in terms of time, whereas for the city of Cluj-Napoca, there is a general clustering of industries with development from the peripheral neighbourhoods towards the centre.

Due to the different spatial extension, both in terms of geometry and in terms of the surface areas of the administrative territories of the two urban centres, a comparative analysis of territorial accessibility cannot be carried out directly. Thus, for the analysis by components (types of creative industries), at city level, it was decided to analyse the surface areas occupied by each accessibility class in relation to the total surface area of the city. Following this methodology, a quantitative analysis was carried out based on values between 0 and 1.

Obtaining the bonus values for each accessibility range based on the proposed equation and methodology involves first calculating the occupied areas of each accessibility range individually, followed by calculating the percentage of land occupancy reported to the total area of the city and integrating them based on the equation system proposed in the analysis methodology. Thus, for the artistic industry, the areas for the accessibility intervals, specific to the city of Pécs, were calculated: 0–5 min (28.12 Km²/17.28%), 5–15 min (41.17 Km²/25.29%), 15–30 min (50.28 Km²/30.89%), 30–60 min (38.41 Km²/23.60%), and >60 min (4.75 Km²/2.91%) and the total area of the city was 162.3 Km². Obtaining the bond value is performed by implementing the equation system of the kind:

For the accessibility interval of 0–5 min:

$$(0.20 \times 17.28)/100 = 0.034$$

$$0 + 0.034 = 0.034$$

For the accessibility interval of 5–15 min:

$$(0.20 \times 25.29)/100 = 0.050$$

$$0.20 + 0.050 = 0.250$$

For the accessibility interval of 15–30 min:

$$(0.20 \times 30.89)/100 = 0.061$$

$$0.40 + 0.061 = 0.461$$

For the accessibility interval of 30–60 min:

$$(0.20 \times 23.60)/100 = 0.047$$

$$0.60 + 0.047 = 0.647$$

For the accessibility interval of >60 min:

$$(0.20 \times 2.91)/100 = 0.005$$

$$0.80 + 0.005 = 0.805$$

where 0.20—the value of the scoring interval; 0.034, 0.050, 0.061, 0.047, and 0.005—the value of the accessibility scoring depending on the area; 0, 0.20, 0.40, 0.60, and 0.80—the basic value of the scoring interval; and 0.034, 0.250, 0.461, 0.647, and 0.805—the value of the accessibility scoring depending on the area.

Implementing the presented equation system, we obtained scoring values for each type of creative industry and each accessibility interval (Table 3). These values were used in the process of spatial comparative analysis, based on the accessibility of the creative industries of the two administrative-territorial units.

Table 3. Rating classes/accessibility intervals.

Industry Type	Accessibility in Minutes									
	0–5		5–15		15–30		30–60		>60	
	Scoring									
	0–0.20		0.20–0.40		0.40–0.60		0.60–0.80		0.80–1	
	Cluj	Pécs	Cluj	Pécs	Cluj	Pécs	Cluj	Pécs	Cluj	Pécs
Ceramic products industry	0.009	0.005	0.229	0.223	0.426	0.439	0.645	0.662	0.888	0.867
Jewellery industry and repair	0.014	0.008	0.230	0.226	0.429	0.440	0.645	0.674	0.880	0.849
Arts industry	0.039	0.034	0.226	0.250	0.434	0.461	0.635	0.647	0.863	0.805
Sports and games industry	0.027	0.009	0.231	0.235	0.428	0.451	0.641	0.683	0.871	0.819
Printing industry	0.028	0.012	0.225	0.228	0.429	0.441	0.639	0.680	0.876	0.836
Media industry	0.048	0.033	0.227	0.243	0.433	0.455	0.632	0.661	0.857	0.805
Film industry	0.031	0.012	0.229	0.231	0.433	0.448	0.637	0.675	0.868	0.831
Radio and TV industry	0.006	0.004	0.225	0.221	0.427	0.446	0.643	0.669	0.896	0.856
Engineering industry	0.053	0.053	0.225	0.249	0.428	0.452	0.630	0.643	0.861	0.800
Research and development industry	0.031	0.026	0.225	0.241	0.434	0.449	0.639	0.671	0.868	0.811
Recreational industry	0.039	0.012	0.225	0.235	0.428	0.447	0.638	0.677	0.868	0.826

Our comparative quantitative analysis of accessibility based on the type of creative industry, intended to highlight functional areas, underscores the impact they have on the territory while also pointing to their functionality or dysfunctionality, which was analysed from the perspective of the characteristics of the respective industry.

Obtaining the bonus values makes it possible to directly compare the access times for the two urban centres for each type of creative industry, without this comparison being influenced by subjectivity. The territorial accessibility component assimilated to the new 5 min city concept, which could be implemented territorially within the territorial development strategies of large urban centres [50,51], is mostly specific to Cluj-Napoca (Figure 4). The sports and games industry, film industry, and recreational industry stand out as creative industries that suggest functionality in Cluj-Napoca for this category of

accessibility. The largest territorial impact in comparative terms is the recreational industry due to the large number of creative industries identified in Cluj-Napoca in relation to the total area of the city. The small surface areas with 0–5 min accessibility compared to the whole administrative territory show, for each creative industry analysed, that interventions in the territorial planning process are necessary so that the mentioned concept can be implemented territorially.

As regards the direct comparison of the two urban centres with the 0–15 min interval (the 15 min interval is specific to the concept city of Pécs), better accessibility specific to the city of Pécs is noticed, as evidenced by the engineering industry and the research and development industry (Figure 4). The large number of creative industries in these areas is responsible for the high functionality of the territory. The city’s polycentricity is also reflected in its easy accessibility, with creative industries in every part of the city, marked by the Garden City hub in the south and the Uranium City nodes in the west. In 2010, the European Capital of Culture project was an initiative to integrate the city’s creative and cultural industries more fully into the life of the city, with renovations and new buildings being located close to the university’s central faculties. The new cultural centres have reinforced the existing CCI, extending the historic city centre east and west.

The comparison for the accessibility intervals with times greater than 15 min (Figure 5), for the rating interval 0.40–1, highlights the similarity in terms of accessibility for the two urban centres. The comparative analysis for each type of creative industry for this range highlights the fact that the city of Cluj-Napoca has a low functionality: the bonus areas in the range 0.8–1 with over 60 min access are significantly higher than for the city of Pécs. The comparative analysis of accessibility for each creative industry highlights a functional pattern that can be analysed in three main categories. The first category is represented by the accessibility interval of 0–5 min, rated with values between 0 and 0.20, which shows an increase in functionality for the city of Cluj-Napoca; the second category is represented by the accessibility interval of 5–60 min, rated with values between 0.20 and 0.80 which shows the same pattern of territorial functionality for both Pécs and Cluj-Napoca; and the third category is represented by the accessibility interval of over 60 min, rated between 0.8 and 1, which shows the less functional character of Cluj-Napoca.



Figure 5. Cont.



Figure 5. Accessibility intervals comparison.

The component analysis does not highlight the general character of territorial accessibility given by the creative industries due to their different importance in terms of impact on territorial development projects. In order to assess the cumulative accessibility and capture the importance of the access generated by each industry in the territory, a spatial analysis of integration through equations, spatial analysis, and spatial database boning was undertaken so that the result obtained—the cumulative accessibility—could be analysed both from the point of view of spatial impact (based on cartographic materials) and the

point of view of the direct comparison of the two urban centres (based on the statistics of the boning values related to the final result).

The implementation of the spatial analysis equation proposed in the research methodology addressed implies that the two types of creative industry considered the most important in terms of territorial impact have the highest impact in the process of the accumulation of accessibility. In order to finalise the spatial analysis and implement the spatial analysis equation, we decided that the research and development industry and the engineering industry were the representative industries of the two cities. This is because they are the industries that give the cities general specificity, and they are the most important in the process of territorial development both in terms of the quality of the workforce employed and the possibilities of carrying out specific activities.

The comparative analysis of the spatial extension of the cumulative accessibility (Figure 6) highlights the unitary character of the territorial areas with 0–5 min accessibility related to Cluj-Napoca. This is primarily due to the co-location of creative industries in the central area and along the main axes (E-V axis and the city centre—S axis), which ensures the functional flows of the city and induces constraints in terms of real estate development or industrial parks and implicitly the location of industries within the administrative-territorial unit. The same constraints are also responsible for the uneven territorial distribution of accessibility ranges in the city of Cluj-Napoca. The development of real estate and related infrastructure in the central-southern and western parts of the city gives a higher functionality in terms of accessibility to creative industries, with most of the territorial areas being located in the 0–15 min intervals, while the northern and south-eastern parts are characterised by a lower functionality, with most of the territorial areas being located in the 15–60 min intervals, with a large extension of the intervals being above 60 min.

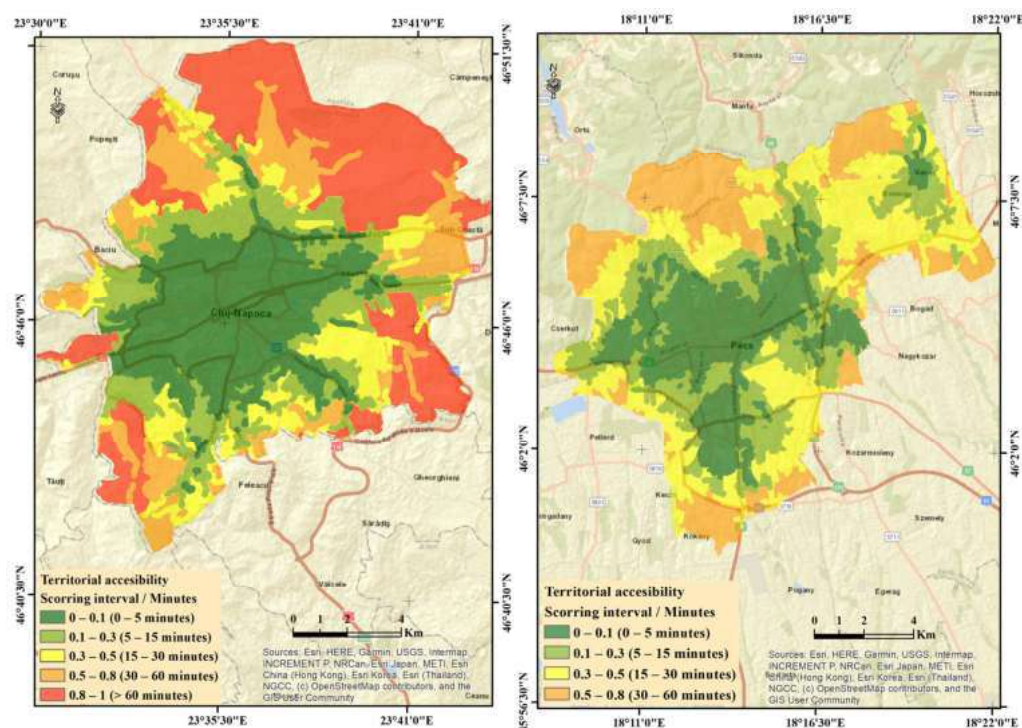


Figure 6. Maps of cumulate accessibility.

The CCI companies located in Pécs are mainly focused on road accessibility, with the main road (Route 6) to the west-east and the southern border being the main access points. In this way, the elongated downtown and the fragmented residential areas, with their smaller hubs, showcase the diversity of the city. The accessibility of the industrial parks in the southern and eastern hubs is historically rooted in the administrative annexation of smaller villages close to Pécs, which has led to a gradual increase in the city's territory but

has also had an impact on the industrial structure and its accessibility. The industrial park in the south is one of the city's newest investments; it is still in the initial, under-construction phase (with several companies settled, but roads and basic infrastructure have not yet been built throughout the entire area). This is why we find this area in the over 15 min category. The northern part of the city is connected to the Mecsek mountain range, which makes access to these areas difficult due to the natural geography.

The 15–30 min accessibility range is spatially underdeveloped in the case of Cluj-Napoca due to the compact nature of the creative industries' locations, with the city's specific constraints also having an impact here. This is due to the spatial arrangement of industry types and spatial development policies. The city of Pécs is developing creative industrial hubs in the form of islands in different parts of the territorial administrative unit (western and southern parts) due to the low restrictiveness imposed by morphometry and access infrastructure, resulting in territorially extended areas without locations of creative industries.

The spatial extension towards the periphery of Pécs of the 30–60 min accessibility range mostly fits the previous accessibility range, re-establishing the fact that the population's access to creative industries decreases from the centre to the periphery primarily due to the clustering of industries in the central area, as well as due to decisions to develop industrial hubs that stand out as islands of local accessibility.

From the point of view of comparing the spatial extension of the accessibility intervals, the interval of more than 60 min stands out very clearly, which, in the case of Cluj-Napoca, characterises the northern and eastern territorial areas, while in the case of Pécs, it is missing. The lack of an accessibility interval of more than 60 min highlights the good management of spatial resources in terms of access infrastructure but also in terms of the territorial distribution of housing and related infrastructures, which are located near the industrial hubs developed in recent years.

The elimination of the territorial dysfunctionality, caused by the large territorial areas occupied by an accessibility interval of more than 60 min in the case of Cluj-Napoca, is a matter for its future development policies. Thus, short- and medium-term development strategies focus on the development of industrial parks in the northern and north-eastern areas of the city—parks that include creativity-based industries, primarily research and development and engineering industries. This policy of developing industrial hubs (mainly green and creative industries) is in line with the spatial development of housing estates in recent years, which tends to exploit the land areas in the north and north-east of the city, resulting in integrated land management that will make the area functional in general but above all functional in terms of access, bringing the human component closer to the workplace and reducing access times.

The quantitative comparative analysis of access times based on the concept of the surface area occupied by the time interval in relation to the total surface area of the administrative-territorial unit reveals the general functionality of the units analysed. Comparing the two urban centres (Figure 7), a relatively similar functionality emerges for the 0–5 min interval, which clearly highlights the compact, sometimes crowded, nature of the layout of the creative industries' locations in the two cities. The difference is in the territorial layout of the industries.

As regards the analysis of the time intervals that define the concepts of functional city, 15 min city, the city of Pécs stands out with high functionality due to the territorial arrangement of industrial centres in the form of hubs throughout the administrative-territorial unit, which eliminates dysfunctions related to access to the territory due to its spatially efficient use. At the same time, the access intervals of 16–60 min have a more regular spatial presence in the city of Pécs but are blurred as a direct territorial effect by the lack of accessibility intervals of more than 60 min, which in the city of Cluj-Napoca is identified over large territorial areas and imposes major territorial dysfunctionality in terms of access to the creative industries.

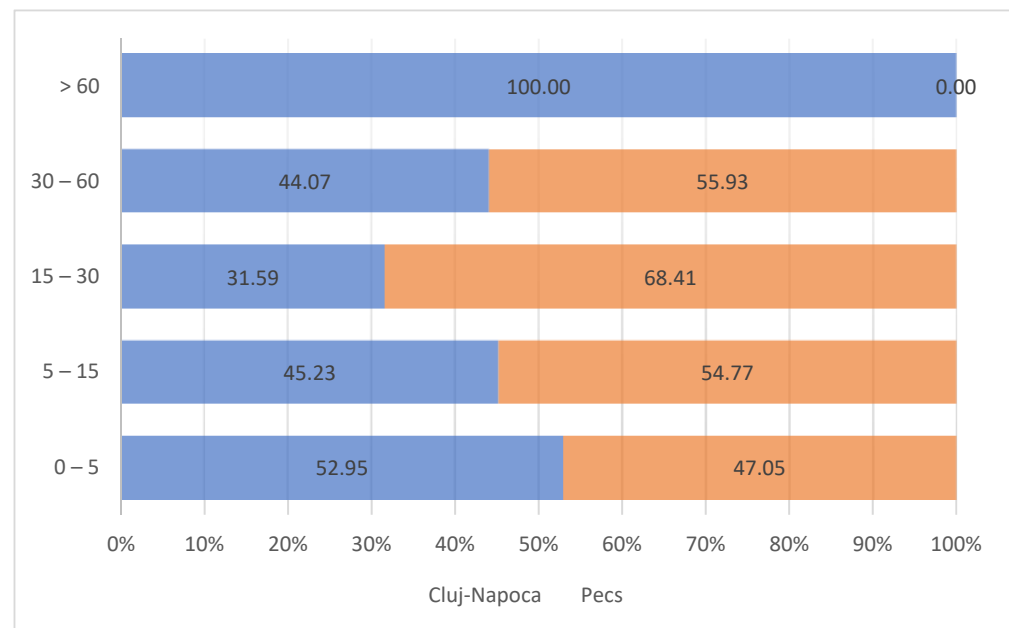


Figure 7. Cumulate accessibility intervals comparison.

The comparative analysis of the functionality of the urban centres in terms of accessibility, both on the basis of the components of the creative industries and the integration of these components to achieve overall accessibility, reveals similar behaviour for the cities of Pécs and Cluj-Napoca. Eliminating discrepancies can be achieved by issuing and implementing sustainable spatial development policies and strategies that put at their core the judicious use of land so that the human component is the main beneficiary of the increase in quality of life by achieving the goals set by highly developed urban centres—goals that are in line with the trend of the 5 or 15 min city.

The identifiable spatial databases, both for the city of Pécs and the city of Cluj-Napoca, under free-source and proprietary formats, make spatial analysis in a GIS environment suitable for the evaluation and comparative analysis of the two cities in terms of territorial functionality, with the analysis being conducted using final database structures with very high accuracy.

In terms of the limitations of this type of spatial analysis, the high processing time of the databases, the high complexity of the integrated analysis of databases representing industries with the same specificity, etc., stand out. The low availability of the databases used in the spatial analysis process (very fast dynamics of the locations of the creative industry and the types of industries identifiable within the TAUs) is another limitation that requires the implementation of the proposed model for analysis times based on characteristic years.

Modelling temporal changes in industrial character can be performed based on probability analysis, which can be implemented in the GIS spatial analysis model using statistical analysis. In this phase of our research, we did not focus on performing a probabilistic analysis, but we analysed the current state of play in terms of the impact of the creative industries and the cumulative impact of all industries identifiable at the time of the analysis within the two urban centres. Future research directions will aim to develop a spatial analysis model that can be the subject of more detailed research—research that can be aggregated, for example, with the trend of population growth or decline, thus removing some of the limitations of the proposed model and at the same time developing it from a methodological and practical application point of view.

5. Conclusions

Urban development is based on strong land and resource management policies that focus on the identification of functional areas for effective exploitation and those with reduced functionality in order to identify problem hot-spots, with the main aim of efficient and sustainable integration into the urban fabric.

The GIS spatial analysis, based on the assessment of territorial accessibility, proposed in the present study for the identification of spatial functionality, is outlined as an open model that can be developed by including in its structure other types of industries, which are cumulatively analysed to identify all areas with reduced functionality. This helps to issue viable solutions for their remediation and contributes to sustainable functional development for administrations at local, regional and national levels.

The dynamics of urban development are determined by the availability and absorption of new knowledge, creativity, innovation and technology. In the international and national competition between cities, the social and economic environment that cities can provide, even for the establishment of a creative economy, is playing an increasingly important role. For this reason, the accessibility of the existing CCI sector within cities is of particular importance. The use of existing infrastructure is a primary factor for urban policy. Culture has become a value-generating economic resource; studies of its accessibility should be a priority in development policy.

This study used two regional centres (Cluj-Napoca and Pécs) as examples to illustrate the possible outputs of the model. It was found that the morphology, natural geography, built environment, and historical image of cities have a strong impact when considering accessibility data. For Cluj-Napoca, we found stronger CCI hubs, mainly in the recreation and R&D sectors. The case of Pécs shows a more balanced CCI sector in terms of accessibility.

Considering that the results of the model proposed in this present study are validated and that the methodology followed allows comparisons to be made for urban centres with different specificities, both in terms of the extension and territorial distribution of the infrastructures analysed, future studies conducted on the basis of this methodology will take into account the analysis of all types of industrial centres identified within the two cities. They will discuss local impact and comparison on a quantitative basis, the cumulative analysis of the impact of all the industries, and the analysis of the comparative result between the two urban centres, in order to highlight the specificities and spatial behaviours of each one.

Author Contributions: Conceptualization, B.Ş., R.H. and S.R.; methodology B.Ş., R.H. and S.R.; software R.S., D.V., V.I. and F.I.; validation P.S., B.Ş. and R.H.; formal analysis S.R., R.S. and F.I.; investigation D.V., P.S. and S.R.; resources B.Ş., R.H. and F.I.; data curation: V.I., F.I. and S.R.; writing—original draft preparation R.H., B.Ş. and R.S.; writing—review and editing B.Ş. and R.H.; visualization S.R., R.S. and V.I.; supervision B.Ş. and R.H.; project administration B.Ş. and R.H.; funding acquisition B.Ş. and R.H. All authors have contributed equally to the work. All authors have read and agreed to the published version of the manuscript.

Funding: The present work has received financial support through the 2024 Development Fund of the Babes-Bolyai University.

Data Availability Statement: Data are contained within the article.

Acknowledgments: This work is part by the project “The relationship between innovation ecosystem and creative industry in the development of regional centres” Romanian Academy—Hungarian Academy of Sciences Joint Research Project. Implementation period 2022–2025, project manager Bilaşco Ştefan and Réka Horeczki. The authors would like to thank the partner listafirme.ro for providing the databases for the current research.

Conflicts of Interest: The authors declare no conflicts of interest.

References

1. European Commission. Green Paper—Unlocking the Potential of Cultural and Creative Industries. 2010. Available online: <https://op.europa.eu/en/publication-detail/-/publication/1cb6f484-074b-4913-87b3-344ccf020eef/language-en> (accessed on 25 May 2023).
2. Dronyuk, I.; Moiseienko, I.; Gregus, J. Analysis of Creative Industries Activities in European Union Countries. *Procedia Comput. Sci.* **2019**, *160*, 479–484. [[CrossRef](#)]
3. Florida, R. *The Rise of the Creative Class: And How It's Transforming Work, Leisure, Community and Everyday Life*; Basic Books: New York, NY, USA, 2002.
4. Faragó, L. A Funkcionális városi térségekre alapozott településhálózat-fejlesztés normatív koncepciója. *Falu Vár. Rég.* **2018**, *3*, 27–31.
5. Szolkai, Z. Lépésről lépésre—A kreatív ipar támogatásának lehe-tőségei a gazdaságicentrumoktól távol eső kis- és közepes városokban. *Terül. Fejleszt. Innov.* **2011**, *5*, 2–15.
6. Zhang, X.; Fang, C.; Wang, Z.; Ma, H. Urban construction land suitability evaluation based on improved multi-criteria evaluation based on GIS (MCE-GIS): Case of New Hefei City, China. *Chin. Geogr. Sci.* **2013**, *23*, 740–753. [[CrossRef](#)]
7. Gao, S.; Janowicz, K.; Couclelis, H. Extracting urban functional regions from points of interest and human activities on location-based social networks. *Trans. GIS* **2017**, *21*, 446–467. [[CrossRef](#)]
8. Tache, A.V.; Popescu, O.C.; Manole, S.D.; Petrişor, A.I. Methodology for assessing the Romanian functional urban areas using GIS and LAU 2 territorial indicators. *Territ. Identity Dev.* **2018**, *3*, 24–37.
9. Picchio, R.; Pignatti, G.; Marchi, E.; Latterini, F.; Benanchi, M.; Foderi, C.; Venanzi, R.; Verani, S. The Application of Two Approaches Using GIS Technology Implementation in Forest Road Network Planning in an Italian Mountain Setting. *Forests* **2018**, *9*, 277. [[CrossRef](#)]
10. Bilaşco, Ş.; Roşca, S.; Păcurar, I.; Moldovan, N.; Vescan, I.; Fodorean, I.; Petrea, D. Roads accesibility to agricultural crops using gis technology. Methodological approach. *Geogr. Tech.* **2018**, *13*, 12–30. [[CrossRef](#)]
11. Ogrodnik, K.; Kolendo, Ł. Application of gis technology and AHP to determine the areas with fully developed, compact functional and spatial structure: A case study of Białystok, Poland. *Land Use Policy* **2021**, *109*, 105616. [[CrossRef](#)]
12. Turek, T.; Stępnia, C. Areas of integration of GIS technology and smart city tools. Research findings. *Procedia Comput. Sci.* **2021**, *192*, 4681–4690. [[CrossRef](#)]
13. Crupi, F. Urban Regeneration and Green and Blue Infrastructure: The Case of the “Acilia–Madonna” Urban and Metropolitan Centrality in the Municipality of Rome. *Urban Sci.* **2022**, *6*, 56. [[CrossRef](#)]
14. Poli, I.; Ravagnan, C.; Ricci, L. A Planning Framework for Urban Resilience toward Climate Adaptation and Mitigation: Potentials and Limits of “Eco-Districts”. *Urban Sci.* **2022**, *6*, 49. [[CrossRef](#)]
15. Mesquitela, J.; Elvas, L.B.; Ferreira, J.C.; Nunes, L. Data Analytics Process over Road Accidents Data—A Case Study of Lisbon City. *ISPRS Int. J. Geo Inf.* **2022**, *11*, 143. [[CrossRef](#)]
16. Blat, J.; Delgado, A.; Ruiz, M.; Segui, J.M. Designing multimedia GIS for territorial planning: The ParcBIT case. *Environ. Plan. B Plan. Des.* **1995**, *22*, 665–678. [[CrossRef](#)]
17. Deravignone, L. GIS data and Territorial Management Approach. In *Urban Coastal Area Conflicts Analysis Methodology*; Department of European, American and Intercultural Studies, Sapienza University of Rome: Rome, Italy, 2013; pp. 267–280.
18. Lytvynchuk, I.; Skydan, O.; Ivaniuk, O. Local governance and territorial development on the basis of gis. *Manag. Theory Stud. Rural. Bus. Infrastruct. Dev.* **2020**, *42*, 422–433. [[CrossRef](#)]
19. Bilous, L.; Samoilenko, V.; Shyshchenko, P.; Havrylenko, O. GIS in landscape architecture and design. *Geoinformatics* **2021**, *2021*, 1–7.
20. Guay, J.F.; Waaub, J.P. SOMERSET-P: A GIS-based/MCDA platform for strategic planning scenarios’ ranking and decision-making in conflictual socioecosystem. *EURO J. Decis. Process.* **2019**, *7*, 301–325. [[CrossRef](#)]
21. Masoudi, M.; Centeri, C.; Jakab, G.; Nel, L.; Mojahedi, M. GIS-based multi-criteria and multi-objective evaluation for sustainable land-use planning (case study: Qaleh Ganj County, Iran) “landuse planning using mce and mola”. *Int. J. Environ. Res.* **2021**, *15*, 457–474. [[CrossRef](#)]
22. Li, X.; Zhang, L.; Liang, C. A GIS-based buffer gradient analysis on spatiotemporal dynamics of urban expansion in Shanghai and its major satellite cities. *Procedia Environ. Sci.* **2010**, *2*, 1139–1156. [[CrossRef](#)]
23. Ghaffar, A.; Kalwar, S.; Memon, I.A.; Brohi, S.; Sahito, N. Evaluating accessibility of public parks through gis: A case study of tando allahyar city. *PalArch's J. Archaeol. Egypt/Egyptol.* **2021**, *18*, 758–771.
24. Al-Mamoori, S.K.; Al-Maliki, L.A.; Al-Sulttani, A.H.; El-Tawil, K.; Al-Ansari, N. Statistical analysis of the best GIS interpolation method for bearing capacity estimation in An-Najaf City, Iraq. *Environ. Earth Sci.* **2021**, *80*, 683. [[CrossRef](#)]
25. Kanakiya, R.S.; Singh, S.K.; Shah, U. GIS Application for spatial and temporal analysis of the air pollutants in urban area. *Int. J. Adv. Remote Sens. GIS* **2015**, *4*, 1120–1129.
26. Chandio, I.A.; Matori, A.N.; Lawal, D.U.; Sabri, S. GIS-based land suitability analysis using AHP for public parks planning in Larkana City. *Mod. Appl. Sci.* **2011**, *5*, 177. [[CrossRef](#)]
27. Roy, S.; Bose, A.; Majumder, S.; Roy Chowdhury, I.; Abdo, H.G.; Almohamad, H.; Abdullah Al Dughairi, A. Evaluating urban environment quality (UEQ) for Class-I Indian city: An integrated RS-GIS based exploratory spatial analysis. *Geocarto Int.* **2022**, *38*, 2153932. [[CrossRef](#)]
28. Khayyal, H.K.; Zeidan, Z.M.; Beshr, A.A. Creation and spatial analysis of 3D city modeling based on GIS data. *Civ. Eng. J.* **2022**, *8*, 105. [[CrossRef](#)]

29. Brennan-Horley, C.; Gibson, C. Where is creativity in the city? Integrating qualitative and GIS methods. *Environ. Plan. A* **2009**, *41*, 2595–2614. [[CrossRef](#)]
30. Liu, H.; Silva, E.A.; Wang, Q. Incorporating GIS data into an agent-based model to support planning policy making for the development of creative industries. *J. Geogr. Syst.* **2016**, *18*, 205–228. [[CrossRef](#)]
31. De Bernard, M.; Comunian, R.; Viganò, F.; Comunian, R.; Faggian, A.; Heinonen, J.; Wilson, N. On GIS and the creative economy: Opportunities and challenges. In *A Modern Guide to Creative Economies*; Edward Elgar Publishing: Glos, UK, 2022; p. 36.
32. Horváth, G. *Spaces and Places in Central and Eastern Europe: Historical Trends and Perspectives of Regional Development*; Routledge: London, UK; New York, NY, USA, 2015.
33. Hajdú, Z.; Horeczki, R. Pécs és Baranya megye fejlődése a történetileg változó földrajzi periférián. *Tér Társad.* **2023**, *37*, 10–31. [[CrossRef](#)]
34. Horváth, G. Régióközpontok Európában. *Magy. Tudomány* **2007**, *168*, 704–720.
35. Ianoş, I. *Oraşele și Organizarea Spațiului Geografic*; Editura Academiei: Bucharest, Romania, 1987.
36. Ianoş, I. *Dinamica Urbană (Aplicații la Oraşul și Sistemul Urban Românesc)*; Editura Tehnică: Bucharest, Romania, 2004.
37. Benedek, J. A romániai urbanizáció jellegzetességei az utolsó évszázad során. In *Kárpát-Medence: Települések, Tájak, Régiók, Tér-Struktúrák*; Hajdú, Z., Györi, R., Eds.; Dialóg Campus Kiadó: Budapest, Romania; Pécs, Hungary, 2006; pp. 77–101.
38. Rác, S. Közép- és Délkelet-Európa az ezredforduló óta. In *A Regionalizmus: Az Elmélettől a Gya-Korlatig: Illés Ivánra Emlékezve 80. Születésnapja Alkalmából*; Nemes, N.J., Pálné, K.I., Eds.; Publikon: Pécs, Hungary, 2022; pp. 59–71.
39. Dörflinger, A.; Bachinger, K.; Enichlmair, C.; Fischl, I.; Gavac, K.; Hausemer, P.; Oberholzner, T.; Spaghetti, V. Boosting the Competitiveness of Cultural and Creative Industries for Growth and Jobs: Final Report. European Commission. 2016. Available online: http://www.dekuzu.com/en/docs/Boosting_the_competitiveness_of_cultural_and_creative_industries.PDF (accessed on 20 November 2022).
40. Deloitte, 2020, Urban Future with a Purpose, 12 Trends Shaping the Future of Cities by 2030. Available online: <https://www.deloitte.com/global/en/Industries/government-public/perspectives/urban-future-with-a-purpose/15-minute-city.html> (accessed on 12 October 2023).
41. Abdelfattah, L.; Deponete, D.; Fossa, G. The 15-minute city: Interpreting the model to bring out urban resiliencies. *Transp. Res. Procedia* **2022**, *60*, 330–337. [[CrossRef](#)]
42. Allam, Z.; Nieuwenhuijsen, M.; Chabaud, D.; Moreno, C. The 15-minute city offers a new framework for sustainability, liveability, and health. *Lancet Planet. Health* **2022**, *6*, e181–e183. [[CrossRef](#)]
43. Ferrer-Ortiz, C.; Marquet, O.; Mojica, L.; Vich, G. Barcelona under the 15-minute city lens: Mapping the accessibility and proximity potential based on pedestrian travel times. *Smart Cities* **2022**, *5*, 146–161. [[CrossRef](#)]
44. Petrea, D.; Bilaşco, Ş.; Roşca, S.; Vescan, I.; Fodorean, I. The determination of the landslide occurrence probability by GIS spatial analysis of the land morphometric characteristics (case study: The Transylvanian Plateau). *Carpathian J. Earth Environ. Sci.* **2014**, *9*, 91–102.
45. Romanian Government. *Government Order No. 447 since 10 April 2003, Concerning the Approval of the Methodological Rules Related to the Drafting and Content of the Natural Hazards at Floods and Landslides Maps*; Monitorul Oficial: Bucharest, Romania, 2013. (In Romanian)
46. PĂCurar, H.; DiRja, M.; Mihai BU, T.A.; PĂCurar, I.; RoŞCa, S.; Bilaşco, Ş. Identification of Soils Factors Influence in the Distributions of Tuber aestivum in Transylvanian Subcarpathian Hill, Romania. *Not. Bot. Horti Agrobot. Cluj-Napoca* **2019**, *47*, 478–486. [[CrossRef](#)]
47. Scott, A. Capitalism and Urbanization in a New Key? The Cogniti-ve-Cultural Dimension. *Soc. Forces* **2007**, *85*, 1465–1482. [[CrossRef](#)]
48. Hesmondhalgh, D. Internationalisation, globalisation and cultural imperialism. In *The Cultural Industries*; Sage: London, UK, 2007.
49. Füzér, K. *A Projektésített Város—Részvételi Városfejlesztés az Ezred-Fordulós Pécsen*; Publikon Kiadó: Pécs, Hungary, 2017.
50. Starrico, L. 15-, 10- or 5-minute city? A focus on accessibility to services in Turin, Italy. *J. Urban Mobil.* **2022**, *2*, 100030. [[CrossRef](#)]
51. Hein, S. The ‘Five Minute City’: A New Way to Imagine a Better Vancouver. 2018. Available online: <https://theyee.ca/opinion/2018/10/17/Five-Minute-City-Better-Vancouver/> (accessed on 12 October 2023).

Disclaimer/Publisher’s Note: The statements, opinions and data contained in all publications are solely those of the individual author(s) and contributor(s) and not of MDPI and/or the editor(s). MDPI and/or the editor(s) disclaim responsibility for any injury to people or property resulting from any ideas, methods, instructions or products referred to in the content.

Research article

FT-IR and HPLC analysis of silver fir (*Abies alba* Mill.) bark compounds from different geographical provenances

Irina M. Morar ^a, Razvan Stefan ^b, Catalina Dan ^c, Radu E. Sestras ^c, Petru Truta ^a, Mădălina Medeleanu ^d, Florica Ranga ^d, Paul Sestras ^e, Alina M. Truta ^a, Adriana F. Sestras ^a

- ^a Department of Forestry, University of Agricultural Sciences and Veterinary Medicine, 400372, Cluj-Napoca, Romania
- ^b Preclinic Department, University of Agricultural Sciences and Veterinary Medicine, 400372, Cluj-Napoca, Romania
- ^c Department of Horticulture and Landscape, University of Agricultural Sciences and Veterinary Medicine, 400372, Cluj-Napoca, Romania
- ^d Department of Food Science and Technology, University of Agricultural Sciences and Veterinary Medicine, 400372, Cluj-Napoca, Romania
- ^e Faculty of Civil Engineering, Technical University of Cluj-Napoca, 400020, Cluj-Napoca, Romania
- ^f Academy of Romanian Scientists, Ilfov 3, 050044, Bucharest, Romania

Recommended articles

Evaluation of the moisture content of *Jatropha curcas* kernels and the heating...

Biosystems Engineering, Volume 130, 2015, pp. 52-59
Jetsada Posom, Panmanas Sirisomboon

Elucidation of molecular interactions in the mixtures of 2-methoxyaniline with alkyl...

Chemical Data Collections, Volume 28, 2020, Article 1...
B. Srikanth, ..., D. Ramachandran

Influence of phylogenetic relatedness on paleoclimate estimation using fossil wood...

Review of Palaeobotany and Palynology, Volume 251, ...
Hugo I. Martínez-Cabrera, Emilio Estrada-Ruiz

Show 3 more articles

Article Metrics

Citations

Citation Indexes: 1

Captures

Readers: FEEDB

HELIYON

Publisher name: CELL PRESS

Journal Impact Factor™

3.4

2023

3.9

Five Year

JCR Category	Category Rank	Category Quartile
MULTIDISCIPLINARY SCIENCES <i>in SCIE edition</i>	28/134	Q1

Source: Journal Citation Reports 2023. [Learn more](#)

Journal Citation Indicator™

0.81

2023

0.8

2022

JCI Category	Category Rank	Category Quartile
MULTIDISCIPLINARY SCIENCES <i>in SCIE edition</i>	37/135	Q2



Research article

FT-IR and HPLC analysis of silver fir (*Abies alba* Mill.) bark compounds from different geographical provenances

Irina M. Morar^a, Razvan Stefan^b, Catalina Dan^{c,**}, Radu E. Sestras^c, Petru Truta^a, Mădălina Medeleanu^d, Florica Ranga^d, Paul Sestras^{e,f,*}, Alina M. Truta^a, Adriana F. Sestras^a

^a Department of Forestry, University of Agricultural Sciences and Veterinary Medicine, 400372, Cluj-Napoca, Romania

^b Preclinic Department, University of Agricultural Sciences and Veterinary Medicine, 400372, Cluj-Napoca, Romania

^c Department of Horticulture and Landscape, University of Agricultural Sciences and Veterinary Medicine, 400372, Cluj-Napoca, Romania

^d Department of Food Science and Technology, University of Agricultural Sciences and Veterinary Medicine, 400372, Cluj-Napoca, Romania

^e Faculty of Civil Engineering, Technical University of Cluj-Napoca, 400020, Cluj-Napoca, Romania

^f Academy of Romanian Scientists, Ilfov 3, 050044, Bucharest, Romania

ARTICLE INFO

Keywords:

Abies alba

Bark

Chemical compounds

Forest

FT-IR

Trees

ABSTRACT

Fourier Transform Infrared Spectroscopy (FT-IR) and High-Performance Liquid Chromatography (HPLC) could be applied to study the provenance of wood, specifically the differentiation of wood resources, as well as the identification of chemical compounds that are connected to the changes that occur in wood as a result of drying treatments. To test this hypothesis, the bark of silver fir (*Abies alba* Mill.) from trees belonging to seven different geographical provenances was studied, using samples dried at three different temperatures (60, 80, and 100 °C). FT-IR spectroscopy revealed different band assignments in the mid-infrared region depending on fir provenances, whereas the vibrational bands of the biomass functional groups tended to shift to lower wavenumbers. Significant differences were identified between the chemical compounds in the bark depending on the provenances. The largest proportion of the total phenolics was represented by the epicatechin gallate, epicatechin, catechin, and procyanidin dimer B1. Exploratory data analysis was performed using principal component analysis (PCA), hierarchical clustering, and Pearson correlations. This allowed a comparative evaluation of the samples and interpret the findings according to the geographical provenances, respectively ecological conditions in the areas of origin, but also the influence of the drying temperatures of the samples on chemical compounds. The precipitation in the areas of origin decreased total phenolics in silver fir bark samples, and total phenolics differed not only due to the geographic provenance, but also due to drying temperature.

* Corresponding author. Faculty of Civil Engineering, Technical University of Cluj-Napoca, 400020, Cluj-Napoca, Romania.

** Corresponding author.

E-mail addresses: irina.todea@usamvcluj.ro (I.M. Morar), rstefan@usamvcluj.ro (R. Stefan), catalina.dan@usamvcluj.ro (C. Dan), rsestras@usamvcluj.ro (R.E. Sestras), petru.truta@usamvcluj.ro (P. Truta), madalinamedeleanu97@gmail.com (M. Medeleanu), floricuta.ranga@usamvcluj.ro (F. Ranga), paul.sestras@mtc.utcluj.ro (P. Sestras), alina.truta@usamvcluj.ro (A.M. Truta), adriana.sestras@usamvcluj.ro (A.F. Sestras).

<https://doi.org/10.1016/j.heliyon.2024.e26820>

Received 2 August 2023; Received in revised form 24 January 2024; Accepted 20 February 2024

Available online 27 February 2024

2405-8440/© 2024 The Authors. Published by Elsevier Ltd. This is an open access article under the CC BY license (<http://creativecommons.org/licenses/by/4.0/>).

1. Introduction

The life and biodiversity of the planet depend critically on forests, which also give people the necessary environmental, social, and economic circumstances for a proper life. Along with their numerous ecosystem functions and services [1–4], forests also supply raw materials and wood for a variety of industries [1,5,6]. Wood is a complex lignocellulosic material composed of cellulose, hemicellulose, lignin, and various extractives. It is accepted that the wood of gymnosperms is of soft essence, and that of angiosperms is of hard essence, and they represent the main types of timber [7,8]. Wood is one of the most popular building materials, as well as being used for furniture and numerous other purposes [9–12].

In the wood business, bark and branches are commonly considered waste; however, this could be a missed opportunity, because such materials can be valuable and are partially underutilized reserves [10]. The bark contains components similar to those present in wood, such as cellulose, hemicellulose, pectin, lignin and various extractive substances [13]. The bark and needles are used to extract the resin that is used for the production of turpentine, drugs, and cosmetics [14].

Information regarding variations in the proportions of the major organic components of wood can be obtained using the Fourier Transform Infrared Spectroscopy (FT-IR) method. It is a method that is frequently used to characterize wood and provides information on functional groups and molecular bonds [7,15], which is valuable for identifying wood components and determining the quality of wood [16–19]. Furthermore, because extracts from the bark of diverse conifer species contain multiple types of polyphenols and have a diversity of actions, including pharmacological ones, reversed-phase High-Performance Liquid Chromatography (HPLC) has been commonly utilized to analyze the extracts of interest [20–22].

Analysis based on FT-IR spectroscopy in conjunction with multivariate statistical approaches provides numerous opportunities for study and data exploration; for example, FT-IR and principal component analysis (PCA) were effective in distinguishing between different wood species [23–25], to describe soil organic matter and microbial communities in forest sites [26], to identify the origin of lignin [27] and to detect pathogens, like *Fusarium* fungi [28]. FT-IR was developed as a tool for the simultaneous and quantitative determination of organic components (e.g., proteins, carbohydrates and lipids), including chemical bonds, being used in multiple fields [29]. PCA analysis has been also used to distinguish very subtle spectral changes in cell walls [30,31]. Gierlinger et al. [25] were able to differentiate between European larch (*Larix decidua*), Japanese larch (*L. kaempferi*) and hybrid larch (*L. eurolepis*) by means of FT-IR in combination with PCA, cluster analysis and independent class analogy modelling. Schimleck et al. [32] discriminated wood from different *Eucalyptus* species, from distant provenances, as well as from the same species grown in different locations, by analyzing NIR spectra by PCA.

Valid, rapid and simple methods of wood identification and certification are needed in forestry for several reasons, such as accurate recognition of the wood source, evaluation of different factors affecting the quality of wood, according to its destination, or even to prevent illegal logging and trade, by identifying and correlating specific components with the ecological conditions from where the trees were developing. Furthermore, forest microclimates influence biodiversity and ecosystem processes in forest landscapes [33–35], most likely also at the level of wood quality and critical wood components. Therefore, the main purpose of the current study was to validate a tool for evaluation of different provenances of Romanian silver fir (*Abies alba*), based on FT-IR and HPLC analyses of the silver fir bark, in order to identify genotypes with a high content of useful components, in regard with the quantity and quality of any lignocellulose or resin constituent and their use within industrial or medicinal purposes. The potential of FT-IR spectroscopy in combination with different multivariate statistical methods is lately used in forestry in order to distinguish wood of the same species, but harvested from different sources. Therefore, in the present study, silver fir bark samples collected from trees grown in seven different areas in Romania, were analyzed through FT-IR and cluster analysis, to identify their biochemical composition. Even more, it was aimed to have a more complete and comprehending image of the data regarding the silver fir bark, so that HPLC was pursued to gain more detailed results, thus to perform a more qualitative and quantitative analysis of the polyphenolic profile of bark extracts.

2. Materials and methods

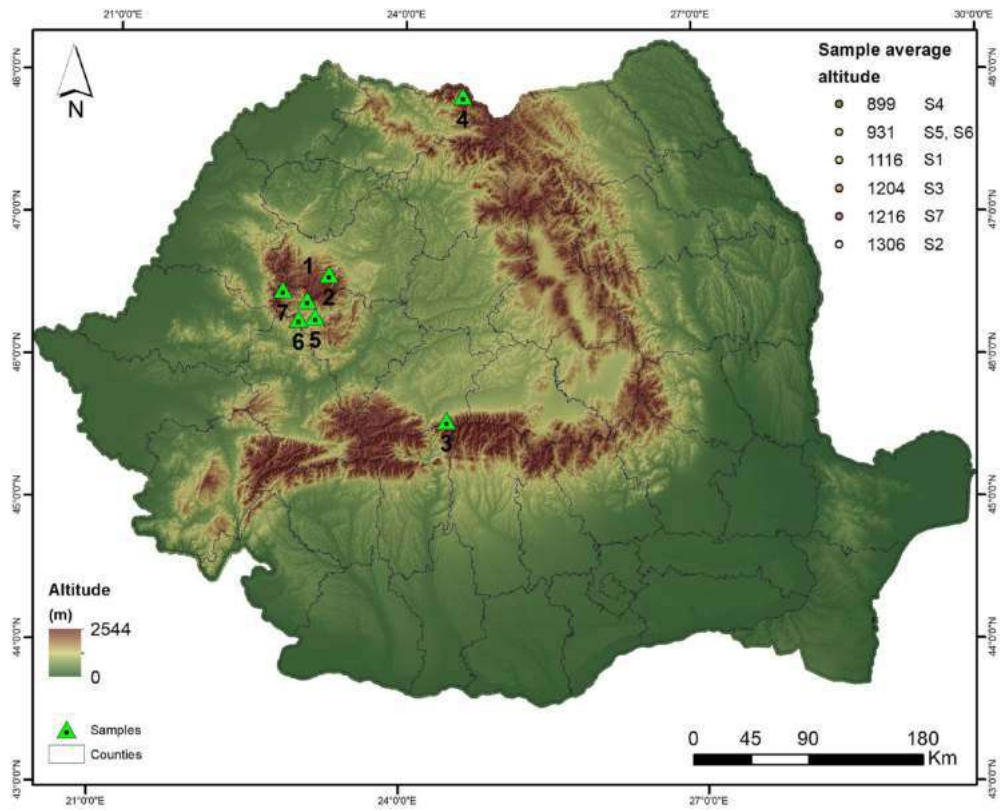
2.1. Field sites and sampling

A. alba samples were collected from mature trees (between 60 and 80 years), chosen randomly to represent seven populations registered as seed source stands in Romania, located in different areas (Table 1).

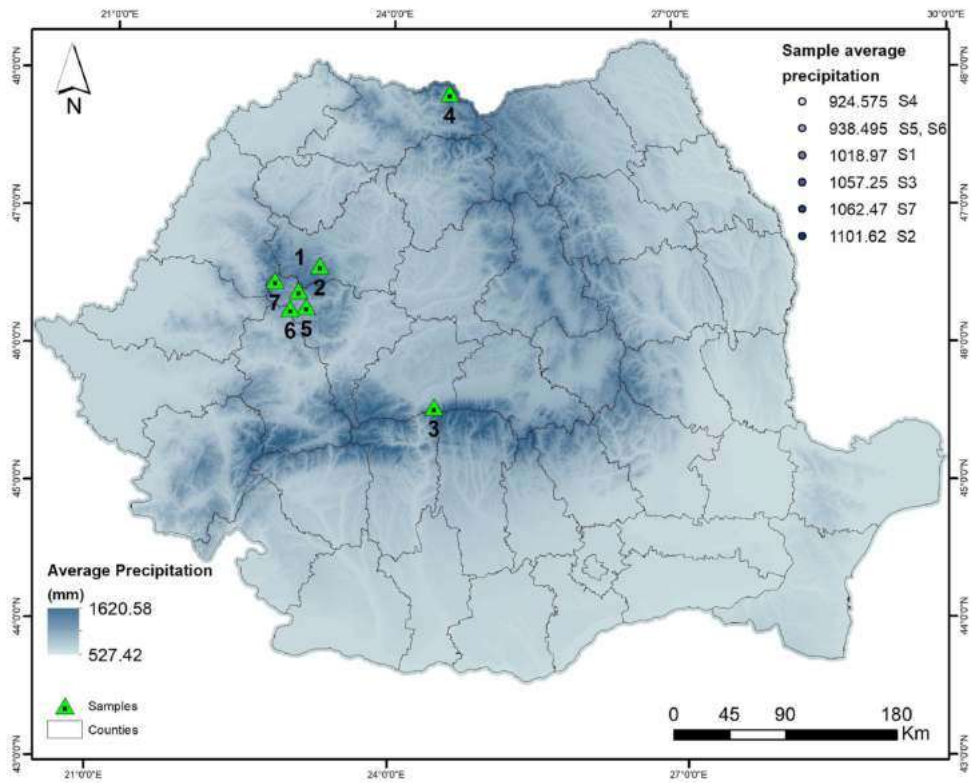
The geographical origins of these provenances (P) were as follows: P1 – Valea Bistrei, P2 – Someșul Rece, P3 – Avrig, P4 – Budescu, P5 – Sohodol, P6 – Valea Morii, P7 – Gârda Seacă (Fig. 1A,B,C). Within all provenances, ten individual trees with similar growth

Table 1
Administrative details of the studied *A. alba* provenances (populations) in regard with their provenance from Romania.

No.	Population	County	Administrative location	Latitude/Longitude
1	Valea Bistrei	Alba	O.S.P. Abrud, UP III, u.a. 228B	46°27' N/23°01' E
2	Someșul Rece	Cluj	O.S. Someșul Rece, UP I, u.a. 92A	46°38' N/23°14' E
3	Avrig	Sibiu	O.S. Izvorul Florii, UP III, u.a. 75A	45°37' N/24°27' E
4	Budescu	Maramureș	O.S. Poieni, UP IV, u.a. 96A	47°54' N/24°36' E
5	Sohodol	Alba	O.S.P. Abrud, UP IV, u.a. 18C	46°20' N/23°06' E
6	Valea Morii	Alba	O.S.P. Abrud, UP, u.a. 39	46°19' N/22°56' E
7	Gârda Seacă	Alba	O.S. Gârda, UP VI, u.a. 20H	46°31' N/22°46' E



A



B

Fig. 1. Location in Romania and the main parameters for investigated *A. alba* populations from which the bark samples were analyzed: Altitude, as m. a.s.l. (metres above sea level) (A); Amount of annual precipitation, as multiannual average, in mm (B); Average annual temperature, in °C (C). Data for mean annual temperature and mean annual precipitation are average values for a ten-year period (2012–2022) from meteorological stations.

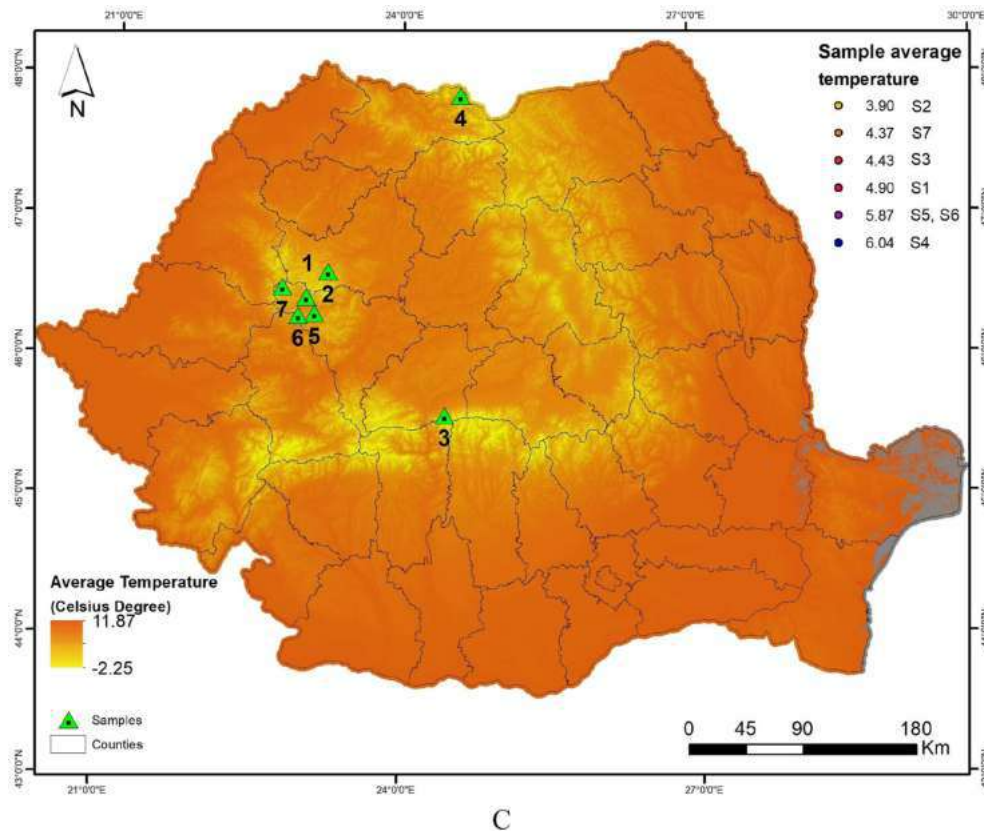


Fig. 1. (continued).

characteristics (habitus and similar dimensions, a straight trunk, without defects, etc.) were randomly chosen for sampling. Stem bark samples were taken only from healthy trees, with no apparent damage. The samples have been taken at a trunk height of approximately 1.3 m above the ground, near the so-called 'diameter at breast height', or DBH), stored in paper tubes, and transported to the spectroscopy laboratory at the University of Agricultural Sciences and Veterinary Medicine of Cluj-Napoca. For FT-IR spectra were used ground bark, belonging to the repeated sampling of the same lot.

2.2. Analyses of silver fir bark by FT-IR

Circular incisions were made on the trunk of selected trees for each population, assuring that the proper bark for the investigation has at least 1 cm thickness. Before the FT-IR analysis, the stem bark samples were dried in the oven at different temperatures (60 °C, 80 °C and 100 °C) for a period of 2 h. The temperatures and the equal interval were established around those used in other similar studies [21,36,37]. In order to generate a composite sample for each provenance, bark samples have been chopped down into small pieces and then ground together in an equal contribution; Grinder Retsch Grindomix GM 200 was used at this stage, with mesh size <300 µm. After that, samples were made by combining 3 mg of the material with two hundred grams of calcined KBr [38]. In order to create a very fine powder, the sample and the KBr were both ground up together once again, until the mixture became completely homogenous. After placing the mixture in a steel spectral pellet kit, verification of the pellet was accomplished using a Specac hydraulic press.

In order to conduct the necessary measurements, each pellet was promptly inserted into a cassette of a Fourier Transform Infrared Spectrometer model Jasco FT/IR 4100. The resolution was 4.0 cm⁻¹, and the scanning range was between 4000 and 350 cm⁻¹. Each spectrum was an average calculated from 256 scans that were carried out on a single sample pellet for each provenance. Spectra Manager was used to make five corrections for CO₂ and five corrections for H₂O for each spectrum. In order to perform a comprehensive study, peak reading was carried out using Origin by OriginLab [39].

2.3. Preparation of extracts

For the extraction of the phenolic compounds, 1 g of ground sample was weighted and extracted with 10 mL methanol, by vortex, for 1 min (Heidolph Reax Top Vortex). After this stage, the extract was placed in an ultrasonication bath for 1 h (Elmasonic E15H). During the final extraction step, the sample was centrifugated at 10,000 RPM, at room temperature, for 10 min (Eppendorf AG 5804). The collected supernatants were filtered through a micro-filter (Chromafil Xtra nylon 0.45 μm) and 20 μL were injected into the HPLC system.

2.3.1. Phytochemical profiling – analysis of bark phenolic extracts by HPLC-DAD-ESI+

Regarding the chromatographic conditions, the separation and identification of the compounds were done by an HPLC system (HPLC Agilent 1200) equipped with a quaternary pump, solvent degasser, autosampler, a UV-VIS detector with a photodiode (DAD) and coupled with a single quadrupole mass spectrometer (Agilent Technologies 6110, CA, USA). The separation was performed on a Kinetex XB C18 column, 4.6 \times 150 mm, 5 μm particle size (Phenomenex, USA), using water (A) and acetonitrile (B) as mobile phases, both containing 0.1% acetic acid (v/v), with a flow rate of 0.5 ml/min. The UV spectra were recorded in the 200–600 nm range for all the peaks, while the chromatograms were registered at the wavelength of 280 nm. The MS detector was used in ESI full positive ionization scanning mode: capillary voltage 3000 V, 350 $^{\circ}\text{C}$, nitrogen flow 7 l/min and m/z 120–1200.

The data acquisition and interpretation of the results were performed using Agilent ChemStation software. Phenolic compounds have been identified by comparing retention time, UV-VIS and mass spectra with standard compounds and data from literature.

2.3.2. Reagents and standards

Hydroxybenzoic acids were quantified as gallic acid equivalents and flavanols as catechin equivalents, so that we used the two phenolic compounds (gallic acid and catechin) as representatives of the polyphenols subclasses. Ultrapure water was purified using a direct-Q UV system from Millipore (USA), and HPLC-purity acetonitrile was acquired from Merck (Germany). Purity levels of >98% HPLC were achieved by using Sigma-Aldrich (USA) gallic acid and catechin.

Calibration curves were performed for the quantification of phenolic compounds by injecting different concentrations of standard substances dissolved in methanol, in the concentration range of 10–100 $\mu\text{g/ml}$ for gallic acid and 10–200 $\mu\text{g/ml}$ for catechin: for calibration curve of gallic acid, we used five concentrations: 100 $\mu\text{g/ml}$, 50 $\mu\text{g/ml}$, 25 $\mu\text{g/ml}$, 12.5 $\mu\text{g/ml}$, 10 $\mu\text{g/ml}$; for calibration curve of catechin the concentrations used were: 200 $\mu\text{g/ml}$, 100 $\mu\text{g/ml}$, 50 $\mu\text{g/ml}$, 25 $\mu\text{g/ml}$ and 10 $\mu\text{g/ml}$ respectively. The calibration curve of gallic acid has the equation $y = 33.624x + 30.68$ ($R^2 = 0.9978$), LOD = 0.35 $\mu\text{g/ml}$, LOQ = 1.05 $\mu\text{g/ml}$; the calibration curve of catechin has the equation $y = 15.224x - 130.24$ ($R^2 = 0.9985$), LOD = 0.18 $\mu\text{g/ml}$, LOQ = 0.72 $\mu\text{g/ml}$.

Table 2

Summary of peak positions for FT-IR spectra within 4000–350 cm^{-1} region of *A. alba* bark subjected to three different drying temperatures.

Peak no.	Wave number (cm^{-1})	Band origin	References
1	820–858	C–H out of plane in position 2, 5, and 6 of guaiacyl units	Faix, 1992 [42]; Boeriu et al., 2004 [43]
2	894	C–H deformation in cellulose	Pandey and Pitman, 2003 [44]
3	1029–1059	Aromatic C–H in plane deformation, guaiacyl type and C–O deformation, primary alcohol in cellulose	Hergert, 1971 [45]; Faix, 1991 [46]; Rana et al., 2008 [47]
4	1062–1076	C–O stretching of secondary alcohols	Faix, 1991 [46]
5	1103–1105	C–O–C stretching in cellulose and hemicellulose	McCann et al., 1992 [30]; Zhang et al., 2010 [48]
6	1146–1147	C–O–C asymmetric stretching in cellulose and hemicellulose	Faix and Bottcher, 1992 [42]; Popescu et al., 2007 [49]; Traoré et al., 2018 [7]
7	1206–1233	Syringyl (phenol) (S) nuclei deformation combined with deformation of cellulose	Evans et al., 1991 [50]
8	1267–1272	C–O vibration in guaiacyl rings	Popescu et al., 2007 [49]; Chen et al., 2010 [51]; Traoré et al., 2018 [7]
9	1315–1317	CH ₂ wagging in crystalline cellulose	Colom and Carrillo, 2005 [52]; Popescu et al., 2007 [49]; Traoré et al., 2018 [7]
10	1339–1374	C–H deformation in cellulose and hemicellulose	Pandey and Pitman, 2003 [44]; Evans et al., 1992 [53]; Mohebbi, 2008 [54]
11	1451–1453	C–H deformation; asymmetric in –CH ₃ and –CH ₂ – for lignins and hemicellulose	Hergert, 1971 [45]; Faix, 1991 [46]; Popescu et al., 2007 [49]; Chen et al., 2010 [51]; Traoré et al., 2018 [7]
12	1515	C=C stretching of the aromatic ring, C=O bond vibrations in extractive compounds	Popescu et al., 2007 [49]; Zhou et al., 2015 [18]; Traoré et al., 2018 [7]
13	1616–1618	C=O stretching conjugated to the aromatic ring, and in carboxylic groups in lignin, carboxylic acid, ester compounds	Zhao et al., 2014 [55]; Traoré et al., 2018 [7]
14	1620	Absorbed O–H and conjugated C–O in polysaccharides	Genest et al., 2013 [56]; Karunakaran et al., 2015 [57]; Traoré et al., 2018 [7]
15	1742–1746	C=O in ester groups, acetyl group in xylan, in unconjugated ketones, carbonyls and in ester groups (frequently of carbohydrate origin)	Bodirlau and Teaca, 2009 [17]; Zhou et al., 2015 [18]; Faix, 1991 [46]; Pandey and Pitman, 2003 [44]
16	2851–2860	CH ₂ stretching of cellulose and hemicelluloses	Longo et al., 2020 [58]
17	2923–2925	CH stretching of cellulose and hemicelluloses	Longo et al., 2020 [58]
18	3399–3426	H-bonded valence vibration, O–H valence vibration of C ₍₆₎ H ₂ O ₍₆₎ –H primary alcohol (main conformation)	Fackler et al., 2010 [59]

2.4. Data analyses

The final data were processed as mean total phenolic values. Analysis of variance (ANOVA) was utilized as a statistical test for a multifactorial experience to find possible differences between the means of the provenances and drying temperatures. Before applying the ANOVA test, the data were tested for normality. If the null hypothesis was rejected, ANOVA was completed using Duncan's test ($\alpha < 0.05$) to separate and highlight the differences between means. Principal component analysis (PCA) and hierarchical clustering analyses utilizing the single linkage technique were performed using PAST software (PALEontological STATistics (PAST) Version 4.09, Natural History Museum, University of Oslo, Norway) [40]. The Pearson correlations between each phenolic compound, respectively total phenolics in the bark, and the main ecological conditions (i.e., temperature, precipitation, amplitude) were computed for the set of geographical provenances, and the graphical representations were made with the NCSS 2023 Statistical Software (NCSS, LLC, Kaysville, Utah) [41]. The P-values below 0.05 were considered statistically significant.

3. Results

3.1. The main FT-IR bands of the silver fir bark and their assignments

The FT-IR bands for the silver fir bark exposed to three different drying temperatures (respectively 60 °C, 80 °C and 100 °C), are presented in Table 2.

One can assign the characteristic functional groups to a class of compounds. Thereafter, it can be recorded that bands in the range of 3399–3426 cm^{-1} correspond to compounds containing functional hydroxyl groups (-OH), including phenolic compounds (e.g., from lignin) such as gallic acids, protocatechuic acid, *p*-coumaric acid or aliphatic structures or hydroxyl group for alpha-cellulose.

Bands no. 13–15 match aldehyde groups (e.g., carbonyl C=O double bond stretching vibration in hemicelluloses (1850–1600 cm^{-1}); the C=O stretching vibration of unconjugated carbonyl group in hemicelluloses (xyloglucan) was identified at 1742–1746 cm^{-1} (connected with the thermal treatment applied). The band no. 12, assigned to C=C vibration can be connected to aromatic ring vibrations of lignin. Further, C–O–C corresponds to vibrations of guaiacyl units, which are clearly evidenced within bark due to the high lignin content. The C–H in-plane bending vibration is represented by the interval 1500–900 cm^{-1} . In lignin, cellulose, and hemicelluloses, C–O and C–C link to skeletal vibrations. Bands 5 and 6 correspond to cellulose and hemicellulose compounds with C–O–C stretching. Compounds with C–O stretching of secondary alcohols have bands in the 1062–1076 cm^{-1} range.

The principal alcohol C–O stretching vibration in cellulose was measured to be between 1029 and 1059 cm^{-1} , depending on the heat treatment. The second peak at 894 cm^{-1} demonstrates aromatic C–H in-plane stretching, guaiacyl type, and C–O deformation. Guaiacyl-syringyl lignin (GS-lignin) found in hardwoods is a copolymer of coniferyl and sinapyl alcohols and was noted with different continents, starting from the C–H group present around 820–858 cm^{-1} .

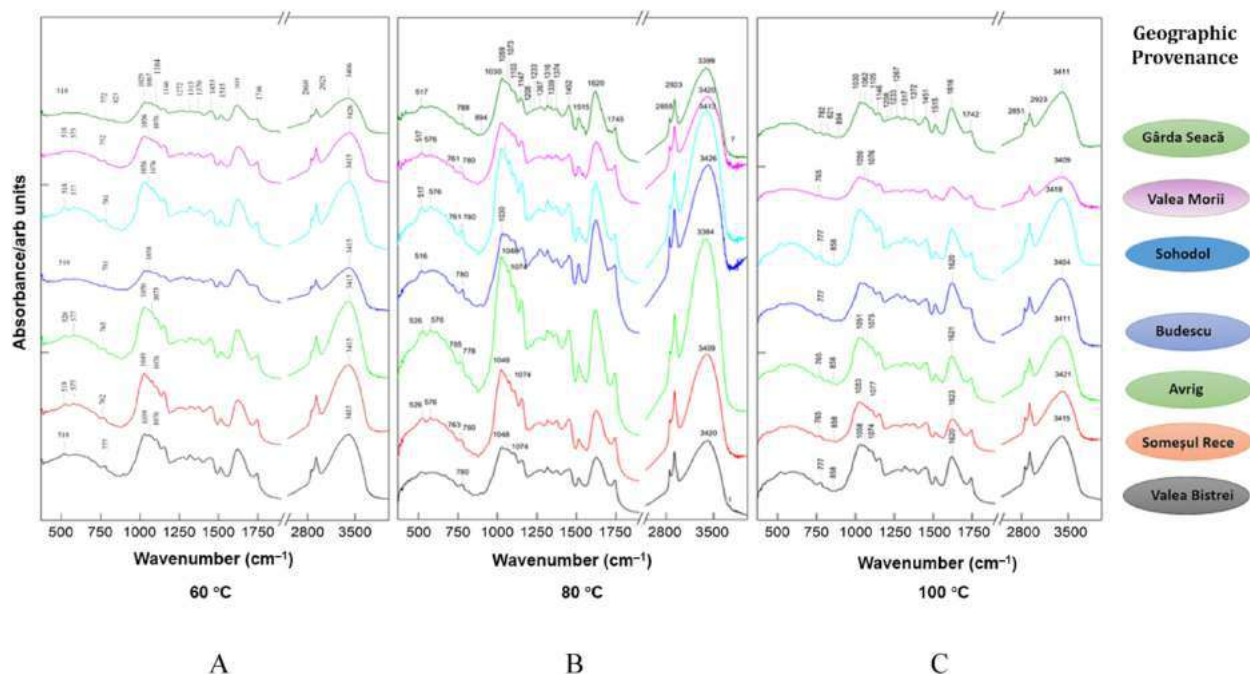


Fig. 2. FT-IR band assignments in the mid-infrared region, after treating silver fir (*A. alba*) bark powder depending on the samples (seven geographical provenances) and the drying temperature: 60 °C (A); 80 °C (B); and 100 °C (C).

3.2. Assignment of FT-IR bands according to bark drying temperature

The results obtained using the FT-IR technique and three drying temperatures (60 °C, 80 °C and 100 °C) demonstrate variations in the chemical composition of the bark within the silver fir provenances (Fig. 2).

Silver fir bark showed 18 prominent peaks in the fingerprint region of the wavenumbers from 3500 to 800 cm^{-1} (Table 2), which represent major cell wall components (i.e., cellulose, hemicelluloses and lignin) [47]. The populations investigated registered comparable peaks, but some migration of bands was noted, depending on the provenance and the drying temperature (Fig. 2A,B,C). The migration of the CH_2 stretching compound of cellulose and hemicelluloses from the wavenumber range of 2860–2851 cm^{-1} , as well as the migration of the C=O stretch in unconjugated ketones, carbonyls, and ester groups, often originating from carbohydrates, from the wavenumber range of 1746–1742 cm^{-1} , was observed in the provenance designated as Gârda Seacă.

FT-IR spectroscopy, which is often used to delineate the presence of the cellulose, hemicelluloses and lignin of different lingo-cellulosic materials [49], revealed different band assignments in the mid-infrared region depending on wood provenances. Strong absorption bands were observed in forest residues from fir bark attributed to O–H and C–H stretching vibrations (3500–3000 cm^{-1} and 3000–2650 cm^{-1}), carbonyl C=O double bond vibration hemicelluloses (1850–1600 cm^{-1}), C=C from aromatic skeletal vibrations, C–H plane bending vibrations and C–O and C–C skeletal vibrations (1500–900 cm^{-1}) within lignin, cellulose and hemicellulose components. It can be noticed that the vibrational bands of the biomass functional groups had a tendency to shift (to lower wavenumbers), similar to other results [12,60]. Changes observed in the FT-IR spectrum for fir bark dried at 100 °C might be due to some different changes in the biomass compared to the samples treated at 60 and 80 °C, respectively changes attributed to unidentified compounds in this study. These bands became less sharp and wider with the increase in treatment temperature. The main bands associated with lignin components were detected between 1620 and 1616 cm^{-1} [7,55], while the cellulose and hemicelluloses were characterized by the bands between 2925 and 2923 cm^{-1} [58]. Group stretching O–H, as well as O–H in lignin, decrease significantly from 60 °C to 100 °C; for example, after the bark was exposed to 60 °C, the peak was found at 3426 cm^{-1} for Valea Morii provenance and migrated to 3409 cm^{-1} after 100 °C; similarly, for Budescu provenance, the band migrated from 3415 cm^{-1} to 3404 cm^{-1} . For nearly all components, among the drying temperature tested for silver fir bark, the bands' position migrated to lower wavenumbers from 60 °C to 100 °C. Such is the case of aromatic C–O vibration in guaiacyl rings, which for the seventh provenance was located at 1272 at 60 °C treatment and shifted to 1267 at 80 °C and 100 °C.

Several studies present well-defined peaks which provide information on various functional groups present in fir wood constituents and their variation depending on the source (needles, bark) that can be identified [12,61]. Differences could also be noticed among samples, according to the wood provenances. This could be explained by the degradation of the lignin, which has become significant at high temperatures.

Peaks in the interval 3399–3426 cm^{-1} indicate an increase of free or only weakly H-bonded O–H groups of cellulose. These evolving O–H bands may suggest the depolymerisation of the polysaccharides and the relative resistance of cellulose crystallites.

3.3. Identification of phenolic compounds in silver fir bark samples by HPLC

Based on their MS fragmentation patterns, high-resolution mass, UV spectra, and retention times, 11 phenolic compounds in total were found in the 21 samples of powder silver fir bark. Representative chromatograms for two selective provenances, respectively P1 – Valea Bistrei and P5 – Sohodol, using the three drying temperatures: T1 = 60 °C; T2 = 80 °C; T3 = 100 °C are illustrated in Figs. 3 and 4). These two provenances have approximately average values for the total phenolics among the populations analyzed, and thus can be considered convenient representations for all chromatograms obtained in the study. Flavonols were responsible for the greatest peaks

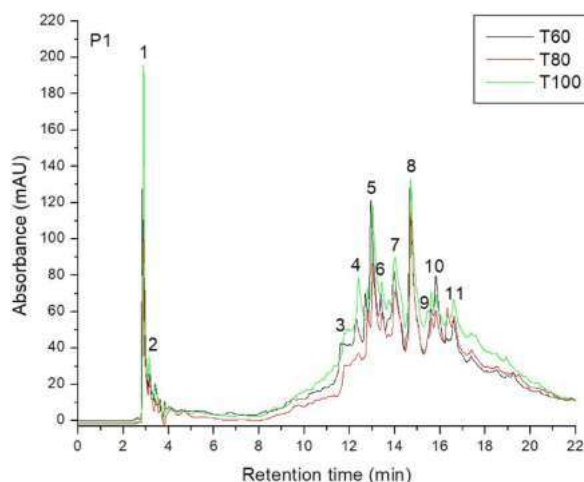


Fig. 3. HPLC chromatogram for *A. alba* from P1 – Valea Bistrei provenance, for the three drying temperatures: T1 = 60 °C; T2 = 80 °C; T3 = 100 °C.

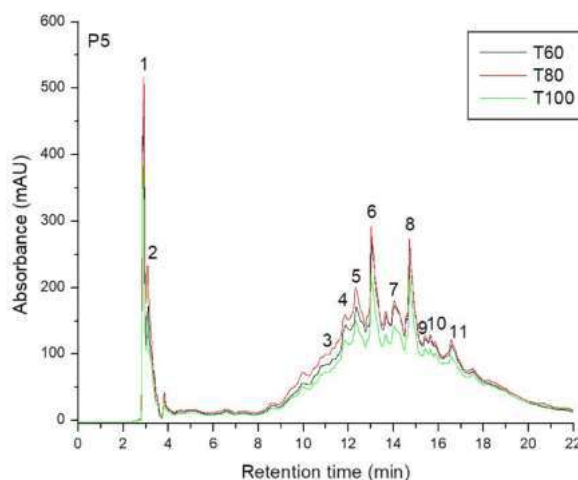


Fig. 4. HPLC chromatogram for *A. alba* originated from P5 – Sohodol provenance, for the three temperatures: T1 = 60 °C; T2 = 80 °C; T3 = 100 °C.

in the HPLC traces of silver fir wood extracts, while the lower peaks were represented by hydroxybenzoic acids.

Peak number identities from all the analyzed provenances are displayed in Table 3, along with quantifications of phenolic compounds (mg/g) depending on the three drying temperature (T1 = 60 °C; T2 = 80 °C; T3 = 100 °C), in silver fir samples from seven geographic provenances, are presented in Tables 4–6.

The obtained chromatograms (21 in total, three temperatures for all seven provenances) look almost similar, whereas the amount of phenolic compounds differs depending on the area. It can be noted that the population with the highest content of phenolic compounds was represented by P3 – Avrig (35.825 mg/g at 60 °C (Table 4), 36.075 mg/g at 80 °C (Table 5), 31.899 mg/g at 100 °C (Table 6), while the one with the lowest content was P4 – Budescu (1.985 mg/g at 60 °C (Table 4), 2.120 mg/g at 80 °C (Table 5), 1.237 mg/g at 100 °C (Table 6). Also, the influence of temperature was marked and can be concluded that 80 °C seems to be the optimal temperature for polyphenol content analysis.

The most abundant compounds in the stem bark samples of silver pin were epicatechingallate, epicatechin, procyanidin dimer B1 and catechin, but their concentration was different depending on the drying temperature applied. Epicatechin and catechin are the first derivative products of flavan-3-ols, while galocatechin forms polymeric tannins.

The results presented in Fig. 5A highlight the significant differences between the content of the fir bark in total phenolics depending on the interaction between provenances and treatments. Drying temperature did not influence the variation of phenolics in the bark in only two provenances, P4 – Budescu and P6 – Valea Morii, which also had the lowest amount of total phenolics (Fig. 5B). Among the provenances, it stood out with a high content of total phenolics P3 – Avrig, followed by P7 – Gârda Seacă and P5 – Sohodol. Unlike the influence of the geographical origin of the samples, drying temperature had significant effects on the phenolics content (Fig. 5C). It had higher values at the treatment with 80 °C and lower at 100 °C, while the treatment with the lowest temperature provided intermediate values.

3.4. Multivariate analysis for *A. alba* provenances related to FT-IR and HPLC bark investigation

Principal component analysis (PCA) was used to explore the three drying temperatures (T1 = 60 °C, T2 = 80 °C, and T3 = 100 °C) for *A. alba* bark, and the findings are displayed in Fig. A1 (A, B, and C). In the PCA dataset for the lowest drying temperature, T1 =

Table 3
Peak number identities and phenolic compounds identified in silver fir samples.

Peak No.	R _t (min)	UV λ _{max} (nm)	[M+H] ⁺ (m/z)	Phenolic compound	Subclass
1	2.91	270	155	2,3-Dihydroxybenzoic acid	Hydroxybenzoic acid
2	3.16	270	139	2-Hydroxybenzoic acid	Hydroxybenzoic acid
3	11.59	280	307	Galocatechin	Flavanol
4	11.96	280	579	Procyanidin dimer B3	Flavanol
5	12.42	280	291	Catechin	Flavanol
6	13.01	280	579	Procyanidin dimer B1	Flavanol
7	14.11	280	291	Epicatechin	Flavanol
8	14.78	280	443	Epicatechingallate	Flavanol
9	15.69	280	453	Catechin-glucose	Flavanol
10	15.89	290	153	Vanilin	Hydroxybenzoic acid
11	16.62	360, 260	303	Ellagic acid	Hydroxybenzoic acid

Table 4

Quantification of phenolic compounds (mg/g), at T = 60 °C (T1 – drying temperature), in silver fir samples from seven geographic provenances.

Peak No.	R _t (min)	Phenolic compound	Provenances						
			P1	P2	P3	P4	P5	P6	P7
			Valea Bistrei	Someșul Rece	Avrig	Budescu	Sohodol	Valea Morii	Gârda Seacă
1	2.91	2,3-Dihydroxybenzoic acid	0.182	1.105	1.343	0.067	1.055	0.160	1.051
2	3.16	2-Hydroxybenzoic acid	0.049	0.307	1.175	0.117	0.757	0.215	0.456
3	11.59	Gallocatechin	0.375	1.367	1.449	0.106	0.937	0.252	1.426
4	11.96	Procyanidin dimer B3	0.290	0.979	5.382	0.166	2.999	0.348	2.585
5	12.42	Catechin	0.796	2.354	5.641	0.201	3.862	0.566	4.414
6	13.01	Procyanidin dimer B1	0.772	2.149	5.388	0.217	4.577	0.602	3.664
7	14.11	Epicatechin	1.412	2.968	6.498	0.196	3.426	0.680	3.970
8	14.78	Epicatechingallate	1.441	3.356	5.252	0.239	4.250	0.811	3.568
9	15.69	Catechin-glucose	0.693	0.681	1.592	0.197	1.071	0.347	1.376
10	15.89	Vanillin	0.335	0.196	1.021	0.055	0.656	0.148	0.915
11	16.62	Ellagic acid	0.367	0.492	1.084	0.424	1.480	0.272	2.323
		Total Phenolics	6.713	15.954	35.825	1.985	25.070	4.400	25.747

Table 5

Quantification of phenolic compounds (mg/g), at T = 80 °C (T2 – drying temperature), in silver fir samples from seven geographic provenances.

Peak No.	R _t (min)	Phenolic compound	Provenances						
			P1	P2	P3	P4	P5	P6	P7
			Valea Bistrei	Someșul Rece	Avrig	Budescu	Sohodol	Valea Morii	Gârda Seacă
1	2.91	2,3-Dihydroxybenzoic acid	0.209	1.226	1.393	0.077	1.227	0.075	1.138
2	3.16	2-Hydroxybenzoic acid	0.050	0.594	1.167	0.089	1.060	0.123	0.946
3	11.59	Gallocatechin	0.334	1.666	1.667	0.096	1.022	0.109	2.379
4	11.96	Procyanidin dimer B3	0.281	2.114	5.365	0.135	3.541	0.202	3.306
5	12.42	Catechin	0.737	2.326	5.764	0.150	4.736	0.622	5.888
6	13.01	Procyanidin dimer B1	1.084	3.055	5.614	0.176	5.059	0.709	4.320
7	14.11	Epicatechin	1.399	4.449	5.432	0.123	3.728	0.543	5.451
8	14.78	Epicatechingallate	1.835	4.911	5.758	0.156	4.551	1.269	3.949
9	15.69	Catechin-glucose	0.470	0.771	1.799	0.168	1.140	0.156	2.150
10	15.89	Vanillin	0.342	1.000	0.986	0.025	0.766	0.168	1.324
11	16.62	Ellagic acid	0.434	1.116	1.130	0.925	1.736	0.322	2.630
		Total Phenolics	7.176	23.228	36.075	2.120	28.567	4.300	33.479

Table 6

Quantification of phenolic compounds (mg/g), at T = 100 °C (T3 – drying temperature), in silver fir samples from seven geographic provenances.

Peak No.	R _t (min)	Phenolic compound	Provenances						
			P1	P2	P3	P4	P5	P6	P7
			Valea Bistrei	Someșul Rece	Avrig	Budescu	Sohodol	Valea Morii	Gârda Seacă
1	2.91	2,3-Dihydroxybenzoic acid	0.191	0.648	0.750	0.096	0.844	0.266	0.694
2	3.16	2-Hydroxybenzoic acid	0.041	0.288	1.098	0.121	0.694	0.205	0.840
3	11.59	Gallocatechin	0.302	1.102	1.866	0.086	0.819	0.509	2.314
4	11.96	Procyanidin dimer B3	0.269	0.828	1.949	0.086	1.280	0.678	2.898
5	12.42	Catechin	0.656	1.933	4.876	0.086	3.275	0.218	5.595
6	13.01	Procyanidin dimer B1	0.722	1.764	5.593	0.086	3.512	0.200	4.290
7	14.11	Epicatechin	1.286	2.572	5.669	0.093	2.666	0.212	5.130
8	14.78	Epicatechingallate	1.738	3.125	6.366	0.086	3.328	0.772	4.054
9	15.69	Catechin-glucose	0.449	0.595	2.120	0.086	0.805	0.405	2.340
10	15.89	Vanillin	0.317	0.500	1.232	0.000	0.418	0.201	1.317
11	16.62	Ellagic acid	0.473	0.789	0.380	0.412	0.926	0.456	2.689
		Total Phenolics	6.445	14.144	31.899	1.237	18.566	4.122	32.159

60 °C, component 1 explains 92.3%, while component 2 has 3.7% of the variation, so cumulatively, the two main components contribute 96.0% of the total variation. At T2 = 80 °C, component 1 accounts for 89.4% and component 2 has 5.4% of the total variation, whereas at T3 = 100 °C, component 1 explains 91.5% and component 2 accounted 5.3% of the total variation. Someșul Rece and Avrig appear as the most distant provenances. All the geographical origins are arranged in the quadrants on the right, quadrant I (upper right), and quadrant II (lower right), both at T1, and at the following two drying temperatures (T2 and T3). In all PCAs, the closest provenances were Valea Morii and Budescu. At T1 and T2, in opposite quadrants and at large distances, epicatechingallate and 2-hydroxybenzoic acid are located, and at T3 epicatechingallate and ellagic acid. At T3, on the other diagonal, catechin is found opposite and distant from 2,3-dihydroxybenzoic acid, 2-hydroxybenzoic acid, and vanillin.

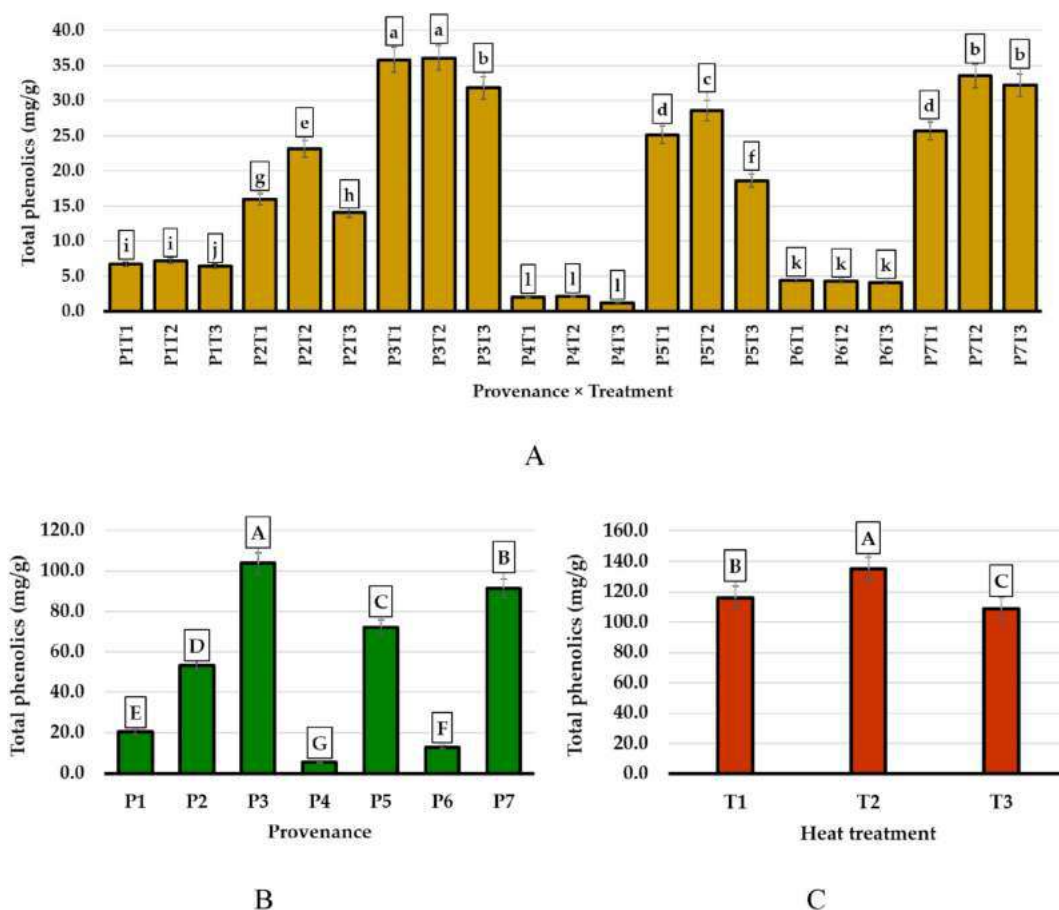


Fig. 5. Total phenolic compounds (mg/g) identified in the bark belonging to different geographical provenances of silver fir, according to (A) the interaction between the geographical origins (seven provenances: P1 – Valea Bistrei, P2 – Someșul Rece, P3 – Avrig, P4 – Budescu, P5 – Sohodol, P6 – Valea Morii, P7 – Gîrda Seacă) and drying temperature (three levels: T1 = 60 °C; T2 = 80 °C; T3 = 100 °C); (B) the unilateral influence of geographical provenances, regardless of the drying temperature; (C) the unilateral influence of the drying temperature, regardless of the geographical provenance. Within the interaction between provenances and treatments (A), respectively, for geographical provenances (B) and treatments (C), significant differences between means are illustrated with different letters (Duncan's Multiple Range Test, $p < 0.05$).

Hierarchical cluster analysis and the corresponding heatmap summarized the relationships between the chemical compounds, in the row dendrogram, but also between the three drying temperatures, in the column dendrogram (Fig. 6). The row dendrogram illustrates the clusters of compounds according to the grouping of observations that were made on the peaks and the levels of similarity between these. The cluster of phenolic compounds has two main branches, the lower one containing only three compounds, two of which are closely placed in a subcluster (CH and CH₂) and one more distant (H, O–H). The upper subcluster has two branches, one represented by a single compound, but the other with numerous branches and subclusters, some finished as four pairs in which the compounds are very close (i.e., C–O–C asym. Stretch. and C–O–C stretch.; C–O stretch. and Aromatic C–H; C=C, C=O and C–H *asym* CH₃ and CH₂; CH₂ wagg. and C–O vibr.). The column dendrogram of drying temperatures shows a closer relationship between the 80 °C and 100 °C levels, which are grouped in a pair subcluster from which the 60 °C level appears more distant.

The Pearson correlations calculated between the main ecological conditions (temperature, precipitation, altitude) of the silver fir geographic provenances and phenolic compounds in the bark revealed that the level of more than half of the phenolic compounds decreased significantly as precipitation increased (Fig. A2). A significant negative correlation ($r = -0.803^*$) was identified both between the total phenolics and precipitation (Fig. A3), illustrating that the amounts of phenolic compounds in the bark are inversely associated with the quantity of precipitation in the areas of the silver fir geographic provenances.

4. Discussion

The current study is a new attempt to evaluate *A. alba* provenances using FT-IR fingerprints and HPLC. FT-IR approach is useful for analyzing wood because it provides information about functional groups and chemical bonds [15,49,50,62], lucrative for identifying wood parts, wood type, and also wood quality assessment [16,19].

FT-IR spectra have been effectively used to characterize the chemical part of wood and bark [42,44,46,62,63], as well as the

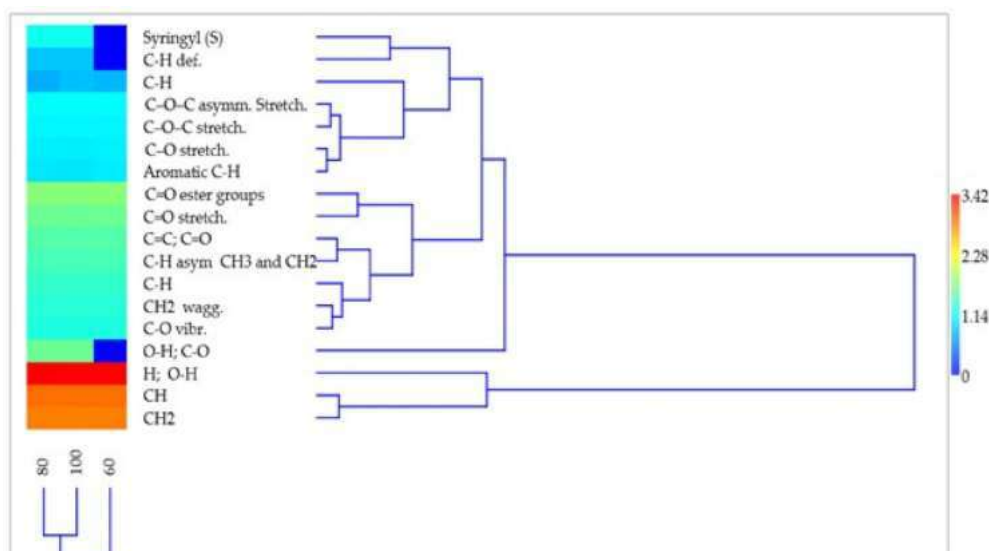


Fig. 6. Hierarchical clustering – paired group UPGMA (unweighted pair group method with arithmetic mean) for 15 components identified in bark of seven provenances of *A. alba* using FT-IR technique, at three different drying temperatures (60, 80, 100 °C).

detection and further the influence of fungi on wood [44,64]. Infrared spectroscopy has also been applied to distinguish tree species. Niemz et al. [65] were able to differentiate between softwoods and hardwoods based on chemical differences in the lignin composition of conifers and angiosperms which were easily detected by FT-IR analyses. However, if differences in chemical composition are small, analysis of individual chemical components is insufficient to group a set of samples by species [47,66].

Chromatography results further revealed that silver fir bark extracts contain large amounts of chemical compounds such as cellulose, hemicellulose, lignin, flavonoids, phenols with antioxidant activity and others, fact that corresponds to other studies carried out [67,68]. Within the same species, genetic variation in the forest can be manifested within and among populations [69]. It is of interest to uncover genetic differences that also determine phenotypic differences in trees, such as growth, resilience to stresses, and useable properties of wood [70–72].

Tree habitus, wood, bark, and chemical compounds can take different peculiarities within species and populations, and under specific ecological conditions, i.e. soil, climate, altitude, forest characteristics, etc. [73]. Bark thickness and constitution depend on the species, the age of the tree, the ecological factors from the origin area, and slightly on different parts of the tree [20]. Bark is also important because it guards trees' stems from fire and other dangers and helps them absorb nutrients, connect to water, and often fix damage [74]. Bark, a non-technical name for tissues located outside the vascular cambium [75], that perform important physiological tasks in a living tree, includes the following: transport and storage of photosynthesis-derived compounds [76], as well as defence against biotic and abiotic stressors [77,78]. Its function can be deduced from the chemical composition, which varies according to the quantities and proportions of structural (cellulose, hemicelluloses, lignin, and suberin) and non-structural (extracts) substances [79]. Conifer bark can contain up to six times more extractives than stemwood (softwood) [78,79], and the bark comprises 10–15% of stem volume [20]. The bark of the silver fir tree comprises various extractable non-structural constituents, including soluble carbohydrates, terpenes, aliphatic alcohols, fatty acids, and polyphenols such as stilbens, flavonoids, lignans, and tannins [78]. The bark is comprised of various tissues encompassing the vascular cambium, encompassing both the periderm and secondary phloem, which is further divided into inner and outer bark [80]. The secondary phloem, which is the layer directly surrounding the vascular cambium, contains polyphenolic parenchyma cells, where the majority of the bark secondary metabolites are produced. These cells also include lipids, carbohydrates, and polyphenolic chemicals [81]. The utilization of bark from commercially cultivated softwood trees presents a promising avenue for accessing secondary metabolites, notably polyphenols such as tannins. These compounds have demonstrated utility in the production of adhesives and resins [20]. A higher total extractive content of the bark was identified in the upper positions of the silver fir trunk [20].

European softwood bark-derived condensed tannins are accepted as an alternative to synthetic phenolics [82]. Due to the composition of the majority of flavonols and acids, the tree bark represents an important source of materials for wood industry. Due to the hydroxyl groups' reactivity with formaldehyde, condensed tannins are ideally suited for the efficient production of adhesives, polymers and foams. Our findings reveal that a significant quantity of catechins and epicatechins (a subgroup of flavanols) were detected in the bark of some provenances, confirming the necessity for proper utilization of this resource in silver fir [11,12,78]. Epicatechin and catechin have been identified in various kinds of trees, including leaf extracts from several *Salix species*, but also in a range of fruits, beans, and chocolate [83]. In comparison to samples from the other provenances, Gârda Seacă contained larger concentrations of ellagic acid. This polyphenol is present in the wood and bark of several forest species, including *Quercus*, *Eucalyptus*, and *Castanea* [84] and has been recognized having antioxidant, anticancer, and antimutagenic activities. As a result, waste from the

forestry, wood-processing, and agro-forestry industries might be used to recover some bioactive chemicals, including ellagic acid [85].

Most infrared bands cannot be traced to a single component due to the intricacy of wood. To improve FT-IR spectral analysis, multivariate statistical approaches can be applied [51]. Similar to the current investigation, principal component analysis (PCA) has been used to discover chemical differences between early-wood and late-wood [86], or to discriminate between trees growing in different places [47]. The hierarchical clustering method enabled the combination of multiple information gathered from detailed sample characterization into a global perspective of the system. Multivariate statistical analysis is frequently used to make clear distinctions based on band positions obtained in FT-IR [51].

In our investigation, infrared spectroscopy and HPLC, in combination with statistical interpretation of data, were valuable instruments to evaluate provenance and characterize the noted differences between the studied samples. The findings provide a potential starting point for selecting appropriate resources represented by natural forests, as well as optimal processes for the utilization of wood from renewable biomass in energy and commodities with added value. Because of the finite nature of fossil-based resources and the negative environmental impact of their use, harnessing renewable biomass is gaining popularity in sustainable forestry. However, for future studies, an in-depth method will be conceived for the assessment of factors (except geographical, respectively genetic, and ecological) that may influence the chemical compounds of interest in fir bark, including age, condition, size of trees, and different sampling heights, cardinal points, different years, but also different seasons.

5. Conclusions

In order to identify prospective uses as sources of significant chemicals, this study includes an in-depth investigation of silver fir bark from seven different geographic provenances in Romania. Among the assessed sources, several populations with high potential for biomass utilization were found, according to the final and compositional analysis. Interpopulation variations of Romanian silver fir caused by genetic and ecological variables appear to be sources of a variety of chemical compounds of interest in tree bark, namely considerable levels of phenolics and flavonoids. Depending on the origins of *A. alba*, the extractive fractions of some provenances contained a significant amount of beneficial compounds and potential antioxidant activity. A negative correlation was identified between total phenolics and precipitation, meaning that as precipitation, respectively the altitude levels increase, the amounts of phenolic compounds in silver fir bark decrease.

Data availability statement

Data associated with the study has not been deposited into a publicly available repository and data will be made available on request.

CRediT authorship contribution statement

Irina M. Morar: Writing – original draft, Project administration, Investigation, Funding acquisition, Conceptualization. **Razvan Stefan:** Writing – review & editing, Validation, Supervision, Resources, Methodology, Formal analysis, Conceptualization. **Catalina Dan:** Writing – original draft, Investigation, Data curation. **Radu E. Sestras:** Writing – review & editing, Formal analysis. **Petru Truta:** Resources, Investigation, Data curation. **Mădălina Medeleanu:** Visualization, Investigation, Formal analysis. **Florica Ranga:** Visualization, Investigation, Formal analysis. **Paul Sestras:** Validation, Supervision, Software, Methodology. **Alina M. Truta:** Resources, Project administration, Methodology, Data curation. **Adriana F. Sestras:** Writing – review & editing, Supervision, Software, Methodology, Formal analysis, Conceptualization.

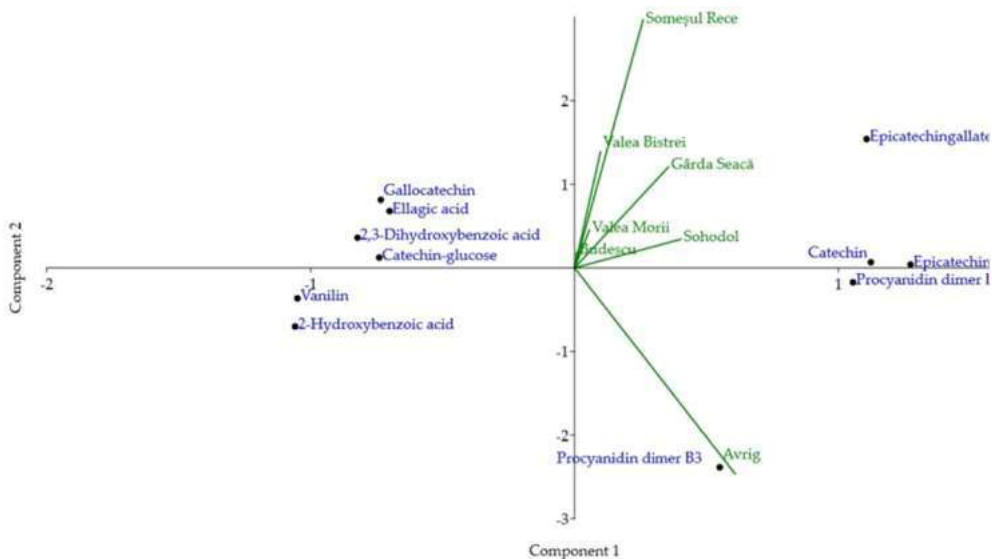
Declaration of competing interest

The authors declare the following financial interests/personal relationships which may be considered as potential competing interests: Irina M. Morar reports financial support and article publishing charges were provided by UEFISCDI, Ministry of Research and Innovation, the project number PN-III-P1-1.1-PD-2021-0651. Irina M. Morar reports article publishing charges was provided by University of Agricultural Sciences and Veterinary Medicine from Cluj-Napoca (USAMVCN).

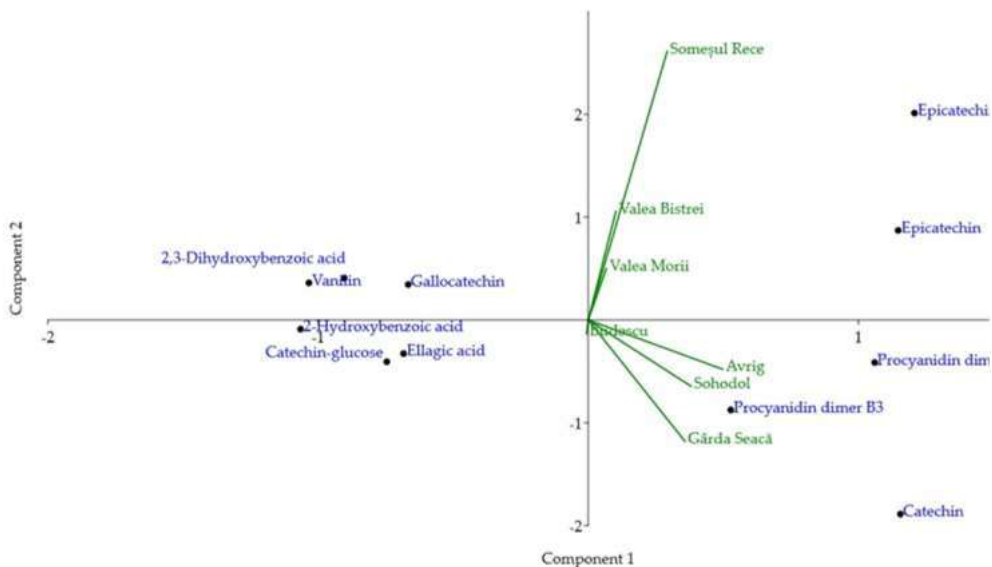
Acknowledgements

UEFISCDI, Ministry of Research and Innovation, Romania; University of Agricultural Sciences and Veterinary Medicine from Cluj-Napoca (USAMVCN), Romania.

Appendix A

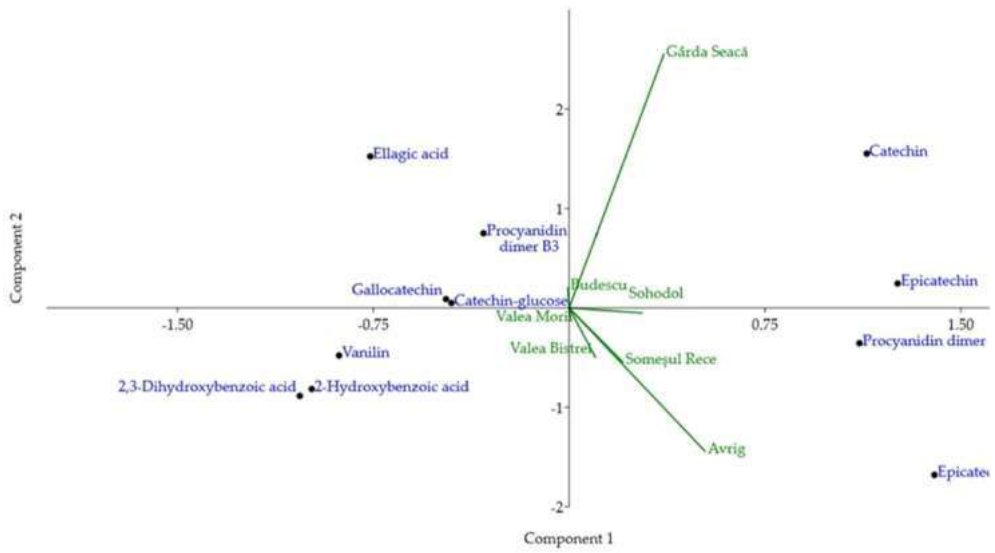


A



B

Fig. A.1. Summarizing datasets and information regarding the origins of silver fir (seven provenances) and phenolic compounds in the bark, using Principal Component Analysis (PCA), depending on the drying temperatures: (A) T = 60 °C (T1 – drying temperature); (B) T = 80 °C (T2 – drying temperature); (C) T = 100 °C (T3 – drying temperature).



C
Fig. A.1. (continued).

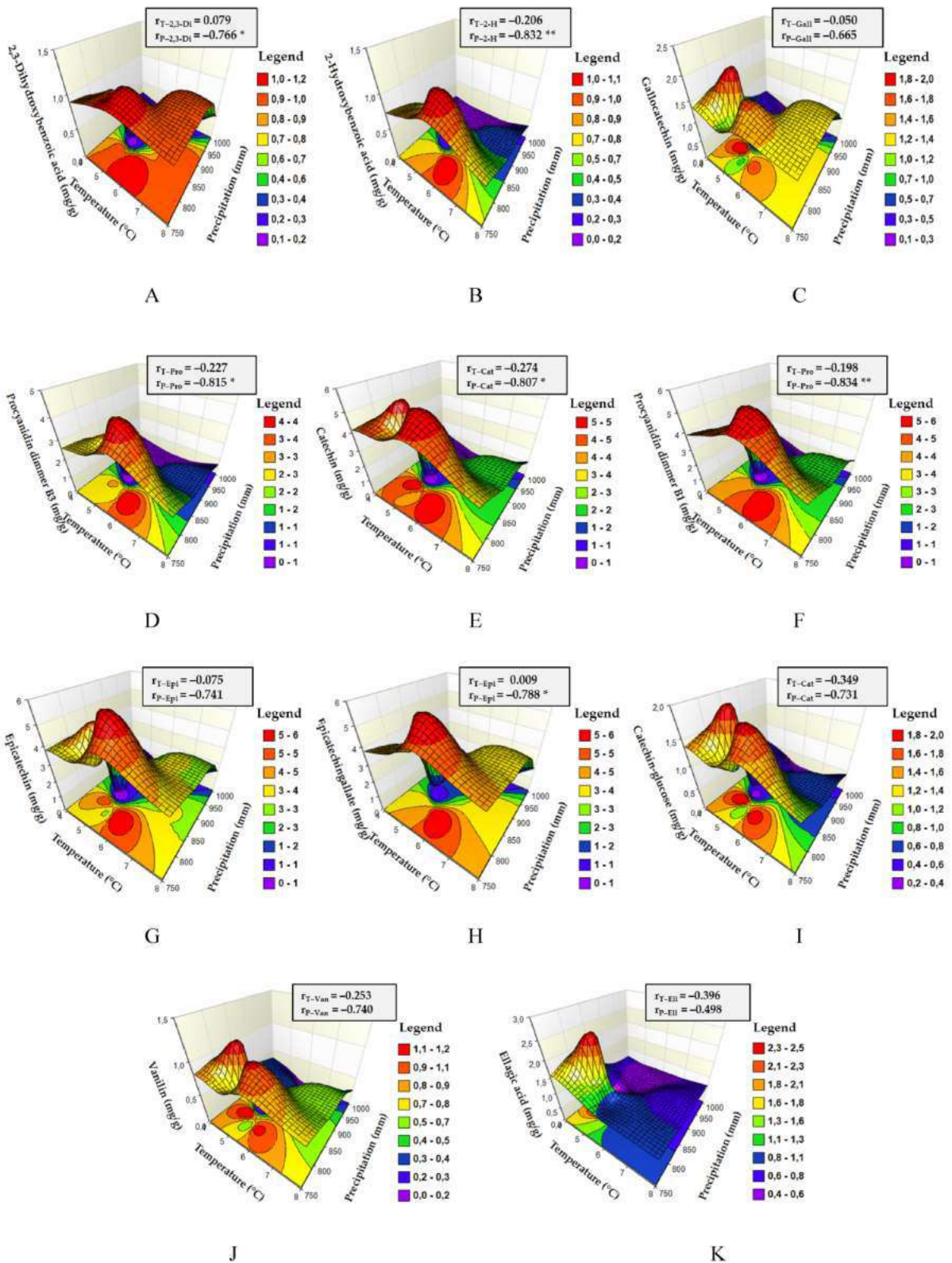


Fig. A.2. The Pearson correlations (r) between the main ecological conditions (i.e., T-temperature, P-precipitation) of the silver fir geographic provenances, and phenolic compounds in the bark: (A) 2,3-Dihydroxybenzoic acid; (B) 2-Hydroxybenzoic acid; (C) Gallic catechin; (D) Procyanidin

dimer B3; (E) Catechin; (F) Procyanidin dimer B1; (G) Epicatechin; (H) Epicatechingallate; (I) Catechin-glucose; (J) Vanillin; (K) Ellagic acid. The 'r' values considered statistically significant were symbolized by * (P value < 0.05) and ** (P value < 0.01).

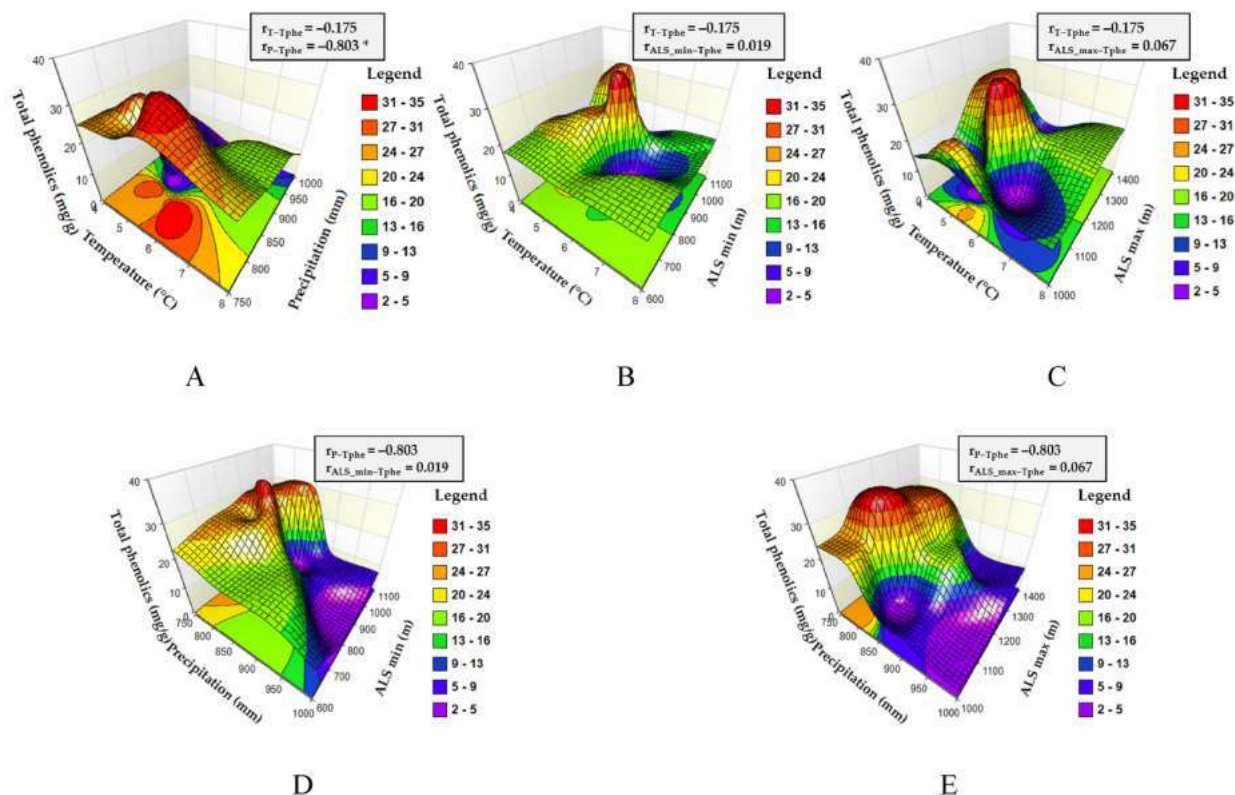


Fig. A.3. The Pearson correlations ('r') between the total phenolics in the bark of the silver fir provenances, and the main ecological conditions of the geographic provenances: (A) temperature, precipitation; (B) temperature, ALS min – minimum altitude; (C) temperature, ALS max – maximum altitude; (D) precipitation, ALS min – minimum altitude; (E) precipitation, ALS max – maximum altitude. The 'r' value considered statistically significant was symbolized by * (P value < 0.05).

References

- [1] R. Costanza, R. d'Arge, R. de Groot, S. Farber, M. Grasso, B. Hannon, K. Limburg, S. Naeem, R.V. O'Neill, J. Paruelo, et al., The value of the world's ecosystem services and natural capital, *Nature* 387 (1997) 253–260, <https://doi.org/10.1038/387253a0>.
- [2] A.S. Mori, K.P. Lertzman, L. Gustafsson, Biodiversity and ecosystem services in forest ecosystems: a research agenda for applied forest ecology, *J. Appl. Ecol.* 54 (2017) 12–27, <https://doi.org/10.1111/1365-2664.12669>.
- [3] E.G. Brockerhoff, L. Barbaro, B. Castagneyrol, D.I. Forrester, B. Gardiner, J.R. González-Olabarria, P.O.B. Lyver, N. Meurisse, A. Oxbrough, H. Taki, et al., Forest biodiversity, ecosystem functioning and the provision of ecosystem services, *Biodivers. Conserv.* 26 (2017) 3005–3035, <https://doi.org/10.1007/s10531-017-1453-2>.
- [4] P. Sestras, M.V. Bondrea, H. Cetean, T. Sălăgean, Ș. Bilașco, S. Naș, V. Spalevic, S. Fountas, S.M. Cîmpeanu, Ameliorative, ecological and landscape roles of Făget Forest, Cluj-Napoca, Romania, and possibilities of avoiding risks based on GIS landslide susceptibility map, *Not. Bot. Horti Agrobot. Cluj-Napoca* 46 (2018) 292–300, <https://doi.org/10.15835/nbha46110866>.
- [5] *Millennium Ecosystem Services, Ecosystems and Human Well-Being*, Island Press, Washington, DC, USA, 2005.
- [6] R. Shmulysky, P.D. Jones, *Forest Products and Wood Science: an Introduction*, seventh ed., Wiley Blackwell, Hoboken, NJ, USA, 2011.
- [7] M. Traoré, J. Kaal, A. Martínez Cortizas, Differentiation between pine woods according to species and growing location using FTIR-ATR, *Wood Sci. Technol.* 52 (2018) 487–504, <https://doi.org/10.1007/s00226-017-0967-9>.
- [8] R.B. Cody, E.O. Espinoza, E.R. Price, P.J. McClure, Wood from hardwood angiosperms and coniferous gymnosperms shows distinctive lignin peaks in Direct Analysis in Real Time (DART) mass spectra, *J. Am. Soc. Mass Spectrom.* 34 (2023) 784–789, <https://doi.org/10.1021/jasms.2c00347>.
- [9] A. Holmgren, B. Bergström, R. Gref, A. Ericsson, Detection of pinosylvins in solid wood of Scots pine using Fourier transform Raman and infrared spectroscopy, *J. Wood Chem. Technol.* 19 (1999) 139–150, <https://doi.org/10.1080/02773819909349604>.
- [10] P. Tiscar, J. Linares, *Pinus nigra* subsp. *Salzmannii* forests from southeast Spain: using structure and process information to guide management, in: C. Frisiras (Ed.), *Pine Forests: Types, Threats and Management*, Nova Science Publishers, Hauppauge, New York, 2011, pp. 1–27.
- [11] E. Benković, T. Grohar, D. Zigon, U. Svajger, D. Janes, S. Kreft, B. Strukelj, Chemical composition of the silver fir (*Abies alba*) bark extract Abigenol (R) and its antioxidant activity, *Ind. Crop. Prod.* 52 (2014) 23–28, <https://doi.org/10.1016/j.indcrop.2013.10.005>.
- [12] E. Butnaru, D. Pamfil, E. Stoleru, M. Brebu, Characterization of bark, needles and cones from silver fir (*Abies alba* Mill.) towards valorization of biomass forestry residues, *Biomass Bioenergy* 159 (2022) 106413.
- [13] J.A. Okolie, S. Nanda, A.K. Dalai, J.A. Kozinski, Chemistry and specialty industrial applications of lignocellulosic biomass, *Waste Biomass Valor* 12 (2021) 2145–2169, <https://doi.org/10.1007/s12649-020-01123-0>.

- [14] N. Papp, D. Purger, S. Czigle, D. Czégényi, S. Stranczinger, M. Tóth, T. Dénes, M. Kocsis, A. Takácsi-Nagy, R. Filep, The importance of pine species in the ethnomedicine of Transylvania (Romania), *Plants* 11 (2022) 2331, <https://doi.org/10.3390/plants11182331>.
- [15] B. Esteves, A. Velez Marques, I. Domingos, H. Pereira, Chemical changes of heat treated pine and eucalypt wood monitored by FTIR, *Maderas Cienc. Tecnol.* 15 (2013) 245–258, <https://doi.org/10.4067/S0718-221X2013005000020>.
- [16] A.K. Moore, N.L. Owen, Infrared spectroscopic studies of solid wood, *Appl. Spectrosc. Rev.* 36 (2001) 65–86.
- [17] R. Bodirlau, C. Teaca, Fourier transform infrared spectroscopy and thermal analysis of lignocellulose fillers treated with organic anhydrides, *Rom. J. Phys.* 54 (2009) 93–104.
- [18] C. Zhou, W. Jiang, Q. Cheng, B.K. Via, Multivariate calibration and model integrity for wood chemistry using Fourier transform infrared spectroscopy, *J. Anal. Methods Chem.* 2015 (2015) 1–9.
- [19] D.S. Gandolfo, H. Mortimer, J.W. Woodhall, N. Boonham, Fourier transform infra-red spectroscopy using an attenuated total reflection probe to distinguish between Japanese larch, pine and citrus plants in healthy and diseased states, *Spectrochim. Acta A Mol.* 163 (2016) 181–188, <https://doi.org/10.1016/j.saa.2016.03.022>.
- [20] M. Brennan, C. Fritsch, S. Cosgun, S. Dumarcay, F. Colin, P. Gerardin, Quantitative and qualitative composition of bark polyphenols changes longitudinally with bark maturity in *Abies alba* Mill, *Ann. For. Sci.* 77 (2020) 1–14.
- [21] F. Ruiz-Aquino, R. Ferial-Reyes, J.G. Rutiaga-Quiñones, L.H. Robledo-Taboada, R. Gabriel-Parra, Characterization of tannin extracts derived from the bark of four tree species by HPLC and FTIR, *For. Sci. Technol.* 19 (2023) 38–46, <https://doi.org/10.1080/21580103.2023.2166593>.
- [22] E.S. Halmemies, H.E. Brännström, M. Karjalainen, J. Nurmi, R. Alén, Availability of extractives from various Norway spruce (*Picea abies*) stumps assortments, *J. Wood Chem. Technol.* 43 (2023) 13–27, <https://doi.org/10.1080/02773813.2022.2152049>.
- [23] M. Brunner, R. Eugster, E. Trenka, L. Bergamin-Strotz, FT-NIR spectroscopy and wood identification, *Holzforschung* 50 (1996) 130–134.
- [24] A. Antti, P. Perre, A microwave applicator for on line wood drying: temperature and moisture distribution in wood, *J. Wood Sci.* 33 (1999) 123–138.
- [25] N. Gierlinger, M. Schwanninger, R. Wimmer, Characteristics and classification of Fourier-transform near infrared spectra of the heartwood of different larch species (*Larix* sp.), *J. Near Infrared Spectrosc.* 12 (2004) 113–119.
- [26] O. Priha, S.J. Grayston, R. Hiukka, T. Pennanen, A. Smolander, Microbial community structure and characteristics of the organic matter in soils under *Pinus sylvestris*, *Picea abies* and *Betula pendula* at two forest sites, *Biol. Fertil. Soils* 33 (2001) 17–24.
- [27] A. Cotrim, A. Ferraz, A. Gonçalves, F. Silva, R. Bruns, Identifying the origin of lignins and monitoring their structural changes by means of FTIR-PCA and-SIMCA, *Bioresour. Technol.* 68 (1999) 29–34.
- [28] G. Kos, H. Lohninger, R. Krška, Fourier transform mid-infrared spectroscopy with attenuated total reflection (FT-IR/ATR) as a tool for the detection of *Fusarium* fungi on maize, *Vib. Spectrosc.* 29 (2002) 115–119.
- [29] A.B.D. Nandiyanto, R. Oktiani, R. Ragadhita, How to read and interpret FTIR spectroscopy of organic material, *Indones. J. Sci. Technol.* 4 (2019) 97–118.
- [30] M. McCann, L. Chen, K. Roberts, E. Kemsley, C. Sene, N. Carpita, N. Stacey, R. Wilson, Infrared microspectroscopy: sampling heterogeneity in plant cell wall composition and architecture, *Physiol. Plantarum* 100 (1997) 729–738.
- [31] L. Chen, N.C. Carpita, W.D. Reiter, R.H. Wilson, C. Jeffries, M.C. McCann, A rapid method to screen for cell-wall mutants using discriminant analysis of Fourier transform infrared spectra, *Plant J.* 16 (1998) 385–392.
- [32] L.R. Schimleck, A.J. Michell, P. Vinden, Eucalypt wood classification by NIR spectroscopy and principal components analysis, *Appita J.* 49 (1996) 319–324.
- [33] P. de Frenne, J. Lenoir, M. Luoto, B.R. Scheffers, F. Zellweger, J. Aalto, M.B. Ashcroft, D.M. Christiansen, G. Decocq, K. De Pauw, et al., Forest microclimates and climate change: importance, drivers and future research agenda, *Global Change Biol.* 27 (2021) 2279–2297, <https://doi.org/10.1111/gcb.15569>.
- [34] M. Curovic, V. Spalevic, P. Sestras, R. Motta, C. Dan, M. Garbarino, A. Vitali, C. Urbinati, Structural and ecological characteristics of mixed broadleaved old-growth forest (Biogradska Gora - Montenegro), *Turk. J. Agric. For.* 44 (2020) 428–438, <https://doi.org/10.3906/tar-2003-103>.
- [35] I.M. Todea, S. González-Orenga, M. Boscaiu, M. Plazas, A.F. Sestras, J. Prohens, O. Vicente, R.E. Sestras, Responses to water deficit and salt stress in silver fir (*Abies alba* Mill.) seedlings, *Forests* 11 (2020) 395, <https://doi.org/10.3390/f11040395>.
- [36] V. Popova, S. Tasheva, T. Ivanova, A. Stoyanova, Coefficient of diffusion of tannins in ethanol extracts from *Physalis alkekengi* L. leaves, *IOP Conf. Ser. Mater. Sci. Eng.* (2021) 1031, <https://doi.org/10.1088/1757-899X/1031/1/012093>.
- [37] R.K. Das, A. Mizan, F.T. Zohra, S. Ahmed, K.S. Ahmed, H. Hossain, Extraction of a novel tanning agent from indigenous plant bark and its application in leather processing, *J. Leather Sci. Eng.* 4 (2022) 18, <https://doi.org/10.1186/s42825-022-00092-5>.
- [38] I. Crișan, R. Vidican, L. Olar, V. Stoian, A. Morea, R. Ștefan, Screening for changes on *Iris germanica* L. rhizomes following inoculation with arbuscular mycorrhiza using Fourier transform infrared spectroscopy, *Agronomy* 9 (2019) 815.
- [39] R. Vârban, I. Crișan, D. Vârban, A. Ona, L. Olar, A. Stoie, R. Ștefan, Comparative FT-IR prospecting for cellulose in stems of some fiber plants: flax, velvet leaf, hemp and jute, *Appl. Sci.* 11 (2021) 8570.
- [40] Ø. Hammer, D.A.T. Harper, P.D. Ryan, PAST: paleontological statistics software package for education and data analysis, *Palaeontol. Electron.* 4 (2001) 4–9.
- [41] L. Ncss, *Ncss 2023 Statistical Software*, Ncss, com/software/ncss: Kaysville, Utah, USA, 2023.
- [42] O. Faix, Fourier transform infrared spectroscopy, *Methods in lignin chemistry* (1992) 83–109.
- [43] C.G. Boeriu, D. Bravo, R.J. Gosselink, J.E. van Dam, Characterisation of structure-dependent functional properties of lignin with infrared spectroscopy, *Ind. Crops Prod.* 20 (2004) 205–218.
- [44] K. Pandey, A. Pitman, FTIR studies of the changes in wood chemistry following decay by brown-rot and white-rot fungi, *Int. Biodeterior. Biodegrad.* 52 (2003) 151–160.
- [45] H.L. Hergert, Infrared spectra, in: K.V. Sarkanen, C.H. Ludwig (Eds.), *Lignins: Occurrence, Formation, Structure and Reactions*, John Wiley & Sons, Inc., New York, NY, USA, 1971, pp. 267–296.
- [46] O. Faix, Classification of lignins from different botanical origins by FT-IR spectroscopy, *Holzforschung* 45 (1991) 21–27.
- [47] R. Rana, G. Müller, A. Naumann, A. Polle, FTIR spectroscopy in combination with principal component analysis or cluster analysis as a tool to distinguish beech (*Fagus sylvatica* L.) trees grown at different sites, *Holzforschung* 62 (2008) 530–538, <https://doi.org/10.1515/HF.2008.104>.
- [48] Y.-i. Zhang, J.-b. Chen, Y. Lei, Q. Zhou, S.-q. Sun, I. Noda, Discrimination of different red wine by Fourier-transform infrared and two-dimensional infrared correlation spectroscopy, *J. Mol. Struct.* 974 (2010) 144–150.
- [49] C.-M. Popescu, M.-C. Popescu, G. Singurel, C. Vasile, D.S. Argyropoulos, S. Willfor, Spectral characterization of eucalyptus wood, *Appl. Spectrosc.* 61 (2007) 1168–1177.
- [50] P. Evans, Differentiating “hard” from “soft” woods using Fourier transform infrared and Fourier transform spectroscopy, *Spectrochim. Acta A Mol.* 47 (1991) 1441–1447.
- [51] H. Chen, C. Ferrari, M. Angiuli, J. Yao, C. Raspi, E. Bramanti, Qualitative and quantitative analysis of wood samples by Fourier transform infrared spectroscopy and multivariate analysis, *Carbohydr. Polym.* 82 (2010) 772–778.
- [52] X. Colom, F. Carrillo, Comparative study of wood samples of the northern area of Catalonia by FTIR, *J. Wood Chem. Technol.* 25 (2005) 1–11.
- [53] P. Evans, A. Michell, K. Schmalzl, Studies of the degradation and protection of wood surfaces, *Wood Sci. Technol.* 26 (1992) 151–163.
- [54] B. Mohebi, Application of ATR infrared spectroscopy in wood acetylation, *J. Agric. Sci.* 10 (2008) 253–259.
- [55] J. Zhao, W. Xiuwen, J. Hu, Q. Liu, D. Shen, R. Xiao, Thermal degradation of softwood lignin and hardwood lignin by TG-FTIR and Py-GC/MS, *Polym. Degrad. Stabil.* 108 (2014) 133–138.
- [56] S. Genest, R. Salzer, G. Steiner, Molecular imaging of paper cross sections by FT-IR spectroscopy and principal component analysis, *Anal. Bioanal. Chem.* 405 (2013) 5421–5430.
- [57] C. Karunakaran, C.R. Christensen, C. Gaillard, R. Lahlali, L.M. Blair, V. Perumal, S.S. Miller, A.P. Hitchcock, Introduction of soft X-ray spectromicroscopy as an advanced technique for plant biopolymers research, *PLoS One* 10 (2015) e0122959.
- [58] S. Longo, S. Capuani, C. Corsaro, E. Fazio, Silver fir characterized by micro-imaging NMR and FTIR spectroscopy, in: *Proceedings of the IOP Conference Series: Materials Science and Engineering*, 2020 012004.

- [59] K. Fackler, J.S. Stevanic, T. Ters, B. Hinterstoisser, M. Schwanninger, L. Salmén, Localisation and characterisation of incipient brown-rot decay within spruce wood cell walls using FT-IR imaging microscopy, *Enzym. Microb. Technol.* 47 (2010) 257–267.
- [60] R.H. Ibrahim, L.I. Darvell, J.M. Jones, A. Williams, Physicochemical characterisation of torrefied biomass, *J. Anal. Appl. Pyrolysis* 103 (2013) 21–30.
- [61] A. Boukir, S. Fellak, P. Doumenq, Structural characterization of *Argania spinosa* Moroccan wooden artifacts during natural degradation progress using infrared spectroscopy (ATR-FTIR) and X-Ray diffraction (XRD), *Heliyon* 5 (2019) e02477.
- [62] K. Pandey, A study of chemical structure of soft and hardwood and wood polymers by FTIR spectroscopy, *J. Appl. Polym. Sci.* 71 (1999) 1969–1975.
- [63] O. Faix, Practical uses of FTIR spectroscopy in wood science and technology, *Mikrochim. Acta* 94 (1988) 21–25.
- [64] A. Naumann, M. Navarro-González, S. Peddireddi, U. Kües, A. Polle, Fourier transform infrared microscopy and imaging: detection of fungi in wood, *Fungal Genom. Biol.* 42 (2005) 829–835.
- [65] P. Niemz, S. Körner, O. Wienhaus, W. Flamme, M. Balmer, Applying NIR spectroscopy for evaluation of the hardwood/softwood ratio and resin content in chip mixtures, *Holz als Roh-und Werkstoff* 50 (1992) 25–28.
- [66] K. Kratzl, H. Tschamler, Infrared spectra of wood and insoluble lignins, *Monatsh. Chem.* 83 (1952) 786–791.
- [67] H. Yang, R. Yan, H. Chen, D.H. Lee, C. Zheng, Characteristics of hemicellulose, cellulose and lignin pyrolysis, *Fuel* 86 (2007) 1781–1788, <https://doi.org/10.1016/j.fuel.2006.12.013>.
- [68] I. Miranda, J. Ferreira, S. Cardoso, H. Pereira, Composition and antioxidant properties of extracts from Douglas fir bark, *Holzforchung* 75 (2021) 677–687, <https://doi.org/10.1515/hf-2020-0097>.
- [69] I.M. Todea Morar, S. Rensen, S. Vilanova, M. Boscaiu, L. Holonec, A.F. Sestras, O. Vicente, J. Prohens, R.E. Sestras, M. Plazas, Genetic relationships and reproductive traits of Romanian populations of silver fir (*Abies alba*): implications for the sustainable management of local populations, *Sustainability* 12 (2020) 4199, <https://doi.org/10.3390/su12104199>.
- [70] Y. Li, M. Suontama, R.D. Burdon, H.S. Dungey, Genotype by environment interactions in forest tree breeding: review of methodology and perspectives on research and application, *Tree Genet. Genomes* 13 (2017) 60, <https://doi.org/10.1007/s11295-017-1144-x>.
- [71] A. Dias, M.J. Gaspar, A. Carvalho, J. Pires, J. Lima-Brito, M.E. Silva, J.L. Louzada, Within- and between-tree variation of wood density components in *Pinus nigra* at six sites in Portugal, *Ann. For. Sci.* 75 (2018) 58, <https://doi.org/10.1007/s13595-018-0734-6>.
- [72] M. Kempf, M. Zarek, J. Paluch, The pattern of genetic variation, survival and growth in the *Abies alba* Mill. population within the introgression zone of two refugial lineages in the Carpathians, *Forests* 11 (2020) 849, <https://doi.org/10.3390/f11080849>.
- [73] T. Oluwajuwon, R. Attafuah, C. Offiah, D. Krabel, Genetic variation in tropical tree species and plantations: a review, *Open J. For.* 12 (2022) 350–366, <https://doi.org/10.4236/ojf.2022.123019>.
- [74] L. Poorter, A. McNeil, V.-H. Hurtado, H.H.T. Prins, F.E. Putz, Bark traits and life-history strategies of tropical dry- and moist forest trees, *Funct. Ecol.* 28 (2014) 232–242, <https://doi.org/10.1111/1365-2435.12158>.
- [75] T. Krekling, V.R. Franceschi, A.A. Berryman, E. Christiansen, The structure and development of polyphenolic parenchyma cells in Norway spruce (*Picea abies*) bark, *Flora* 195 (2000) 354–369.
- [76] V. De Schepper, T. De Swaef, I. Bauweraerts, K. Steppe, Phloem transport: a review of mechanisms and controls, *J. Exp. Bot.* 64 (2013) 4839–4850.
- [77] V.R. Franceschi, P. Krokene, E. Christiansen, T. Krekling, Anatomical and chemical defenses of conifer bark against bark beetles and other pests, *New Phytol.* 167 (2005) 353–376.
- [78] V. Vek, T. Šmidovnik, M. Humar, I. Poljanšek, P. Oven, Comparison of the content of extractives in the bark of the trunk and the bark of the branches of silver fir (*Abies alba* Mill.), *Molecules* 28 (2023) 225.
- [79] J. Routa, H. Brännström, P. Anttila, M. Mäkinen, J. Jänis, A. Asikainen, Wood extractives of Finnish pine, spruce and birch—availability and optimal sources of compounds, *Natural Resources and Bioeconomy Studies* 73 (2017) 6–55.
- [80] B. Konópka, J. Pajtlík, V. Šebeň, K. Merganičová, Modeling bark thickness and bark biomass on stems of four broadleaved tree species, *Plants* 11 (2022) 1148, <https://doi.org/10.3390/plants11091148>.
- [81] C. Bark Romero, Structure and functional ecology, in: A.B. Cunningham, B.M. Campbell, M.K. Luckert (Eds.), *Bark: Use, Management, and Commerce in Africa*, *ume 17*, New York Botanical Garden Press, New York, NY, USA, 2013, pp. 5–25.
- [82] S. Bianchi, I. Krosiakova, R. Janzon, I. Mayer, B. Saake, F. Pichelin, Characterization of condensed tannins and carbohydrates in hot water bark extracts of European softwood species, *Phytochemistry* 120 (2015) 53–61, <https://doi.org/10.1016/j.phytochem.2015.10.006>.
- [83] E. Piąteczak, M. Dybowska, E. Pluciennik, K. Kośla, J. Kolniak-Ostek, U. Kalinowska-Lis, Identification and accumulation of phenolic compounds in the leaves and bark of *Salix alba* (L.) and their biological potential, *Biomolecules* 10 (2020) 1391, <https://doi.org/10.3390/biom10101391>.
- [84] J. Sharifi-Rad, C. Quispe, C.M.S. Castillo, R. Caroca, M.A. Lazo-Vélez, H. Antonyak, A. Polishchuk, R. Lysiuk, P. Oliinyk, L. De Masi, et al., Ellagic acid: a review on its natural sources, chemical stability, and therapeutic potential, *Oxid. Med. Cell. Longev.* 2022 (2022) 3848084, <https://doi.org/10.1155/2022/3848084>.
- [85] F.M. Vella, L. De Masi, R. Calandrelli, A. Morana, B. Laratta, Valorization of the agro-forestry wastes from Italian chestnut cultivars for the recovery of bioactive compounds, *Eur. Food Res. Technol.* 245 (2019) 2679–2686, <https://doi.org/10.1007/s00217-019-03379-w>.
- [86] R. Hori, J. Sugiyama, A combined FT-IR microscopy and principal component analysis on softwood cell walls, *Carbohydr. Polym.* 52 (2003) 449–453, [https://doi.org/10.1016/S0144-8617\(03\)00013-4](https://doi.org/10.1016/S0144-8617(03)00013-4).



Evaluation of tectonic activity using morphometric indices: Study of the case of Taililoute ridge (middle-Atlas region, Morocco)

Driss Sadkaoui ^a, Benzougagh Brahim ^b, Shuraik Kader ^c, Kamal Agharroud ^d, Abdel-Ilah Mihraje ^a, Khadija Aluni ^a, Habiba Aassoumi ^a, Slimane Sassioui ^e, Velibor Spalevic ^f, Paul Sestras ^{g, h}

- ^a Abdelmlek Essaâdi University, Faculty of Sciences, Department of Geology, Laboratory: Environmental Geology and Natural Resources, Tetouan, Morocco
- ^b Geophysics and Natural Hazards Laboratory, Department of Geomorphology and Geomatics (D2G), Scientific Institute, Mohammed V University in Rabat, Avenue Ibn Batouta, Agdal, PO Box 703, 10106, Rabat-City, Morocco
- ^c School of Engineering and Built Environment, Griffith University, 170 Kessels Road, Nathan, QLD, 4111, Australia
- ^d Earth Sciences Department, Ain Chock Faculty of Sciences, University Hassan II of Casablanca, Morocco
- ^e Laboratory of Analysis and Modeling of Water and Natural Resources, Mohammadia School of Engineers, Mohammed V University in Rabat, Morocco
- ^f Biotechnical Faculty, University of Montenegro, Podgorica, 81000, Montenegro
- ^g Faculty of Civil Engineering, Technical University of Cluj-Napoca, 400020, Cluj-Napoca, Romania
- ^h Academy of Romanian Scientists, Ilfov 3, 050044, Bucharest, Romania

Recommended articles

New geostatistical approach to the analysis of structural lineaments: Case study in th...

Journal of African Earth Sciences, Volume 213, 2024, Ar...
Abdelfattah Aboulfaraj, ..., Abdelouahed Farah

Integrating 3D subsurface imaging, seismic attributes, and wireline logging analyses:...

Journal of African Earth Sciences, Volume 213, 2024, Ar...
Amir Ismail, ..., Emad A. Eysa

Aouelloul impact crater, Mauritania: New structural, lithological, and petrographic...

Journal of African Earth Sciences, Volume 214, 2024, A...
E. Ould Mohamed Navee, ..., H. Si Mhamdi

Show 3 more articles

Article Metrics

Citations

Citation Indexes: 2

Captures

Readers: 3



View details

JOURNAL OF AFRICAN EARTH SCIENCES

Publisher name: PERGAMON-ELSEVIER SCIENCE LTD

Journal Impact Factor™

2.2 (2023) 2.3 (Five Year)

JCR Category	Category Rank	Category Quartile
GEOSCIENCES, MULTIDISCIPLINARY in SCIE edition	120/253	Q2

Source: Journal Citation Reports 2023. Learn more

Journal Citation Indicator™

0.6 (2023) 0.59 (2022)

JCI Category	Category Rank	Category Quartile
GEOSCIENCES, MULTIDISCIPLINARY in SCIE edition	134/253	Q3





Evaluation of tectonic activity using morphometric indices: Study of the case of Taililoute ridge (middle-Atlas region, Morocco)

Driss Sadkaoui^a, Benzougagh Brahim^b, Shuraik Kader^{c,*}, Kamal Agharroud^d, Abdel-Ilah Mihraje^a, Khadija Aluni^a, Habiba Aassoumi^a, Slimane Sassioui^e, Velibor Spalevic^f, Paul Sestras^{g,h}

^a Abdelmlek Essaâdi University, Faculty of Sciences, Department of Geology, Laboratory: Environmental Geology and Natural Resources, Tetouan, Morocco

^b Geophysics and Natural Hazards Laboratory, Department of Geomorphology and Geomatics (D2G), Scientific Institute, Mohammed V University in Rabat, Avenue Ibn Batouta, Agdal, PO Box 703, 10106, Rabat-City, Morocco

^c School of Engineering and Built Environment, Griffith University, 170 Kessels Road, Nathan, QLD, 4111, Australia

^d Earth Sciences Department, Ain Chock Faculty of Sciences, University Hassan II of Casablanca, Morocco

^e Laboratory of Analysis and Modeling of Water and Natural Resources, Mohammedia School of Engineers, Mohammed V University in Rabat, Morocco

^f Biotechnical Faculty, University of Montenegro, Podgorica, 81000, Montenegro

^g Faculty of Civil Engineering, Technical University of Cluj-Napoca, 400020, Cluj-Napoca, Romania

^h Academy of Romanian Scientists, Ilfov 3, 050044, Bucharest, Romania

ARTICLE INFO

Handling Editor: M Mapeo

Keywords:

Morocco
Middle atlas region
Morphometric indices
Satellite image analysis
Tectonic activity
Tizi N'Teghtène fault system

ABSTRACT

In the Middle Atlas region, the Tizi N'Teghtène Fault System is a network of faults inherited from the Hercynian orogeny, which operated as normal faults during the Jurassic and reverse faults since the Miocene. The issue at hand is whether this fault system continues to be active today. To address this concern, focus has been placed on a central portion of the Tizi N'Teghtène Fault System, specifically the anticlinal ridge of Taililoute. Determining the tectonically active segments of this ridge is crucial for structural analysis and the Quaternary evolution of this mountain chain. To achieve this, morphometric indices related to the evolution of watersheds and their streams have been employed. These indices include hypsometry, elongation ratio (Re), drainage asymmetry factor (AF), and the elongation profiles of various watercourses. These indicators provide insights into the degree of active longitudinal growth of the Taililoute ridge. These parameters were determined through satellite image analysis using suitable software and geographic information systems (GIS). Tectonic activity analyses reveal that both flanks of this ridge exhibit ongoing tectonic activity, marked by the occurrence of normal faults and strike-slip faults during the Quaternary phase of the Alpine orogeny. It is concluded that the Tizi N'Teghtène Fault system remains tectonically active. This research contributes to a deeper understanding of the ongoing tectonic activities within the Tizi N'Teghtène Fault System, a matter of geological significance. By employing morphometric indices and modern satellite image analysis techniques, a methodological innovation is presented by this study in assessing tectonic activity in mountainous regions. These results provide valuable insights into structural dynamics of the Middle Atlas, aiding in the understanding of its geological evolution. Furthermore, this research can have broader applications in seismic hazard assessment and land use planning, making it relevant beyond the immediate geographical boundaries of the study area.

1. Introduction

Assessing tectonic activity using morphometric indices is an

important tool for understanding the tectonic evolution of a region. Morphometric indices are mathematical parameters that describe the shape, size and spatial distribution of landforms, such as mountains,

* Corresponding author.

E-mail addresses: d.sadkaoui@uae.ac.ma (D. Sadkaoui), brahim.benzougagh@is.um5.ac.ma (B. Brahim), shuraik10@gmail.com, shuraik.mohamedabdulkader@griffithuni.edu.au, s.mohamedabdulkader@griffith.edu.au (S. Kader), kamal.gharroud@etu.uae.ac.ma (K. Agharroud), mihrajeabdellilah@gmail.com (A.-I. Mihraje), khadijaaluni@gmail.com (K. Aluni), habibaassoumi@gmail.com (H. Aassoumi), sassiouislimane@gmail.com (S. Sassioui), velibor.spalevic@gmail.com (V. Spalevic), psestras@yahoo.com, psestras@mail.utcluj.ro (P. Sestras).

<https://doi.org/10.1016/j.jafrearsci.2024.105219>

Received 9 October 2023; Received in revised form 20 February 2024; Accepted 6 March 2024

Available online 8 March 2024

1464-343X/© 2024 The Author(s). Published by Elsevier Ltd. This is an open access article under the CC BY license (<http://creativecommons.org/licenses/by/4.0/>).

valleys and river networks (Kelemen et al., 2023). These indices are used to quantify the degree of tectonic deformation and uplift, and to distinguish between active and inactive tectonic regions (Alizadeh et al., 2020; Baruah et al., 2022; Parrino et al., 2023).

One of the most widely used morphometric indices to assess tectonic activity is the hypsometric integral (Hi), which is a measure of the elevation distribution of a landscape. Hi is calculated by dividing the area between the hypsometric curve which is a graph of percent area versus elevation and the datum line which is a straight line connecting the highest and lowest elevations, by the total area of the watershed (Bashir et al., 2024; Ji et al., 2021; Othman & Omar, 2023). Other morphometric indices used to assess tectonic activity include aspect ratio (Re) and basin shape (Bs). Re is a measure of the degree of elongation of a basin and is calculated by dividing the maximum length of the basin by its maximum width (Bhat et al., 2020). Bs is a measure of the asymmetry of a basin and is calculated by dividing the basin area on the longest side of the long axis by the basin area on the shortest side (Taib et al., 2023). Drainage asymmetry factor (FA) and longitudinal stream profiles can also be used to assess tectonic activity. AF is a measure of the degree of asymmetry of a river network and Longitudinal profiles of rivers can also provide information about tectonic activity, as changes in channel slope and inclination can indicate active faults or an uprising (Jani et al., 2021). The Middle Atlas is part of the Atlas Mountain range, which spans Morocco's central-northern region. The region is situated between the High Atlas and the Rif Mountains (Ouallali et al., 2024). This Mountain range is a 300-km-long mountain range that stretches from southwest to northeast. To the northwest the Middle Atlas Causse and southeast the folded Middle Atlas, it is essentially made up of tabular carbonate deposits. Unlike the southern front of the Rif, which corresponds to the hinterland of the Middle Atlas (Agharroud et al., 2021; Amine et al., 2020), evidence of Quaternary tectonic activity in this chain have not been thoroughly studied. From Lake Ouiuane in the southwest to the town of Sefrou in the northeast, the Middle Atlas causse

is crossed longitudinally by a network of faults known as the Tizi n'Teghtène Accident (TTA). This accident is considered as an anticlinal ridge which overlooks the Ifrane and Guigou causes and the Azrou plateau between Lake Ifrah and the town of Azrou. Although seismic activity along the Middle Atlas is generally moderate with magnitudes not exceeding 5, this seismicity could be of local origin.

Located at the westernmost tip of African plate, Morocco exhibits slow-evolving active tectonics. However, the seismicity database shows a potential threat in this region to host earthquakes of high intensity/magnitude. Examples include the historical earthquake in Fès-Meknès region at 1755 along the southern border of the Rif chain (Poujol et al., 2017), the Agadir earthquake of 1960 at the southern border of the Atlas chain (Paradise, 2005), the occurrence in Al Hoceima at 2004 along the Trans-Alboran shear zone at 6.4 Mw (van der Woerd et al., 2014), and the most recent catastrophe in El Haouz in 2023 within the High Atlas Chain (Fig. 1) at 6.8 Mw (Errazzouki, 2023; Hughes et al., 2024). The identification of active deformations in such regions has been a tough challenge since the distribution of tectonic activity may extend across various fault segments instead of being concentrated on a singular fault (Agharroud et al., 2021). Consequently, the seismogenic potential of such fault may be obscured, as seen in the recent reactivation of Tizi n'test fault system in the High Atlas the El Haouz earthquake of 2023.

The Middle Atlas appears to exhibit less tectonic activity when compared to the Rif and High Atlas chains. However, it remains an active mountain range, and the ongoing deformation is influenced by the plate convergence occurring between Africa and Eurasia (Lázaro et al., 2011; Sébrier et al., 2006). The instrumental seismicity shows various seismic events with magnitudes reaching up to 5.2 magnitude. The latest of which identified in 2024 is located 25 km north of Ifran city (Fig. 1). However, historical seismicity is limited and notably incomplete for the Middle Atlas. As a result, they do not provide sufficient information to supplement instrumental data. The seismic activity is potentially associated with NE-SW Tizi N'trettenne fault system, which

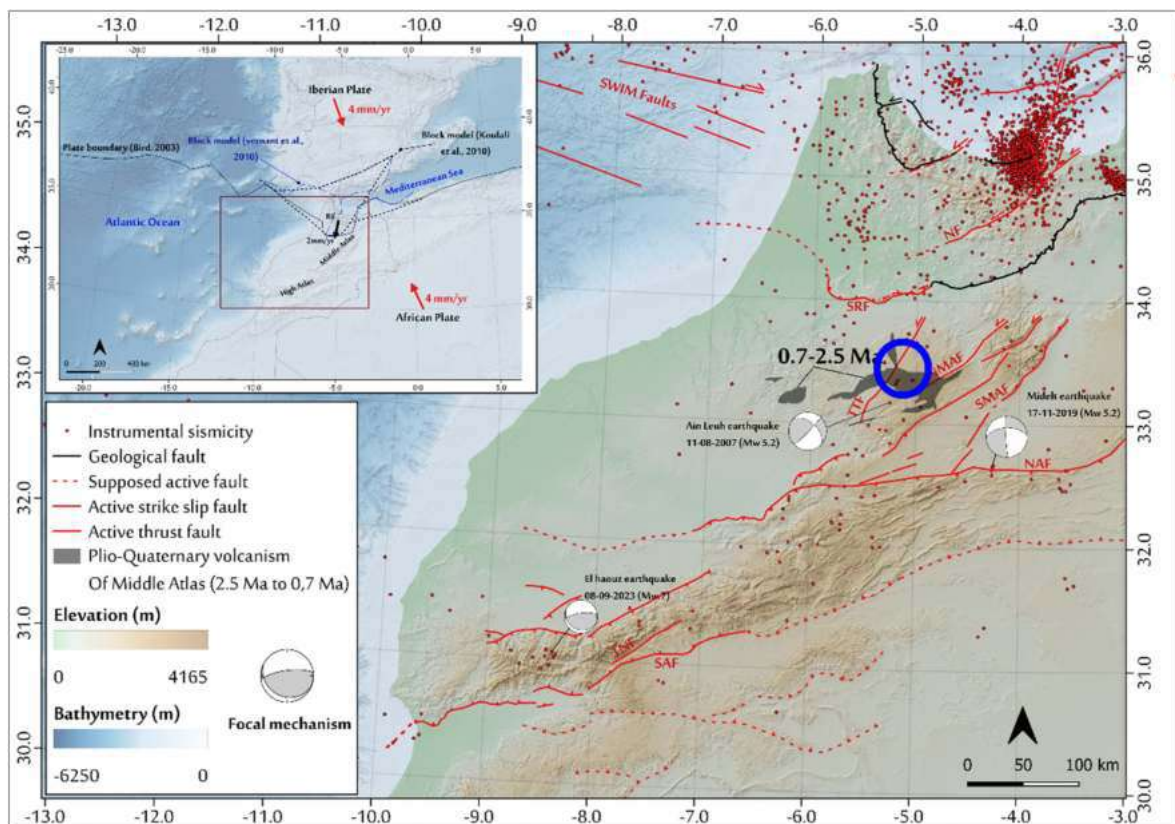


Fig. 1. Localization of the study area.

overlaps with the Middle Atlas Causse (Fig. 1). This is supported by the fact that (1) the seismicity distribution highlights a significant NE-SW trend that follows the Moroccan Hot Line, and (2) findings from micro-seismic monitoring campaign conducted by (Ramdani and Tadili, 1980).

The focal mechanism of these events involves a left lateral strike-slip with a shortening axis-oriented N-S to NW-SE (Aydin and Page, 1984; Hatzfeld and Frogneux, 1981; Kapetanidis and Kassaras, 2019). The Tizi n'trettenne fault system accommodates the displacement of the Prerif Ridge about 2 mm/yr, located at the southern border of the Rif chain, to SW and SSW with respect to stable Africa (Chalouan et al., 2014; Fadil et al., 2006). Additional faults in the Middle Atlas, as El Hajeb Fault, accommodate the deformation resulting from the displacement of the Prerif Ridge.

This study allows to highlight the active tectonics of an area which coincides with the trans-Moroccan Agadir-Nekkor fracture (Ait Brahim and Chotin, 1984) and at which a mantle rise is interpreted by (Frizon de Lamotte et al., 2000; Spakman and Wortel, 2004). The objective of this study is to identify regions where recent TTA activity has been active and where tectonic movement is strong by analyzing landscape change and how it relates to TTA activity. To do this, were used measurements of morphometric indices of the watersheds and the different watercourses coming from the Taïliloute anticlinal ridge. In this work, we are limited to the calculation and study of the following morphometric indices: Elongation index (Re), Asymmetry (AF), Hypsometric curve, Longitudinal profile standardized.

2. Data and methodology

The Tizi n'Teghtène Fault System, which stretches from the Ouiuane region (An Leuh Causse) in the south to the southern Rif valley in the north, is represented by the Taïliloute ridge (Fig. 1). It should be noted that this hill divides the Guigou Causse from the northwest by the Ifrane Causse. The ridge is oriented NE-SW between Lake Ifrah in the northeast and the Michlifène station in the southwest. It then shifts to an E-W orientation between Michlifène and the city of Azrou. A cluster of volcanoes that spew lava onto the Azrou plateau are what define the ridge's southern region (Baadi et al., 2021).

Instrumental seismicity data covers the period from 1950 to 2023 and is sourced from the Earthquake Hazards Program, available at <https://earthquake.usgs.gov/>. The active faults of the Moroccan Atlas are from (Sébrier et al., 2006). The SWIM faults in the Gulf of Cadiz are taken from (Serpelloni et al., 2007). Rif and Alboran faults are from (Galindo-Zaldívar et al., 2009; Poujol et al., 2017), and the southern Rif front is from (Agharroud et al., 2021). Focal mechanism data is sourced from the Harvard global centroid moment tensor catalog, adhering with the approaches of (Ekström et al., 2012). The data on elevation and bathymetry in background originate from the General Bathymetric Chart of the Oceans (GEBCO) (Sandwell et al., 2002).

The outcrops in the study area are largely carbonate and formed mainly of dolomites and limestones with different facies of lower and middle Lias age, currently strongly karstified. Volcanic cones, craters and huge basaltic outpourings cover the Azrou plateau in particular (Fig. 1). The quaternary volcanic products emitted are of a much more considerable quantity (i.e., >1500 km²) and represented by volcanics and very poorly evolved basic lavas (Garzanti et al., 2021; Verolino et al., 2022).

The shape of hydrographic networks and watersheds can provide indications of tectonics. Slow tectonic deformations can cause lateral migration of watercourses and watershed divides between basins (Kader et al., 2023; Kader et al., 2023; Vojtko et al., 2012). Thus, the slow tilting of a block stimulates the regressive erosion of small streams draining the uplifted part, which promotes the lateral migration of the main course towards the subsiding part (Kader et al., 2022; Puliti et al., 2022; Sestras et al., 2023). The 3rd order watersheds that exhibit lateral migrations during the Pleistocene (Gupta et al., 2022) are chosen for a study of

active faults in order to emphasize the significance and direction of watercourse displacement.

This work suggests using morphometric indices at eleven 3rd order watersheds to assess the tectonic activity at the Taïliloute ridge described by Table 1. The digital terrain model (DTM) for this study must be created using the geological map of Azrou at a scale of 1/50 000 and Shuttle Radar Topography Mission (SRTM) pictures. These photos are processed using remote sensing and geographic information system-specific features of software.

3. Results

3.1. Hypsometric curve and Hi

The hypsometric curve represents the distribution of a watershed's surface area as a function of elevation. The percentage of the watershed's surface area that is located above a particular altitude is expressed hypsometric curve (Bajracharya and Jain, 2022). The resulting hypsometric curve can take on a variety of shapes, including convex if the watershed is less damaged and tends to be younger, S-shaped when the watershed is mature, and concave when the watershed is very ancient and has experienced significant erosion. The hypsometric curve aids in identifying regions with younger and more active watersheds, which suggests a likelihood of relatively recent tectonic uplift in terms of active tectonics. Data from 11 watersheds around the Taïliloute anticlinal ridge in the study area's digital elevation model (DEM) were extracted to produce the hypsometric curves (Fig. 2).

The analysis of hypsometric curves (Fig. 3) shows that, apart from Tigriga 3 and Tizguite watersheds, which have concave curves, most of the watersheds have "S" shaped curves, indicating their maturity.

The Hi reflects the non-eroded relative volume: it is low for highly evolved watersheds known as concave curve and high for more immature watersheds commonly referred as convex curve (Banerjee et al., 2023; Ben Hassen et al., 2014; Khan et al., 2021). This index are calculated using a simple equation:

$$Hi = (H_{\text{mean}} - H_{\text{min}}) / (H_{\text{max}} - H_{\text{min}}) \quad (\text{Eq } 1)$$

Where.

Table 1
Different morphometric indices used in the evaluation of the active tectonics of the Taïliloute wrinkle.

Morphometric indices	Formulas	Description	Reference
Elongation index (Re)	$Re = \frac{2}{Lm} \left(\frac{A}{\pi} \right)^{0.5}$	A: total area of a watershed Lm: length of the watershed	Bull and McFadden (2020)
Watershed shape	$Bs = Lm/lm$	Lm: length of sub-basin; lm: width of sub-basin	Ramírez-Herrera (1998)
Asymmetry (AF)	$AF = 100(Ar/At)$	Ar: surface of the right part of a sub-basin. At: total surface of a watershed	Taloor et al. (2021)
Hypsometric curve	–	Distribution of the surface of a given sub-basin (a) as a function of its elevation (h)	Bajracharya and Jain (2022)
Hypsometric Index (HI)	$HI = (Hm - Hmin) / (Hmax - Hmin)$	Hm: average altitude; Hmax: maximum altitude; Hmin: minimum altitude	Ben Hassen et al. (2014)
Longitudinal profile standardized	Concavity IC	Ratio of normalized drain elevations to their normalized distance, plotted in a dimensionless graph	Phillips and Lutz (2008)

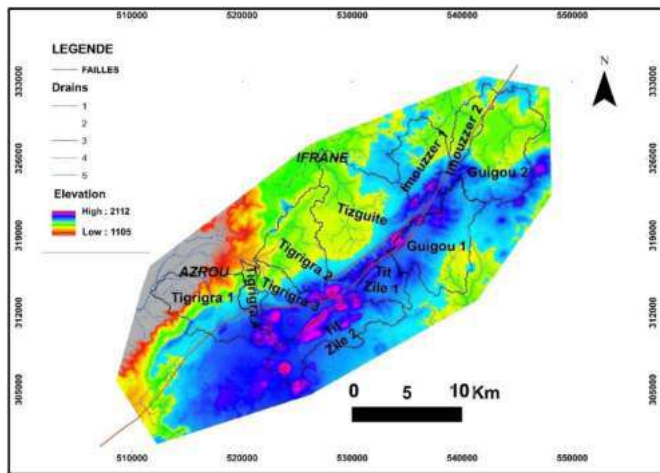


Fig. 2. Location of watersheds around the Taïliloute anticlinal ridge.

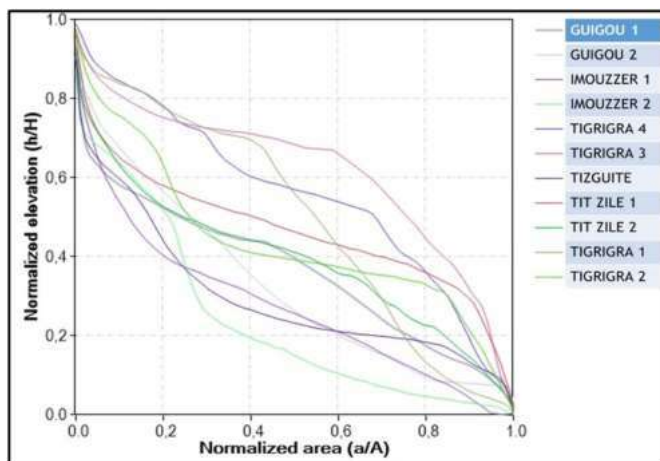


Fig. 3. Hypsometric curves of the watersheds around the Taïliloute anticlinal ridge.

- Hmean is the mean elevation of the watershed.
- Hmax is the maximum elevation.
- Hmin is the minimum elevation.

HI ranges from 0 to 1, and this range is subdivided into three subclasses.

- $HI \leq 0.3$ for an old watershed.
- $0.3 < HI \leq 0.6$ for a mature watershed
- $0.6 < HI \leq 1$ for a young watershed

Only the Imouzzar and Tizguite watersheds have HI values below 0.3, indicating that they are older watersheds. The watersheds in Guigou, Tit Zile, and Tigrigra 1, 2, and 4 are mature (0.3 HI 0.6), though. Thus, it may be deduced that the only younger watershed is the Tigrigra 3 one (Table 2).

3.2. Re and watershed shape

The Re of a watershed is defined as the ratio between the diameter of a circle with the same area as the watershed and the maximum length of the watershed (Benzougagh et al., 2022; Sutradhar and Mondal, 2023). It is calculated as follows:

Table 2

Some morphometric indices of the Taïliloute anticline.

Watershed	Area (Km ²)	RE	Bs	AF	Hi	IC
Tigrigra1	41,18	0,63	1,57	31,70	0,499	0,08
Tigrigra2	41,29	0,50	2,33	39,62	0,44	0,34
Tigrigra3	28,66	0,78	1,20	33,63	0,619	-0,11
Tigrigra4	9,02	0,49	2,52	60,13	0,558	-0,29
Tizguite	72,82	0,77	1,11	60,17	0,3	0,15
Imouzer1	26,06	0,73	1,65	35,40	0,277	-0,15
Imouzer2	17,90	0,44	3,91	63,32	0,239	0,05
Guigou1	47,02	0,72	1,57	18,33	0,368	0,36
Guigou2	52,34	0,73	1,63	46,80	0,332	0,37
Tit zile1	15,99	0,79	1,11	52,11	0,468	-0,04
Tit Zile2	35,01	0,49	3,25	19,83	0,396	0,01
Total	387,27					

$$Re = \frac{2}{Lm} \left(\frac{A}{\pi} \right)^{0,5} \tag{Eq 2}$$

Where.

- Re is the elongation ratio.
- A is the total area of the watershed, $2 (A/\pi)^{0,5}$ is the diameter of a circle with the same area as the basin.
- π is the mathematical constant pi.
- Lmax is the maximum length of the watershed.

The Re is an important parameter that characterizes the shape of a watershed. Re's are grouped into three categories (Patel and Parekh, 2021): circular (>0.9), oval (0.9–0.8), and elongated (<0.7).

The shape of watersheds (Bs) varies from elongated in highly active regions to circular in older watersheds (Taye et al., 2023). The watershed shape index is defined as follows:

$$Bs = \frac{Lm}{lm} \tag{Eq 3}$$

Where.

- Bs is the watershed shape index.
- Lmax is the maximum length of the watershed.
- Lmin is the minimum length of the watershed.

High values of Bs characterize elongated watersheds in active regions, while low values are typical of circular older watersheds. Based on the Re index, the maximum elongation is observed in the Imouzzar 2 watershed ($Re = 0.44$) northwest of the Taïliloute ridge, while the minimum elongation is observed in the Tit Zile 2 watershed ($Re = 0.79$) southeast of the ridge. However, the Bs index shows maximum elongation in the Imouzzar 2 watershed ($Bs = 3.91$) and minimum elongation in the Tit Zile 1 and Tizguite watersheds ($Bs = 1.1$).

The relationship between the Bs and Re indices can provide information on watersheds where tectonics are more active (Alizadeh et al., 2020). This relationship is illustrated in Fig. 4, the blue curve shows the variation of Bs, and the red curve shows the variation of Re in the different watersheds. Active tectonics are more significant where the Bs and Re curves diverge from each other and less significant where the watershed shape becomes almost circular, and the curves converge. These results show that five watersheds have a relatively high elongation, namely Tigrigra 2, Tigrigra 4, Imouzzar 2 on the Cause d'Ifrane, and Tit Zile 2 on the Guigou Plateau. Therefore, it is in these watersheds that tectonics are more active compared to the other watersheds where tectonics are less active.

It was observed that the watersheds with maximum elongation are located at the NE and SW ends of the Taïliloute anticlinal ridge (Fig. 5).

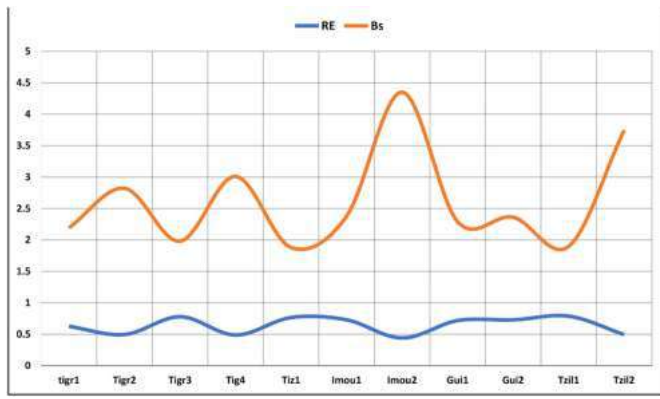


Fig. 4. Comparison between Bs and Re.

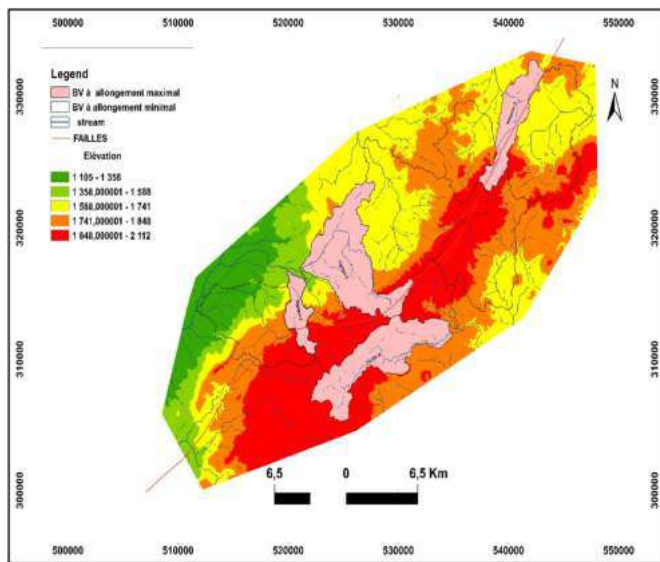


Fig. 5. Location of watersheds with maximum elongation in the Taililoute wrinkle.

3.3. Computation of AF

Formula for AF was developed to detect the tectonic tilting of watersheds as a whole due to asymmetric uplift across a specific landscape (Taloor et al., 2021). The asymmetry factor is calculated as follows:

$$AF = 100 \frac{Ar}{At} \quad (\text{Eq 4})$$

Where.

- AF: Asymmetry factor
- At: Total area of a watershed.
- Ar: Area on the right side of the mainstream in the watershed.

In stable regions, AF should be equal to or close to 50. Values above and below 50 for AF indicate uplift of the right and left sides of the watershed, respectively. The AF value in the Tigrigra 4, Tizguite 1, and Imouzzar 2 watersheds is greater than 50 (Table 2) and demonstrates uplift of the right side of these watersheds, while the AF value in the other watersheds is less than 50 and shows uplift of the left side of these watersheds. It should be noted that all watersheds on the Guigou plateau have an AF index <50 (Fig. 6). There are 7 watersheds with low AF and are located at the NE and SW ends of the Taililoute anticlinal ridge.

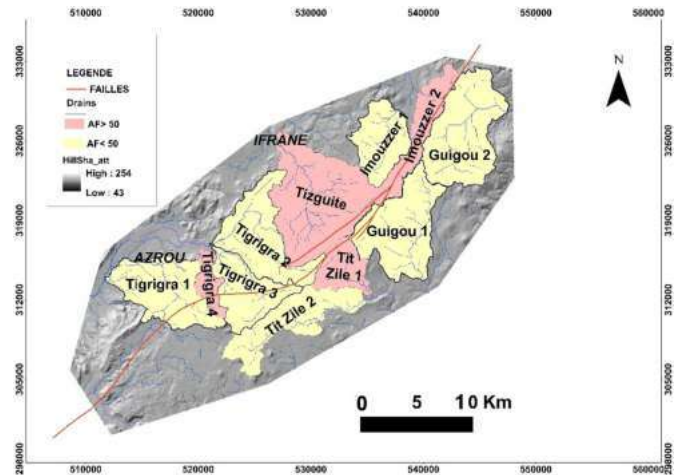


Fig. 6. Distribution of watersheds by AF

3.4. The longitudinal profiles of the wadis of the TTF

The longitudinal profile of a river is a graph that shows the variation of the elevation of the bed or valley floor with distance. The longitudinal profiles of rivers result from the interaction between fluvial incision, tectonics, and lithology (Fisher et al., 2022). According to models of longitudinal profile evolution, the older a river is, the more concave and closer to dynamic equilibrium its profile becomes. Most geomorphologists consider that longitudinal profiles of rivers exhibit the shape of an exponential concave curve (Billi, 2022; Khan et al., 2021). However, these curves may have interruptions by knickpoints, which are points where an abrupt change in slope is observed. The presence of knickpoints on a profile is often associated with instability of the control variables. In the study area, the Guigou 1, Guigou 2, Tizguite, and Tigrigra 2 streams are concave, indicating that they are older. The Imouzzar 1, Tigrigra 3, and Tigrigra 4 streams are convex, while the other streams are linear, indicating that they are young. All the streams have at least two knickpoints each (Fig. 7).

To evaluate and compare the concavities of longitudinal profiles, the concavity indices IC of Langbein (Mvondo Owono et al., 2016) were used:

$$IC = 2A/H \quad (\text{Eq 5})$$

Where.

- A = difference in altitude between the profile at midstream and a straight line joining the two ends of the profile,
- H = difference in height between the source and the outlet of the drain.

The profile tends to be straight when the value of IC is close to 0; conversely, when IC = -1 the profile is extremely convex and when IC = 1 the profile is extremely concave. In the Taililoute anticlinal ridge (Table 2), the IC values of 7 streams are close to zero or negative. This suggests that the flow profiles tend to be convex, as also shown by the general shape of the longitudinal profiles.

4. Discussion

The Taililoute anticlinal ridge, a section of the Middle Atlas Thrust that is considered a positive flower structure (Driss, 2016), is a watershed divide between the tributaries of the Beht and El Kantra rivers to the NW and the tributaries of the Guigou river to the SE. Analysis of 3rd order watersheds shows that they are elongated in the same direction as the Middle Atlas (NE-SW) and not in the direction of the flow, which is

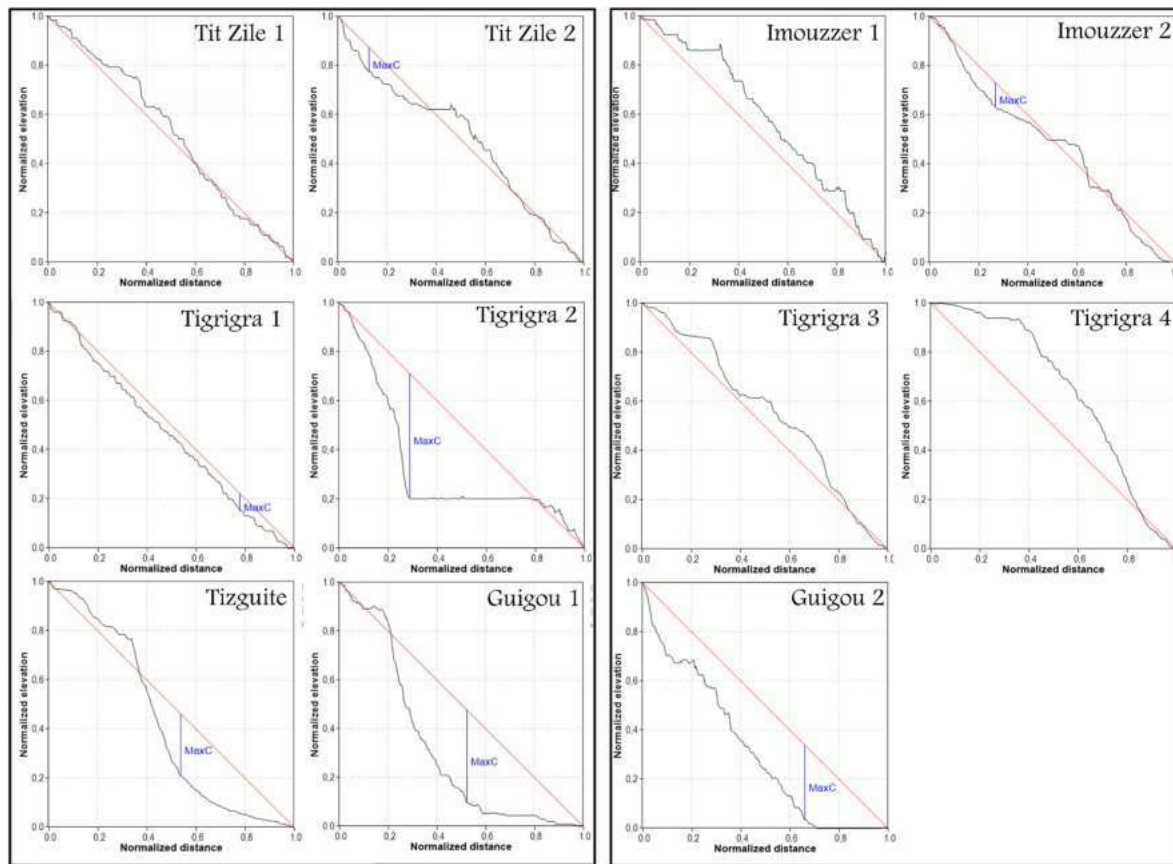


Fig. 7. Longitudinal profiles of the rivers of the Taililoute rift.

NW-SE. This suggests that there is a strike-slip reactivation leaving pull-apart basins at the relay of fault segments. These watersheds are mostly convex, with a H_i close to 0.40, indicating that the watersheds are in a juvenile stage and controlled by tectonic uplift that is being discussed in past studies like (Baranov et al., 2023; Ngapna et al., 2020; Séranne and Anka, 2005; Strahler, 1952). Analysis of the main streams in the study area shows that their longitudinal profiles are generally straight into convex and each present at least two knickpoints. This indicates that these streams are more recent, and the slope interruptions are explained by fault crossings.

The TTF is a fault inherited from the opening of the Tethys Ocean and acted as a normal fault during the Tethys rifting period. During the early Cenozoic era, inversion tectonics occurred as a result of the African and Eurasian plates convergence, leading to the formation of the Atlas Mountains, which includes the Taililoute anticlinal ridge. Due to oblique stresses resulting from this convergence, the TTF fault switched to left-lateral strike-slip, contributing to the development of the flower structure fold observed in the Taililoute anticlinal ridge. The TTF exhibited left-lateral strike-slip movement during the Quaternary period. Evidence of this Quaternary phase of the Alpine orogeny has been identified in the sedimentary archives of Lake Ifrah, which date from 8640 years BP (El Bait et al., 2014), and the basalts of the Middle Atlas volcanic province, including the age varies between 2.5 and 0.7 Ma (Azenoud et al., 2022; El Azzouzi et al., 2010). Continually reactivating TTF faults are inferred from morphometric indices conducted on the Taililoute anicline ridge. These reactivations induce polje-shaped depressions when the bottom of the poljes reaches the Triassic clays, the depression is filled with water and forms a lake, as is the case with Lake Ifrah in the NE of the Taililoute anticlinal ridge. Other studies of geomorphological indices in the Moulouya watershed, which crosses a part of the Middle Atlas, have confirmed the recent activity of the TTF (Díaz-Azpiroz et al., 2014; El Hmaidi et al., 2022), which is

characterized by significant uplift and a high distribution of slope breaks.

The activity of the TTF could be related to inherited NW-SE oriented faults that cross the southern front of the Rif chain towards the Middle Atlas. These faults control the evolution of the landscape in this sector (Agharroud et al., 2021; Youssef et al., 2023), and they extend towards the Middle Atlas where they may propagate tectonic activity. This activity is marked by seismicity in this zone. It appears that the recent tectonic activity of the TTF is generally related to regional geodynamics explained by a model of lithospheric delamination or the rollback process of a subducting slab (Bezada et al., 2013). This geodynamics results from a collision between the African and Iberian plates and the Betic-Alboran-Rif block (Baratin et al., 2016), where the Middle Atlas is situated directly at the boundary between Africa and the southern front of the BAR block.

5. Conclusion

This research study highlighted the importance of geomorphological indices as powerful tools to assess tectonic activity within the Taililoute anticlinal ridge and the broader Middle Atlas region. It was observed that most of the hypsometric curves are convex, the H_i index is greater than 0.3 for most watersheds in the study area. According to the findings, the watersheds are elongated ($Re < 0.7$ and $Bs > 1$) which confirms that the watersheds are young, therefore susceptible for tectonic activities. The study of the longitudinal profiles of the rivers of the Taililoute anticlinal ridge are for the most part convex and the IC index of seven drains is close to zero or negative. This suggests that flow profiles tend to be convex, so they are tectonically active. The results unequivocally demonstrate that the Taililoute anticlinal ridge is actively undergoing deformation. This conclusion is supported by convincing evidence of reactivated TTF left-lateral strike slip fault encountered in the recent

sedimentary deposits of Lake Ifrah and in the Quaternary basalts of the Azrou Plateau.

The use of geomorphological indices in this study holds great promise for advancing the understanding of tectonic evolution in the Middle Atlas region. These indices not only effectively distinguish between active and dormant tectonic zones, but also provide essential information on the extent of deformation and uplift. Therefore, we advocate for the continued application of these indices in future investigations focused on the Tailililoute anticlinal ridge and the broader Middle Atlas region. Such efforts will undoubtedly contribute to a better understanding of the dominant tectonic dynamics in this area, which may have considerable implications for seismic risk assessment and informed land use planning, thereby extending the relevance of the research beyond immediate geographic boundaries.

Declarations

Ethical Approval	Not Applicable
Consent to Participate	Not Applicable
Consent to Publish	Not Applicable
Authors Contributions	<ol style="list-style-type: none"> 1. Conceived and designed the studies - Driss Sadkaoui, Benzougagh Brahim, Kamal Agharroud, Abdel-Ilah Mihraje, Khadija Aluni, Habiba Aassoumi, and Slimane Sassioui 2. Performed the analysis - Driss Sadkaoui, Kamal Agharroud, Abdel-Ilah Mihraje, Khadija Aluni, Habiba Aassoumi, and Slimane Sassioui 3. Analyzed and interpreted the data - Driss Sadkaoui, Benzougagh Brahim, Shuraik Kader, Kamal Agharroud, Abdel-Ilah Mihraje, Khadija Aluni, Habiba Aassoumi, Slimane Sassioui, Velibor Spalevic, and Paul Sestras 4. Contributed materials, analysis tools or data - Kamal Agharroud, Abdel-Ilah Mihraje, and Slimane Sassioui 5. Authored the paper - Driss Sadkaoui, Benzougagh Brahim, Shuraik Kader, Kamal Agharroud, Abdel-Ilah Mihraje, Khadija Aluni, Habiba Aassoumi, Slimane Sassioui, Velibor Spalevic, Paul Sestras 6. Internal reviewers –Benzougagh Brahim, Shuraik Kader, Kamal Agharroud, Velibor Spalevic, Paul Sestras 7. Project administration – Driss Sadkaoui, Benzougagh Brahim, Shuraik Kader and Velibor Spalevic <p>All authors have read and approved the final version of the manuscript.</p>
Funding	Not Applicable
Competing interests	The authors have no relevant financial or non-financial interests to disclose
Availability of data and materials	The data and materials will be available for review upon request by the journal to the corresponding author.
Computer Code Availability section	"No code or software has been developed for this research."

CRediT authorship contribution statement

Driss Sadkaoui: Writing – original draft, Visualization, Validation, Software, Resources, Methodology, Investigation, Formal analysis, Data curation, Conceptualization. **Benzougagh Brahim:** Writing – review & editing, Writing – original draft, Visualization, Validation, Supervision, Software, Resources, Project administration, Methodology, Investigation, Data curation, Conceptualization. **Shuraik Kader:** Writing – review & editing, Writing – original draft, Visualization, Validation, Software, Methodology, Investigation, Formal analysis, Data curation. **Kamal Agharroud:** Writing – review & editing, Writing – original draft, Visualization, Validation, Software, Resources, Methodology, Investigation, Formal analysis, Data curation, Conceptualization. **Abdel-Ilah Mihraje:** Writing – original draft, Visualization, Validation, Software,

Resources, Methodology, Investigation, Formal analysis, Data curation, Conceptualization. **Khadija Aluni:** Writing – original draft, Visualization, Validation, Software, Resources, Methodology, Investigation, Formal analysis, Data curation, Conceptualization. **Habiba Aassoumi:** Writing – original draft, Visualization, Validation, Methodology, Investigation, Formal analysis, Data curation, Conceptualization. **Slimane Sassioui:** Writing – original draft, Visualization, Validation, Software, Resources, Methodology, Investigation, Formal analysis, Data curation, Conceptualization. **Velibor Spalevic:** Writing – review & editing, Writing – original draft, Visualization, Validation, Supervision, Project administration, Methodology, Investigation, Formal analysis, Data curation. **Paul Sestras:** Writing – original draft, Visualization, Validation, Methodology, Investigation, Formal analysis, Data curation.

Declaration of competing interest

The authors declare that they have no known competing financial interests or personal relationships that could have appeared to influence the work reported in this paper.

Data availability

Data will be made available on request.

References

- Agharroud, K., Siame, L.L., Ben Moussa, A., Bellier, O., Guillou, V., Fleury, J., El Kharim, Y., 2021. Seismo-tectonic model for the southern Pre-Rif border (Northern Morocco): insights from morphochronology. *Tectonics* 40 (4), e2021T0006633. <https://doi.org/10.1029/2020T0006633>.
- Ait Brahim, L., Chotin, P., 1984. Mise en évidence d'un changement de direction de compression dans l'avant-pays rifain (Maroc) au cours du Tertiaire et du Quaternaire. *Bull. Soc. Geol. Fr.* 7 (4), 681–691. <https://doi.org/10.2113/gssgfbull.S7-XXVI.4.681>.
- Alizadeh, A., Hormozi Moghadam, H., Seraj, M., 2020. DEM-derived geomorphic indices for assessment of tectonic activity at the Dara anticlinal oil structure within the Zagros fold-thrust belt, southwestern Iran. *Arabian J. Geosci.* 13 (4), 192. <https://doi.org/10.1007/s12517-020-5156-8>.
- Amine, A., El Ouardi, H., Zebari, M., El Makrini, H., 2020. Active tectonics in the moulay idriss massif (south rifian ridges, NW Morocco): new insights from geomorphic indices and drainage pattern analysis. *J. Afr. Earth Sci.* 167, 103833 <https://doi.org/10.1016/j.jafrearsci.2020.103833>.
- Aydin, A., Page, B.M., 1984. Diverse pliocene-quaternary tectonics in a transform environment, San Francisco Bay region, California. *Geol. Soc. Am. Bull.* 95 (11), 1303–1317. [https://doi.org/10.1130/0016-7606\(1984\)95<1303:DPTIAT>2.0.CO;2](https://doi.org/10.1130/0016-7606(1984)95<1303:DPTIAT>2.0.CO;2).
- Azenoud, K., Baali, A., El Asmi, H., Ait Brahim, Y., Hakam, O., Hayati, A., El Kamel, T., 2022. Soft-sediment deformation structures recognised in a reverse-drag associated with normal faulting (Lake Ifrah, Northwest Africa): palaeoseismic assessment and neotectonic implications. *Sediment. Geol.* 441, 106264 <https://doi.org/10.1016/j.sedgeo.2022.106264>.
- Baadi, K., Amine, A., Zangmo Tefogoum, G., Sabaoui, A., Teikiout, B., 2021. Volcanic geosites assessment in the plio-quaternary azrou-timahdite plateau (middle Atlas, Morocco). *J. Afr. Earth Sci.* 184, 104352 <https://doi.org/10.1016/j.jafrearsci.2021.104352>.
- Bajracharya, P., Jain, S., 2022. Hydrologic similarity based on width function and hypsometry: an unsupervised learning approach. *Comput. Geosci.* 163, 105097 <https://doi.org/10.1016/j.cageo.2022.105097>.
- Banerjee, M., Ghosh, D., Pal, S., Karmakar, M., 2023. Geomorphic assessment of longitudinal profile of the Kanchi river basin, India: recognition of dynamic equilibrium condition. *Phys. Geogr.* 44 (2), 162–185. <https://doi.org/10.1080/02723646.2021.1978139>.
- Baranov, A., Tenzer, R., Eitel Kemgang Ghomsfi, F., 2023. A new Moho map of the African continent from seismic, topographic, and tectonic data. *Gondwana Res.* 124, 218–245. <https://doi.org/10.1016/j.jgr.2023.06.019>.
- Baratin, L.-M., Mazzotti, S., Chéry, J., Vernant, P., Tahayt, A., Mourabit, T., 2016. Incipient mantle delamination, active tectonics and crustal thickening in Northern Morocco: insights from gravity data and numerical modeling. *Earth Planet Sci. Lett.* 454, 113–120. <https://doi.org/10.1016/j.epsl.2016.08.041>.
- Baruah, M.P., Bezbaruah, D., Goswami, T., 2022. Active tectonics deduced from geomorphic indices and its implication on economic development of water resources in South-Eastern part of Mikir massif, Assam, India. *Geology, Ecology, and Landscapes* 6 (2), 99–112.
- Bashir, O., Bangroo, S.A., Shafai, S.S., Senesi, N., Kader, S., Alamri, S., 2024. Geostatistical modeling approach for studying total soil nitrogen and phosphorus under various land uses of North-Western Himalayas. *Ecol. Inf.* 80, 102520 <https://doi.org/10.1016/j.ecoinf.2024.102520>.

- Ben Hassen, M., Deffontaines, B., Turki, M.M., 2014. Recent tectonic activity of the Gafsa fault through morphometric analysis: southern Atlas of Tunisia. *Quat. Int.* 338, 99–112. <https://doi.org/10.1016/j.quaint.2014.05.009>.
- Benzougagh, B., Meshram, S.G., Dridri, A., Boudad, L., Baamar, B., Sadkaoui, D., Khedher, K.M., 2022. Identification of critical watershed at risk of soil erosion using morphometric and geographic information system analysis. *Appl. Water Sci.* 12, 1–20. <https://doi.org/10.1007/s13201-021-01532-z>.
- Bezada, M.J., Humphreys, E.D., Toomey, D.R., Harnafi, M., Dávila, J.M., Gallart, J., 2013. Evidence for slab rollback in westernmost Mediterranean from improved upper mantle imaging. *Earth Planet. Sci. Lett.* 368, 51–60. <https://doi.org/10.1016/j.epsl.2013.02.024>.
- Bhat, M.A., Dar, T., Bali, B.S., 2020. Morphotectonic analysis of Aripal Basin in the North-Western Himalayas (India): an evaluation of tectonics derived from geomorphic indices. *Quat. Int.* 568, 103–115. <https://doi.org/10.1016/j.quaint.2020.10.032>.
- Billi, P., 2022. Geomorphology of Eritrean river systems. In: *Landscapes and Landforms of the Horn of Africa: Eritrea, Djibouti, Somalia*. Springer, pp. 125–153.
- Bull, W.B., McFadden, L.D., 2020. Tectonic geomorphology north and south of the Garlock fault, California. In: *Geomorphology in Arid Regions*. Routledge, pp. 115–138.
- Chalouan, A., Gil, A.J., Galindo-Zaldívar, J., Ahmamou, M.F., Ruano, P., de Lacy, M.C., Riguzzi, F., 2014. Active faulting in the frontal Rif cordillera (Fes region, Morocco): constraints from GPS data. *J. Geodyn.* 77, 110–122. <https://doi.org/10.1016/j.jog.2014.01.002>.
- Díaz-Azpiroz, M., Barcos, L., Balanyá, J.C., Fernández, C., Expósito, I., Czeck, D.M., 2014. Applying a general triclinic transpression model to highly partitioned brittle-ductile shear zones: a case study from the Torcal de Antequera massif, external Betics, southern Spain. *J. Struct. Geol.* 68, 316–336. <https://doi.org/10.1016/j.jsg.2014.05.010>.
- Driss, S., 2016. Etude géomorpho-structurale de la région d'Ifrane-Guigou (Moyen Atlas, Maroc).
- Ekström, G., Nettles, M., Dzierwowski, A.M., 2012. The global CMT project 2004–2010: centroid-moment tensors for 13,017 earthquakes. *Phys. Earth Planet. In.* 200–201, 1–9. <https://doi.org/10.1016/j.pepi.2012.04.002>.
- El Azzouzi, M.H., Maury, R.C., Bellon, H., Youbi, N., Cotten, J., Kharbouch, F., 2010. Petrology and K-Ar chronology of the neogene-quaternary middle Atlas basaltic province, Morocco. *Bull. Soc. Geol. Fr.* 181 (3), 243–257.
- El Bait, M.N., Rhoujjati, A., Eynaud, F., Benkaddour, A., Dezileau, L., Wainer, K., Cheddadi, R., 2014. An 18 000-year pollen and sedimentary record from the cedar forests of the Middle Atlas, Morocco. *J. Quat. Sci.* 29 (5), 423–432. <https://doi.org/10.1002/jqs.2708>.
- El Hmaidi, A., Talhaoui, A., Manssouri, I., Jaddi, H., Ben-Daoud, M., Kasse, Z., Essahlaoui, A., 2022. Assessment of the physicochemical water quality of the Moulouya River, Morocco, using the SEQ-Eau index. *Environ. Monit. Assess.* 194, 1–17. <https://doi.org/10.1007/s10661-021-09636-4>.
- Errazouki, S., 2023. Between rubble and rage: reflections on the earthquake in Morocco and its aftermath. *J. N. Afr. Stud.* 1–9. <https://doi.org/10.1080/13629387.2023.2294509>.
- Fadil, A., Vernant, P., McClusky, S., Reilinger, R., Gomez, F., Ben Sari, D., Barazangi, M., 2006. Active tectonics of the western Mediterranean: geodetic evidence for rollback of a delaminated subcontinental lithospheric slab beneath the Rif Mountains, Morocco. *Geology* 34 (7), 529–532. <https://doi.org/10.1130/G22291.1>.
- Fisher, J., Pazzaglia, F., Anastasio, D., Gallen, S., 2022. Linear inversion of fluvial topography in the northern apennines: comparison of base-level fall to crustal shortening. *Tectonics* 41 (11), e2022TC007379. <https://doi.org/10.1029/2022TC007379>.
- Frizon de Lamotte, D., Saint Bezar, B., Bracène, R., Mercier, E., 2000. The two main steps of the Atlas building and geodynamics of the western Mediterranean. *Tectonics* 19 (4), 740–761. <https://doi.org/10.1029/2000TC900003>.
- Galindo-Zaldívar, J., Chalouan, A., Azzouz, O., Sanz de Galdeano, C., Anahnah, F., Ameza, L., Chabli, A., 2009. Are the seismological and geological observations of the Al Hoceima (Morocco, Rif) 2004 earthquake (M=6.3) contradictory? *Tectonophysics* 475 (1), 59–67. <https://doi.org/10.1016/j.tecto.2008.11.018>.
- Garzanti, E., Capaldi, T., Vezzoli, G., Limonta, M., Sosa, N., 2021. Transcontinental retroarc sediment routing controlled by subduction geometry and climate change (Central and Southern Andes, Argentina). *Basin Res.* 33 (6), 3406–3437. <https://doi.org/10.1111/bre.12607>.
- Gupta, L., Agrawal, N., Dixit, J., Dutta, S., 2022. A GIS-based assessment of active tectonics from morphometric parameters and geomorphic indices of Assam Region, India. *J. Asian Earth Sci.* X 8, 100115. <https://doi.org/10.1016/j.jaesx.2022.100115>.
- Hatzfeld, D., Frogneux, M., 1981. Intermediate depth seismicity in the western Mediterranean unrelated to subduction of oceanic lithosphere. *Nature* 292 (5822), 443–445. <https://doi.org/10.1038/292443a0>.
- Hughes, P.D., Bell, B.A., Fletcher, W.J., Braithwaite, R.J., Cornelissen, H.L., Fink, D., Rhoujjati, A., 2024. Chapter 24 - holocene glacial landscapes of the Atlas mountains, Morocco. In: Palacios, D., Hughes, P.D., Jomelli, V., Tanarro, L.M. (Eds.), *European Glacial Landscapes*. Elsevier, pp. 475–491.
- Jani, C., Kandregula, R.S., Bhosale, S., Chavan, A., Lakhote, A., Bhandari, S., Thakkar, M. G., 2021. Delineation of tectonically active zones in the Island Belt Uplift region, Kachchh Basin, western India: a geomorphic and geodetic approach. *Quaternary Science Advances* 4, 100034. <https://doi.org/10.1016/j.qsa.2021.100034>.
- Ji, Y., Su, S., Liu, Z., Huang, Q., 2021. Assessment of tectonic activity based on the geomorphic indices in the middle reaches of the upstream of Jinsha River, China. *Geol. J.* 56 (8), 3974–3991. <https://doi.org/10.1002/gj.4148>.
- Kader, S., Jauffer, L., Bashir, O., Raimi, M.O., 2023a. A comparative study on the stormwater retention of organic waste substrates biochar, sawdust, and wood bark recovered from psidium guajava L. Species. *Agric. For.* 69 (1), 105–112. <https://doi.org/10.17707/AgricForest.69.1.09>.
- Kader, S., Novicevic, R., Jauffer, L., 2022. Soil management in sustainable agriculture: analytical approach for the ammonia removal from the dairy manure. *J. Agric. For.* 68 (4), 69–78. <https://doi.org/10.17707/AgricForest.68.4.06>.
- Kader, S., Raimi, M.O., Spalevic, V., Iyngiala, A.-A., Bukola, R.W., Jauffer, L., Butt, T.E., 2023b. A concise study on essential parameters for the sustainability of Lagoon waters in terms of scientific literature. *Turk. J. Agric. For.* 47 (3), 288–307. <https://doi.org/10.55730/1300-011X.3087>.
- Kapetanidis, V., Kassaras, I., 2019. Contemporary crustal stress of the Greek region deduced from earthquake focal mechanisms. *J. Geodyn.* 123, 55–82. <https://doi.org/10.1016/j.jog.2018.11.004>.
- Kelemen, P., Dunkl, I., Csillag, G., Mindszenty, A., Józsa, S., Fodor, L., von Eynatten, H., 2023. Origin, timing and paleogeographic implications of Paleogene karst bauxites in the northern Transdanubian range, Hungary. *Int. J. Earth Sci.* 112 (1), 243–264. <https://doi.org/10.1007/s00531-022-02249-3>.
- Khan, S., Fryirs, K.A., Ralph, T.J., 2021. Geomorphic controls on the diversity and patterns of fluvial forms along longitudinal profiles. *Catena* 203, 105329. <https://doi.org/10.1016/j.catena.2021.105329>.
- Lázaro, E.M., Harrath, A.H., Stocchino, G.A., Pala, M., Bagnà, J., Riutort, M., 2011. Schmidtea mediterranea phylogeography: an old species surviving on a few Mediterranean islands? *BMC Evol. Biol.* 11, 1–15. <https://doi.org/10.1186/1471-2148-11-274>.
- Mvondo Owono, F., Ntamak-Nida, M.-J., Dauteuil, O., Guillocheau, F., Njom, B., 2016. Morphology and long-term landscape evolution of the South African plateau in South Namibia. *Catena* 142, 47–65. <https://doi.org/10.1016/j.catena.2016.02.012>.
- Ngapna, M.N., Owona, S., Owono, F.M., Ateba, C.B., Tsimi, V.M., Ondoa, J.M., Ekodeck, G.E., 2020. Assessment of relative active tectonics in edea – eseka region (SW Cameroon, central Africa). *J. Afr. Earth Sci.* 164, 103798. <https://doi.org/10.1016/j.jafrearsci.2020.103798>.
- Othman, A.T., Omar, A.A., 2023. Evaluation of relative active tectonics by using geomorphic indices of the Bamo anticline, Zagros Fold-Thrust Belt, Kurdistan Region of Iraq. *Heliyon* 9 (7), 44001. <https://doi.org/10.1016/j.heliyon.2023.e17970>.
- Ouallali, A., Kader, S., Bammou, Y., Aqnoy, M., Courba, S., Beroho, M., Hysa, A., 2024. Assessment of the erosion and outflow intensity in the Rif region under different land use and land cover scenarios. *Land* 13 (2). <https://doi.org/10.3390/land13020141>.
- Paradise, T.R., 2005. Perception of earthquake risk in Agadir, Morocco: a case study from a Muslim community. *Global Environ. Change B Environ. Hazards* 6 (3), 167–180. <https://doi.org/10.1016/j.hazards.2006.06.002>.
- Parrino, N., Burrato, P., Sulli, A., Gasparo Morticelli, M., Agate, M., Srivastava, E., Di Maggio, C., 2023. Plio-Quaternary coastal landscape evolution of north-western Sicily (Italy). *J. Maps* 1–13. <https://doi.org/10.1080/17445647.2022.2159889>.
- Patel, S.N., Parekh, F., 2021. Analysis of river meandering and morphometric parameters using remote sensing and GIS. In: *Paper Presented at the International Conference on Hydraulics, Water Resources and Coastal Engineering*.
- Phillips, J.D., Lutz, J.D., 2008. Profile convexities in bedrock and alluvial streams. *Geomorphology* 102 (3), 554–566. <https://doi.org/10.1016/j.geomorph.2008.05.042>.
- Poujol, A., Ritz, J.-F., Vernant, P., Huot, S., Maate, S., Tahayt, A., 2017. Which fault destroyed Fes city (Morocco) in 1755? A new insight from the Holocene deformations observed along the southern border of Gibraltar arc. *Tectonophysics* 712–713, 303–311. <https://doi.org/10.1016/j.tecto.2017.05.036>.
- Puliti, I., Pucci, S., Villani, F., Porreca, M., Benedetti, L., Robustelli, G., Stella, G., 2022. Estimating the long-term slip rate of active normal faults: the case of the Paganica Fault (Central Apennines, Italy). *Geomorphology* 415, 108411. <https://doi.org/10.1016/j.geomorph.2022.108411>.
- Ramandi, M., Tadili, B., 1980. Sismicité détaillée du Moyen-Atlas: sondages sismiques profonds dans le Maroc central. *Th&e Dr. de 3e cycl. Université Scientifique Grenoble*.
- Ramírez-Herrera, M.T., 1998. Geomorphic assessment of active tectonics in the Acambay Graben, Mexican volcanic belt. *Earth Surf. Process. Landforms: The journal of the british Geomorphological Group* 23 (4), 317–332. [https://doi.org/10.1002/\(SICI\)1096-9837\(199804\)23:4%3C317::AID-ESP845%3E3.0.CO;2-V](https://doi.org/10.1002/(SICI)1096-9837(199804)23:4%3C317::AID-ESP845%3E3.0.CO;2-V).
- Sandwell, D.T., Sichoix, L., Smith, B., 2002. The 1999 Hector Mine earthquake, southern California: vector near-field displacements from ERS InSAR. *Bull. Seismol. Soc. Am.* 92 (4), 1341–1354. <https://doi.org/10.1785/0120000901>.
- Sébrier, M., Siamé, L., Zouine, E.M., Winter, T., Missenard, Y., Leturmy, P., 2006. Active tectonics in the Moroccan high Atlas. *Compt. Rendus Geosci.* 338 (1), 65–79. <https://doi.org/10.1016/j.crte.2005.12.001>.
- Séranne, M., Anka, Z., 2005. South Atlantic continental margins of Africa: a comparison of the tectonic vs climate interplay on the evolution of equatorial west Africa and SW Africa margins. *J. Afr. Earth Sci.* 43 (1), 283–300. <https://doi.org/10.1016/j.jafrearsci.2005.07.010>.
- Serpelloni, E., Vannucci, G., Pondrelli, S., Argani, A., Casula, G., Anzidei, M., Gasperini, P., 2007. Kinematics of the Western Africa-Eurasia plate boundary from focal mechanisms and GPS data. *Geophys. J. Int.* 169 (3), 1180–1200. <https://doi.org/10.1111/j.1365-246X.2007.03367.x>.
- Sestras, P., Mircea, S., Roşca, S., Bilaşco, Ş., Sălăgean, T., Dragomir, L.O., Kader, S., 2023. GIS based soil erosion assessment using the USLE model for efficient land management: a case study in an area with diverse pedo-geomorphological and bioclimatic characteristics. *Not. Bot. Horti Agrobot. Cluj-Napoca* 51 (3). <https://doi.org/10.15835/nbha51313263, 13263-13263>.
- Spakman, W., Wortel, R., 2004. A tomographic view on western Mediterranean geodynamics. In: *The TRANSMED Atlas. The Mediterranean Region from Crust to*

- Mantle: Geological and Geophysical Framework of the Mediterranean and the Surrounding Areas. Springer, pp. 31–52.
- Strahler, A.N., 1952. Hypsometric (area-altitude) analysis of erosional topography. *Geol. Soc. Am. Bull.* 63 (11), 1117–1142.
- Sutradhar, S., Mondal, P., 2023. Prioritization of watersheds based on morphometric assessment in relation to flood management: a case study of Ajay river basin, Eastern India. *Watershed Ecology and the Environment* 5, 1–11. <https://doi.org/10.1016/j.wsee.2022.11.011>.
- Taib, H., Hadji, R., Hamed, Y., Bensalem, M.S., Amamria, S., 2023. Exploring Neotectonic Activity in a Semiarid Basin: a Case Study of the Ain Zerga Watershed. *Journal of Umm Al-Qura University for Applied Sciences*. <https://doi.org/10.1007/s43994-023-00072-3>.
- Taloor, A.K., Joshi, L.M., Kotlia, B.S., Alam, A., Kothiyari, G.C., Kandregula, R.S., Dumka, R.K., 2021. Tectonic imprints of landscape evolution in the Bhilangana and Mandakini basin, Garhwal Himalaya, India: a geospatial approach. *Quat. Int.* 575–576, 21–36. <https://doi.org/10.1016/j.quaint.2020.07.021>.
- Taye, G., Vanmaercke, M., van Wesemael, B., Tesfaye, S., Tekla, D., Nyssen, J., Poesen, J., 2023. Estimating the runoff response from hillslopes treated with soil and water conservation structures in the semi-arid Ethiopian highlands: is the curve number method applicable? *Scientific African* 20, e01620. <https://doi.org/10.1016/j.sciaf.2023.e01620>.
- van der Woerd, J., Dorbath, C., Ousadou, F., Dorbath, L., Delouis, B., Jacques, E., Haessler, H., 2014. The Al Hoceima Mw 6.4 earthquake of 24 February 2004 and its aftershocks sequence. *J. Geodyn.* 77, 89–109. <https://doi.org/10.1016/j.jog.2013.12.004>.
- Verolino, A., Jenkins, S.F., Sieh, K., Herrin, J.S., Schonwalder-Angel, D., Sihavong, V., Oh, J.H., 2022. Assessing volcanic hazard and exposure to lava flows at remote volcanic fields: a case study from the Bolaven Volcanic Field, Laos. *Journal of Applied Volcanology* 11 (1), 6. <https://doi.org/10.1186/s13617-022-00116-z>.
- Vojtko, R., Petro, L.u., Benová, A., Bóna, J., Hók, J., 2012. Neotectonic evolution of the northern Laborec drainage basin (northeastern part of Slovakia). *Geomorphology* 138 (1), 276–294. <https://doi.org/10.1016/j.geomorph.2011.09.012>.
- Youssef, B., Bouskri, I., Brahim, B., Kader, S., Brahim, I., Abdelkrim, B., Spalević, V., 2023. The contribution of the frequency ratio model and the prediction rate for the analysis of landslide risk in the Tizi N' tichka area on the national road (RN9) linking Marrakech and Ouarzazate. *Catena* 232, 107464. <https://doi.org/10.1016/j.catena.2023.107464>.



Evaluation of tectonic activity using morphometric indices: Study of the case of Taililoute ridge (middle-Atlas region, Morocco)

Driss Sadkaoui ^a, Benzougagh Brahim ^b, Shuraik Kader ^c, Kamal Agharroud ^d, Abdel-Ilah Mihraje ^e, Khadija Aluni ^e, Habiba Aassoumi ^e, Slimane Sassioui ^e, Velibor Spalevic ^f, Paul Sestras ^{g, h}

- ^a Abdelmlek Essaâdi University, Faculty of Sciences, Department of Geology, Laboratory: Environmental Geology and Natural Resources, Tetouan, Morocco
- ^b Geophysics and Natural Hazards Laboratory, Department of Geomorphology and Geomatics (D2G), Scientific Institute, Mohammed V University in Rabat, Avenue Ibn Batouta, Agdal, PO Box 703, 10106, Rabat-City, Morocco
- ^c School of Engineering and Built Environment, Griffith University, 170 Kessels Road, Nathan, QLD, 4111, Australia
- ^d Earth Sciences Department, Ain Chock Faculty of Sciences, University Hassan II of Casablanca, Morocco
- ^e Laboratory of Analysis and Modeling of Water and Natural Resources, Mohammadia School of Engineers, Mohammed V University in Rabat, Morocco
- ^f Biotechnical Faculty, University of Montenegro, Podgorica, 81000, Montenegro
- ^g Faculty of Civil Engineering, Technical University of Cluj-Napoca, 400020, Cluj-Napoca, Romania
- ^h Academy of Romanian Scientists, Ilfov 3, 050044, Bucharest, Romania

Recommended articles

New geostatistical approach to the analysis of structural lineaments: Case study in th...

Journal of African Earth Sciences, Volume 213, 2024, Ar...
Abdelfattah Aboulfaraj, ..., Abdelouahed Farah

Integrating 3D subsurface imaging, seismic attributes, and wireline logging analyses:...

Journal of African Earth Sciences, Volume 213, 2024, Ar...
Amir Ismail, ..., Emad A. Eysa

Aouelloul impact crater, Mauritania: New structural, lithological, and petrographic...

Journal of African Earth Sciences, Volume 214, 2024, A...
E. Ould Mohamed Navee, ..., H. Si Mhamdi

Show 3 more articles

Article Metrics

Citations

Citation Indexes: 2

Captures

Readers: 3



View details

JOURNAL OF AFRICAN EARTH SCIENCES

Publisher name: PERGAMON-ELSEVIER SCIENCE LTD

Journal Impact Factor™

2.2 (2023) 2.3 (Five Year)

JCR Category	Category Rank	Category Quartile
GEOSCIENCES, MULTIDISCIPLINARY <i>in SCIE edition</i>	120/253	Q2

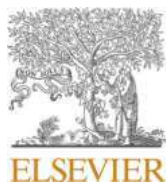
Source: Journal Citation Reports 2023. [Learn more](#)

Journal Citation Indicator™

0.6 (2023) 0.59 (2022)

JCI Category	Category Rank	Category Quartile
GEOSCIENCES, MULTIDISCIPLINARY <i>in SCIE edition</i>	134/253	Q3





Machine learning models for gully erosion susceptibility assessment in the Tensift catchment, Haouz Plain, Morocco for sustainable development

Youssef Bammou^a, Brahim Benzougagh^b, Ouallali Abdessalam^c, Igmoullan Brahim^a, Shuraik Kader^{d,*}, Velibor Spalevic^e, Paul Sestras^{f,g}, Sezai Ercişli^h

^a Department of Geology, Faculty of Science and Technology, Laboratory of Geo-Resources, Geo-Environment and Civil Engineering (L3G), Cadi Ayad University, Morocco

^b Department of Geomorphology and Geomatics, Scientific Institute, Mohammed V, University in Rabat, Avenue Ibn Battouta, Agdal, P.B 703, 10106, Rabat-City, Morocco

^c Process Engineering and Environment Laboratory, Hassan II University of Casablanca, Faculty of Sciences and Techniques of Mohammedia, BP 146, Mohammedia, 28806, Morocco

^d School of Engineering and Built Environment, Griffith University, Nathan, QLD, 4111, Australia

^e Biotechnical Faculty, University of Montenegro, Podgorica, 81000, Montenegro

^f Faculty of Civil Engineering, Technical University of Cluj-Napoca, 400020, Cluj-Napoca, Romania

^g Academy of Romanian Scientists, Ilfov 3, 050044, Bucharest, Romania

^h Faculty of Agriculture, Department of Horticulture, Ataturk University, Erzurum, 25240, Turkiye

ARTICLE INFO

Handling Editor: DR Damien Delvaux

Keywords:

Digital surface models
Gully erosion susceptibility
Land degradation
Machine learning
Factor importance
Morocco

ABSTRACT

Gully erosion is a widespread environmental danger, threatening global socio-economic stability and sustainable development. This study comprehensively applied seven machine learning (ML) models including SVM, KNN, RF, XGBoost, ANN, DT, and LR, and evaluated gully erosion susceptibility in the Tensift catchment and predict it within the Haouz plain, Morocco. To ensure the reliability of the findings, the study employed a robust combination of gully erosion inventory, sentinel images, and Digital Surface Model. Eighteen predictors, encompassing topographical, geomorphological, environmental, and hydrological factors, were selected after multicollinearity analyses. The gully erosion susceptibility of the study revealed that approximately 28.18% of the Tensift catchment is at a very high risk of erosion. Furthermore, 15.13% and 31.28% of the catchment are categorized as low and very low respectively. These findings extend to the Haouz plain, where 7.84% of the surface area are very highly risking erosion, while 18.25% and 55.18% are characterized as low and very low risk areas. To gauge the performance of the ML models, an array of metrics including specificity, precision, sensitivity, and accuracy were employed. The study highlights XGBoost and KNN as the most promising models, achieving AUC ROC values of 0.96 and 0.93 in the test phase. The remaining models namely RF (AUC ROC = 0.89), LR (AUC ROC = 0.80), SVM (AUC ROC = 0.81), DT (AUC ROC = 0.86), and ANN (AUC ROC = 0.78), also displayed commendable performance. The novelty of this research is its innovative approach to combat gully erosion through cutting edge ML models, offering practical solutions for watershed conservation, sustainable management, and the prevention of land degradation. These insights are invaluable for addressing the challenges posed by gully erosion within the region, and beyond its geographical boundaries and can be used for defining appropriate mitigation strategies at local to national scale.

1. Introduction

Water erosion, a common natural phenomenon, causes substantial

environmental and socioeconomic issues (Borrelli et al., 2020; Hassen and Bantider, 2020; Micić Ponjiger et al., 2021, 2023; Wassie, 2020). The complicated interplay between water, land topography, land use, and climate significantly result in erosions (Bammou et al., 2023;

* Corresponding author. School of Engineering and Built Environment, Griffith University, Nathan, QLD, 4111, Australia.

E-mail addresses: youssef.bammou@ced.uca.ma, igmoullan@gmail.com (Y. Bammou), brahim.benzougagh@is.um5.ac.ma (B. Benzougagh), abdessalam.ouallali@univh2c.ma (O. Abdessalam), igmoullan@gmail.com (I. Brahim), shuraik10@gmail.com, shuraik.mohamedabdulkader@griffithuni.edu.au, s.mohamedabdulkader@griffith.edu.au (S. Kader), velibor.spalevic@gmail.com (V. Spalevic), psestras@yahoo.com, psestras@mail.utcluj.ro (P. Sestras), sercisli@gmail.com, sezai.ercisli@tubitak.gov.tr (S. Ercişli).

<https://doi.org/10.1016/j.jafrearsci.2024.105229>

Received 27 October 2023; Received in revised form 4 February 2024; Accepted 8 March 2024

Available online 11 March 2024

1464-343X/© 2024 The Authors. Published by Elsevier Ltd. This is an open access article under the CC BY license (<http://creativecommons.org/licenses/by/4.0/>).

Luetzenburg et al., 2020; Sestras et al., 2023). Understanding and managing the consequences of erosion become even more critical in

and geographical constraints such as radioisotope tracing techniques.

As a result, gully erosion stands out as an interesting study target due

Nomenclature	
ABHT	Tensift Basin Hydraulic Agency
ANN	Artificial Neural Network
AUC-ROC	Area Under Curve of the Receiver Operating Characteristic
CM	Correlation Matrix
DEM	Digital Elevation Model
DSM	Digital Surface Model
DT	Decision tree
FAO	Food and Agriculture Organisation
FR	Frequency Ratio
GES	Gully Erosion susceptibility
GIS	Geographic Informatic System
HSG	Hydrologic Soil Group
HWSD	Harmonized World Soil Database
IDW	Inverse distance weighted
KNN	K-Nearest Neighbor
LR	Logistic Regression
LULC	Land Use and Land Cover
LS	Slope Length
MAE	Mean Absolute Error
MI	Mutual Information
ML	Machine Learning
NDVI	Normalized Difference Vegetation Index
NFR	Normalized Frequency Ratio
RMSE	Root Mean Square Error
RF	Random Forests
SAGA	System for Automated Geoscientific Analyses
SPI	Stream Power Index
SVM	Support vector Machines
TOL	Tolerance
TPI	Topographic Position Index
TRI	Topographic Roughness Index
TWI	Topographic Wetness Index
USGS	United States Geological Survey
VIF	Variance Inflation Factor
XGBoost	eXtreme Gradient Boosting contraction

semi-arid places like Haouz Plain in central Morocco due to limited water supplies and fragile ecosystems.

Erosion can have negative repercussions in both erosion and deposition zones. Organic and mineral matter is washed away from the soil in erosion-prone areas, resulting in lower water retention available for plants, poor infiltration, and unfavorable soil drainage conditions (Kader et al., 2022; Naorem et al., 2023; Xiao et al., 2023). Soil depletion and fertility deterioration are difficult to repair in the short term and results to soil erosion and loss of soil quality pose a severe threat to food security (Kader et al., 2023; Salhi et al., 2023; Saljnikov et al., 2022). Erosion's consequences in deposition zones can appear as undesirable sediment deposition, reduced retention capacity of hydraulic structures (Yu and Deng, 2022), floods (Kader et al., 2023), those lead to the prolonged water pollution and resulting on lowering the water quality.

Studying, analyzing, and mapping erosion susceptibility is essential beyond its academic value. Erosion directly influences water supplies, soil fertility, reservoir sedimentation, and overall landscape integrity. Understanding erosion patterns and susceptibilities is critical for protecting essential natural resources and directing successful land management methods (Ahmed et al., 2024; Asempah et al., 2024). Numerous methods for investigating and mapping erosion have been developed over time. In the Moroccan context, notable examples of applications adhered diverse methodologies such as the Universal Soil Loss Equation (Elaloui et al., 2017), Revised Universal Soil Loss Equation (RUSLE) (Bammou et al., 2023) the Soil and Water Assessment Tool (SWAT) (Briak et al., 2016; Echogdali et al., 2022; Ouallali et al., 2020), radioisotope tracing techniques such as ^{137}Cs (M. Meliho et al., 2019) and ^{210}Pb (Moustakim et al., 2022), and the Erosion Potential Method (EPM) (Elaloui et al., 2022). These models help identify areas of concern and project probable erosion rates, making it easier to develop soil and water conservation measures.

These models, however, have several limitations. Except for the EPM, most of these approaches and models produce conclusions primarily concerned with sheet erosion. However, rill and gully erosion are responsible for most material flowing downstream in watersheds. These approaches frequently simplify complicated erosive processes, which might result in approximations. Furthermore, accurate calibration using local data is required for these models to produce meaningful forecasts. They can also be limited by the unpredictability of atmospheric deposits

to its significant sediment transport capability compared to other types and forms of water erosion. In this context, gully erosion is a distinct and devastating type that deserves special consideration. Gullies can transform landscapes, ruin agricultural fields, and disrupt biological balances (Geng et al., 2021; Mosaffaie et al., 2021; Zhang et al., 2021) because of their deep incisions and substantial sediment transport capabilities. Gully erosion develops as a critical factor in land degradation, given the particular characteristics of semi-arid areas, typified by heavy rainfall occurrences and deforestation (Garosi et al., 2019). Therefore, using precise mapping tools to identify areas vulnerable to gully erosion is critical for proactive erosion management and mitigation.

Traditionally, the procedures indicated above, including qualitative and quantitative approaches, have been employed to assess erosion susceptibility. However, these techniques frequently fail to completely capture the intricate dynamics of erosion processes, particularly in changing landscapes and climatic conditions. Artificial intelligence, notably machine learning (ML) algorithms, may help improve erosion susceptibility mapping by considering many aspects and interactions (Arabameri et al., 2021; Cimusa Kulimushi et al., 2023).

An ML model's viability depends on accuracy, which is evaluated by discriminating capacity and dependability. Discrimination measures a model's capacity to discriminate between the presence and absence of gully erosion (Bashir et al., 2024). The concordance between the expected probability of events such as gully erosion and the observed proportions of their occurrences is measured by reliability (Youssef et al., 2023). However, for several studies, intense discrimination and good dependability are both essential components of an efficient model (Hembram et al., 2021; Saha et al., 2021). In this paper, seven of the most prominent ML algorithms in the state-of-the-art namely SVM, KNN, RF, XGBoost, ANN, DT, and LR examined to predict and map GES in a previously unstudied semi-arid region of Morocco.

This study aims to fill current gaps in erosion assessment methodologies by leveraging ML capabilities to generate accurate and actionable susceptibility maps. The main goal of gully erosion risk management is to identify and locate areas considered to be at high risk. However, achieving this objective can be time-consuming and costly. Therefore, employing predictive models based on ML offers significant advantages in tackling this issue efficiently. The primary objective of this study is twofold: first, to demonstrate the capability of ML

algorithms in mapping GES and comparing the predictive performance of each ML model entails evaluating the model's specificity, precision, sensitivity, accuracy, and reliability (as assessed by RMSE and MAE). Secondly, to give valuable insights into a high-risk semi-arid region's sensitivity to gully erosion.

A solid foundation for predictive analysis is provided by incorporating data from 1220 field samples uniformly split across eroded and non-eroded regions into ML models. The findings of this study not only serve to improve erosion control but also to advance geospatial analysis and environmental modeling in general. This study in the other terms is the first-of-its-kind in the North African context where the findings of this research have huge potentials to contribute to developing sustainable land use plans and erosion mitigation initiatives in semi-arid regions by thoroughly investigating the usefulness of ML with novel applications through systematic integration of gully erosion inventory, sentinel images, and Digital Surface Model (DSM).

2. Materials and methods

2.1. Study area

The Tensift watershed, located in the central part of Morocco near Marrakech, has an area of 20,000 km² (Fig. 1). It is made up of two separate hydrological zones with opposing tendencies. The southern slopes of the Atlas Mountains, which stand above 4000 m in height, get significant precipitation and snowfall, amounting to up to 600 mm every year. These mountains provide an important source of water for the large Haouz plain downstream, which is semi-arid with an annual

precipitation of 250 mm. Particularly, irrigation operations benefit a substantial area of this plain, notably the 2000 km² irrigated Haouz plain.

Geologically, there are three primary geological formations that make up the watershed of the High Atlas near Marrakech: (1) The Permo-triassic is the dominating formation in the east. It frequently coexists with Precambrian and Ordovician schistose rocks; (2) Precambrian eruptive and metamorphic rocks may be found in the central region, which is home to the highest peaks of the Atlas; and (3) primary and secondary limestone formations can be found in the western region (Duclaux, 2005). As most of these geological formations have limited permeability, continuous surface runoff and, possibly, the development of considerable runoff after heavy rainfall, are encouraged the risk of gully erosion. In addition, this area has varied and unpredictable hydrological behavior that is influenced by its geomorphological and climatic factors. It gives rise to long-lasting storms that frequently cause significant soil degradation and loss.

2.2. Methodology

This research applies an approach based on the integration of ML into a system and remote sensing, using 18 factors conditioning gully erosion, namely topographical, geological, geomorphological, hydrological, climatic and anthropogenic factors, to create prediction maps. The methodology adopted for this study is summarized in the flow chart in Fig. 2. The main steps are as follows 1) Database preparation refers to the creation of a geographic database composed of eighteen factors that condition landslides and inventory points that include landslide and

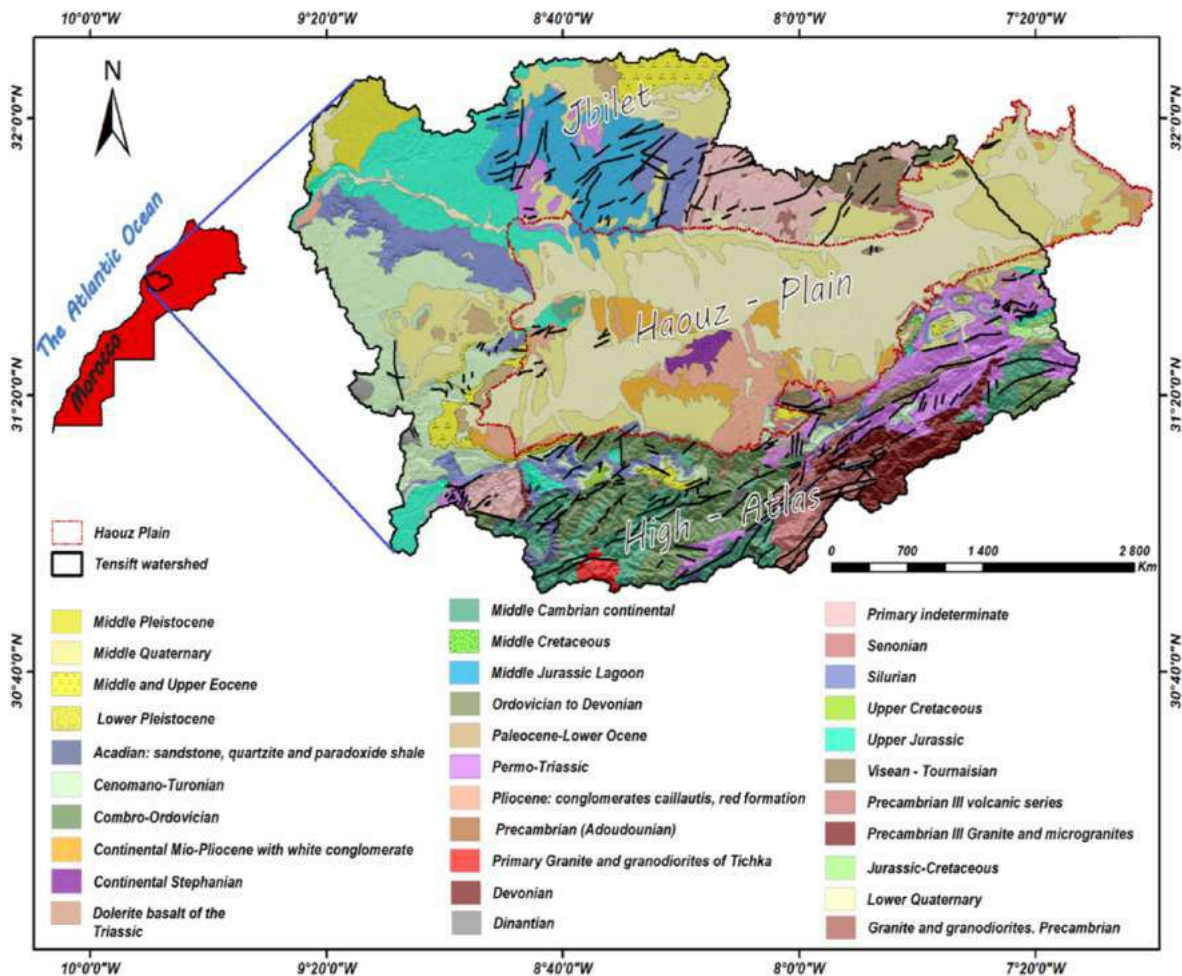


Fig. 1. Geographical location and geological properties of the Haouz Plain and Tensift Watershed (Morocco).

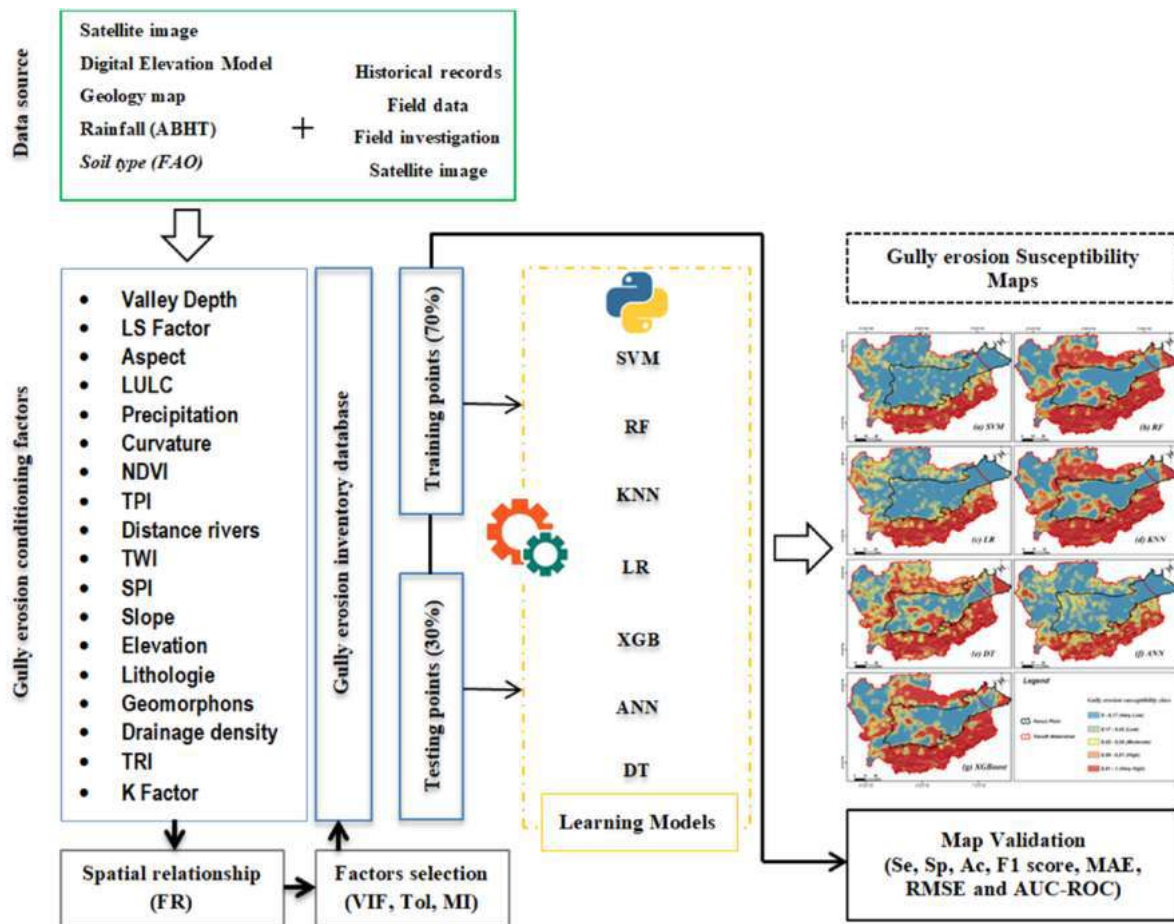


Fig. 2. Flowchart of the developed methodology.

non-slide points. After assembling the databases, we extracted the values of the landslide causal factors to the landslide and non-slide locations concerned, which correspond to the following code (1,0, 2) Analysis of the multicollinearity and importance of the factors using the variance inflation factor (VIF), tolerance (TOL) and mutual information (MI) 3) Application of the seven selected ML models and validation of the results using several statistical parameters 4) Production of gully erosion vulnerability maps.

The inventory map of eroded and non-eroded sites shown in Fig. 3 was compiled from a number of data sources, the collection of points through field missions in 2022 using a GPS (Fig. 3a, b, 3c, 3d, 3e and 3f), an analysis of sentinel satellite images (Fig. 3g) and the interpretation of DSM, provided by ALOS Global Digital Surface Model "ALOS World 3D - 30m (AW3D30)" (Fig. 3h). Afterwards, 620 gully locations were verified and located. On the other hand, for the analysis process to be effective it is important to homogenize the partitioning of locations into gullies and non-gullies (Conoscenti et al., 2014; Rahmati et al., 2016).

The application of ML models frequently requires two types of data inputs for a reliable estimation of gully erosion vulnerability (non-eroded 0 and eroded 1). The sample ratio, eroded/non-eroded, must be close to 1 to obtain a reliable result (Nefeslioglu et al., 2008; Schicker and Moon, 2012). The non-eroded points are selected from the high-resolution Google Earth Pro images and are located at a logical distance from the erosion points. When applying ML models, the data is usually separated into two sets of training and testing where 70% of the total were used to train the seven ML models and the remaining 30% of the total were used to test the seven models.

The study was carried out on the fascia that make up the study area shows two types of erosion. Strong erosion in areas with an abundance

of friable materials such as Neogene phosphate marl, clays and tertiary deposits, and weak erosion in the Jibelt, which is characterized by rocky outcrops that are highly resistant to erosion and gentle slopes.

There are various limits to the research approach that need to be taken into account. Its reliance on remote sensing and machine learning integration into a system is one of its limitations. Although these methods can be effective in forecasting gully erosion, they are not perfect and are prone to mistakes and uncertainties.

The choice of the eighteen parameters conditioning gully erosion is another drawback. Although topographical, geological, geomorphological, hydrological, climatic, and anthropogenic factors are among the many characteristics covered by these components, it is crucial to recognize that additional factors that might also affect gully erosion may not have been considered for this study. Thus, these omissions could have an impact on the model's predicted accuracy.

Furthermore, the quality and resolution of the remote sensing data used may have an impact on the prediction maps' accuracy made using this methodology. The reliability of the prediction maps can be affected by the data's accuracy as well as any possible mistakes or flaws in the data processing methods.

It is critical to remember that the projections of models are predicted on assumptions and previous facts. Future modifications to the land use, environmental conditions, or other variables not included in the model could have an impact on how accurate and useful the prediction maps are. Overall, although the study approach has its merits, it is crucial to acknowledge these constraints and take them into account when analyzing the findings and utilizing the prediction maps.

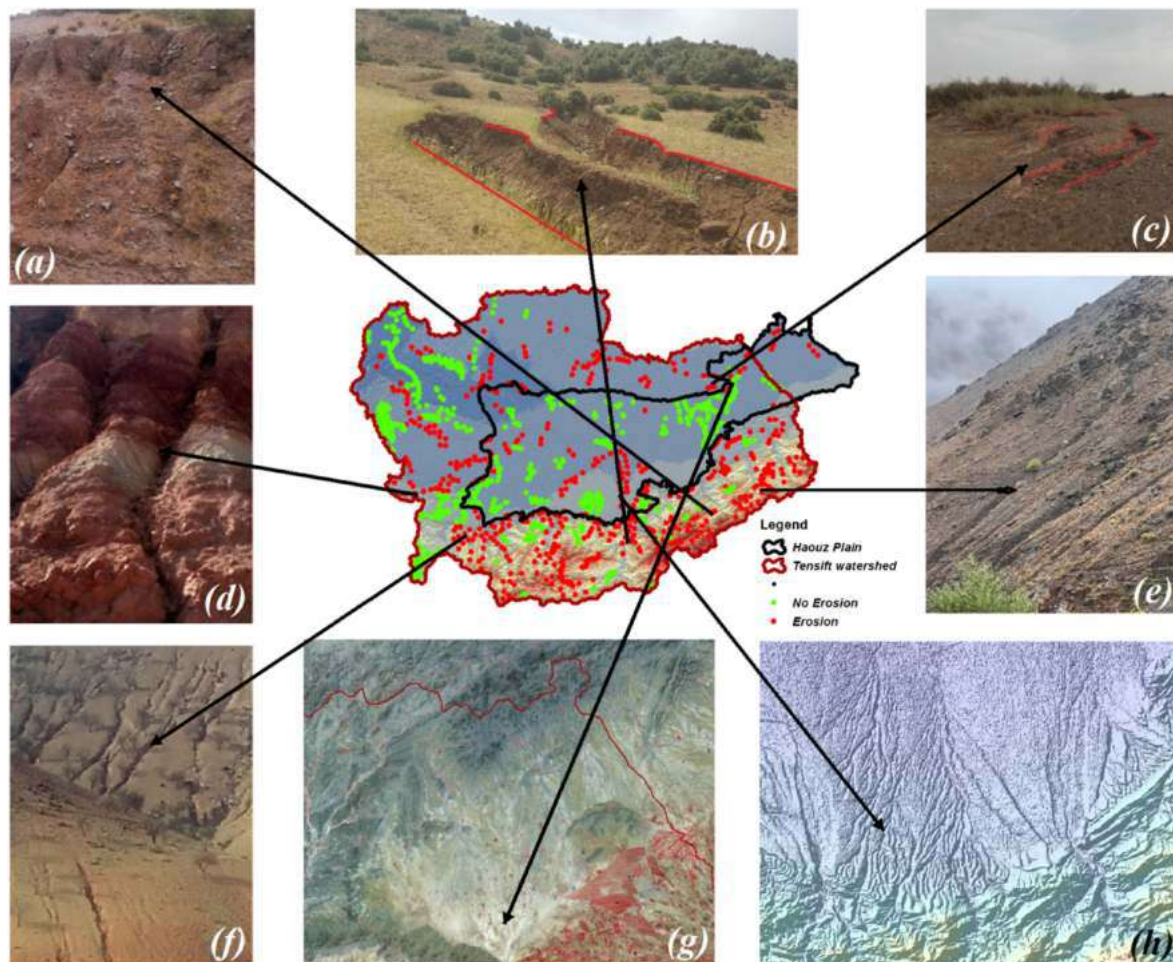


Fig. 3. Inventory map of the Tensift watershed and the Haouz plain and examples of gully erosion areas (a, b, c, d, e, and f) field photos (g) Sentinel satellite image and (h) Digital Surface Model.

2.2.1. Gully erosion conditioning factors

The development of the Gully Erosion Spatial Model is a comprehensive process that involves carefully selecting conditioning factors using various techniques and employing spatial modeling techniques to understand gully erosion (Pourghasemi et al., 2020). In this study, there were 18 qualitative and quantitative variables meticulously reconstructed, encompassing crucial aspects like topography, geomorphology, environment, and hydrology. These variables include altitude, slope, aspect, rainfall, LULC, geomorphons, TPI, distance to rivers, valley depth, curvature, lithology, NDVI, TWI, TRI, LS, drainage density, and SPI.

The selection of these factors has been driven by a thorough analysis of data from previous research and careful consideration of multicollinearity. Notably, for the classification of quantitative factors, the study adopts the widely acknowledged natural break technique, a classification method frequently recommended by significant studies like (Tiwari et al., 2021). By incorporating these essential variables and advanced modeling techniques, the Gully Erosion Spatial Model aims to offer valuable insights into the complex processes of gully erosion, contributing significantly to the understanding and management of this critical environmental issue.

The altitude of the study area was divided into nine classes with a minimum value of less than 300m and a maximum value of more than 3100m, see Fig. 4c, created using the 30m resolution DEM obtained from the USGS. Slope generally has a remarkable effect on gully formation. The slope map extracted from the DEM has been divided into nine classes with values between 0° and 71°, see Fig. 4a. Similarly, the aspect

map has been divided into nine classes shown in Fig. 4b. The curvature map is also extracted from the DEM and classified into three classes: concave representing negative pixel values, flat corresponding to zero values and positive shown by a convex shape as shown in Fig. 4d.

Water erosion energy and transport potential affect and accelerate susceptibility to gully erosion, represented by the Sediment Power Index (SPI) which is calculated from the equation given in Table 1 and has been classified into six sub-classes in Fig. 4o. The TWI is one of the main factors in gully erosion. It is calculated from the equation presented in Table 1, based on DEM data. It is divided into six classes as shown in Fig. 4h. The LS factor is one of the main factors in the RUSLE equation was also calculated from the DEM using the equation represented in Table 1 and this factor has been classified into six classes, as illustrated by Fig. 4m.

The difference in elevation between pixels in a DEM is expressed by the TRI, which in this study has been classified into six categories shown in Fig. 4p. The TPI is also calculated using the DEM and used to classify and calculate the difference in height between each data point, or pixel in a raster DEM, and its immediate surroundings. The TPI was classified into seven categories; see Fig. 4f. Drainage density factors were used and classified into five categories (Fig. 4j). The distance to the river was prepared by applying the Euclidean distance tool in ArcGIS. It was classified into six sub-classes (Fig. 4n). Gully erosion depends strongly on the nature of the lithological facies and the types of soil exposed on the surface, these indicators playing an important role in the acceleration of gully erosion (Rahmati et al., 2017).

The lithological map was drawn up on the basis of the geological data

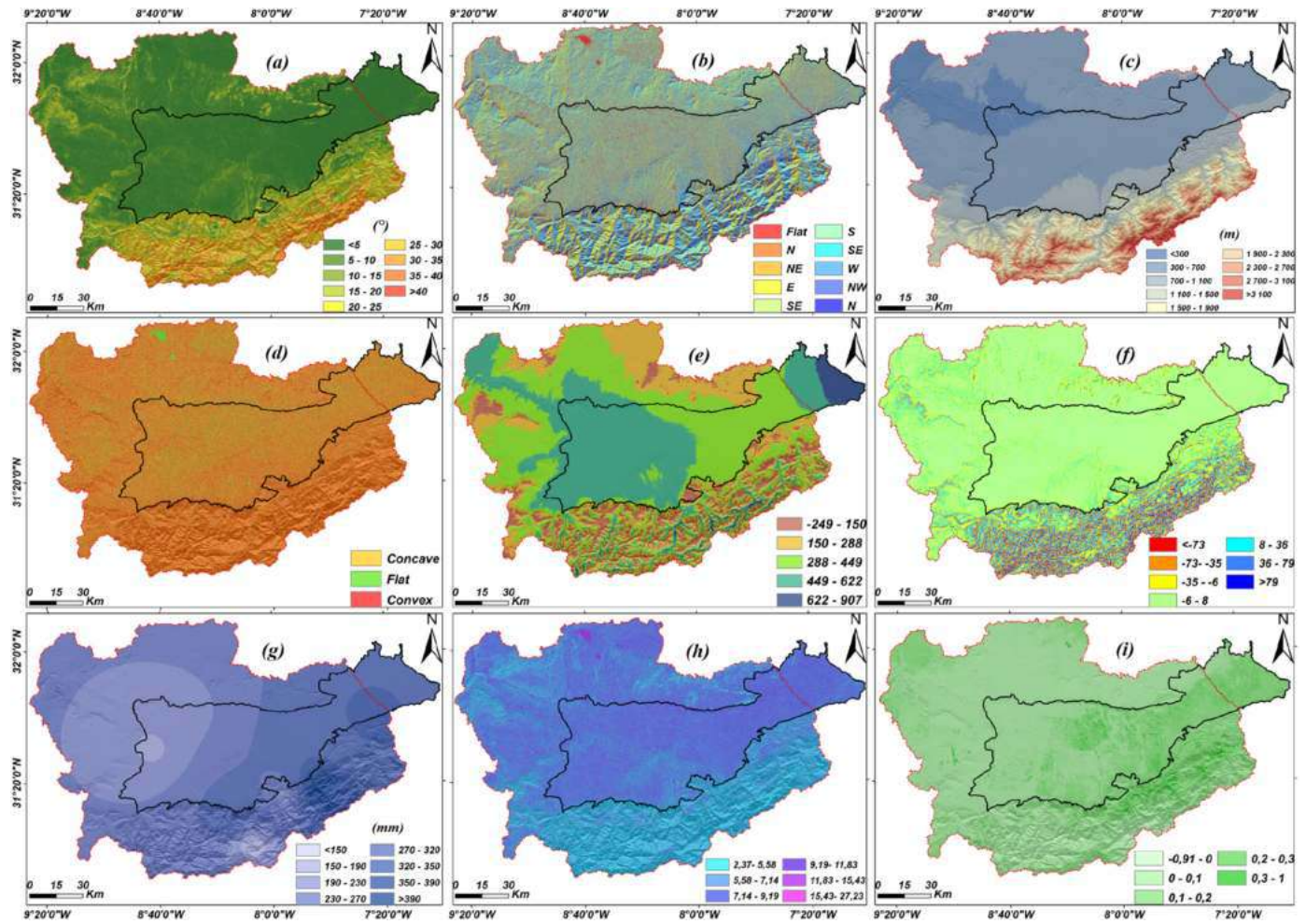


Fig. 4. Landslide conditioning factors within study area (a) Slope in °, (b) Aspect, (c) Elevation, (d) Curvature, (e) Valley depth, (f) TPI, (g) Rainfall, (h) TWI, (i) NDVI, (j) Drainage Density (k) Lithology, (l) LULC, (m) LS Factor (n) Distance to rivers, (o) SPI, (p) TRI, (q) Geomorphons and (r) Factor K.

available in Morocco and was classified into nine classes numbered from 1 to 32, as shown in the legend to Fig. 4k). For the K-factor map, which is one of the important factors in the RUSLE equation, the equation presented in Table 1 is based on soil type data provided by FAO- HWSD.

NDVI was calculated using Sentinel-2 imagery according to the equation in Table 1, classified into five classes with values ranging from -0.91 to 1 (Fig. 4i). The LULC map was produced from the same Sentinel-2 imagery scene after a supervised classification process using ArcGIS software. The LULC classes are water, trees, vegetation, crops, built-up areas, bare soil and rangeland (Fig. 4l). The geomorphology and valley depth factors were developed using SAGA GIS software. The former was classified into ten classes: flat, summit, ridge, shoulder, spur, slope, trough, bottom of slope and valley depression (Fig. 4q). The second was classified into five classes ranging from -249 to 907 (Fig. 4e). The last factor addressed concerns the climatic component, which contributes directly to gully erosion, annual rainfall, based on analysis of a time series from 1992 to 2020 at several climate stations in the Tensift catchment area. The result of this map was subdivided into eight classes with a spatiotemporal variation between less than 150 mm in the western part of the study area and more than 390 mm generally in the High Atlas and in areas to the east of the study area (Fig. 4g).

2.2.2. Gully erosion factor classification analysis

In the current study, seven prediction models were used to enhance the ML prediction of gully erosion risk. Various statistical tests were

performed on these models to discover strong linear connections between different components. These tests, which included CM analysis, VIF (Eq. (1)), TOL (Eq. (2)), and MI (Eq. (3)), aided in identifying and eliminating non-significant components. VIF values larger than 10 and TOL values of 0.1, in particular, revealed significant multicollinearity amongst components (Miao et al., 2023). If two variables were significantly correlated and satisfied the multicollinearity criterion, the one with the higher VIF was eliminated based on the CM analysis. The MI analysis revealed the significance of factors causing of gully erosion, with low MI values suggesting little influence and leading to their removal.

$$VIF_j = \left[\frac{1}{Tol_j} \right] \quad \text{Eq.1}$$

$$Tol = 1 - R_j^2 \quad \text{Eq.2}$$

$$MI(n, j) = H(n) - H\left(\frac{n}{j}\right) \quad \text{Eq.3}$$

Where j is the GES influence factor, n is the subclass of GES influence factors, Tol i is the tolerance of j, VIF j is the variance inflation factor of j, MI (n; j) is the mutual information for n and j, R is the determining coefficient of the regression for the predisposition of j, on all other predisposition factors, H(n) is the entropy of n, and H (n/j) is the conditional entropy for n given the eroded area state factor j.

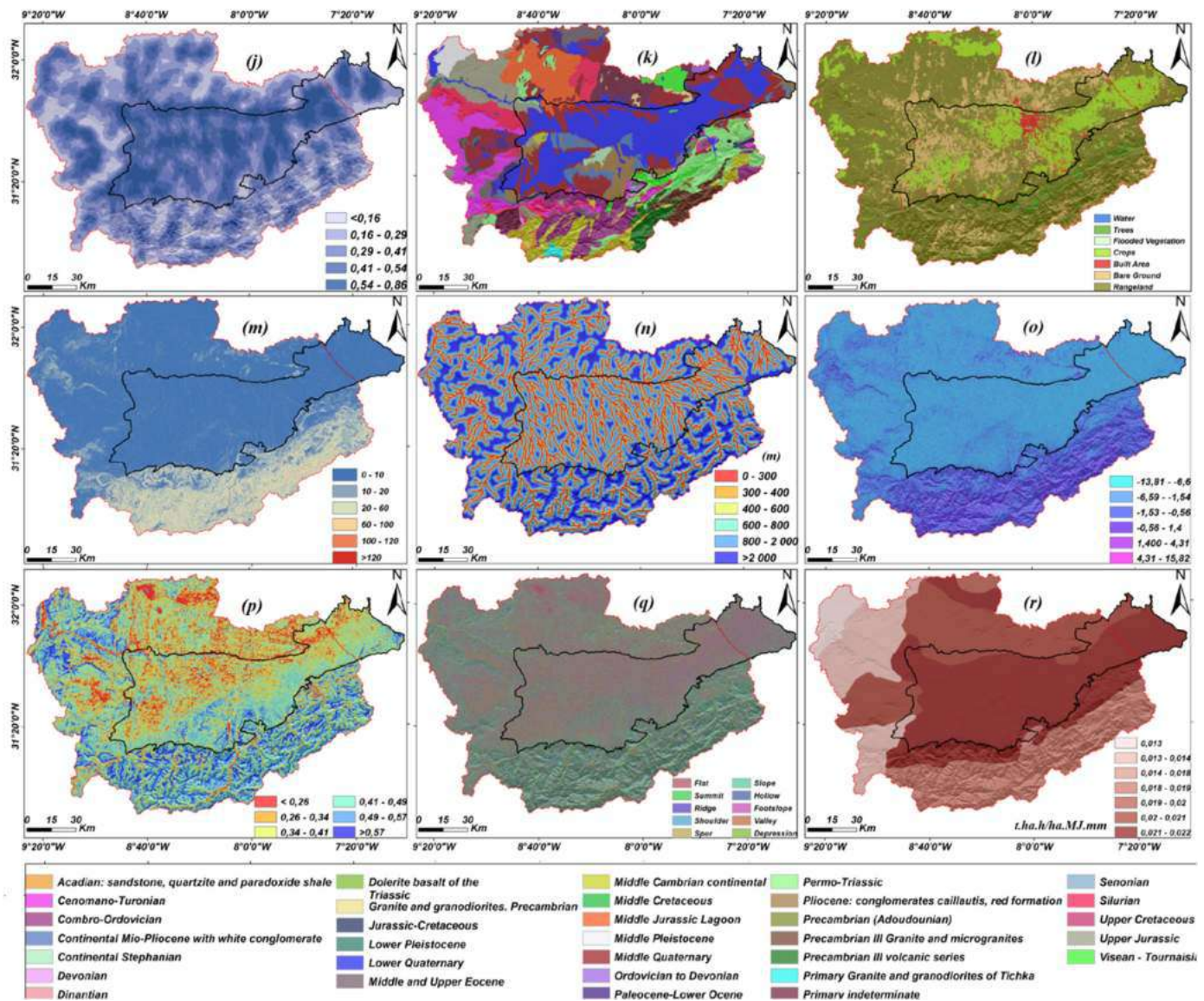


Fig. 4. (continued).

The optimized selection analysis of GES influencing factors and model application was based on the determination of the normalized frequency ratio (NFR) (Eq. (4)), which has recently been a recommended step to unify the importance of the type of input data for the different factors (Mao et al., 2022; Namous et al., 2021). Consequently, the frequency ratio (FR) (Eq. (5)) was assigned to the subclass of factors influencing the GES in the sense of defining the relationship between the eroded locations at GES and the factors influencing the GES (Masoud et al., 2022). The results were then normalized using equation (5). As a result, all the maps used were converted to an NFR between 0 (low GES) and 1 (high GES).

$$NFR_n = \frac{FR_n - \text{Max}(FR_n)}{\text{Max}(FR_n) - \text{Min}(FR_n)} * (0.99 - 0.01) + 0.01 \quad \text{Eq.4}$$

$$FR_n = \frac{W_n}{P_n} \cdot \frac{P_t}{W_t} \quad \text{Eq.5}$$

Where n represents the subclass of factors influencing GES, FRn is the frequency ratio of n, NFRn is the normalized frequency ratio of n, Wn is the number of water sampling points located in n, Wt is the total number of water sampling points, Pn is the number of pixels in n, and Pt is the

total number of all pixels.

The GES influencing factors were categorized into subclasses by analyzing the maps generated through Jenks' natural break technique (Ouallali et al., 2024; Sarker, 2021). However, it is important to note that the exceptions are aspect, LULC, geomorphons and lithology, which were classified according to directional units, supervised classification, and lithological units, respectively.

2.2.3. Description of the learning algorithms

This work is based on the implementation of seven algorithms used to estimate susceptibility to gully erosion: SVM, RF, K-NN, LR, ANN, DT and XGBoost, which has already been tested for flood risk (Bammou et al., 2023). Table 2 contains descriptions of the selected algorithms.

2.3. Validation techniques

The results of the proposed technique were validated for the seven models generated from various performance measures, including specificity, precision, sensitivity, and accuracy. If there is a geographical link between the measured eroded and non-eroded areas and the anticipated eroded areas, the performance indices are considered significant, in

Table 1
Sources, equations and data processing used in this study.

Factors	Data Layers	Equation & Processing	Source
Topographic factors	Elevation	Fill tool for correction in ArcGIS	SRTM-DEM (Digital Elevation Model) were downloaded from the website of United States Geological Survey (USGS) https://earthexplorer.usgs.gov/
	Slope (°)	Processing in ArcGIS	
	SPI	$SPI = As \times \tan\beta$ As is the upstream drainage area and β is the slope degree.	
	TPI	Processing in ArcGIS	
	LS	$LS = (m + 1) \times [As/22] \times [sin\beta/0.0896]$ As is the upstream drainage area and β is the slope degree	
	Aspect	Processing in ArcGIS	
	Curvature	Processing in ArcGIS	
	TWI	$TWI = \ln (As/\tan\beta)$ As is the upstream drainage area and β is the slope degree	
	TRI	Processing in ArcGIS	
	Geomorphological factors	Geomorphons	Processing in SAGA GIS
Geological factors	Valley Depth		
	K Factor	$K = fcsand * fcl - si * forge * fhisand$ Where: fcsand: fraction of soils with high coarse sand content, fcl-si: fraction of soils with high silt/clay ratio. forge: fraction of soils with high organic carbon content and fhisand: fraction of soils with extremely high sand content	https://www.fao.org/soils-portal/data-hub/soil-maps-and-databases/faunesco-soil-ma p-of-the-world/en/
Climatic factors	Lithology	Mapping	Geological map of Marrakech 500,000 scale
	Rainfall (mm)	Interpolation of monthly rainfall using the Kriging method	Tensift Hydraulic Basin Agency (ABHT)
LAND cover factors	NDVI	$NDVI = \frac{B8 - B4}{B8 + B4}$ B8=NIR & B4= RED	Sentinel-2 Images https://earthexplorer.usgs.gov/
	LULC	Supervised classification using the Maximum Likelihood method	

reference to (Costache, 2019; Costache and Bui, 2020).

$$\text{Specificity} = \frac{TN}{FP + TN} \tag{Eq.6}$$

$$\text{Sensitivity} = \frac{TP}{FN + TP} \tag{Eq.7}$$

$$\text{Accuracy} = \frac{TN + TP}{FP + TP + FN + TN} \tag{Eq.8}$$

Table 2
Description of the four algorithms applied in this study.

Model	Developed by	Description	Applied by
KNN	Fix and Hodges (1952)	One of the ML algorithms, the K-NN algorithm is based on the supervised learning method. It places the new case in the category that is most like the existing categories by assuming that there is a likelihood that the new case/data will be like the current cases. (that is, eroded and non-eroded points).	(Avand et al., 2019; Barakat et al., 2023; Mokarram and Zarei, 2021)
SVM	(Bottou and Vapnik, 1992; Cortes and Vapnik, 1995)	Each datum is represented by a point in an n-dimensional space (n denotes the number of features) in the SVM method, with each feature's value denoting a specific position. The best hyperplane that effectively distinguishes the two classes is then found when we go on to classification. The prediction of GES is done using the radial basis function.	(Aouragh et al., 2023; Pal et al., 2022; Pourghasemi et al., 2020)
RF	Breiman (2001)	Based on various groups of the GES-influencing variables identified using the bootstrap aggregation (also known as bagging) and random feature selection procedures, a meta-estimator called random forest updates a specific number of DT classifiers. It enhances the model's propensity to predict outcomes.	(Shruthi et al., 2021; Rahmati et al., 2017; Wang et al., 2021)
XGBoost	Chen and Guestrin (2016)	An enhanced Gradient Boosting. Second-order derivatives are used, which lower the loss function and provide more precise trees.	(Chapi et al., 2017; Hosseini et al., 2020; Mosavi et al., 2018)
ANN	Hopfield (1982)	(ANN) has been developed from the multi-layer perceptron with three neural layers: a primary layer and an intermediate or hidden layer. In the first stage of learning, the network predicts the label of everyone (eroded or non-eroded) using its weights and bias values. A cost function determines the difference between the calculated value and the observed value. In the backpropagation step, each weight is updated according to the gradient of the cost function. This process continues until convergence is reached or a maximum number of learning epochs is reached.	(Modeste Meliho et al., 2022; Parvin et al., 2022)

(continued on next page)

Table 2 (continued)

Model	Developed by	Description	Applied by
DT	Breiman (2001)	This algorithm selects the most suitable features (the factor influencing gully erosion) as the root and generates child nodes. Based on the top-down observations and the processing results at each level, predictions are obtained, from the root to the child nodes corresponding to the new data (eroded and/or non-eroded).	(Choubin et al., 2019; Seydi et al., 2022; Wang et al., 2015)
LR	Cox (1958)	This generalized linear statistical model uses a logistic function as the link function. It is used to study the relationships between a set of qualitative and qualitative variables. This model can be used to predict the probability of an eroded occurring (value of 1) or not (value of 0), by optimizing the regression coefficients. The values are in a range from 0 to 1.	Zhao et al. (2019)

$$\text{Precision} = \frac{TP}{FP + TP} \tag{Eq.9}$$

$$F1 \text{ score} = \frac{2}{\frac{1}{Pr} + \frac{1}{Recal}} \text{ Recall} = \frac{TP}{TP + FN} \tag{Eq.10}$$

With TP (true positives), TN (true negatives), FP (false positives) and FN (false negatives). The analysis also used another popular measure known as the ROC (Aleksova et al., 2023). The most used ROC curve analyzes the area under the curve to determine the accuracy of prediction models. Mapping GES has also used RMSE and MAE. Both types of indices have been used in several academic studies.

$$AUC = \frac{(\sum TP + \sum TN)}{(P + N)} \tag{Eq.11}$$

Where P and N are the total number of pixels with and without torrential events respectively, TP represent the true positive and TN represent the true negative.

$$RMSE = \sqrt{\frac{1}{n} \sum_{i=1}^n (X_{\text{predicted}} - X_{\text{actual}})^2} \tag{Eq.12}$$

$$MAE = \sqrt{\frac{1}{n} \sum_{i=1}^n |X_{\text{predicted}} - X_{\text{actual}}|} \tag{Eq.13}$$

.Where n is the total number of samples in the learning or testing phase, X predicted is the projected value from the GES model, and X actual is the observed value. The AUC value characterizes the quality of the probabilistic model by indicating its reliability in predicting the occurrence or non-occurrence of erosion events. A good fit is represented by AUC values ranging from 0.5 to 1, while values below 0.5 indicate a random fit (Aleksova et al., 2023).

3. Results

3.1. Multicollinearity and factor selection

The results of the CM shown in Fig. 6 represent Pearson’s association

analysis between 18 influencing variables namely the Drainage density, Aspect, K Factor, TPI, TWI, Geomorphons, NDVI, LULC, Rainfall, Distance from Rivers, Curvature, Elevation, Slope, SPI, LS Factor, Lithology, and TRI. As the results show, the highest positive correlation value (0.69) was found between the LS factor and slope, and a strong linear correlation was found between the following factors: Elevation and slope, drainage density and valley depth, TWI and Geomorphons, SPI and Geomorphons, SPI and LS factor, Rainfall and elevation, slope, and TRI. The results of the tolerance and VIF applied to check the multicollinearity of the feed influence factors in this study show a Tol value between 0.15 and 0.94 for Geomorphons and TWI, respectively, as well as a maximum VIF value of 6.35 for Geomorphons and a minimum value of 1.05 for TWI (Fig. 5).

According to the Tol and VIF requirements among the 18 factors used in this study, the Geomorphons factor was removed in the following analysis. Next, the MI of the other 17 factors (Fig. 7) shows positive values ranging from 0.261 (Slope) to 0.029 (Aspect). Consequently, slope is ranked as the most important factor, followed by LS factor (MI = 0.227), TPI (MI = 0.226) and lithology (MI = 0.213).

3.2. Gully erosion susceptibility maps

The GES model was developed by applying seven different algorithms. The results were presented in the form of probability predictions, ranging from 0 to 1, indicating the lowest to highest GES values, respectively. To make the visualization more informative, the generated maps were classified into five distinct zones using Jenks’ classification of natural breaks. These zones are as follows: very low, low, moderate, high, and very high.

Upon conducting an initial visual analysis of the seven maps produced by the SVM (Fig. 8a), RF (Fig. 8b), LR (Fig. 8c), KNN (Fig. 8d), DT (Fig. 8e), ANN (Fig. 8f), and XGBoost (Fig. 8g) algorithms, certain patterns emerged. Specifically, areas with very high GES values were found to be concentrated in the southern part of the Tensift watershed, encompassing the lowland area (Haouz) and the foothills of the High Atlas. Additionally, there were localized occurrences of very high GES values in the western and northern regions of the Jbilet. Conversely, areas with very low GES values were predominantly observed in the central part of the Haouz plain. This initial visual analysis provides valuable insights into the spatial distribution of GES across the Tensift watershed, highlighting regions of high and low susceptibility. The information derived from these maps is crucial for understanding the potential risk and guiding management efforts in the study area.

The geospatial distribution of the degree of GES is quite remarkable in the very strong degree in the High Atlas and certain area of Jbilet. The SVM, LR and ANN models generally show low to very low sensitivity in Jbilet and the Haouz plain, with an increase in sensitivity in the Talmezt region. However, the DT model also shows an increase in sensitivity in Jbilet in the Kettara region and in other regions of the Haouz plain such as Mejjat, Chichaoua, Lataouia and Takarkoust. For the RF, KNN and XGBoost models, the strong to very strong sensitivity is noticeable in the

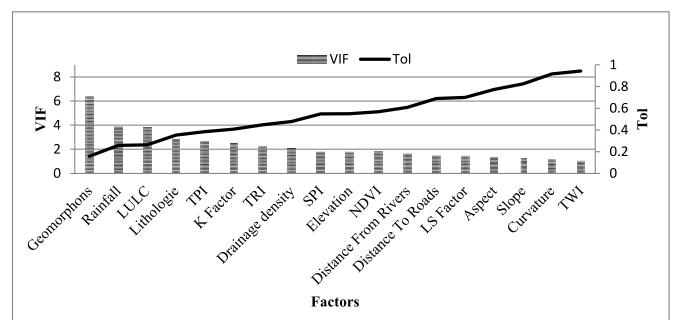


Fig. 5. Multicollinearity analysis of conditioning factors by VIF and TOL.

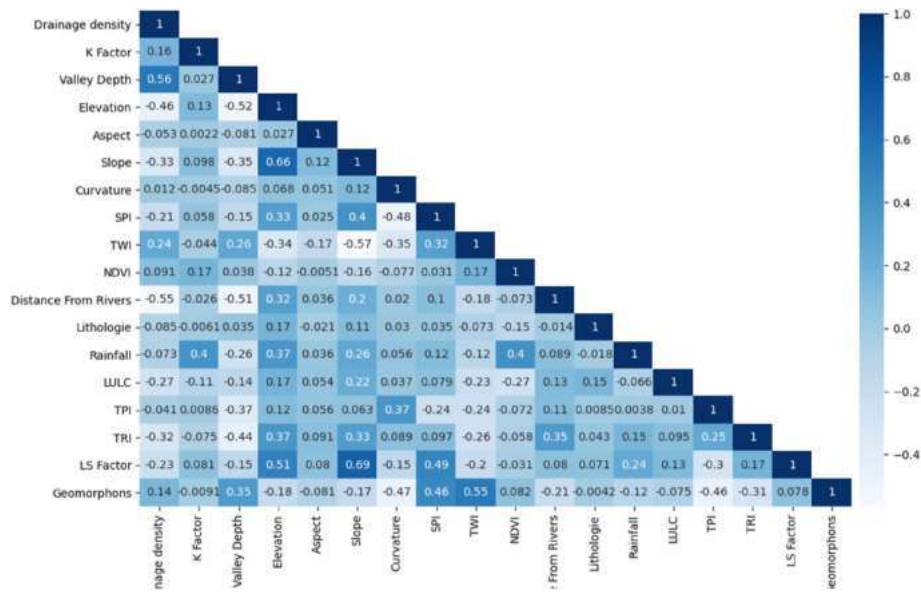


Fig. 6. Multicollinearity analysis of conditioning factors using the correlation matrix.

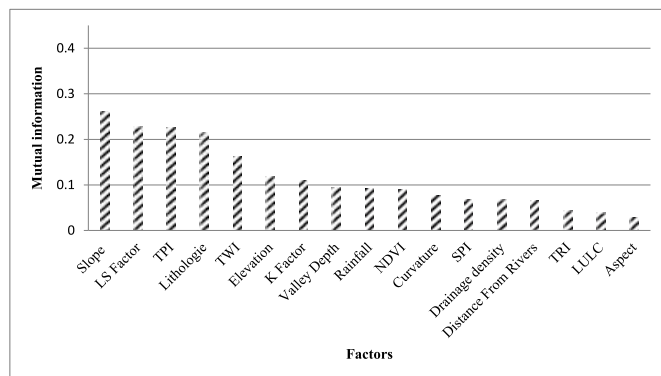


Fig. 7. Flash gully erosion conditioning factors in relation to predictive strength for all models.

same places with a slight difference in the areas covered. This sensitivity is located in the Ourika, Ait Ourir, Laataouia, Kettara, Takarkoust, Chichaoua Talmest, Mejjat and Ijjoukak areas.

According to the results shown in Fig. 9, the spatial distribution of GES in the Tensift catchment area for the seven models applied shows that the percentage area for very low sensitivity ranged from a minimum of 17.11% to a maximum of 43.99% for the DT and SVM models respectively, the percentage area for low sensitivity ranged from a minimum of 9.38% to a maximum of 22.12% recorded respectively for the DT and SVM models recorded respectively for the (RF and KNN) and ANN models, for moderate sensitivity the percentage area varied between 8.03% noticed for the (RF and KNN) models and 18.58% noticed for DT, the lowest percentage area 7.25% and the highest 19.56% are represented respectively by the SVM and DT models for strong sensitivities, finally for very strong sensitivities the lowest area is 15.40% and the highest is 37.88% recorded respectively for the ANN and XGBoost models.

On the other hand, the results elaborated by Fig. 10 in the Haouz plain, where all the characteristics, in particular at the topographic level, present a large difference with those of the High Atlas. The spatial distribution of GES in this area, for the seven models applied show that the percentage area for very low sensitivity varied between the minimum 33.74% and the maximum 77.26% recorded respectively for the DT and LR models, the percentage area for low sensitivity varied

between the minimum 13.26% and the maximum 21.50% recorded respectively for the two models (RF and KNN) and SVM recorded respectively for the XGBoost model, for moderate sensitivity the percentage area varied between 5.56% recorded for the LR model and 17.70% recorded for DT, the lowest percentage area 0.77% and the highest 14.86% are represented respectively by the SVM model and the two models (RF and KNN) for strong sensitivities, finally for very strong sensitivities the lowest area is 0.12% and the highest is 18.32% recorded respectively for the LR and DT models.

In the Tensift watershed, most areas are expected to have very low (31.28%) and low (15.13%) GES values. The other regions of the watershed are distributed as follows: moderate (12.34%), high (13.07%) and very high (28.18%) GES values (Fig. 9). In contrast, the Haouz plain area shows a different distribution pattern. Here, there is a notable decrease in the areas associated with very high (7.84%) and high (7.82%) GES values. Instead, the dominant categories in this region are moderate (10.88%), low (18.25%) and very low (55.18%) GES values (Fig. 10).

3.3. Performance of the models used

This study employed seven models, SVM, RF, KNN, DT, ANN, LR, and XGBoost, to predict GES. The effectiveness of these models was evaluated using both training data (70%) and test data (30%). Various performance metrics were considered, including Precision, Sensitivity, Specificity, Accuracy, Recall, F1 score, FPR, MAE, RMSE, and the Area Under Curve of the Receiver Operating Characteristic (AUC-ROC).

The results from the training and validation phases were meticulously recorded and summarized in Table 3 and Table 4. Additionally, Fig. 11 illustrates the performance outcomes of the different models. By assessing these metrics and comparing the results of each model, this study provides a comprehensive evaluation of the predictive capabilities of the algorithms in determining GES. These findings contribute significantly to understanding the effectiveness of the models and their potential utility in practical applications related to gully erosion management and prevention.

In this research, the XGBoost and KNN models demonstrated outstanding performance when evaluated on the testing data. The XGBoost model achieved impressive scores for various metrics, such as Precision = 0.93, Sensitivity = 0.89, Specificity = 0.95, Accuracy = 0.91, Recall = 0.89, F1 score = 0.91, FPR = 0.07, MAE = 0.03, and AUC-ROC = 91.07%. Similarly, the KNN model showed excellent results with

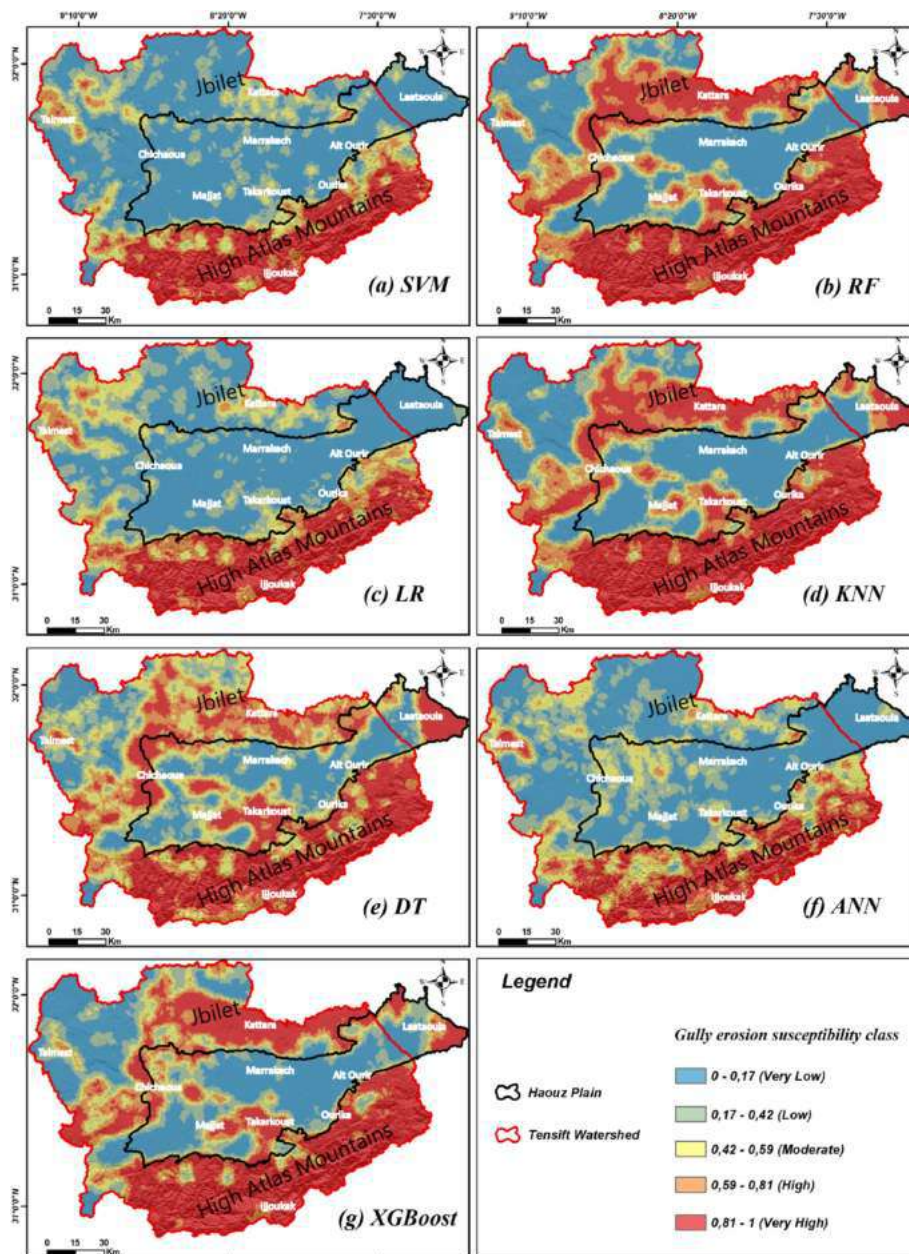


Fig. 8. GES maps of the Tensift catchment and the Haouz plain predicted by the (a) SVM, (b) RF, (c) LR, (d) KNN, (e) DT, (f) ANN and (g) XGBoost models.

Precision = 0.95, Sensitivity = 0.92, Specificity = 0.95, Accuracy = 0.93, Recall = 0.92, F1 score = 0.93, FPR = 0.05, MAE = 0.53, and AUC-ROC = 93.13%. The other six models, RF, LR, SVM, DT, and ANN, also showed high performance on the training data. These models exhibited Sensitivity, Specificity, Precision, Accuracy, AUC, and F1 values all above 0.78, along with negligible FPR and MAE scores.

When evaluated on the test data set, all the applied models showed high or very high performance as illustrated by Fig. 11. Sensitivity values varied between 0.78 for the ANN model and 0.92 for the LR model. Other metrics, such as Precision, Accuracy, F1 score, FPR, and MAE, demonstrated values ranging from 0.80 to 0.95, 0.78 to 0.93, 0.79 to 0.93, 0.09 to 0.21, and 0.11 to 0.27, respectively. The KNN and XGBoost models achieved the maximum AUC-ROC values 93.13% and 91.07% respectively, while the ANN model had the minimum AUC-ROC value of 78.60%.

In addition to evaluating sensitivity and specificity, statistical comparisons were performed using the RMSE, as presented in Tables 3 and 4. The results revealed that the RMSE values for the seven models utilized

in this study ranged from 0.18 to 0.52 during the training and test phases. Fig. 12 illustrates the overall ranking of RMSE values. The RMSE values demonstrated a close alignment between the observed and generated values, indicating an optimal match with the expected susceptibility probability. This achievement confirms the accuracy and reliability of the models in predicting GES. The low RMSE values signify that the models have effectively captured and represented the underlying patterns in the data, further validating their performance in practical applications related to gully erosion management and prediction.

4. Discussion

4.1. Assessing the accuracy of the seven models

The performance of the seven GES sensitivity models was evaluated according to the random split (70/30%) by validation using several statistical measures, namely AUC, RMSE and MAE.

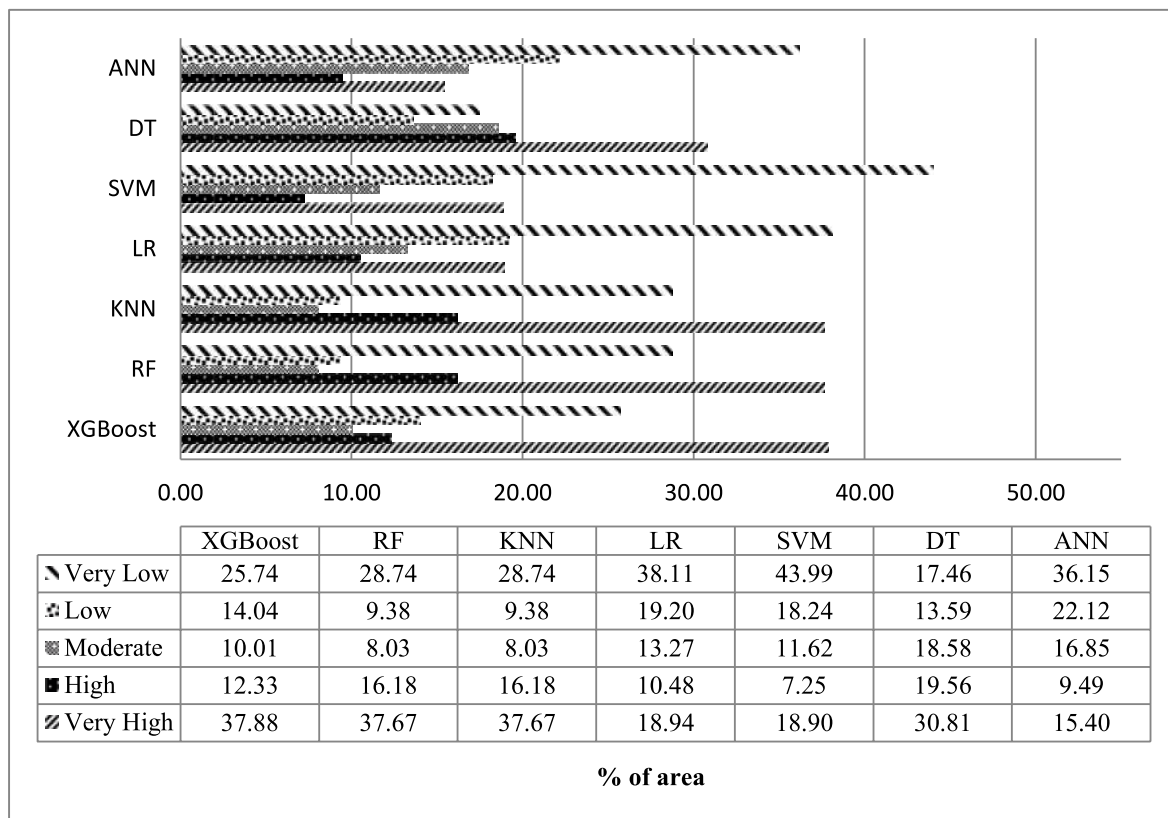


Fig. 9. Percentage of eroded gully areas in the Tensift watershed for the models used.

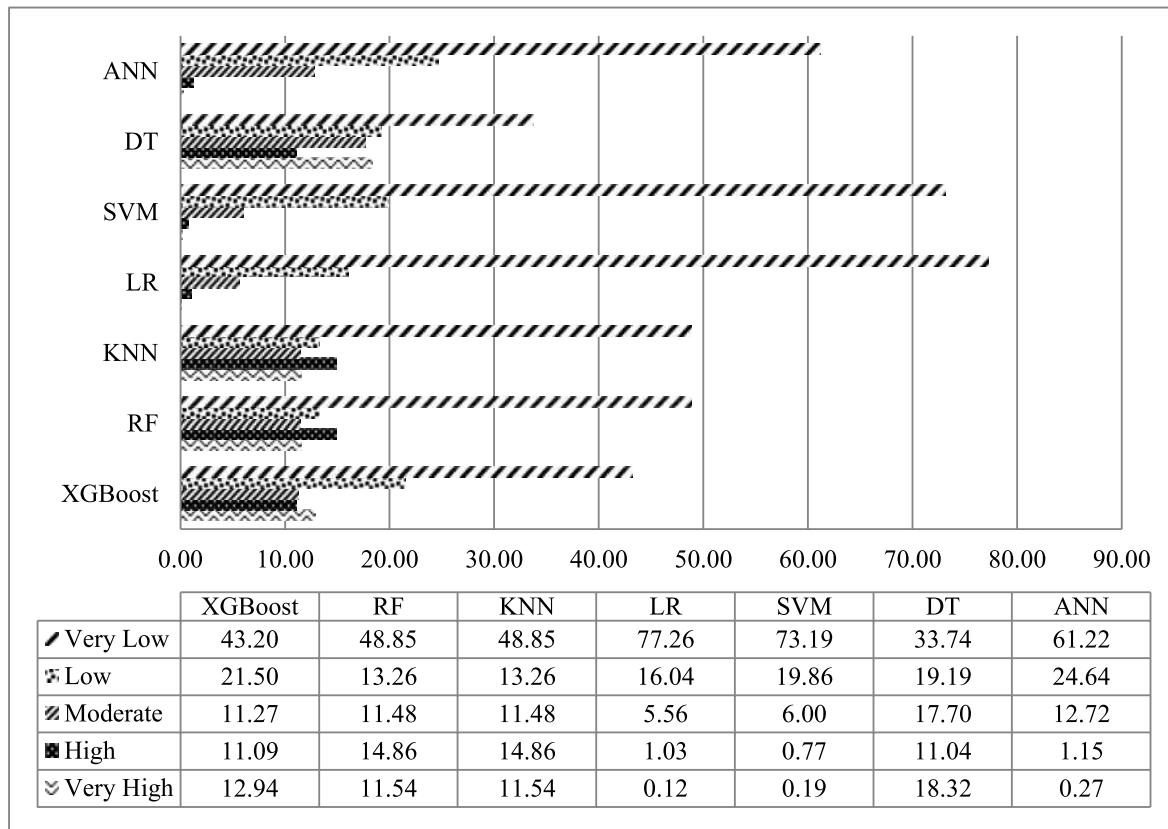


Fig. 10. Percentage of eroded gully areas in the Haouz plain for the models used.

Table 3
Performance of the seven models using training data.

Performance Indicators	Model							Training Data
	XGBoost	RF	KNN	LR	SVM	DT	ANN	
Precision	0.9924	0.9695	0.9695	0.9695	0.9084	0.8636	0.5758	Training Data
Sensitivity	0.9489	0.9621	0.9621	0.9338	0.7727	0.9194	0.8837	
Specificity	0.9906	0.9640	0.9640	0.9626	0.8652	0.8487	0.6433	
False positive rate (FPR)	0.0094	0.0360	0.0360	0.0374	0.1348	0.1513	0.3567	
Accuracy	0.9671	0.9630	0.9630	0.9465	0.8066	0.8848	0.7284	
Recall	0.9489	0.9621	0.9621	0.9338	0.7727	0.9194	0.8837	
F1 score	0.9701	0.9658	0.9658	0.9513	0.8351	0.8906	0.6972	
MAE	0.0329	0.0370	0.0371	0.1810	0.1934	0.1152	0.2716	
RMSE	0.1814	0.1924	0.1924	0.4255	0.4397	0.3394	0.5211	
AUC	96.71	94.65	94.65	81.89	80.66	88.48	72.84	

Table 4
Performance of the seven models using testing data.

Performance Indicators	Model							Testing Data
	XGBoost	RF	KNN	LR	SVM	DT	ANN	
Precision	0.9399	0.9217	0.9520	0.9520	0.9608	0.9054	0.8088	Testing Data
Sensitivity	0.8955	0.8825	0.9240	0.9240	0.7556	0.8416	0.7838	
Specificity	0.9294	0.9085	0.9406	0.9406	0.9378	0.8872	0.7885	
False positive rate (FPR)	0.0706	0.0915	0.0594	0.0594	0.0622	0.1128	0.2115	
Accuracy	0.9107	0.8942	0.9313	0.9313	0.8159	0.8616	0.7860	
Recall	0.8955	0.8825	0.9240	0.9240	0.7556	0.8416	0.7838	
F1 score	0.9172	0.9017	0.9378	0.9378	0.8460	0.8723	0.7961	
MAE	0.0329	0.0370	0.0221	0.1810	0.1934	0.1152	0.2716	
RMSE	0.1814	0.1924	0.1714	0.4255	0.4397	0.3394	0.5211	
AUC	91.07	89.42	93.13	80.25	81.59	86.59	78.60	

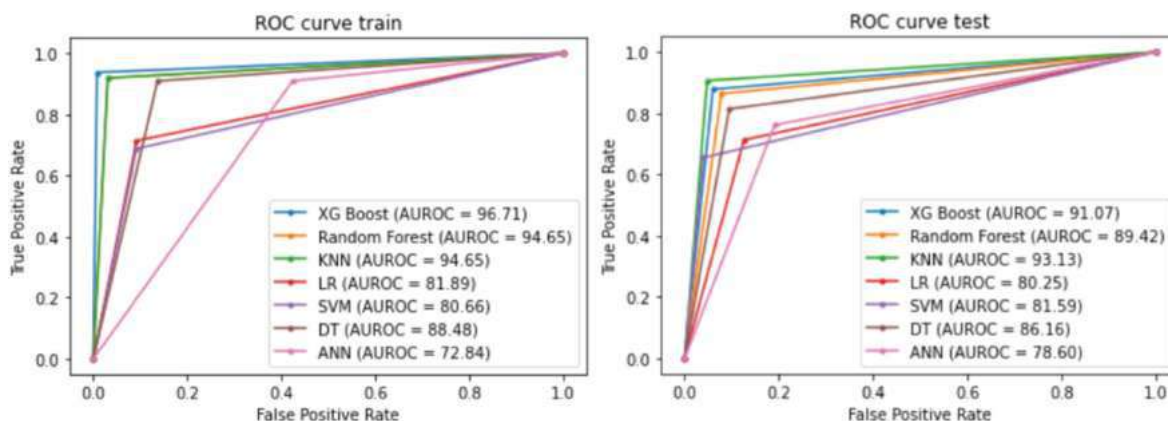


Fig. 11. ROC curve analysis of different gully erosion models using (a) training data, (b) validation data.

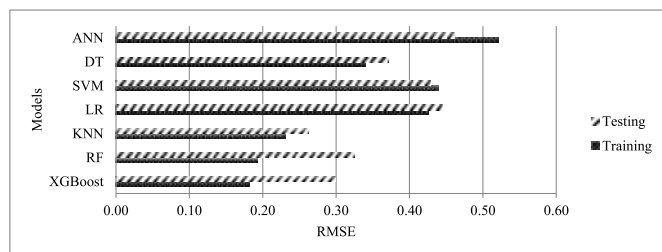


Fig. 12. The performance of the various gully erosion models using RMSE values.

The accuracy values indicate that the XGBoost and KNN models demonstrated a very high level of performance and robustness, the other DT, RF, LR and SVM models demonstrated a high level of performance, and the only ANN model showed an average performance. This

performance indicates that it can be applied to various fields of study and to the monitoring of natural hazards such as soil erosion, landslides, floods, and others (Guo et al., 2021; Sahour et al., 2020).

Sometimes the use of a single type of accuracy indicator can vary the margin of error and lead to more or less inaccurate results (Tehrany et al., 2015). In this way, the performance of the seven models used in this study is confirmed by other additional indices such as MAE and RMSE, which can consolidate the reliability of the models used (Pham et al., 2019). The RMSE and MAE values are lower, indicating that a large proportion of the inventories were recognized in the outcomes of the GES maps.

4.2. The importance of conditioning factors

The important variables affecting gully erosion in our study area, derived using mutual information analysis, which showed that topographic factors namely slope, LS factor and TPI and geological factors

represented by lithology are more important than the other variables. This fact is largely in agreement with the results obtained in the sub-basin of Chichaoua by (Baiddah et al., 2023) for the factors of LS and lithology, his study also shows the importance of other factors such as distance to rivers and elevation. This differentiation can be explained by the choice of a mixed area which shows a contrast between the values of altitude, married a plain and mountain area and by the large area of our study area.

The combination of very friable lithologies such as phosphatic marls from the Neogene and tertiary clays and deposits, and high altitudes with little vegetation, facilitates the creation and development of this type of erosion, particularly on steep slopes and in areas where the vegetation cover is damaged (Arabameri et al., 2020). On the other hand, there is little erosion in a large part of the areas where the rocky outcrop of the Hercynian basement, which is essentially made up of shale rocks, grauwackes, limestone bars and volcanic matrix of primary age (i.e., Cambro-Ordovician), comprising flat land with very gentle slopes in the north of the study area, in the Jibelt and land protected by extensive plant cover.

Vegetation cover generally plays a very important role in soil protection, and its degradation, especially by the numerous activities of the population in the various villages of the Tensift catchment area, such as deforestation and grazing, increases the risk of gully formation (Arabameri et al., 2020). In addition, numerous studies in arid and semi-arid contexts on the importance of topographical factors on gully formation have shown direct effects on rainfall trends, runoff kinetic energy and vegetation cover (Beullens et al., 2014; Nazari Samani et al., 2009).

4.3. Susceptibility to gully erosion maps

The seven models used to produce vulnerability maps reveal that certain factors have a greater influence than others on the spatial variability of vulnerability. For example, the variation in the proportions of sensitivity to the risk of gully erosion at high altitudes towards the plain is directly attributable to the topographical impact. This is consistent with the substantial geographical link between these sites and the TRI classes greater than 0.57 and slopes greater than 30°.

Comparing the resulting maps generated by the seven models, the KNN, RF and XGBoost models show the same percentage area in zones representing very high vulnerability and very low vulnerability. ML methods can produce Gully Erosion Spatial Models with a high degree of accuracy. This can be seen as a fundamental tool to help planners and managers ensure sustainable and effective management of areas affected by soil erosion in mountainous and semi-arid environments.

5. Conclusion

This study has shown how important it is to comprehend the spatial spread of gully erosion in order to effectively control the phenomenon. SVM, RF, KNN, DT, ANN, LR, and XGBoost are the seven-machine learning (ML) models that were used in this study to examine the impact of 17 parameters on gully formation in a mountainous semi-arid landscape. Of the significant variables found, lithology, slope, LS factor, and TPI stood out as being crucial in the creation of gullies. After evaluating these models' robustness in the face of changing input data, seven maps of erosion vulnerability were produced, showcasing their dependability and resilience in forecasting the susceptibility of gully erosion. The performance of the seven GES sensitivity models was examined by applying a random split (70/30%) and validated using multiple statistical metrics, including AUC, RMSE, and MAE. The accuracy results suggest that the XGBoost and KNN models revealed an exceptionally high degree of performance and robustness. The study found that approximately 28.18% of the Tensift catchment is at a very high risk of erosion, while 15.13% and 31.28% are categorized as low and very low risk areas. The study highlights XGBoost and KNN as the most promising models, achieving AUC ROC values of 0.96 and 0.93 in

the test phase.

The study on gully erosion has highlighted the significance of machine learning methods for managing it. However, the methodological approach of this study has its own limitations that need to be addressed in future studies. The chosen machine learning models are sensitive to changes in specific input data, and for their accessibility and quality. Additionally, the study's findings may not be generalizable to other regions with dissimilar geological features or environmental circumstances.

In the future, research may be directed into a number of interesting scopes. First, in order to determine whether the results are generally applicable and take regional differences into consideration, the use of ML models could be expanded to various geographic areas. Furthermore, adding more extensive datasets and investigating cutting-edge machine learning algorithms might improve the models' precision and predictive power. Future research may also look into the long-term evolution of gully erosion and how it interacts with the dynamics of climate change. This would assist direct adaptive management techniques and offer insights into the possible effects of climate change on gully formation.

The susceptibility maps generated by this work are extremely useful for planning areas impacted by gully erosion and for sustainable management in semi-arid highland regions. They offer vital information needed to put conservation and erosion control plans into action. The study emphasizes how crucial machine learning approaches are to understanding the complexity of gully erosion and provides workable answers to this urgent problem. This study has advanced knowledge among the scientific community regarding the gully erosion and brought attention to the significance of machine learning methods for managing it. Researchers can further expand understanding in this field and create more effective techniques for minimizing gully erosion in a range of environments by addressing the recommended directions for future research.

Ethical approval

Not Applicable.

Consent to participate

Not Applicable.

Consent to publish

Not Applicable.

Funding

Not Applicable.

Availability of data and materials

The data and materials will be available for review upon request by the journal to the corresponding author.

CRedit authorship contribution statement

Youssef Bammou: Conceptualization, Data curation, Formal analysis, Investigation, Methodology, Resources, Software, Validation, Visualization, Writing – original draft. **Brahim Benzougagh:** Conceptualization, Data curation, Formal analysis, Investigation, Methodology, Project administration, Resources, Software, Supervision, Validation, Visualization, Writing – original draft, Writing – review & editing. **Ouallali Abdessalam:** Formal analysis, Investigation, Methodology, Resources, Software, Supervision, Validation, Visualization, Writing – original draft. **Igmoullan Brahim:** Conceptualization, Data curation,

Formal analysis, Funding acquisition, Investigation, Methodology, Resources, Software, Supervision, Validation, Visualization, Writing – original draft. **Shuraik Kader:** Conceptualization, Data curation, Formal analysis, Investigation, Methodology, Project administration, Resources, Software, Supervision, Validation, Visualization, Writing – original draft, Writing – review & editing. **Velibor Spalevic:** Conceptualization, Data curation, Formal analysis, Investigation, Methodology, Project administration, Resources, Software, Supervision, Validation, Visualization, Writing – original draft, Writing – review & editing. **Paul Sestras:** Data curation, Formal analysis, Investigation, Methodology, Validation, Visualization, Writing – original draft, Writing – review & editing. **Sezai Ercişli:** Data curation, Formal analysis, Investigation, Resources, Validation, Visualization, Writing – original draft.

Declaration of competing interest

The authors declare that they have no known competing financial interests or personal relationships that could have appeared to influence the work reported in this paper.

Data availability

Data will be made available on request.

References

- Ahmed, I.A., Talukdar, S., Baig, M.R.I., Shahfahad, Ramana G.V., Rahman, A., 2024. Quantifying soil erosion and influential factors in Guwahati's urban watershed using statistical analysis, machine and deep learning. *Remote Sens. Appl.: Society and Environment* 33, 101088. <https://doi.org/10.1016/j.rsae.2023.101088>.
- Aleksova, B., Lukić, T., Milevski, I., Spalević, V., Marković, S.B., 2023. Modelling water erosion and mass movements (wet) by using GIS-based multi-hazard susceptibility assessment approaches: a case study—kratovska Reka Catchment (North Macedonia). *Atmosphere* 14 (7), 1139. <https://doi.org/10.3390/atmos14071139>.
- Aouragh, M.H., Ijlil, S., Essahlaoui, N., Essahlaoui, A., El Hmaidi, A., El Ouali, A., Mridekh, A., 2023. Remote sensing and GIS-based machine learning models for spatial gully erosion prediction: a case study of Rdat watershed in Sebou basin, Morocco. *Remote Sens. Appl.: Society and Environment* 30, 100939. <https://doi.org/10.1016/j.rsae.2023.100939>.
- Arabameri, A., Chandra Pal, S., Costache, R., Saha, A., Rezaie, F., Seyed Danesh, A., Hoang, N.-D., 2021. Prediction of gully erosion susceptibility mapping using novel ensemble machine learning algorithms. *Geomatics, Nat. Hazards Risk* 12 (1), 469–498. <https://doi.org/10.1080/19475705.2021.1880977>.
- Arabameri, A., Tiefenbacher, J.P., Blaschke, T., Pradhan, B., Tien Bui, D., 2020. Morphometric analysis for soil erosion susceptibility mapping using novel GIS-based ensemble model. *Rem. Sens.* 12 (5), 874. <https://doi.org/10.3390/rs12050874>.
- Asemphang, M., Shisanya, C.A., Schütt, B., 2024. Modeling of soil erosion risk in a typical tropical savannah landscape. *Scientific African* 23, e02042. <https://doi.org/10.1016/j.sciaf.2023.e02042>.
- Avand, M., Janizadeh, S., Naghibi, S.A., Pourghasemi, H.R., Khosrobeigi Bozchaloei, S., Blaschke, T., 2019. A comparative assessment of random forest and k-nearest neighbor classifiers for gully erosion susceptibility mapping. *Water* 11 (10), 2076. <https://doi.org/10.3390/w11102076>.
- Baiddah, A., Krimissa, S., Hajji, S., Ismaili, M., Abdelrahman, K., El Bouzekraoui, M., Badredin, N., 2023. Head-cut gully erosion susceptibility mapping in semi-arid region using machine learning methods: insight from the high atlas, Morocco. *Front. Earth Sci.* 11, 1184038. <https://doi.org/10.3389/feart.2023.1184038>.
- Bammou, Y., Benzougagh, B., Bensaid, A., Igmoullan, B., Al-Quraishi, A.M.F., 2023. Mapping of current and future soil erosion risk in a semi-arid context (haouz plain-Marrakech) based on CMIP6 climate models, the analytical hierarchy process (AHP) and RUSLE. *Modeling Earth Systems and Environment* 1–14. <https://doi.org/10.1007/s40808-023-01845-9>.
- Barakat, A., Rafai, M., Mosaid, H., Islam, M.S., Saeed, S., 2023. Mapping of water-induced soil erosion using machine learning models: a case study of Oum Er Rbia Basin (Morocco). *Earth Systems and Environment* 7 (1), 151–170. <https://doi.org/10.1007/s41748-022-00317-x>.
- Bashir, O., Bangroo, S.A., Shafai, S.S., Senesi, N., Kader, S., Alamri, S., 2024. Geostatistical modeling approach for studying total soil nitrogen and phosphorus under various land uses of North-Western Himalayas. *Ecol. Inf.* 80, 102520. <https://doi.org/10.1016/j.ecoinf.2024.102520>.
- Beullens, J., Van de Velde, D., Nyssen, J., 2014. Impact of slope aspect on hydrological rainfall and on the magnitude of rill erosion in Belgium and northern France. *Catena* 114, 129–139. <https://doi.org/10.1016/j.catena.2013.10.016>.
- Borrelli, P., Robinson, D.A., Panagos, P., Lugato, E., Yang, J.E., Alewell, C., Ballabio, C., 2020. Land use and climate change impacts on global soil erosion by water (2015–2070). *Proc. Natl. Acad. Sci. USA* 117 (36), 21994–22001. <https://doi.org/10.1073/pnas.2001403117>.
- Bottou, L., Vapnik, V., 1992. Local learning algorithms. *Neural Comput.* 4 (6), 888–900. <https://doi.org/10.1162/neco.1992.4.6.888>.
- Breiman, L., 2001. Random forests. *Mach. Learn.* 45, 5–32. <https://doi.org/10.1023/A:1010933404324>.
- Briak, H., Moussadek, R., Aboumaria, K., Mrabet, R., 2016. Assessing sediment yield in Kalaya gauged watershed (Northern Morocco) using GIS and SWAT model. *International Soil and Water Conservation Research* 4 (3), 177–185. <https://doi.org/10.1016/j.iswcr.2016.08.002>.
- Chapi, K., Singh, V.P., Shirzadi, A., Shahabi, H., Bui, D.T., Pham, B.T., Khosravi, K., 2017. A novel hybrid artificial intelligence approach for flood susceptibility assessment. *Environ. Model. Software* 95, 229–245. <https://doi.org/10.1016/j.envsoft.2017.06.012>.
- Chen, T., Guestrin, C., 2016. Xgboost: a scalable tree boosting system. In: *Paper Presented at the Proceedings of the 22nd Acm Sigkdd International Conference on Knowledge Discovery and Data Mining*.
- Choubin, B., Rahmati, O., Soleimani, F., Ailou, H., Moradi, E., Alamdari, N., 2019. Regional groundwater potential analysis using classification and regression trees. In: *Spatial Modeling in GIS and R for Earth and Environmental Sciences*. Elsevier, pp. 485–498.
- Cimusa Kulimushi, L., Bigabwa Bashagaluke, J., Prasad, P., Heri-Kazi, A.B., Lal Kushwaha, N., Masroor, M., Mohammed, S., 2023. Soil erosion susceptibility mapping using ensemble machine learning models: a case study of upper Congo river sub-basin. *Catena* 222, 106858. <https://doi.org/10.1016/j.catena.2022.106858>.
- Conoscenti, C., Angileri, S., Cappadonia, C., Rotigliano, E., Agnesi, V., Märker, M., 2014. Gully erosion susceptibility assessment by means of GIS-based logistic regression: a case of Sicily (Italy). *Geomorphology* 204, 399–411. <https://doi.org/10.1016/j.geomorph.2013.08.021>.
- Cortes, C., Vapnik, V., 1995. Support-vector networks. *Mach. Learn.* 20, 273–297. <https://doi.org/10.1007/BF00994018>.
- Costache, R., 2019. Flash-Flood Potential assessment in the upper and middle sector of Prahova river catchment (Romania). A comparative approach between four hybrid models. *Sci. Total Environ.* 659, 1115–1134. <https://doi.org/10.1016/j.scitotenv.2018.12.397>.
- Costache, R., Bui, D.T., 2020. Identification of areas prone to flash-flood phenomena using multiple-criteria decision-making, bivariate statistics, machine learning and their ensembles. *Sci. Total Environ.* 712, 136492. <https://doi.org/10.1016/j.scitotenv.2019.136492>.
- Cox, D.R., 1958. The regression analysis of binary sequences. *J. Roy. Stat. Soc. B Stat. Methodol.* 20 (2), 215–232.
- Duclaux, A., 2005. Modélisation hydrologique de 5 Bassins Versants du Haut-Atlas Marocain avec SWAT (Soil and Water Assessment Tool). Mémoire du diplôme d'Ingénieur Agronome de l'Institut National Agronomique de Paris-Grignon.
- Echogdali, F.Z., Kpan, R.B., Ouchchen, M., Id-Belqas, M., Dadi, B., Ikirri, M., Boutaleb, S., 2022. Spatial prediction of flood frequency analysis in a semi-arid zone: a case study from the Seyad Basin (Guelmim Region, Morocco). *Geospatial technology for landscape and environmental management: sustainable assessment and planning* 49–71. https://doi.org/10.1007/978-981-16-7373-3_3.
- Elaloui, A., Khalki, E.M.E., Namous, M., Ziadi, K., Eloudi, H., Faouzi, E., Boudhar, A., 2022. Soil erosion under future climate change scenarios in a semi-arid region. *Water* 15 (1), 146. <https://doi.org/10.3390/w15010146>.
- Elaloui, A., Marrakchi, C., Fekri, A., Maimouni, S., Aradi, M., 2017. USLE-based assessment of soil erosion by water in the watershed upstream Tessaout (Central High Atlas, Morocco). *Modeling Earth Systems and Environment* 3, 873–885. <https://doi.org/10.1007/s40808-017-0340-x>.
- Fix, E., Hodges, J.L., 1952. *Discriminatory Analysis: Nonparametric Discrimination: Small Sample Performance*.
- Garosi, Y., Sheklabadi, M., Conoscenti, C., Pourghasemi, H.R., Van Oost, K., 2019. Assessing the performance of GIS-based machine learning models with different accuracy measures for determining susceptibility to gully erosion. *Sci. Total Environ.* 664, 1117–1132. <https://doi.org/10.1016/j.scitotenv.2019.02.093>.
- Geng, R., Zhang, G.-H., Hong, D.-L., Ma, Q.-H., Jin, Q., Shi, Y.-Z., 2021. Response of soil detachment capacity to landscape positions in hilly and gully regions of the Loess Plateau. *Catena* 196, 104852. <https://doi.org/10.1016/j.catena.2020.104852>.
- Guo, Z., Shi, Y., Huang, F., Fan, X., Huang, J., 2021. Landslide susceptibility zonation method based on C5.0 decision tree and K-means cluster algorithms to improve the efficiency of risk management. *Geosci. Front.* 12 (6), 101249. <https://doi.org/10.1016/j.gsf.2021.101249>.
- Hassen, G., Bantider, A., 2020. Assessment of drivers and dynamics of gully erosion in case of Tabota Koromo and Koromo Danshe watersheds, South Central Ethiopia. *Geoenvironmental Disasters* 7, 1–13.
- Hembram, T.K., Saha, S., Pradhan, B., Abdul Maulud, K.N., Alamri, A.M., 2021. Robustness analysis of machine learning classifiers in predicting spatial gully erosion susceptibility with altered training samples. *Geomatics, Nat. Hazards Risk* 12 (1), 794–828. <https://doi.org/10.1080/19475705.2021.1890644>.
- Hopfield, J.J., 1982. Neural networks and physical systems with emergent collective computational abilities. *Proc. Natl. Acad. Sci. USA* 79 (8), 2554–2558. <https://doi.org/10.1073/pnas.79.8.2554>.
- Hosseini, F.S., Choubin, B., Mosavi, A., Nabipour, N., Shamshirband, S., Darabi, H., Haghghi, A.T., 2020. Flash-flood hazard assessment using ensembles and Bayesian-based machine learning models: application of the simulated annealing feature selection method. *Sci. Total Environ.* 711, 135161. <https://doi.org/10.1016/j.scitotenv.2019.135161>.
- Kader, S., Jauffer, L., Bashir, O., Raimi, M.O., 2023a. A comparative study on the stormwater retention of organic waste substrates biochar, sawdust, and wood bark recovered from psidium guajava L. Species. *Agric. For.* 69 (1), 105–112. <https://doi.org/10.17707/AgricForest.69.1.09>.

- Kader, S., Novicevic, R., Jauffer, L., 2022. Soil management in sustainable agriculture: analytical approach for the ammonia removal from the dairy manure. *J. Agric. For.* 68 (4), 69–78. <https://doi.org/10.17707/AgricultForest.68.4.06>.
- Kader, S., Raimi, M.O., Spalevic, V., Iyngiala, A.-A., Bukola, R.W., Jauffer, L., Butt, T.E., 2023b. A concise study on essential parameters for the sustainability of Lagoon waters in terms of scientific literature. *Turk. J. Agric. For.* 47 (3), 288–307. <https://doi.org/10.55730/1300-011X.3087>.
- Luetzenburg, G., Bittner, M.J., Calsamiglia, A., Renschler, C.S., Estrany, J., Poepl, R., 2020. Climate and land use change effects on soil erosion in two small agricultural catchment systems Fugnitz – Austria, Can Revull – Spain. *Sci. Total Environ.* 704, 135389 <https://doi.org/10.1016/j.scitotenv.2019.135389>.
- Mao, W., Xu, C., Yang, Y., 2022. Investigation on strength degradation of sandy soil subjected to concentrated particle erosion. *Environ. Earth Sci.* 81, 1–10. <https://doi.org/10.1007/s12665-021-10123-9>.
- Masoud, A.M., Pham, Q.B., Alezabawy, A.K., El-Magd, S.A.A., 2022. Efficiency of geospatial technology and multi-criteria decision analysis for groundwater potential mapping in a Semi-Arid region. *Water* 14 (6), 882. <https://doi.org/10.3390/w14060882>.
- Meliho, M., Khattabi, A., Driss, Z., Orlando, C.A., 2022. Spatial prediction of flood-susceptible zones in the Ourika watershed of Morocco using machine learning algorithms. *Appl. Comput. Inform.* <https://doi.org/10.1108/ACI-09-2021-0264>.
- Meliho, M., Noura, A., Benmansour, M., Boulmane, M., Khattabi, A., Mhammedi, N., Benkdad, A., 2019. Assessment of soil erosion rates in a Mediterranean cultivated and uncultivated soils using fallout ¹³⁷Cs. *J. Environ. Radioact.* 208–209, 106021 <https://doi.org/10.1016/j.jenvrad.2019.106021>.
- Miao, F., Zhao, F., Wu, Y., Li, L., Török, Á., 2023. Landslide susceptibility mapping in Three Gorges Reservoir area based on GIS and boosting decision tree model. *Stoch. Environ. Res. Risk Assess.* 1–21. <https://doi.org/10.1007/s00477-023-02394-4>.
- Micić Ponjiger, T., Lukić, T., Basarin, B., Jokić, M., Wilby, R.L., Pavić, D., Morar, C., 2021. Detailed analysis of spatial-temporal variability of rainfall erosivity and erosivity density in the central and southern Pannonian basin. *Sustainability* 13 (23), 13355. <https://doi.org/10.3390/su132313355>.
- Micić Ponjiger, T., Lukić, T., Wilby, R.L., Marković, S.B., Valjarević, A., Dragičević, S., Milanović, M.M., 2023. Evaluation of rainfall erosivity in the western balkans by mapping and clustering ERA5 reanalysis data. *Atmosphere* 14 (1), 104. <https://doi.org/10.3390/atmos14010104>.
- Mokarram, M., Zarei, A.R., 2021. Determining prone areas to gully erosion and the impact of land use change on it by using multiple-criteria decision-making algorithm in arid and semi-arid regions. *Geoderma* 403, 115379. <https://doi.org/10.1016/j.geoderma.2021.115379>.
- Mosaffaie, J., Salehpour Jam, A., Tabatabaei, M.R., Kousari, M.R., 2021. Trend assessment of the watershed health based on DPSIR framework. *Land Use Pol.* 100, 104911 <https://doi.org/10.1016/j.landusepol.2020.104911>.
- Mosavi, A., Ozturk, P., Chau, K.-w., 2018. Flood prediction using machine learning models: literature review. *Water* 10 (11), 1536. <https://doi.org/10.3390/w10111536>.
- Moustakim, M., Benmansour, M., Noura, A., Benkdad, A., Damnati, B., 2022. Caesium-137 re-sampling approach and excess Lead-210 sediment dating to assess the impacts of climate change and agricultural practices on soil erosion and sedimentation in Northwest Morocco. *Environ. Earth Sci.* 81 (10), 278. <https://doi.org/10.1007/s12665-022-10409-6>.
- Namous, M., Hssaisoune, M., Pradhan, B., Lee, C.-W., Alamri, A., Elaloui, A., Ouayah, M., 2021. Spatial prediction of groundwater potentiality in large semi-arid and karstic mountainous region using machine learning models. *Water* 13 (16), 2273. <https://doi.org/10.3390/w13162273>.
- Naorem, A., Jayaraman, S., Dang, Y.P., Dalal, R.C., Sinha, N.K., Rao, C.S., Patra, A.K., 2023. Soil constraints in an arid environment—challenges, prospects, and implications. *Agronomy* 13 (1), 220. <https://doi.org/10.3390/agronomy13010220>.
- Nazari Samani, A., Ahmadi, H., Jafari, M., Boggis, G., Ghoddousi, J., Malekian, A., 2009. Geomorphic threshold conditions for gully erosion in Southwestern Iran (Boushehr-Samal watershed). *J. Asian Earth Sci.* 35 (2), 180–189. <https://doi.org/10.1016/j.jseas.2009.02.004>.
- Nefeslioglu, H.A., Duman, T.Y., Durmaz, S., 2008. Landslide susceptibility mapping for a part of tectonic kelkit valley (eastern black sea region of Turkey). *Geomorphology* 94 (3), 401–418. <https://doi.org/10.1016/j.geomorph.2006.10.036>.
- Ouallali, A., Briak, H., Aassoumi, H., Beroho, M., Bouhsane, N., Moukchane, M., 2020. Hydrological foretelling uncertainty evaluation of water balance components and sediments yield using a multi-variable optimization approach in an external Rif's catchment. Morocco. *Alex. Eng. J.* 59 (2), 775–789. <https://doi.org/10.1016/j.aej.2020.02.017>.
- Ouallali, A., Kader, S., Bammou, Y., Aqnoy, M., Courba, S., Beroho, M., Hysa, A., 2024. Assessment of the erosion and outflow intensity in the rif region under different land use and land cover scenarios. *Land* 13 (2). <https://doi.org/10.3390/land13020141>.
- Pal, S., Paul, S., Debanshi, S., 2022. Identifying sensitivity of factor cluster based gully erosion susceptibility models. *Environ. Sci. Pollut. Control Ser.* 29 (60), 90964–90983. <https://doi.org/10.1007/s11356-022-22063-3>.
- Parvin, F., Ali, S.A., Calka, B., Bielecka, E., Linh, N.T.T., Pham, Q.B., 2022. Urban flood vulnerability assessment in a densely urbanized city using multi-factor analysis and machine learning algorithms. *Theor. Appl. Climatol.* 149 (1–2), 639–659. <https://doi.org/10.1007/s00704-022-04068-7>.
- Pham, B.T., Prakash, I., Singh, S.K., Shirzadi, A., Shahabi, H., Tran, T.-T.-T., Bui, D.T., 2019. Landslide susceptibility modeling using Reduced Error Pruning Trees and different ensemble techniques: hybrid machine learning approaches. *Catena* 175, 203–218. <https://doi.org/10.1016/j.catena.2018.12.018>.
- Pourghasemi, H.R., Sadhasivam, N., Kariminejad, N., Collins, A.L., 2020. Gully erosion spatial modelling: role of machine learning algorithms in selection of the best controlling factors and modelling process. *Geosci. Front.* 11 (6), 2207–2219. <https://doi.org/10.1016/j.gsf.2020.03.005>.
- Rahmati, O., Pourghasemi, H.R., Zeinivand, H., 2016. Flood susceptibility mapping using frequency ratio and weights-of-evidence models in the Golastan Province, Iran. *Geocarto Int.* 31 (1), 42–70. <https://doi.org/10.1080/10106049.2015.1041559>.
- Rahmati, O., Tahmasebipour, N., Haghizadeh, A., Pourghasemi, H.R., Feizizadeh, B., 2017. Evaluation of different machine learning models for predicting and mapping the susceptibility of gully erosion. *Geomorphology* 298, 118–137. <https://doi.org/10.1016/j.geomorph.2017.09.006>.
- Saha, S., Sarkar, R., Thapa, G., Roy, J., 2021. Modeling gully erosion susceptibility in Phuentsholing, Bhutan using deep learning and basic machine learning algorithms. *Environ. Earth Sci.* 80, 1–21. <https://doi.org/10.1007/s12665-021-09599-2>.
- Sahour, H., Gholami, V., Vazifedan, M., 2020. A comparative analysis of statistical and machine learning techniques for mapping the spatial distribution of groundwater salinity in a coastal aquifer. *J. Hydrol.* 591, 125321 <https://doi.org/10.1016/j.jhydrol.2020.125321>.
- Salhi, A., El Hasnaoui, Y., Pérez Cutillas, P., Heggy, E., 2023. Soil erosion and hydroclimatic hazards in major African port cities: the case study of Tangier. *Sci. Rep.* 13 (1), 13158 <https://doi.org/10.1038/s41598-023-40135-3>.
- Saljnikov, E., Lavrishchev, A., Römbke, J., Rinklebe, J., Scherber, C., Wilke, B.-M., Eulenstein, F., 2022. Understanding and monitoring chemical and biological soil degradation. *Advances in Understanding Soil Degradation* 75–124. https://doi.org/10.1007/978-3-030-85682-3_3.
- Sarker, I.H., 2021. Machine learning: algorithms, real-world applications and research directions. *SN computer science* 2 (3), 160. <https://doi.org/10.1007/s42979-021-00592-x>.
- Schicker, R., Moon, V., 2012. Comparison of bivariate and multivariate statistical approaches in landslide susceptibility mapping at a regional scale. *Geomorphology* 161–162, 40–57. <https://doi.org/10.1016/j.geomorph.2012.03.036>.
- Sestras, P., Mircea, S., Roşca, S., Bilaşco, Ş., Sălăgean, T., Dragomir, L.O., Kader, S., 2023. GIS based soil erosion assessment using the USLE model for efficient land management: a case study in an area with diverse pedo-geomorphological and bioclimatic characteristics. *Not. Bot. Horti Agrobot. Cluj-Napoca* 51 (3), 13263. <https://doi.org/10.15835/nbha51313263>.
- Seydi, S.T., Kanani-Sadat, Y., Hasanlou, M., Sahraei, R., Chanussot, J., Amani, M., 2022. Comparison of machine learning algorithms for flood susceptibility mapping. *Rem. Sens.* 15 (1), 192. <https://doi.org/10.3390/rs15010192>.
- Shruthi, G., Krishna Raj, 2021. Local frequency descriptor and hybrid features for classification of brain magnetic resonance images using ensemble classifier. *Int. J. Adv. Comput. Sci. Appl.* 12 (11). <https://doi.org/10.14569/IJACSA.2021.0121122>.
- Tehrany, M.S., Pradhan, B., Mansor, S., Ahmad, N., 2015. Flood susceptibility assessment using GIS-based support vector machine model with different kernel types. *Catena* 125, 91–101. <https://doi.org/10.1016/j.catena.2014.10.017>.
- Tiwari, A., G., Vishwakarma, B.D., 2021. Parameter importance assessment improves efficacy of machine learning methods for predicting snow avalanche sites in Leh-Manali Highway, India. *Sci. Total Environ.* 794, 148738 <https://doi.org/10.1016/j.scitotenv.2021.148738>.
- Wang, Z., Lai, C., Chen, X., Yang, B., Zhao, S., Bai, X., 2015. Flood hazard risk assessment model based on random forest. *J. Hydrol.* 527, 1130–1141. <https://doi.org/10.1016/j.jhydrol.2015.06.008>.
- Wang, Z., Liu, Y., He, D., Chan, S., 2021. Intrusion detection methods based on integrated deep learning model. *Comput. Secur.* 103, 102177. <https://doi.org/10.1016/j.cose.2021.102177>.
- Wassie, S.B., 2020. Natural resource degradation tendencies in Ethiopia: a review. *Environmental Systems Research* 9 (1), 1–29. <https://doi.org/10.1186/s40068-020-00194-1>.
- Xiao, S., Hou, R., Li, T., Meng, F., Fu, Q., Li, M., Dong, S., 2023. Mechanism of microbial inhibition of rainfall erosion in black soil area, as a soil structure builder. *Soil Tillage Res.* 233, 105819 <https://doi.org/10.1016/j.still.2023.105819>.
- Youssef, B., Bouskri, I., Brahim, B., Kader, S., Brahim, I., Abdelkrim, B., Spalević, V., 2023. The contribution of the frequency ratio model and the prediction rate for the analysis of landslide risk in the Tizi N'tichka area on the national road (RN9) linking Marrakech and Ouarzazate. *Catena* 232, 107464. <https://doi.org/10.1016/j.catena.2023.107464>.
- Yu, Z., Deng, X., 2022. Assessment of land degradation in the North China Plain driven by food security goals. *Ecol. Eng.* 183, 106766 <https://doi.org/10.1016/j.ecoleng.2022.106766>.
- Zhang, H., Liang, X., Chen, H., Shi, Q., 2021. Spatio-temporal evolution of the socio-ecological landscape resilience and management zoning in the loess hill and gully region of China. *Environmental Development* 39, 100616. <https://doi.org/10.1016/j.envdev.2021.100616>.
- Zhao, G., Pang, B., Xu, Z., Peng, D., Xu, L., 2019. Assessment of urban flood susceptibility using semi-supervised machine learning model. *Sci. Total Environ.* 659, 940–949. <https://doi.org/10.1016/j.scitotenv.2018.12.217>.

Optimizing flood susceptibility assessment in semi-arid regions using ensemble algorithms: a case study of Moroccan High Atlas

Original Paper | Open Access
Volume 120, pages 1–15 (2023)

Download PDF

Paul Sestras

Faculty of Civil Engineering, Technical University of Cluj-Napoca, 400020, Cluj-Napoca-Napoca, Romania

Academy of Romanian Scientists, Ilfov 3, 50044, Bucharest, Romania

[View author publications](#)

You can also search for this author in [PubMed](#) | [Google Scholar](#)

Youssef Bammou

Velibor Spalevic, Paul Sestras, Paolo Billi & Slobodan B. Marković

2082 Accesses 2 Citations [Explore all metrics](#) →



Natural Hazards

[Aims and scope](#) →

[Submit manuscript](#) →

[Use our pre-submission checklist](#) →

Avoid common mistakes on your manuscript.

NATURAL HAZARDS

Publisher name: SPRINGER

Journal Impact Factor™

3.3

2023

3.6

Five Year

JCR Category	Category Rank	Category Quartile
GEOSCIENCES, MULTIDISCIPLINARY <i>in SCIE edition</i>	65/253	Q2
METEOROLOGY & ATMOSPHERIC SCIENCES <i>in SCIE edition</i>	43/110	Q2
WATER RESOURCES <i>in SCIE edition</i>	35/127	Q2

Source: Journal Citation Reports 2023. [Learn more](#)

Journal Citation Indicator™

0.82

2023

0.82

2022





Optimizing flood susceptibility assessment in semi-arid regions using ensemble algorithms: a case study of Moroccan High Atlas

Youssef Bammou¹ · Brahim Benzougagh² · Brahim Igmoullan¹ · Abdessalam Ouallali³ · Shuraik Kader^{4,5} · Velibor Spalevic⁶ · Paul Sestras^{7,8} · Paolo Billi^{9,10} · Slobodan B. Marković¹¹

Received: 14 November 2023 / Accepted: 4 March 2024 / Published online: 21 March 2024
© The Author(s) 2024

Abstract

This study explores and compares the predictive capabilities of various ensemble algorithms, including SVM, KNN, RF, XGBoost, ANN, DT, and LR, for assessing flood susceptibility (FS) in the Houz plain of the Moroccan High Atlas. The inventory map of past flooding was prepared using binary data from 2012 events, where “1” indicates a flood-prone area and “0” a non-flood-prone or extremely low area, with 762 indicating flood-prone areas. 15 different categorical factors were determined and selected based on importance and multicollinearity tests, including slope, elevation, Normalized Difference Vegetation Index, Terrain Ruggedness Index, Stream Power Index, Land Use and Land Cover, curvature plane, curvature profile, aspect, flow accumulation, Topographic Position Index, soil type, Hydrologic Soil Group, distance from river and rainfall. Predicted FS maps for the Tensift watershed show that, only 10.75% of the mean surface area was predicted as very high risk, and 19% and 38% were estimated as low and very low risk, respectively. Similarly, the Haouz plain, exhibited an average surface area of 21.76% for very-high-risk zones, and 18.88% and 18.18% for low- and very-low-risk zones respectively. The applied algorithms met validation standards, with an average area under the curve of 0.93 and 0.91 for the learning and validation stages, respectively. Model performance analysis identified the XGBoost model as the best algorithm for flood zone mapping. This study provides effective decision-support tools for land-use planning and flood risk reduction, across globe at semi-arid regions.

Keywords Flood susceptibility · GIS · Machine learning · Factor importance · Tensift watershed

Abbreviations

ABHT	Tensift Basin Hydraulic Agency
ANN	Artificial neural network
AUC-ROC	Area under curve of the receiver operating characteristic
CM	Correlation matrix
DEM	Digital elevation model

Extended author information available on the last page of the article

DT	Decision tree
FAO	Food and Agriculture Organisation
FR	Frequency ratio
FS	Flood susceptibility
GIS	Geographic informatic system
HSG	Hydrologic Soil Group
IDW	Inverse distance weighted
KNN	K-nearest neighbor
LR	Logistic regression
LULC	Land use and land cover
MAE	Mean absolute error
MI	Mutual information
ML	Machine learning
NFR	Normalized frequency ratio
RMSE	Root mean square error
RF	Random forests
SPI	Stream power index
SVM	Support vector machines
TOL	Tolerance
TPI	Topographic position index
TRI	Topographic roughness index
TWI	Topographic wetness index
USGS	United States Geological Survey
VIF	Variance inflation factor
XGBoost	EXtreme Gradient Boosting contraction

1 Introduction

The current technological advancements are dealing hard to cope with the recovery from various natural disasters across the world because of their unpredictability, and the enormous damages result as consequences. Among these natural occurrences, flooding stands out as destructive phenomenon that directly impact about 200 million people annually in terms of infrastructural, economic detriments, and loss of lives (Abdulrazzak et al. 2019; Sivakumar 2005). In the twentieth century, more than 100,000 lives were killed by floods and affected over 1.4 billion people in terms of infrastructure and economic destructions (El Alfy 2016; Han and Sharif 2021). Systematic risk reduction strategies with the integration of sophisticated scientific technology to forecast flooding scenarios in advance, that would incorporate all the associated parameters in particular regions related to climatic and geographic features are necessary to mitigate the adverse impacts of floods.

In contrary to popular beliefs, floods are more damaging in semi-arid and desert areas than in wetlands. The main reason for these drastic losses is the absence of a systematic prediction tool for runoffs in these areas because of the lack of hydrometeorological data and gauging of the flash floods (Aryal et al. 2020). After earthquakes, floods are the most frequent natural catastrophe in Morocco in terms of fatalities and injuries. The Tensift watershed and the Haouz plain are very vulnerable to flooding. In fact, the sub-catchment regions of the Tensift have witnessed disastrous floods because of torrential rains in 1995

and 2002, which not only caused the deaths of more than 200 people but also enormous material damage (Youssef et al. 2023a, b).

The Haouz plain and Tensift watershed are categorized as belonging to semi-arid zones on the Kopper-Geiger world climate map (Bouramtane et al. 2020), where it is exceedingly challenging and complex to investigate these phenomena. Due to climatic changes in rainfall, urbanization, and variables relating to the sub-watersheds of Ourika, R'dat, Zat, Rheraya, Assif El Mal, N'fis and Seksaou, the flood disaster in the Tensift watershed and the Haouz plain has gotten worse. Consequently, comprehensive research and investigations on flood susceptibility (FS) have become imperative in accurately identifying high-risk areas and implementing effective preventative measures (Echogdali et al. 2022).

Apart from climate-related influences, various other factors play a crucial role in determining flood dynamics, necessitating their consideration for accurate flood risk evaluation. Among these factors, slope characteristics directly affect hydrological processes, influencing the direction of precipitation. A higher permeability of the topsoil layer on the land enhances the infiltration capacity and reduces runoff (Bennani et al. 2019; Benssaou et al. 2003). Additionally, factors such as geological formations and land use changes, such as transitions from forested areas to agricultural fields or from agricultural zones to urbanized regions, play significant roles in flood management (Kader et al. 2023). Additionally, there are climatic factors that affect flood risk, including precipitation rate and volume and melting (Anjos et al. 2015; Bennani et al. 2019; Soulaïmani and Bouabdelli 2005).

Recent advances in ML algorithms have been combined with GIS and remote sensing methods, greatly enhancing the mapping of flood risk and spatial variability. The commonly used ML techniques for predicting flood risk are the ANN—Artificial Neural Network (Dahri et al. 2022), SVM—Support Vector Machine (Choubin et al. 2019a, b), RF—Random Forests (Billah et al. 2023), LR—logistic Regression (Ali et al. 2020), adaptive neuro-fuzzy inference systems (Ahmadlou et al. 2019), and long-term memory (Apyadin et al. 2020; Dazzi et al. 2021). In order to predict the spatial and temporal variation of flood risk by relating runoff to precipitation and which require field observation data, several studies on the likelihood of flood occurrence have been conducted using various models and techniques, such as rainfall runoff like GSSHA (Kirker and Toran 2023), MIKE DHI (Beden and Ulke Keskin 2021), HEC-HMS (El Alfy 2016), and SWAT (Tan et al. 2020). The regions vulnerable to flooding in this model are divided into two categories (1) not floodable (2) floodable: on the basis of historical and geo-environmental data (Benkirane et al. 2020), which do not consider the field observation data. To forecast floods by incorporating all three data types including the field observation data, further models based on GIS and remote sensing have been developed (Costache et al. 2022; Mosavi et al. 2018).

Despite the publication of considerable studies, the use of machine learning (ML) techniques to analyze floods in the Tensift watershed and Haouz plain has lacked the required attention. These methodologies must be incorporated to map and forecast FS in the locations, and it is an utmost important to identify the best feasible model that is suitable for the study area in terms of relevance and serviceability. To resolve this identified research gap, this study was designed based on the following primary objectives: were firstly to evaluate the ability of the SVM, KNN, RF, XGBoost, ANN, DT, and LR methods to predict flood susceptibility areas, secondly to study the role that each flood conditioning factor plays in the development of flood susceptibility maps, Thirdly to create flood susceptibility maps using an ensemble modelling strategy for each model and finally to identify the areas at risk of flooding in the Haouz plain and the Tensift catchment.)

The novelty of this study lies in the comprehensive evaluation of the multiple advanced algorithms on flood prediction, offering a diverse toolkit for tackling this complex issue.

Unlike the published research sources available within this field in scientific literature, this research is structured on a systematic comparison of various ensembled algorithms, including RF, SVM, k-nearest neighbor (KNN), and eXtreme Gradient Boosting contraction (XGBoost). This study is first-of-its-kind to the North African region, providing a comprehensive FS assessment crucial for risk management in the study region.

This research study offers a sophisticated methodology for scientific community to assess floods that integrates a Multifactor analysis approach by integrating various influential factors, such as slope, elevation, vegetation index, terrain ruggedness, land use and land cover. By analyzing the binary data from past flooding events, the study skillfully produced a FS map that delineates risk levels across the landscape. This research is especially significant since it can provide extremely precise flood prediction models, which are useful for reducing the likelihood of future floods and lessening their negative effects. These findings hold valuable implications for flood management and risk reduction strategies and offers insights for policymakers, enabling informed decisions for land use planning and disaster preparedness. This research's outcome furnishes decision-support tools crucial for informed land-use planning and mitigation efforts.

2 Material and methods

2.1 Study area

The Tensift watershed, located in the central part of Morocco near Marrakech, has an area of 20,000 km² (Fig. 1). It is made up of two separate hydrological zones with opposing tendencies. The southern slopes of the Atlas Mountains, which stand above 4000 m in height, get significant precipitation and snowfall, amounting to up to 600 mm every year. These mountains provide an important source of water for the large Haouz plain downstream, which is semi-arid with an annual precipitation of 250 mm. Particularly, irrigation operations benefit a substantial area of this plain, notably the 2000 km² irrigated Haouz plain.

Geologically, there are three primary geological formations that make up the watershed of the High Atlas near Marrakech (Duclaux 2005): (1) The Permo-Triassic is the dominant formation in the east. It frequently coexists with Precambrian and Ordovician schistose

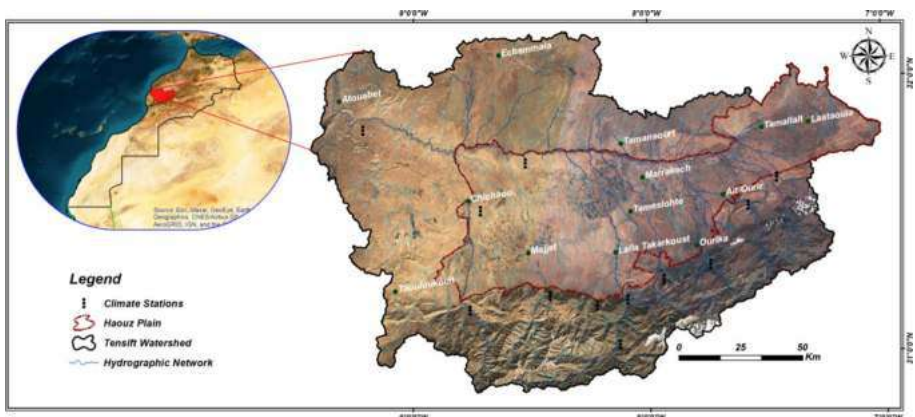


Fig. 1 Study area of the Tensift watershed and the Haouz plain [Source – Study authors]

rocks; (2) Precambrian eruptive and metamorphic rocks may be found in the central region, which is home to the highest peaks of the Atlas; and (3) primary and secondary limestone formations can be found in the western region. Since most of these geological formations have limited permeability, continuous surface runoff and, eventually, the development of considerable runoff after heavy rains, are encouraged.

In addition, this area has a varied and unpredictable hydrological behavior that is influenced by its geomorphological and climate factors. It gives rise to long-lasting storms that frequently result in significant damage, such as the inundations that occurred in Ourika on August 17, 1995, and October 28, 1999, which resulted in 200 fatalities, the destruction of 142 buildings, and the inundation of more than 300 ha of agricultural land. These events were reported by the Tensift Basin Hydraulic Agency (ABHT).

2.2 Predictors and conditioning factors of flooding

Based on the research area and data available, the flood-conditioning parameters, including topography, elevation, slope, aspect, lithology, land use, precipitation, and habitation, were taken into consideration. The four categories of these flood conditioning elements are hydrology, geography, environment, and ethnography. In this study, the following factors were taken into account from the Digital Elevation Model (DEM) at a resolution of 30 m, downloaded from Were downloaded from the website of United States Geological Survey (USGS); slope, aspect, elevation, flow accumulation, topographic position index (TPI), topographic roughness index (TRI), stream power index (SPI), plane curvature, topographic wetness index (TWI), profile curvature, distance to river, for precipitation, this factor is calculated by interpolating data from 9 climate stations supplied by ABHT using IDW method, for land use and land cover (LULC) is extracted by supervised classification using the Maximum Likelihood method from a Sentinel 2A satellite scene supplied by Scihub Copernicus, the soil type factor was developed using the database provided by the FAO, the Hydrologic Soil Group (HSG) factor was developed using data from EARTH-DATA, illustrated by Fig. 2 and Table 1.

Precipitation is an important climatic factor that impacts the likelihood of floods. As a result, it is critical to underline that the annual mean rainfall acts as a core component in most flood vulnerability studies. Hydrometeorological aspect has been proven as an indispensable flood predictor due to its substantial relationship with soil moisture changes (Ighile et al. 2022; Verma et al. 2022). The aspect grid values were used to construct a single flat region as well as the ninth north, northeast, east, southeast, southwest, west, and northwest divisions. The TPI which makes it possible to identify one of these most recent cells, considers the height of the surrounding cells (Jenness, 2000). The following classes have been defined for the TPI card in this study: $(-198)-(-123)$; $(-123)-(-40)$; $(-40)-(-10)$; $(-10)-40$; $40-140$; and $140-247$.

SPI is another morphometric parameter that will be utilized for flood forecasting. Erosive force and transport capacity are included while calculating the water values. The SPI maps have been divided into the following categories based on professional opinion: <1 ; $1-2$; $2-6$; $6-8$ and $8-15$.

Similarly, slope is a major morphometric feature that has a significant impact on flooding (Ganie et al. 2022). It is well known that an area with a steep slope that causes significant surface runoff is more prone to flooding than a flat area. The slope was separated into the following ranges: $0-5$; $5-12$; $12-22$; $22-33$; and $33-71$ to create the slope map. Due to the permeability of the rock, the soil types primarily control the amount of water

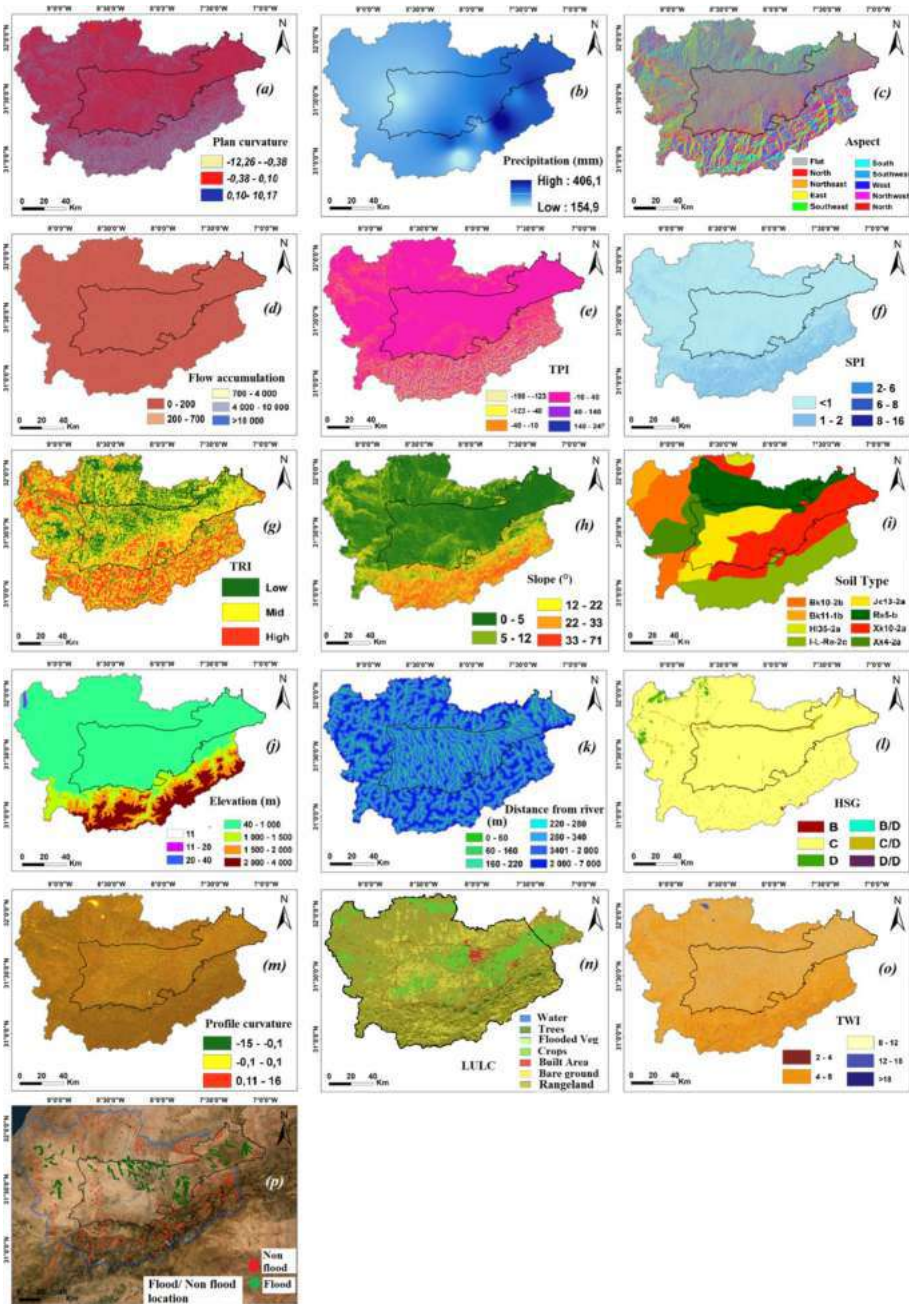


Fig. 2 The fifteen flood factors developed for the study area **a** plan curvature, **b** precipitation, **c** Aspect, **d**: Flow accumulation, **e** TPI, **f** SPI, **g** TRI, **h** Slope, **i** Soil type, **j** Elevation, **k** Distance from river, **l** HSG, **m** Profile-curvature, **n** LULC, **o** TWI, and **p** inventory of flooded and non-flooded areas). [Source – Study authors]

Table 1 Sources, equations and data processing used in this study

Factors	Layers and units	Equation & Processing	Source
Topographic factors	Elevation (m)	Fill tool for correction in ArcGIS	SRTM-DEM (Digital Elevation Model) were downloaded from the website of United States Geological Survey (USGS) https://earthexplorer.usgs.gov/
	Slope (°)	Processing in ArcGIS	
	Stream Power Index (SPI)	$SPI = As \times \tan\beta$ As is the upstream drainage area and β is the slope degree	
	Topographic Position Index (TPI)	Processing in ArcGIS	
	Aspect	Processing in ArcGIS	
	Plan Curvature	Processing in ArcGIS	
Geomorphological factors	Profile Curvature	Processing in ArcGIS	
	Topographic Wetness Index (TWI)	$TWI = \ln(As/\tan\beta)$ As is the upstream drainage area and β is the slope degree	
	Topographic Roughness Index (TRI)	Processing in ArcGIS	
	Distance to rivers (m)	Processing in SAGA GIS	
	Flow Accumulation		

Table 1 (continued)

Factors	Layers and units	Equation & Processing	Source
Geological factors	Soil Type	Xk10-2a: (48.7% sand, 29.9% silt, 21.6% caly and 0.64 orgC) Bk10-2b: (81.6% sand, 6.8% silt, 11.7% caly and 0.44 orgC) Re5-b: (68.3% sand, 15.1% silt, 16.6% caly and 0.5 orgC) Xk4-2a: (47.7% sand, 30.9% silt, 22.6% caly and 0.65 orgC) Je13-2a: (39.6% sand, 39.9% silt, 20.6% caly and 0.65 orgC) IL-Re-2c: (58.9% sand, 16.2% silt, 24.9% caly and 0.97 orgC)	https://www.fao.org/soils-portal/data-hub/soil-maps-and-databases/faounesco-soil-map-of-the-world/en
Climatic factors	Rainfall (mm)	HSG B: moderately low runoff potential (50–90% sand and 10–20% clay) C: moderately high runoff potential (<50% sand and 20–40% clay) D: high runoff potential (<50% sand and >40% clay) B/D: high runoff potential unless drained (50–90% sand and 10–20% clay) C/D: high runoff potential unless drained (<50% sand and 20–40% clay) D/D: high runoff potential unless drained (<50% sand and >40% clay) Interpolation of monthly rainfall using the IDW method	https://daac.ornl.gov/SOILS/guides/Global_Hydro_logic_Soil_Group.html Tensift Hydraulic Basin Agency (ABHT)
LAND cover factors	LandUse-LandCover (LULC)	Supervised classification using the Maximum Likelihood method	Sentinel-2 Images https://scihub.copernicus.eu/dhus/#/home

penetration, which in turn affects the flooding occurrence (Tariq et al. 2022). Eight classes were discovered in this research region: (Bk10-2b; Bk11-1b; HI35-2a; I-L-Re-2c; Jc13-2a; Re5-b Xk10-2a and Xk4-2a). Because flooding is more common in low-lying areas, elevation is a second critical morphometric component in determining flood vulnerability. The elevation map for the case study was created using the following seven elevation classes: 11 m, 11–20 m, 20–40 m, 40–1000 m, 1000–1500 m, 1500–2000 m, and 2000–4000 m. The flood control parameter known as the hydrologic soil group has a big influence on how much water infiltration occurs.

Soil texture has a direct impact on infiltration due to its influence on hydraulic conductivity. There are six main hydrological soil types in the Tensift watershed: B, C, D, B/D, C/D and D/D. The direction of the slope in the vertical plane influences the curvature of the soil profile. Positive numbers indicate that surface runoff is decreasing, while negative values suggest that surface runoff is increasing. Three classes were used to create the profile curvature map: -15 to -0.1 , -0.1 to 0.1 , and 0.1 to 16 . LULC, a factor in flood forecasting, has a considerable impact on processes involving surface runoff and water storage. There are seven main types of land use in the Tensift watershed: water bodies, forest areas, flooded areas, vegetation, crops, built-up areas, bare lands, and rangeland. The slope angle and catchment area measurements are used to calculate the TWI. This metric highlights the role that geography plays in the phenomena of water accumulation. The classes described below were developed using the natural breaks approach to produce the topographic moisture index map: 1–4; 4–8; 8–12; 12–18 and > 18 .

2.3 Flood Locations Inventory

For management and mitigation strategies to be effective, it is crucial to comprehend and analyze the flood inventory. The past flood occurrences serve as crucial input variables for calculating FS. The origin of the flood inventory varies by geographic region, but commonly include previous engineering and scientific work, the hydraulic agency, field surveys, or recently developing technology. Variables that affect flood vulnerability have been employed as points for flood placement in several published studies including (Chapi et al. 2017; Costache et al. 2022; Wang et al. 2018). Based on information from scholarly journals, historical data, Google Earth, and satellite image analysis, the current study created a flood inventory map. As a result, the flooding that occurred in the Tensift watershed and the Haouz plain utilized a total of 890 flood event sites (Figs. 2 and 3). These selected flood plain locations were considered relevant in the study area, as they shed light on the complex issues associated with flooding.

2.4 Flood factor classification analysis

In the current study, seven prediction models were used to enhance the (ML) prediction of flood hazards. Various statistical tests were performed on these models to discover strong linear connections between different components. These tests, which included correlation matrix (CM) analysis, variance inflation factor (VIF) (Eq. 1), tolerance (TOL) (Eq. 2), and mutual information (MI) (Eq. 3), aided in identifying and eliminating non-significant components. VIF values larger than 10 and TOL values of 0.1, in particular, revealed significant multicollinearity amongst components (Miao et al. 2023). If two variables were significantly correlated and satisfied the multicollinearity criterion, the one with the higher VIF was eliminated based on the CM analysis. The MI

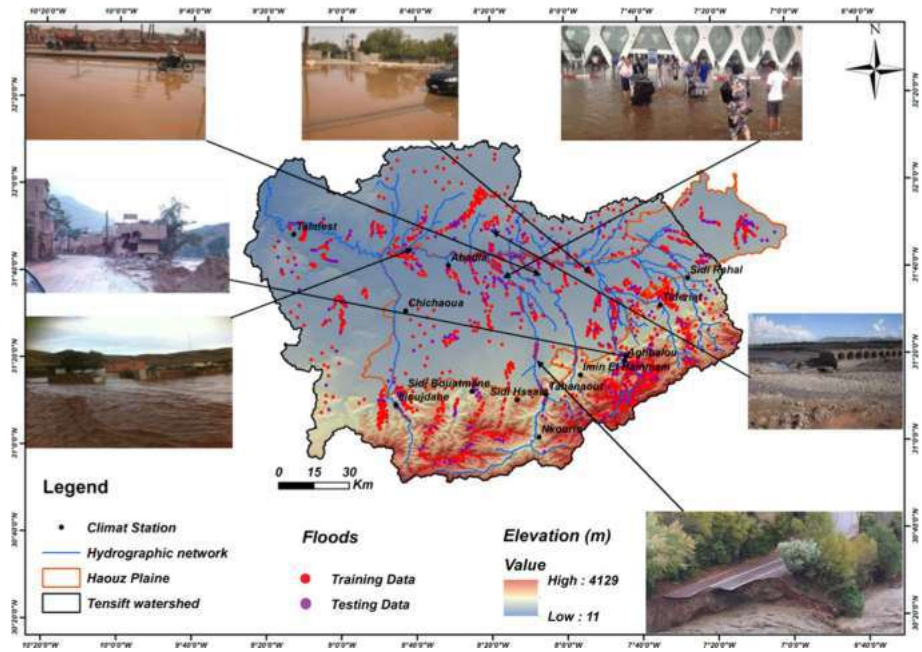


Fig. 3 Inventory map and examples of floods in the Tensift watershed and the Haouz plain [Source – Study authors]

analysis revealed the significance of factors causing floods, with low MI values suggesting little influence and leading to their removal.

$$VIF_j = \left[\frac{1}{Tol_j} \right] \tag{1}$$

$$Tol = 1 - R_j^2 \tag{2}$$

$$MI(n, j) = H(n) - H\left(\frac{n}{j}\right) \tag{3}$$

where j is the FS influence factor, n is the subclass of FS influence factors, Tol_i is the tolerance of j , VIF_j is the variance inflation factor of j , $MI(n; j)$ is the mutual information for n and j , R is the determining coefficient of the regression for the predisposition of j , on all other predisposition factors, $H(n)$ is the entropy of n , and $H(n/j)$ is the conditional entropy for n given the flooded area state factor j .

The optimized selection analysis of FS influencing factors and model application was based on the determination of the normalized frequency ratio (NFR) (Eq. 4), which has recently been a recommended step to unify the importance of the type of input data for the different factors (Mao et al. 2022; Namous et al. 2021). Consequently, the frequency ratio (FR) (Eq. 5) was assigned to the subclass of factors influencing the FS in the sense of defining the relationship between the flooded locations and the factors influencing the

FS (Masoud et al. 2022). The results were then normalized using Eq. (5). As a result, all the maps used were converted to an NFR between 0 for low FS, and 1 for high FS.

$$NFR_n = \frac{FR_n - \text{Max}(FR_n)}{\text{Max}(FR_n) - \text{Min}(FR_n)} * (0.99 - 0.01) + 0.01 \tag{4}$$

$$FR_n = \frac{\frac{W_n}{W_t}}{\frac{P_n}{P_t}} \tag{5}$$

where n represents the subclass of factors influencing FS, FRn is the frequency ratio of n, NFRn is the normalized frequency ratio of n, Wn is the number of water sampling points located in n, Wt is the total number of water sampling points, Pn is the number of pixels in n, and Pt is the total number of all pixels.

The subclasses of FS influencing factors were determined by classifying maps produced using Jenks’ natural break technique (Sarker 2021); the exceptions are aspect, LULC, and lithology, which have been classified according to directional units, supervised classification, and lithological units, respectively.

2.5 Methodology flowchart

This research suggests the use of seven different ML models as well as GIS and remote sensing to monitor flooding. As our model uses a binary categorization (0: no flooding; 1: flooded), the location of non-flooded areas is included in the susceptibility mapping process. The methodological strategy used to draw up the susceptibility maps for this study involves the following main stages, described in Fig. 4.

The construction of the initial GIS database, which includes two types of data, namely the historical flooded areas extracted through different and the development of different maps of flood conditioning factors.

The transformation of this database into numerical mode used the FR method to indicate the relationships between the influencing factors and the FS. After applying multicollinearity analyses such as correlation matrix analysis (CM), VIFs, Tol and the mutual information test (MI), the factors influencing the FS according to their importance were selected. The second step consists of evaluating the performance and effectiveness of the seven algorithms applied, namely DT, ANN, LR, KNN, SVM, RF, XGBoost for training and test data, according to validation criteria such as specificity, sensitivity, false positive rate, precision, F1 score, accuracy, mean absolute error, root-mean-square error and the area under curve of the receiver operating characteristic (AUC-ROC). In the final stage, the database was divided into training and test data, with 70% and 30% of the total data sample being flooded and non-flooded respectively for the generation of the FS maps. External validation of the random sample for each site was carried out using ArcGIS 10.5.1 software to ensure a non-objective sampling process.

2.6 Description of the learning algorithms

In this work, seven algorithms were used to estimate flooding susceptibility: SVM, RF, K-NN, LR, ANN, DT, and XGBoost. Table 2 contains descriptions of the algorithms that were

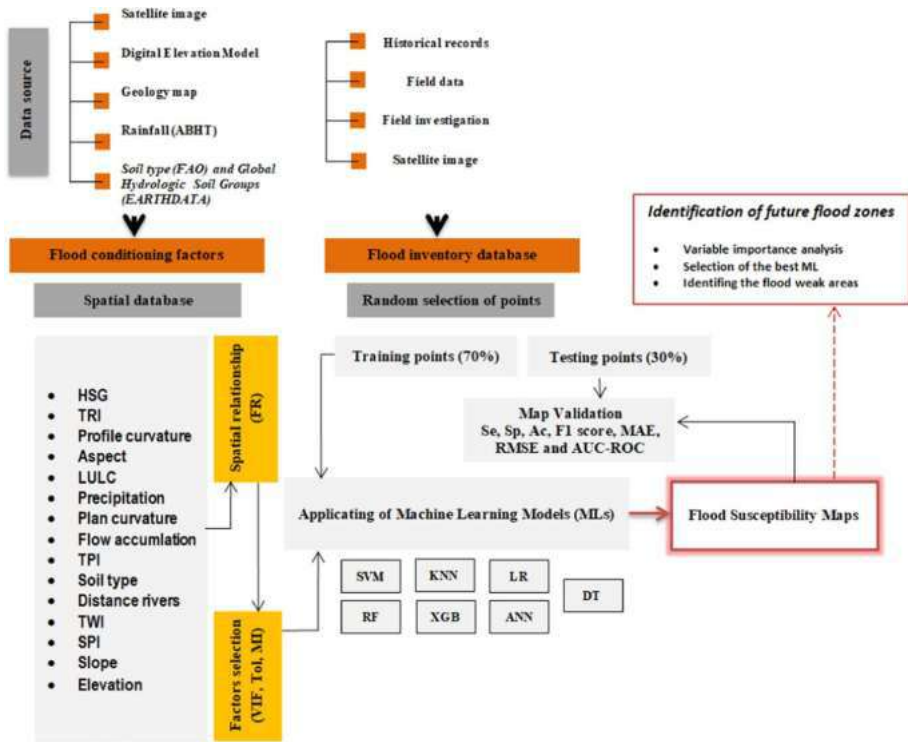


Fig. 4 Outline of the methodological workflow adopted in this study

chosen. Furthermore, there are surveys with scientific establishments that discuss the parameters, classification, and functioning of these systems (Liu and Lang 2019; Sarker 2021).

2.7 Validation techniques

The results of the proposed technique were validated for the seven models generated from various performance measures including specificity, precision, sensitivity, and accuracy. If there is a geographical connection between the measured floodable and non-floodable regions and the anticipated floodable areas, the performance indices are deemed significant, according to the outcomes of (Costache 2019a; Costache and Bui 2020).

The following parameters TP (true positives), TN (true negatives), FP (false positives) and FN (false negatives) were used to find Specificity, Sensitivity, Accuracy, Precision, recall and F1 score (Eqs. 6–10). The analysis also used another popular measure known as the receiver operating characteristic (ROC) curve. The most used ROC curve analyzes the area under the curve to determine the accuracy of prediction models (AUC) illustrated by Eq. 11. FS mapping has also used root mean square error (RMSE) and mean absolute error (MAE) as of Eqs. 12 and 13. Both types of indices have been used in several previous research studies.

$$\text{Specificity} = \frac{\text{TN}}{\text{FP} + \text{TN}} \quad (6)$$

Table 2 Description of the four algorithms applied in this study

Model	Developed by	Description	Applied by
KNN	Fix and Hodges (1952) and Cover and Hart (1967)	One of the ML algorithms, the K-NN algorithm is based on the supervised learning method. It places the new case in the category that is most like the existing categories by assuming that there is a likelihood that the new case/data will be like the current cases. That is, flooded and non-flooded points	Costache (2019b), Sami and Ibrahim (2021), Shah et al. (2020), Thi Thuy Linh et al. (2022)
SVM	Bottou and Vapnik (1992) and Cortes and Vápnik (1995)	Each datum is represented by a point in an n-dimensional space (n—the number of features) in the SVM method, with each feature’s value denoting a specific position. The best hyperplane that effectively distinguishes the two classes is then found during the classification. The prediction of FS is done using the radial basis function	Dazzi et al. (2021), Tehrani et al. (2014)
RF	Breiman (2001)	Based on various groups of the FS-influencing variables identified using the bootstrap aggregation (also known as bagging) and random feature selection procedures, a meta-estimator called random forest updates a specific number of DT classifiers. It enhances the model’s propensity to predict outcomes	Chapi et al. (2017), Hosseini et al. (2020), Mosavi et al. (2018)
XGBoost	Chen and Guestrin (2016)	An enhanced Gradient Boosting second-order tree boosting is known as eXtreme Gradient Boosting second-order derivatives are used, which lower the loss function and provide more precise trees	Thi Thuy Linh et al. (2022)
ANN	Hopfield (1982)	(ANN) has been developed from the multi-layer perceptron with three neural layers: a primary layer and an intermediate or hidden layer. In the first stage of learning, the network predicts the label of everyone (flooded or non-flooded) using its weights and bias values. A cost function determines the difference between the calculated value and the observed value. In the backpropagation step, each weight is updated according to the gradient of the cost function. This process continues until convergence is reached or a maximum number of learning epochs is reached	Melitho et al. (2022), Parvin et al. (2022)

Table 2 (continued)

Model	Developed by	Description	Applied by
DT	Breiman (2001)	This algorithm selects the most suitable features (the factor influencing flooding) as the root and generates child nodes. Based on the top-down observations and the processing results at each level, predictions are obtained, from the root to the child nodes corresponding to the new data (flooded and/or non-flooded)	Choubin et al. (2019b), Seydi et al. (2022), Wang et al. (2015)
LR	Cox (1958)	This generalized linear statistical model uses a logistic function as the link function. It is used to study the relationships between a set of qualitative and qualitative variables. This model can be used to predict the probability of a flood occurring (value of 1) or not (value of 0), by optimizing the regression coefficients. The values are in a range from 0 to 1	Zhao et al. (2019)

$$\text{Sensitivity} = \frac{TP}{FN + TP} \tag{7}$$

$$\text{Accuracy} = \frac{TN + TP}{FP + TP + FN + TN} \tag{8}$$

$$\text{Precision} = \frac{TP}{FP + TP} \tag{9}$$

$$\text{F1score} = \frac{2}{\frac{1}{Pr} + \frac{1}{Recal}} \text{Recall} = \frac{TP}{TP + FN} \tag{10}$$

$$\text{AUC} = \frac{(\sum TP + \sum TN)}{(P + N)} \tag{11}$$

where P and N are the total number of pixels with and without torrential events respectively, TP represent the true positive and TN represent the true negative.

$$RMSE = \sqrt{\frac{1}{n} \sum_{i=1}^n (X_{predicted} - X_{actual})^2} \tag{12}$$

$$MAE = \sqrt{\frac{1}{n} \sum_{i=1}^n |X_{predicted} - X_{actual}|} \tag{13}$$

where n is the total number of samples in the learning or testing phase, X predicted is the projected value from the FS model, and X actual is the observed value.

3 Results

3.1 Multicollinearity and factor selection

In Fig. 5, the correlation matrix (CM) represents Pearson’s association analysis between fifteen influencing variables that are briefly elaborated in Fig. 2. As the results show, the highest positive correlation value (0.75) was found between elevation and slope, and a strong linear correlation between the following factors: TWI and SPI, rainfall and slope, SPI and Profile curvature, TRI and distance to river, TRI, and elevation.

The results of the tolerance and VIF applied to check the multicollinearity of the feed influence factors in this study show a Tol value between 0.12 and 0.97 for TWI and HSG, respectively, as well as a maximum VIF value of 8.02 for TWI and a minimum value of 1.02 for HSG (Fig. 6). In accordance with the Tol and VIF requirements among the fifteen factors used in this study, TWI and SPI were removed in the following analysis. Next, the MI of the other thirteen factors (Fig. 7) shows positive values ranging from 0.382 (distance to river) to 0.013 (HSG). Consequently, distance from the river is ranked as the most important factor, followed by elevation (MI=0.245), Accumulation flow (MI=0.183) and slope (MI=0.159).

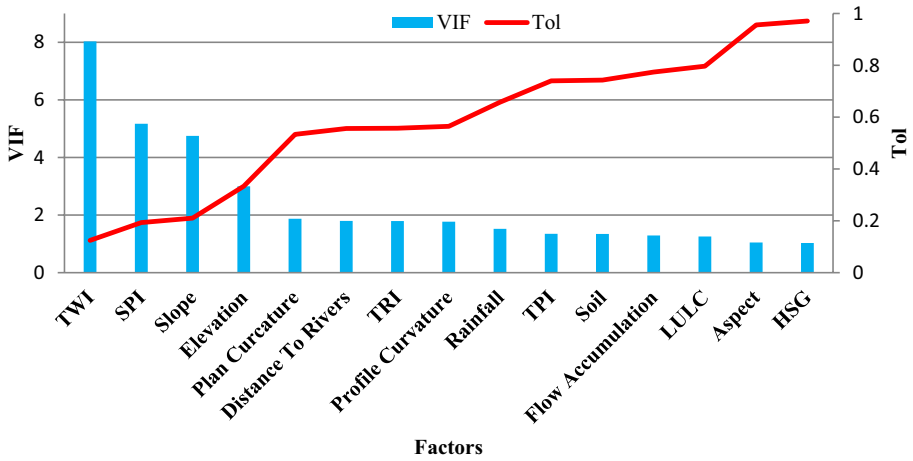


Fig. 5 Multicollinearity analysis of conditioning factors using the correlation matrix

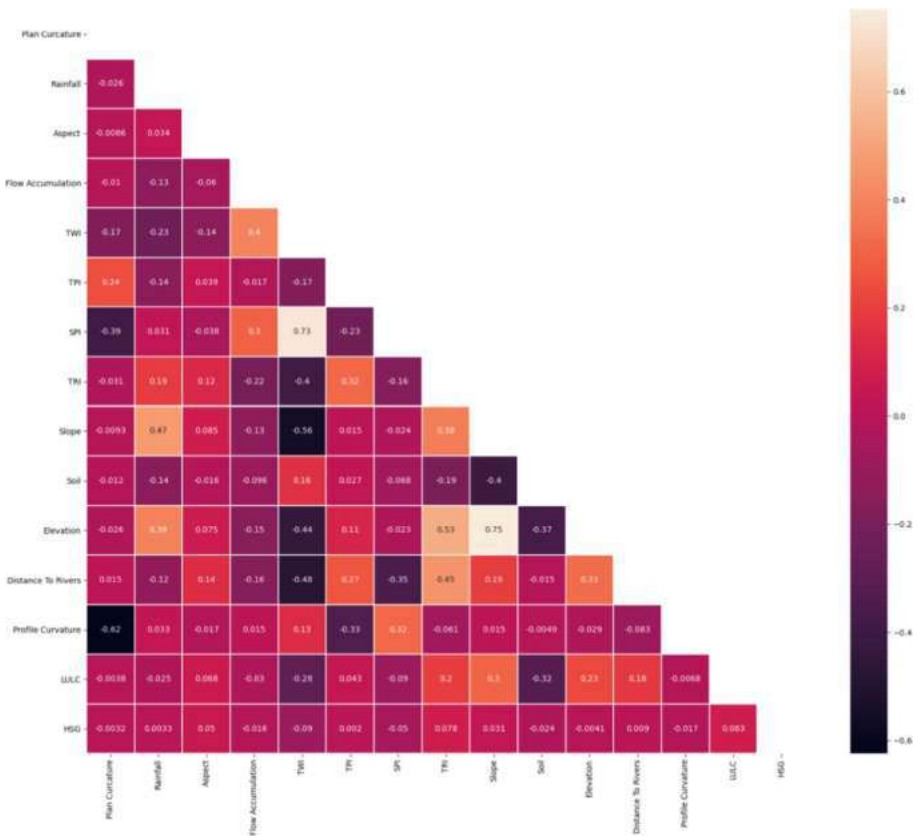


Fig. 6 Multicollinearity analysis of conditioning factors by variance inflation factor (VIF) and tolerance (TOL)

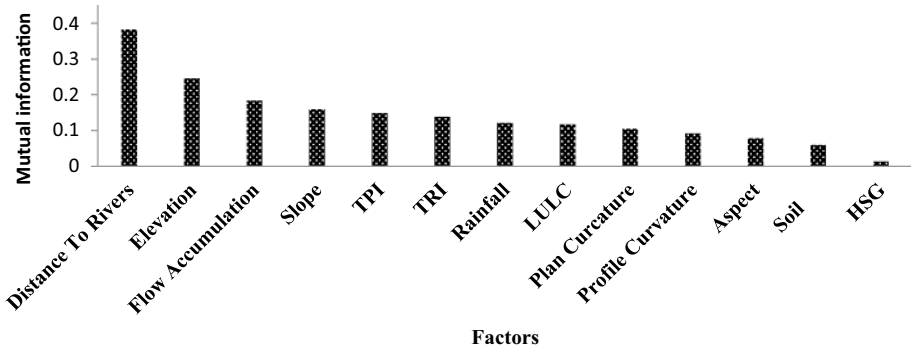


Fig. 7 Flash flood conditioning factors in relation to predictive strength for all models

3.2 Flood susceptibility maps

The FS development of the FS model was based on the application of the seven algorithms. The results were presented as a probability prediction ranging from 0 to 1, corresponding to the lowest and highest FS values respectively. Subsequently, the generated maps were then classified into the following five different zones using Jenks’ natural break classification: very low, low, moderate, high, and very high.

Initial visual analysis of the seven maps produced by the SVM (Fig. 8a), RF (Fig. 8b), LR (Fig. 8c), KNN (Fig. 8d), DT (Fig. 8e), ANN (Fig. 8f) and XGBoost (Fig. 8g) models shows that very high FS values are concentrated in the downstream part of the Tensift watershed, particularly in the lowland area (Haouz), and are slightly localized in the western part and in the Jbilet. On the other hand, very low FS values are found in the upstream part of the High Atlas chain.

The spatial distribution of the degree of sensitivity to flooding is quite remarkable in the very strong and very weak degrees especially in the Haouz plain, all the models used show a very weak sensitivity and the same differing degrees of sensitivity in the high altitudes of the High Atlas and the Ourika area except for the XGBoost model which also shows a weak sensitivity in the Jebilet area.

For the Haouz plain, the SVM model shows 23% of very weak sensitivity surfaces in the Majjat and Ait Ourir area and 20% of very strong sensitivity surfaces located in the centre of the area, the RF model shows 11% of very weak sensitivity surfaces scattered in several areas in the Mjjat and Takarkoust and 20% of very strong sensitivity surfaces generally in the Laataouia area, the LR model shows 14% of very low sensitivity surfaces in the middle altitudes of certain areas of Mjjat, Takarkoust, Ait Ourir and Lataouia and 19% of very high sensitivity surfaces located slightly in the centre of the area, the KNN model shows 11% of very low sensitivity surfaces and 18% of very high sensitivity surfaces, with the same geospatial distribution of the RF model, the DT model shows 13% of very weak sensitivity surface located in the region of Ait Ourir, Mejjat and 23% of very strong sensitivity surface observed over a large region of Laataouia and the urban area of Marrakech, the ANN model shows 33% of very weak sensitivity surface over a large area of Majjat, Takarkoust and Ait ourir and 23% of very strong sensitivity surfaces generally observed in Marrakech and Ourika and finally the XGBoost model, which shows 23% of very low sensitivity surfaces over large areas of

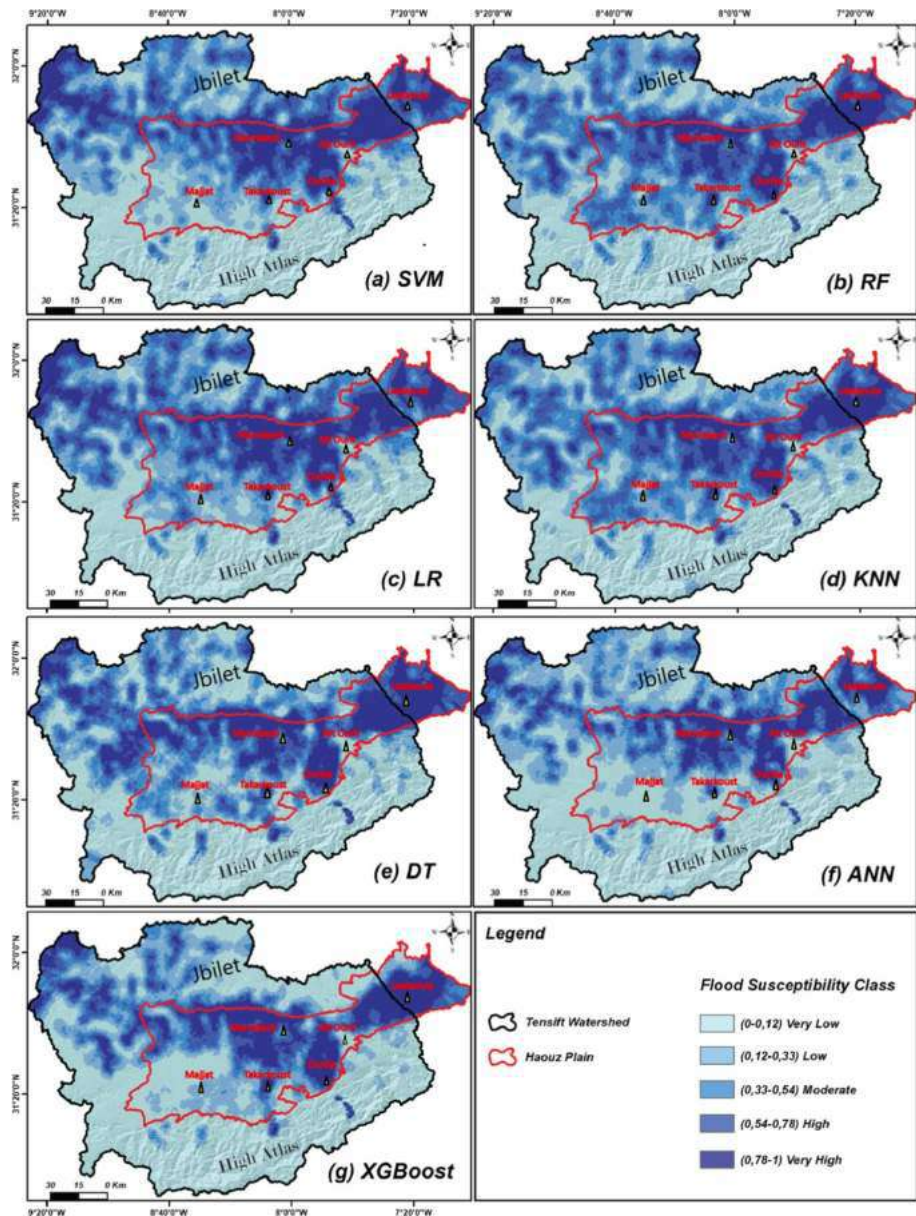


Fig. 8 FS maps Tensift watershed predicted by the SVM, RF, LR, KNN, DT, ANN and XGBoost models [Source Study authors]

Majjat and the surrounding Laataouia region and 30% of very high sensitivity surfaces concentrated in Ourika, Laataouia and Marrakech.

In the Tensift watershed, most areas are predicted to have very low (39.89%) and low (23.97%) FS, and the remaining areas are associated with moderate (15.72%), high (13.86%) and very high (10.75%) FS values provided by Fig. 9. In the Haouz plain zone,

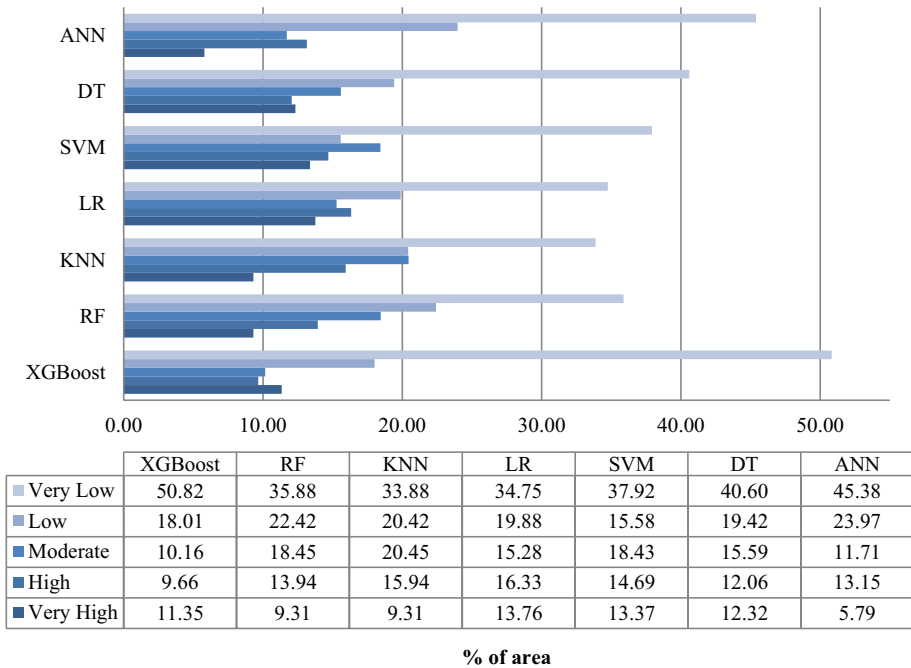


Fig. 9 Percentage of FS area in the Tensift watershed of the models used

on the other hand, there is an increase in the areas associated with high (22.14%) and very high (21.76%) FS values while the remaining areas show moderate (19.02%), low (18.88%) and very low (18.18%) percentages (Fig. 10).

Overall, Fig. 9 illustrates that the low and very low FS classes are predominant in the Tensift watershed, encompassing more than 59.85% of the total surface area. Conversely, Fig. 10 demonstrates that the high and very high FS classes dominate the Haouz plain, covering over 43.91% of the total surface area.

3.3 Performance of the seven ML models used

The results of this study were constructed using seven ML models to predict FS, namely SVM, RF, KNN, DT, ANN, LR and XGBoost, and evaluated the effectiveness of the training (70%) and test (30%) data used, and the performance indicators. Precision, Sensitivity, specificity, (FPR) false positive rate, accuracy, recall, F1 score, MAE, RMSE and AUC-ROC. The results of the training and validation phases were recorded as shown in Tables 3, 4, and Fig. 11.

In this research, for the training data set, the XGBoost model shows excellent performance, presented by scores (Precision = 0.95), (Sensitivity = 0.97), (Specificity = 0.95), (Accuracy = 0.97), (Recall = 0.96), (F1 score = 0.95), (FPR = 0.05), (MAE = 0.04) and AUC-ROC (values = 96.21%). The other six models RF, KNN, LR, SVM, DT, and ANN show high performance, indicated by Sensitivity, Specificity, Precision, Accuracy, AUC-ROC and F1 score values above 0.88 and negligible FPR and MAE scores. For the test data set, all models applied show high to very high performance. Sensitivity values

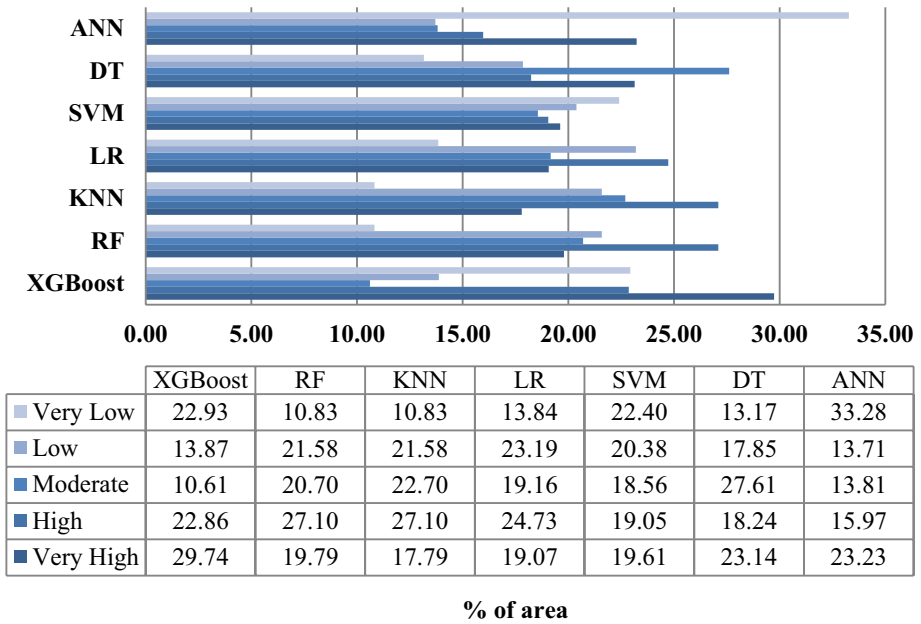


Fig. 10 Percentage of FS surface in the Haouz plain of the models used

Table 3 Performance of the four models using training data

Performance Indicators	Models						
	XGBoost	RF	KNN	LR	SVM	DT	ANN
<i>Training data</i>							
Precision	0.95	0.92	0.88	0.88	0.86	0.92	0.84
Sensitivity	0.97	0.96	0.96	0.95	0.94	0.95	0.98
Specificity	0.95	0.92	0.92	0.88	0.86	0.90	0.84
False positive rate (FPR)	0.05	0.08	0.08	0.12	0.14	0.10	0.16
Accuracy	0.97	0.94	0.94	0.92	0.91	0.93	0.91
recall	0.96	0.93	0.88	0.92	0.90	0.90	0.97
F1 score	0.95	0.93	0.92	0.90	0.88	0.92	0.90
MAE	0.04	0.06	0.06	0.08	0.09	0.07	0.09
RMSE	0.19	0.23	0.24	0.28	0.31	0.26	0.30
AUC-ROC	96.21	94.48	94.31	91.96	90.69	93.38	91.01

ranged from a minimum of 0.90 to a maximum of 0.98 for DT and ANN respectively, parameter values for Precision, Accuracy, F1-score, FPR, MAE varied between 0.78 and 0.93, 0.88 and 0.94, 0.87 and 0.92, 0.07 and 0.22, 0.06 and 0.12 respectively, maximum AUC-ROC values were all marked for the XGBoost model (0.9378), and minimum values were all marked for the ANN model (0.8756).

Table 4 Performance of the four models using testing data

Performance Indicators	Models						
	XGBoost	RF	KNN	LR	SVM	DT	ANN
<i>Testing data</i>							
Precision	0.93	0.93	0.89	0.90	0.91	0.91	0.78
Sensitivity	0.94	0.94	0.94	0.94	0.93	0.90	0.98
False positive rate (FPR)	0.07	0.07	0.14	0.10	0.09	0.09	0.22
Specificity	0.93	0.93	0.86	0.90	0.91	0.91	0.78
Accuracy	0.94	0.94	0.91	0.92	0.92	0.91	0.88
recall	0.92	0.91	0.93	0.91	0.89	0.86	0.98
F1 score	0.92	0.92	0.91	0.91	0.90	0.88	0.87
MAE	0.06	0.06	0.09	0.08	0.08	0.08	0.12
RMSE	0.25	0.25	0.31	0.28	0.28	0.31	0.38
AUC-ROC	93.78	93.71	90.53	92.29	92.02	90.67	87.56

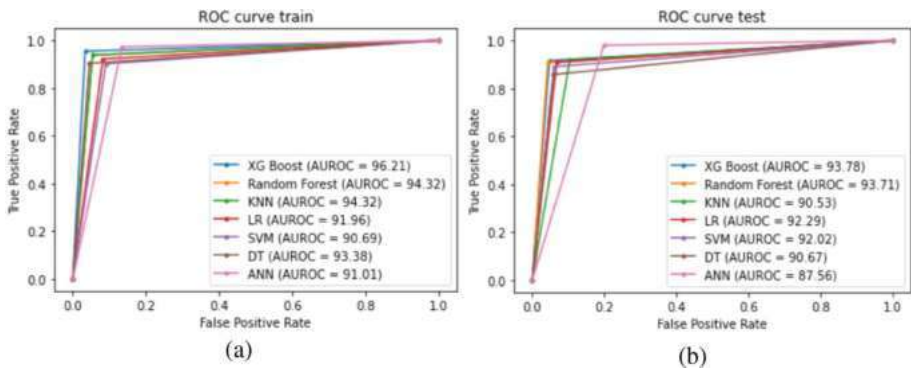


Fig. 11 ROC curve analysis of different flooding models using **a** training data, **b** validation data

Nonetheless, XGBoost outperforms the other four models in terms of accuracy, mostly because to its integration of all base learners’ prediction outcomes, which boosts the model’s recognition rate and generalization capacity. To address missing values on various nodes, distinct techniques will be applied while determining and storing the best course of action. In the meanwhile, XGBoost increases the learning rate by adding a regular term to the objective function and supporting custom loss functions, which prevent overfitting and simplify the learning model. Therefore, the XGBoost model eventually produces better simulation results, and the flood susceptibility mapping approach based on XGBoost is effective and workable.

In addition to the sensitivity and specificity criteria, statistical evaluations were conducted to make the comparison using RMSE, as shown in Tables 3 and 4. The overall RMSE ranking is shown in Fig. 12. The RMSE values for XGBoost indicate an optimal match with the observed and generated values; thus, the expected susceptibility probability has been achieved.

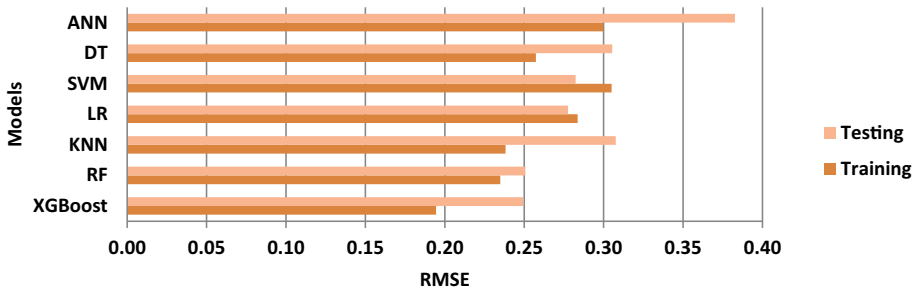


Fig. 12 The performance of different flooding models using RMSE values

3.4 Prioritization of the seven models used

The performance of each model in this study suggests that the XGBoost and RF models had the greatest accuracy in predicting FS for both the training and test datasets. For the training dataset, they are followed by LR, SVM, DT, KNN, and ANN. The following algorithms were ranked for the test dataset: KNN, DT, LR, ANN, and SVM mentioned by Fig. 13.

4 Discussion

In a semi-arid flood-prone area such as the Tensift catchment and the Haouz plain, it is important to categorize and develop FS maps for success and failure rates that ensure flood risk planning and management. In most research and studies, test data sets have been used to construct the reliability performance of flood models. According to (Janizadeh et al.

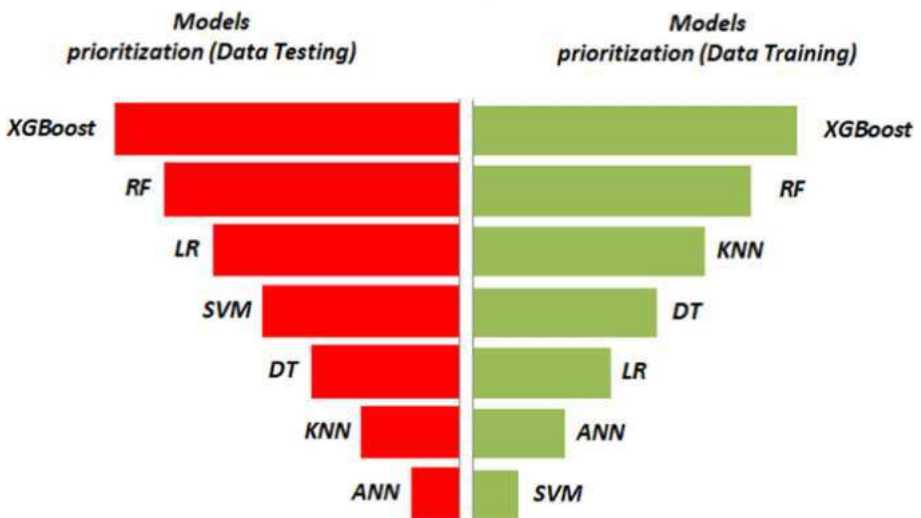


Fig. 13 Prioritization of models in the training and testing phases

2021; Sestras et al. 2023), the spatial prediction of flood risk areas has been attributed to the probability of different thematic flood risk maps. In addition, research and studies have investigated the impact of influential geo-environmental factors and the benefits of several ML algorithms in the mapping of FS in different regions of the world affected by this phenomenon.

The use of the ensemble modelling technique, which combines the seven models to provide more accurate forecasts than each of them in isolation, has increased the accuracy of the results. As a result, the ensemble models gained in importance and were able to anticipate future events more accurately than the individual models.

The importance of the variables affecting vulnerability to flooding, the effectiveness and periodicity of the models used, and the reliability of the technique chosen, are discussed in this section.

4.1 Factors influencing susceptibility to flooding

After the preparation of the inventory maps through field surveys, the collection of data from the processing of satellite scenes, and the analysis of the ABHT historical flood database, the first step in the spatial prediction of FS was the preparation of the set of influencing factors. Of the fifteen factors prepared, TWI and SPI were eliminated because of their collinearity with other factors, which limits the performance of the prediction. Furthermore, according to MI, the most important factor is the distance to the river, which is not consistent with the results of (Meliho et al. 2022), applied in the Ourika catchment which is a totally manganese area. But they are consistent with the results of (Al-Areeq et al. 2022), applied in a mixed area between low and high altitude, followed by elevation. The least important factor in our study is the HSG. In addition, Flow accumulation, Slope, TPI, TRI, Rainfall, LULC, Curvature Plane, Curvature Profile, Aspect, and soil type had a considerable impact on FS, respectively.

The results indicate that the most important locations at a distance from the river, particularly those of Tensift and Ourika along the Haouz plain at low altitude, were highly susceptible to flooding with a high density. The results obtained indicate that high susceptibility is associated with elevation, slope, TPI and TRI along the roads and sub-watersheds of Tensift, the sub-watersheds of Ourika, Zat and Rheraya. This assessment is confirmed by our results. The results and actions of the flood predictors also demonstrate that frequent flooding is expected due to the morphology of the Tensift catchment. In the Kingdom of Morocco, a great deal of research has been carried out to map regions and areas vulnerable to flooding to take targeted measures to reduce the incidence of these risks in the future. Information on the characteristics and impacts of floods is important for administrations and decision-makers to help them formulate policies, as well as flood management strategies, such as the construction of flood-resistant structures to improve emergency response plans in the event of flooding.

4.2 Performance of the models and effectiveness of the methodology

The 70/30% as of Fig. 4 split was used in this study for the choice of training and validation datasets shows high performance. The seven algorithms applied in this study have a high to very high efficiency for the prediction of the FS after the evaluation of the models, despite a slight weakness of the ANN which shows a (AUC-ROC=87.56% in the test stage), is

which has been reported by previous studies in the same theme (Mia et al. 2023; Towfiqul Islam et al. 2021; Youssef et al. 2023a, b).

According to the results, the XGBoost model obtained excellent results in both phases, as it is the case in other studies as well. Methodology adopted in this research, and the results are consistent with recent research studies of Parvin et al. (2022), Seydi et al. (2022), which have highlighted the high and rapid efficiency of ML-DL, RS and GIS in geo-spatial prediction in semi-arid and arid areas characterized by irregular and dangerous flood periods. It is based on a set of geo-environmental factors.

The XGBoost algorithm predicts the FS map effectively, making it a viable alternative for flood risk management in both the Tensift catchment and the Haouz plain. It can specifically help in detecting and classifying regions at high risk of flooding, allowing for the establishment of a monitoring system.

The effective result of this method reflected by the targeted choice of maximum available spatial data of the study area, also to the set of input data, as well as to the application and validation of the algorithm and finally by an extensive field survey, the historical database of the ABHT and satellite scenes of the inventory, the application and evaluation of seven models applied based on the same set of data and parameterized allowed a more logical prioritization of models. Optimizing the performance of the seven models is an essential objective that can be achieved in two significant ways. The first approach consists of enriching all these models by subjecting them to intensive training with a considerable mass of observed data. The second approach relies on the power of the synergy generated by combining these models.

5 Conclusion

This research examined some ML models RF, SVM, KNN, DT, ANN, LR, and XGBoost to map and predict FS in the Tensift watershed and Haouz plain. To this end, mutual information (MI) analysis was used for factor selection and classification. Of these, distance to river and elevation factors were identified as the main factors influencing FS, while TWI and SPI were eliminated from the analysis based on the multicollinearity test and the importance of MI. In addition, the performance measures (Precision, Sensitivity, specificity, FPR, accuracy, recall, F1 score, MAE, RMSE and AUC-ROC) were tested simultaneously with the model evaluation to validate the FS maps. The results for the FS prediction training and validation tests showed that all the models applied met the validation standards. The results of the analysis of the priorities of the models for the prediction of flood risk phenomena demonstrated the superiority of the XGBoost model (AUC-ROC training = 96.21%, AUC-ROC test = 93.78%) and, consequently, the effectiveness of the FS map as predicted by this model. The approach followed in this research has generated an essential ML-RS-GIS-based tool for flood vulnerability mapping, designed to implement prevention and protection plans in a semi-arid context.

It is inevitable to mention certain limitations encountered throughout this research study. The research uses binary flood data from 2012 to create the inventory map of past flooding. This data is from single year, which might not capture the full spectrum of flooding patterns. Future studies should consider using longer time series data to better understand FS, especially in regions with variable climate conditions. In terms of research context, a key concern is that the FS can change over time due to factors like urbanization,

climate change, and land-use modifications. Addressing these limitations will enhance the accuracy and applicability of FS models, improving land-use planning and risk efforts.

This study and its methodology were designed and developed such a way to be more applicable and generalizable across globe. Outcomes of this research highlights the role of advanced algorithms in enhancing precision for flood risk assessments, applicable globally. Methodology and insights can influence policies and practices in regions facing similar environmental challenges. Findings on the efficacy of XGBoost compared to other ML models have broader applications for FS mapping in similar semi-arid regions across globe.

Future research works should extend the study with temporal data to capture changes in FS patterns over time. Also, the integration of dynamic factors like urbanization trends, socio-economic factors, real-time remote sensing data would provide a more holistic assessment for real-time monitoring and would provide a broader understanding regarding the flood impacts on communities and infrastructure. It would be more comprehensive if future works conducted based on comparative studies across different regions to validate the effectiveness of the developed algorithm in varied contexts.

Authors contributions 1. Conceived and designed the studies—Bammou Youssef, Benzougagh Brahim, Igmoullan Brahim, Shuraik Kader, Velibor Spalevic, Paolo Billi, and Slobodan B. Marković. 2. Performed the analysis—Bammou Youssef, Benzougagh Brahim, Igmoullan Brahim, Ouallali Abdessalam, Shuraik Kader, Velibor Spalevic, Paul Sestras, Paolo Billi, and Slobodan B. Marković. 3. Analyzed and interpreted the data—Bammou Youssef, Benzougagh Brahim, Igmoullan Brahim, Ouallali Abdessalam, Shuraik Kader, Velibor Spalevic, Paolo Billi, and Slobodan B. Marković. 4. Contributed materials, analysis tools or data—Bammou Youssef, Benzougagh Brahim, Igmoullan Brahim, Ouallali Abdessalam, Shuraik Kader. 5. Preparation of draft—Bammou Youssef, Benzougagh Brahim, Igmoullan Brahim, Ouallali Abdessalam, Shuraik Kader, Velibor Spalevic, Paul Sestras, Paolo Billi, and Slobodan B. Marković. 6. Internal reviewers – Velibor Spalevic, Paolo Billi, and Slobodan B. Marković. 7. Project administration – Benzougagh Brahim, Shuraik Kader, Velibor Spalevic, Paolo Billi, and Slobodan B. Marković. All authors have read and agreed to the submitted version.

Funding Open Access funding enabled and organized by CAUL and its Member Institutions. No fundings were received for this research.

Availability of data and materials The data and materials will be available on request.

Declarations

Competing interests The authors have no relevant financial or non-financial interests to disclose.

Ethical approval Not applicable.

Consent to participate Not applicable.

Consent to publish Not applicable.

Open Access This article is licensed under a Creative Commons Attribution 4.0 International License, which permits use, sharing, adaptation, distribution and reproduction in any medium or format, as long as you give appropriate credit to the original author(s) and the source, provide a link to the Creative Commons licence, and indicate if changes were made. The images or other third party material in this article are included in the article's Creative Commons licence, unless indicated otherwise in a credit line to the material. If material is not included in the article's Creative Commons licence and your intended use is not permitted by statutory regulation or exceeds the permitted use, you will need to obtain permission directly from the copyright holder. To view a copy of this licence, visit <http://creativecommons.org/licenses/by/4.0/>.

References

- Abdulrazzak M, Elfeki A, Kamis A, Kassab M, Alamri N, Chaabani A, Noor K (2019) Flash flood risk assessment in urban arid environment: case study of Taibah and Islamic universities' campuses, Medina, Kingdom of Saudi Arabia. *Geomat Nat Hazards Risk* 10(1):780–796. <https://doi.org/10.1080/19475705.2018.1545705>
- Ahmadlou M, Karimi M, Alizadeh S, Shirzadi A, Parvinnejhad D, Shahabi H, Panahi M (2019) Flood susceptibility assessment using integration of adaptive network-based fuzzy inference system (ANFIS) and biogeography-based optimization (BBO) and BAT algorithms (BA). *Geocarto Int* 34(11):1252–1272. <https://doi.org/10.1080/10106049.2018.1474276>
- Al-Areeq AM, Abba S, Yassin MA, Benaafi M, Ghaleb M, Aljundi IH (2022) Computational machine learning approach for flood susceptibility assessment integrated with remote sensing and GIS techniques from Jeddah. *Saudi Arabia Remote Sens* 14(21):5515. <https://doi.org/10.3390/rs14215515>
- Ali SA, Parvin F, Pham QB, Vojtek M, Vojteková J, Costache R et al (2020) GIS-based comparative assessment of flood susceptibility mapping using hybrid multi-criteria decision-making approach, naïve Bayes tree, bivariate statistics and logistic regression: a case of Topľa basin. *Slovakia Ecol Indic* 117:106620. <https://doi.org/10.1016/j.ecolind.2020.106620>
- Anjos L, Gaistardo CC, Deckers J, Dondeyne S, Eberhardt E, Gerasimova M et al (2015) World reference base for soil resources 2014 International soil classification system for naming soils and creating legends for soil maps
- Apaydin H, Feizi H, Sattari MT, Colak MS, Shamshirband S, Chau K-W (2020) Comparative analysis of recurrent neural network architectures for reservoir inflow forecasting. *Water* 12(5):1500. <https://doi.org/10.3390/w12051500>
- Aryal SK, Silberstein RP, Fu G, Hodgson G, Charles SP, McFarlane D (2020) Understanding spatio-temporal rainfall-runoff changes in a semi-arid region. *Hydrol Process* 34(11):2510–2530. <https://doi.org/10.1002/hyp.13744>
- Beden N, Ulke Keskin A (2021) Flood map production and evaluation of flood risks in situations of insufficient flow data. *Nat Hazards* 105(3):2381–2408. <https://doi.org/10.1007/s11069-020-04404-y>
- Benkirane M, Laftouhi N-E, El Mansouri B, Salik I, Snineh M, El Ghazali FE et al (2020) An approach for flood assessment by numerical modeling of extreme hydrological events in the Zat watershed (High Atlas, Morocco). *Urban Water J* 17(5):381–389. <https://doi.org/10.1080/1573062X.2020.1734946>
- Bennani O, Druon E, Leone F, Trambly Y, Saidi MEM (2019) A spatial and integrated flood risk diagnosis: relevance for disaster prevention at Ourika valley (High Atlas-Morocco). *Disaster Prev Manag Int J* 28(5):548–564. <https://doi.org/10.1108/DPM-12-2018-0379>
- Benssaou M, Hamoumi NM (2003) Le graben de l'Anti-Atlas occidental (Maroc): contrôle tectonique de la paléogéographie et des séquences au Cambrien inférieur. *CR Geosci* 335(3):297–305. [https://doi.org/10.1016/S1631-0713\(03\)00033-6](https://doi.org/10.1016/S1631-0713(03)00033-6)
- Billah M, Islam AKMS, Mamooun WB, Rahman MR (2023) Random forest classifications for landuse mapping to assess rapid flood damage using Sentinel-1 and Sentinel-2 data. *Remote Sens Appl Soc Environ* 30:100947. <https://doi.org/10.1016/j.rsase.2023.100947>
- Bottou L, Vapnik V (1992) Local learning algorithms. *Neural Comput* 4(6):888–900. <https://doi.org/10.1162/neco.1992.4.6.888>
- Bouramtane T, Yameogo S, Touzani M, Tiouiouine A, Elanati MH, Ouadi J et al (2020) Statistical approach of factors controlling drainage network patterns in arid areas (Morocco). Application to the Eastern Anti Atlas Morocco. *J Afr Earth Sci* 162:103707. <https://doi.org/10.1016/j.jafrearsci.2019.103707>
- Breiman L (2001) Random forests. *Mach Learn* 45:5–32. <https://doi.org/10.1023/A:1010933404324>
- Chapi K, Singh VP, Shirzadi A, Shahabi H, Bui DT, Pham BT, Khosravi K (2017) A novel hybrid artificial intelligence approach for flood susceptibility assessment. *Environ Model Softw* 95:229–245. <https://doi.org/10.1016/j.envsoft.2017.06.012>
- Chen T, Guestrin C (2016) Xgboost: A scalable tree boosting system. Paper presented at the Proceedings of the 22nd acm sigkdd international conference on knowledge discovery and data mining
- Choubin B, Moradi E, Golshan M, Adamowski J, Sajedi-Hosseini F, Mosavi A (2019a) An ensemble prediction of flood susceptibility using multivariate discriminant analysis, classification and regression trees, and support vector machines. *Sci Total Environ* 651:2087–2096. <https://doi.org/10.1016/j.scitotenv.2018.10.064>
- Choubin B, Rahmati O, Soleimani F, Alilou H, Moradi E, Alamdari N (2019) Regional groundwater potential analysis using classification and regression trees. In: *Spatial modeling in GIS and R for earth and environmental sciences*, Elsevier, pp 485–498

- Cortes C, Vapnik V (1995) Support-vector networks. *Mach Learn* 20:273–297. <https://doi.org/10.1007/BF00994018>
- Costache R (2019a) Flash-Flood Potential assessment in the upper and middle sector of Prahova river catchment (Romania). A comparative approach between four hybrid models. *Sci Total Environ* 659:1115–1134. <https://doi.org/10.1016/j.scitotenv.2018.12.397>
- Costache R (2019b) Flood susceptibility assessment by using bivariate statistics and machine learning models—a useful tool for flood risk management. *Water Resour Manag* 33(9):3239–3256. <https://doi.org/10.1007/s11269-019-02301-z>
- Costache R, Bui DT (2020) Identification of areas prone to flash-flood phenomena using multiple-criteria decision-making, bivariate statistics, machine learning and their ensembles. *Sci Total Environ* 712:136492. <https://doi.org/10.1016/j.scitotenv.2019.136492>
- Costache R, Pham QB, Arabameri A, Diaconu DC, Costache I, Crăciun A et al (2022) Flash-flood propagation susceptibility estimation using weights of evidence and their novel ensembles with multicriteria decision making and machine learning. *Geocarto Int* 37(25):8361–8393. <https://doi.org/10.1080/10106049.2021.2001580>
- Cover T, Hart P (1967) Nearest neighbor pattern classification. *IEEE Trans Inf Theory* 13(1):21–27
- Cox DR (1958) The regression analysis of binary sequences. *J R Stat Soc Ser B Stat Methodol* 20(2):215–232
- Dahri N, Yousfi R, Bouamrane A, Abida H, Pham QB, Derdous O (2022) Comparison of analytic network process and artificial neural network models for flash flood susceptibility assessment. *J Afr Earth Sc* 193:104576. <https://doi.org/10.1016/j.jafrearsci.2022.104576>
- Dazzi S, Vacondio R, Mignosa P (2021) Flood stage forecasting using machine-learning methods: a case study on the Parma River (Italy). *Water* 13(12):1612. <https://doi.org/10.3390/w13121612>
- Duclaux A (2005) Modélisation hydrologique de 5 Bassins Versants du Haut-Atlas Marocain avec SWAT (Soil and Water Assessment Tool). Mémoire du diplôme d'Ingénieur Agronome de l'Institut National Agronomique de Paris-Grignon.
- Echogdali FZ, Kpan RB, Ouchchen M, Id-Belqas M, Dadi B, Ikirri M et al (2022) Spatial prediction of flood frequency analysis in a semi-arid zone: a case study from the Seyad Basin (Guelmim Region, Morocco). *Geospatial Technol Landsc Environ Manag Sustain Assess Plann*. https://doi.org/10.1007/978-981-16-7373-3_3
- El Alfy M (2016) Assessing the impact of arid area urbanization on flash floods using GIS, remote sensing, and HEC-HMS rainfall–runoff modeling. *Hydrol Res* 47(6):1142–1160. <https://doi.org/10.2166/nh.2016.133>
- Fix E, Hodges JL (1952) Discriminatory analysis: nonparametric discrimination: Small sample performance
- Ganie PA, Posti R, Kunal K, Kunal G, Sarma D, Pandey PK (2022) Insights into the morphometric characteristics of the Himalayan River using remote sensing and GIS techniques: a case study of Saryu basin, Uttarakhand, India. *Appl Geomat* 14(4):707–730. <https://doi.org/10.1007/s12518-022-00461-z>
- Han Z, Sharif HO (2021) Analysis of flood fatalities in the United States, 1959–2019. *Water* 13(13):1871. <https://doi.org/10.3390/w13131871>
- Hopfield JJ (1982) Neural networks and physical systems with emergent collective computational abilities. *Proc Natl Acad Sci* 79(8):2554–2558. <https://doi.org/10.1073/pnas.79.8.2554>
- Hosseini FS, Choubin B, Mosavi A, Nabipour N, Shamsirband S, Darabi H, Haghghi AT (2020) Flash-flood hazard assessment using ensembles and Bayesian-based machine learning models: application of the simulated annealing feature selection method. *Sci Total Environ* 711:135161. <https://doi.org/10.1016/j.scitotenv.2019.135161>
- Ighile EH, Shirakawa H, Tanikawa H (2022) Application of GIS and machine learning to predict flood areas in Nigeria. *Sustainability* 14(9):5039. <https://doi.org/10.3390/su14095039>
- Janizadeh S, Chandra Pal S, Saha A, Chowdhuri I, Ahmadi K, Mirzaei S et al (2021) Mapping the spatial and temporal variability of flood hazard affected by climate and land-use changes in the future. *J Environ Manag* 298:113551. <https://doi.org/10.1016/j.jenvman.2021.113551>
- Kader S, Raimi MO, Spalevic V, Iyngiala AA, Bukola RW, Jaufer L, Butt TE (2023) A concise study on essential parameters for the sustainability of Lagoon waters in terms of scientific literature. *Turk J Agric* for 47(3):288–307. <https://doi.org/10.55730/1300-011X.3087>
- Kirker AN, Toran L (2023) When impervious cover doesn't predict urban runoff: Lessons from distributed overland flow modeling. *J Hydrol* 621:129539. <https://doi.org/10.1016/j.jhydrol.2023.129539>
- Liu H, Lang B (2019) Machine learning and deep learning methods for intrusion detection systems: a survey. *Appl Sci* 9(20):4396. <https://doi.org/10.3390/app9204396>
- Mao W, Xu C, Yang Y (2022) Investigation on strength degradation of sandy soil subjected to concentrated particle erosion. *Environ Earth Sci* 81:1–10. <https://doi.org/10.1007/s12665-021-10123-9>

- Masoud AM, Pham QB, Alezabawy AK, El-Magd SAA (2022) Efficiency of geospatial technology and multi-criteria decision analysis for groundwater potential mapping in a Semi-Arid region. *Water* 14(6):882. <https://doi.org/10.3390/w14060882>
- Meliho M, Khattabi A, Driss Z, Orlando CA (2022) Spatial prediction of flood-susceptible zones in the Ourika watershed of Morocco using machine learning algorithms. *Appl Comput Inf.* <https://doi.org/10.1108/ACI-09-2021-0264>
- Mia MU, Chowdhury TN, Chakraborty R, Pal SC, Al-Sadoon MK, Costache R, Islam ARMT (2023) Flood susceptibility modeling using an advanced deep learning-based iterative classifier optimizer. *Land* 12(4):810. <https://doi.org/10.3390/land12040810>
- Miao F, Zhao F, Wu Y, Li L, Török Á (2023) Landslide susceptibility mapping in Three Gorges Reservoir area based on GIS and boosting decision tree model. *Stoch Environ Res Risk Assess.* <https://doi.org/10.1007/s00477-023-02394-4>
- Mosavi A, Ozturk P, Chau K-W (2018) Flood prediction using machine learning models: literature review. *Water* 10(11):1536. <https://doi.org/10.3390/w10111536>
- Namous M, Hssaisoune M, Pradhan B, Lee C-W, Alamri A, Elaloui A et al (2021) Spatial prediction of groundwater potentiality in large semi-arid and karstic mountainous region using machine learning models. *Water* 13(16):2273. <https://doi.org/10.3390/w13162273>
- Parvin F, Ali SA, Calka B, Bielecka E, Linh NTT, Pham QB (2022) Urban flood vulnerability assessment in a densely urbanized city using multi-factor analysis and machine learning algorithms. *Theor Appl Climatol* 149(1–2):639–659. <https://doi.org/10.1007/s00704-022-04068-7>
- Sami NA, Ibrahim DS (2021) Forecasting multiphase flowing bottom-hole pressure of vertical oil wells using three machine learning techniques. *Pet Res* 6(4):417–422. <https://doi.org/10.1016/j.ptlrs.2021.05.004>
- Sarker IH (2021) Machine learning: algorithms, real-world applications and research directions. *SN Comput Sci* 2(3):160. <https://doi.org/10.1007/s42979-021-00592-x>
- Sestras P, Mircea S, Roșca S, Bilașco Ș, Sălăgean T, Dragomir LO et al (2023) GIS based soil erosion assessment using the USLE model for efficient land management: a case study in an area with diverse pedo-geomorphological and bioclimatic characteristics. *Notulae Botanicae Horti Agrobotanici Cluj-Napoca* 51(3):13263–13263. <https://doi.org/10.15835/nbha51313263>
- Seydi ST, Kanani-Sadat Y, Hasanlou M, Sahraei R, Chanussot J, Amani M (2022) Comparison of machine learning algorithms for flood susceptibility mapping. *Remote Sens* 15(1):192. <https://doi.org/10.3390/rs15010192>
- Shah K, Patel H, Sanghvi D, Shah M (2020) A comparative analysis of logistic regression, random forest and KNN models for the text classification. *Augment Hum Res* 5:1–16. <https://doi.org/10.1007/s41133-020-00032-0>
- Sivakumar MV (2005) Impacts of natural disasters in agriculture, rangeland and forestry: an overview. *Nat Disasters Extreme Events Agric Impacts Mitig.* https://doi.org/10.1007/3-540-28307-2_1
- Soulaimani A, Bouabdelli M (2005) Le Plateau de Lakhssas (Anti-Atlas occidental, Maroc): un graben finiprécambrien réactivé à l'hercynien. *Ann Soc Géol Nord* 2(2):177–184
- Tan ML, Gassman PW, Yang X, Haywood J (2020) A review of SWAT applications, performance and future needs for simulation of hydro-climatic extremes. *Adv Water Resour* 143:103662. <https://doi.org/10.1016/j.advwatres.2020.103662>
- Tariq A, Yan J, Ghaffar B, Qin S, Mousa B, Sharifi A et al (2022) Flash flood susceptibility assessment and zonation by integrating analytic hierarchy process and frequency ratio model with diverse spatial data. *Water* 14(19):3069. <https://doi.org/10.3390/w14193069>
- Tehrany MS, Pradhan B, Jebur MN (2014) Flood susceptibility mapping using a novel ensemble weights-of-evidence and support vector machine models in GIS. *J Hydrol* 512:332–343. <https://doi.org/10.1016/j.jhydrol.2014.03.008>
- Thi Thuy Linh N, Pandey M, Janizadeh S, Sankar Bhunia G, Norouzi A, Ali S et al (2022) Flood susceptibility modeling based on new hybrid intelligence model: optimization of XGboost model using GA metaheuristic algorithm. *Adv Space Res* 69(9):3301–3318. <https://doi.org/10.1016/j.asr.2022.02.027>
- Towfiqul Islam ARM, Talukdar S, Mahato S, Kundu S, Eibek KU, Pham QB et al (2021) Flood susceptibility modelling using advanced ensemble machine learning models. *Geosci Front* 12(3):101075. <https://doi.org/10.1016/j.gsf.2020.09.006>
- Verma S, Bhatla R, Shahi N, Mall R (2022) Regional modulating behavior of Indian summer monsoon rainfall in context of spatio-temporal variation of drought and flood events. *Atmos Res* 274:106201. <https://doi.org/10.1016/j.atmosres.2022.106201>
- Wang Z, Lai C, Chen X, Yang B, Zhao S, Bai X (2015) Flood hazard risk assessment model based on random forest. *J Hydrol* 527:1130–1141. <https://doi.org/10.1016/j.jhydrol.2015.06.008>

- Wang Y, Hong H, Chen W, Li S, Pamučar D, Gigović L et al (2018) A hybrid GIS multi-criteria decision-making method for flood susceptibility mapping at Shangyou, China. *Remote Sens* 11(1):62. <https://doi.org/10.3390/rs11010062>
- Youssef AM, Mahdi AM, Pourghasemi HR (2023a) Optimal flood susceptibility model based on performance comparisons of LR, EGB, and RF algorithms. *Nat Hazards* 115(2):1071–1096. <https://doi.org/10.1007/s11069-022-05584-5>
- Youssef B, Bouskri I, Brahim B, Kader S, Brahim I, Abdelkrim B, Spalević V (2023b) The contribution of the frequency ratio model and the prediction rate for the analysis of landslide risk in the Tizi N'tichka area on the national road (RN9) linking Marrakech and Ouarzazate. *CATENA* 232:107464. <https://doi.org/10.1016/j.catena.2023.107464>
- Zhao G, Pang B, Xu Z, Peng D, Xu L (2019) Assessment of urban flood susceptibility using semi-supervised machine learning model. *Sci Total Environ* 659:940–949. <https://doi.org/10.1016/j.scitotenv.2018.12.217>

Publisher's Note Springer Nature remains neutral with regard to jurisdictional claims in published maps and institutional affiliations.

Authors and Affiliations

Youssef Bammou¹ · Brahim Benzougagh² · Brahim Igmoullan¹ · Abdessalam Ouallali³ · Shuraik Kader^{4,5}  · Velibor Spalevic⁶ · Paul Sestras^{7,8} · Paolo Billi^{9,10} · Slobodan B. Marković¹¹

✉ Shuraik Kader
shuraik10@gmail.com; shuraik.mohamedabdulkader@griffithuni.edu.au; s.mohamedabdulkader@griffith.edu.au

Youssef Bammou
youssef.bammou@ced.uca.ma

Brahim Benzougagh
brahim.benzougagh@is.um5.ac.ma; benzougaghbrahim@gmail.com

Brahim Igmoullan
igmoullan@gmail.com

Abdessalam Ouallali
abdessalam.ouallali@univh2c.ma

Velibor Spalevic
velibor.spalevic@gmail.com

Paul Sestras
psestras@yahoo.com; psestras@mail.utcluj.ro

Paolo Billi
bli@unife.it

¹ Laboratory of Geo-Resources, Department of Geology, Faculty of Science and Technology, Geo-Environment and Civil Engineering (L3G), Cadi Ayyad University, Marrakech, Morocco

² Department of Geomorphology and Geomatics, Scientific Institute, Mohammed V, University in Rabat, Avenue Ibn Battouta, Agdal, P.B. 703, 10106 Rabat-City, Morocco

³ Process Engineering and Environment Laboratory, Faculty of Sciences and Techniques of Mohammedia, Hassan II University of Casablanca, BP 146, 28806 Mohammedia, Morocco

⁴ School of Engineering and Built Environment, Griffith University, Nathan, QLD 4111, Australia

⁵ Green Infrastructure Research Labs (GIRLS), Cities Research Institute, Griffith University,

Nathan, QLD 4111, Australia

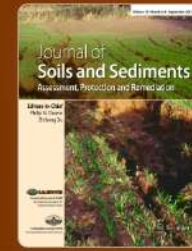
- ⁶ Biotechnical Faculty, University of Montenegro, 81000 Podgorica, Montenegro
- ⁷ Faculty of Civil Engineering, Technical University of Cluj-Napoca, 400020 Cluj-Napoca-Napoca, Romania
- ⁸ Academy of Romanian Scientists, Ilfov 3, 50044 Bucharest, Romania
- ⁹ Department of Earth Sciences, University of Ferrara, 44121 Ferrara, Italy
- ¹⁰ International Platform for Dryland Research and Education, Tottori University, 680-0945 Tottori, Italy
- ¹¹ Department of Geography, Tourism and Hotel Management, Faculty of Sciences, University of Novi Sad, Trg Dositeja Obradovića 3, 21000 Novi Sad, Serbia

Mathematical vs. machine learning models for particle size distribution in fragile soils of North-Western Himalayas

Soils, Sec 2 · Global Change, Environmental Risk Assessment, Sustainable Land Use · Research Article | [Open access](#)

Published: 06 June 2024

Volume 24, pages 2294–2308, (2024) [Cite this article](#)



[Download PDF](#)

You have full access to this article

Paul Sestras [View ORCID ID profile](#)

Faculty of Civil Engineering, Technical University of Cluj-Napoca, 400020, Cluj-Napoca-Napoca, Romania

Academy of Romanian Scientists, Ilfov 3, 50044, Bucharest, Romania

[View author publications](#)

You can also search for this author in [PubMed](#) | [Google Scholar](#)

Owais Bashir, Shabir Ahmad Bangroo, Shahid Shaukat, Jaufer, Nicola Senesi, Alban Kuriqi, Negar Omidvari

Ruby Michael, Mohamed Ksibi, Velibor Spalevic, Paul Sestras, Slobodan B. Marković, Paolo Billi, Sezai

Ercişli & Artan Hysa

manuscript.

JOURNAL OF SOILS AND SEDIMENTS

Publisher name: SPRINGER HEIDELBERG

Journal Impact Factor™

2.8

2023

3.3

Five Year

JCR Category	Category Rank	Category Quartile
ENVIRONMENTAL SCIENCES <i>in SCIE edition</i>	187/358	Q3
SOIL SCIENCE <i>in SCIE edition</i>	21/49	Q2

Source: Journal Citation Reports 2023. [Learn more](#)

Journal Citation Indicator™

0.68

2023

0.72

2022

JCI Category	Category Rank	Category Quartile
ENVIRONMENTAL SCIENCES <i>in SCIE edition</i>	161/359	Q2



Mathematical vs. machine learning models for particle size distribution in fragile soils of North-Western Himalayas

Owais Bashir¹ · Shabir Ahmad Bangroo¹ · Shahid Shuja Shafai¹ · Tajamul Islam Shah¹ · Shuraik Kader² · Lizny Jauffer³ · Nicola Senesi⁴ · Alban Kuriqi⁵ · Negar Omidvar⁶ · Soora Naresh Kumar⁷ · Ayyanadar Arunachalam⁸ · Ruby Michael² · Mohamed Ksibi⁹ · Velibor Spalevic¹⁰ · Paul Sestras^{11,12} · Slobodan B. Marković¹³ · Paolo Billi^{14,15} · Sezai Erciqli¹⁶ · Artan Hysa^{17,18}

Received: 11 April 2024 / Accepted: 10 May 2024 / Published online: 6 June 2024
© The Author(s) 2024

Abstract

Purpose Particle size distribution (PSD) assessment, which affects all physical, chemical, biological, mineralogical, and geological properties of soil, is crucial for maintaining soil sustainability. It plays a vital role in ensuring appropriate land use, fertilizer management, crop selection, and conservation practices, especially in fragile soils such as those of the North-Western Himalayas.

Materials and methods In this study, the performance of eleven mathematical and three Machine Learning (ML) models used in the past was compared to investigate PSD modeling of different soils from the North-Western Himalayan region, considering that an appropriate model must fit all PSD data.

Results and discussion Our study focuses on the significance of evaluating the goodness of fit in particle size distribution modeling using the coefficient of determination ($R^2_{adj} = 0.79$ to 0.45), the Akaike information criterion ($AIC = 67$ to 184), and the root mean square error ($RMSE = 0.01$ to 0.09). The Fredlund, Weibull, and Rosin Rammler models exhibited the best fit for all samples, while the performance of the Gompertz, S-Curve, and Van Genuchten models was poor. Of the three ML models tested, the Random Forest model performed the best ($R^2 = 0.99$), and the SVM model was the lowest ($R^2 = 0.95$). Thus, the PSD of the soil can be best predicted by ML approaches, especially by the Random Forest model.

Conclusion The Fredlund model exhibited the best fit among mathematical models while random forest performed best among the machine learning models. As the number of parameters in the model increased better was the accuracy.

Keywords Soil sustainability · Land use management · Model evaluation · Conservation practices · Random Forest model

1 Introduction

Particle size distribution (PSD), which consists of a cumulative percentage curve constructed from particle diameter values, is one of the most important soil physical characteristics as it influences almost all soil chemical, physical, biological, mineralogical, mechanical, and hydrological properties, and processes (Ließ and Sakhae 2023; Sowiński et al. 2023). In particular, PSD affects (i) soil chemical properties - base saturation, organic carbon content, adsorption properties, cation exchange capacity, and buffering capacity (Curtin and

Trolove 2013; Yang et al. 2020); (ii) soil physical properties - water retention, thermal conductivity, permeability, residual water content, soil aggregate formation, porosity, bulk density, soil aeration, and saturated and unsaturated hydraulic conductivity (Kader et al. 2022a; Minasny and Hartemink 2011); (iii) soil biological properties- bacterial, fungal and actinomycete populations, the carbon content of soil biomass, decomposition and mineralization of organic matter, length, weight and volume of plant roots and mycorrhizal population (Beylich et al. 2010; Ouallali et al. 2024; Sestras et al. 2023); (iv) soil mechanical properties- atterberg limits, tensile strength, soil strength, penetration resistance, compatibility, soil void ratio and compression index (Hartge et al. 2016; Lal and Shukla 2004). Soil PSD also strongly affects soil fertility parameters such as primary and

Responsible editor: Mohammad Valipour

Extended author information available on the last page of the article

m micronutrients, fixation, and de-fixation of ammonia (Kader et al. 2022b), availability of phosphorus, and potassium fixation (Bashir et al. 2024; Ljavić et al. 2023; Zolfaghari Nia et al. 2022). In addition, PSD strongly influences erosion, deposition, illuviation, calcification, and decalcification processes, the transfer of soluble and insoluble substances, and the distribution of horizons (Kader et al. 2022c; Knapen et al. 2007; Youssef et al. 2023).

Various mathematical models have been used to investigate the PSD of soils. The crucial aspect here is that the PSD should be determined precisely, whereby the difference between measured and estimated data should be as small as possible. Mathematical modeling of PSD is an important means (a) to characterize and classify soils by using the most appropriate parameters to design drainage systems properly (Esmaeelnejad et al. 2016); (b) to estimate soil hydraulic properties such as hydraulic conductivity and water retention and define appropriate particle sizes and uniformity coefficients (Rehman et al. 2022); and (c) to describe the entire curve of measured data points and thus improve the ability to find similar soil databases (Mozaffari et al. 2022). In addition, various Machine learning (ML) models, such as decision trees, Random Forest (RF), multiple linear regressions, and Artificial Neural Networks (ANN), have recently been used to analyze and classify soil texture classes (Rodriguez-Galiano et al. 2015).

Due to their robustness to noise and minimal bias when working with large datasets, ML models such as RF and gradient boosting have outperformed linear statistical approaches such as multiple linear regression in predicting some soil properties (Gao and Ding 2022; Wang et al. 2023). In addition, decision trees and ANN are popular ML approaches due to their high accuracy rate and kappa coefficients that measure the agreement between predicted and actual values. However, the overall result of a preliminary literature review shows that there is no systematic research focusing on the feasibility of different mathematical and ML algorithms to analyze soil texture categorization via PSD.

The North-Western Himalayas is an agriculture-oriented region encompassing diverse ecosystems including high-altitude farmlands, valleys, and foothills. Understanding the soil properties in this region is essential due to its unique climatic conditions, topography, and vegetation (Sidhu 2016). PSD exhibits spatial variability across landscapes (Millar et al. 1958). Mathematical models and ML models allow us to predict and generalize patterns to estimate PSD across large areas based on existing data, which is crucial for efficient land management and resource allocation (Feng et al. 2020; Wang et al. 2024).

The present study aims to utilize the great potential of mathematical models and ML algorithms in assessing the PSD of many soils collected in the North-Western Himalayan region and under different land uses, i.e., agriculture, horticulture, forest, and fallow. The specific objectives of

this work were (a) to compare the performance of different mathematical and ML models in predicting the PSD of soils, (b) to determine the effectiveness of different mathematical models and their fitting ability, and (c) to evaluate the ability of three ML models in classifying these soils and to find the best-performing model. The ultimate goal of this study is to provide a comprehensive way of PSD assessment for researchers that could help farmers and policymakers from the North-Western Himalayas and similar regions across the globe to tailor the fertilization, irrigation, and crop selection based on localized soil information, leading to improved yield and sustainable land development practices.

2 Materials and methods

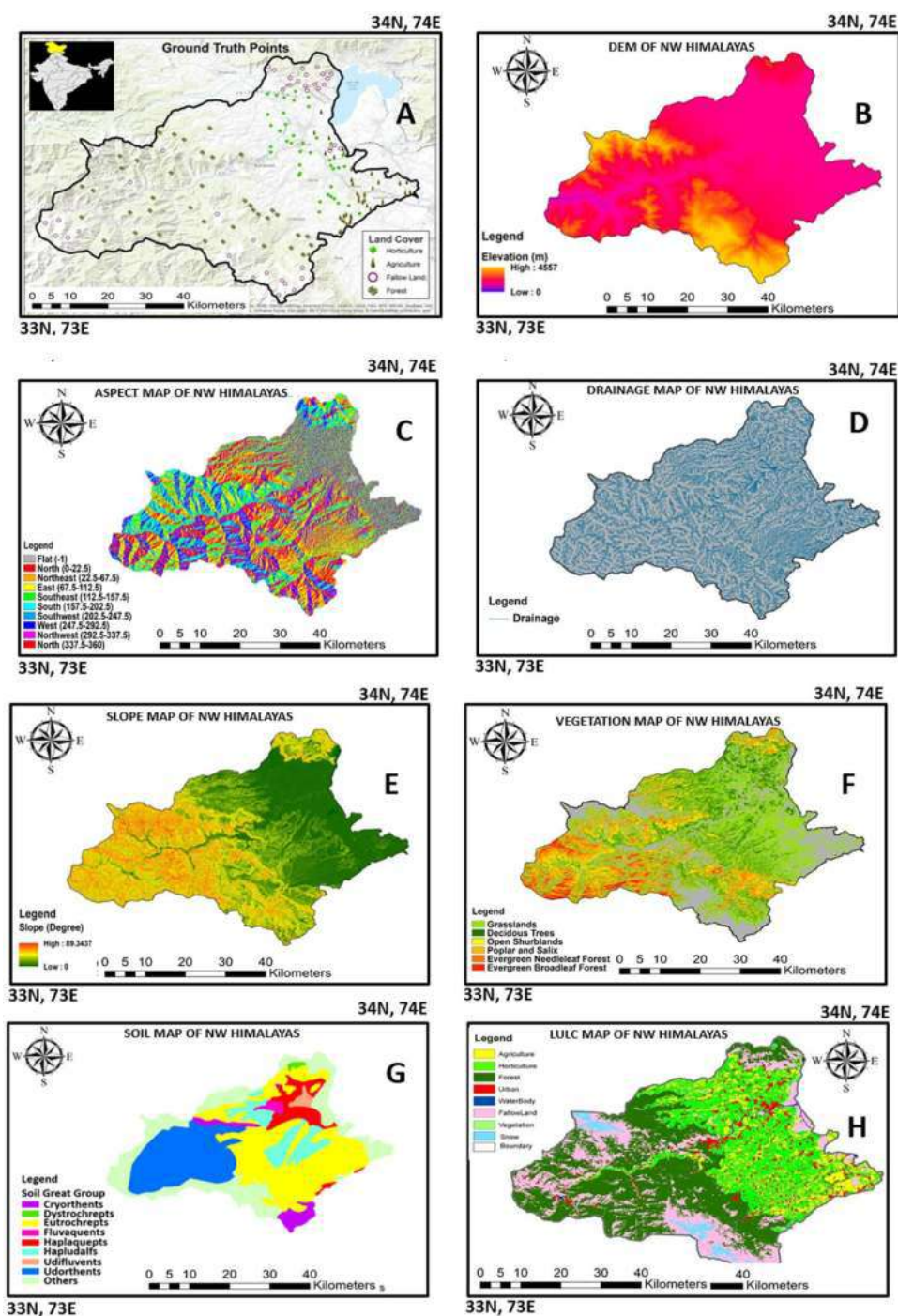
2.1 Study area

The research area was located in Jammu and Kashmir, in the North-Western Himalayas in the far north of India, on the border with Pakistan in locations 34° 16'–34° 40', 73° 45'–75° 35', 1060 to 3400 m altitude (Fig. 1). This area, known as the “snow-water-erosion crossing zone,” harbors some protected species and a considerable variety of medicinal and horticultural crops and is subject to severe erosion (Hossain et al. 2023). The average temperature is 25 °C, and the average annual rainfall is between 860 and 1050 mm, with heavy snowfall in winter. The heaviest precipitation occurs between March and July, with March being the rainiest. The topography is characterized by mountains and valleys, where the Jhelum River and its tributaries are the main source of irrigation. The North-Western side of Lake Wular, the largest freshwater lake in Asia, is also part of the region. The native vegetation of the area consists of *Pinus* spp, *Fir* spp, *Citrus* spp, *Salix* spp, *Populus* spp, and *Ulmus* spp (Bashir et al. 2022; Sharma et al. 2023).

2.2 Soil samples and particle size analysis

Three hundred soil samples were collected from different land uses (agriculture, horticulture, forest, and fallow) and the collected soil was air-dried and cleaned of pebbles and roots. A 50-gram aliquot of each sample was first treated with H₂O₂ to remove organic material and iron and aluminum oxides, then with 100 ml of a 5% sodium hexametaphosphate and water to reach a final volume of 1 L. The mixture was kept overnight, shaking back and forth. The sand fraction was then separated by sieving (2 mm), and the silt and clay fractions were separated by the hydrometric sedimentation method. An ASTM No. 152 H hydrometer was used with a bouyoucos gram scale per liter. The fine fractions collected after wet sieving (< 75 µm) were transferred to soil structure cylinders, while the coarse fraction retained by the 75-µm sieve was dried in an oven at 105

Fig. 1 The North-Western Himalayas study area in northern India with the indication of the 300 sampling sites (Ground Truth Points) (A); DEM (Digital Evaluation Model) map (B); aspect map (C); drainage map (D); slope map (E); vegetation map (F); soil map (G); LULC (Land Use and Land Cover) map (H)



°C and then weighed. Several measurements were taken after 30 s and 1, 2, 10, 30, 60, 90, 120, 300, 600, 1440, and 2880 min to determine the finer fractions (Esmaelnejad et al. 2016). The results obtained were divided into the following textural categories: Sand, sandy loam, loamy sand, loam, silty loam, silt, sandy loam, loamy loam, silty loam, sandy loam, silty loam, and clay, as described in Fig. 2.

Specifically, particle size distribution was related to several factors, including topography, such as slope,

aspect, drainage, and parent material; Remote Sens data, such as normalized difference vegetation index (NDVI) and brightness index (BI); climate and site variables; and category maps. The topographic variables were calculated using a GIS software called SAGA, while the Remote sensing data were derived from Landsat 8 imagery. In addition, topography, latitude, and longitude were also considered due to the complexity of the study area (Bashir et al. 2022).

Table 1 List of the various models applied to study soil PSD.

S. No.	Model	Equation
I.	Weibull Three Parameter	$P(d) = a - \exp\left[-\left(\frac{d}{b}\right)^c\right]$
II.	Gompertz model	$P(D) = a + b \times \exp\{-\exp[-c(D - d)]\}$
III.	S-curve	$\frac{P}{100} = e^{-nx}$ $x = \left[k \times \ln\left(\frac{d}{d_{min}}\right)\right]^{\frac{d}{d_0}}$
IV.	Logarithm-Exponential	$P(d) = A \times \exp(B \times \log d)$
V.	Jaky model	$P(d) = \exp\left\{-\frac{1}{p^2} \left[\ln\left(\frac{d}{d_{max}}\right)\right]^2\right\}$
VI.	Fredlund bimodal	$P = \left\{ w \left[\frac{1}{\left(\ln \left[\exp(1) + \left(\frac{d_{bi}}{d} \right)^{n_{bi}} \right] \right)^{m_{bi}}} \right] \right. \\ \left. + (1 - w) \left[\frac{1}{\left(\ln \left[\exp(1) + \left(\frac{J_{bi}}{d} \right)^{K_{bi}} \right] \right)^{l_{bi}}} \right] \right\} \\ \times \left\{ 1 - \left(\frac{\ln \left(1 + \frac{d_{rbi}}{d} \right)}{\ln \left(1 + \frac{d_{rbi}}{d_m} \right)} \right)^7 \right\}$
VII.	Best model	$P(d) = \left[1 + \left(\frac{d_x}{d} \right)^n \right]^{-m}$ $m = 1 - \frac{2}{n}$
VIII.	Van Genuchten or HP model	$P(d) = \left[1 + \left(\frac{k_1}{d} \right)^{k_2} \right]^{\frac{1}{k_2} - 1}$
IX.	Power law	$P(d) = \left(\frac{k_1}{1 - k_2} \right) \times d^{(1 - k_2)}$
X.	Rosin-Rammler	$P(d) = 1 - \exp\left[-k_1 \times \left(\frac{d}{L}\right)^{k_2}\right]$ $P(d) = 1 - \exp\left[-\left(\frac{d}{L}\right)^k\right]$
XI.	Exponential Power	$P(d) = \exp(-\beta_1 \times d^{\beta_2})$

and most appropriate for PSD modeling (Cheshmberah et al. 2022). Recently (Zhang et al. 2022), the fitting performance of the lognormal models was tentatively improved by adding an error function. Still, this modification was found to apply to only half of all soil texture classes. Later attempts such as (Sun et al. 2022) to improve the applicability of the models by shifting or scaling the model were unsuccessful, and their inaccuracy was attributed to the assumption of a symmetric PSD curve, which is not always true for all soil particle sizes.

In contrast to the other PSD models, the log-exponential model first proposed by Jaky contained only one parameter that is compatible with only certain soil texture classes and was unsuitable for soil samples with a large or non-uniform PSD range (Zhang et al. 2022). Since the fitting performance of a model is known to improve as the number of fitting parameters increases, most PSD models include two or three parameters. However, this increases model complexity and

requires more sample points to fit the parameters. The most commonly used log-exponential models include the methods proposed by two studies (Deviren Saygin and Erpul 2019), which have higher applicability and versatility, while the Gompertz model is based on the logistic growth function and the Fredlund model is based on the soil-water characteristic curve (Bayat et al. 2017; Cheshmberah et al. 2022).

Power function models can be divided into two categories. The first includes models obtained by modifying the Weibull distribution, such as the models of Rosin Rosin – Rammler–Sperling – Bennett (RRSB) (Bayat et al. 2017; Zhang et al. 2022). The second category includes models based on fractal theory, which focuses on the self-similarity of porous media. An example of this is the Tyler model (Tyler and Wheatcraft 1992), which was later improved based on the multi-fractal concept (Wang et al. 2015). However, fractal models have poor fitting performance resulting

from the difficulty of identifying self-similarity due to the different sizes of soil samples in the various databases, so they were not tested in this study.

One of the objectives of this work is to identify the best-performing model among those listed in Table 2. The model that best fits the data with the least number of fitting parameters while holding all other circumstances constant, thus minimizing the variability between the predicted and observed data. The PSD models evaluated in this work contained one to four fitting parameters, the values of which were determined using the Microsoft Excel Solver routine operator, allowing the best fit between predicted and observed data to be plotted. In addition, the performance of the eleven PSD models listed in Table 1 was evaluated using three statistical indices, namely the root mean square error (RMSE), the adjusted coefficient of determination (R^2_{adj}), and the Akaike information criterion (AIC), which assesses the complexity of the model and its goodness of fit by discouraging overfitting and encouraging fitting.

In Table 2, SSE and SST stand for the residual and total sum of squares, respectively, N for the number of PSD data points for soil *i*, P for model parameters, and Y_e and Y_o for the predicted and cumulative mass fractions, respectively. In this study, the model with the lowest AIC value was considered the best-performing. In addition to AIC, the indices, R^2_{adj} and RMSE were also used to test the quality of fit. The R^2_{adj} is often used to measure goodness of fit in statistical software programs and scientific papers, but its applicability to nonlinear regression analysis has been controversial in recent years. Therefore, RMSE and AIC are expected to be more appropriate in measuring goodness of fit for nonlinear models. A general principle when comparing PSD models is that a model with a higher R^2_{adj} value and lower RMSE and AIC values provide a better fit for a single data set, i.e., the closer RMSE and AIC are to 0 and the closer R^2_{adj} is to 1, the better the model performs.

Table 2 Statistical indexes are used to evaluate the performance of each model

Akaike information criteria (AIC)	$N \ln(SSE) - N \ln N + 2$
SSE	$\sum_{i=1}^N (Y_e - Y_o)^2$
RMSE	$\sqrt{\frac{SSE}{N-P}}$
R^2_{adj}	$1 - \left(\frac{SSE}{N-P} \middle \frac{SST}{N-1} \right)$

2.4 ML models and parameter optimization and validation

2.4.1 The Artificial Neural Network (ANN) model

The ANN model simulates the brain's information processing system by identifying the nonlinear system behavior that current regression-based approaches do not exploit. An ANN model consists of an input layer, a hidden layer, and an output layer (Wang et al. 2022) and involves a few constraints on model structure and assumptions as the shape of the connections is determined during learning (Zhang et al. 2022). In this work, the default settings were used, and a hidden layer with four neurons with hyperbolic tangent activation and identity output was created.

2.4.2 The Random Forest (RF) model

The RF model presented integrates a bagging strategy with the selection of random variables (Breiman 2001), which aims to combine a “weak learner” set to obtain a “strong learner.” The R package “Random Forest” was used in this work to perform the RF model. A bootstrap sample was used for each RF tree, and different methods were used to split the binary data for regression and classification questions. The data were separated using the Gini index for classification, and each tree model was trained by minimizing the sum of squares of mean deviations for regression.

In addition, RF is quite robust to overfitting and is indifferent to the range of input values, so standardization or normalization is not required in this process. The main objective of the RF model is to adjust two parameters, namely the number of trees (ntree) and the number of attributes randomly selected at each split (mtry).

2.4.3 The Support Vector Machine (SVM) model

The SVM model, introduced by Cortes and Vapnik in 1995 (Qin and Li 2023), is a generalized linear classifier often used in classification and regression problems in soil science. The main goal of SVM is structural risk minimization, which is to find different classes by creating an ideal separation hypersurface in the feature space. SVM support vector regression, or regression problem, can be solved by minimizing the structural risk using loss functions (Panup et al. 2022). The R package “e1071” was used to develop the SVM model in this work. The kernel function for the SVM was assumed to be a linear function. The other factors that needed to be adjusted were “cost” and “gamma,” which govern the trade-off between classification complexity and accuracy and the radial effect ranges.

2.4.4 Parameter optimization and validation method

Optimal parameters are defined as those with the lowest RMSE for regression and the largest kappa coefficient for classification using cross-validation. In this work, the R package “caret” (Carl et al. 2018) for SVM, the R package “random forest” for RF, and the R package “ann” for ANN were used to optimize the considered parameters. Two hundred fifty soil samples (75% of the original dataset) were used for training and 50 soil samples (25% of the total data) for validation, and the procedure was repeated ten times.

The overall accuracy consists of the count of all soil texture types used in the validation divided by the number of those accurately recognized by the machine-learning model:

$$\text{Overall accuracy} = \frac{\text{TP} + \text{TN}}{\text{TP} + \text{TN} + \text{FP} + \text{FN}} \quad (1)$$

where TP, TN, FP, and FN stand for true positives, true negatives, false positives, and false negatives.

The confusion matrix is used to determine the kappa coefficient that indicates how well the predicted classes and measured classes agree, according to:

$$\text{kappa} = \frac{p_o - p_e}{1 - p_e} \quad (2)$$

where p_e is the probability of agreement when two classes are unconditionally independent, and p_o is the probability of observed agreement (general accuracy). Thus, a value of the kappa coefficient from 0.00 to 0.19 indicates a sufficient agreement, from 0.20 to 0.39 a moderate agreement, from 0.40 to 0.60 a considerable agreement, from 0.61 to 0.80 a near-perfect agreement, and from 0.81 to 1.00 a near perfect agreement between the two classes of data.

The probabilities of the different soil texture types obtained by the training and prediction methods of the ML models are used to calculate the precision (Eq. 3) and the recall (Eq. 4). These probabilities sum up to 1 and are chosen as the mean value for the degree of recognition of positive instances (Flach and Kull 2015).

$$\text{Precision} = \frac{\text{TP}}{\text{TP} + \text{FP}} \quad (3)$$

$$\text{Recall} = \frac{\text{TP}}{\text{TP} + \text{FN}} \quad (4)$$

The soil texture data set used was unbalanced, as 43.8% of the samples belong to the silt loam class, and the remaining belong to other classes. This imbalance of classes would mean that the negative classifier would give an overemphasized result due to the large number of negative values.

Consequently, the results could be too optimistic and should be interpreted cautiously.

The confusion index (COI) (Eq. 5) depends on the prediction probability developed when evaluating the ambiguities of ML models for categorization.

$$\text{COI} = \sum_{i=1}^n \frac{[1 - (\text{Pmax}, i - \text{Psecmax}, i)]}{n} \quad (5)$$

Pmax, i denotes the greatest possible probability of soil sample i , and $\text{Psecmax}, i$ denotes the second-highest likely likelihood. The model performance is improved as the COI is lower.

2.4.5 Cluster analysis

Cluster analysis, also called numerical taxonomy or classification analysis, aims to sort objects into groups based on their similarities using measured variables. This approach is the main goal of exploratory data mining and a common way to look at statistical data. In cluster analysis, there is no prior information about belonging to a cluster. It involves choosing a distance criterion, selecting a clustering method, determining the number of clusters, reading the profile cluster correctly, and finally deciding whether the cluster is valid (Backhaus et al. 2023; Templ et al. 2008). Cluster analysis can be hierarchical or non-hierarchical and is considered more accurate when there are fewer similarities and more differences between the clusters. Cluster analysis uses different algorithms, each with its own approach, to identify clusters efficiently. These algorithms use other methods to group similar data points based on certain criteria, such as distance or similarity. Therefore, the appropriate algorithm's choice depends on the data's characteristics and the analysis's specific goals. In this work, the most common approaches to cluster analysis were used, i.e., the Ward method and Euclidean distance in the software R (Ultsch and Löttsch 2022).

3 Results and discussion

3.1 Mathematical/statistical modeling of PSD

The fitting performance of mathematical PSD models depends on the data set's quantity and quality, i.e., the accuracy and reliability, and the distribution among the different soil texture groups. In particular, the performance of any model depends on five important factors: accuracy and flexibility, overprediction, overlap or non-overlap, a difficult fitting procedure, and a complex equation form. In this paper, three statistical indices, i.e., AIC, RMSE, and R^2_{adj} were used to determine the performance of PSD models. Although goodness of fit is

Table 3 Accuracy is achieved by the various statistical models used in fitting PSD data of all soil samples

	Sand			Silt			Clay		
	AIC	R ²	RMSE	AIC	R ²	RMSE	AIC	R ²	RMSE
Fredlund	184 ± 7.9	0.76 ± 0.03	0.011 ± 0.001	159.7 ± 14.4	0.76 ± 0.03	0.031 ± 0.021	119.4 ± 24.4	0.80 ± 0.002	0.018 ± 0.014
Weibull	174 ± 6.80	0.75 ± 0.03	0.014 ± 0.002	153.4 ± 14.2	0.76 ± 0.03	0.033 ± 0.024	114.1 ± 21.6	0.80 ± 0.003	0.021 ± 0.015
Rossin Rammler	169 ± 3.40	0.75 ± 0.04	0.015 ± 0.006	151.1 ± 15.3	0.76 ± 0.04	0.037 ± 0.024	113.8 ± 20.4	0.80 ± 0.000	0.026 ± 0.015
Exponential power	166 ± 5.2	0.73 ± 0.08	0.024 ± 0.000	148.2 ± 13.6	0.75 ± 0.04	0.041 ± 0.026	110.1 ± 18.6	0.80 ± 0.002	0.031 ± 0.017
Power Law	123 ± 4.7	0.64 ± 0.01	0.032 ± 0.004	129.1 ± 14.2	0.71 ± 0.06	0.055 ± 0.033	98.4 ± 22.6	0.78 ± 0.001	0.051 ± 0.028
Jaky	119 ± 3.9	0.63 ± 0.07	0.056 ± 0.002	124.3 ± 14.4	0.70 ± 0.06	0.061 ± 0.003	95.7 ± 17.7	0.77 ± 0.004	0.059 ± 0.031
BEST	98 ± 2.8	0.69 ± 0.06	0.068 ± 0.007	118.7 ± 13.6	0.70 ± 0.05	0.064 ± 0.003	90.2 ± 18.1	0.76 ± 0.001	0.081 ± 0.024
Simple law	91 ± 1.4	0.57 ± 0.05	0.073 ± 0.001	108.9 ± 15.3	0.61 ± 0.07	0.088 ± 0.049	84.2 ± 23.3	0.76 ± 0.003	0.096 ± 0.031
Gompertz	82 ± 0.8	0.54 ± 0.08	0.089 ± 0.000	106.4 ± 11.4	0.70 ± 0.08	0.104 ± 0.062	81.3 ± 14.4	0.72 ± 0.002	0.116 ± 0.024
S-curve	80 ± 1.2	0.46 ± 0.11	0.092 ± 0.005	103.1 ± 8.8	0.63 ± 0.11	0.164 ± 0.044	67.6 ± 5.9	0.70 ± 0.001	0.164 ± 0.026
Van Genutchen	67 ± 1.4	0.45 ± 0.13	0.097 ± 0.007	97.5 ± 10.6	0.58 ± 0.14	0.181 ± 0.065	62.2 ± 8.8	0.68 ± 0.001	0.181 ± 0.042

generally evaluated based on the R^2_{adj} value, its application to nonlinear models has been questioned by several researchers. The AIC and RMSE indices would more accurately assess the goodness of fit of non-linear models.

For the PSD models used in this work, the value of R^2_{adj} for sand, silt, and clay was between 0.799 and 0.458, that of AIC between 184 and 67, and that of RMSE between 0.011 and 0.097 (Table 3).

The models were listed, starting with the model with the lowest RMSE value. In that order, the Fredlund, Weibull, Rossin-Rammler, and Exponential Power models best fit the PSD curve for all samples (Hwang et al. 2002). The best performance of the Fredlund model can be attributed to the highest clay content of all soil samples, while the almost similar performance of the Weibull model could be due to its good fitting accuracy (Bayat et al. 2017). The Rossin-Rammler model showed better fitting ability than the Exponential Power, Power Law, Jaky, and BEST models, possibly due to its ability to differentiate particles more accurately. The better performance of the BEST model in fitting PSD curves compared to the Simple Law, S-Curve, and Gompertz models could be due to the smaller number of fitting parameters (Hwang et al. 2002), which would result in less overfitting and better adaptation to new data sets. The Gompertz model showed lower performance compared to the previously mentioned models. In contrast, the S-curve and Van Genutchen models showed the worst performance, which could be due to their inflexible nature leading to a high overlap effect (Abkenar et al. 2019).

3.1.1 R^2_{adj} values of sand, silt, and clay

The R^2_{adj} values for sand, silt, and clay listed in Table 3 show that the Fredlund, Weibull, Rossin-Rammler, and Exponential Power models have higher accuracy than all other

models at a significance level of $p \leq 0.05$. In particular, the Fredlund model performed best regarding R^2_{adj} for all particle sizes, and its effectiveness increased with increasing clay content. However, studies based on the properties and fit of PSD (Bayat et al. 2015) found that the Weibull model had the highest fit over a wide range of particle sizes. The Power Law, Jaky, and BEST models also showed comparable and relatively low R^2_{adj} values for the sandy texture. In contrast, the Simple Law, Gompertz, S-curve, and Van Genutchen models showed the significantly lowest R^2_{adj} values compared to the other models (Abkenar et al. 2019; Afrasiabi et al. 2019; Bayat et al. 2015; Rastgou et al. 2021; Weipeng et al. 2015). To summarize, the R^2_{adj} index does not appear to be effective for comparing the performance of nonlinear models, as it does not convincingly differentiate between models. This is likely because it measures the arbitrary variation each model allows, making it difficult to determine which model best fits the data.

3.1.2 RMSE values of sand, silt, and clay

The classification of the models according to the value of the RMSE index showed that the Fredlund model had the lowest RMSE value and the highest goodness of fit for all soil samples, which is why it was placed at the top of Table 3. However, the difference between Fredlund, Weibull, Rossin-Rammler, and exponential power models was not significant ($p \leq 0.05$), as previously observed (Abkenar et al. 2019; Bayat et al. 2015; Botula et al. 2013). The power law and Jaky models showed similarly low performance and goodness of fit, as previously reported (Bayat et al. 2015; Botula et al. 2013; Carl et al. 2018). Finally, the Simple log, Gompertz, S-curve, and Van Genutchen models showed the lowest goodness-of-fit performance, significantly different from the other models.

3.1.3 AIC values of sand, silt, and clay

The AIC index imposes a penalty on supplemental adjustment coefficients and discourages overfitting. The Fredlund model showed the highest AIC values and was the best model with the highest accuracy and fit to the data (Table 3). The Weibull model follows it, followed by the Rossin-Rammler and exponential power models, which had similar AIC values. The Power Law and Jaky models showed lower AIC values, with the latter performing better than the former for silt texture, as previously noted (Afrasiabi et al. 2019; Bayat et al. 2015; Rastgou et al. 2021; Weipeng et al. 2015). Lower AIC values were shown by the BEST, Simple log, Gompertz, and S-curve models, which had significantly low goodness of fit, while the Van Genuchten model showed the lowest AIC value.

3.2 ML modelling of PSD

Of the three ML models evaluated, the RF model had the highest overall accuracy (0.992), followed by ANN (0.966) and SVM (0.950), as shown in Fig. 3. In addition, the RF algorithm yielded the highest kappa coefficient (0.242), followed by ANN (0.238) and SVM (0.213). However, regarding COI, SVM (COI=0.278) performed the best, while RF (COI=0.501) performed the least.

The results obtained in this study might differ from those obtained with common fraction modeling techniques, as it focused on using independent modeling or component-wise techniques, which capture the results of common fraction modeling only to a limited extent. Although the RF ML model appeared to perform better than ANN and SVM, as previously observed (Heung et al. 2016), it exhibited the longest overall computation time in classification and interpolation mode. In contrast, the ANN model performed better than the other two models when finding a trade-off between model accuracy and total computation time by drastically reducing the latter without compromising accuracy. This result is related to the fact that the training phase of the ANN model can automatically perform parallel computations, making ANN results up to ten times faster than current gradient-boosting models, which is a key advantage when working with large datasets (Chen and Guestrin 2016). When working with large data sets, ANN is recommended due to its speed, even if the accuracy achieved is not entirely satisfactory.

In addition, several joint component approaches, such as compositional kriging, characterized by highly accurate soil modeling, and Dirichlet regression, which uses an incentive, can contribute to a multidimensional prescription for soil PSD (Savelonas et al. 2022). However, ML algorithms such as ANN, RF, and SVM appeared more powerful in integrating ecological covariates. They could also be used in

conjunction with multivariate vectors and log-ratio methods in future studies. For example, the extended form of RF, Multivariate Random Forest (MRF), can make valuable predictions for all output attributes with a single model (Kazemi and Mohorko 2017).

3.3 Cluster analysis

Cluster analysis is a means by which different objects can be categorized into other groups, i.e., clusters, based on measured characteristics, with similar objects placed in the same cluster. It is a popular method for analyzing statistical information and a main technique in exploratory data mining. Based on the RMSE values (Table 3), the data processing with the Fredlund, Weibull, Rossin-Rammler, and Exponential Power models could be assigned to the same cluster. In contrast, the data processed with the Power, Jaky, Best, Simple law, and Gompertz models could be assigned to a second cluster, and a third cluster comprised the data analyzed with the less powerful S-curve and Van Genuchten models (Fig. 4).

The fitting performance of mathematical PSD models plays a crucial role in understanding soil texture characteristics (Muniruzzaman and Pedretti 2021; Pham et al. 2023). Three statistical indices, namely AIC, RMSE, and R^2_{adj} , were employed to evaluate the performance of PSD models. The results, summarized in Table 3, indicate varying performance across different models. The Fredlund, Weibull, Rossin-Rammler, and Exponential Power models best fit PSD curves across all soil samples. The Fredlund model exhibited superior performance, attributed to its efficacy in handling high clay content.

Examining the R^2_{adj} values for sand, silt, and clay (Table 3) reaffirms the superiority of the Fredlund, Weibull, Rossin-Rammler, and Exponential Power models. The Fredlund model demonstrated consistently high accuracy, especially with increased clay content. However, it's noteworthy that R^2_{adj} alone may not effectively differentiate the performance of nonlinear models.

The classification based on RMSE values highlighted the Fredlund model's outstanding performance, closely followed by the Weibull, Rossin-Rammler, and Exponential Power models. The Power Law, Jaky, and BEST models demonstrated comparable performance, while the Simple Law, Gompertz, S-Curve, and Van Genuchten models exhibited significantly lower goodness-of-fit.

The AIC index, penalizing overfitting, placed the Fredlund model at the top, followed by the Weibull, Rossin-Rammler, and Exponential Power models. Power Law and Jaky models displayed lower AIC values, with the BEST, Simple Law, Gompertz, and S-Curve models showing the least goodness of fit.

The ML models, including Random Forest (RF), Artificial Neural Network (ANN), and Support Vector Machine

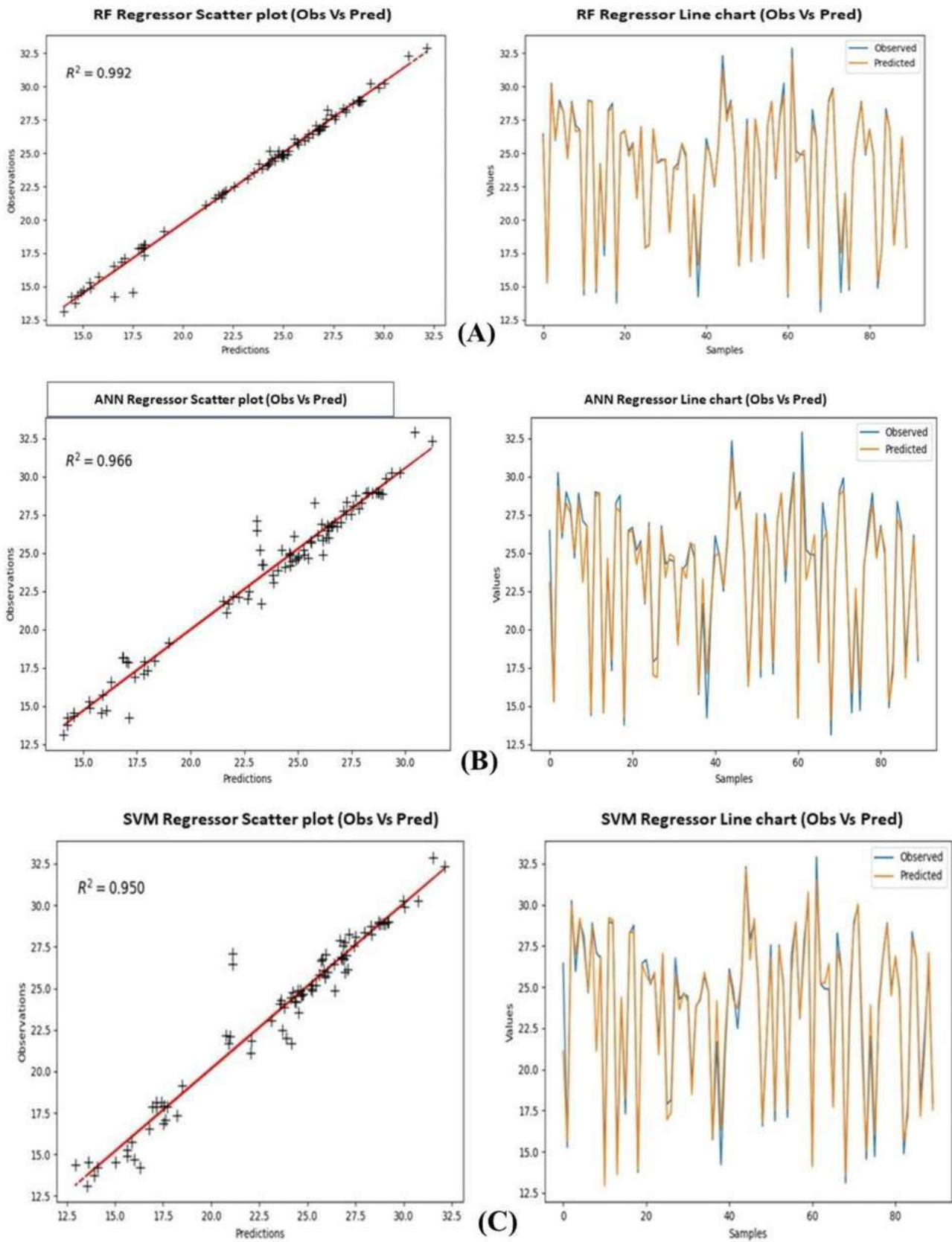
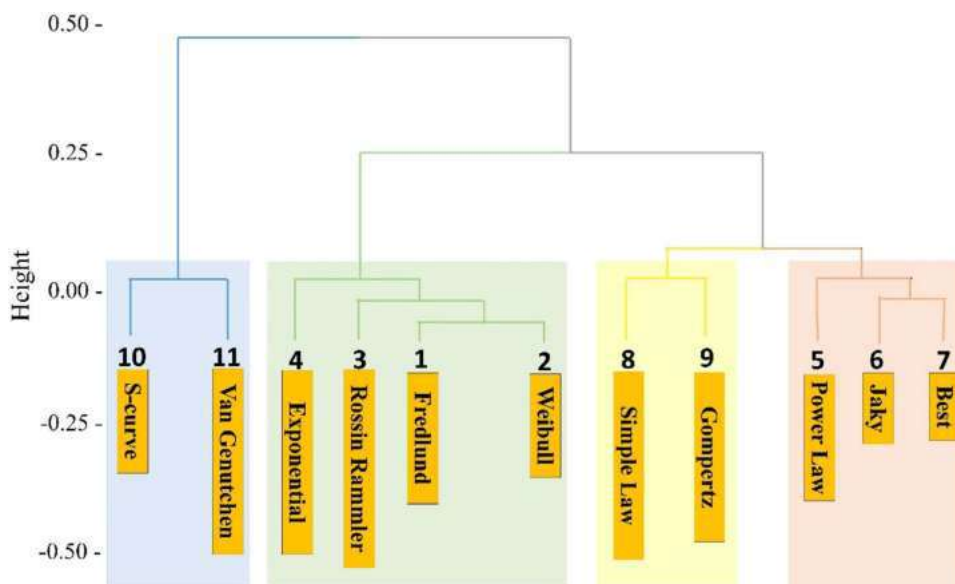


Fig. 3 Comparison of the performance of the three machine-learning models RF (A), ANN (B), and SVM (C)

Fig. 4 Cluster diagram of the accuracy achieved by the various models applied based on RMSE values



(SVM), were evaluated for their accuracy. The RF model demonstrated the highest overall accuracy, with ANN and SVM following. However, SVM performed the best concerning the Correctly Outlined Instances (COI) metric. The results indicate that while RF exhibited superior accuracy, ANN offered a notable advantage in computation time efficiency, crucial for handling large datasets.

Cluster analysis based on RMSE values revealed three distinct clusters. The first cluster included data processed by the Fredlund, Weibull, Rossin-Rammler, and Exponential Power models, emphasizing their consistent accuracy. The second cluster comprised data processed by the Power, Jaky, BEST, Simple Law, and Gompertz models. The third cluster represented less accurate models, namely S-Curve and Van Genuchten.

In conclusion, the comprehensive evaluation using multiple statistical indices provides valuable insights into the performance of various mathematical and ML models for PSD. The Fredlund and other top-performing models are reliable for accurate soil texture prediction. ML models, particularly Random Forest, show promise in enhancing accuracy, with considerations for computation efficiency. The cluster analysis further supports categorizing models based on their fitting performance, aiding in selecting appropriate models for different soil conditions.

4 Conclusion

In general, the performance of most of the eleven mathematical models evaluated in this work was satisfactory regarding predicting PSD curves in soil. Based on the three validation criteria, the three-parametric Fredlund model was the most

reliable and accurate for predicting soil PSD curves. However, the Weibull, Rossin-Rammler, and Exponential Power models also showed high prediction accuracy. In contrast, the Power, Jaky, Best, Simple Law, and Gompertz models performed moderately well when fitting the soil texture data. In summary, the predictive accuracy of models with a higher or comparable number of parameters was higher than that of models based on a smaller or equivalent number of parameters. However, using additional parameters does not always mean the model performs better.

The results of this study have also confirmed the importance of comparative goodness of fit testing in the form of R^2_{adj} , AIC, and RMSE values for PSD models before using them for PSD parameter estimation. The Fredlund, Weibull, and Rossin-Rammler mathematical models can provide a satisfactory PSD curve and acceptable accuracy, essential for soil mechanics, physics applications, and hydraulic parameter assessment. However, ML models performed better than mathematical models, and RF outperformed ANN and SVM.

The novelty of the study lies in the comprehensive comparison of eleven mathematical models and three ML models for PSD modeling, considering the diverse soil characteristics prevalent in the North-Western Himalayan region. The model performance was systematically evaluated using established metrics such as coefficient of determination (R^2_{adj}), Akaike information criterion (AIC), and root mean square error (RMSE), providing a robust assessment of model fit across different soil samples.

The findings of this study underscore the significance of ML approaches, particularly the Random Forest model, in accurately predicting PSD in fragile soils. While traditional mathematical models such as Fredlund, Weibull,

and Rosin Rammler exhibited commendable performance, the superiority of ML models, especially in handling complex soil dynamics, is evident from the results of this study. Notably, the Random Forest model outperformed all the other models tested, highlighting its potential for precise PSD prediction in similar environments. Future research studies can be designed based on the investigation to confirm these results and determine the best approach for specific applications based on regional and geographical requirements.

The implications of this research are significant for soil science and land management practices in fragile ecosystems. By elucidating the strengths and limitations of both mathematical and ML models, this study offers valuable insights for researchers and practitioners engaged in soil resources management, agricultural planning, and environmental conservation in mountainous regions.

Author contributions Conceived and designed the studies - Owais Bashir, Shabir Ahmad Bangroo, Shahid Shuja Shafai, Shuraik Kader, Nicola Senesi, Slobodan B. Marković, Paolo Billi and Alban Kuriqi. Performed the analysis - Owais Bashir, Shabir Ahmad Bangroo, Shahid Shuja Shafai, Soora Naresh Kumar, Ayyanadar Arunachalam, Shuraik Kader, Lizny Jaufer, Nicola Senesi, Velibor Spalevic, Negar Omidvar, Artan Hysa, Paul Sestras, Paolo Billi and Alban Kuriqi. Analysed and interpreted the data - Owais Bashir, Shabir Ahmad Bangroo, Shahid Shuja Shafai, Shuraik Kader, Lizny Jaufer, Negar Omidvar, Mohamed Ksibi, Nicola Senesi and Alban Kuriqi. Contributed materials, analysis tools or data - Owais Bashir, Shabir Ahmad Bangroo, Shahid Shuja Shafai, Soora Naresh Kumar, Ayyanadar Arunachalam, Shuraik Kader, Lizny Jaufer, Velibor Spalevic, Slobodan B. Marković, Artan Hysa, Paul Sestras, Sezai Ercişli, Tajamul Islam Shah and Alban Kuriqi. Wrote the paper and proof-reading - Owais Bashir, Shabir Ahmad Bangroo, Shahid Shuja Shafai, Tajamul Islam Shah, Shuraik Kader, Lizny Jaufer, Nicola Senesi, Ruby Michael, Mohamed Ksibi, Velibor Spalevic, Alban Kuriqi, Negar Omidvar, Slobodan B. Marković, Artan Hysa, Paul Sestras, Sezai Ercişli, Slobodan B. Marković and Paolo Billi. Internal reviewers – Alban Kuriqi, Nicola Senesi, Ruby Michael, Mohamed Ksibi, Velibor Spalevic, Slobodan B. Marković, Sezai Ercişli, and Paolo Billi. Project administration – Owais Bashir, Nicola Senesi, Slobodan B. Marković and Paolo Billi. All authors have read and agreed to the published version of the manuscript.

Funding Open Access funding enabled and organized by CAUL and its Member Institutions No fundings received.

Availability of data and materials No research data were used outside of the submitted manuscript file. All the available data were mentioned within the manuscript.

Declarations

Ethical approval Not applicable.

Consent to participate Not applicable.

Consent to publish Not applicable.

Competing interests The authors have no relevant financial or non-financial interests to disclose.

Open Access This article is licensed under a Creative Commons Attribution 4.0 International License, which permits use, sharing, adaptation, distribution and reproduction in any medium or format, as long as you give appropriate credit to the original author(s) and the source, provide a link to the Creative Commons licence, and indicate if changes were made. The images or other third party material in this article are included in the article's Creative Commons licence, unless indicated otherwise in a credit line to the material. If material is not included in the article's Creative Commons licence and your intended use is not permitted by statutory regulation or exceeds the permitted use, you will need to obtain permission directly from the copyright holder. To view a copy of this licence, visit <http://creativecommons.org/licenses/by/4.0/>.

References

- Abkenar FZ, Rasoulzadeh A, Asghari A (2019) Performance evaluation of different soil water retention functions for modeling of water flow under transient condition. *Bragantia* 78:119–130. <https://doi.org/10.1590/1678-4499.2017406>
- Afrasiabi F, Khodaverdiloo H, Asadzadeh F, Van Genuchten MT (2019) Comparison of alternative soil particle-size distribution models and their correlation with soil physical attributes. *J Hydrol Hydromech* 67:179–190. <https://doi.org/10.2478/johh-2018-0009>
- Backhaus K, Erichson B, Gensler S, Weiber R, Weiber T (2023) Cluster analysis. In: *Multivariate analysis: an application-oriented introduction*. Springer, pp 453–532
- Bashir O, Bangroo SA, Guo W, Meraj G, T Ayele G, Naikoo NB, Taddese H (2022) Simulating spatiotemporal changes in land use and land cover of the North-Western Himalayan Region using Markov chain analysis. *Land* 11:2276. <https://doi.org/10.3390/land11122276>
- Bashir O, Bangroo SA, Shafai SS, Senesi N, Kader S, Alamri S (2024) Geostatistical modeling approach for studying total soil nitrogen and phosphorus under various land uses of North-Western Himalayas. *Ecol Inf* 80:102520. <https://doi.org/10.1016/j.ecoinf.2024.102520>
- Bayat H, Rastgo M, Mansouri Zadeh M, Vereecken H (2015) Particle size distribution models, their characteristics and fitting capability. *J Hydrol* 529:872–889. <https://doi.org/10.1016/j.jhydrol.2015.08.067>
- Bayat H, Rastgou M, Nemes A, Mansourizadeh M, Zamani P (2017) Mathematical models for soil particle-size distribution and their overall and fraction-wise fitting to measurements. *Eur J Soil Sci* 68:345–364. <https://doi.org/10.1111/ejss.12423>
- Beylich A, Oberholzer HR, Schrader S, Höper H, Wilke BM (2010) Evaluation of soil compaction effects on soil biota and soil biological processes in soils. *Soil Tillage Res* 109:133–143. <https://doi.org/10.1016/j.still.2010.05.010>
- Botula YD, Cornelis WM, Baert G, Mafuka P, Van Ranst E (2013) Particle size distribution models for soils of the humid tropics. *J Soil Sediment* 13:686–698. <https://doi.org/10.1007/s11368-012-0635-5>
- Breiman L (2001) Random forests. *Mach Learn* 45:5–32. <https://doi.org/10.1023/A:1010933404324>
- Carl G, Levin SC, Kühn I (2018) spind: an R package to account for spatial autocorrelation in the analysis of lattice data. *Biodivers Data J*. <https://doi.org/10.3897/BDJ.6.e20760>

- Chen T, Guestrin C (2016) Xgboost: A scalable tree boosting system. In: Proceedings of the 22nd acm sigkdd international conference on knowledge discovery and data mining
- Cheshmberah F, Zolfaghari AA, Taghizadeh-Mehrjardi R, Scholten T (2022) Evaluation of mathematical models for predicting particle size distribution using digital soil mapping in semiarid agricultural lands. *Geocarto Int* 37:13016–13038. <https://doi.org/10.1080/10106049.2022.2076911>
- Curtin D, Trolove S (2013) Predicting pH buffering capacity of New Zealand soils from organic matter content and mineral characteristics. *Soil Res* 51:494–502. <https://doi.org/10.1071/SR13137>
- Deviren Saygin S, Erpul G (2019) Modeling aggregate size distribution of eroded sediment resulting from rain-splash and raindrop impacted flow processes. *Int J Sediment Res* 34:166–177. <https://doi.org/10.1016/j.ijsrc.2018.10.004>
- Esmaelnejad L, Siavashi F, Seyedmohammadi J, Shabanpour M (2016) The best mathematical models describing particle size distribution of soils. *Model Earth Syst Env* 2:1–11. <https://doi.org/10.1007/s40808-016-0220-9>
- Feng X, Qu J, Tan L, Fan Q, Niu Q (2020) Fractal features of sandy soil particle-size distributions during the rangeland desertification process on the eastern Qinghai-Tibet Plateau. *J Soils Sediments* 20(1):472–485. <https://doi.org/10.1007/s11368-019-02392-6>
- Flach P, Kull M (2015) Precision-recall-gain curves: PR analysis done right. In: Cortes C, Lawrence N, Lee D, Sugiyama M, Garnett R (eds) *Advances in Neural Information Processing Systems* 28 (NIPS 2015). https://papers.nips.cc/paper_files/paper/2015/hash/33e8075e9970de0cfea955afd4644bb2-Abstract.html. ISBN: 9781510825024
- Gao Z, Ding M (2022) Application of convolutional neural network fused with Mach Learn modeling framework for geospatial comparative analysis of landslide susceptibility. *Nat Hazard* 113:833–858. <https://doi.org/10.1007/s11069-022-05326-7>
- Hartge KH, Horn R, Horton R, Bachmann J, Peth S (2016) Essential soil physics
- Heung B, Ho HC, Zhang J, Knudby A, Bulmer CE, Schmidt MG (2016) An overview and comparison of machine-learning techniques for classification purposes in digital soil mapping. *Geoderma* 265:62–77. <https://doi.org/10.1016/j.geoderma.2015.11.014>
- Hossain F, Kamal AM, Sadeak S, Gazi MY (2023) Quantitative soil erosion risk assessment due to rapid urbanization in the Cox's Bazar district and Rohingya refugee camps in Bangladesh. *Stoch Env Res Asses* 37:989–1006. <https://doi.org/10.1007/s00477-022-02314-y>
- Hwang SI, Lee KP, Lee DS, Powers SE (2002) Models for estimating soil particle-size distributions. *Soil Sci Soc Amer J* 66:1143–1150. <https://doi.org/10.2136/sssaj2002.1143>
- Kader S, Chadalavada S, Jauffer L, Spalevic V, Dudic B (2022c) Green roof substrates—a literature review. *Front Built Env*. <https://doi.org/10.3389/fbuil.2022.1019362>
- Kader S, Novicevic R, Jauffer L (2022b) Soil management in sustainable agriculture: analytical approach for the ammonia removal from the dairy manure. *Agric For* 68:69–78. <https://doi.org/10.17707/AgricultForest.68.4.06>
- Kader S, Spalevic V, Dudic B (2022a) Feasibility study for estimating optimal substrate parameters for sustainable green roof in Sri Lanka. *Env Dev Sustain*. <https://doi.org/10.1007/s10668-022-02837-y>
- Kazemi F, Mohorko R (2017) Review on the roles and effects of growing media on plant performance in green roofs in world climates. *Urban Urban Green* 23:13–26. <https://doi.org/10.1016/j.ufug.2017.02.006>
- Knapen A, Poesen J, Govers G, Gyssels G, Nachtergaele J (2007) Resistance of soils to concentrated flow erosion: A review. *Earth Sci Rev* 80:75–109. <https://doi.org/10.1016/j.earscirev.2006.08.001>
- Lal R, Shukla MK (2004) Principles of soil physics. CRC Press
- Ließ M, Sakhaee A (2023) Deep learning with a multi-task convolutional neural network to generate a national-scale 3D soil data product: particle size distribution of the German agricultural soil-landscape. *EGUsphere* 2023:1–23. <https://doi.org/10.5194/egusphere-2023-2386>
- Ljavić D, Radović M, Kulina M, Zejak D, Spalević V, Kader S, Jauffer L (2023) Influence of cultivar and fertilization treatment on the yield and leaf nutrients content of apple (*Malus domestica* Borkh). *Heliyon*. <https://doi.org/10.1016/j.heliyon.2023.e16321>
- Millar CE, Turk LM, Foth HD (1958) Fundamentals of soil science. *Soil Sci* 86:168
- Minasny B, Hartemink AE (2011) Predicting soil properties in the tropics. *Earth Sci Rev* 106:52–62. <https://doi.org/10.1016/j.earscirev.2011.01.005>
- Mozaffari H, Moosavi AA, Dematte JAM (2022) Estimating particle-size distribution from limited soil texture data: Introducing two new methods. *Biosyst Eng* 216:198–217. <https://doi.org/10.1016/j.biosystemseng.2022.02.007>
- Muniruzzaman M, Pedretti D (2021) Mechanistic models supporting uncertainty quantification of water quality predictions in heterogeneous mining waste rocks: a review. *Stoch Env Res Assess* 35:985–1001. <https://doi.org/10.1007/s00477-020-01884-z>
- Ouallali A, Kader S, Bammou Y, Aqnouy M, Courba S, Beroho M, Briak H, Spalevic V, Kuriqi A, Hysa A (2024) Assessment of the erosion and outflow intensity in the Rif region under different land use and land cover scenarios. *Land*. <https://doi.org/10.3390/land13020141>
- Panup W, Ratipapongton W, Wangkeeree R (2022) A novel twin support vector machine with generalized pinball loss function for pattern classification. *Symmetry* 14:289. <https://doi.org/10.3390/sym14020289>
- Pham K, Kim D, Le CV, Won J (2023) Mach Learn-based pedotransfer functions to predict soil water characteristics curves. *Transp Geotech* 42:101052. <https://doi.org/10.1016/j.trgeo.2023.101052>
- Qin Z, Li Q (2023) An uncertain support vector machine with imprecise observations. *Fuzzy Optim Decis Mak*. <https://doi.org/10.1007/s10700-022-09404-0>
- Rastgou M, Bayat H, Mansoorzadeh M, Gregory AS (2021) Prediction of soil hydraulic properties by Gaussian process regression algorithm in arid and semiarid zones in Iran. *Soil Tillage Res* 210:104980. <https://doi.org/10.1016/j.still.2021.104980>
- Rehman ZU, Khalid U, Ijaz N, Mujtaba H, Haider A, Farooq K, Ijaz Z (2022) Mach Learn-based intelligent modeling of hydraulic conductivity of sandy soils considering a wide range of grain sizes. *Eng Geol* 311:106899. <https://doi.org/10.1016/j.enggeo.2022.106899>
- Rodriguez-Galiano V, Sanchez-Castillo M, Chica-Olmo M, Chica-Rivas M (2015) Mach Learn predictive models for mineral prospectivity: An evaluation of neural networks, random forest, regression trees and support vector machines. *Ore Geol Rev* 71:804–818. <https://doi.org/10.1016/j.oregeorev.2015.01.001>
- Savelonas MA, Veinidis CN, Bartsokas TK (2022) Computer vision and pattern recognition for the analysis of 2D/3D remote sens data in Geoscience: a survey. *Remote Sens* 14:6017. <https://doi.org/10.3390/rs14236017>
- Sestrars P, Mircea S, Roşca S, Bilaşco Ştefan, Sălăgean T, Dragomir Lo H, Mv, Bruma S, Sabou C, Marković R, Kader S (2023) GIS based soil erosion assessment using the USLE model for efficient land management: A case study in an area with diverse pedo-geomorphological and bioclimatic characteristics. *Notulae Botanicae Horti Agrobotanici Cluj-Napoca* 51(3):13263–13263. <https://doi.org/10.15835/nbha51313263>
- Sharma H, Pant KS, Bishist R, Lal Gautam K, Ludarmani Dogra R, Kumar A (2023) Estimation of biomass and carbon storage potential

- in agroforestry systems of north western Himalayas, India. *CATENA* 225:107009. <https://doi.org/10.1016/j.catena.2023.107009>
- Sidhu GS (2016) Soil conservation of Northwestern Himalayas (NWH): their constraints and potentials for sustainable hill agriculture. *Conservation agriculture: an approach to combat climate change in Indian Himalaya*. 315, 338. https://doi.org/10.1007/978-981-10-2558-7_12
- Sowiński P, Smólczyński S, Orzechowski M, Kalisz B, Bieniek A (2023) Effect of soil agricultural use on particle-size distribution in young glacial landscape slopes. *Agriculture* 13:584. <https://doi.org/10.3390/agriculture13030584>
- Sun X, She D, Wang H, Fei Y, Gao L (2022) Modelling soil hydraulic properties with an improved pore-solid fractal (PSF) model through image analysis. *Eur J Soil Sci* 73:e13156. <https://doi.org/10.1111/ejss.13156>
- Templ M, Filzmoser P, Reimann C (2008) Cluster analysis applied to regional geochemical data: problems and possibilities. *Appl Geochem* 23:2198–2213. <https://doi.org/10.1016/j.apgeochem.2008.03.004>
- Tyler SW, Wheatcraft SW (1992) Fractal scaling of soil particle-size distributions: analysis and limitations. *Soil Sci Soc Amer J* 56:362–369. <https://doi.org/10.2136/sssaj1992.03615995005600020005x>
- Ullsch A, Lötsch J (2022) Euclidean distance-optimized data transformation for cluster analysis in biomedical data (EDOtrans). *BMC Bioinform* 23:233. <https://doi.org/10.1186/s12859-022-04769-w>
- Wang C, Cai G, Liu X, Wu M (2022) Prediction of soil thermal conductivity based on Intelligent computing model. *Heat Mass Transf* 58:1695–1708. <https://doi.org/10.1007/s00231-022-03209-y>
- Wang J, Zhang M, Bai Z, Guo L (2015) Multi-fractal characteristics of the particle distribution of reconstructed soils and the relationship between soil properties and multi-fractal parameters in an opencast coal-mine dump in a loess area. *Environ Earth Sci* 73:4749–4762. <https://doi.org/10.1007/s12665-014-3761-0>
- Wang Z, Cai Y, Liu D, Qiu F, Sun F, Zhou Y (2023) Intelligent classification of coal structure using multinomial logistic regression, random forest and fully connected neural network with multi-source geophysical logging data. *Int J Coal Geol* 268:104208. <https://doi.org/10.1016/j.coal.2023.104208>
- Wang Z, Hasi E, Han X, Qingda M (2024) Fractal characterization of soil particle size distribution under different land use patterns on the north slope of Wula Mountain in China. *J Soils Sediments* 24(3):1148–1164. <https://doi.org/10.1007/s11368-024-03722-z>
- Weipeng W, Jianli L, Bingzi Z, Jiabao Z, Xiaopeng L, Yifan Y (2015) Critical evaluation of particle size distribution models using soil data obtained with a laser diffraction method. *PLoS ONE* 10:e0125048. <https://doi.org/10.1371/journal.pone.0125048>
- Yang Y, Wang Y, Peng Y, Cheng P, Li F, Liu T (2020) Acid-base buffering characteristics of non-calcareous soils: Correlation with physicochemical properties and surface complexation constants. *Geoderma* 360:114005. <https://doi.org/10.1016/j.geoderma.2019.114005>
- Youssef B, Bouskri I, Brahim B, Kader S, Brahim I, Abdelkrim B, Spalević V (2023) The contribution of the frequency ratio model and the prediction rate for the analysis of landslide risk in the Tizi N'tichka area on the national road (RN9) linking Marrakech and Ouarzazate. *CATENA* 232:107464. <https://doi.org/10.1016/j.catena.2023.107464>
- Zhang H, Wang C, Chen Z, Kang Q, Xu X, Gao T (2022) Performance comparison of different particle size distribution models in the prediction of soil particle size characteristics. *Land* 11:2068. <https://doi.org/10.3390/land11112068>
- Zolfaghari Nia M, Moradi M, Moradi G, Taghizadeh-Mehrjardi R (2022) Machine learning models for prediction of soil properties in the riparian forests. *Land* 12(1):32. <https://doi.org/10.3390/land12010032>

Publisher's Note Springer Nature remains neutral with regard to jurisdictional claims in published maps and institutional affiliations.

Authors and Affiliations

Owais Bashir¹ · Shabir Ahmad Bangroo¹ · Shahid Shuja Shafai¹ · Tajamul Islam Shah¹ · Shuraik Kader² · Lizny Jaufer³ · Nicola Senesi⁴ · Alban Kuriqi⁵ · Negar Omidvar⁶ · Soora Naresh Kumar⁷ · Ayyanadar Arunachalam⁸ · Ruby Michael² · Mohamed Ksibi⁹ · Velibor Spalevic¹⁰ · Paul Sestras^{11,12} · Slobodan B. Marković¹³ · Paolo Billi^{14,15} · Sezai Ercişi¹⁶ · Artan Hysa^{17,18}

✉ Shuraik Kader
s.mohamedabdulkader@griffith.edu.au;
shuraik.mohamedabdulkader@griffithuni.edu.au;
shuraik10@gmail.com

✉ Negar Omidvar
n.omidvar@griffith.edu.au

Owais Bashir
owaisbashir10@skuastkashmir.ac.in

Shabir Ahmad Bangroo
shabir@skuastkashmir.ac.in

Shahid Shuja Shafai
shahidshafai@gmail.com

Tajamul Islam Shah
3tjamul@gmail.com

Lizny Jaufer
lizny96@gmail.com

Nicola Senesi
nicola.senesi@uniba.it

Alban Kuriqi
alban.kuriqi@tecnico.ulisboa.pt

Soora Naresh Kumar
nareshkumar@iari.res.in; nareshkumar.soora@gmail.com

Ayyanadar Arunachalam
arun70@gmail.com; arun.icar@yahoo.com

Ruby Michael
ruby.michael@griffith.edu.au

Mohamed Ksibi
mohamed.ksibi@isbs.usf.th

Velibor Spalevic
velibor.spalevic@gmail.com

Paul Sestras
psestras@yahoo.com; psestras@mail.utcluj.ro

Slobodan B. Marković
baca.markovic@gmail.com

Paolo Billi
paolo.billi@unife.it

Sezai Ercişli
sercisli@gmail.com; sercisli@atauni.edu.tr

Artan Hysa
artan.hysa@tum.de

- ¹ Division of Soil Science, Sher-e-Kashmir University of Agricultural Sciences and Technology of Kashmir, 190025 Srinagar, India
- ² School of Engineering and Built Environment, Griffith University, 4111 Brisbane, Australia
- ³ School of Architecture, Liverpool John Moores University, L3 5UX Liverpool, UK
- ⁴ Department of Soil, Plant and Food Sciences, University of Bari “Aldo Moro”, 70121 Bari, Italy
- ⁵ CERIS, Instituto Superior Técnico, University of Lisbon, 1649-004 Lisbon, Portugal
- ⁶ Centre for Planetary Health and Food Security, Griffith University, 4111 Brisbane, Australia
- ⁷ ICAR-Indian Agricultural Research Institute, 110012 New Delhi, India
- ⁸ ICAR-Central Agroforestry Research Institute, 284001 Jhansi, India
- ⁹ High Institute of Biotechnology of Sfax (ISBS) Laboratory of Environmental Engineering and Ecotechnology (LGEET) at the National Engineering School of Sfax (ENIS), University of Sfax, Sfax, Tunisia
- ¹⁰ Biotechnical Faculty, University of Montenegro, 81000 Podgorica, Montenegro
- ¹¹ Faculty of Civil Engineering, Technical University of Cluj-Napoca, 400020 Cluj-Napoca-Napoca, Romania
- ¹² Academy of Romanian Scientists, Ilfov 3, 50044 Bucharest, Romania
- ¹³ Department of Geography, Tourism and Hotel Management, Faculty of Sciences, University of Novi Sad, Trg Dositeja Obradovića 3, 21000 Novi Sad, Serbia
- ¹⁴ Department of Earth Sciences, University of Ferrara, 44121 Ferrara, Italy
- ¹⁵ International Platform for Dryland Research and Education, Tottori University, 680-0945 Tottori, Italy
- ¹⁶ Faculty of Agriculture, Department of Horticulture, Ataturk University, 25240 Erzurum, Türkiye
- ¹⁷ School of Life Sciences, Technical University of Munich, Freising 85354, Germany
- ¹⁸ Faculty of Architecture and Engineering, Epoka University, 1032 Tirana, Albania



Spatial Mapping for Multi-Hazard Land Management in Sparsely Vegetated Watersheds Using Machine Learning Algorithms

Youssef Bammou¹ · Brahim Benzougagh² · Brahim Igmoullan¹ · Shuraik Kader³ · Abdessalam Ouallali⁴ · Velibor Spalevic⁵ · Paul Sestras^{6,7} · Alban Kuriqi^{8,9}

Received: 4 December 2023 / Accepted: 30 June 2024
© The Author(s) 2024

Abstract

This study breaks new ground by developing a multi-hazard vulnerability map for the Tensift watershed and the Haouz plain in the Moroccan High Atlas area. The unique juxtaposition of flat and mountainous terrain in this area increases sensitivity to natural hazards, making it an ideal location for this research. Previous extreme events in this region have underscored the urgent need for proactive mitigation strategies, especially as these hazards increasingly intersect with human activities, including agriculture and infrastructure development. In this study six advanced machine learning (ML) models were used to comprehensively assess the combined probability of three significant natural hazards: flooding, gully erosion, and landslides. These models rely on causal factors derived from reputable sources, including geology, topography, meteorology, human activities, and hydrology. The research's rigorous validation process, which includes metrics such as specificity, precision, sensitivity, and accuracy, underlines the robust performance of all six models. The validation process involved comparing the model's predictions with actual hazard occurrences over a specific period. According to the outcomes in terms of the area under curve (AUC), the XGBoost model emerged as the most predictive, with remarkable AUC values of 93.41% for landslides, 91.07% for gully erosion and 93.78% for flooding. Based on the overall findings of this study, a multi-hazard risk map was created using the relationship between flood risk, gully erosion, and landslides in a geographic information system (GIS) architecture. The innovative approach presented in this work, which combined ML algorithms with geographical data, demonstrates the power of these tools in sustainable land management and the protection of communities and their assets in the Moroccan High Atlas and regions with similar topographical, geological, and meteorological conditions that are vulnerable to the aforementioned risks.

Keywords Natural hazards · Geographic information system (GIS) · Hazard susceptibility assessment · Machine learning (ML) · Area under curve (AUC)

Introduction

Numerous research projects have highlighted the undeniable increase in the frequency of natural disasters worldwide, predominantly caused by changes in climate (Pei et al. 2023; Zhang et al. 2023). Therefore, protection against natural disasters has become an absolute priority, and forecasting and prevention measures are still among the steps that need to be taken to move towards good planning (Bashir et al. 2024a, b; Yousefi et al. 2020). Creating thematic data to map catastrophe susceptibility is still among the most crucial methods for foreseeing and managing natural risks (Khan et al. 2020; Youssef et al. 2023). These maps are essential in natural risk

management and developing risk reduction strategies. They make it possible to visualize and classify at-risk areas, identify vulnerable populations and infrastructures, and better understand the risk factors specific to each region.

However, most current research into natural hazards is limited to the analysis of individual risks (Bammou et al. 2024b; Razavi-Termeh et al. 2023). These studies, which focus on particular threats, generally consider risks as independent phenomena without considering the combined degree of vulnerability of relationships between several risks (Panahi et al. 2020; Yousefi et al. 2020). Thus, assessing and looking into the interactions between different risks is fundamental. Various hazard investigations are crucial, as they allow us to find far more significant concentrations of harm and risk than studies focusing on a single type of

Extended author information available on the last page of the article

hazard (Hillier et al. 2020). For this kind of research, the geographical distribution of natural hazards in the area has to be reevaluated. This strategy aids in lowering the likelihood of occurrence and the possibility of cumulative risks brought on by the interplay of several hazards, such as landslides, financial losses, and fatalities (Bammou et al. 2024d; Sestras et al. 2023; Stalhandske et al. 2024). By mapping vulnerability holistically and considering the complex interactions between natural hazards, it is possible to predict, prevent, and proactively manage threats to communities and the environment.

Multi-hazard vulnerability mapping is a method that aims to consider multiple types of threats simultaneously at each location. It makes it possible to assess the complex spatial relationships between different high-risk events, including the possibility for these events to occur concurrently or cumulatively, as well as any potential interactions between them (Aksha et al. 2020; Ming et al. 2022). According to Bammou et al. (2024a, b, c, d), the Tensift catchment consists of well-correlated risk zones with certain common conditioning factors, such as increased water erosion risk from runoff-induced flooding and landslides from heavy rainfall and flooding. Multi-hazard mapping is a powerful tool for understanding better and managing the complex risks that threaten communities (Lombardo et al. 2020; Saunders and Kilvington 2016).

Various techniques have been used to model multiple hazards, such as using two decision aids, namely the sequential Monte Carlo technique and a decision aid (Guo et al. 2020; Zhao et al. 2024). Another method combines empirical data with deterministic, equation-based (i.e., theoretical) discoveries (Bout et al. 2018; Mondini et al. 2023). Furthermore, a method integrating multi-criteria analysis and geographic information systems (GIS) has been applied to produce successful outcomes, as demonstrated by Lyu and Yin (2023), Sestras et al. (2023). Recently, a lot of research has employed the integration of machine learning methods, including Boosted Regression Tree (BRT), Generalized Additive Model (GAM), Random Forest (RF), and Support Vector Machine (SVM) for risk prediction (Bammou et al. 2024a; Kohansarbaz et al. 2022; Ye et al. 2020).

The development of a multi-hazard map using ML models is based on the study of the leading natural hazards in the study area, namely gullying, landslides, and flooding (Bammou et al. 2023). The production of such a map is essential for a good understanding of the association of these risks. This study, therefore, compared the effectiveness and accuracy of different machine learning models, such as SVM, RF, ANN, KNN, DT and XGBoost, in producing risk maps for the Tensift catchment and the Haouz plain.

This would be a pioneering study in the scientific literature that combines three natural hazards: landslide, gully erosion and flood risks together to construct. This work uses

state-of-the-art ML models to develop a novel multi-hazard assessment strategy to understand the interrelationships and assess the dangers of landslides, gully erosion, and floods. This study aims to answer the research questions: Why is a multi-hazard assessment necessary rather than a single-hazard approach, and what are the benefits? The findings of this research are helpful for researchers, authorities, developers, and decision-makers involved in land management and risk mitigation strategies in the Moroccan High Atlas and regions across the globe with similar topographical, geological, and meteorological conditions.

Material and methods

Study area

The High Atlas in Marrakech is formed by three primary geological formations, according to Duclaux (2005): (1) the Permo-Triassic is the most common formation in the east. The highest peaks of the Atlas are located in the central region, home to (2) Precambrian igneous and metamorphic rocks. The western area is home to (3) primary and secondary limestone formations, most of which have limited permeability, continuous surface runoff, and the potential to develop significant runoff after heavy rainfall. It often occurs in conjunction with Ordovician and Precambrian shales.

The central Moroccan region around Marrakesh is home to the Tensift watershed. Its 20,000 km² surface consists mainly of two zones that behave differently hydrologically as illustrated by Fig. 1. With an elevation gain of over 4000 m, the Atlas Mountains' southern slopes receive a substantial amount of precipitation and snowfall (up to 600 mm/year) in the catchment region. These mountains act as a "water tower" for the large, semi-arid Haouz plain, which is situated downstream and receives 250 mm of precipitation annually. More specifically, irrigation covers a sizable portion of the 2000 km³ Haouz plain.

Numerous lithological and structural elements and a varied and erratic hydrological behavior driven by geomorphological and climatic conditions define the research region. They give rise to various threats, such as the floods in Ourika on August 17, 1995, and October 28, 1999, which destroyed 142 structures that regularly caused severe damage, caused 200 fatalities, and flooded over 300 ha of arable land. More recently, on July 18, 2023, they also caused significant damage in Moulay Brahim. The landslides in this area, especially along the Tizi N'tichka national route, which links Ouarzazate and Marrakech, and the village of Ijoukak, where a dramatic landslide occurred in July 2019 that killed over 20 people due to the landslide and gully erosion, were also documented by the Hydraulic Agency of the Tensift Basin (ABHT).

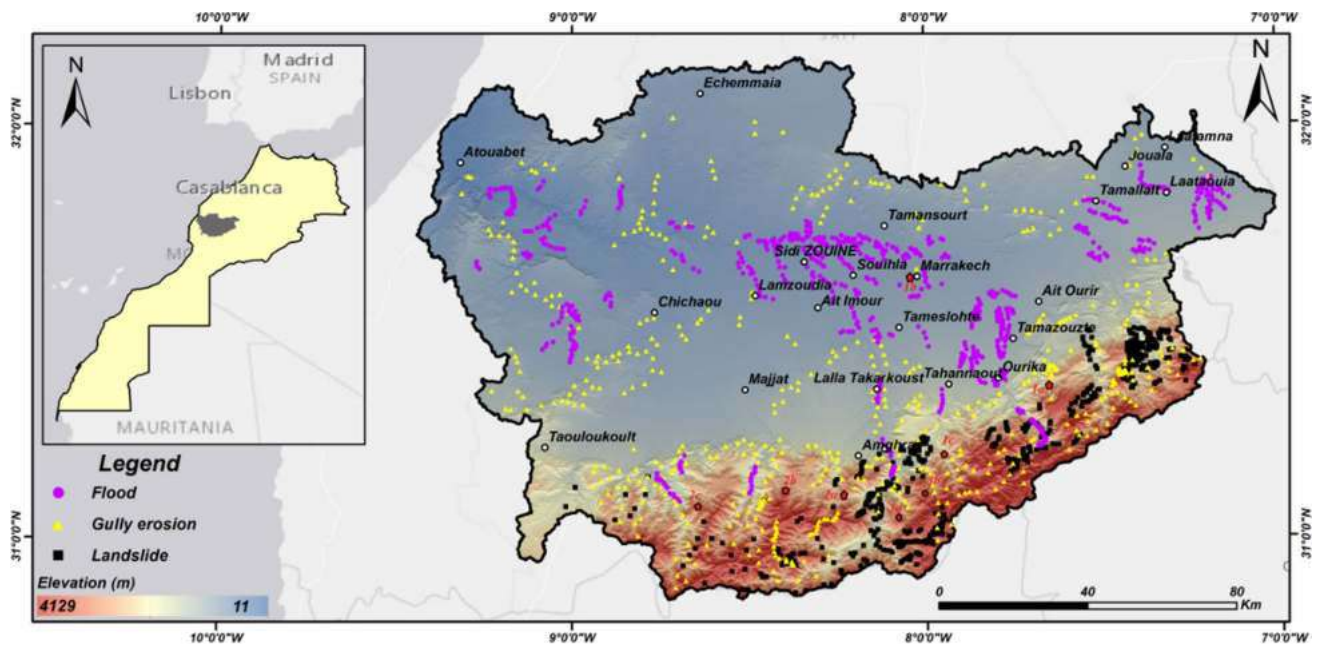


Fig. 1 The Haouz Plain and the Tensift watershed are study areas

Multi-hazard inventory

Compiling an inventory is a crucial step in assessing the hazard. Based on GPS-based field surveys, regional and national statistics from many sources, including the Tensift Hydraulic Basin Agency (ABHT) and analysis of Google Earth imagery of vulnerable areas in mountainous regions, the comprehensive A list of gully erosion, floods, and landslides in the Tensift watershed is available given by Fig. 2. The inventory maps were created using this information, and 620 gully erosion sites, 1291 landslide sites, and 762 inundation sites as of Fig. 1. The training and validation sites for each hazard class in the inventory map were selected by random selection. In the literature, the percentage ratio of 70/30% is frequently utilized for training and validation datasets (Bammou et al. 2024a; Hong et al. 2016; Pourghasemi and Rahmati 2018) and it is being continued in this study as well. This study applies this percentage ratio by integrating binary codings (0, 1), i.e., values associated with landslide-relevant and non-landslide-relevant pixels. The landslide inventory map was then converted into raster data at a resolution of thirty meters (30 m).

Data collection

The creation of the landslide susceptibility grids was based on different data sources. Table 1 shows a description of the other media used.

Multi-hazard conditioning factors (MCFs)

Multi-hazard conditioning factors (MCFs) was also conducted to determine the most pertinent criteria for each risk category. Table 2 and Fig. 3 provide a quick overview of the rasters and data layers of topography, climate, hydrology, vegetation, land use, and geology that were constructed using GIS software.

These include 25 conditioning factors, namely slope given in Fig. 3a, aspect given by Fig. 4b, elevation given by Fig. 3c, and precipitation given in Fig. 3d, which were generated from data from 14 precipitation stations provided by ABHT for the period 1992 to 2020. The Topographic Moisture Index (TWI) illustrated in Fig. 3e was calculated using Eq. (1). Normalised Differential Vegetation Index (NDVI) illustrated by Fig. 3f was determined using Eq. (2).

Other parameters such as drainage density (Fig. 3g), lithology (Fig. 3h) which includes 32 facies was derived from a 1:500,000 scale geological map of Marrakech, LULC (Fig. 3i), which was generated from Sentinel-2 images with 10 m resolution from 2022, LS factor (Eq. (3) and Fig. 3j) is one of the critical elements in the RUSLE equation, along with the distances to faults (Fig. 3u) and rivers (Fig. 3k), developed using spatial analyst Euclidean distance tool, SPI illustrated by Fig. 3l was calculated using Eq. (6), TRI illustrated by Fig. 3m was calculated using Eq. (4), geomorphons (Fig. 3n), factor K illustrated by Fig. 3o was calculated using Eq. (5), HSG (Fig. 3p), distance to roads (Fig. 3q), soil type (Fig. 3r), river accumulation (Fig. 3s),

Fig. 2 Photographs of the three hazards in the Tensift catchment collected in the field. **1a**, **1b** and **1c** Flooding; **2a**, **2b** and **2c** gully erosion; **3a** and **3b** landslides. NB: their locations are shown in Fig. 1

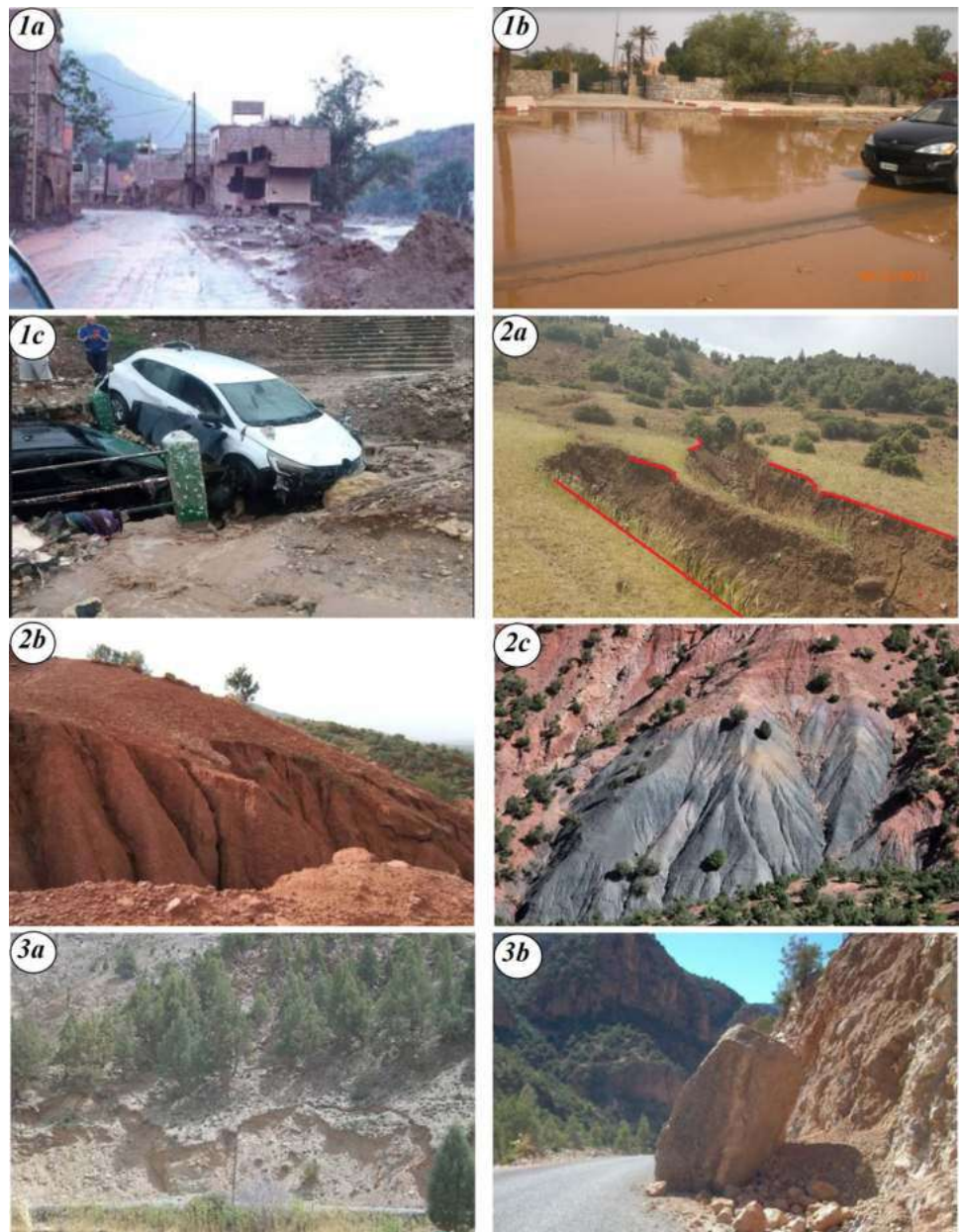


Table 1 Data used and sources

Database and source	Scale/resolution	Acquisition date
SRTM-DEM (digital elevation model) United States Geological Survey (USGS) https://earthexplorer.usgs.gov/	30 m	2018
Soil type https://www.fao.org/soils-portal/data-hub/soil-maps-anddatabases/faounesco-soil-map-of-the-world/en/	1:5 000 000 scale	1981
Sentinel-2 images (B02–B03–B04–B08) https://code.earthengine.google.com/	10 m	01-01-2022 to 30-01-2022
Geological map of Marrakech	1: 500 000 scale	
Rainfall data Tensift Hydraulic Basin Agency (ABHT)	14 stations	1992 to 2020
Global Hydrologic Soil Groups (HYSOGs) https://cmr.earthdata.nasa.gov/search/concepts/C2216864285-ORNL_CLOUD.html	250 m	2017-11-28

Table 2 Conditioning factors tested and used to map vulnerability to natural hazards

Hazard-indicator factors	Description			Hazard type		
	Type	Range	Units	Flood	Landslide	Gully erosion
Valley depth	Grid	(− 249.95) to 907.68	m	x	x	✓
LS factor	Grid	0–5350.66	L in m, S in %	x	x	✓
Aspect	Grid	9 directions + flat	–	✓	✓	✓
LULC	Grid	7 classes	–	✓	✓	✓
Precipitation	point	154.90–406.10	mm	✓	✓	✓
Curvature	Grid	(− 27.22) to 21.22	–	x	x	✓
NDVI	Grid	(− 0.91) to 10	–	x	✓	✓
TPI	Grid	(− 198.12) to 247.74	–	✓	✓	✓
Distance to rivers	Polyline	0–7597.17	m	✓	✓	✓
TWI	Grid	2.37–27.24	–	□	✓	✓
SPI	Grid	(− 13.82) to 15.24	–	□	x	✓
Slope	Grid	0–71.02	°	✓	✓	✓
Elevation	Grid	11–4129	m	✓	✓	✓
Lithology	Polygone	32 facies	–	x	✓	✓
Geomorphons	Grid	10 classes	–	x	x	□
Drainage density	Grid	0–0.86	Km/Km ²	x	x	✓
TRI	Grid	0.0009–0.99	–	✓	x	✓
Flow accumulation	Grid	0–22,498,869	–	✓	x	x
K factor	Grid	0.0135–0.0228	t ha h/ha MJ mm	x	x	✓
Soil type	Grid	Eight classes	–	✓	✓	x
HSG	Grid	6 groupes	–	✓	x	x
Distance to faults	Polyline	0–48,835.9	m	x	✓	x
Profile curvature	Grid	(− 15.72) to 16.11	–	✓	✓	x
Distance to roads	Polyline	0–12,322.7	M	x	✓	x
Plan curvature	Grid	(− 12.27) to 10.17	–	✓	x	x

✓—factor used, x—factor not used, □—eliminated after multicollinearity analysis

profile curvature (Fig. 3t), curvature (Fig. 3v), valley depth (Fig. 3w), TPI (Fig. 3x) and plan curvature (Fig. 3y). At a resolution of thirty (30 m) meters, the topographic variables were extracted using the digital elevation model (DEM).

Each layer shown in Fig. 3 was standardized to a pixel resolution of 30 m*30 m using software GIS in the WGS 84/UTM zone 29N projection system. Many factor sets were employed to generate the maps of hazard sensitivity, as indicated in Table 1: following the removal of two components, there are 13 factors for floods, 17 for gully erosion, and 14 for landslides.

$$TWI = \ln (As/\tan\beta) \tag{1}$$

- As: drainage area of the upstream,
- B: slope degree (Nellemann and Reynolds 1997).

$$TRI = Y \left[\sum (X_{ij} - X_{00})^2 \right]^{\frac{1}{2}} \tag{2}$$

- x_{ij} : each pixel's height next to (0, 0). roughened areas with steep slopes have positive TRI values, whereas regions with zero gradient have zero TRI values (Jones and Vaughan 2010).

$$NDVI = \frac{B8 - B4}{B8 + B4} \tag{3}$$

- B8 = NIR and B4 = RED.

$$LS = (m + 1) \times [As/22] \times [\sin\beta/0.0896] \tag{4}$$

- As: upstream drainage area.
- β : slope degree.

$$K = f_{csand} * f_{cl-si} * f_{orgc} * f_{hisand} \tag{5}$$

- f_{csand} : portion of soils that have a lot of gritty sand.
- f_{cl-si} : portion of soils with a high percentage of clay to silt.
- f_{orgc} : portion of soils that contain a lot of organic carbon.
- f_{hisand} : portion of very high sand-content soils.

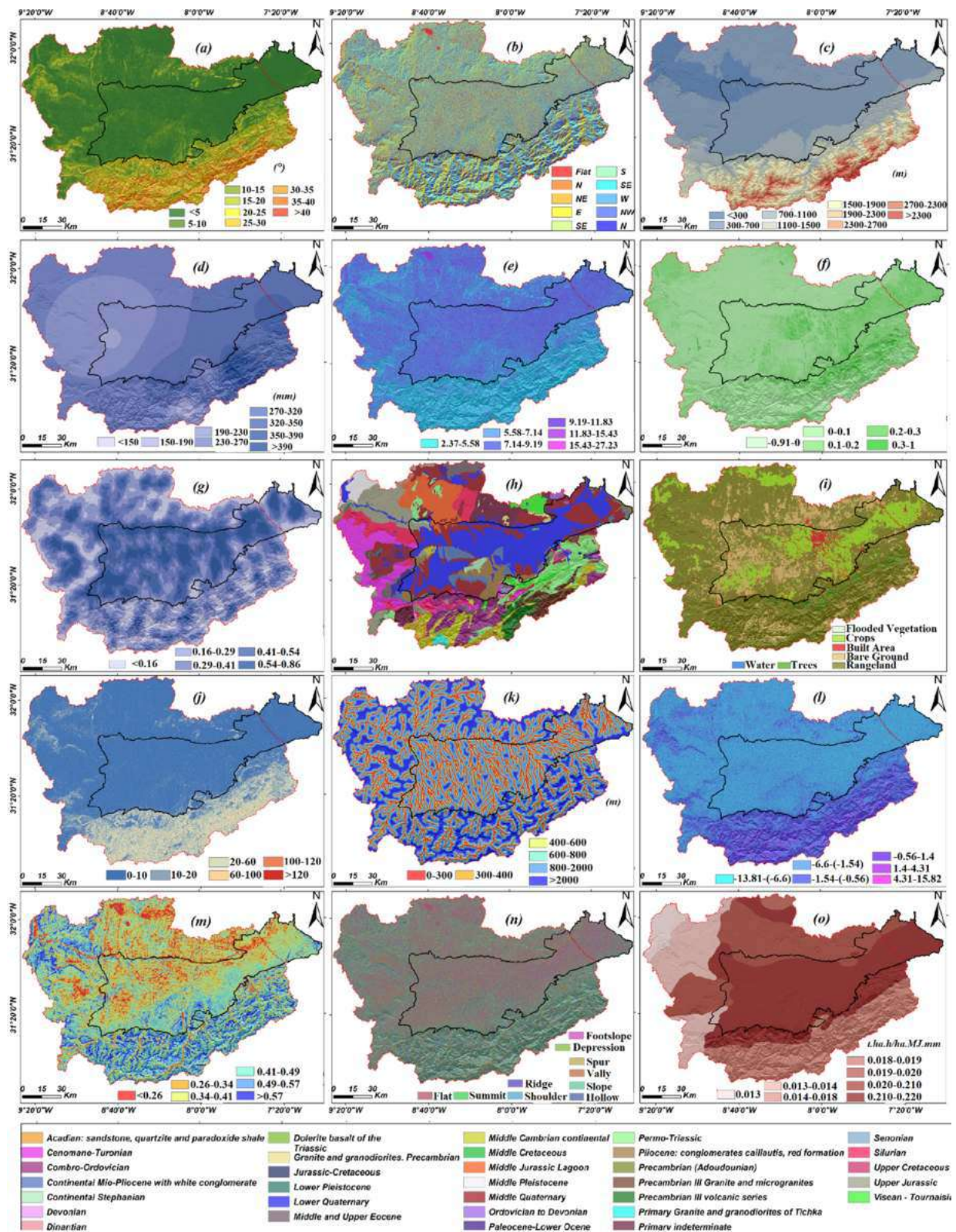


Fig. 3 a Slope in $^{\circ}$, b aspect, c elevation, d rainfall, e TWI, f NDVI, g drainage density, h lithology, i LULC, j LS factor, k distance to rivers, l SPI, m TRI, n geomorphons, o factor K, p HSG, q distance to

roads, r soil type, s flow accumulation, t profile curvature, u distance to faults, v curvature, w valley depth, x TPI and y plan curvature

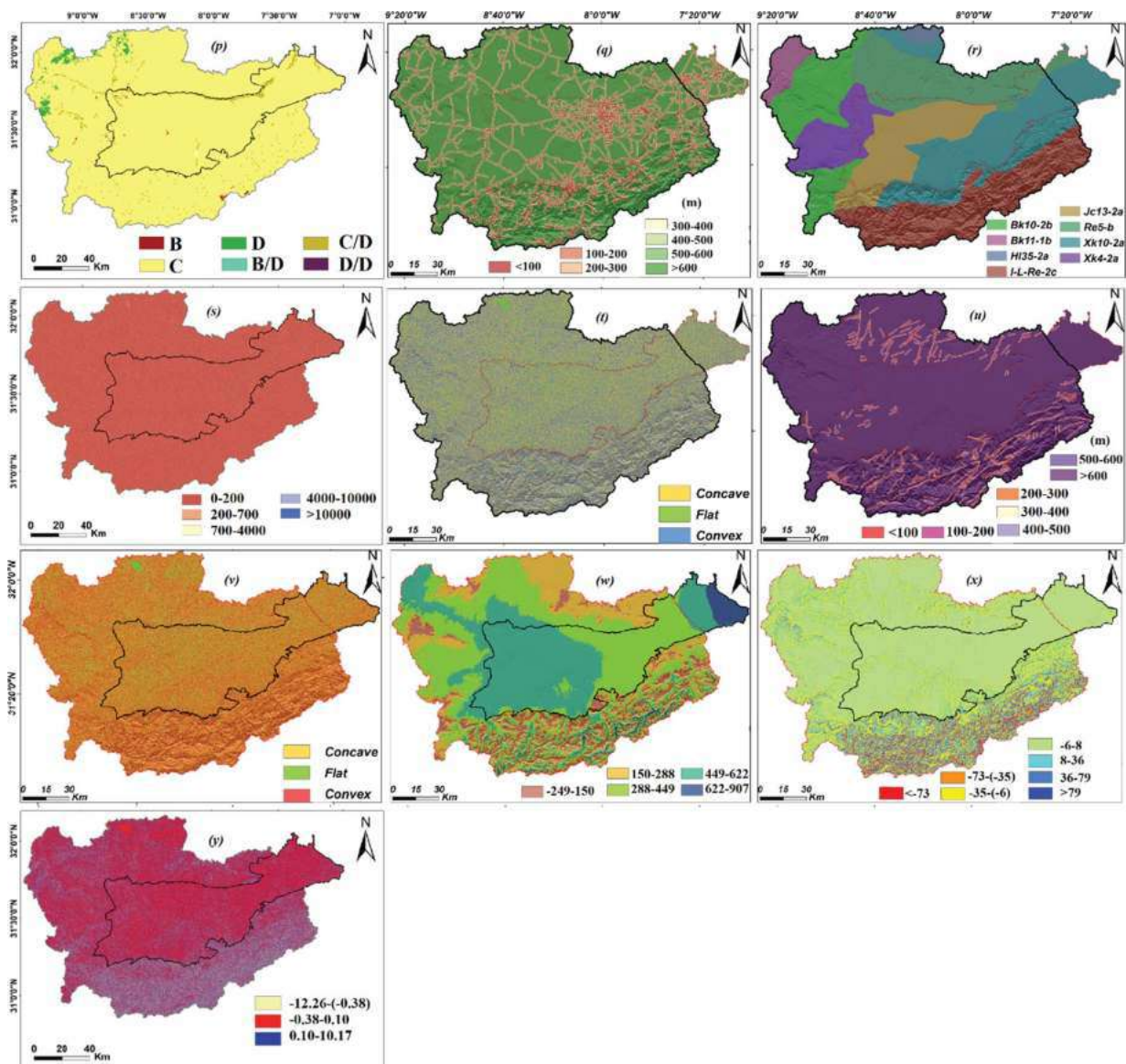


Fig. 3 (continued)

$$SPI = A_s \times \tan\beta$$

- A_s : upstream drainage area.
- β : slope degree.

Selection of multi-hazard factors

The present study used six predictive models to improve ML prediction of susceptibility to floods, landslides, and water erosion. These models were subjected to several statistical tests to identify solid and linear correlations between the various components. These tests, which included variance inflation factor (VIF) calculated using

(6) Eq. (7) and correlation matrix analysis (CM), were used to identify and exclude the non-significant components, tolerance (TOL) calculated using Eq. (8), and mutual information (MI) calculated using Eq. (9). Low MI values indicated a minor effect and led to eliminating the causes producing flooding, landslides, and gully erosion. The MI analysis demonstrated the relevance of these components.

$$VIF_j = \left[\frac{1}{Tol_j} \right] \tag{7}$$

$$Tol = 1 - R_j^2 \tag{8}$$

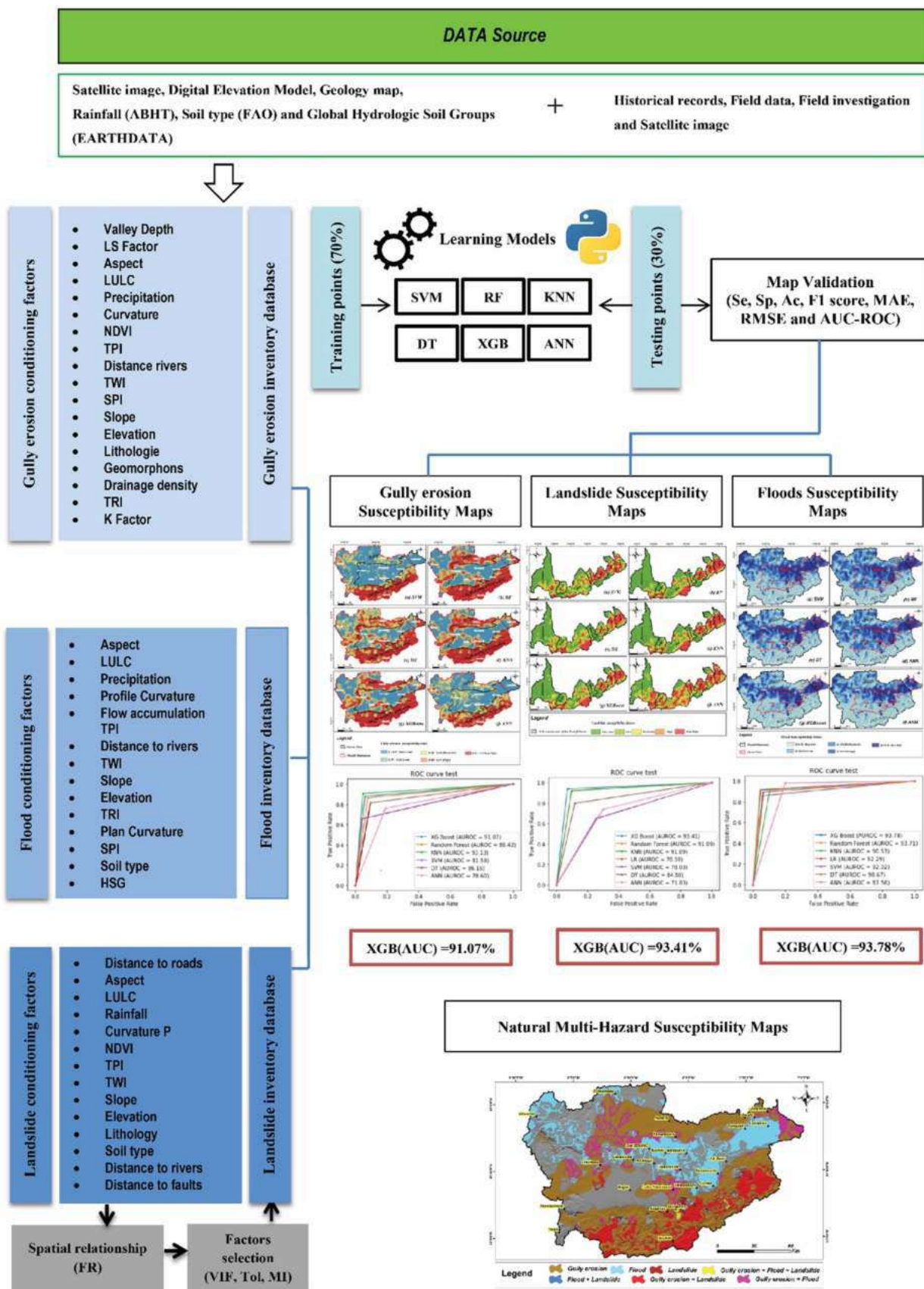


Fig. 4 Flowchart of the methodology developed for this study

$$MI(n, j) = H(n) - H(n/j) \tag{9}$$

- j: affects landslide susceptibility (LS), flood susceptibility (FS), and gully erosion susceptibility (GES).
- n: subclass of LS, FS, and GES impact factors.
- Tol_j: j tolerance.
- VIF_j: j inflation factor.
- MI (n; j): n and j data exchange.
- R: the propensity of j's regression coefficient on all other predisposition components.
- H(n): conditional entropy for n given the landslide, flooded, and eroded zone j. is the entropy of n - H(n/j).

Using Eq. (10), the normalized frequency ratio (NFR) was calculated, the basis for the model's application and the optimal analysis of the factors that affected LS, FS, and GES. This approach is the most widely recommended method for standardizing the significance regarding the variety of data used as input for the different factors (Mao et al. 2021; Youssef et al. 2023). Therefore, to define the link between the factors affecting LS, FS, and GES and the susceptible locations, the frequency ratio (FR) derived from Eq. (11) was allocated to the subclass of factors impacting LS, FS, and GES, as similar to the approach followed by Masoud et al. (2022). Afterwards, Eq. (10) was used to standardize the data. This led to the transformation of each map into an NFR of 1 for high LS, FS, and GES and 0 for low LS, FS, and GES.

$$NFR_n = \frac{FR_n - \text{Max}(FR_n)}{\text{Max}(FR_n) - \text{Min}(FR_n)} * (0.99 - 0.01) + 0.01 \tag{10}$$

$$FR_n = \frac{W_n}{\frac{W_t}{\frac{P_n}{P_t}}} \tag{11}$$

- n: is the category of variables affecting the likelihood of landslides, floods, and gully erosion.
- FR_n: n frequency ratio
- NFR_n: n normalized frequency ratio
- W_n: n is the number of risk sample points.
- W_t: points in the overall risk sample.
- P_n: n number of pixels
- P_t: total amount of all pixels

The determining factors Jenks' natural break approach was utilized to analyze the maps and classify LS, FS, and GES into subclasses (Sarker 2021).

Methodology flowchart

The current study was carried out in five different phases. Phase 1 involved the identification of the three natural hazards dealt with in this study to collect exhaustive data on various events from other sources; Phase 2 involved the differentiation of the different events based on an in-depth analysis of the published literature; Phase 3 dealt with the modelling of the various types of hazard using six ML models; phase 4 involved the validation of the models and the selection of the most appropriate model for each hazard. Finally, in phase 5, a multi-hazard susceptibility map (MHSM) was created by integrating the model with the best AUC for each type of hazard. Figure 4 illustrates the overall methodology of this research.

The methodology employed in this research is robust, multifaceted, and based on several key elements. Firstly, it begins with carefully curating high-quality data to ensure its reliability and relevance to the study objectives. Secondly, rigorous validation techniques are applied to assess the accuracy and integrity of the data collected, thereby enhancing the credibility of subsequent analyses. In addition, the methodology recognizes the importance of carefully selecting and prioritizing conditioning factors and using diverse inventories from reputable sources by integrating multiple data sets of varying spatial and temporal dimensions. Finally, the systematic comparison of different machine learning models is an integral part of the methodology, ensuring a rigorous evaluation is employed to select the best-performing model.

Methods of validation

For the six models developed using different performance measures, such as specificity (Eq. 12), precision (Eq. 15), sensitivity (Eq. 13), F1 score (Eq. 16), and accuracy (Eq. 14), the outcomes of the suggested approach were validated. The performance indices are deemed significant if there is a geographic correlation between the areas that represent the risks of flooding, landslides, and gully erosion and the measured stable regions and the predicted risk areas of indicated risks (Costache 2019; Costache and Tien Bui 2020).

$$\text{Specificity} = \frac{TN}{FP + TN} \tag{12}$$

$$\text{Sensitivity} = \frac{TP}{FN + TP} \tag{13}$$

$$\text{Accuracy} = \frac{TN + TP}{FP + TP + FN + TN} \tag{14}$$

$$\text{Precision} = \frac{\text{TP}}{\text{FP} + \text{TP}} \quad (15)$$

$$\text{F1 score} = \frac{2}{\frac{1}{\text{Pr}} + \frac{1}{\text{Recal}}} \quad \text{Recall} = \frac{\text{TP}}{\text{TP} + \text{FN}} \quad (16)$$

While TP (true positives), TN (true negatives), FP (false positives), and FN (false negatives).

The investigation also used the ROC (receiver operating characteristic) curve, another widely utilized metric. The most popular ROC curve calculates the prediction models' accuracy (AUC) by analyzing the area under the curve (Eq. 17). Additionally, mean absolute error (MAE) (Eq. 19) and root mean square error (RMSE) (Eq. 18) were used to map the vulnerability to landslides, floods, and gully erosion. Numerous scholarly research have made use of both of these types of indexes.

$$\text{AUC} = \frac{(\sum \text{TP} + \sum \text{TN})}{(\text{P} + \text{N})} \quad (17)$$

where TP stands for the real positive, TN for the actual negative, and P and N, respectively, are the total numbers of pixels with and without torrential events.

$$\text{RMSE} = \sqrt{\frac{1}{n} \sum_{i=1}^n (X_{\text{predicted}} - X_{\text{actual}})^2} \quad (18)$$

$$\text{MAE} = \sqrt{\frac{1}{n} \sum_{i=1}^n |X_{\text{predicted}} - X_{\text{actual}}|} \quad (19)$$

n: is the total number of samples in the learning or testing phase, $X_{\text{predicted}}$: the projected value from the susceptibility models (landslides, floods, and gully erosion), X_{actual} : the observed value.

Results

Factor selection and multicollinearity

The Pearson correlation analysis between fifteen influencing factors (LULC, soil type, topographic wetness index, precipitation, elevation, slope, river accumulation, TPI, SPI, elevation, plan curvature, HSG, and aspect) and flood risk is shown in Fig. 5A. In contrast, Fig. 5B illustrates the Pearson analysis between eighteen influencing variables (drainage density, aspect, LS-factor, lithology, drainage density, K-factor, TPI, TWI, precipitation, distance to rivers, curvature, elevation, slope, NDVI, LULC, and TRI) for gully erosion risk. The following factors were considered for the

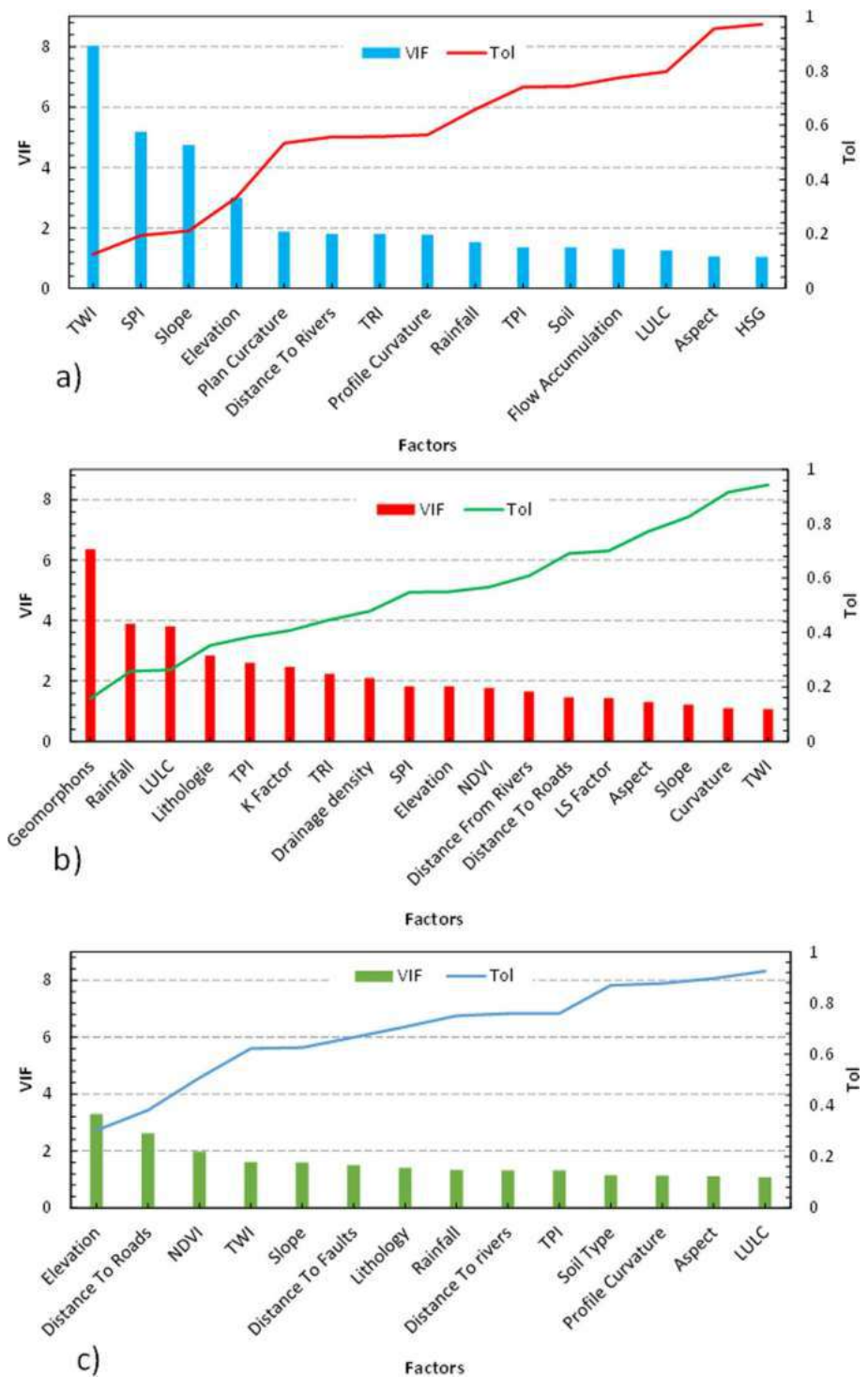
landslide risk shown in Fig. 5C: soil type, proximity to rivers, topographic position index (TPI), topographic wetness index (TWI), and linkage to faults.

To ensure the complexity of the input variables investigated in this study, the findings of the tolerance and inflation coefficients of variance (VIF) indicate a Tol value between 0.12 and 0.97 for HSG and TWI, respectively, and between 1.02 and 8.02 for TWI and 8.02 for HSG at the lowest VIF value as illustrated by Fig. 5A. Among the fifteen indicators taken into consideration in this study, The Tol and VIF criteria led to the exclusion of TWI and SPI from additional inquiry. Subsequently, the MI of the remaining thirteen elements (distance to the river) to 0.013 (HSG) is computed and produces positive results as described by Fig. 6A. Thus, the most significant aspect is the distance to the river, which is followed by slope (MI=0.159), height (MI=0.245), and backwater (MI=0.183).

Figure 6 showed that the LS factor and slope for the gully erosion risk had the most substantial positive correlation (0.69). Elevation and slope, drainage density and gully depth, TWI and gramophone, SPI and gramophone, SPI and LS factor, precipitation, elevation, slope, and TRI all showed significant linear connections. Figure 5B illustrates the results of the tolerance and variance information factors (VIF) used in this study to test the overlap of the forage influencing factors. For Geomorphone and TWI, respectively, the Tol value falls between 0.15 and 0.94, and the maximum VIF value for Geomorphones is 6.35, while the minimum value for TWI is 1.05. The gramophone component was removed from the 18 variables utilized in this analysis because of Tol and VIF constraints. The MI of the parameters displayed in Fig. 6B is then calculated, and the findings show positive values in the range of 0.261 (slope) to 0.029 (aspect). As a result, slope is the most significant factor, followed by lithology (MI=0.213), TPI (MI=0.226), and LS (MI=0.227).

A significant linear relationship was found between the following variables: NDVI and precipitation, elevation and slope, lithology and elevation, slope and lithology, and slope and lithology and the distance between roads and rivers. The results for landslide risk indicate that the highest positive correlation value (0.63) was a correlation between road mileage and height. The findings of the tolerance and variance information factors (VIF), which were utilized in this study to examine the multicollinearity of the forage-affecting variables, show that the LULC values and elevation range from 0.30 to 0.92 in terms of Tol and that the values of LULC and elevation range from 1.08 to 3.30 on the maximum VIF value (Fig. 5C). The MI of the remaining 14 components (Fig. 7B) indicates positive values between 0.132 (inclination) to 0.021 (LULC). Thus, the slope is the most significant component, followed by the following: height (MI=0.120),

Fig. 5 The conditioning factors for **A** flood, **B** gully erosion, and **C** landslide were studied using the variance inflation factor (VIF) and tolerance (TOL) multicollinearity



lithology (MI=0.118), road distance (MI=0.095), and fault distance (MI=0.091).

Six machine learning models were applied to generate sensitivity maps for floods (Fig. 8A), gully erosion (Fig. 8B), and landslides (Fig. 8C) based on risk predictions using independent variables and the actual risk

condition using dependent variables. Based on the Jenks classifier for natural breaks (Jenks and Caspall 1971). Five classifications were applied to each sensitivity map: very low, low, moderate, high, and very high. Maps showing the flood sensitivity of the Tensift watershed and the Haouz plain were created using the SVM, RF, KNN, DT,

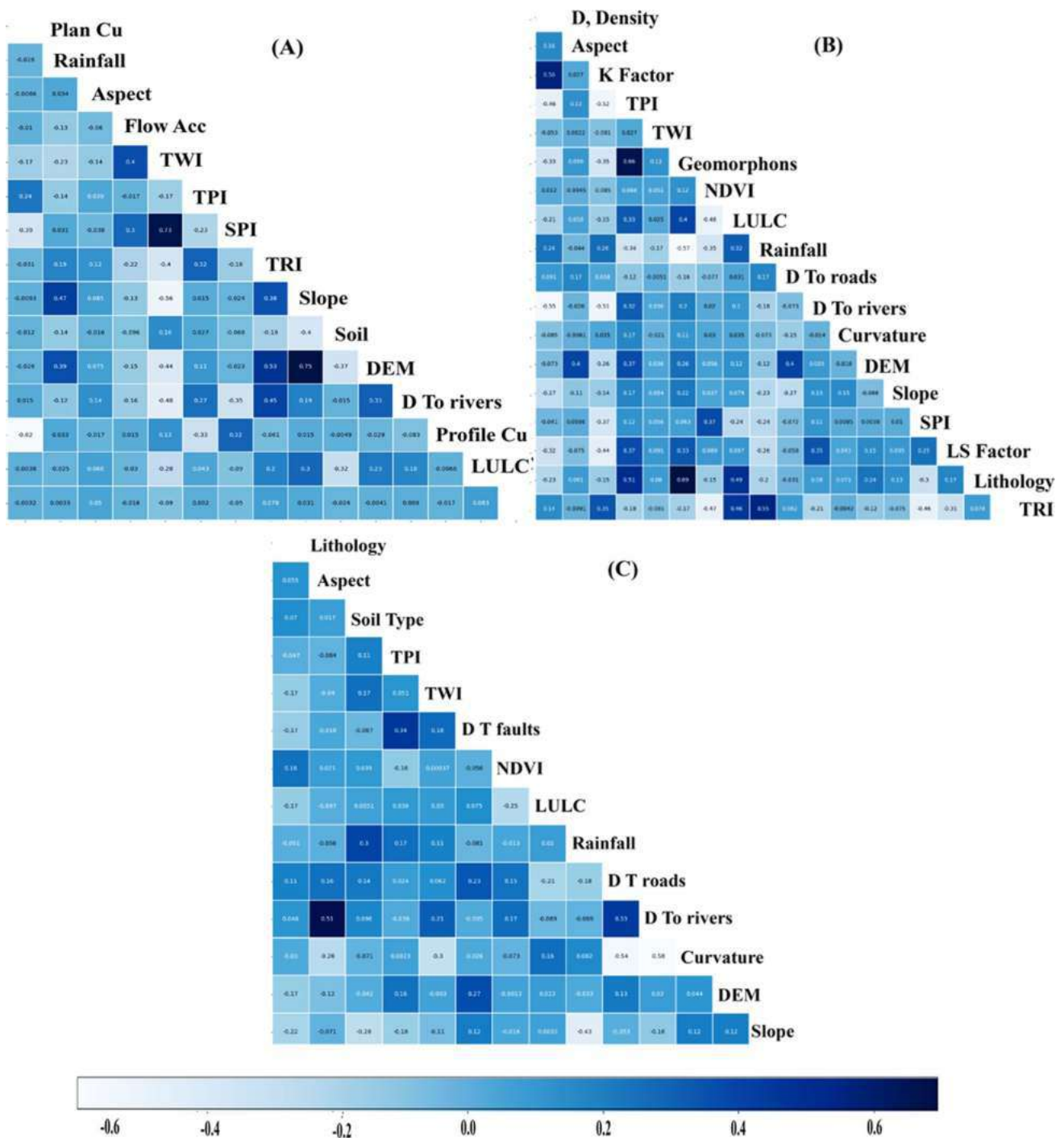


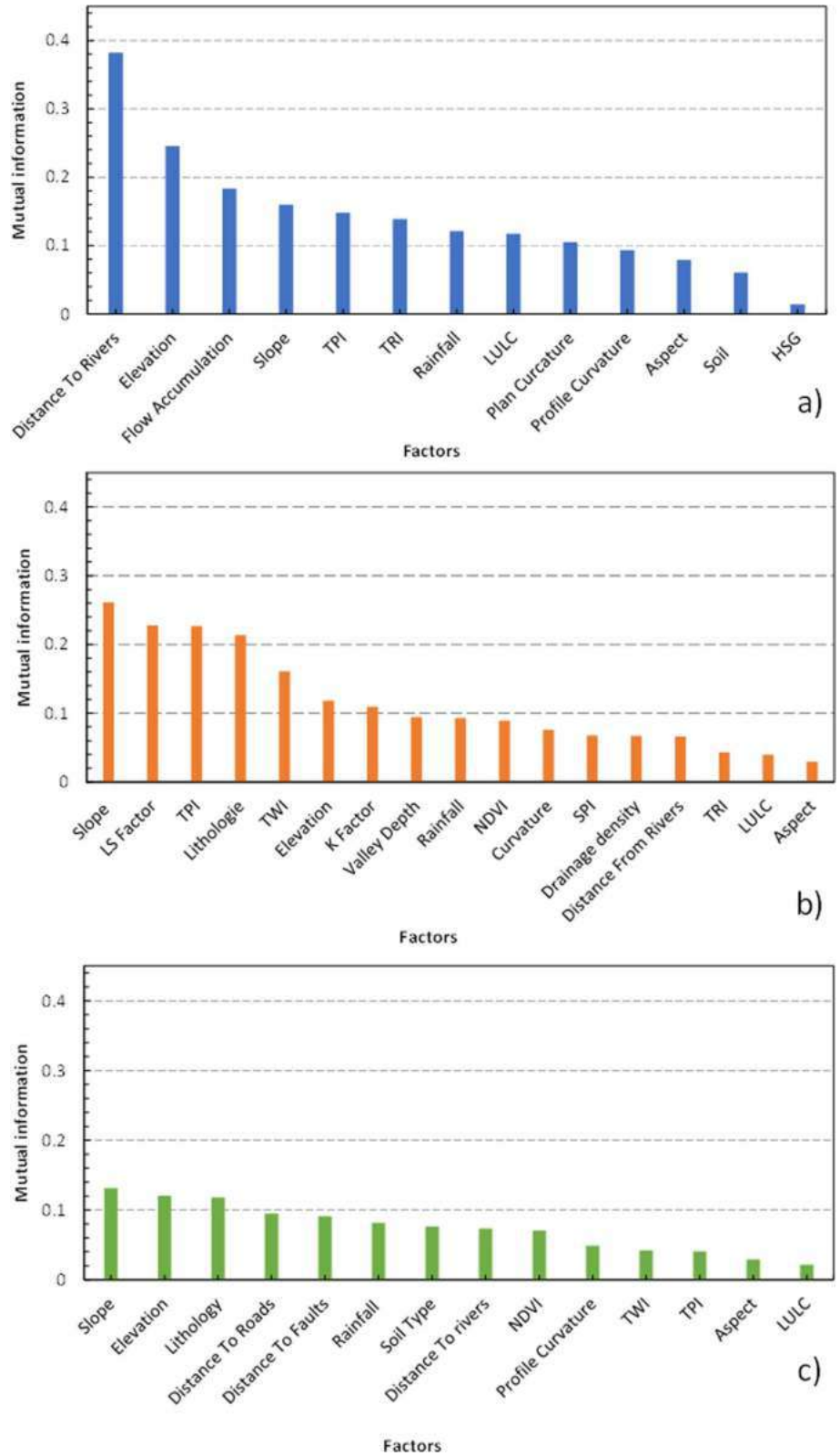
Fig. 6 Analysis of conditioning components' multicollinearity using the correlation matrix for **A** flood, **B** gully erosion, and **C** landslide

ANN, and XGBoost models (Fig. 8A(a–g)). Furthermore, gully erosion sensitivity maps were created for the same watershed using the same models (Fig. 8B(a–g)). Finally, landslide sensitivity maps were produced using the same models (Fig. 8C(a–g)).

Validation of models

The AUC curves for the six machine learning models that were utilized to develop the models for landslides, floods, and gully erosion are shown in Fig. 9. The results show that the AUCs for the different flood vulnerability models range from 90.69 to 96.21% in the training phase and from

Fig. 7 The importance of selected hazard predictive factors for **A** flood, **B** gully erosion, and **C** landslide



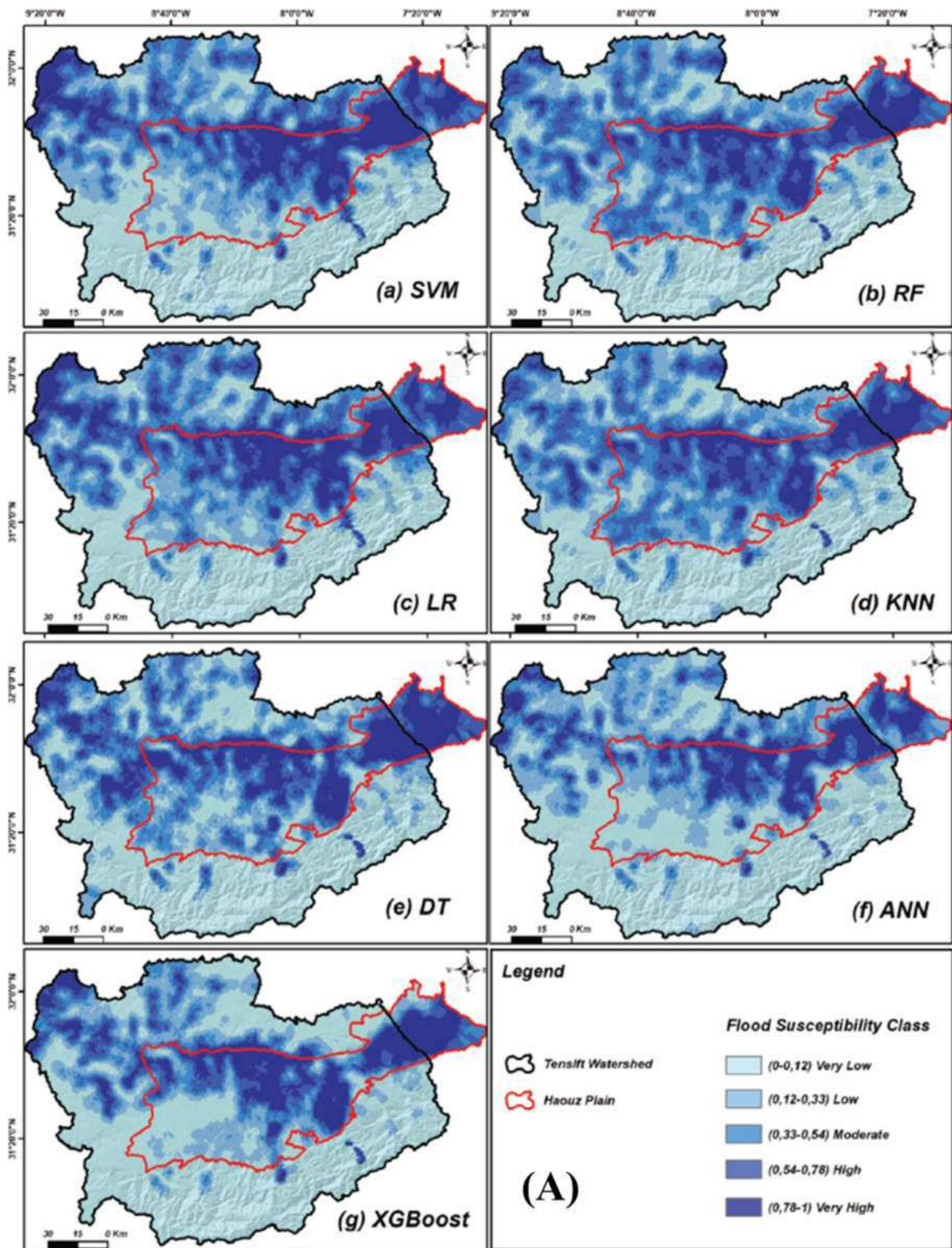


Fig. 8 Susceptibility maps for **A** flooding, **B** gully erosion, and **C** landslide, predicted by the (a) SVM, (b) RF, (e) DT, (d) KNN, (g) XGBoost, and (f) ANN models

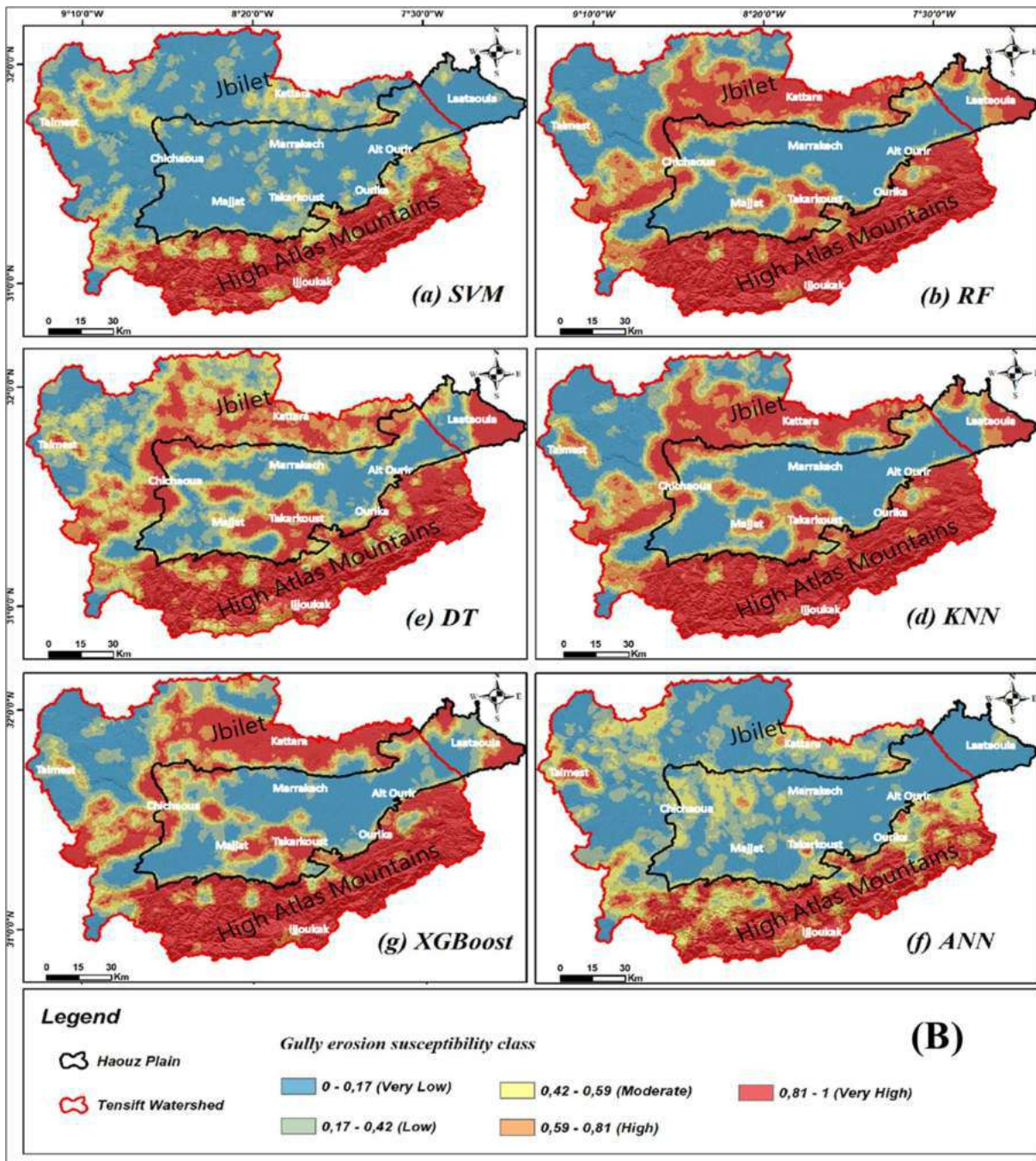


Fig. 8 (continued)

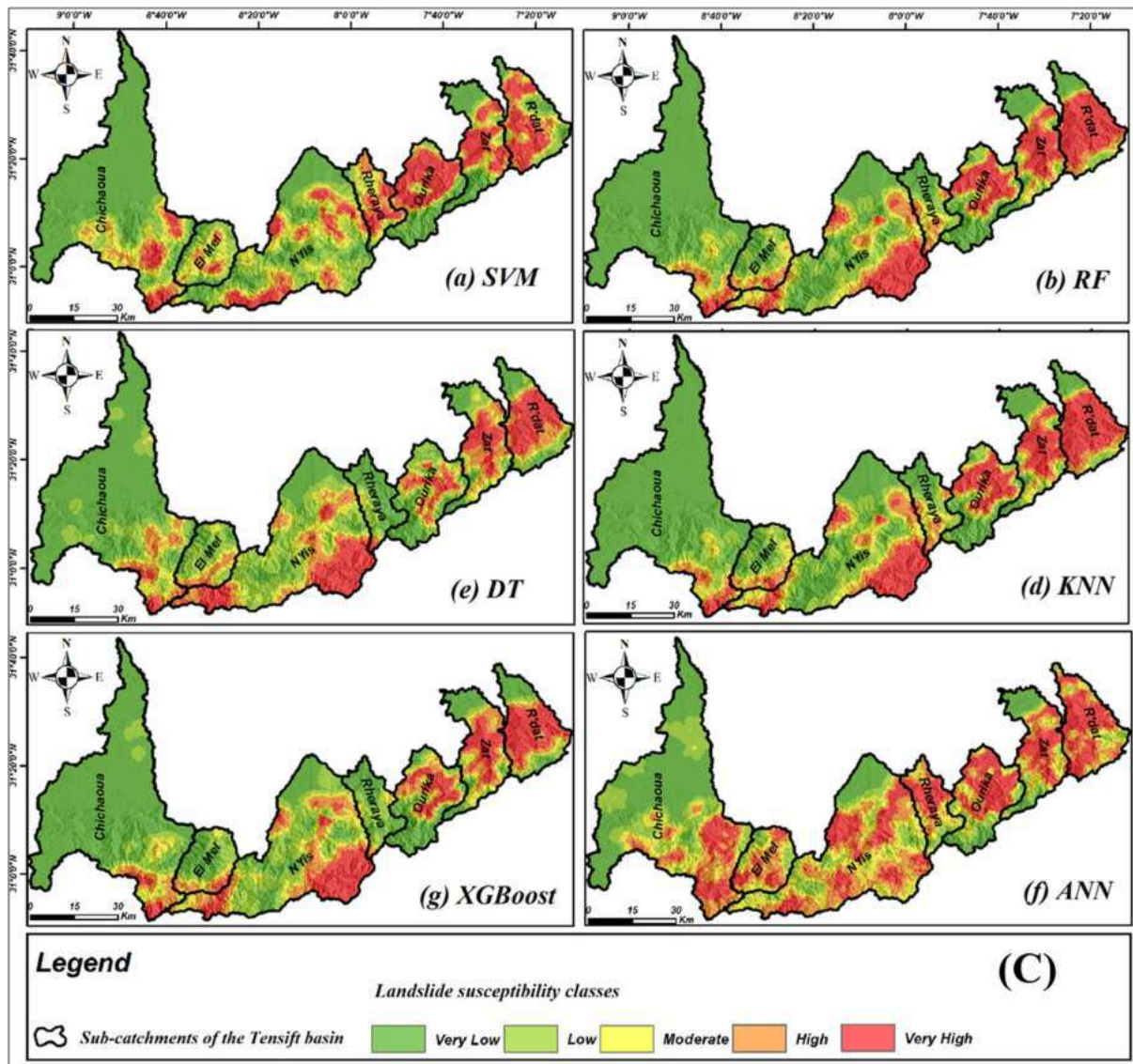


Fig. 8 (continued)

87.56 to 93.78% in the testing phase, corresponding to high to extremely high performance. The XGBoost, RF, KNN, DT, ANN, and SVM models achieved AUCs of (96.21%), (94.32%), (94.32%), (93.38%), (91.01%) and (90.01%) in the training phase and AUCs of (93.78%), (93.71%), (90.53%), (90.67%), (87.56%) and (92.02%) in the test phase (Fig. 9A), for gully erosion the results show an AUC that varies from 96.71 to 72.84% in the training phase and from 91.07 to 78.60% in the test phase, for landslides, the results show an AUC that varies from 94.57 to 70.03% in the training phase and from 93.41 to 70.03% in the test phase.

The effectiveness of the chosen XGBoost FS, GES, and LS prediction models throughout the training and validation stages is displayed in Tables 4 and 5. Along with the effectiveness of the training data used (30%) and test data used

(70%), the following metrics are evaluated by adhering to the approaches of (Bammou et al. 2024d): Pr (precision), Se (sensitivity), Sp (specificity), Ac (accuracy), F1 score, FPR (false positive rate), MAE (mean absolute error), RMSE (root mean square error), and AUC-ROC (area under the receiver operating characteristic curve).

The XGBoost model performed exceptionally well for all training data, as evidenced by the following values: (Pr = 0.95), (Se = 0.97), (Sp = 0.95), (Ac = 0.97), (Recall = 0.96), (F1 score = 0.95), (MAE = 0.04), and RMSE (values = 0.19) for the risk of flooding; (Pr = 0.99), (Se = 0.94), (Sp = 0.99), (Ac = 0.96), (Recall = 0.95), (F1 score = 0.97), (FPR = 0.009), (MAE = 0.03) and RMSE (values = 0.12) for the risk of gully erosion; and

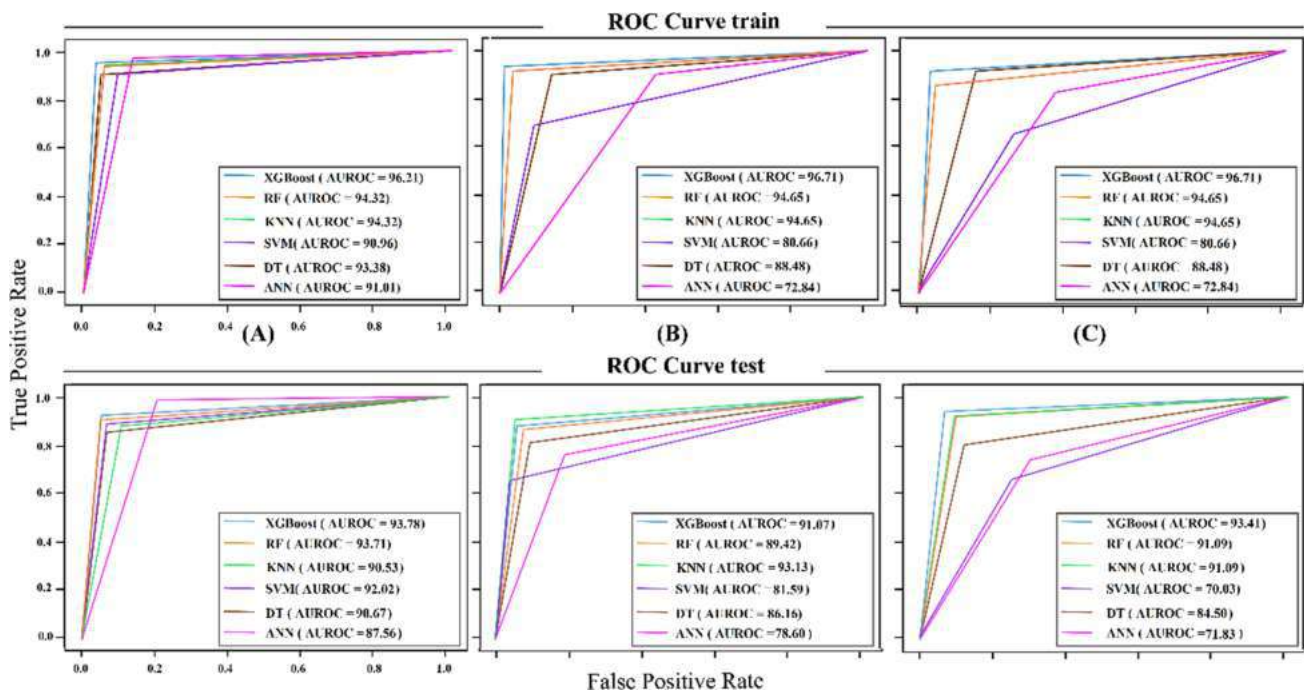


Fig. 9 ROC curve analysis of different models of A flooding, B gully erosion, and C landslide for training and validation data

Table 3 Performance of best XGBoost model based on training data

Performance indicators	XGBoost model			
	Flood	Gully erosion	Landslide	
Precision	0.95	0.99	0.97	Training data
Sensitivity	0.97	0.94	0.98	
Specificity	0.95	0.99	0.96	
False positive rate (FPR)	0.05	0.0094	0.0344	
Accuracy	0.97	0.96	0.97	
Recall	0.96	0.95	0.98	
F1 score	0.95	0.97	0.98	
MAE	0.04	0.0371	0.0542	
RMSE	0.1900	0.1924	0.2329	
AUC (%)	96.21	96.71	94.57	

Table 4 Performance of best XGBoost model based on testing data

Performance indicators	XGBoost model			
	Flood	Gully erosion	Landslide	
Precision	0.93	0.94	0.93	Testing data
Sensitivity	0.94	0.90	0.95	
Specificity	0.93	0.93	0.92	
False positive rate (FPR)	0.0700	0.0706	0.0854	
Accuracy	0.94	0.91	0.93	
Recall	0.92	0.90	0.95	
F1 score	0.92	0.92	0.94	
MAE	0.0600	0.0329	0.0658	
RMSE	0.2500	0.1814	0.2566	
AUC	93.78	91.07	93.41	

lastly, (Pr = 0.97), (Se = 0.98), (Sp = 0.96), (Ac = 0.97), (Recall = 0.98), (F1 score = 0.98), (FPR = 0.03), (MAE = 0.05) and RMSE (values = 0.23) for the risk of landslides, as shown by Tables 3 and 4.

For all test data, the XGBoost model performed excellently, as confirmed by the values (Pr = 0.93), (Se = 0.94), (Sp = 0.93), (Ac = 0.94), (Recall = 0.92), (F1 score = 0.92), (FPR = 0.07), (MAE = 0.06) and RMSE (values = 0.25) for the flood risk, the values (Pr = 0.94), (Se = 0.90), (Sp = 0.93), (Ac = 0.91), (Recall = 0.90), (F1 score = 0.92), (FPR = 0.07), (MAE = 0.03) and RMSE (values = 0.118) for gully erosion risk and lastly the values (Pr = 0.93), (Se = 0.95), (Sp = 0.92),

(Ac = 0.93), (Recall = 0.95), (F1 score = 0.94), (FPR = 0.08), (MAE = 0.06) and RMSE (values = 0.25) for the risk of landslides as described by Table 5.

Multi-hazard maps

The multi-hazard map was produced by constructing and evaluating three separate hazard susceptibility maps, each correlated with a distinct hazard (FL, GES, and LS). Using the XGBoost model, this development was based on the link between independent factors, i.e., hazard indicators, and dependent variables, i.e., locations at risk of flooding,

gully erosion, and landslides. The three vulnerability maps (flooding, gully erosion, and landslides) were then integrated into Software GIS to create the comprehensive multi-hazard risk map shown in Fig. 10.

As illustrated by Fig. 11, the results indicate that the research region is separated into seven vulnerability groups. The region is exposed to various risks to the extent of around 71.03%, with the percentage breakdown as follows: 36.05% of the total area is made up of gully erosion (GES), 16.92% of floods (FS), 10.59% of landslides and gully erosion (GES-LS), 6.54% of floods and gully erosion (FS-GES), 0.56% of landslides (LS), 0.33% of floods and landslides (FS-LS), and 0.31% of floods, gully erosion, and landslides (FL-GES-LS).

Discussion

A range of modelling techniques can significantly enhance the understanding of risk management. In a semi-arid area prone to many hazards such as flooding, gully erosion, landslides, and, more recently, earthquakes, such as the catastrophic earthquake of September 8, 2023, in the research region, there has been an acceleration in the establishment of landslide hazard zones.

This study investigated three natural hazards in the Tensift watershed, a region in the Moroccan High Atlas with mountain and lowland characteristics. The aim was to perform multi-hazard modelling to understand the relationships

and to assess the susceptibility to landslides, gully erosions and flood risks in the study area. To this end, six ML models were used to study flooding, gully erosion, and landslides: DT, RF, SVM, KNN, ANN, and XGBoost. The analysis of (CM), (TOL), (VIF), and (MI) led to the conclusion that the selected factors can influence flooding, gully erosion, and landslides in the Tensift catchment. To evaluate the models' success, training datasets, validation, and evaluation metrics were employed to assess the ML models' performance. Accuracy, precision, recall, F1 score, mean absolute error (MAE), root mean square error (RMSE), and area under the receiver characteristic curve (AUC-ROC) are examples of standard measurements. The XGBoost model for the three hazards showed an average accuracy of (AUC = 95.83%) and (AUC = 92.75%) in the training and test phases, respectively.

The spatial prediction of FS is dependent on several affecting variables. Due to their collinearity with other factors, which reduced the prediction's efficacy, TWI and SPI were eliminated from this study's original set of fifteen components. Additionally, MI claims that the most crucial element is the distance to the river. According to the spatial prediction results of (Al-Areeq et al. 2022; Meliho et al. 2022) regarding FS, the most critical areas at a given distance from the river were considered very vulnerable to high-density floods. Since the Haouz Plain is located at low elevations, the findings of the present study are being validated by the previous scientific literature, notably (Melihio et al. 2022), which shows that high susceptibility

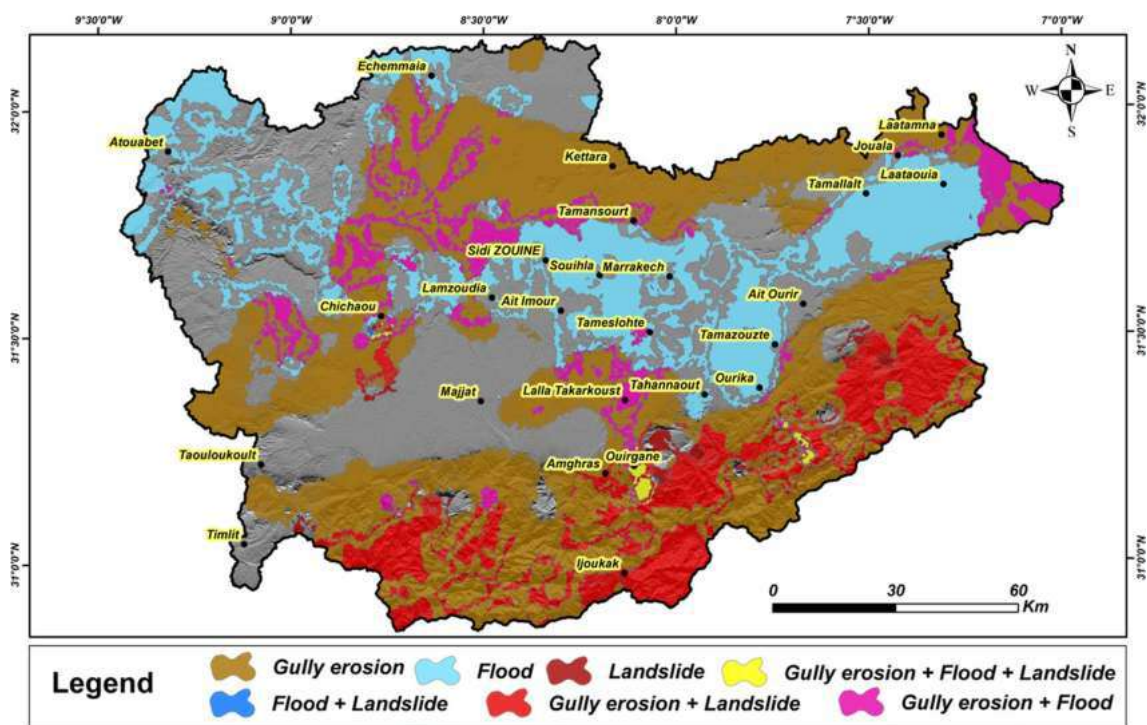
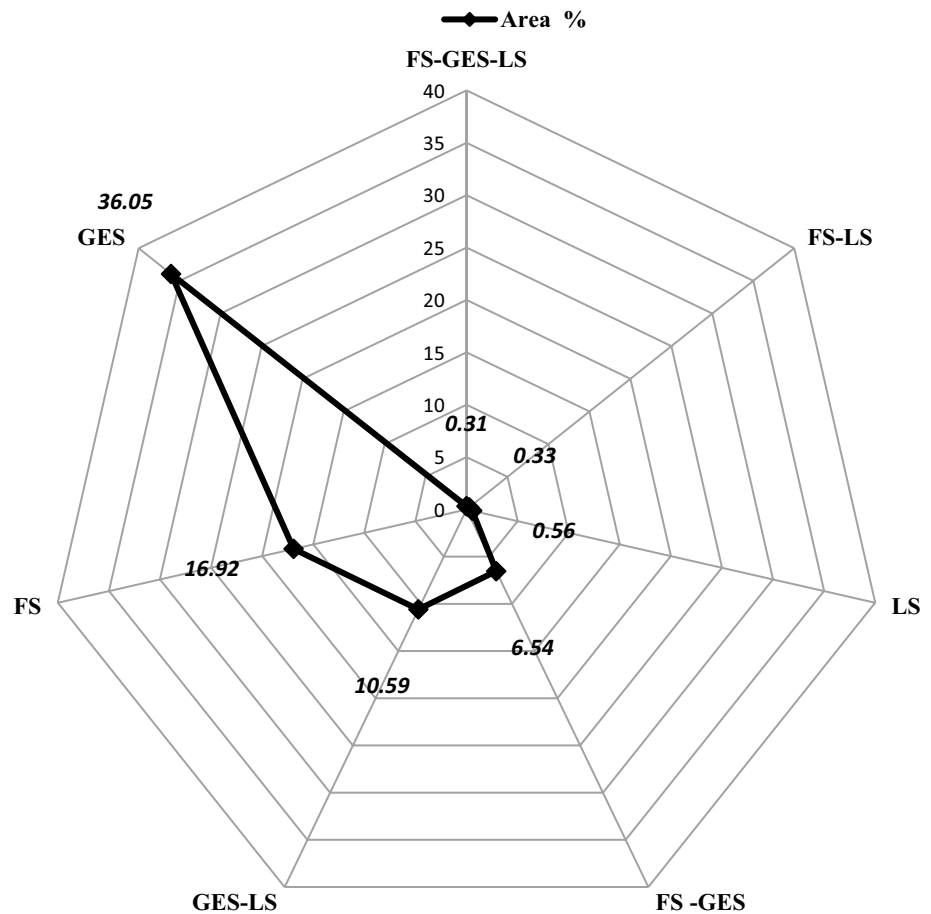


Fig. 10 A multi-hazard risk map was developed using the most potent XGBoost model

Fig. 11 Percentages of various hazard types in the research region



is connected with elevation, slope, TPI, and TRI in Tensift rivers and sub-catchments, especially the Ourika, Zat, and Rheraya sub-catchments.

The key variables influencing gully erosion in the research region for the spatial prediction of GES indicate that geological factors, represented by lithology and topographic factors, such as slope, LS factor, and TPI, are more significant than other variables. This fact is primarily in line with the findings of (Baiddah et al. 2023) for lithology and the LS variables in the Chichaoua sub-basin; his work also highlights the importance of additional elements like altitude and proximity to rivers. Selecting a mixed zone, which compares altitude values by combining a lowland, a mountainous zone, and the study zone's broad area, can help to understand this divergence.

The combination of exceptionally highly friable lithologies, such as Tertiary clays and sediments and Neogene phosphate marls, with high altitudes and little vegetation, especially on steep slopes and in areas where the vegetation cover is damaged, favors the occurrence and development of this type of erosion (Arabameri et al. 2020; Bammou et al. 2024c). Lastly, spatial prediction of LS findings demonstrates that the following five factors—slope gradient, height, lithology, proximity to highways,

and proximity to rivers—are critical in determining the likelihood of landslides. Unstable soils migrate along slopes due to the constant action of gravity and the slope gradient and elevation variables. Steeper hills are more likely to cause landslides. In addition to affecting slope stability, excavation activities related to the building or extension of road networks can raise the danger of landslides in locations near highways. Another critical factor in landslides is the proximity to rivers. The stability of slopes next to rivers is threatened by bank and gully erosion, raising the possibility of landslides in these locations.

Compared to the other six models, the XGBoost model is more accurate primarily because it uses all base learners' prediction outcomes, improving its recognition rate and generalization capacity. When determining and preserving the optimal path of action, several techniques will be employed to address missing values that may have occurred on other nodes. XGBoost adds a regular term to the objective function and allows custom loss functions, but it also minimizes the learning model and avoids overfitting, which accelerates learning. Because of this, the XGBoost model ultimately produces improved simulation results, and the XGBoost-based method is practical

and efficient for mapping the susceptibility of landslides, floods, and gully erosion.

The use of the XGBoost algorithm, which has shown excellent predictive capabilities in this study, has many advantages. One notable advantage is its simple implementation, which does not require prior data preprocessing and its built-in mechanisms for handling missing data. In addition, the ensembled algorithm employs bias reduction techniques by sequentially combining multiple weak learners to improve the quality of predictions iteratively (Bashir et al. 2024a, b; Benzougagh et al. 2024; Zounemat-Kermani et al. 2021). This approach effectively mitigates the significant biases that often occur in ML models. In addition, XGBoost prioritizes features in the training phase that contribute to improved prediction accuracy to increase computational efficiency. This feature can be beneficial in reducing data attributes and efficiently managing large data sets.

It is essential to know that the presence of one danger can cause the occurrence of another. For example, knowledge of multiple hazards, their interrelationships, linkages, and cascading effects can increase awareness of their processes and the best methods to prevent and reduce catastrophic losses while supporting good land management (Godschall et al. 2020; Msabi and Makonyo 2021; Ouallali et al. 2024). The resulting maps provide essential information to prepare and monitor existing and future anthropogenic activities.

Conclusion

The research has substantially contributed to the knowledge of how vulnerable Morocco's Northern and High Atlas areas are to different threats. Due to their distinct geography and dense population, these mountainous areas face an intricate web of natural threats. The primary goal was to give decision-makers the necessary information to identify and demarcate high-risk zones. This research yields a thorough multi-hazard vulnerability map incorporating these three main natural risks.

This map divides the research area into six danger zones, accounting for 71.03% of the area. Three zones are linked to specific hazards: the landslide risk zone (0.56%), which is situated in steep, high-altitude Tensift sub-basins; the erosion risk zone (36.05%), which is concentrated along major rivers like the R'dat, Zat, and Ourika; and the flood risk zone (16.92%), which primarily affects the Haouz plains and certain tributaries of the High Atlas.

Additionally, the study showed that there are three zones—the flood and landslide hazard zone (0.33%), the flood and gully erosion hazard zone (6.54%), and the landslide and gully erosion hazard zone (10.59%)—where two types of risks overlap. Surprisingly, the High Atlas has multi-hazard zones, especially in the Ourika and N'fis

catchments, which comprise 0.31% of the study area and are impacted by all three hazards: landslides, gully erosion, and floods.

The XGBoost machine learning model demonstrated exceptional dependability and yielded precise forecasts for several categories of hazards. Our multi-hazard map was the result, and it achieved an impressive average of (AUC = 95.83%) during the training phase and (AUC = 92.75%) during the testing phase. The multi-hazard analysis is essential for sustainable growth in these hilly and flood-prone areas as infrastructure and urban and rural development continue to rise. Based on the multi-hazard risk map, policy recommendations for sustainable land management and hazard mitigation could be proposed in the context of the High Atlas landscape. Developing strategies for increasing public awareness and education about these hazards and the importance of sustainable land management could also contribute to a more comprehensive understanding of multi-hazard assessments and more effective land management and hazard mitigation.

Albeit it is a pioneering study in the field of multi-hazard assessment, this study has a few identified limitations that could be rectified in future research studies. Firstly, the study's geographical focus might limit the results' applicability to other regions with different topographical, geological, and meteorological conditions. Conducting similar studies in the future in various geographical areas could validate the applicability of the models and allow for comparison of the results. The ML models used in this study rely on causal factors derived from reputable and trusted sources. Future studies could incorporate real-time or dynamic data into ML models to study the reflection of changing conditions and enhance prediction accuracy. Lastly, this study does not extensively acknowledge how the changes in anthropogenic activities could impact the three aforementioned hazards. It is highly encouraged to encapsulate in-depth studies on how the changes in anthropogenic activities such as urbanization, deforestation, and land use dynamics could impact landslides, soil erosion and flood risks could get incorporated into ML models.

Author contributions Conceived and designed the studies—Youssef Bammou, Brahim Benzougagh, Brahim Igmoullan, Shuraik Kader, and Velibor Spalevic. Performed the analysis—Youssef Bammou, Brahim Benzougagh, Brahim Igmoullan, Abdessalam Ouallali, Shuraik Kader, Velibor Spalevic, Paul Sestras, and Alban Kuriqi. Analyzed and interpreted the data—Youssef Bammou, Brahim Benzougagh, Brahim Igmoullan, Abdessalam Ouallali, Shuraik Kader, Velibor Spalevic, Paul Sestras, and Alban Kuriqi. Contributed materials, analysis tools, or data—Youssef Bammou, Brahim Benzougagh, Brahim Igmoullan, Abdessalam Ouallali, Shuraik Kader, and Velibor Spalevic. Authored the paper—Youssef Bammou, Brahim Benzougagh, Brahim Igmoullan, Abdessalam Ouallali, Shuraik Kader, Velibor Spalevic, Paul Sestras, and Alban Kuriqi. Internal reviewers – Brahim Benzougagh, Shuraik Kader, Velibor Spalevic, Paul Sestras, and Alban Kuriqi. Project

administration – Brahim Benzougagh, Velibor Spalevic, and Alban Kuriqi. All authors have read and agreed to the published version of the manuscript.

Funding Open Access funding enabled and organized by CAUL and its Member Institutions No funding was received for this research project.

Availability of data and materials All data used in this research were described within the manuscript.

Declarations

Conflict of interest The authors have no relevant financial or non-financial interests to disclose.

Ethical approval Not applicable.

Consent to participate Not applicable.

Consent to publish Not applicable.

Open Access This article is licensed under a Creative Commons Attribution 4.0 International License, which permits use, sharing, adaptation, distribution and reproduction in any medium or format, as long as you give appropriate credit to the original author(s) and the source, provide a link to the Creative Commons licence, and indicate if changes were made. The images or other third party material in this article are included in the article's Creative Commons licence, unless indicated otherwise in a credit line to the material. If material is not included in the article's Creative Commons licence and your intended use is not permitted by statutory regulation or exceeds the permitted use, you will need to obtain permission directly from the copyright holder. To view a copy of this licence, visit <http://creativecommons.org/licenses/by/4.0/>.

References

- Aksha SK, Resler LM, Juran L, Carstensen LW Jr (2020) A geospatial analysis of multi-hazard risk in Dharan, Nepal. *Geomat Nat Hazards Risk* 11(1):88–111. <https://doi.org/10.1080/19475705.2019.1710580>
- Al-Areeq AM, Abba S, Yassin MA, Benaafi M, Ghaleb M, Aljundi IH (2022) Computational machine learning approach for flood susceptibility assessment integrated with remote sensing and GIS techniques from Jeddah, Saudi Arabia. *Remote Sens* 14(21):5515. <https://doi.org/10.3390/rs14215515>
- Arabameri A, Saha S, Roy J, Chen W, Blaschke T, Tien Bui D (2020) Landslide susceptibility evaluation and management using different machine learning methods in the Gallicash River Watershed, Iran. *Remote Sens* 12(3):475. <https://doi.org/10.3390/rs12030475>
- Baiddah A, Krimissa S, Hajji S, Ismaili M, Abdelrahman K, El Bouze-kraoui M et al (2023) Head-cut gully erosion susceptibility mapping in semi-arid region using machine learning methods: insight from the High Atlas, Morocco. *Front Earth Sci* 11:1184038. <https://doi.org/10.3389/feart.2023.1184038>
- Bammou Y, Benzougagh B, Bensaid A, Igmoullan B, Al-Quraishi AMF (2023) Mapping of current and future soil erosion risk in a semi-arid context (haouz plain-Marrakech) based on CMIP6 climate models, the analytical hierarchy process (AHP) and RUSLE. *Model Earth Syst Environ*. <https://doi.org/10.1007/s40808-023-01845-9>
- Bammou Y, Benzougagh B, Abdessalam O, Brahim I, Kader S, Spalevic V et al (2024a) Machine learning models for gully erosion susceptibility assessment in the Tensift catchment, Haouz Plain, Morocco for sustainable development. *J Afr Earth Sci* 213:105229. <https://doi.org/10.1016/j.jafrearsci.2024.105229>
- Bammou Y, Benzougagh B, Bensaid A, Igmoullan B, Al-Quraishi AMF (2024b) Mapping of current and future soil erosion risk in a semi-arid context (haouz plain-Marrakech) based on CMIP6 climate models, the analytical hierarchy process (AHP) and RUSLE. *Model Earth Syst Environ* 10(1):1501–1514. <https://doi.org/10.1007/s40808-023-01845-9>
- Bammou Y, Benzougagh B, Igmoullan B, Al-Quraishi AMF, Ghaib FA, Kader S (2024c) Assessing soil erosion vulnerability in semi-arid Haouz Plain, Marrakech, Morocco: land cover, socio-spatial mutations, and climatic variations. In: Al-Quraishi AMF, Mustafa YT (eds) *Natural resources deterioration in MENA Region: land degradation, soil erosion, and desertification*. Springer International Publishing, Cham, pp 113–133. https://doi.org/10.1007/978-3-031-58315-5_7
- Bammou Y, Benzougagh B, Igmoullan B, Ouallali A, Kader S, Spalevic V et al (2024d) Optimizing flood susceptibility assessment in semi-arid regions using ensemble algorithms: a case study of Moroccan High Atlas. *Nat Hazards*. <https://doi.org/10.1007/s11069-024-06550-z>
- Bashir O, Bangroo SA, Shafai SS, Senesi N, Kader S, Alamri S (2024a) Geostatistical modeling approach for studying total soil nitrogen and phosphorus under various land uses of North-Western Himalayas. *Eco Inform* 80:102520. <https://doi.org/10.1016/j.ecoinf.2024.102520>
- Bashir O, Bangroo SA, Shafai SS, Senesi N, Naikoo NB, Kader S, Jauffer L (2024b) Unlocking the potential of soil potassium: geostatistical approaches for understanding spatial variations in Northwestern Himalayas. *Eco Inform* 81:102592. <https://doi.org/10.1016/j.ecoinf.2024.102592>
- Benzougagh B, Al-Quraishi AMF, Bammou Y, Kader S, El Brahim M, Sadkaoui D, Ladel L (2024) Spectral Angle Mapper Approach (SAM) for land degradation mapping: a case study of the Oued Lahdar Watershed in the Pre-Rif Region (Morocco). In: Al-Quraishi AMF, Mustafa YT (eds) *Natural Resources deterioration in MENA Region: land degradation, soil erosion, and desertification*. Springer International Publishing, Cham, pp 15–35. https://doi.org/10.1007/978-3-031-58315-5_2
- Bout B, Lombardo L, van Westen CJ, Jetten VG (2018) Integration of two-phase solid fluid equations in a catchment model for flash-floods, debris flows and shallow slope failures. *Environ Model Softw* 105:1–16. <https://doi.org/10.1016/j.envsoft.2018.03.017>
- Costache R (2019) Flash-Flood Potential assessment in the upper and middle sector of Prahova river catchment (Romania). A comparative approach between four hybrid models. *Sci Total Environ* 659:1115–1134. <https://doi.org/10.1016/j.scitotenv.2018.12.397>
- Costache R, Tien Bui D (2020) Identification of areas prone to flash-flood phenomena using multiple-criteria decision-making, bivariate statistics, machine learning and their ensembles. *Sci Total Environ* 712:136492. <https://doi.org/10.1016/j.scitotenv.2019.136492>
- Duclaux A (2005) Modélisation hydrologique de 5 Bassins Versants du Haut-Atlas Marocain avec SWAT (Soil and Water Assessment Tool). Mémoire du diplôme d'Ingénieur Agronome de l'Institut National Agronomique de Paris-Grignon. p 53
- Godschall S, Smith V, Hubler J, Kremer P (2020) A decision process for optimizing multi-hazard shelter location using global data. *Sustainability* 12(15):6252. <https://doi.org/10.3390/su12156252>
- Guo Z, Chen L, Yin K, Shrestha DP, Zhang L (2020) Quantitative risk assessment of slow-moving landslides from the viewpoint of decision-making: a case study of the Three Gorges Reservoir in China. *Eng Geol* 273:105667. <https://doi.org/10.1016/j.enggeo.2020.105667>

- Hillier JK, Matthews T, Wilby RL, Murphy C (2020) Multi-hazard dependencies can increase or decrease risk. *Nat Clim Change* 10(7):595–598. <https://doi.org/10.1038/s41558-020-0832-y>
- Hong H, Pourghasemi HR, Pourtaghi ZS (2016) Landslide susceptibility assessment in Lianhua County (China): a comparison between a random forest data mining technique and bivariate and multivariate statistical models. *Geomorphology* 259:105–118. <https://doi.org/10.1016/j.geomorph.2016.02.012>
- Jenks GF, Caspall FC (1971) Error on choroplethic maps: definition, measurement, reduction. *Ann Assoc Am Geogr* 61(2):217–244. <https://doi.org/10.1111/j.1467-8306.1971.tb00779.x>
- Jones HG, Vaughan RA (2010) Remote sensing of vegetation: principles, techniques, and applications. Oxford University Press, Oxford
- Khan A, Gupta S, Gupta SK (2020) Multi-hazard disaster studies: monitoring, detection, recovery, and management, based on emerging technologies and optimal techniques. *Int J Disaster Risk Reduct* 47:101642. <https://doi.org/10.1016/j.ijdrr.2020.101642>
- Kohansarbaz A, Kohansarbaz A, Shabanlou S, Yosefvand F, Rajabi A (2022) Modelling flood susceptibility in northern Iran: application of five well-known machine-learning models. *Irrig Drain* 71(5):1332–1350. <https://doi.org/10.1002/ird.2745>
- Lombardo L, Tanyas H, Nicu IC (2020) Spatial modeling of multi-hazard threat to cultural heritage sites. *Eng Geol* 277:105776. <https://doi.org/10.1016/j.enggeo.2020.105776>
- Lyu H-M, Yin Z-Y (2023) An improved MCDM combined with GIS for risk assessment of multi-hazards in Hong Kong. *Sustain Cities Soc* 91:104427. <https://doi.org/10.1016/j.scs.2023.104427>
- Mao W, Xu C, Yang Y (2021) Investigation on strength degradation of sandy soil subjected to concentrated particle erosion. *Environ Earth Sci* 81(1):1. <https://doi.org/10.1007/s12665-021-10123-9>
- Masoud AM, Pham QB, Alezabawy AK, El-Magd SAA (2022) Efficiency of geospatial technology and multi-criteria decision analysis for groundwater potential mapping in a semi-arid region. *Water* 14(6):882. <https://doi.org/10.3390/w14060882>
- Melhi M, Khattabi A, Driss Z, Orlando CA (2022) Spatial prediction of flood-susceptible zones in the Ourika watershed of Morocco using machine learning algorithms. *Appl Comput Inform*. <https://doi.org/10.1108/ACI-09-2021-0264>
- Ming X, Liang Q, Dawson R, Xia X, Hou J (2022) A quantitative multi-hazard risk assessment framework for compound flooding considering hazard inter-dependencies and interactions. *J Hydrol* 607:127477. <https://doi.org/10.1016/j.jhydrol.2022.127477>
- Mondini AC, Guzzetti F, Melillo M (2023) Deep learning forecast of rainfall-induced shallow landslides. *Nat Commun* 14(1):2466. <https://doi.org/10.1038/s41467-023-38135-y>
- Msabi MM, Makonyo M (2021) Flood susceptibility mapping using GIS and multi-criteria decision analysis: a case of Dodoma region, central Tanzania. *Remote Sens Appl Soc Environ* 21:100445. <https://doi.org/10.1016/j.rsae.2020.100445>
- Nellemann C, Reynolds PE (1997) Predicting Late Winter Distribution of Muskoxen Using an Index of Terrain Ruggedness. *Arctic Alpine Res* 29(3):334–338. <https://doi.org/10.2307/1552148>
- Ouallali A, Kader S, Bammou Y, Aqnouy M, Courba S, Beroho M et al (2024) Assessment of the erosion and outflow intensity in the Rif Region under different land use and land cover scenarios. *Land*. <https://doi.org/10.3390/land13020141>
- Panahi M, Gayen A, Pourghasemi HR, Rezaie F, Lee S (2020) Spatial prediction of landslide susceptibility using hybrid support vector regression (SVR) and the adaptive neuro-fuzzy inference system (ANFIS) with various metaheuristic algorithms. *Sci Total Environ* 741:139937. <https://doi.org/10.1016/j.scitotenv.2020.139937>
- Pei Y, Qiu H, Yang D, Liu Z, Ma S, Li J et al (2023) Increasing landslide activity in the Taxkorgan River Basin (eastern Pamirs Plateau, China) driven by climate change. *CATENA* 223:106911. <https://doi.org/10.1016/j.catena.2023.106911>
- Pourghasemi HR, Rahmati O (2018) Prediction of the landslide susceptibility: which algorithm, which precision? *CATENA* 162:177–192. <https://doi.org/10.1016/j.catena.2017.11.022>
- Razavi-Termeh SV, Hatamiafkoueh J, Sadeghi-Niaraki A, Choi S-M, Al-Kindi KM (2023) A GIS-based multi-objective evolutionary algorithm for landslide susceptibility mapping. *Stoch Environ Res Risk Assess*. <https://doi.org/10.1007/s00477-023-02562-6>
- Sarker IH (2021) Machine learning: algorithms, real-world applications and research directions. *SN Comput Sci* 2(3):160. <https://doi.org/10.1007/s42979-021-00592-x>
- Saunders WSA, Kilvington M (2016) Innovative land use planning for natural hazard risk reduction: a consequence-driven approach from New Zealand. *Int J Disaster Risk Reduct* 18:244–255. <https://doi.org/10.1016/j.ijdrr.2016.07.002>
- Sestras P, Mircea S, Roșca S, Bilașco Ș, Sălăgean T, Dragomir LO et al (2023) GIS based soil erosion assessment using the USLE model for efficient land management: a case study in an area with diverse pedo-geomorphological and bioclimatic characteristics. *Notulae Botanicae Horti Agrobotanici Cluj-Napoca* 51(3):13263–13263. <https://doi.org/10.15835/nbha51313263>
- Stalhandske Z, Steinmann CB, Meiler S, Sauer IJ, Vogt T, Bresch DN, Kropf CM (2024) Global multi-hazard risk assessment in a changing climate. *Sci Rep* 14(1):5875. <https://doi.org/10.1038/s41598-024-55775-2>
- Ye T, Liu W, Mu Q, Zong S, Li Y, Shi P (2020) Quantifying livestock vulnerability to snow disasters in the Tibetan Plateau: comparing different modeling techniques for prediction. *Int J Disaster Risk Reduct* 48:101578. <https://doi.org/10.1016/j.ijdrr.2020.101578>
- Yousefi S, Pourghasemi HR, Emami SN, Pouyan S, Eskandari S, Tiefenbacher JP (2020) A machine learning framework for multi-hazards modeling and mapping in a mountainous area. *Sci Rep* 10(1):12144. <https://doi.org/10.1038/s41598-020-69233-2>
- Youssef B, Bouskri I, Brahim B, Kader S, Brahim I, Abdelkrim B, Spalevič V (2023) The contribution of the frequency ratio model and the prediction rate for the analysis of landslide risk in the Tizi N'tichka area on the national road (RN9) linking Marrakech and Ouarzazate. *CATENA* 232:107464. <https://doi.org/10.1016/j.catena.2023.107464>
- Zhang T, Wang W, An B, Wei L (2023) Enhanced glacial lake activity threatens numerous communities and infrastructure in the Third Pole. *Nat Commun* 14(1):8250. <https://doi.org/10.1038/s41467-023-44123-z>
- Zhao T, Peng H, Xu L, Sun P (2024) Statistical landslide susceptibility assessment using Bayesian logistic regression and Markov Chain Monte Carlo (MCMC) simulation with consideration of model class selection. *Georisk Assess Manag Risk Eng Syst Geohazards* 18(1):211–227. <https://doi.org/10.1080/17499518.2023.2288600>
- Zounemat-Kermani M, Batelaan O, Fadaee M, Hinkelmann R (2021) Ensemble machine learning paradigms in hydrology: a review. *J Hydrol* 598:126266. <https://doi.org/10.1016/j.jhydrol.2021.126266>

Publisher's Note Springer Nature remains neutral with regard to jurisdictional claims in published maps and institutional affiliations.

Authors and Affiliations

Youssef Bammou¹ · Brahim Benzougagh² · Brahim Igmoullan¹ · Shuraik Kader³ · Abdessalam Ouallali⁴ · Velibor Spalevic⁵ · Paul Sestras^{6,7} · Alban Kuriqi^{8,9}

✉ Shuraik Kader
s.mohamedabdulkader@griffith.edu.au;
shuraik.mohamedabdulkader@griffithuni.edu.au;
shuraik10@gmail.com

Youssef Bammou
youssef.bammou@ced.uca.ma

Brahim Benzougagh
brahim.benzougagh@is.um5.ac.ma;
benzougaghbrahim@gmail.com

Brahim Igmoullan
igmoullan@gmail.com

Abdessalam Ouallali
abdessalam.ouallali@univh2c.ma;
abdessalamouallali@gmail.com

Velibor Spalevic
velibor.spalevic@gmail.com

Paul Sestras
psestras@yahoo.com; psestras@mail.utcluj.ro

Alban Kuriqi
alban.kuriqi@tecnico.ulisboa.pt

¹ Laboratory of Geo-Resources, Geo-Environment and Civil Engineering (L3G), Department of Geology, Faculty

of Science and Technology, Cadi Ayyad University, Marrakesh, Morocco

² Department of Geomorphology and Geomatics, Scientific Institute, Mohammed V, University in Rabat, Avenue Ibn Battouta, Agdal, P.B 703, 10106 Rabat-City, Morocco

³ School of Engineering and Built Environment, Griffith University, Nathan, QLD 4111, Australia

⁴ Process Engineering and Environment Laboratory, Faculty of Sciences and Techniques of Mohammedia, Hassan II University of Casablanca, BP 146, 28806 Mohammedia, Morocco

⁵ Biotechnical Faculty, University of Montenegro, 81000 Podgorica, Montenegro

⁶ Department of Civil Engineering, Technical University of Cluj-Napoca, 400020 Cluj-Napoca, Romania

⁷ Academy of Romanian Scientists, Ilfov 3, 050044 Bucharest, Romania

⁸ CERIS, Instituto Superior Técnico, University of Lisbon, 1649-004 Lisbon, Portugal

⁹ Civil Engineering Department, University for Business and Technology, 10000 Pristina, Kosovo

 [View PDF](#)

[Download full issue](#)



Journal of African Earth Sciences

Volume 218, October 2024, 105361



Assessing landslide susceptibility in northern Morocco: A geostatistical mapping approach in Al Hoceima-Ajdir

Ayyoub Sbihi ^a✉, Mohamed Mastere ^a✉, Brahim Benzougagh ^a  ✉, Velibor Spalevic ^b✉, Paul Sestras ^{c,h}✉, Mirjana Radovic ^d✉, Slobodan B. Marković ^e✉, Lizny Jaufer ^f✉, Shuraik Kader ^g  ✉

Paul Sestras

[View in Scopus](#) 

Faculty of Civil Engineering,
Technical University of Cluj-Napoca, 400020, Cluj-Napoca,
Romania

Academy of Romanian Scientists,
Ilfov 3, 50044, Bucharest, Romania

 psestras@mail.utcluj.ro

More documents by Paul Sestras

Provided by Scopus

[Spatial Mapping for Multi-Hazard Land Management in...](#)

JOURNAL OF AFRICAN EARTH SCIENCES

Publisher name: PERGAMON-ELSEVIER SCIENCE LTD

Journal Impact Factor™

2.2
2023

2.3
Five Year

JCR Category	Category Rank	Category Quartile
GEOSCIENCES, MULTIDISCIPLINARY <i>in SCIE edition</i>	120/253	Q2

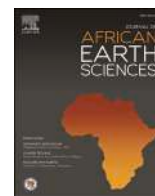
Source: Journal Citation Reports 2023. [Learn more](#) 

Journal Citation Indicator™

0.6
2023

0.59
2022

JCI Category	Category Rank	Category Quartile
GEOSCIENCES, MULTIDISCIPLINARY <i>in SCIE edition</i>	134/253	Q3



Assessing landslide susceptibility in northern Morocco: A geostatistical mapping approach in Al Hoceima-Ajdir

Ayyoub Sbihi^a, Mohamed Mastere^a, Brahim Benzougagh^{a,**}, Velibor Spalevic^b, Paul Sestras^{c,h}, Mirjana Radovic^d, Slobodan B. Marković^e, Lizny Jaufer^f, Shuraik Kader^{g,*}

^a Geophysics and Natural Hazards Laboratory, Department of Geomorphology and Geomatics (D2G), Scientific Institute, Mohammed V University in Rabat, Avenue Ibn Batouta, Agdal, PO Box 703, 10106, Rabat-City, Morocco

^b Biotechnical Faculty, University of Montenegro, Podgorica, 81000, Montenegro

^c Faculty of Civil Engineering, Technical University of Cluj-Napoca, 400020, Cluj-Napoca, Romania

^d University of East Sarajevo, Faculty of Agriculture, Lukavica, 71126, East Sarajevo, Bosnia and Herzegovina

^e Department of Geography, Tourism and Hotel Management, Faculty of Sciences, University of Novi Sad, Trg Dositeja Obradovića 3, 21000, Novi Sad, Serbia

^f School of Architecture, Liverpool John Moores University, L3 5UX, Liverpool, United Kingdom

^g School of Engineering and Built Environment, Griffith University, Nathan Campus, 170 Kessels road, 4111, QLD, Australia

^h Academy of Romanian Scientists, Ilfov 3, 50044, Bucharest, Romania

ARTICLE INFO

Handling Editor: DR Damien Delvaux

Keywords:

Geohazards
Tectonic movements
Geomatic tools
Predisposing factors
Receiver operating characteristics (ROC)
Morocco

ABSTRACT

Landslides are a significant global risk due to their impact on nature, society, and the economy. The Al Hoceima-Ajdir region is highly susceptible to geohazards such as earthquakes and ground instabilities caused by local tectonic movements and specific climatic and geomorphological conditions. This study aims to assess landslide susceptibility in Al Hoceima-Ajdir using a digital mapping approach that integrates the geostatistical Frequency Ratio tool, geomatic tools, and field observations. The frequency ratio method, a widely used technique in geospatial analysis, evaluates the relative frequency of landslides based on the spatial distribution of conditioning factors such as slope, lithology and land use – land cover. This method calculates the ratio of the frequency of landslides within specific classes of these factors to their respective frequencies in the entire study area. This research introduces a novel susceptibility map highlighting major threats to several natural and touristic sites crucial to the region's socio-economic activities. The susceptibility map was developed by analyzing 40 historical landslides along various predisposing factors, including topographic, geo-hydrological, and anthropogenic parameters. The results identify areas prone to landslides and classify their susceptibility into five levels ranging from very high to very low, with each level indicating a different degree of risk and requiring a specific set of preventive measures. The reliability of this map was evaluated using the Receiver Operating Characteristics (ROC) method, demonstrating a high accuracy of 89%, further validated by field visits. This high-precision susceptibility map is significant for pre- and post-risk management, enhancing prevention and mitigation strategies. It also protects society, the economy, and the environment by providing a reliable regional planning and hazard management tool. The findings of this study offer a significant advancement in the methodology for landslide susceptibility assessment and present a model that can be adapted to other regions facing similar geohazards. The research underscores the importance of integrating geostatistical tools with field data to produce accurate and actionable susceptibility maps, benefitting the global scientific community by improving hazard prediction and management strategies.

* Corresponding author.

** Corresponding author.

E-mail addresses: ayyoub.sbihi@um5r.ac.ma (A. Sbihi), mohamed.mastere@is.um5.ac.ma (M. Mastere), brahim.benzougagh@is.um5.ac.ma (B. Benzougagh), velibor.spalevic@gmail.com (V. Spalevic), psestras@mail.utcluj.ro (P. Sestras), mirjana.radovic@pof.ues.rs.ba (M. Radovic), baca.markovic@gmail.com (S.B. Marković), lizny96@gmail.com (L. Jaufer), s.mohamedabdulkader@griffith.edu.au, shuraik.mohamedabdulkader@griffithuni.edu.au, shuraik10@gmail.com (S. Kader).

<https://doi.org/10.1016/j.jafrearsci.2024.105361>

Received 23 May 2024; Received in revised form 18 July 2024; Accepted 26 July 2024

Available online 27 July 2024

1464-343X/© 2024 The Authors. Published by Elsevier Ltd. This is an open access article under the CC BY license (<http://creativecommons.org/licenses/by/4.0/>).

1. Introduction

Landslides are natural phenomena that occur when soil or rock masses rapidly move along a slope. They can have devastating consequences, threatening human life and causing considerable damage to infrastructure (Glade and Crozier, 2005; Zorn and Komac, 2007). The province of Al Hoceima in Morocco is not spared from these landslides due to hydro-geological, topographical and climatic anomalies, so the vulnerability of this region is exacerbated by unstable geological formations, frequent seismic activities, and steep topography, making it a significant concern for the local population and environment (El Fahchouch et al., 2015; Rahali, 2019).

In the context of risk prevention and management in this province, numerous studies have been conducted to assess the susceptibility of mass movements in different city outskirts. These studies have utilized various methods, including geological, geomatic, geotechnical, and geostatistical approaches (Labriki et al., 2016; Rfif and Ait Brahim, 2018; Benzougagh et al., 2024). However, the present work is the first to evaluate the susceptibility of mass movements in the urban municipalities of Al Hoceima - Ajdir using the statistical method of Frequency Ratio. This statistical tool provides a method to quantitatively analyze the relationship between the inventory of historical landslides and the predisposing factors to landslides as well as the calculations from this method allow for deducing the frequency of past landslides and examining how these events are related to certain geological, hydrological, topographic, and environmental variables extracted from various approaches, such as remote sensing, geographic information systems, and field surveys.

The seismic history of the Al Hoceima area has experienced several earthquakes, resulting in soil instabilities and ground movements (Talhaoui et al., 2005). Furthermore, the local topography, characterized by steep slopes and specific geological formations, contributes to an increased risk of landslides. The climate, with abundant precipitation and alternating dry and wet periods, also significantly influences soil stability.

The inventory of historical landslides is of paramount importance in natural risk management. This process provides essential data for assessing these events' frequency, intensity, and geographical location (G.D. Bathrellos et al., 2021; Ouallali et al., 2024; Bashir et al., 2024). This knowledge is critical for defining high-risk areas and implementing specific protective measures, such as prohibiting construction in sensitive areas or adapting construction standards. Moreover, by analyzing the characteristics of past landslides, common triggering factors can be identified, such as steep slopes or unstable materials (Mastere et al., 2020).

Mapping landslide susceptibility is crucial for assessing and predicting high-risk landslide areas. Numerous methods have been developed for mapping based on geological, topographic, and climatic factors. The results of these methods have enabled the production of an accurate landslide susceptibility map, which helps plan risk management measures (Akgun et al., 2008; Guzzetti et al., 2006; Lee and Min, 2001). This work aims to determine the levels of landslide susceptibility in the Al Hoceima - Ajdir region by utilizing the results of frequency ratio analysis and analyzing them with geomatics tools and discovering the most influential parameters on terrain instability. The results of this study provide an essential tool for preventive risk management and mitigation, thereby improving regional planning and protecting the society, economy and environment of the region. This research proposes a methodology applicable to other regions, highlighting the importance of combining geostatistical tools with field data for effective geohazards management. The uniqueness of the approach adopted in this study compared to previous research lies in its detailed zoning of areas prone to soil instabilities. Indeed, we conducted detailed mapping that accurately distinguishes between various zones and local tourist sites threatened by this hazard.

2. Materials and methods

2.1. Study area

The province of Al-Hoceima is located in the northern part of Morocco, forming an integral part of the Tanger-Tétouan-Al-Hoceima region. This study specifically focuses on the province's northeastern region, home to two rural communities, Al Hoceima and Ajdir (Fig. 1), characterized by a total area not exceeding 33 square kilometers and distinguished by a very high level. This study area is located in the western part of Al Hoceima Bay. It is bounded by Izzemouren to the west and the community of Aït Youssef ou Ali to the south, while the Mediterranean Sea borders its northern and eastern sides.

In the geological context, its location in northern Morocco indicates that this area belongs to the Rif domain. According to its positioning, the area is characterized by its affiliation with the Bokkoya massif, which represents a dominance of carbonate formations originating from a limestone ridge that concentrated in the area in the form of windows "klippes", forming remarkable reliefs such as the one at Sidi Abid Point. These klippes are also composed of Paleozoic materials with a Mesozoic age cover, indicating the presence of Ghomarids, locally known as the Al-Hoceima klippe (Azzouz et al., 2002) which is illustrated by (Fig. 2), with metamorphosed units exposed, known as the Sebides (Azzouz, 1992; Chalouan et al., 1995; Michard et al., 2002).

2.2. Research method

In the framework of this study, the methodology followed several key steps (Fig. 3). It began by collecting data from different sources, such as satellite imagery, geological and topographic maps, and field excursions, which provides a solid foundation for this work. The data analysis was based on nine main parameters: slope, aspect, lithology, faults, elevation, roads, hydrographic network, land use, and historical inventory. These parameters were carefully examined to understand their influence on landslide susceptibility (Kanungo et al., 2009; Fallah-Zazuli et al., 2019; Pourghasemi et al., 2012; Chen et al., 2019a,b). The development of the landslide susceptibility map was based on applying the recognized statistical model, the Frequency Ratio (FR); this model utilized the previously analyzed parameters to generate a map indicating the levels of susceptibility to this hazard in the study area. Finally, the Receiver Operating Characteristic (ROC) method and field visits were used to assess the reliability and verify the obtained results.

Data extraction was performed using various methods and sources. Using a digital elevation model with a resolution of 30m facilitated the processing of crucial information such as elevation, slope, relief aspect, and the hydrographic network. This allowed us to understand the terrain topography and the distribution and connectivity of watercourses. The geological map of Al-Hoceima at a scale of 1/50,000 provided information on the different geological formations in the area and potential faults. Sentinel-2 satellite images were used to map land uses and roads accurately.

The landslide inventory phase is carried out using two methods. The first involves exploiting regional satellite images to detect their geographical locations and track the history of these collapses. At the same time, the second is based on field excursions to assess the geomorphological state and type of landslide. These two methods have led to the discovery and measure more than 40 landslides of different types (Fig. 4) distributed throughout the study area, which will be the crucial factor in this evaluation.

2.3. Topographic parameters

Previous studies have shown that steep slopes combined with specific exposure and high elevation can create predisposing conditions favoring landslides (Montgomery and Dietrich, 1994; Bammou et al., 2024). Therefore, topography is considered one of the main factors of

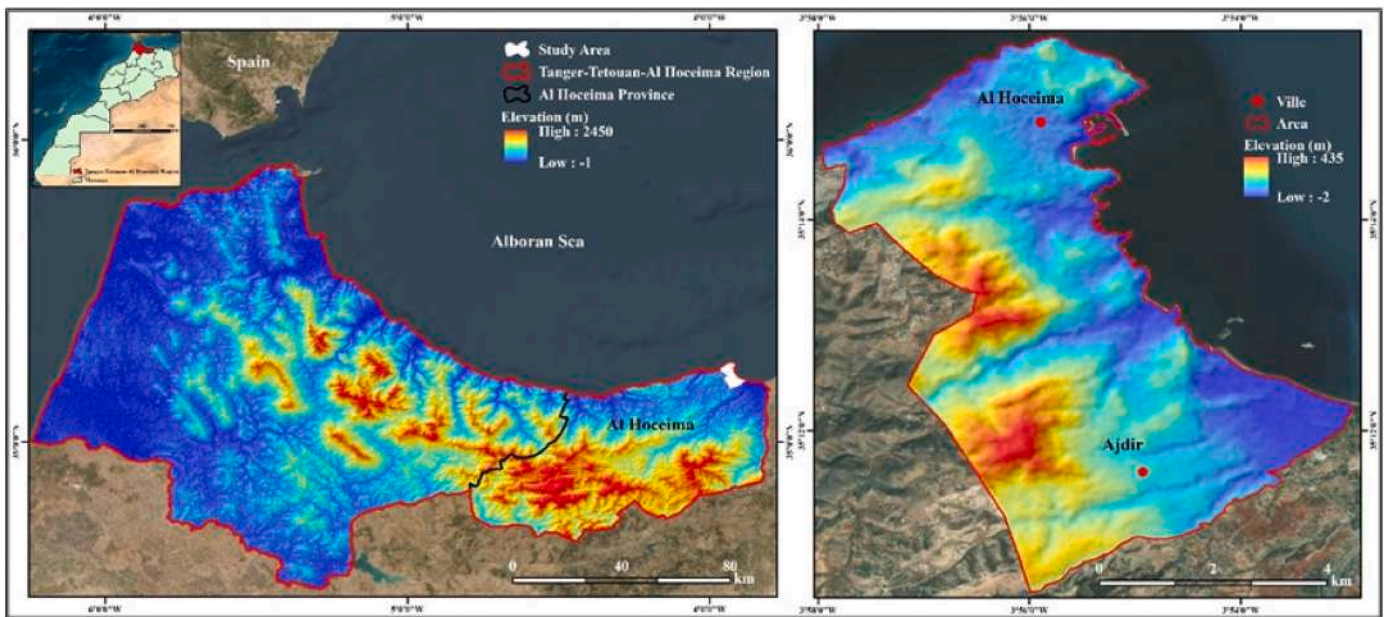


Fig. 1. Geographical location of study area.

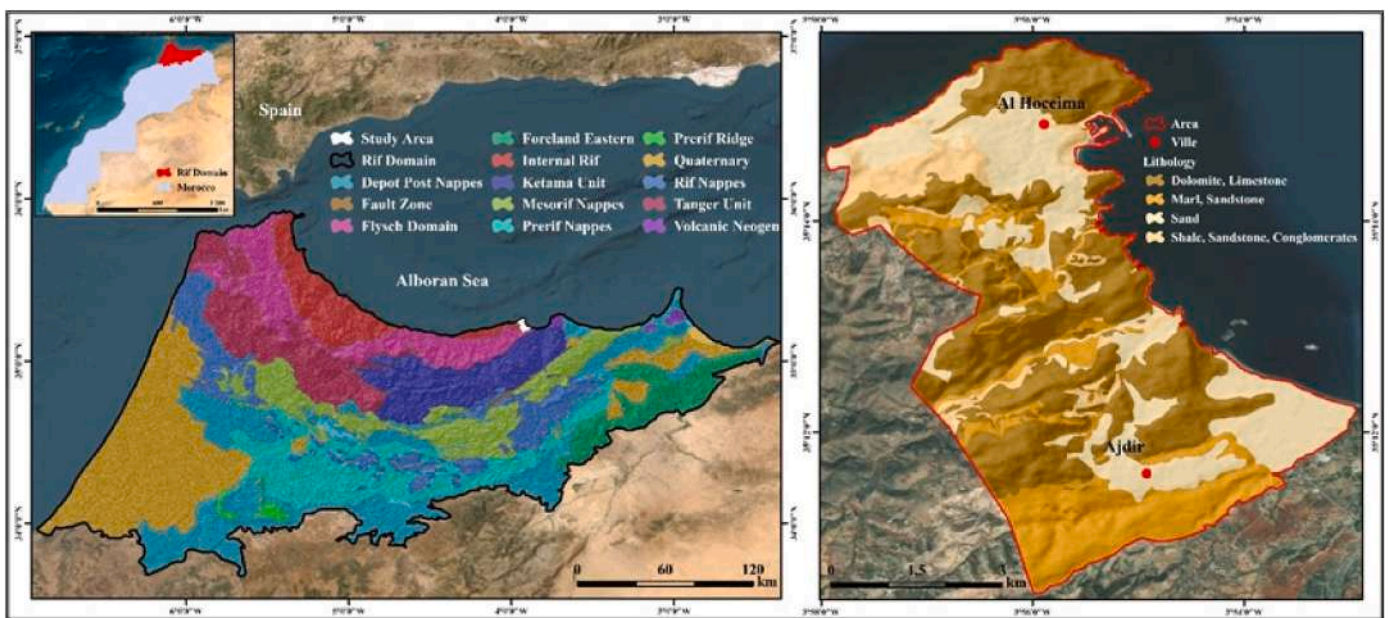


Fig. 2. Geological map of the study area.

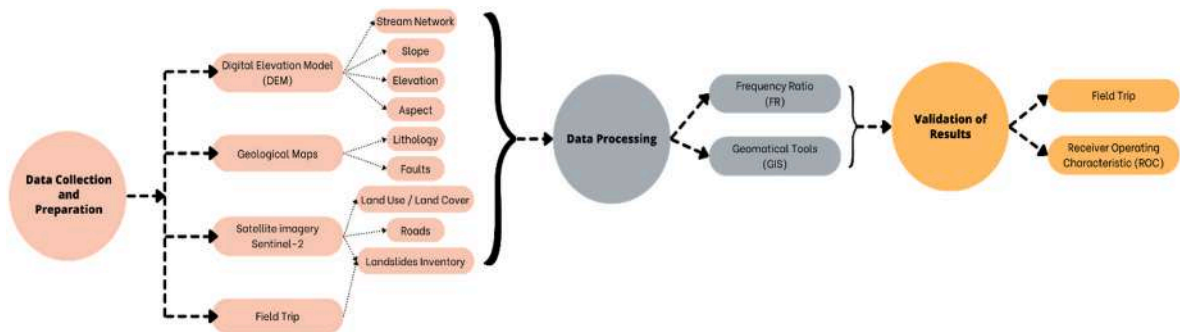


Fig. 3. Methodological flowchart for mapping landslide susceptibility.



Fig. 4. Some examples of historical landslides in the study area (Left: Extracted by satellite imagery from Google Earth between July and August 2023; Right: extracted by field visit during June, 2023).

terrain instability due to the effect of its parameters.

The slope of the terrain plays a crucial role in landslide initiation, as steep inclines increase the risk of soil destabilization (Sadkaoui et al., 2024; Sidle and Bogaard, 2016). Furthermore, the direction or aspect of the slope can indirectly influence landslide initiation by impacting vegetation cover and soil moisture retention, this orientation affects the amount of solar radiation received, which can modulate vegetation cover and the soil's stability to retain moisture. For instance, a north-facing slope tends to receive less direct sunlight, promoting denser vegetation cover and higher soil moisture retention, thereby reducing the risk of landslides (García-Rodríguez et al., 2008; Basharat et al., 2014). High-altitude areas are often characterized by steeper slopes, increasing soil susceptibility to failure and promoting landslide occurrences (Chen et al., 2019a,b).

2.4. Geological-hydrological parameters

The complex interactions between geological and hydrological parameters require in-depth studies to understand lithology, which refers

to the composition and nature of rocks and how they can influence landslides in various ways (G.D. Bathrellos et al., 2024). Faults can also play an essential role in landslides. When a fault intersects a slope, it creates a vulnerable point where the soil is less stable. This structural weakness makes it easier for the earth masses to break and slide, especially when triggered by factors such as heavy rainfall or earthquakes.

The distribution of hydrographic networks in high rainfall areas can accelerate slope erosion and increase the probability of landslides (Benzougagh et al., 2020; Bammou et al., 2024a,b), as well as increase the interstitial pressure of adjacent soils, reducing their cohesion (Crozier and Glade, 2010).

2.5. Natural-anthropogenic parameters

Land use and roads are closely related to landslides, as these natural phenomena can significantly impact their construction, maintenance, and landscape. The construction of roads on steep slopes or in geologically unstable regions can lead to modifications in natural drainage systems, which facilitate water condensation in the soil and increase the

potential for landslides (Harmouzi et al., 2019). In other words, when natural drainage systems are disrupted by road construction, water can accumulate more easily in the soil. This increase hydrostatic pressure and can contribute to soil destabilization, thereby increasing the risk of landslides. Increasing population and the growing demand for buildable land can expand urban areas into landslide-prone areas (Guzzetti et al., 1999; Glade et al., 2005). Removing natural vegetation to make way for construction and adding artificial structures can disrupt soil balance, thereby increasing the probability of ground movements (Mohamed and Lahsen, 2018).

2.6. Frequency ratio

The frequency ratio method is commonly used for mapping landslide susceptibility (Yilmaz, 2009). This method quantifies the probability of landslide occurrence using statistical techniques and geomatics tools to generate a landslide susceptibility map. It integrates historical landslide data collected from satellite images between July and August 2023, along with field mission data from June 2023, incorporating relevant environmental factors such as slope, soil type, tectonic structures and proximity to watercourses (Ding et al., 2017). The frequency ratio (FR) of each variable involved in landslide formation measures the relative frequency at which each environmental factor contributes to these events. It assesses how parameters influence the probability of landslides occurring in the study area. It is calculated using the following equation (1):

$$FR = \frac{Nb(Px1)/Nb(Px2)}{\sum (Nb(Px3)/Nb(Px4))} \quad (1)$$

Where.

- **Nb (Px1)**: Number of pixels representing landslides in a class.
- **Nb (Px2)**: Total number of pixels in each class.
- **Nb (Px3)**: Total number of pixels representing landslides in the entire area.
- **Nb (Px4)**: Total number of pixels in the entire area.

After calculating the frequency ratio (FR) for all parameters contributing to landslide susceptibility, the weight of influence for each factor can be determined using equation (2). This equation helps to determine the landslide susceptibility index (IS) using equation (3).

$$RF = \frac{FR_{1a}}{FR_1} \quad \text{and} \quad w = \frac{Max(RF) - Min(RF)}{Min_{[Max(RF) - Min(RF)]}} \quad (2)$$

Where.

- **FR_{1a}**: Frequency ratio of a subclass factor.
- **FR₁**: Frequency ratio of a factor.
- **Max (RF)**: the maximum value of RF of each factor.
- **Min (RF)**: the minimum value of RF of each factor.
- **Min [Max (RF)-Min (RF)]**: the minimum value of the difference between max and min of all factors.
- **n**: number of term (i.e. nth term)

$$IS = (Factor_1 \times w_1) + (Factor_2 \times w_2) + (Factor_n \times w_n) \quad (3)$$

The verification of the obtained results is carried out through two approaches. The first approach is the Area Under the Curve (AUC), which allows deducing the reliability and performance of the method used through a quantitative analysis between the utilized data (historical landslides and causative factors) and the obtained results (Ja, 1988; Lee and Talib, 2005). The second approach involves field visits to verify the risk levels indicated in the generated map through on-site observations.

3. Results

3.1. Predisposing factors

3.1.1. Slope

The treatments applied to a digital terrain model reveal that the Al Hoceima - Ajdir sector is characterized by a maximum slope reaching 55°. Given that the slope factor has a maximum inclination of 55° degrees, an approach was adopted to divide this parameter into five equally distributed classes. The threshold value of 11 was chosen as the dividing point between these classes, thereby facilitating a clear and coherent classification of terrains based on their slope (Fig. 5A). The first category includes the gentlest slopes, with inclinations ranging from 0 to 11°. The second category consists of slopes with inclinations ranging from 11 to 22°. The third category pertains to slopes with inclinations ranging from 22 to 33°, and these slopes are considered the first level that can cause soil instability.

The fourth category includes slopes with inclinations ranging from 33 to 44°; these slopes can pose a relatively high risk of landslides. Finally, the fifth category comprises the steepest slopes, with 44 to 55-degree inclinations. These slopes are highly vulnerable to landslides and require special attention. The frequency ratio for this factor is estimated to be a total of 4.20. Sloped terrains, with an inclination ranging between 33 and 44°, are considered the most susceptible to soil instability. This is indicated by their FR value reaching 1.74, the highest among the classes of this factor.

3.1.2. Elevation

The location of the sector in a mountainous region confirms the elevation of the relief in this area, as indicated by the presence of maximum altitudes exceeding 400 m (Fig. 5B). Based on the classification of this factor, six distinct classes are identified: (0–80 m), (80–160 m), (160–240 m), (240–320 m), (320–400 m), (>400 m). Applying equation (1), it is determined that the frequency ratio (FR) associated with this factor does not exceed 3.67, with a maximum value of 1.61 corresponding to areas with altitudes ranging from 0 to 80 m.

3.1.3. Aspect

The watersheds in this area exhibit exposures distributed in eight distinct directions (Fig. 5C): (North), (Northeast), (East), (Southeast), (South), (Southwest), (West), (Northwest). Among these directions, the north represents the highest frequency, with a coefficient of 1.55 out of a total of 7.81, which is the sum of the frequencies of all directions.

3.1.4. Lithology

The geology of the Al-Hoceima-Ajdir municipalities is characterized by its lithological diversity, encompassing several types of soils. The lithological mapping of this area (Fig. 5D) reveals the presence of four lithological groups distributed throughout the study area: (G1: Shale - Sandstone - Conglomerates), (G2: Sand), (G3: Marl and Sandstone), (G4: Dolomite and Limestone).

The examination of frequency ratio values for each group highlights that soils composed of shale, sandstone, and conglomerates exhibit a stronger predisposition to landslides, as indicated by their high value of 3.86. This quantitative analysis confirms the greater propensity of these soil types to be involved in ground movements.

3.1.5. Tectonic structures

The presence of our study area in a highly tectonic zone allowed us to consider the distribution of faults in the Al-Hoceima - Ajdir region. The treatments applied to this factor are of significant interest as they enable us to assess the proximity of landslides to faults and determine the maximum distance of tectonic effects capable of triggering a landslide. Fig. 5 illustrates six classes, each representing the distance of landslides from faults. This distance is classified as follows: (0–60 m), (60–120 m), (120–180 m), (180–240 m), (240–300 m), (>300 m). This factor's

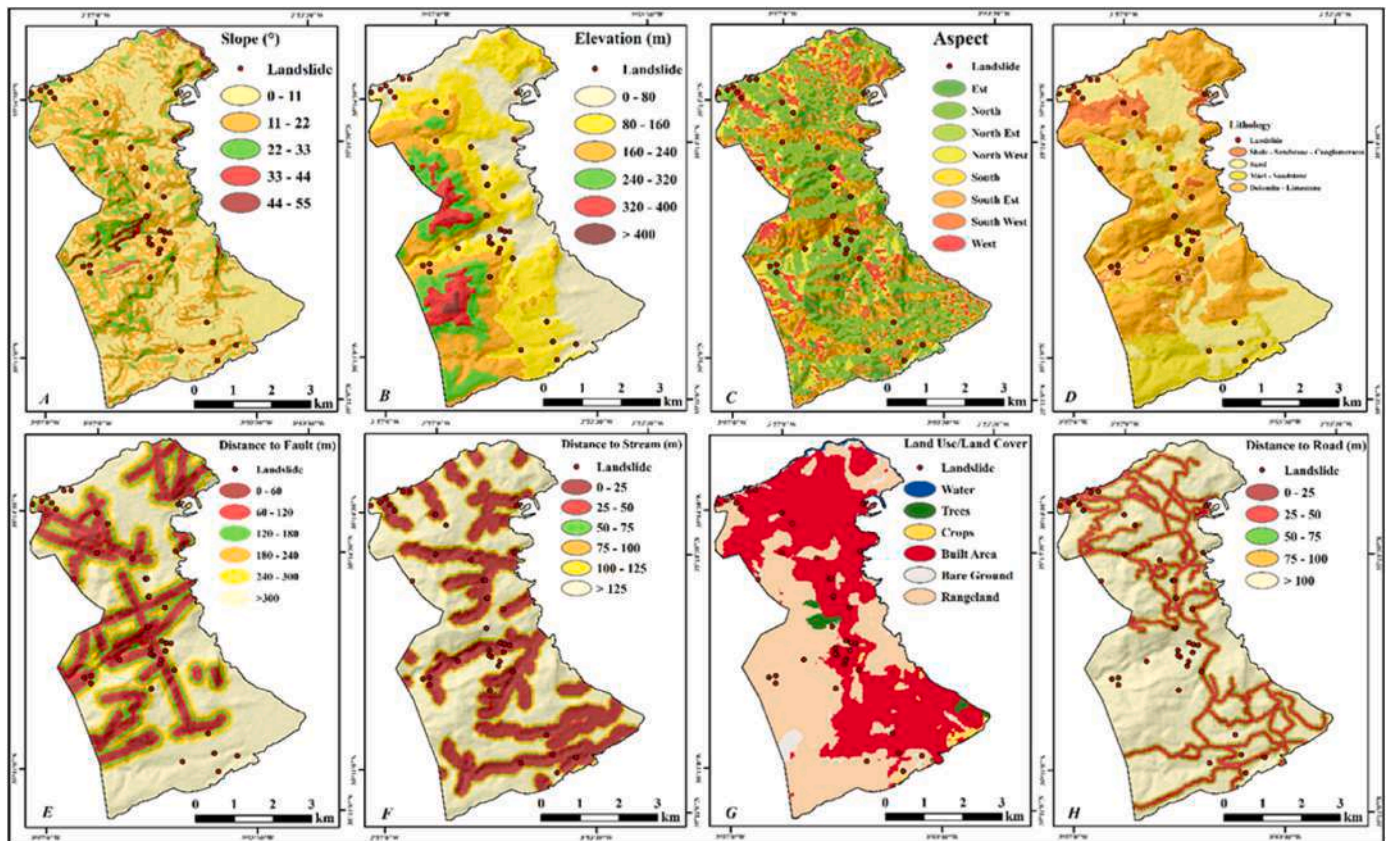


Fig. 5. Maps of the parameters used in this study area. A) Slope, B) Elevation, C) Aspect, D) Lithology, E) Distance to fault, F) Distance to stream, G) Land Use/Land Cover, H) Distance to road.

calculated frequency ratio values indicate that the tectonic effect on landslides will be more pronounced in areas closest to faults. For example, the class (0–60 m) has a maximum FR value of 1.81, demonstrating a significant influence.

3.1.6. Hydrographic networks

In our study area, we observed the presence of numerous interconnected hydrographic networks distributed throughout the zone. The purpose of this map is to determine the relationship between hydrographic networks and landslides in the Al Hoceima-Ajdir area (Fig. 5F). This map was generated through a series of treatments to illustrate the proximity of hydrographic networks to landslides. The distance was divided into six distinct classes to understand this complex relationship better: (0–25 m), (25–50 m), (50–75 m), (75–100 m), (100–125 m), (>125 m).

The frequency ratio results obtained for this parameter highlight the substantial impact of hydrodynamics on landslides, particularly in areas adjacent to watercourses. For instance, the class corresponding to a distance of 0–25 m has the highest value compared to other classes, which is 1.81, indicating a significant influence.

3.1.7. Land use/land cover

For this factor, an analysis was conducted on the relationship between land use and landslides in the Al Hoceima-Ajdir municipalities. The focus was on six main categories: water, forests, agricultural lands, residential areas, bare soils, and pastures (Fig. 5G). Each category represents a specific type of land use that can be considered a cause and/or stake related to landslide occurrences. The frequency ratio calculations for various land use categories highlight that bare soils exhibit the highest FR value of 1.89. This significant value identifies them as areas prone to landslides, where their occurrence is more frequent.

3.1.8. Road network

Understanding the relationship between roads and terrain instability in our study area was achieved through treatments that categorized the distance between roads and landslides into five classes: (0–25 m), (25–50 m), (50–75 m), (75–100 m), (>100 m) (Fig. 5H). The second class, which corresponds to a distance ranging from 25 to 50 m, has a maximum FR value of 1.56. These findings emphasize the importance of considering the proximity of roads when assessing landslide risks and planning preventive measures.

3.2. Frequency ratio

The analysis of landslide-predisposing factors in the Al-Hoceima - Ajdir area was conducted using the Frequency Ratio (FR) method. This approach revealed the distribution of landslides relative to all parameters integrated into this hazard, in order to identify the most influential parameters in these deformations and evaluate their level of influence on the genesis of soil movement.

In general, the gathered results illustrate a correlation between the landslide areas and each parameter associated with this risk. “w” represents the weight assigned to each factor in the calculation of the landslide susceptibility index. The table below (Table 1) demonstrates that as the weight value of a factor increases, its influence on the susceptibility index becomes more significant. According to the histogram below (Fig. 6), certain parameters stand out with a significant weight of influence, notably lithology, land use, elevation and slope. The Lithology exhibits the maximum weight of influence in these results, reaching a remarkable value of 21.19%. The three other parameters, namely elevation, slope, and land use, are also ranked among the most influential factors on this phenomenon in the area, with influence weights ranging from 12.43% to 17.10%. However, it is essential not to neglect other parameters such as faults, roads, and hydrographic

Table 1
The results of the causative parameters for landslides using the frequency ratio.

Factor	Classes (Degree)	Number of Pixel	Percentage number of pixels (%)	Number of landslide pixels	Percentage number of landslide pixels (%)	FR	RF	W
Slope	1 (0° - 11°)	15802	43.11008048	37	18.1372549	0.420719579	0.099977	
	2 (11° - 22°)	15128	41.2713136	118	57.84313725	1.40153371	0.33305	
	3 (22° - 33°)	4745	12.94502796	46	22.54901961	1.741905825	0.413933	
	4 (33° - 44°)	857	2.283453826	3	1.470588235	0.644019256	0.15304	
	5 (44° - 55°)	143	0.39012413					
	Total	36655	100	204	100	4.208178369	1	2.1363651
Aspect	N	6722	18.33856227	58	28.43137255	1.550359954	0.198287	
	NE	5991	16.34429137	45	22.05882353	1.349634746	0.172611	
	E	5067	13.82348929	18	8.82329912	0.638299725	0.081635	
	SE	5173	14.66838037	12	5.88232941	0.401298431	0.051324	
	S	4315	11.77192243	10	4.901960784	0.41641106	0.053257	
	SW	2214	6.040103669	14	6.862745098	1.136196574	0.145313	
	W	2554	6.967671532	14	6.862745098	0.984940962	0.125968	
	NW	4419	12.05565407	33	16.17647059	1.341816088	0.171611	
Total	36655	100	204	100	3.810997584	1	1	
Lithology	Shale, Sandstone, Conglomerates	2121	7.781801113	62	30.09708738	3.867624852	0.5691	
	Sand	8525	28.58244485	56	27.18446602	0.951089599	0.139948	
	Marl, Sandstone	5488	18.40005364	66	32.03883495	1.741235953	0.256213	
	Dolomite, Limestone	13492	45.2357004	22	10.67961165	0.236088124	0.034739	
	Total	29826	100	206	100	6.296038529	1	3.6361365
Distance to Fault	0 - 60	5841	16.01458613	58	29.14572864	1.819494914	0.240642	
	60 - 120	4679	12.82866778	22	11.05527638	0.881763401	0.113946	
	120 - 180	4266	11.69632331	36	18.09045226	1.54667854	0.204509	
	180 - 240	3466	9.502919668	27	13.5678392	1.427754758	0.188784	
	240 - 300	3186	8.73228799	27	13.5678392	1.552322263	0.205375	
	>300	15035	41.22227401	29	14.57286432	0.353519176	0.046744	
	Total	36473	100	199	100	7.582897052	1	1.3194066
Distance to stream	0 - 25	11176	29.61785127	119	57.76699029	1.95041249	0.348584	
	25 - 50	3270	8.66592463	18	8.737864078	1.008301416	0.180207	
	50 - 75	2241	5.938941008	13	6.310679612	1.062593416	0.18991	
	75 - 100	2183	5.78523476	9	4.368923939	0.753186814	0.134669	
	100 - 125	2100	5.56522698	4	1.941747373	0.3489943	0.062357	
	>125	16764	44.42677691	43	20.87378641	0.469846967	0.083973	
	Total	37734	100	206	100	5.595244162	1	1.9476609
Distance to road	0 - 25	2285	6.05546722	6	2.912621359	0.480984045	0.089456	
	25 - 50	5487	14.54126252	47	22.81553398	1.569020155	0.291814	
	50 - 75	3371	8.93387746	28	13.59233301	1.52147529	0.282972	
	75 - 100	2875	7.819123337	15	7.281553398	0.955694386	0.177245	
	>100	23716	62.85047967	110	53.39805825	0.849604626	0.1188014	
	Total	37734	100	206	100	5.376778501	1	1.3769772
Elevation	0 - 80	10217	27.06920305	90	43.68932039	1.613986208	0.438835	
	80 - 160	13181	34.92310682	75	36.40776699	1.042542112	0.283462	
	160 - 240	7628	20.29983468	39	18.93303883	0.936773563	0.254704	
	240 - 320	4332	11.4773209	2	0.970873786	0.084590628	0.023	
	320 - 400	2217	5.873781263					
	>400	169	0.447753285					
	Total	37744	100	206	100	3.677892511	1	2.8296086
LULC	Water	4104	0.87311004	0	0			
	Trees	5705	1.15672168	0	0			
	Crops	4562	0.924972222	0	0			
	Built Area	24320	49.41565762	147	71.3592233	1.444060987	0.372339	
	Bare Ground	11345	2.300262505	9	4.368932039	1.899316666	0.489723	
	Rangeland	223768	45.37027275	50	24.27184466	0.534972421	0.137938	
Total	493204	100	206	100	3.878350074	1	3.3937706	

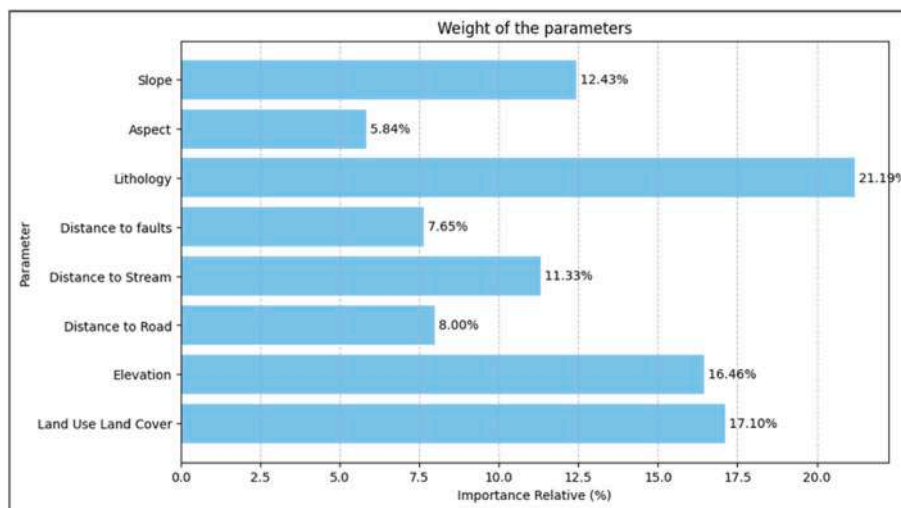


Fig. 6. The weight of the parameter influence.

networks, as they exert a significant influence on terrain instability. Nevertheless, their weight of influence on this hazard remains relatively low compared to the aforementioned parameters.

3.3. Landslide susceptibility

The mapping of landslide susceptibility in the Al Hoceima - Ajdir region was conducted using geomatics tools, utilizing the results obtained from the FR method (Table 1). This process involves combining the responsible factors with their influence weights, resulting in a map (Fig. 8) that illustrates different levels of landslide susceptibility and the intensity of this risk, divided into five levels covering the entire area

(Low, Moderate, Moderate, High, Very High), with the subdivision of these levels primarily associated with the existence of the most influential parameters in terrain instability.

The susceptibility map shows that only 27% of the total area of Al Hoceima-Ajdair exhibits low susceptibility to this risk. In comparison, 73% of the zone's area displays moderate to very high susceptibility. Moderate susceptibility predominates, covering 57% of the total area (Fig. 7). This indicates that three-quarters of the study area has a high probability of terrain instability occurrences.

The images below serve as evidence for the results presented in the landslide susceptibility map in the study area. During these field visits, we observed several areas prone to landslides, which are already

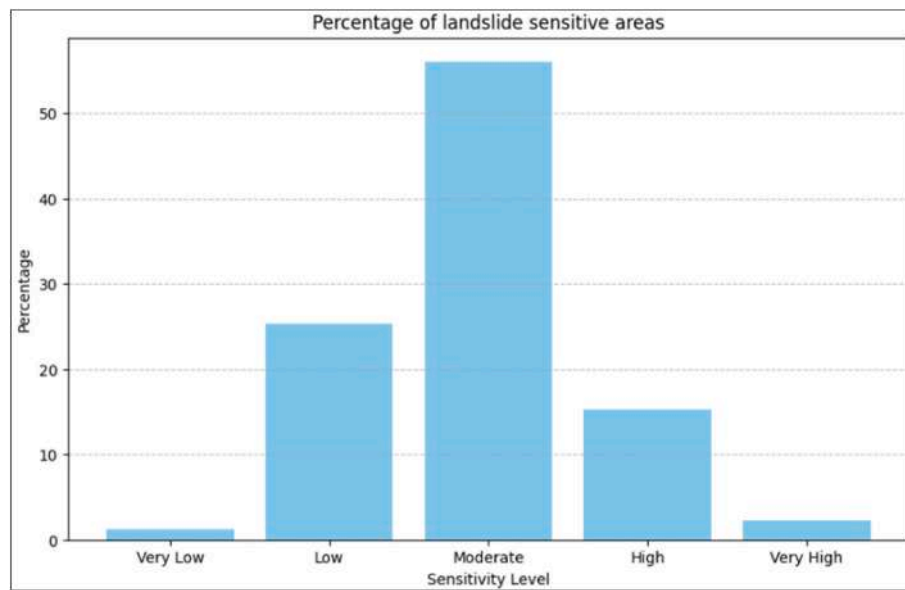


Fig. 7. Percentage of landslide sensitive areas.

indicated in the generated map. The study sector is facing a significant challenge, as most areas affected by this phenomenon are located in highly tourist-attractive and residential zones. Among these areas is Boujibar National Park, considered a valuable natural heritage site in the province of Al-Hoceima. This park stands out for its vast forest, housing different biozones, as well as providing a panoramic view of the city and local islands such as Isla de Mar, Isla de Tierra, and Peñón de Alhucemas (Fig. 9e). Furthermore, the Sabadía road, located along the coast, is also highly susceptible to this phenomenon. This road is renowned as the city's most famous promenade and is a heavily travelled route to other beaches in the region (Fig. 9a, c).

The port and the maritime station are also highly exposed to landslides (Fig. 9d). At the same time, the residential complex of Badés remains a popular tourist destination for residents wishing to enjoy the natural beauty of the region. However, its susceptibility to land movements can be a disadvantage for this tourist site (Fig. 9b). The Al-Hoceima provincial road, which is the only access route for tourists to Al-Hoceima, exhibits considerable vulnerability near this road (Fig. 9f, g). This can result in temporary closures or traffic restrictions, thereby impacting tourism by limiting accessibility to Al-Hoceima and its surroundings.

The findings provide a clear and concise perspective on predisposing factors to mass movements in the Al Hoceima-Ajdir region. However, a thorough analysis underscores the imperative to integrate effective mitigation measures, particularly through optimized land use. In addition to reducing slope length through alternative construction methods, strategies such as constructing retaining walls to stabilize critical slopes are essential. Furthermore, installing effective drainage systems to manage runoff can prevent water accumulation and mitigate landslide risks.

Following these field verifications, the ROC function also strengthened the significant validity and reliability of the model. Consequently, this graphical representation demonstrates a performance reaching up to 89.63%, obtained from a quantitative analysis comparing the interaction of historical landslides and their characteristics with the results collected by the FR model (Fig. 10), which form the two axes of this graph: the true positive rate and false positive rate, or sensitivity and specificity. From these two validation approaches, one can observe a tangible conformity between the results of the frequency ratio and the susceptibility levels observed in the area.

4. Discussion

The present study addresses the issue of landslides in the Al Hoceima-Ajdir region, particularly their natural and touristic sites, which are the sole regional economic sources. It also aims to identify the susceptibility level of these sites and the natural anomalies that trigger the genesis of this hazard. Using geostatistical tools contributes to obtaining compelling results through an in-depth spatial analysis of unstable terrains and their characteristics in the studied factors (Karpouza et al., 2021).

These approaches highlight that the Al Hoceima-Ajdir region is highly exposed to landslide hazards due to the convergence of several characteristics facilitating soil instability. Although the susceptibility map to this hazard illustrates a variation in risk levels, the most sensitive and vital sites in the study area, such as the national park and the maritime port, are the most threatened by soil instabilities due to the fragility of their lithologies and the irregularity of their topographies. The development of this map results from a set of processes of the frequency ratio model, already recognized for its performance and results in several similar studies, thus reaffirming the reliability of this model in this study, which reaches 89% through the receiver operating characteristic.

The Al Hoceima region has experienced significant seismic activity that can disturb some soil masses, distinguished by geological, geomorphological, and climatic properties, making these soils vulnerable and less resistant. The results gathered, as well as those from previous studies conducted using different approaches, show consistency, highlighting that in-depth statistical analysis of causal factors illustrates that the low stability of these terrains is closely related to their soil nature, distinguished by significant fragility, as indicated by geotechnical analyses of this area (Labriki et al., 2016; Bashir et al., 2024b). Furthermore, numerous fundamental or applied studies lead to conclusions similar to this work, demonstrating that topographic anomalies and land cover have significantly contributed to these geomorphological deformations. This underscores the need to pay particular attention to areas characterized by these anomalies to reduce the stakes of this risk (Azzouz et al., 2002; El Khattabi, 2023).

The analysis of the interrelations between soil movements and the parameters responsible for their formation reflects that soils composed of schists and detrital sediments such as sandstones and conglomerates are particularly unstable (Bashir et al., 2024c). This fragility is closely associated with their physical properties, characterized by low cohesion between particles, high porosity, and significant permeability,

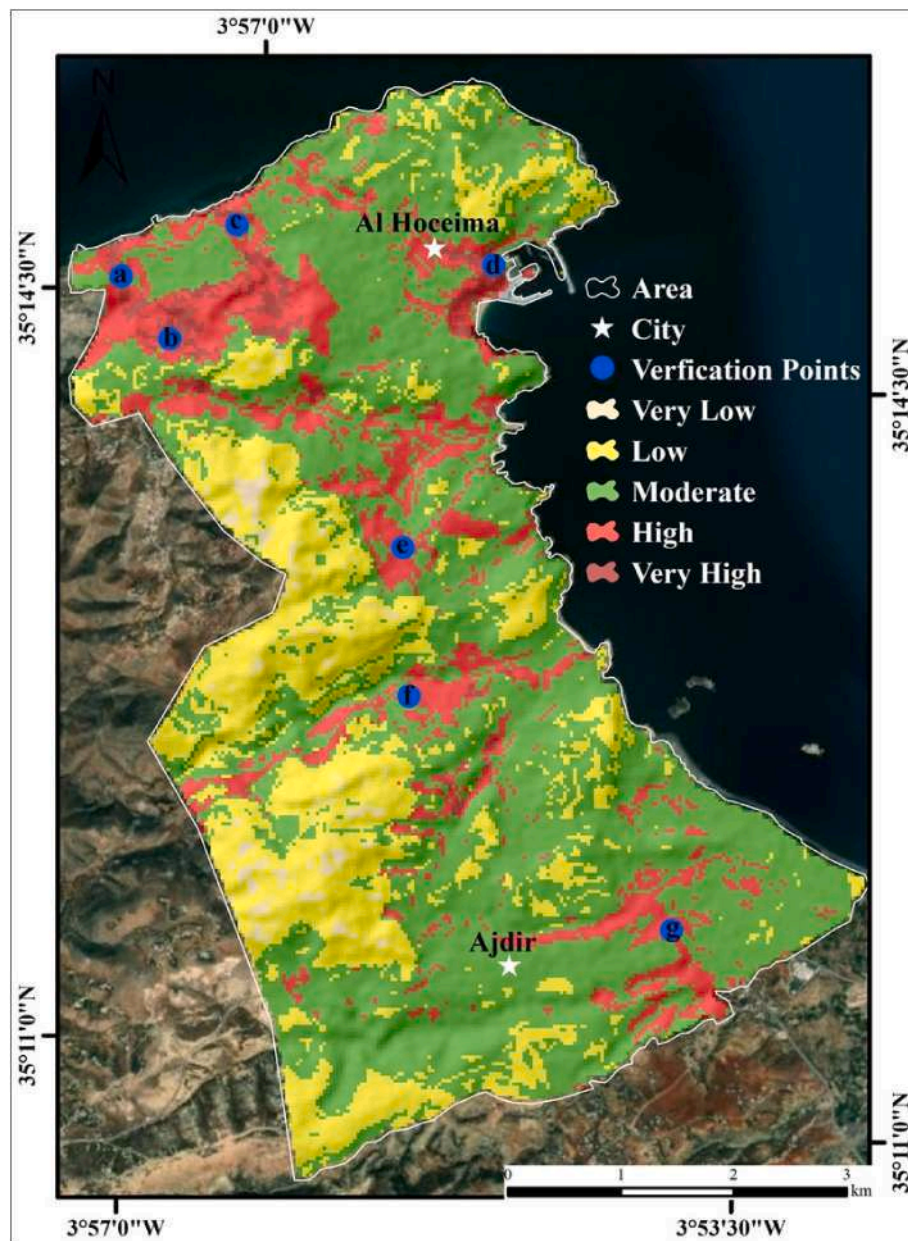


Fig. 8. Landslide susceptibility map.

facilitating rapid water infiltration into their structure. This results in a loss of strength, reduced compaction, and friction between particles, leading to an increased probability of soil instability.

The analysis also demonstrates that topographic parameters play a crucial role in contributing to this hazard through gravitational force, which is associated with the slope and altitude of local relief. This can exert significant traction on soil materials when the slope of the soil is steep and at a very high altitude. Knowing that the Al Hoceima region is located in an active seismotectonic zone, with the dominance of numerous active faults, the occurrence of landslides will be higher near these faults, as they can influence the soil through the effects of seismic activities, which are controlled by the significant faults present in the area, where these effects may diminish as one moves away from the fault. In addition to geological factors, hydrodynamic anomalies also contribute to the creation of these soil movements, where the hydrographic networks of the studied area influence geomorphological deformation due to variations in water levels stored in rivers and their flows, which can exert pressure on banks, especially during periods of

floods or high flows. This hydraulic pressure can lead to soil erosion and weaken their stability, thus increasing the risk of landslides, knowing that hydraulic erosion is often the initial phase of terrain instabilities.

The validation of the results could be made more robust by following these recommendations: (i) Conduct a more thorough sensitivity analysis: In addition to using the ROC method to evaluate the accuracy of the susceptibility map, other validation methods could be tested, such as cross-validation or splitting the data into training and test sets. This would allow for evaluating the stability and generalization of the model. (ii) Increase the sample size of historical landslides: The study is based on 40 historical landslides. It would be beneficial to increase the sample size, if possible, to get a more complete picture of the spatial distribution of the landslides and their relationship with the conditioning factors. (iii) Incorporate additional field data: In addition to the field observations carried out, more field data could be collected, such as geotechnical measurements, soil profiles, precipitation records, etc. This additional data could improve the characterization of the conditioning factors and the understanding of the landslide processes. (iv) Compare



Fig. 9. Same areas susceptible to landslides. (a, c). the Sabadia coastal road, (b). the Badés residential complex road, (d). The port maritime of Al Hoceima, (e). the Boujibar National Park, (f, g). National Highway of Al Hoceima.

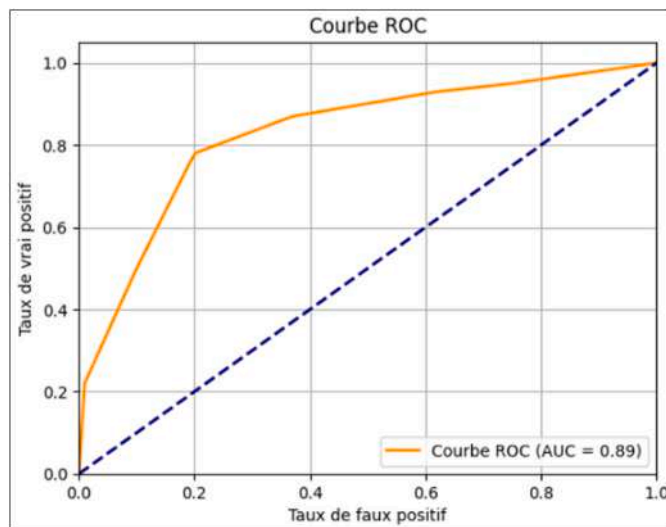


Fig. 10. The reliability rate of the results by AUC.

with other susceptibility methods: It would be useful to compare the results of the Frequency Ratio method used in this study with other susceptibility assessment approaches, such as expert knowledge-based models, alternative statistical methods, or even machine learning techniques. This would allow for evaluating the robustness and consistency of the results. (v) Validation through future landslide events: As new landslides occur in the study area; it would be beneficial to update and re-validate the susceptibility map using these data on recent events. This would help assess the long-term predictive capability of the map.

The limitations of the study: (i) While the use of the historical landslide inventory is crucial for validating the susceptibility model, it is recognized that these data can be incomplete or biased, particularly in regions where events are poorly documented. This can affect the accuracy of the model performance evaluation. (ii) The weighting of the different parameters influencing landslide susceptibility is a significant methodological challenge. Although the Frequency Ratio method has been applied, the choice of weights assigned to each factor involves a degree of subjectivity that can limit the reproducibility of the approach. (iii) Additional data, such as more detailed field observations, geotechnical measurements, or information on historical landslide

triggers, could help strengthen the validation of the model and evaluate its limitations more precisely. (iv) The integration of other validation techniques, such as sensitivity analyses or comparisons with other susceptibility assessment methods, could also contribute to a more robust analysis of the limitations of the developed model.

5. Conclusion

The Al Hoceima-Ajdjr region is considered an attractive tourist destination for all social categories, national or international, due to its mild climate, magnificent beaches, and preserved nature. These tourist activities constitute the main driver of the regional economy, and any change can negatively influence the socio-economic fabric, including landslides, which are prevalent throughout the region, especially in tourist sites.

Resolving this issue and achieving a result can contribute to the protection and prevention of this territory, done through the utilization of the frequency ratio model, which has been able to process a database containing more than 40 historical landslide incidents based on eight predisposing parameters to this hazard. To deduce the relationship between these parameters and the probability of soil instability and to develop a regional map of susceptibility to this risk, the frequency ratio used 70% of these data for model training. At the same time, the rest was reserved for testing, which allowed the model to predict the susceptibility weight of each section more easily.

The steps followed yield conclusions similar to those of previous studies of different approaches addressing this risk in this area. Furthermore, new findings mention the correlation and interaction between various factors and mass movements. These results illustrate that the Al Hoceima - Ajdir municipalities are almost entirely susceptible to terrain instability, with moderate to very high levels, particularly in their tourist areas, due to the conjunction of conditions conducive to landslides. This includes soil weakness characterized by a predominance of fragile, inconsistent soils prone to instability and the effective contribution of topographic parameters such as slope, where most unstable terrains are located in steep areas. Not to mention the influence of hydrographic networks and tectonic structures contribute to land deformations and show a significant prevalence of these landslides at their ends. Additionally, other parameters such as roads and land use may have contradictory impacts in this context, potentially accelerating soil instability processes and becoming post-collapse issues, especially as the inventory of historical landslides shows a high prevalence in residential areas.

The results collected by RF were evaluated by the ROC curve, yielding an AUC value of 0.89, thus reflecting the performance and reliability of the model. Despite these results and their validation in the field, the Al Hoceima-Ajdir area requires high-resolution and reliable results, which could be achieved in the future through new techniques and models, such as those based on machine learning or deep learning. Finally, the aspect of geostatistical methods and geomatics tools in the field can significantly contribute to identifying responsible consequences in the development of actionable risk maps, which can facilitate the implementation of plans and strategies for the prevention and protection of the environment, social, tourism, and economy against natural risks.

Funding

No funds were received for this research.

Ethical approval

Not applicable.

Consent to participate

Not applicable.

Consent to publish

Not applicable.

CRedit authorship contribution statement

Ayyoub Sbihi: Writing – original draft, Visualization, Validation, Supervision, Software, Resources, Methodology, Investigation, Formal analysis, Data curation, Conceptualization. **Mohamed Mastere:** Writing – review & editing, Writing – original draft, Visualization, Validation, Supervision, Software, Resources, Project administration, Methodology, Investigation, Formal analysis, Data curation, Conceptualization. **Brahim Benzougagh:** Writing – review & editing, Writing – original draft, Visualization, Validation, Supervision, Software, Resources, Project administration, Methodology, Investigation, Formal analysis, Data curation, Conceptualization. **Velibor Spalevic:** Writing – review & editing, Writing – original draft, Visualization, Validation, Resources, Project administration, Methodology, Investigation, Formal analysis, Data curation. **Paul Sestras:** Writing – original draft, Visualization, Validation, Software, Resources, Methodology, Investigation, Formal analysis, Data curation. **Mirjana Radovic:** Writing – original draft, Visualization, Validation, Software, Methodology, Investigation. **Slobodan B. Marković:** Writing – review & editing, Writing – original draft, Visualization, Validation, Software, Resources, Methodology, Investigation, Formal analysis, Data curation. **Lizny Jaufer:** Visualization, Software, Resources, Methodology, Investigation, Formal analysis, Data curation. **Shuraik Kader:** Writing – review & editing, Writing – original draft, Visualization, Validation, Resources, Project administration, Methodology, Investigation, Formal analysis, Data curation, Conceptualization.

Declaration of competing interest

The authors declare that they have no known competing financial interests or personal relationships that could have appeared to influence the work reported in this paper.

Data availability

Data will be made available on request.

References

- Akgun, A., Dag, S., Bulut, F., 2008. Landslide susceptibility mapping for a landslide-prone area (Findikli, NE of Turkey) by likelihood-frequency ratio and weighted linear combination models. *Environ. Geol.* 54, 1127–1143. <https://doi.org/10.1007/s00254-007-0882-8>.
- Azzouz, O., El Fellah, B., Chalouan, A., 2002. *Processus de glissement dans le Massif de Bokoya (Rif interne, Maroc) : exemple de Cala Bonita*. Bulletin de l'Institut scientifique, Rabat, section Sciences de la Terre 24, 33–40.
- Azzouz, O., 1992. *Lithostratigraphie et tectonique hercynienne des terrains paléozoïques ghomarides du Massif des Bokoya (Rif Interne, Maroc)*. These 3eme Cycles. Faculté des Sciences 208.
- Basharat, M., Rohn, J., Baig, M.S., Khan, M.R., 2014. Spatial distribution analysis of mass movements triggered by the 2005 Kashmir earthquake in the Northeast Himalayas of Pakistan. *Geomorphology* 206, 203–214. <https://doi.org/10.1016/j.geomorph.2013.09.025>.
- Bammou, Y., Benzougagh, B., Abdessalam, O., Brahim, I., Kader, S., Spalevic, V., Sestras, P., Ercişli, S., 2024a. Machine learning models for gully erosion susceptibility assessment in the Tensift catchment, Haouz Plain, Morocco for sustainable development. *J. Afr. Earth Sci.* 213, 105229 <https://doi.org/10.1016/j.jafrearsci.2024.105229>.
- Bammou, Y., Benzougagh, B., Igmoullan, B., Ouallali, A., Kader, S., Spalevic, V., Marković, S.B., 2024b. Optimizing flood susceptibility assessment in semi-arid regions using ensemble algorithms: a case study of Moroccan High Atlas. *Nat. Hazards*. <https://doi.org/10.1007/s11069-024-06550-z>.
- Bashir, O., Bangroo, S.A., Shafai, S.S., Senesi, N., Kader, S., Alamri, S., 2024a. Geostatistical modeling approach for studying total soil nitrogen and phosphorus under various land uses of North-Western Himalayas. *Ecol. Inf.* 80, 102520 <https://doi.org/10.1016/j.ecoinf.2024.102520>.
- Bashir, O., Bangroo, S.A., Shafai, S.S., Senesi, N., Naikoo, N.B., Kader, S., Jaufer, L., 2024b. Unlocking the potential of soil potassium: geostatistical approaches for understanding spatial variations in Northwestern Himalayas. *Ecol. Inf.* 81, 102592 <https://doi.org/10.1016/j.ecoinf.2024.102592>.
- Bashir, O., Bangroo, S.A., Shafai, S.S., Shah, T.I., Kader, S., Jaufer, L., Michael, R., Ksibi, M., Spalevic, V., Sestras, P., Marković, S.B., Billi, P., Ercişli, S., Hysa, A., 2024c. Mathematical vs. machine learning models for particle size distribution in fragile soils of North-Western Himalayas. *J. Soils Sediments*. <https://doi.org/10.1007/s11368-024-03820-y>.
- Bathrellos, G.D., Koukouvelas, I.K., Skilodimou, H.D., Nikolakopoulos, K., Vgenopoulos, A.L., 2024. Landslide causative factors evaluation using GIS in the tectonically active Glafkos River area, northwestern Peloponnese, Greece. *Geomorphology* 461, 109285. <https://doi.org/10.1016/j.geomorph.2024.109285>.
- Bathrellos, G.D., Skilodimou, H.D., Zygouri, V., Koukouvelas, I., 2021. Landslide: a recurrent phenomenon? Landslide hazard assessment in mountainous areas of central Greece. *Z. Geomorphol.* 63 (1), 95–114. <https://doi.org/10.1127/zfg/2021/0670>.
- Benzougagh, B., Al-Quraishi, A.M.F., Bammou, Y., Kader, S., El Brahimi, M., Sadkaoui, D., Ladel, L., 2024. Spectral angle mapper approach (sam) for land degradation mapping: a case study of the oued lahdar watershed in the pre-rif region (Morocco). In: *Natural Resources Deterioration in MENA Region: Land Degradation, Soil Erosion, and Desertification*. Springer International Publishing, Cham, pp. 15–35. <https://doi.org/10.1007/978-3-031-58315-2>.
- Benzougagh, B., Meshram, S.G., Baamar, B., Dridri, A., Boudad, L., Sadkaoui, D., Mimich, K., 2020. Relationship between landslide and morpho-structural analysis: a case study in Northeast of Morocco. *Appl. Water Sci.* 10 (7), 1–10. <https://doi.org/10.1007/s13201-020-01258-4>.
- Chalouan, A., Ouazani-Touham, A., Mouhir, L., Saji, R., Benmakhlof, M., 1995. *Les failles normales à faible pendage du Rif interne (Maroc) et leur effet sur l'amincissement crustal du domaine D'Alboran*.
- Chen, W., Panahi, M., Tsangaratos, P., Shahabi, H., Ilia, I., Panahi, S., Li, S., Jaafari, A., Ahmad, B.B., 2019a. Applying population-based evolutionary algorithms and a neuro-fuzzy system for modeling landslide susceptibility. *Catena* 172 (Complete), 212–231. <https://doi.org/10.1016/j.catena.2018.08.025>.
- Chen, W., Li, J., Li, L., Wang, G., 2019b. Landslide susceptibility assessment based on random forest algorithm in an earthquake-prone area, China. *Nat. Hazards* 98 (2), 605–621. <https://doi.org/10.1117/12.2538059>.
- Crozier, M., Glade, T., 2010. Hazard assessment for risk analysis and risk management. In: Alcántara-Ayala, I., Goudie, A.S. (Eds.), *Geomorphological Hazards and Disaster Prevention*. Cambridge University Press, Cambridge, pp. 221–232. <https://doi.org/10.1017/CBO9780511807527.018> chapter.
- Ding, Q., Chen, W., Hong, H., 2017. Application of frequency ratio, weights of evidence and evidential belief function models in landslide susceptibility mapping. *Geocarto Int.* 32 (6), 619–639. <https://doi.org/10.1080/10106049.2016.1165294>.
- El Fahchouch, A.N., Brahim, L.A., Raji, O., Khouakhi, A., 2015. Apport du SIG et de la télédétection dans la modélisation spatiale de la susceptibilité aux mouvements de terrain dans la région d'Al Hoceima, Rif Oriental, Maroc. *Afrique Science. Revue Internationale des Sciences et Technologie* 11 (2), 44–57.
- El Khattabi, M., 2023. *Etude et gestion des risques liés aux glissements de terrain en milieu urbain : application à la ville d'Al Hoceima (Nord du Maroc)*. Université de Lille ; Université Mohammed Premier Oujda (Maroc). Doctoral dissertation.
- Fallah-Zazuli, M., Vafaiejad, A., Alesheykh, A.A., Modiri, M., Aghamohammadi, H., 2019. Mapping landslide susceptibility in the Zagros Mountains, Iran: a comparative study of different data mining models. *Earth Sci Inform* 12 (4), 615–628. <https://doi.org/10.1007/s12145-019-00389-w>.
- García-Rodríguez, M.J., Malpica, J.A., Benito, B., Díaz, M., 2008. Susceptibility assessment of earthquake-triggered landslides in El Salvador using logistic

- regression. *Geomorphology* 95 (3), 172–191. <https://doi.org/10.1016/j.geomorph.2007.06.001>.
- Glade, T., Anderson, M.G., Crozier, M.J., 2005. Landslide hazard and risk: issues, concepts, and approach. In: *Landslide Risk Assessment*. John Wiley & Sons, pp. 1–40. <https://doi.org/10.1002/9780470012659.ch1>.
- Glade, T., Crozier, M.J., 2005. Landslide hazard and risk: concluding comment and perspectives. In: *Landslide Hazard and Risk*. Wiley, Chichester, pp. 767–774. <https://doi.org/10.1002/9780470012659.ch26>.
- Guzzetti, F., Carrara, A., Cardinali, M., Reichenbach, P., 1999. Landslide hazard evaluation: a review of current techniques and their application in a multi-scale study, Central Italy. *Geomorphology* 31 (1–4), 181–216. [https://doi.org/10.1016/S0169-555X\(99\)00078-1](https://doi.org/10.1016/S0169-555X(99)00078-1).
- Guzzetti, F., Reichenbach, P., Ardizzone, F., Cardinali, M., Galli, M., 2006. Estimating the quality of landslide susceptibility models. *Geomorphology* 81 (1–2), 166–184. <https://doi.org/10.1016/j.geomorph.2006.04.007>.
- Harmouzi, H., Nefeslioglu, H.A., Rouai, M., Sezer, E.A., Dekayir, A., Gokceoglu, C., 2019. Landslide susceptibility mapping of the Mediterranean coastal zone of Morocco between Oued Laou and El Jebha using artificial neural networks (ANN). *Arabian J. Geosci.* 12, 1–18. <https://doi.org/10.1007/s12517-019-4892-0>.
- Ja, S., 1988. Measuring the accuracy of diagnostic systems. *Science (New York, N.Y.)* 240 (4857). <https://doi.org/10.1126/science.3287615>.
- Kanungo, D., Arora, M., Sarkar, S., Gupta, R.P., 2009. Landslide susceptibility zonation (Ish) mapping – a review. *J. South Asia Disaster Stud.* 2, 81–105. https://doi.org/10.1142/98127016050038_0038.
- Karpouza, M., Chousianitis, K., Bathrellos, G.D., Skilodimou, H.D., Kaviris, G., Antonarakou, A., 2021. Hazard zonation mapping of earthquake-induced secondary effects using spatial multi-criteria analysis. *Nat. Hazards* 109 (1), 637–669. <https://doi.org/10.1007/s11069-021-04852-0>.
- Labriki, A., Chakiri, S., Nouaim, W., Allouza, M., Bejjaji, Z., Ezzayani, J., 2016. Etude géotechnique et modélisation volumique des zones instables ; processus d'effondrement de la falaise adjacente à la voie de contournement du port d'Al Hoceima (Rif, Maroc). *Eur. Sci. J.* 13 (9), 251–265. <https://doi.org/10.19044/esj.2017.v13n9p251>.
- Lee, S., Talib, J.A., 2005. Probabilistic landslide susceptibility and factor effect analysis. *Environ. Geol.* 47 (7), 982–990. <https://doi.org/10.1007/s00254-005-1228-z>.
- Lee, S., Min, K., 2001. Statistical analysis of landslide susceptibility at Yongin, Korea. *Environ. Geol.* 40, 1095–1113. <https://doi.org/10.1007/s002540100310>.
- Mastere, M., El Fellah, B., Maquaire, O., 2020. Landslides inventory map as a first step for hazard and risk assessment: Rif mountains, Morocco. *Bulletin de l'institut Scientifique, Rabat, Section Sciences De La Terre* 42, 49–62.
- Michard, A., Chalouan, A., Feinberg, H., Goffé, B., Montigny, R., 2002. How does the Alpine belt end between Spain and Morocco? *Bull. Soc. Geol. Fr.* 173 (1), 3–15.
- Mohamed, R., Lahsen, A.B., 2018. Qualitative and quantitative evaluation of the ground movement risk on an urban cartographic scale Example of QUEMADO (Eastern Rif, Morocco). In: *MATEC Web of Conferences*, vol. 149. EDP Sciences, 02039. <https://doi.org/10.1051/mateconf/201814902039>.
- Montgomery, D.R., Dietrich, W.E., 1994. A physically based model for the topographic control on shallow landsliding. *Water Resour. Res.* 30 (4), 1153–1171. <https://doi.org/10.1029/93WR02979>.
- Ouallali, A., Kader, S., Bammou, Y., Aqnouy, M., Courba, S., et al., 2024. Assessment of the erosion and outflow intensity in the Rif region under different land use and land cover scenarios. *Land* 13 (2). <https://doi.org/10.3390/land13020141>.
- Pourghasemi, H.R., Pradhan, B., Gokceoglu, C., 2012. Application of fuzzy logic and analytical hierarchy process (AHP) to landslide susceptibility mapping at Haraz watershed, Iran. *Nat. Hazards* 63 (2), 965–996. <https://doi.org/10.1007/s11069-012-0217-2>.
- Rahali, H., 2019. Improving the reliability of landslide susceptibility mapping through spatial uncertainty analysis: a case study of Al Hoceima, Northern Morocco. *Geocarto Int.* 34 (1), 43–77. <https://doi.org/10.1080/10106049.2017.1357767>.
- Sadkaoui, D., Brahim, B., Kader, S., Agharroud, K., Miharaje, A.-I., Aluni, K., Aassoumi, H., Sassioui, S., Spalevic, V., Sestras, P., 2024. Evaluation of tectonic activity using morphometric indices: study of the case of Taïliloute ridge (middle-Atlas region, Morocco). *J. Afr. Earth Sci.* 213, 105219. <https://doi.org/10.1016/j.jafrearsci.2024.105219>.
- Sidle, R.C., Bogaard, T.A., 2016. Dynamic earth system and ecological controls of rainfall-initiated landslides. *Earth Sci. Rev.* 159, 275–291. <https://doi.org/10.1016/j.earscirev.2016.05.013>.
- Talhaoui, A., Aberkan, M., Brahim, I., El Mouraouah, A., 2005. Risques géologiques et activité sismique dans la région d'Al Hoceima (Maroc): Approche de la quantification des facteurs responsables du déclenchement des instabilités de terrain Geological hazards and seismic activity within the area of Al Hoceima (Morocco): Approach of quantifying factors responsible for the triggering of the ground instabilities. *Pangea infos* 43, 3–18.
- Yilmaz, I., 2009. Landslide susceptibility mapping using frequency ratio, logistic regression, artificial neural networks and their comparison: a case study from Kat landslides (Tokat—Turkey). *Comput. Geosci.* 35 (6), 1125–1138. <https://doi.org/10.1016/j.cageo.2008.08.007>.
- Zorn, M., Komac, B., 2007. Probability modelling of landslide hazard. *Acta Geogr. Slov.* 47 (2), 139–169.

Rainfall-runoff modeling based on HEC-HMS model: a case study in an area with increased groundwater discharge potential

[view article impact >](#)



[View altmetric score >](#)

Share on

- Mihai Valentin Herbei¹ Codruța Bădăluță-Minda² Cosmin Alin Popescu¹
 Adina Horablagă^{1*} Lucian Octavian Dragomir^{1*} George Popescu¹
 Shuraik Kader^{3,4} Paul Sestras^{5,6,7}

Edited by



Velibor Spalevic

Reviewed by



Rastko Marković



Ana M. Pop



Abdessalam OUALALI

[Download a PDF](#)

¹ Department of Sustainable Development and Environmental Engineering, University of Life Sciences "King Mihai I" from Timisoara, Timisoara, Romania

² Department of Hydrotechnical, Politehnica University Timisoara, Timisoara, Romania

³ School of Engineering and Built Environment, Griffith University, Nathan, QLD, Australia

⁴ Green Infrastructure Research Labs (GIRLS), Cities Research Institute, Griffith University, Gold Coast, QLD, Australia

⁵ Faculty of Civil Engineering, Technical University of Cluj-Napoca, Cluj-Napoca, Romania

⁶ Faculty of Forestry and Cadastre, University of Agricultural Sciences and Veterinary Medicine Cluj-Napoca, Cluj-Napoca, Romania

⁷ Academy of Romanian Scientists, Bucharest, Romania

FRONTIERS IN WATER

Publisher name: FRONTIERS MEDIA SA

Journal Impact Factor™

2.6

2023

2.6

Five Year

JCR Category	Category Rank	Category Quartile
WATER RESOURCES <i>in ESCI edition</i>	51/128	Q2

Source: Journal Citation Reports 2023. [Learn more](#)

Journal Citation Indicator™

0.6

2023

0.64

2022

JCI Category	Category Rank	Category Quartile
WATER RESOURCES	57/128	Q2





OPEN ACCESS

EDITED BY

Velibor Spalevic,
University of Montenegro, Montenegro

REVIEWED BY

Ana M. Petrović,
Serbian Academy of Sciences and Arts, Serbia
Rastko Marković,
University of Niš, Serbia
Abdessalam Ouallali,
University of Hassan II Casablanca, Morocco

*CORRESPONDENCE

Adina Horablaga
✉ adinahorablaga@usvt.ro
Lucian Octavian Dragomir
✉ luciandragomir@usvt.ro

RECEIVED 02 August 2024

ACCEPTED 24 September 2024

PUBLISHED 11 October 2024

CITATION

Herbei MV, Bădăluță-Minda C, Popescu CA, Horablaga A, Dragomir LO, Popescu G, Kader S and Sestras P (2024) Rainfall-runoff modeling based on HEC-HMS model: a case study in an area with increased groundwater discharge potential.
Front. Water 6:1474990.
doi: 10.3389/frwa.2024.1474990

COPYRIGHT

© 2024 Herbei, Bădăluță-Minda, Popescu, Horablaga, Dragomir, Popescu, Kader and Sestras. This is an open-access article distributed under the terms of the [Creative Commons Attribution License \(CC BY\)](https://creativecommons.org/licenses/by/4.0/). The use, distribution or reproduction in other forums is permitted, provided the original author(s) and the copyright owner(s) are credited and that the original publication in this journal is cited, in accordance with accepted academic practice. No use, distribution or reproduction is permitted which does not comply with these terms.

Rainfall-runoff modeling based on HEC-HMS model: a case study in an area with increased groundwater discharge potential

Mihai Valentin Herbei¹, Codruța Bădăluță-Minda²,
Cosmin Alin Popescu¹, Adina Horablaga^{1*},
Lucian Octavian Dragomir^{1*}, George Popescu¹, Shuraik Kader^{3,4}
and Paul Sestras^{5,6,7}

¹Department of Sustainable Development and Environmental Engineering, University of Life Sciences "King Mihai I" from Timisoara, Timisoara, Romania, ²Department of Hydrotechnical, Politehnica University Timisoara, Timisoara, Romania, ³School of Engineering and Built Environment, Griffith University, Nathan, QLD, Australia, ⁴Green Infrastructure Research Labs (GIRLS), Cities Research Institute, Griffith University, Gold Coast, QLD, Australia, ⁵Faculty of Civil Engineering, Technical University of Cluj-Napoca, Cluj-Napoca, Romania, ⁶Faculty of Forestry and Cadastre, University of Agricultural Sciences and Veterinary Medicine Cluj-Napoca, Cluj-Napoca, Romania, ⁷Academy of Romanian Scientists, Bucharest, Romania

The Hydrologic Modeling System (HEC-HMS), designed to accurately simulate precipitation-runoff processes in various watershed types, was employed in our study to establish a model for a particular watershed. Consequently, we planned to create a rainfall-runoff model to investigate the specific characteristics of floods, assess some pre-diction models, and issue assumptions about their viability, which could be beneficial in establishing flood warning systems. The model was developed using daily precipitation data collected from different rain gauge stations in the Gilort watershed, located in southern Romania. The study employed the HEC-GeoHMS terrain processing tool, utilizing a digital elevation design to build a hydrological model. The statistical indicators used to evaluate the runoff mechanisms, specifically regression, coefficient of determination, correlation coefficient, index of agreement (Willmott index), and the root mean squared error (RMSE), showed a strong relationship between the simulated and recorded flow of the watershed. The leaking model was assessed using other statistical parameters, including the deviation of runoff volumes ($Dv = 6.40\%$), Nash–Sutcliffe efficiency ($NSE = 0.908$), and Kling-Gupta efficiency ($KGE = 0.901$). These parameters confirmed that the simulated data closely matched the observed data, indicating an effective association, and were considered reliable indicators of the model's goodness of fit, ensuring its reliability and efficacy.

KEYWORDS

catchment area, discharge, hydrologic processes, precipitation, runoff, watershed systems

1 Introduction

Floods are typically responsible for around one-third of all global disasters. Unfortunately, these extraordinary phenomena spread quickly, and it is predicted that both the frequency and intensity of damage will increase in the future (Jonkman, 2005; Bronstert, 2003; Angelakis et al., 2023; Balica et al., 2023). Floods are the predominant form of natural calamity, arising

from the inundation of territory that is typically dry due to an excess of water (Dixit, 2003; Merz et al., 2021). In tropical regions, floods frequently result from storms generated by tropical cyclones or tsunamis along the coast. Conversely, in temperate regions, floods are commonly triggered by intense rainfall or the rapid thawing of snow (Woodruff et al., 2013; Eccles et al., 2019). Flooding can lead to extensive destruction, causing fatalities and harm to private possessions and vital public health facilities. The occurrence and strength of floods are on the rise, and this trend is projected to increase as a result of climate change (Whitfield, 2012; Kron et al., 2012; Jain and Lall, 2001).

Basins are crucial elements for the hydrological regulation and sustainable utilization of natural resources within this system. The main factors that determine drainage networks are the geological and morphological structure, topography, and climatic elements (Tariq et al., 2023; Bryndal, 2023; Bouramtane et al., 2020). Morphometric studies are valuable tools for planners to enhance the effectiveness of urbanization, agricultural, and industrial activities within a watershed (Venkatesh and Anshumali, 2019; Ghosh and Gope, 2021). Several studies using the geoprocessing features of ArcGIS software have shown that different drainage networks are viable and sustainable, depending on the shape of the basin, the texture of the drainage, and the morphometric parameters of the relief (Bharath et al., 2021; Bahiru et al., 2024; Kumar Rai et al., 2017). Remote sensing is a beneficial technique for quickly obtaining data about the Earth's surface, including Digital Elevation Models (DEM) and Land Use and Land Cover (LULC) information (Al-Taei et al., 2023; Ahmad et al., 2023; Sestras et al., 2019). This data can be employed as input for hydrological models (Bilaşco et al., 2021). In addition, Geographic Information Systems (GIS) provide a platform for simulating hydrological models (Gambolati et al., 2002; Knebl et al., 2005; Thakur et al., 2017).

Adequate understanding of watershed runoff is crucial for the planning and design of water resources and associated projects (Zezelew and Melesse, 2018; Sudriani et al., 2023). The runoff simulation model is a hydrological model that analyses the response of a water basin to precipitation and predicts floods. It is used to enhance water resource management and implement preventive measures against floods in specific hydrographic basins (Teng et al., 2017; Du et al., 2012; Al-Sabhan et al., 2003). The Hydrologic Engineering Centre-Hydrologic Modeling System (HEC-HMS) model is a hydrological model that has been effectively employed with conclusive results (Visweshwaran, 2017). This model possesses the capacity to replicate floods in both immediate and prolonged scenarios. The timing of runoff can occasionally affect the effects of flooding. Consequently, a specific amount of rainfall can lead to a substantial flood in certain areas of the watershed, while causing a modest flood in other areas (Natarajan and Radhakrishnan, 2019; Masseroni et al., 2016; Ben Khélifa and Mosbahi, 2022; Ansari et al., 2023).

The process of flood modeling may be efficiently conducted by utilizing HEC-HMS and GIS. The outcomes of this modeling aid in making informed decisions and implementing protective measures to mitigate the adverse impacts of floods (Dunca and Bădăluță-Minda, 2018; Kumar et al., 2023). ArcGIS utilizes HEC-GeoHMS as a preliminary tool for the hydrologic models. The outputs produced by HEC-GeoHMS, such as the grid, watershed boundary, sub-river basin boundary, and the centroid of the watershed and sub-watershed, are

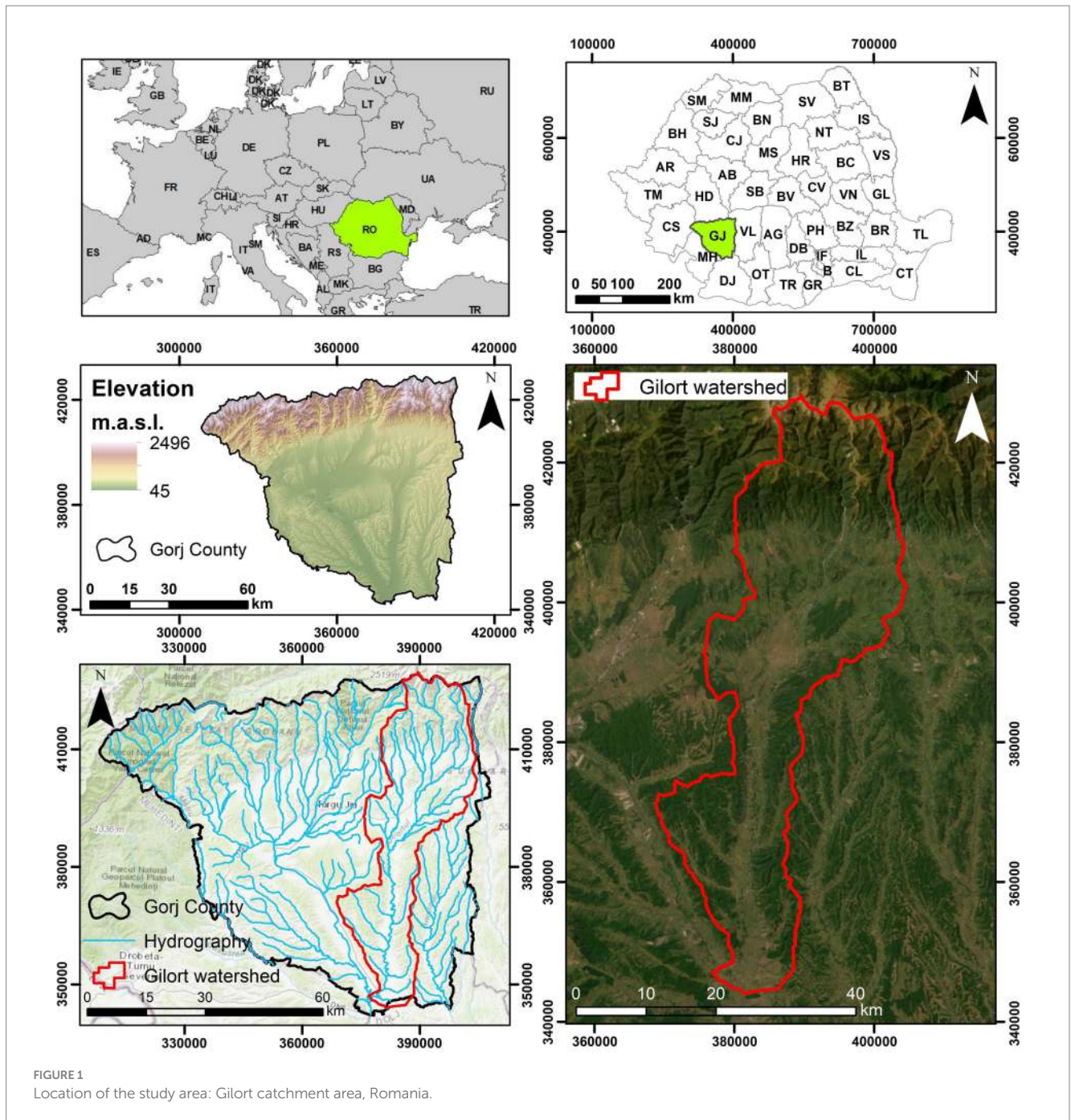
subsequently imported into the Hydrologic Modeling System for the purpose of conducting the simulation (Castro and Maidment, 2020; Ramly and Tahir, 2016). HEC HMS and GIS technologies have undergone extensive testing and have been actively utilized globally for flood modeling purposes for numerous years (Seth et al., 2006; Pullar and Springer, 2000; Natarajan and Radhakrishnan, 2019; Natarajan and Radhakrishnan, 2020). The demand for a modeling system is also driven by the necessity to effectively plan and manage hydrographic basins, enabling accurate decision-making regarding timely flood alerts and the identification of flood risk zones (Taherizadeh et al., 2023; Mustafa et al., 2023; Bilaşco et al., 2022).

Climate change, extreme weather events, deforestation, and anthropogenic interference adversely affect the environment and the socio-economic conditions of contemporary society. These factors have intensified catastrophic events, resulting in fatalities and considerable material devastation. Floods are a substantial global issue, resulting in adverse economic consequences. Consequently, the attention of scientists and society in this area is current. Significant emphasis was placed on evaluating and mitigating the impacts of floods globally, including in Europe and Romania (Peptenatu et al., 2020; Petrişor et al., 2020; Grecu et al., 2017; Ionita and Nagavciuc, 2021; Sestras et al., 2023b; Svetlana et al., 2015). The primary objective of this hydrological inquiry and modeling was to conduct a quantitative analysis of the surface flows within the Gilort watershed, located in the southern region of Romania, in order to produce simulation outcomes. Subsequently, these can be employed in combination with various software applications to analyze water availability, topography drainage, flow prediction, future climatic effects, reservoir spillway design, flood damage mitigation, floodplain regulation, and systems operation. To validate the precision of the prediction models for the match between simulated flows and real flows, it was proposed to utilize multiple statistical indicators. Hence, the validation of the models was performed using regression, coefficient of determination (R^2), Pearson correlation coefficient (r), the root mean squared error (RMSE). In addition, the index of agreement (d) as stated by Willmott (1981) was computed, as well as other relevant indicators, as an established measure for evaluating the precision of the model's predictions. Consequently, the objectives of this study were to evaluate the reliability of the HEC-HMS hydrological modeling system in estimating and simulating the rainfall-runoff process in a certain area of Romania, associated with excessive rainfall. Using statistical indicators, we also examined the reliability of the model developed for the Gilort watershed.

2 Materials and methods

2.1 The study area and timeframe used for creating the proposed model

The research was conducted in a region associated with the Gilort River, which is a left tributary of the Jiu River, located in the southern region of Romania (Figure 1). The Gilort river spans 116 kilometers in length and originates from the Parâng Mountains, namely from the Parângul Mare Peak (2,519 m a.s.l.). It is fed by two primary springs located at an altitude of 2,350 m a.s.l. The river is immediately bordered on the right by Mândra Peak and on the left by Gruiu Peak. The river traverses the western section of the Subcarpathian Olt region,



encompassing a drainage basin of more than 1,348 km², with the area having an average elevation of 544 m.a.s.l. Upstream, prior to exiting the Parâng Mountains, the river exhibits a characteristic mountain valley with steep slopes exceeding 65%, a bed profile in the shape of a V, and the formation of gorges on a small section with calcareous deposits.

The daily rainfall data from 2015 to 2020 obtained from the rain gauge stations in the basin were used as reference data for the development of the proposed model. During the year 2015, the month of July experienced a significant amount of rainfall, with precipitation levels ranging from 176.5 mm in Săcelu to 231.8 mm in Turburea (Table 1). Precipitation started on July 2, with recorded amounts ranging from 33.4 mm in Ciocadia to 53.3 mm in Turburea. The precipitation occurred as a result of the expansion of the Azoric

anticyclone, combined with a rain front originating from the Mediterranean Sea. Consequently, during the period of July 2015, substantial amounts of precipitation were recorded (Administratia Nationala De Meteorologie, 2024; Meteoblue AG, 2024). Figure 2 depicts the flood hydrographs recorded at hydrometric stations in the Gilort hydrographic basin from July 8 to 23, 2015.

2.2 Hydrological modeling

To perform the desired hydrologic simulations, the Hydrologic Modeling System (HEC-HMS), an open-source software developed by the US Army Corps of Engineers Hydrologic Engineering Center, was

TABLE 1 Rainfall regime in July 2015 (Administratia Nationala De Meteorologie, 2024).

No.	River	Hydrometric station	Rainfall recorded on 2015.07.02 (mm)	Max rainfall in 24 h from per. 10–2015.07.13 (mm)	Total rainfall July 2015 (mm)
1	Galbenu	Baia de Fier	41.7	26.0	206.7
2	Ciocadia	Ciocadia	33.4	49.6	211.9
3	Blahnița	Săcelu	50.8	14.3	176.5
5	Gilort	Târgu Cărbunești	34.1	34.2	187.0
6	Gilort	Turburea	53.3	26.1	231.8

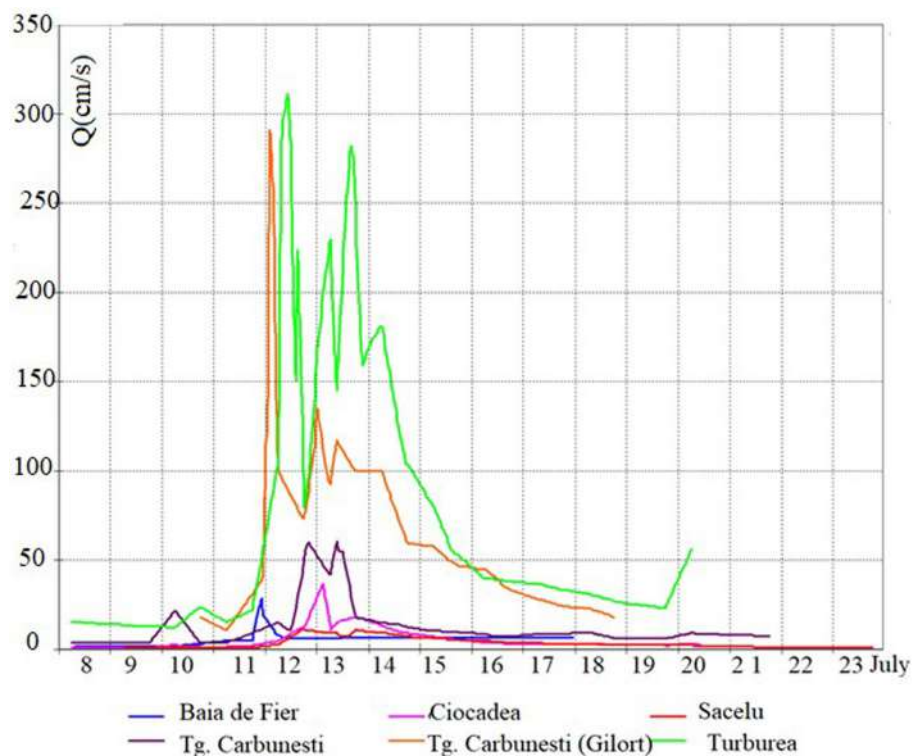


FIGURE 2
Flood hydrographs at hydrometric stations in the Gilort hydrographic basin from July 8–23, 2015.

used to estimate the hydrologic response of the chosen basin, with precipitation as input. In addition, HEC-Geo HMS was used as a geospatial hydrological tool that allows the visualization of spatial information, the extraction of physical characteristics of watersheds from SRTM DEM (Shuttle Radar Topography Mission Digital Elevation Model) data (Yang et al., 2011), in order to develop hydrological parameters, as well as the construction of inputs to hydrological models (Fan et al., 2013; Fleming and Doan, 2013). Figure 3 depicts the hydrological modeling in our context. For this study, the Soil Conservation Service (SCS) Curve Number (CN) method (SCS CN) was chosen, which implements the curve number (CN) methodology, depending on the basin characteristics that generate the runoff such as soil type, land use, soil surface conditions and previous moisture conditions. A digital elevation model (DEM) with a cell size of 30×30 m was utilized, together with land use coverage records, to obtain the curve number (CN). CN is the parameter on which the SCS method can be applied (Ponce and Hawkins, 1996; Ross et al., 2018). Based on land use, for the territory of Romania, the values of the CN index were

established (Chendeş, 2007). Furthermore, the SCS unit hydrograph method was used to simulate the flows in certain sections of the watercourses, using several input parameters (delay time, curve number, etc.). Given that soil moisture significantly influences the infiltration of water into the soil, impacting the amount and speed of runoff (Hawley and McCuen, 1982), the simulation method took into account the AMC index (antecedent moisture conditions) based on the AMC class (Chow et al., 1988) provided in Table 2.

The SCS – CN approach converts precipitation within the hydrographic basin into surface runoff. The designation of the drainage curve is determined by the hydrological soil group of the region, land utilization, treatment, and hydrological condition. The CN (curve number) values increase linearly with runoff potential and decrease inversely with infiltration coefficient. The categorization and allocation of values to the CN index have been modified and implemented (Chendeş, 2007) using both USDA textbooks and other established classifications found in the global literature. The SCS model is based on an extensively utilized equation for drainage layer,

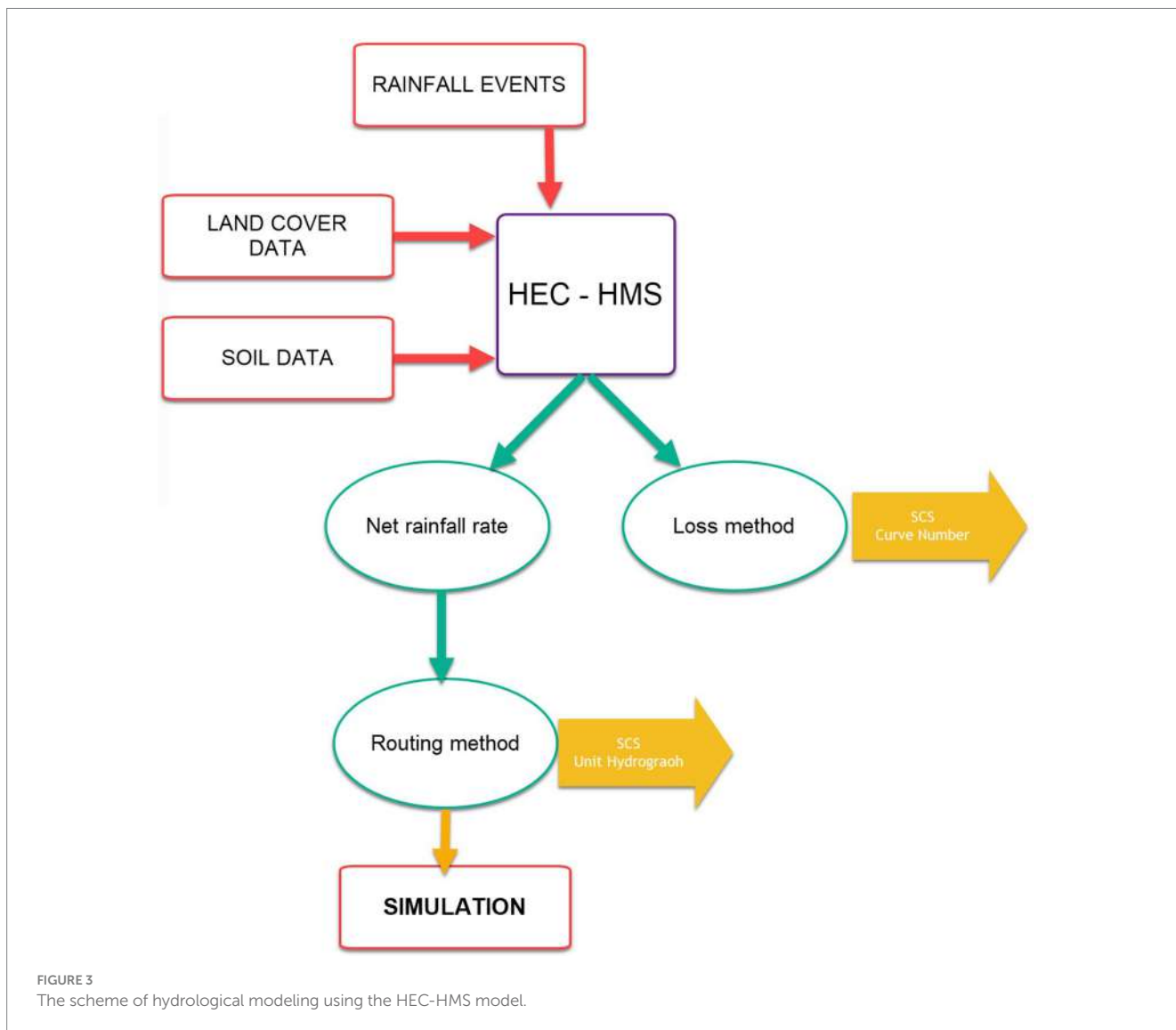


TABLE 2 Description of AMC classes (antecedent moisture conditions) considered in the simulation process (Chow et al., 1988).

AMC class	Description	Rainfall
I	Dry soil	< 12.7 mm during the summer and when there is rainfall < 35.6 mm during the autumn-spring precipitation
II	Soils with normal infiltration conditions	12.7–28 mm in the rainfall range of a high frequency
III	Saturated soil	< 28 mm when there is no heavy rainfall > 35.4 mm when large amounts of precipitation are recorded

which does not directly account for the quantity of infiltrating water. The equation is as follows (Equation 1; Mihalik et al., 2008):

$$Q = \frac{(P - I_a)^2}{P - I_a + S} \tag{1}$$

where: Q – accumulated runoff depth (mm); P – accumulated rainfall depth (mm); I_a – initial abstraction (mm); S – potential maximum retention after runoff begins.

Different soil groups have different infiltration rate and CN values (Muthu and Santhi, 2015; Table 3).

For the transfer function, the unitary hydrograph SCS method was used, which is successfully applied to simulate the flow rates of water courses. This method requires a lag time parameter in h, which is defined as the length of time between the centroid of the precipitation mass and the peak discharges (Equations 2, 3; Fleming and Brauer, 2016).

$$T_{Lag} = 0.6 \times T_c \tag{2}$$

$$T_c = 0.0195 \times L^{0.77} \times S^{-0.385} \tag{3}$$

where: T_c – concentration time (h); L – the channel flow length (m); S – dimensionless main channel slope.

The excess rain was transformed into direct runoff by means of the SCS unitary hydrograph method, and the parameters required to

TABLE 3 SCS soil hydrologic groups and infiltration rates (Muthu and Santhi, 2015).

Soil group	Runoff potential	Infiltration rate (mm/h)	Observation
A	Low	> 7.5	High rate of water transmission
B	Moderate	3.8–7.5	Moderate rate of water transmission
C	Moderately high	1.3–3.8	Moderate rate of water transmission
D	High	< 1.3	Low rate of water transmission

TABLE 4 The hydrological model of the HEC-HMS catchment (Chendes, 2007).

No.	Model	Method	Parameter required (unit) Initial abstraction (mm)
1	Lost rate parameter	SCS curve number	Curve number and impervious area (%)
2	Runoff transform	SCS unit hydrograph	Lag time (min)
3	Routing method constants	Muskingum	Travel time (K) and dimensionless weight (X)

run this model are shown in Table 4. Basin lag time values were calculated using Equation (4) (Mishra and Singh, 2013):

$$\text{Lag} = \frac{(S + 1)^{0.7} \cdot L^{0.8}}{1900 \cdot Y^{0.5}} \tag{4}$$

where: S – maximum retention (mm); Lag – basin lag time (hour); L – hydraulic length of the catchment (longest flow path) (feet); Y – basin slope (%).

The standard error of the estimate of the dependent variable is equal to the standard deviation of the residuals with the root mean square error (RMSE) and determined by Equation (5):

$$\hat{\sigma} = \text{RMSE} = S_y \sqrt{1 - R^2} = \sqrt{\frac{\sum_{j=1}^N (y_j - \hat{y}_j)^2}{N}} \tag{5}$$

where: N is the number of data points; y_j is the actual values; \hat{y}_j is the predicted values. The larger the RMSE, the larger the difference between the predicted and observed values, meaning that the regression model fits the data worse. Conversely, the smaller the RMSE, the better a model is able to fit the data.

The Pearson correlation method is one of the most used methods for numerical variables and assigns a value between –1 and 1, where 0 is no correlation, 1 is total positive correlation and –1 is total negative correlation (Mudelsee, 2014). This is calculated with Equation (6):

$$r = \frac{\sum (x - m_x)(y - m_y)}{\sqrt{\sum (x - m_x)^2 \sum (y - m_y)^2}} \tag{6}$$

where: m_x and m_y are the means of x and y variables.

The index of agreement (d), introduced by Willmott (1981), is a standardized metric used to quantify the extent of error in model predictions. It was calculated using Equation (7).

$$d = 1 - \frac{\sum_{i=1}^n (O_i - P_i)^2}{\sum_{i=1}^n (|P_i - \bar{O}| + |O_i - \bar{O}|)^2} \tag{7}$$

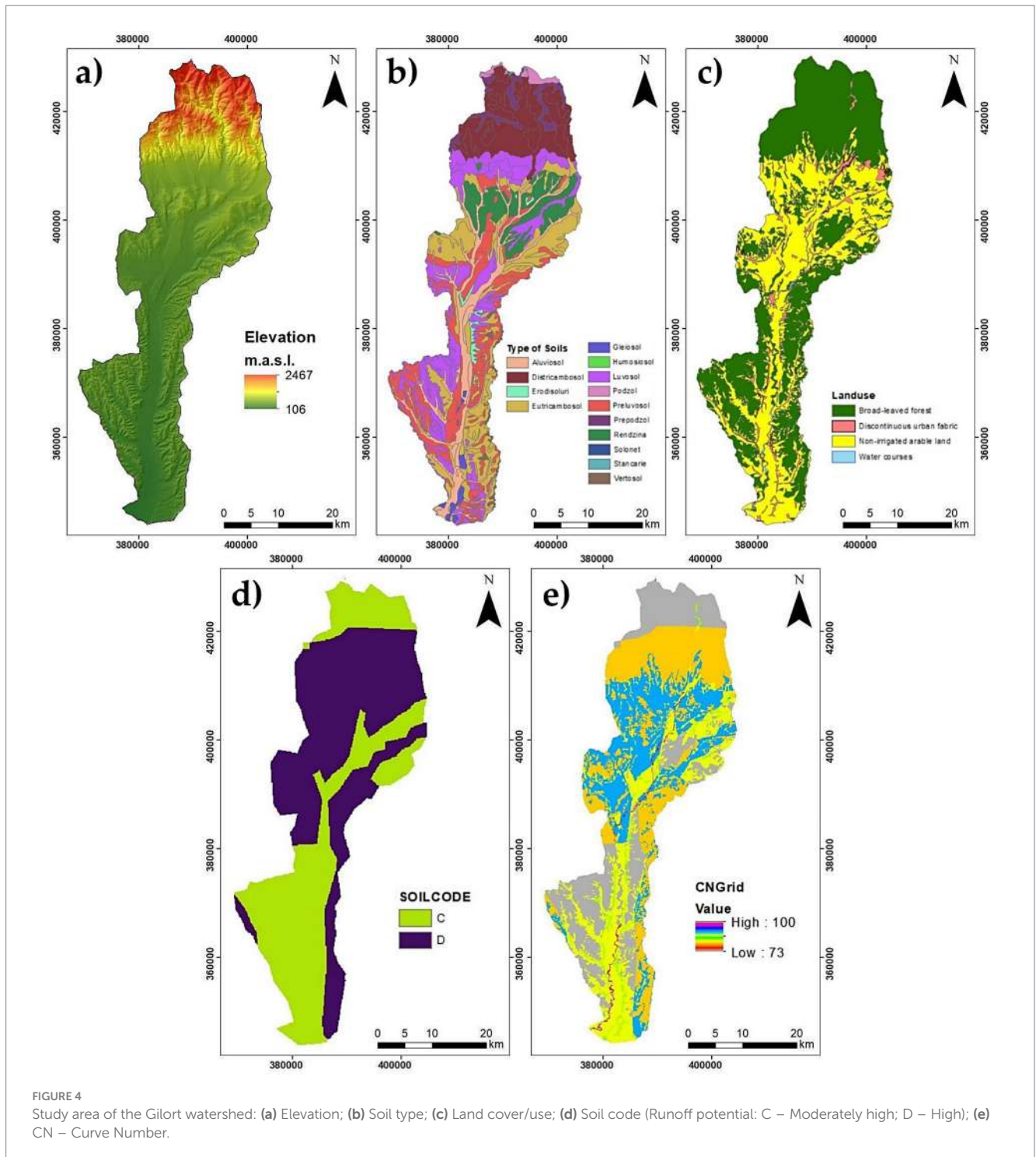
The variables in the equation are defined as follows: O_i represents the observation value; P_i represents the forecast value, \bar{O} represents the average observation values, and \bar{P} represents the average forecast values. As a measure that quantifies the relationship between the mean square error and the potential error, “d” values range from 0 to 1. A number of 1 in the agreement indicates a complete match, whereas a value of 0 shows no agreement all.

The soils were classified into four hydrological groups, namely A, B, C, and D, based on their texture. Group A comprises soils with a coarse texture, which exhibit the lowest runoff capacity. Group B consists of soils with a medium texture, which are either deep or of medium depth, and have good drainage. Group C comprises soils characterized by a restrictive layer that impedes the downward movement of water in the soil profile. These soils have a moderately fine to fine texture. In contrast, soils classified as Group D possess a fine structure characterized by a high clay content, resulting in a greater susceptibility to leakage and a reduced capacity for infiltration. The land use/cover map of the Gilort watershed (Figure 4) was created from the Corine Land Cover 2006 dataset.

Considering the soil and land use data in the study region of the Gilort watershed, the curve number (CN) accurately depicted the potential for runoff. The selection of the CN value was determined by considering key factors such as the soil composition in each sub-basin, the initial moisture level, and the type of vegetation covering the sub-basin. The CN is a dimensionless index used to measure leakage, ranging from 1 to 100. Higher values of CN implied a higher degree of leakage (USDA, 1972; USGS, 2017). The initial phase involved determining the moisture conditions under normal circumstances (CN II), which were then adjusted based on the prior moisture conditions (AMC I, AMC II, and AMC III). In the SCS Curve Number approach, each sub-basin was assigned a Curve Number value, which was obtained using the HEC Geo-HMS program. The data collected in this phase was used to do hydrological modeling using the HEC-HMS software. The modeling process involved four components: basin model, meteorological model, time series data, and specification control, based on which modeled basins were obtained such as for the Superior Barzava catchment presented in Figure 5.

2.3 Data processing and statistics

The values of the individual parameters were estimated through manual calibration. The optimal values of the parameters (K, X) for the Muskingum model were determined by comparing the observed



and simulated flows in the examined portions. In the current study, regression analysis, Pearson's correlation coefficient (r) and coefficient of determination (R^2) were utilized as effective tools in operational hydrological forecasting among the event-based rainfall-runoff models (Mekanik et al., 2013; De La Fuente et al., 2019; Yan et al., 2023; Liu et al., 2021). Additional quantitative models, such as root mean square error (RMSE), Nash–Sutcliffe efficiency (NSE), and others, were applied and assessed for evaluation (Ajmal et al., 2015; Mustafa et al., 2018; Franz and Hogue, 2011; Moriasi et al., 2007), some of them using AgriMetSoft software (AgriMetSoft, 2019). The

model was calibrated using daily precipitation data from the hydrological year intervals spanning from 2015 to 2020. Two precipitation events were chosen annually from the years 2015 to 2017, for the purpose of calibrating and validating the data. The model was adjusted for the time frame from 8 to 23 July 2015 and verified for the year 2017. The parameters, including initial abstraction, CN number, percentage impermeability, and lag time, were adjusted to match the conditions of the SCS curve number technique for the year 2015. A one-sample t -test was used to test the regression hypothesis that the simulated and observed data were identical ($p < 0.05$).

Calculations, including regression model fitting, used standardized variables and compared their absolute values.

3 Results

The results of the three stations (Săcelu, Târgu Cărbunești, and Turburea) for the introduction of precipitation data in the meteorological sheet, corresponding to the intervals of the hydrological years 2015–2020, are presented in Figures 6, 7. For the control run, daily rainfall began on 8 July and ended on 23 July. In our model, the HEC-HMS was used to simulate both a single watershed and a system of multiple hydrologically connected watersheds. The simulation of

precipitation-runoff for the Gilort watershed done for a single rain event from July 8, 2015, to July 23, 2015, using HEC-HMS is presented in Figures 8–10. The data were obtained as hydrologic simulation models with the integrated use of remote sensing and GIS. Because a lack of reliable recorded data on precipitation and runoff is a serious problem for the planning and sustainable management of water resources in a river basin, we used the downpour from July 8 to 23, 2015, to simulate the precipitation-runoff model (HEC-HMS hydrological model). Calibration was undertaken to ensure that the empirical results for peak flow and peak time during the simulation matched the observed data. After the calibration procedure, the HEC-HMS model produced a simulated hydrograph for the Turburea sub-watershed (Figure 11) and simulated outflow data for the Gilort watershed (Figure 12) during the storm event that occurred from July 8 to 23, 2015. The calibration approach encompassed the utilization of standard parameters, including impermeability, delay duration, and curve number, which were tailored to our specific dataset.

The statistical parameters used to estimate the runoff process revealed a good match between the observed and simulated discharges for the hydrographic basin under consideration (Figure 13). Therefore, the coefficient of determination (R^2) for the simulated vs observed flows has a high value (0.9113), indicating that the simulation accurately captures over 91% of the entire variation in the data. The regression equation and the regression line indicate the tight, directly proportional positive relationship between the two variables. The regression line has a sharp upward trend. In addition, the observed flows and the simulated flows have a Pearson correlation coefficient of 0.954, which indicates that there is a very close relationship between the two variables, respectively $p < 0.001$. Therefore, the t -test is likewise statistically significant, confirming the robust association between the observed and simulated runoff. Finally, the index of agreement (d) exhibited a significantly high value, nearly reaching 1, specifically 0.975, meaning that between the observed and simulated means and variances, there was almost a perfect match.

Other assessment methods were also used to statistically test the predictions of the simulated model against the real data obtained in the Gilort basin throughout the investigated period.

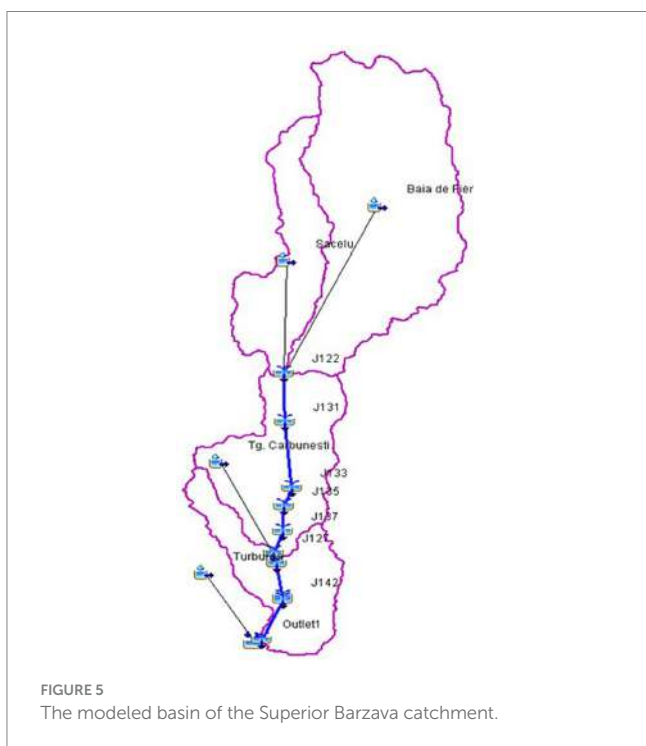


FIGURE 5 The modeled basin of the Superior Barzava catchment.

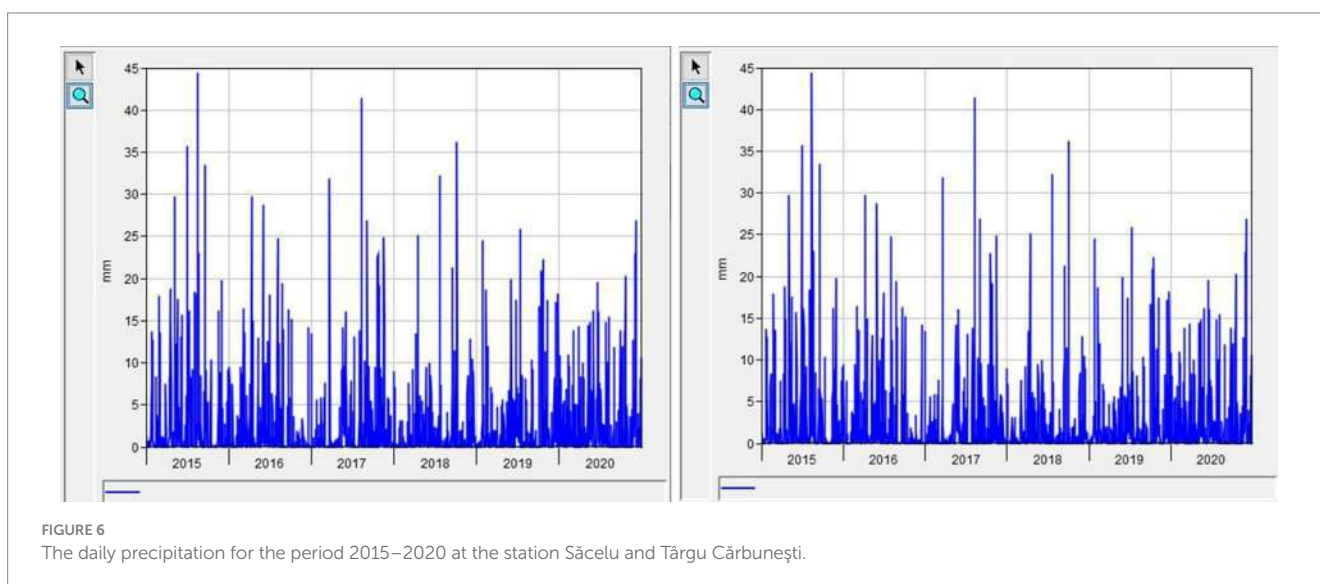


FIGURE 6 The daily precipitation for the period 2015–2020 at the station Săcelu and Târgu Cărbunești.

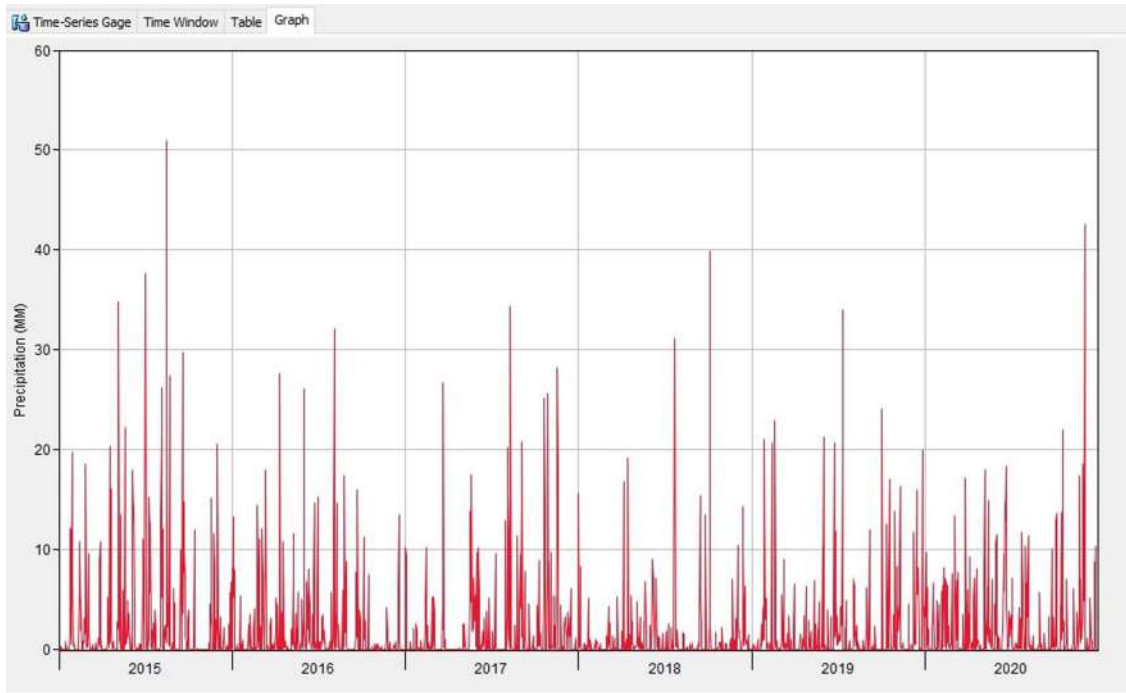


FIGURE 7
Daily precipitation for the period 2015–2020 at Turburea station.

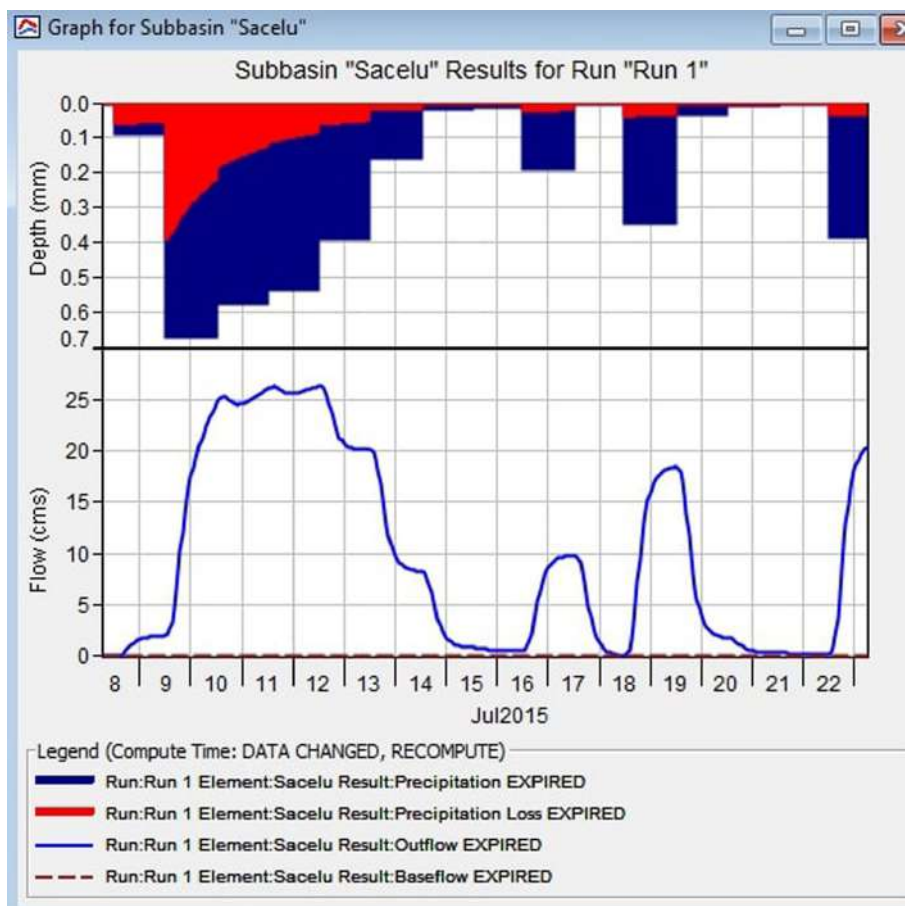


FIGURE 8
HEC-HMS simulated hydrograph of sub-watershed Săcelu shows the total precipitation, soil infiltration and total outflow.

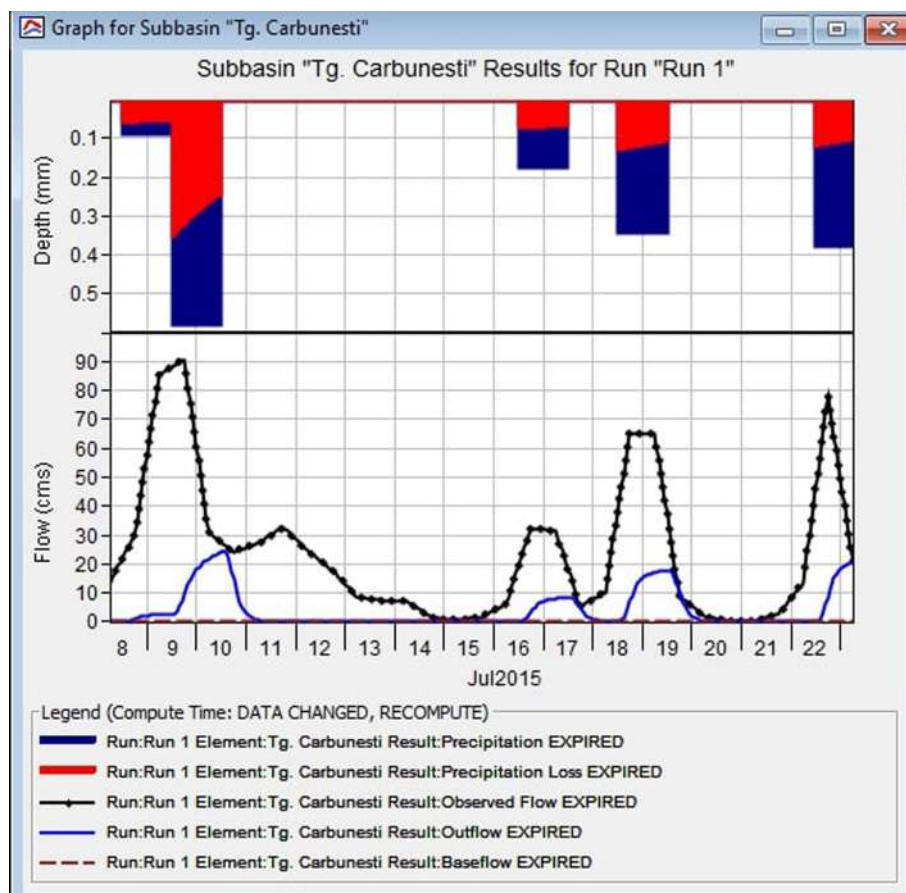


FIGURE 9
HEC-HMS simulated hydrograph of sub-watershed Târgu Cărbunești shows the total precipitation, soil infiltration and total outflow.

Figure 14 displays the findings obtained from different methods used to measure the accuracy of the model's estimated values compared to the actual observations. These various models performed using AgriMetSoft (2019) also confirmed the accuracy of the previously reported values of the presented parameters. It can be noted that under the conditions that a reduced deviation of runoff volume value indicates superior model performance, the deviation of runoff volumes (Dv) was 6.40%. In addition, the Nash–Sutcliffe efficiency (NSE) of 0.908 indicates a strong agreement between the observed and simulated data, suggesting a nearly perfect fit of the model to the observed data, when $NSE = 1$ (AgriMetSoft, 2019). In general, the values of the other parameters that were estimated are consistent with these findings (i.e., Kling-Gupta efficiency) and offer support for the validity of the model. Residuals, which in the context of our investigation represented the portion of the validation data that the model did not explain, were used in conjunction with RMSE to assess the predictability of the model for observed and simulated datasets (Figure 15). The regression equation produced a negative result, suggesting a pronounced downward trend in the regression line. However, the coefficient of determination reveals that 88.1% of the variance in a component may be attributed to its association with the other factor. The correlation coefficient exhibited a high value, indicating a robust association between the variables. The data were evaluated using the *t*-test, resulting in statistical findings which certified that

the regression coefficient between the two analyzed parameters is significant ($p < 0.001$).

4 Discussion

The data collected in the Gilort hydrographic basin, Romania, namely the leakage in the closure section, were utilized in our study to construct a simulation-based model for the purpose of verification and validation. The results were utilized in the model by computing the precipitation-runoff in the Gilort hydrographic basin, using the precipitation data that occurred on the surface of the investigated region as input. The highest recorded flow rates ranged from 10.9 m³/s in Săcelu to 311 m³/s in Turburea, while the flood volumes varied from 1.57 million m³ in Baia de Fier to 58.8 million m³ in Turburea. It is important to mention that although the caution limits in the study period were surpassed at Ciocadia, Săcelu, Tg-Cărbunești (Gilort), and the flood limit at Turburea, no physical harm was reported. The highest water flows were successfully channeled down the main riverbed.

The simulated and real flows of the hydrographic basin under study were precisely matched by the statistical indicators, particularly the coefficient of determination, coefficient of correlation, index of agreement, and RMSE, that were used to assess the runoff mechanisms. Other statistical parameters used to evaluate the runoff model, including the deviation of runoff volumes (Dv) and the Nash–Sutcliffe

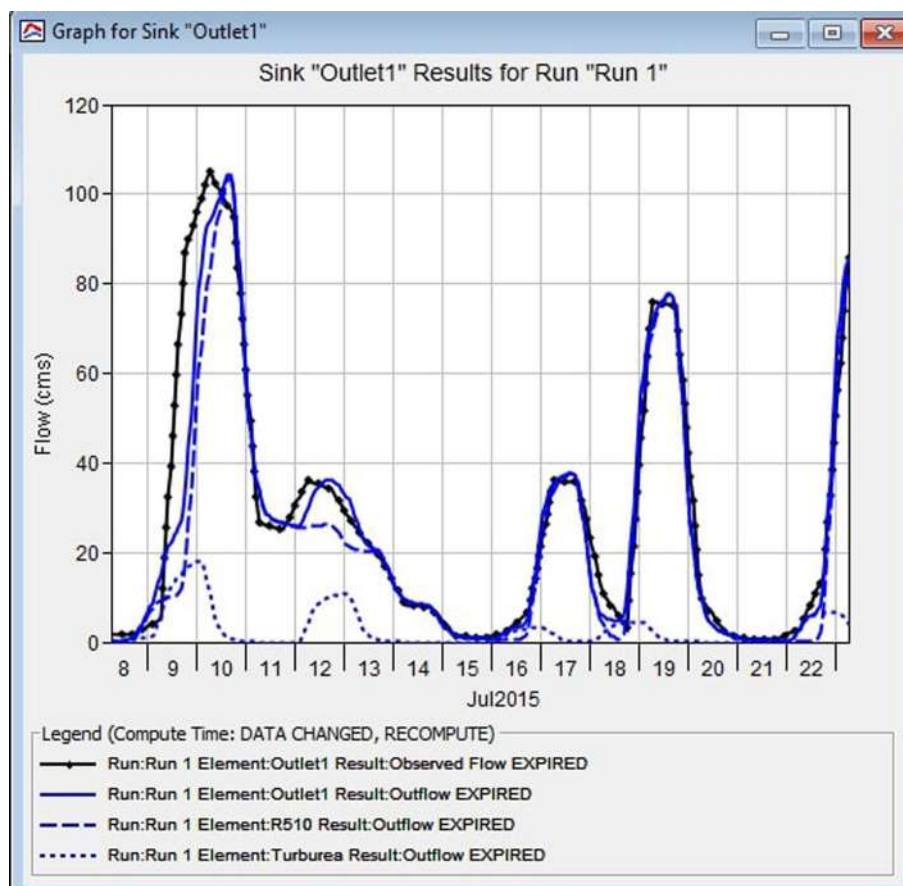


FIGURE 10
Simulated and observed the outflow graph of Gilort watershed on a storm event from 8 July 2015 to 23 July 2015.

efficiency (NSE) confirmed the appropriate matching of the simulated and observed data. Both Dv (WMO, 1986; Wagener et al., 2004) and NSE (Nash and Sutcliffe, 1970) could be considered appropriate measures of goodness of fit which ensure model reliability and performance. Furthermore, the Kling-Gupta efficiency (KGE) appears to be comparable to the Nash–Sutcliffe efficiency (NSE), particularly in cases where there are no biases (Mathevet et al., 2023; Skaugen and Weltzien, 2016; Rezaei-Sadr, 2020). This is because both metrics assess the relative strength of distortion compared to the variability in observations (Duc and Sawada, 2023). The values of these two parameters in our investigation were highly comparable (KGE = 0.901; NSE = 0.908). The statistical comparisons of the model predictions with the real observations and the quantification of the goodness-of-fit of observations to the simulated values by the model were facilitated by the software and information support implemented by AgriMetSoft (2019). The index of agreement value, or Willmott index ($d = 0.975$), was near 1, indicating a perfect match, whereas 0 means no agreement (Aboelkhair et al., 2019; Biudes et al., 2014). The deviation of runoff volumes (Dv) had a quite small value in our investigation, which was a favorable result because a smaller Dv indicates superior model performance (knowing that in the case of a perfect model, Dv equals zero) (Mediero et al., 2010). The root mean square error (RMSE), which quantifies the discrepancy between two datasets by comparing the predicted and actual outcomes of individual differences, was calculated to be 8.659. The NSA value was very close to 1, a value that,

on a scale of 0–1, indicates a perfect alignment between the simulated model and the observed data. When multiple criteria are utilized, particularly over a certain season or a series of seasons, evaluating a model's success becomes challenging for a potential user (Martinez and Rango, 1989). Therefore, we tried to determine whether the relationship between the RMSE and the residuals may be employed as a potential method to assess the accuracy of the model. The results unequivocally demonstrated a robust negative correlation between these two variables, which was further supported by the t-test. The utilization of the regression equation in the investigation may be advantageous in predicting one variable, contingent upon the value of the other variable. Therefore, the model allows for the calculation (including both interpolation and extrapolation) of the extent to which the variables of interest can vary. This pertains to the problem of limited or insufficient data regarding rainfall and water flow, which has been an ongoing challenge in hydrological modeling (Demisse et al., 2021; Ben Khélifa and Mosbahi, 2022; Teng et al., 2018; Halwatura and Najim, 2013).

The findings of this study support the model's validity and usefulness for developing flood mapping and designing flood mitigation measures in the studied area. Such generated models can be used to other hydrological basins with similar hydrological circumstances, allowing for modifications based on general and local variables. Furthermore, a multitude of studies emphasize these facets, conducted in various regions across the world, including

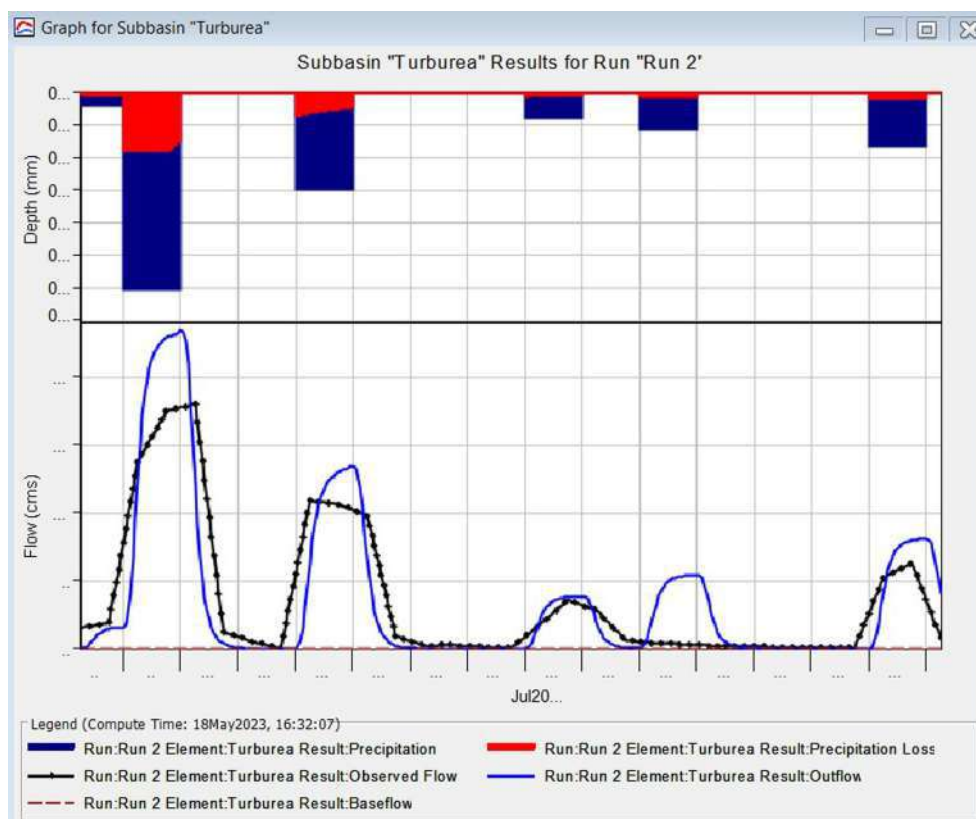


FIGURE 11
HEC-HMS simulated hydrograph of sub-watershed Turburea after calibration.

diverse geographical and meteorological circumstances (Sahu et al., 2023; Yimer et al., 2009; Verma et al., 2022; Rahman et al., 2017; Shah and Lone, 2022; Bammou et al., 2024; Ouallali et al., 2024). Examining the intricacy of the hydrological process in a specific area relies on the attributes of precipitation and the qualities of the watershed (Sidle, 2021). Applying rainfall-runoff models involves distinct challenges and opportunities, which vary depending on a variety of factors, such as the geographical characteristics of the land and the specific meteorological circumstances of the area (Ranjan and Singh, 2022; Choudhari et al., 2014; Ramly and Tahir, 2016; Sarminingsih et al., 2019; Gholami and Khaleghi, 2021; Hamdan et al., 2021). An essential obstacle lies in the inherent uncertainty of precipitation and its dynamic formation and evolution throughout time. Predicting the spatial distribution of rainfall over the catchment region is particularly challenging since rainfall serves as the main input in hydrological models (Todini, 2007; Loritz et al., 2021; Salvatore et al., 2015). This could compel the researcher to reduce the number of research questions, thus leading to an increase in model uncertainty (Abushandi and Merkel, 2013). Hydrologic models may require substantial modifications to global data storage systems for geology and soils, which may be frequently necessary. In order to improve hydrological processes, it is essential to categorize various types of soil and rock classes into distinct groupings (Costea et al., 2022; Sestras et al., 2023a). When determining the scale of spatial discretization and routing in catchment models, it is essential to take into account the topographical data and the desired level of precision required by other modeling communities and

organizations. The topography data is the primary factor that determines this (Olayinka and Irvbogbe, 2017; Fathalizadeh et al., 2020; Azizi et al., 2021). Enhancing the geological databases would be facilitated and rendered more valuable through increased collaboration and communication among hydrologists, geographers, and other researchers studying the Earth's surface (Archfield et al., 2015; Qi et al., 2021).

In Romania, due to the increased frequency of floods, a Flood Risk Management Plan was developed (Ministerul Mediului, 2023; Diaconu, 2022), with the main goal of reducing the negative consequences of floods for human health, economic activity, the environment, and cultural heritage through a synergy of prevention, protection, preparation, emergency management, and post-flood measures (reconstruction and recovery). Flood Risk Management Plans address all areas of flood risk management, focusing on prevention, protection, and readiness while taking into account the features of the catchment or sub-catchment, such as flood forecasting and early warning systems. Hydrological modeling systems, such as HEC-HMS, can be beneficial for understanding rainfall-runoff mechanisms in high-risk watersheds and implementing the most effective remedies.

5 Conclusion

The current research employed the HEC-HMS model to simulate runoff in watersheds, facilitating flood modeling,

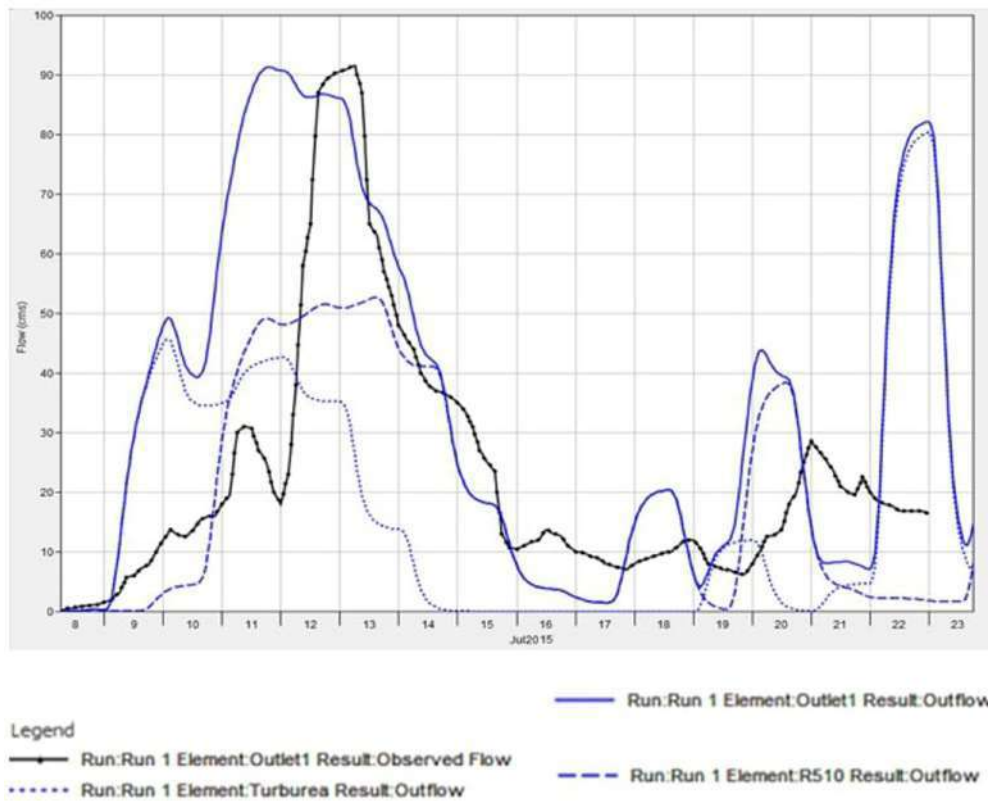


FIGURE 12
HEC-HMS simulated hydrograph of Gilort watershed after calibration.

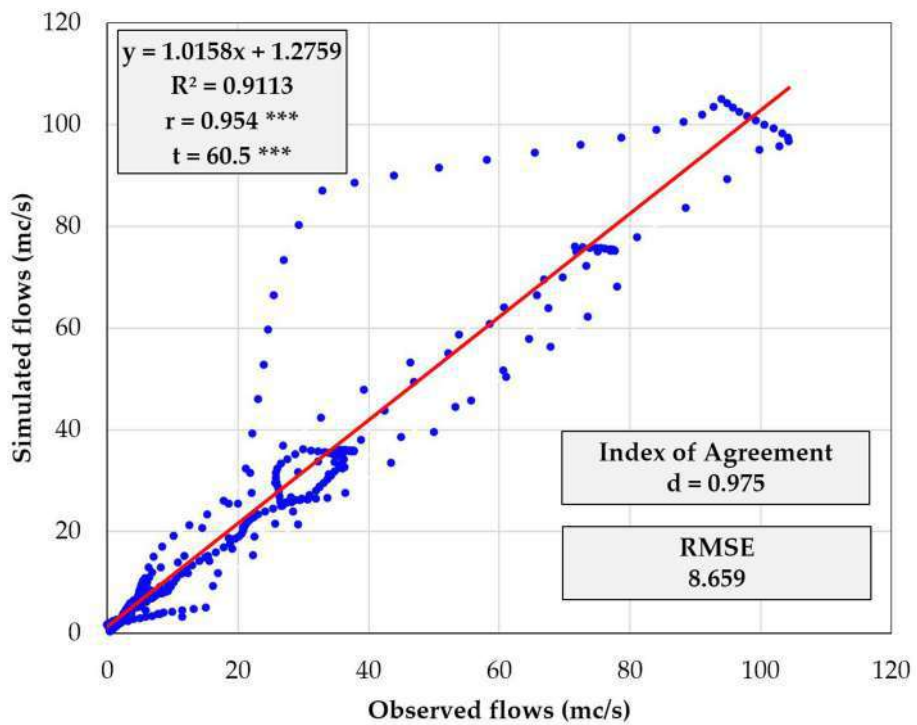


FIGURE 13
Simulated versus observed flows before the validation (8–23 July 2015).

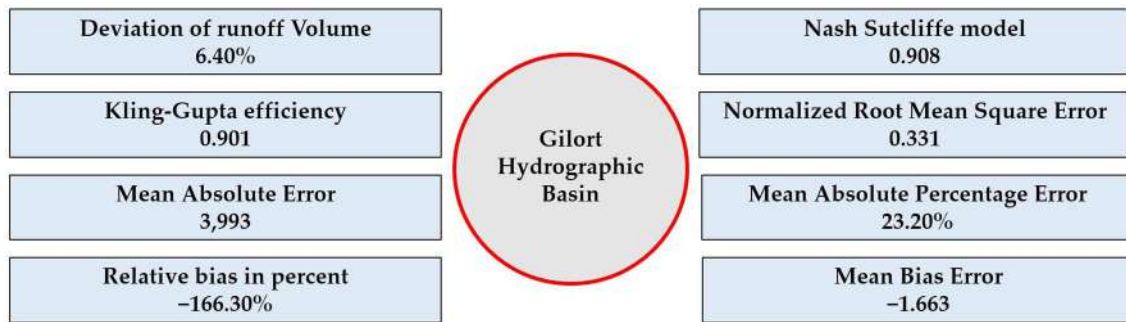


FIGURE 14

Calculated indices for statistical comparisons of model predictions with actual observations (simulated flows - observed flows) in Gilort Hydrographic Basin.

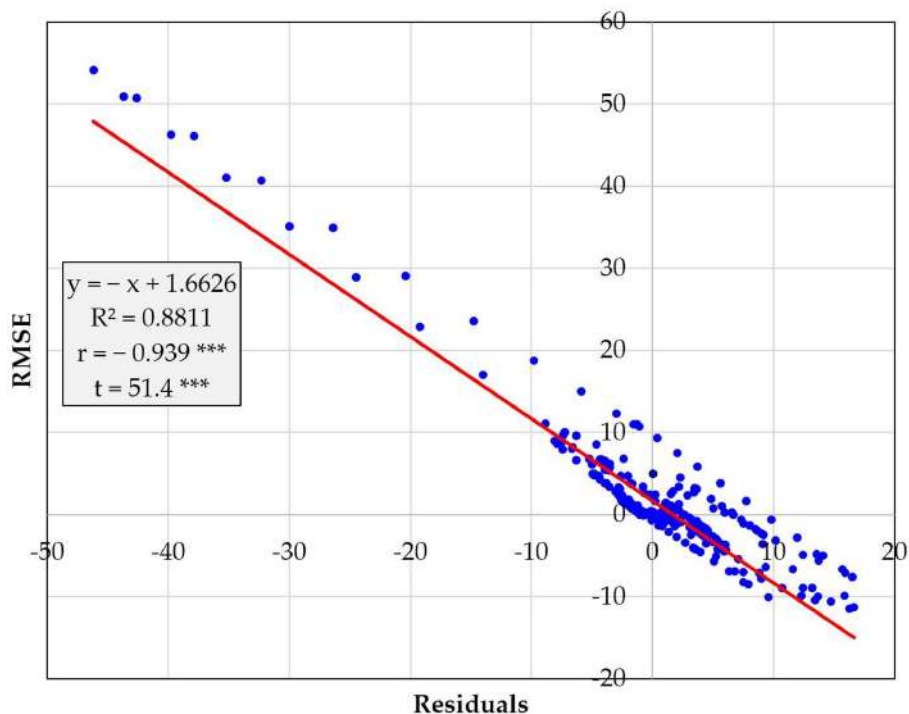


FIGURE 15

Simulated versus observed flows before the validation (8–23 July 2015).

water resource planning, and management applications. The regression equation, coefficient of determination, correlation coefficient, and various indices such as root mean squared error (RMSE), index of agreement (d), deviation of runoff volumes (Dv), Nash–Sutcliffe efficiency (NSE), and Kling-Gupta efficiency (KGE) have shown a strong correlation between simulated flows and observed flows. Hence, these statistical features have demonstrated the reliability of the model for the Gilort watershed. They contributed to comparing simulated and observed data and probably could be of interest to the forecast of discharges from the studied hydrographic region. The presented model can be utilized to predict river flow and aid in flood mitigation efforts. Furthermore, the findings derived from

this study can serve as a valuable reference for forthcoming endeavors in assessing flood risks within the study region. Subsequent research will concentrate on creating a database for improved regionalization of the rainfall-runoff model and validating the model across a wide range of catchments in the current study area.

Data availability statement

The original contributions presented in the study are included in the article/supplementary material, further inquiries can be directed to the corresponding authors.

Author contributions

MH: Conceptualization, Methodology, Visualization, Writing – original draft. CB-M: Formal analysis, Investigation, Software, Validation, Visualization, Writing – original draft. CP: Funding acquisition, Project administration, Resources, Supervision, Writing – original draft. AH: Data curation, Investigation, Validation, Visualization, Writing – original draft. LD: Data curation, Formal analysis, Investigation, Supervision, Writing – review & editing. GP: Data curation, Formal analysis, Investigation, Methodology, Software, Validation, Visualization, Writing – original draft. SK: Formal analysis, Software, Validation, Visualization, Writing – review & editing. PS: Conceptualization, Formal analysis, Investigation, Visualization, Writing – review & editing.

Funding

The author(s) declare that financial support was received for the research, authorship, and/or publication of this article. This work was supported by the project “Increasing the impact of excellence research on the capacity for innovation and technology transfer within USV Timișoara” code 6PFE, submitted in the competition Program 1 - Development of the national system of research - development, Subprogram 1.2 - Institutional

References

- Abouelkhair, H., Morsy, M., and El Afandi, G. (2019). Assessment of agroclimatology Nasa power reanalysis datasets for temperature types and relative humidity at 2 m against ground observations over Egypt. *Adv. Space Res.* 64, 129–142. doi: 10.1016/j.asr.2019.03.032
- Abushandi, E., and Merkel, B. (2013). Modelling rainfall runoff relations using HEC-HMS and Ihares for a single rain event in an arid region of Jordan. *Water Resour. Manag.* 27, 2391–2409. doi: 10.1007/s11269-013-0293-4
- Administriația Națională De Meteorologie. (2024). Meteo Romania. București. Available at: <https://www.meteoromania.ro/> (Accessed November 24, 2023).
- AgriMetSoft. (2019). Online calculators. Korea, Seoul National University's BK Residence Halls is, A1201. Available at: <https://agrimetsoft.com/calculators> (Accessed December 10, 2023).
- Ahmad, M. N., Shao, Z., and Javed, A. (2023). Modelling land use/land cover (Lulc) change dynamics, future prospects, and its environmental impacts based on geospatial data models and remote sensing data. *Environ. Sci. Pollut. Res.* 30, 32985–33001. doi: 10.1007/s11356-022-24442-2
- Ajmal, M., Waseem, M., Ahn, J.-H., and Kim, T.-W. (2015). Improved runoff estimation using event-based rainfall-runoff models. *Water Resour. Manag.* 29, 1995–2010. doi: 10.1007/s11269-015-0924-z
- Al-Sabhan, W., Mulligan, M., and Blackburn, G. A. (2003). A real-time hydrological model for flood prediction using Gis and the www. *Comput. Environ. Urban. Syst.* 27, 9–32. doi: 10.1016/S0198-9715(01)00010-2
- Al-Taei, A. I., Alesheikh, A. A., and Darvishi Boloorani, A. (2023). Land use/land cover change analysis using multi-temporal remote sensing data: a case study of Tigris and Euphrates Rivers Basin. *Land* 12:1101. doi: 10.3390/land12051101
- Angelakis, A. N., Capodaglio, A. G., Valipour, M., Krasilnikoff, J., Ahmed, A. T., Mandi, L., et al. (2023). Evolution of floods: from ancient times to the present times (ca 7600 BC to the present) and the future. *Land* 12:1211. doi: 10.3390/land12061211
- Ansari, M. Z., Ahmad, I., Rautela, K. S., Goyal, M. K., and Singh, P. K. (2023). “Hydrological modelling using HEC-HMS and estimation of the flood peak by Gumbel's method” in Ecosystem restoration: towards sustainability and resilient development. eds. A. K. Gupta, M. K. Goyal and S. P. Singh (Singapore: Springer Nature Singapore).
- Archfield, S. A., Clark, M., Arheimer, B., Hay, L. E., Mcmillan, H., Kiang, J. E., et al. (2015). Accelerating advances in continental domain hydrologic modeling. *Water Resour. Res.* 51, 10078–10091. doi: 10.1002/2015WR017498
- Azizi, S., Ilderomi, A. R., and Noori, H. (2021). Investigating the effects of land use change on flood hydrograph using HEC-HMS hydrologic model (case study: Ekbatan Dam). *Nat. Hazards* 109, 145–160. doi: 10.1007/s11069-021-04830-6
- Bahiru, T. K., Aldosary, A. S., Kafy, A. A., Rahman, M. T., Nath, H., Kalaivani, S., et al. (2024). Geospatial approach in modeling linear, areal, and relief morphometric interactions in Dabus river basin ecology for sustainable water resource management. *Groundw. Sustain. Dev.* 24:101067. doi: 10.1016/j.gsd.2023.101067
- Balica, S. F., Dinh, Q., and Popescu, I. (2023). Vulnerability and exposure in developed and developing countries. In: J. F. Shroder, P. Paron and Baldassarre G. Di. (eds.) Hydro-meteorological hazards, risks, and disasters. Boston: Elsevier.
- Bammou, Y., Benzougagh, B., Igmoullan, B., Ouallali, A., Kader, S., Spalevic, V., et al. (2024). Optimizing flood susceptibility assessment in semi-arid regions using ensemble algorithms: a case study of Moroccan high atlas. *Nat. Hazards* 120, 7787–7816. doi: 10.1007/s11069-024-06550-z
- Ben Khélifa, W., and Mosbahi, M. (2022). Modeling of rainfall-runoff process using HEC-HMS model for an urban ungauged watershed in Tunisia. *Model. Earth Syst. Environ.* 8, 1749–1758. doi: 10.1007/s40808-021-01177-6
- Bharath, A., Kumar, K. K., Maddamsetty, R., Manjunatha, M., Tangadagi, R. B., and Preethi, S. (2021). Drainage morphometry based sub-watershed prioritization of Kalinadi basin using geospatial technology. *Environ. Chall.* 5:100277. doi: 10.1016/j.envc.2021.100277
- Bilașco, Ș., Hognogi, G.-G., Roșca, S., Pop, A.-M., Iuliu, V., Fodorean, I., et al. (2022). Flash flood risk assessment and mitigation in digital-era governance using unmanned aerial vehicle and GIS spatial analyses case study: small river basins. *Remote Sens.* 14:2481. doi: 10.3390/rs14102481
- Bilașco, Ș., Roșca, S., Vescan, I., Fodorean, I., Dohotar, V., and Sestras, P. (2021). A Gis-based spatial analysis model approach for identification of optimal Hydrotechnical solutions for gully Erosion stabilization: case study. *Appl. Sci.* 11:4847. doi: 10.3390/app11114847
- Biudes, M. S., Machado, N. G., Danelichen, V. H. D. M., Souza, M. C., Vourlitis, G. L., and Nogueira, J. D. S. (2014). Ground and remote sensing-based measurements of leaf area index in a transitional forest and seasonal flooded forest in Brazil. *Int. J. Biometeorol.* 58, 1181–1193. doi: 10.1007/s00484-013-0713-4
- Bouramtane, T., Tiouiouine, A., Kacimi, I., Valles, V., Talih, A., Kassou, N., et al. (2020). Drainage network patterns determinism: a comparison in arid, semi-arid and semi-humid area of Morocco using multifactorial approach. *Hydrology* 7:87. doi: 10.3390/hydrology7040087
- Bronstert, A. (2003). Floods and climate change: interactions and impacts. *Risk Anal.* 23, 545–557. doi: 10.1111/1539-6924.00335
- Bryndal, T. (2023). Changes in the active drainage network and their impact on the hydrological response and flood risk management process: a case study for a Flysch Mountain catchment. *Resources* 12:146. doi: 10.3390/resources12120146

performance, Institutional development projects - Development projects of excellence in RDI.

Acknowledgments

The authors thank the GEOMATICS Research Laboratory, ULS “King Mihai I” from Timisoara, for the facility of the software use for this study.

Conflict of interest

The authors declare that the research was conducted in the absence of any commercial or financial relationships that could be construed as a potential conflict of interest.

Publisher's note

All claims expressed in this article are solely those of the authors and do not necessarily represent those of their affiliated organizations, or those of the publisher, the editors and the reviewers. Any product that may be evaluated in this article, or claim that may be made by its manufacturer, is not guaranteed or endorsed by the publisher.

- Castro, C. V., and Maidment, D. R. (2020). Gis preprocessing for rapid initialization of HEC-HMS hydrological basin models using web-based data services. *Environ. Model Softw.* 130:104732. doi: 10.1016/j.envsoft.2020.104732
- Chendeş, V. (2007). Liquid and solid runoff in curvature Subcarpathian. Doctoral thesis.: Romanian Academy, Institute of Geography.
- Choudhari, K., Panigrahi, B., and Paul, J. C. (2014). Simulation of rainfall-runoff process using HEC-HMS model for Balijore Nala Watershed, Odisha, India. *Int. J. Geom. Geosci.* 5, 253–265.
- Chow, V. T., Maidment, D. R., and Mays, L. W. (1988). *Applied hydrology*. New York, NY: McGraw-Hill.
- Costea, A., Bilasco, S., Irimus, I.-A., Rosca, S., Vescan, I., Fodorean, I., et al. (2022). Evaluation of the risk induced by soil Erosion on land use. Case study: Guruslău depression. *Sustain. For.* 14:652. doi: 10.3390/su14020652
- De La Fuente, A., Meruane, V., and Meruane, C. (2019). Hydrological early warning system based on a deep learning runoff model coupled with a meteorological forecast. *Water* 11:1808. doi: 10.3390/w11091808
- Demisse, H., Ayalew, A., Ayana, M., and Lohani, T. (2021). Extenuating the parameters using HEC-HMS hydrological model for ungauged catchment in the central Omo-Gibe Basin of Ethiopia. *J. Groundwater Sci. Eng.* 9, 317–325. doi: 10.19637/j.cnki.2305-7068.2021.04.005
- Diaconu, D. C. (2022). Flood risk management in Romania: flood handbook. CRC Press, 179–200.
- Dixit, A. (2003). Floods and vulnerability: need to rethink flood management. *Nat. Hazards* 28, 155–179. doi: 10.1023/A:1021134218121
- Du, J., Qian, L., Rui, H., Zuo, T., Zheng, D., Xu, Y., et al. (2012). Assessing the effects of urbanization on annual runoff and flood events using an integrated hydrological modeling system for Qinhuai River basin, China. *J. Hydrol.* 464–465, 127–139. doi: 10.1016/j.jhydrol.2012.06.057
- Duc, L., and Sawada, Y. (2023). A signal-processing-based interpretation of the Nash–Sutcliffe efficiency. *Hydrol. Earth Syst. Sci.* 27, 1827–1839. doi: 10.5194/hess-27-1827-2023
- Dunca, A.-M., and Bădăluță-Minda, C. (2018). The determination of the maximum runoff in the representative and experimental hydrographical basin of Sebes River (Banat, Romania). *Rocznik Ochrona Środowiska* 20, 54–72.
- Eccles, R., Zhang, H., and Hamilton, D. (2019). A review of the effects of climate change on riverine flooding in subtropical and tropical regions. *J. Water Clim. Change* 10, 687–707. doi: 10.2166/wcc.2019.175
- Fan, Y., Li, H., and Miguez-Macho, G. (2013). Global patterns of groundwater table depth. *Science* 339, 940–943. doi: 10.1126/science.1229881
- Fathalizadeh, B., Abedini, M., and Rajabi, M. (2020). Investigating the causes and hazards of flood in Zunuzchay watershed using HEC-HMS hydrological model and fuzzy logic. *J. Quant. Geomorphol. Res.* 9, 134–155. doi: 10.22034/gmpj.2020.109539
- Fleming, M., and Brauer, T. (2016). Hydrologic modelling system HEC-HMS quick start guide. Version 4.2: US Army Corps of Engineers, Institute of Water Resources.
- Fleming, M. J., and Doan, J. H. (2013). HEC-GeoHMS geospatial hydrologic modeling extension user's manual. Davis, CA: US Army Corps of Engineers, Hydrologic Engineering Center.
- Franz, K. J., and Hogue, T. S. (2011). Evaluating uncertainty estimates in hydrologic models: borrowing measures from the forecast verification community. *Hydrol. Earth Syst. Sci.* 15, 3367–3382. doi: 10.5194/hess-15-3367-2011
- Gambolati, G., Teatini, P., and Gonella, M. (2002). Gis simulations of the inundation risk in the coastal lowlands of the northern Adriatic Sea. *Math. Comput. Model.* 35, 963–972. doi: 10.1016/S0895-7177(02)00063-8
- Gholami, V., and Khaleghi, M. R. (2021). A simulation of the rainfall-runoff process using artificial neural network and HEC-HMS model in forest lands. *J. For. Sci.* 67, 165–174. doi: 10.17221/90/2020-JFS
- Ghosh, M., and Gope, D. (2021). Hydro-morphometric characterization and prioritization of sub-watersheds for land and water resource management using fuzzy analytical hierarchical process (FAHP): a case study of upper Rihand watershed of Chhattisgarh state, India. *Appl Water Sci* 11:17. doi: 10.1007/s13201-020-01340-x
- Greuc, F., Zaharia, L., Ioana-Toroimac, G., and Armaş, I. (2017). "Floods and flash-floods related to river channel dynamics" in Landform dynamics and evolution in Romania. eds. M. Radoane and A. Vespremeanu-Stroe (Cham: Springer International Publishing).
- Halwatura, D., and Najim, M. M. M. (2013). Application of the HEC-HMS model for runoff simulation in a tropical catchment. *Environ. Model Softw.* 46, 155–162. doi: 10.1016/j.envsoft.2013.03.006
- Hamdan, A. N. A., Almuktar, S., and Scholz, M. (2021). Rainfall-runoff modeling using the HEC-HMS model for the Al-Adhaim River catchment, northern Iraq. *Hydrology* 8:58. doi: 10.3390/hydrology8020058
- Hawley, M. E., and McCuen, R. H. (1982). Water yield estimation in Western United States. *J. Irrig. Drain Div.* 108, 25–34.
- Ionita, M., and Nagavciuc, V. (2021). Extreme floods in the eastern part of Europe: large-scale drivers and associated impacts. *Water* 13:1122. doi: 10.3390/w13081122
- Jain, S., and Lall, U. (2001). Floods in a changing climate: does the past represent the future? *Water Resour. Res.* 37, 3193–3205. doi: 10.1029/2001WR000495
- Jonkman, S. N. (2005). Global perspectives on loss of human life caused by floods. *Nat. Hazards* 34, 151–175. doi: 10.1007/s11069-004-8891-3
- Knebl, M. R., Yang, Z. L., Hutchison, K., and Maidment, D. R. (2005). Regional scale flood modeling using Nexrad rainfall, Gis, and HEC-HMS/RAS: a case study for the San Antonio River basin summer 2002 storm event. *J. Environ. Manag.* 75, 325–336. doi: 10.1016/j.jenvman.2004.11.024
- Kron, W., Steuer, M., Löw, P., and Wirtz, A. (2012). How to deal properly with a natural catastrophe database – analysis of flood losses. *Nat. Hazards Earth Syst. Sci.* 12, 535–550. doi: 10.5194/nhess-12-535-2012
- Kumar Rai, P., Narayan Mishra, V., and Mohan, K. (2017). A study of morphometric evaluation of the son basin, India using geospatial approach. *Remote Sens. Appl. Soc. Environ.* 7, 9–20. doi: 10.1016/j.rsase.2017.05.001
- Kumar, V., Sharma, K. V., Caloiero, T., Mehta, D. J., and Singh, K. (2023). Comprehensive overview of flood modeling approaches: a review of recent advances. *Hydrology* 10:141. doi: 10.3390/hydrology10070141
- Liu, Y., Zhang, T., Kang, A., Li, J., and Lei, X. (2021). Research on runoff simulations using deep-learning methods. *Sustain. For.* 13:1336. doi: 10.3390/su13031336
- Loritz, R., Hrachowitz, M., Neuper, M., and Zehe, E. (2021). The role and value of distributed precipitation data in hydrological models. *Hydrol. Earth Syst. Sci.* 25, 147–167. doi: 10.5194/hess-25-147-2021
- Martinez, J., and Rango, A. (1989). Merits of statistical criteria for the performance of hydrological MODELS1. *Jawra J. Am. Water Resour. Assoc.* 25, 421–432. doi: 10.1111/j.1752-1688.1989.tb03079.x
- Masseroni, D., Cislighi, A., Camici, S., Massari, C., and Brocca, L. (2016). A reliable rainfall-runoff model for flood forecasting: review and application to a semi-urbanized watershed at high flood risk in Italy. *Hydrol. Res.* 48, 726–740. doi: 10.2166/nh.2016.037
- Mathevet, T., Le Moine, N., Andréassian, V., Gupta, H., and Oudin, L. (2023). Multi-objective assessment of hydrological model performances using Nash–Sutcliffe and Kling–Gupta efficiencies on a worldwide large sample of watersheds. *Comptes Rendus. Géosci.* 355, 117–141. doi: 10.5802/crgeos.189
- Mediero, L., Jiménez-Álvarez, A., and Garrote, L. (2010). Design flood hydrographs from the relationship between flood peak and volume. *Hydrol. Earth Syst. Sci.* 14, 2495–2505. doi: 10.5194/hess-14-2495-2010
- Mekanic, F., Imteaz, M. A., Gato-Trinidad, S., and Elmahdi, A. (2013). Multiple regression and artificial neural network for long-term rainfall forecasting using large scale climate modes. *J. Hydrol.* 503, 11–21. doi: 10.1016/j.jhydrol.2013.08.035
- Merz, B., Blöschl, G., Vorogushyn, S., Dottori, F., Aerts, J. C. J. H., Bates, P., et al. (2021). Causes, impacts and patterns of disastrous river floods. *Nat. Rev. Earth Environ.* 2, 592–609. doi: 10.1038/s43017-021-00195-3
- Meteoblue AG. Meteoblue weather. Basel. (2024) Available at: <https://content.meteoblue.com/en> (Accessed November 24, 2023).
- Mihalik, E. N., Levine, N. S., and Amatya, D. M. (2008). Rainfall-runoff modeling of the chapel branch creek watershed using GIS-based rational and SCS-CN methods. St. Joseph, MI: American Society of Agricultural and Biological Engineers.
- Ministerul Mediului. (2023). Planul de Management al Riscului la Inundații (Romania). București. Available at: <https://www.mmediu.ro/categorie/planul-de-management-al-riscului-la-inundatii/376> (Accessed December 12, 2023).
- Mishra, S. K., and Singh, V. P. (2013). *Soil conservation service curve number (SCS-CN) methodology (Vol. 42)*. Springer Science & Business Media.
- Moriassi, D. N., Arnold, J. G., van Liew, M. W., Bingner, R. L., Harmel, R. D., and Veith, T. L. (2007). Model evaluation guidelines for systematic quantification of accuracy in watershed simulations. *Trans. ASABE* 50, 885–900. doi: 10.13031/2013.23153
- Mudelsee, M. (2014). *Climate time series analysis: Classical statistical and bootstrap methods. 2nd Edn.* Cham: Springer International Publishing.
- Mustafa, M., Barnhart, B., Babbar-Sebens, M., and Ficklin, D. (2018). Modeling landscape change effects on stream temperature using the soil and water assessment tool. *Water* 10:1143. doi: 10.3390/w10091143
- Mustafa, A., Szydłowski, M., Veysipanah, M., and Hameed, H. M. (2023). GIS-based hydrodynamic modeling for urban flood mitigation in fast-growing regions: a case study of Erbil, Kurdistan region of Iraq. *Sci. Rep.* 13:8935. doi: 10.1038/s41598-023-36138-9
- Muthu, A. L., and Santhi, M. H. (2015). Estimation of surface runoff potential using SCS-CN method integrated with GIS. *Indian J. Sci. Technol.* 8, 1–6. doi: 10.17485/ijst/2015/v8i28/83324
- Nash, J. E., and Sutcliffe, J. V. (1970). River flow forecasting through conceptual models part I — a discussion of principles. *J. Hydrol.* 10, 282–290. doi: 10.1016/0022-1694(70)90255-6

- Natarajan, S., and Radhakrishnan, N. (2019). Simulation of extreme event-based rainfall-runoff process of an urban catchment area using HEC-HMS. *Model. Earth Syst. Environ.* 5, 1867–1881. doi: 10.1007/s40808-019-00644-5
- Natarajan, S., and Radhakrishnan, N. (2020). Flood hazard delineation in an ungauged catchment by coupling hydrologic and hydraulic models with geospatial techniques—a case study of Koraiyar basin, Tiruchirappalli City, Tamil Nadu, India. *Environ. Monit. Assess.* 192:689. doi: 10.1007/s10661-020-08650-2
- Olayinka, D., and Irvibogbe, H. (2017). Estimation of hydrological outputs using HEC-HMS and GIS. *Nig. J. Environ. Sci. Technol.* 1, 390–402. doi: 10.36263/nijest.2017.02.0054
- Ouallali, A., Kader, S., Bammou, Y., Aqnoy, M., Courba, S., Beroho, M., et al. (2024). Assessment of the erosion and outflow intensity in the Rif region under different land use and land cover scenarios. *Land* 13:141. doi: 10.3390/land13020141
- Peptenatu, D., Grecu, A., Simion, A. G., Gruia, K. A., Andronache, I., Draghici, C. C., et al. (2020). “Deforestation and frequency of floods in Romania” in Water resources management in Romania. eds. A. M. Negm, G. Romanescu and M. Zelenáková (Cham: Springer International Publishing).
- Petrişor, A.-I., Sirodoev, I., and Ianoş, I. (2020). Trends in the national and regional transitional dynamics of land cover and use changes in Romania. *Remote Sens.* 12:230. doi: 10.3390/rs12020230
- Ponce, V. M., and Hawkins, R. H. (1996). Runoff curve number: has it reached maturity? *J. Hydrol. Eng.* 1, 11–19. doi: 10.1061/(ASCE)1084-0699(1996)1:1(11)
- Pullar, D., and Springer, D. (2000). Towards integrating Gis and catchment models. *Environ. Model. Softw.* 15, 451–459. doi: 10.1016/S1364-8152(00)00023-2
- Qi, W., Ma, C., Xu, H., Chen, Z., Zhao, K., and Han, H. (2021). A review on applications of urban flood models in flood mitigation strategies. *Nat. Hazards* 108, 31–62. doi: 10.1007/s11069-021-04715-8
- Rahman, K. U., Balkhair, K. S., Almazroui, M., and Masood, A. (2017). Sub-catchments flow losses computation using Muskingum-Cunge routing method and HEC-HMS GIS based techniques, case study of Wadi Al-Lith, Saudi Arabia. *Model. Earth Syst. Environ. Saudi Arabia. Model. Earth Syst. Environ.* 3, 1–19. doi: 10.1007/s40808-017-0268-1
- Ramly, S., and Tahir, W. (2016). “Application of HEC-GeoHMS and HEC-HMS as rainfall-runoff model for flood simulation” in *Isfram 2015*. eds. W. Tahir, P. I. D. S. H. Abu Bakar, M. A. Wahid, S. R. Mohd Nasir and W. K. Lee (Singapore: Springer Singapore), 181–192.
- Ranjan, S., and Singh, V. (2022). HEC-HMS based rainfall-runoff model for Punpun river basin. *Water Pract. Technol.* 17, 986–1001. doi: 10.2166/wpt.2022.033
- Rezaei-Sadr, H. (2020). Flood hydrograph prediction in a semi-arid mountain catchment: the role of catchment subdivision. *J. Flood Risk. Manag.* 13:e12568. doi: 10.1111/jfr3.12568
- Ross, C., Prihodko, L., Anchang, J., Kumar, S., Ji, W., and Hanan, N. (2018). Global hydrologic soil groups (HYSOGs250m) for curve number-based runoff modeling. Oak Ridge, TN: ORNL DAAC.
- Sahu, M. K., Shwetha, H. R., and Dwarakish, G. S. (2023). State-of-the-art hydrological models and application of the HEC-HMS model: a review. *Model. Earth Syst. Environ.* 9, 3029–3051. doi: 10.1007/s40808-023-01704-7
- Salvadore, E., Bronders, J., and Batelaan, O. (2015). Hydrological modelling of urbanized catchments: a review and future directions. *J. Hydrol.* 529, 62–81. doi: 10.1016/j.jhydrol.2015.06.028
- Sarminingsih, A., Rezagama, A., and Ridwan. (2019). Simulation of rainfall-runoff process using HEC-HMS model for Karang watershed, Semarang, Indonesia. *J. Phys. Conf. Ser.* 1217:012134. doi: 10.1088/1742-6596/1217/1/012134
- Sestras, P., Mircea, S., Cimpeanu, S. M., Teodorescu, R., Roşca, S., Bilaşco, Ş., et al. (2023a). Soil Erosion assessment using the intensity of Erosion and outflow model by estimating sediment yield: case study in river basins with different characteristics from Cluj County, Romania. *Appl. Sci.* 13:9481. doi: 10.3390/app13169481
- Sestras, P., Mircea, S., Roşca, S., Bilaşco, Ş., Sălăgean, T., Dragomir, L. O., et al. (2023b). Gis based soil erosion assessment using the Usle model for efficient land management: a case study in an area with diverse pedo-geomorphological and bioclimatic characteristics. *Not. Bot. Hort. Agrob.* 51:13263. doi: 10.15835/nbha51313263
- Sestras, P., Salagean, T., Bilasco, S., Bondrea, M. V., Nas, S., Fountas, S., et al. (2019). Prospect of a Gis based digitization and 3D model for a better management and land use in a specific micro-areal for crop trees. *Environ. Eng. Manag. J.* 18, 1269–1277. doi: 10.30638/eemj.2019.121
- Seth, N., Deshmukh, S. G., and Vrat, P. (2006). A conceptual model for quality of service in the supply chain. *Int. J. Phys. Distri. Logist. Manag.* 36, 547–575. doi: 10.1108/09600030610684971
- Shah, M., and Lone, M. A. (2022). Hydrological modeling to simulate stream flow in the Sindh Valley watershed, Northwest Himalayas. *Model. Earth Syst. Environ.* 8, 2461–2470. doi: 10.1007/s40808-021-01241-1
- Sidle, R. C. (2021). Strategies for smarter catchment hydrology models: incorporating scaling and better process representation. *Geosci. Lett.* 8:24. doi: 10.1186/s40562-021-00193-9
- Skaugen, T., and Weltzien, I. H. (2016). A model for the spatial distribution of snow water equivalent parameterized from the spatial variability of precipitation. *Cryosphere* 10, 1947–1963. doi: 10.5194/tc-10-1947-2016
- Sudriani, Y., Sebestyén, V., and Abonyi, J. (2023). Surface water monitoring systems—the importance of integrating information sources for sustainable watershed management. *IEEE Access* 11, 36421–36451. doi: 10.1109/ACCESS.2023.3263802
- Svetlana, D., Radovan, D., and Ján, D. (2015). The economic impact of floods and their importance in different regions of the world with emphasis on Europe. *Proc. Econ. Fin.* 34, 649–655. doi: 10.1016/S2212-5671(15)01681-0
- Taherizadeh, M., Niknam, A., Nguyen-Huy, T., Mezósi, G., and Sarli, R. (2023). Flash flood-risk areas zoning using integration of decision-making trial and evaluation laboratory, Gis-based analytic network process and satellite-derived information. *Nat. Hazards* 118, 2309–2335. doi: 10.1007/s11069-023-06089-5
- Tariq, A., Hashemi Beni, L., Ali, S., Adnan, S., and Hatamleh, W. A. (2023). An effective geospatial-based flash flood susceptibility assessment with hydrogeomorphic responses on groundwater recharge. *Groundw. Sustain. Dev.* 23:100998. doi: 10.1016/j.gsd.2023.100998
- Teng, F., Huang, W., Cai, Y., Zheng, C., and Zou, S. (2017). Application of hydrological model Prms to simulate daily rainfall runoff in Zamask-Yingluoxia subbasin of the Heihe River basin. *Water* 9:769. doi: 10.3390/w9100769
- Teng, F., Huang, W., and Ginis, I. (2018). Hydrological modeling of storm runoff and snowmelt in Taunton River basin by applications of HEC-HMS and PRMS models. *Nat. Hazards* 91, 179–199. doi: 10.1007/s11069-017-3121-y
- Thakur, J. K., Singh, S. K., and Ekanthalu, V. S. (2017). Integrating remote sensing, geographic information systems and global positioning system techniques with hydrological modeling. *Appl. Water Sci.* 7, 1595–1608. doi: 10.1007/s13201-016-0384-5
- Todini, E. (2007). Hydrological catchment modelling: past, present and future. *Hydrol. Earth Syst. Sci.* 11, 468–482. doi: 10.5194/hess-11-468-2007
- USDA (1972). Soil conservation service national engineering handbook. Section 4: hydrology. Washington, DC: USDA.
- USGS. (2017). Runoff: surface and overland water runoff. Water Science School. Available at: <https://www.usgs.gov/> (Accessed December 12, 2023).
- Venkatesh, M., and Anshumali. (2019). A GIS-based assessment of recent changes in drainage and morphometry of Betwa River basin and sub-basins, Central India. *Appl. Water Sci.* 9:157. doi: 10.1007/s13201-019-1033-6
- Verma, R., Sharif, M., and Husain, A. (2022). Application of HEC-HMS for hydrological modeling of upper Sabarmati River basin, Gujarat, India. *Model. Earth Syst. Environ.* 8, 5585–5593. doi: 10.1007/s40808-022-01411-9
- Visweshwaran, R. (2017). Application of the HEC-HMS model for runoff simulation in the Krishna basin. Master of Technology in Remote Sensing and Geographic Information System, National Institute of Technology Karnataka Surathkal.
- Wagener, T., Wheeler, H., and Gupta, H. V. (2004). Rainfall-runoff modelling in gauged and ungauged catchments. London: World Scientific.
- Whitfield, P. H. (2012). Floods in future climates: a review. *J. Flood Risk. Manag.* 5, 336–365. doi: 10.1111/j.1753-318X.2012.01150.x
- Willmott, C. J. (1981). On the validation of models. *Phys. Geogr.* 2, 184–194. doi: 10.1080/02723646.1981.10642213
- WMO (1986). Intercomparison of models of snowmelt runoff. Geneva: World Meteorological Organization.
- Woodruff, J. D., Irish, J. L., and Camargo, S. J. (2013). Coastal flooding by tropical cyclones and sea-level rise. *Nature* 504, 44–52. doi: 10.1038/nature12855
- Yan, Y., Zhang, W., Liu, Y., and Li, Z. (2023). Simulated annealing algorithm optimized Gru neural network for urban rainfall-inundation prediction. *J. Hydroinf.* 25, 1358–1379. doi: 10.2166/hydro.2023.006
- Yang, L., Meng, X., and Zhang, X. (2011). SRTM DEM and its application advances. *Int. J. Remote Sens.* 32, 3875–3896. doi: 10.1080/01431161003786016
- Yimer, G., Jonoski, A., and Griensven, A. V. (2009). Hydrological response of a catchment to climate change in the upper Beles river basin, upper blue Nile, Ethiopia. *Nile Basin Water Eng. Sci. Mag.* 2, 49–59.
- Zezelew, D. G., and Melesse, A. M. (2018). Applicability of a spatially semi-distributed hydrological model for watershed scale runoff estimation in Northwest Ethiopia. *Water* 10:923. doi: 10.3390/w10070923

Home > Euro-Mediterranean Journal for Environmental Integration > Article

Exploring soil pedogenesis through frequency-dependent magnetic susceptibility in varied lithological environments



Euro-Mediterranean Journal for Environmental Integration

[Aims and scope](#) →

[Submit manuscript](#) →

[Use our pre-submission checklist](#) →

Avoid common mistakes on your manuscript.



Paul Sestras [View ORCID ID profile](#)

Faculty of Civil Engineering, Technical University of Cluj-Napoca, 400020, Cluj-Napoca-Napoca, Romania

Academy of Romanian Scientists, Ilfov 3, 050044, Bucharest, Romania

[View author publications](#)

You can also search for this author in [PubMed](#) | [Google Scholar](#)

Original Paper (2024)

Download

Abdessa

Michael & Paul Sestras

EURO-MEDITERRANEAN JOURNAL FOR ENVIRONMENTAL INTEGRATION

Publisher name: SPRINGER HEIDELBERG

Journal Impact Factor™

1.8

2023

2

Five Year

JCR Category	Category Rank	Category Quartile
ENVIRONMENTAL SCIENCES <i>in ESCI edition</i>	267/358	Q3

Source: Journal Citation Reports 2023. [Learn more](#)

Journal Citation Indicator™

0.32

2023

0.32

2022

JCI Category	Category Rank	Category Quartile
--------------	---------------	-------------------





Exploring soil pedogenesis through frequency-dependent magnetic susceptibility in varied lithological environments

Abdessalam Ouallali¹ · Naima Bouhsane² · Saidati Bouhlassa² · Velibor Spalevic³ · Shuraik Kader⁴ · Ruby Michael⁴ · Paul Sestras^{5,6}

Received: 4 March 2024 / Accepted: 21 September 2024
© The Author(s) 2024

Abstract

The use of percent frequency-dependent magnetic susceptibility ($\chi_{fd}\%$) is well-established for detecting superparamagnetic (SP) components in fine-grained soils and sediments. This study employs $\chi_{fd}\%$ as a direct indicator of pedogenetic processes in soils from the Moroccan Rif region. Three soil transects (T1, T2, and T3), each comprising four soil cores with depths reaching 100 to 120 cm, were sampled from distinct lithological formations within an area subject to moderate to intense erosion. A total of 272 soil samples were collected and analyzed using MS2 Bartington Instruments, providing values to calculate $\chi_{fd}\%$ and identify ultrafine ferrimagnetic minerals (SP, $<0.03 \mu\text{m}$). In Quaternary fluvial terraces (T1) soils, approximately 60% of the samples indicate a mixture of SP, multidomain (MD), and Single Stable Domain (SSD) magnetic grains, while 30% contained coarser MD grains. Only 10% of the samples exhibit predominantly superparamagnetic (SP) grains. Soils on marly substrates (T2) showed 90% of samples with a combination of SP, MD, and SSD, and just 10% had SP grains. In contrast, soils from Villafranchian sandy deposits displayed $\chi_{fd}\%$ values exceeding 10% in over 50% of samples, indicating that almost all iron components consist of SP grains. Physico-chemical analyses of the soils in profiles T1, T2, and T3 reveal distinct characteristics, including variations in clay content, organic matter, nutrient levels, and proportions of free and total iron. These results are important for understanding soil evolution and pedogenesis, with profiles T1 and T3 showing advanced development marked by high mineral iron, clay, and organic matter content. In contrast, profile T2 reflects a weak stage, influencing nutrient availability and contributing to overall soil dynamics in the respective profiles. The results of this study suggest that magnetic susceptibilities in these samples primarily originate from pedogenetic sources, revealing significantly advanced pedogenesis compared to T1 and T2 soils. The findings of this study align with previous research on soil erosion and degradation in the region, demonstrating that soils developed on terraces and marly substrates are more degraded and less stable than those on sandy substrates. This study underscores the utility of magnetic susceptibility as a rapid and effective indicator for initial soil assessment and gauging the degree of pedogenesis.

Keywords Percent frequency-dependent magnetic susceptibility · Superparamagnetic components · Pedogenetic processes · Ferrimagnetic minerals · Soil erosion

Introduction

Magnetic susceptibility verifies the magnetizability of materials found in soils, rocks, dust, and sediments, particularly iron-containing minerals (Balsam et al. 2011). Dearing (1994) states these measures supplement data provided by mineralogical procedures such as X-ray diffraction or heavy mineral analysis. In summary, these measures allow

researchers to identify the minerals in a sample, estimate their concentration or total volume with high precision, classify distinct types of material, identify the processes that govern their generation or movement, and establish "ecological footprints" for the corresponding materials. The conventional soil maps only show their physical and chemical characteristics and spatial extent. Therefore, additional knowledge about the magnetism of soils and sediments is required (Silva et al 2016; Brito et al. 2022). The scientific community stands as the primary entity engrossed in the electromagnetic and magnetic properties of soils and rocks, particularly within various research domains such as soil

Responsible Editor: Mohamed Ksibi.

Extended author information available on the last page of the article

erosion (Moukhchane et al. 1998; Bouhlassa & Bouhsane 2019), geophysics, and environmental sciences (Singer et al. 1996; Dakir et al. 2020), soil development, and contamination (Hanesch et al. 2007). Archaeological surveys (Linford et al. 2005), planetary studies (Kletetschka et al. 2000), as well as mineral detection and mining exploration (Hannam et Dearing, 2008) also rely on this method. The pedogenetic process of soils, encompassing the formation and development of soils over geological time, holds crucial significance in various science and environmental management fields (Ma et al. 2019; Lal et al. 2021). A comprehensive assessment of this process is particularly relevant regarding soil resource management (Sabri et al. 2022; Stefanidis et al. 2022). Understanding how soils evolve and form allows us to better anticipate their physical, chemical, and biological characteristics, directly impacting sustainable and rational land use. In-depth knowledge of soil pedogenesis also contributes to developing effective strategies to combat soil degradation (Debebe et al. 2023; Wang et al. 2023). By figuring out the causes and mechanisms of soil evolution and degradation, environmental management experts can put targeted preventive and corrective measures into place to preserve long-term fertility and productivity (Cai et al. 2023; Liliwirianis et al. 2023).

Using magnetic susceptibility to assess soils' mineralogy and grain size offers a powerful tool to probe the pedogenetic processes in depth (Ding et al. 2020; Cao et al. 2021). Magnetic susceptibility, which measures a material's response to an external magnetic field, is directly linked to magnetic minerals such as magnetite and maghemite in soils (Shirzaditabar et al. 2021). By studying spatial and vertical variations in magnetic susceptibility within a soil profile, it is possible to recreate the geochemical history of the soil, offering useful insights into past and current soil formation processes (De Mello et al. 2020). Additionally, the size of the magnetic particles in the soil may be determined by measuring the magnetic grain size, which can be used to determine the parent material sources and comprehend the movement and redeposition of particles within the soil profile (Wang et al. 2022; Ouallali et al. 2023). Incorporating this data into a study of soil formation can provide valuable insights. For instance, changes in magnetic susceptibility in soil profiles can indicate periods of intense soil formation, chemical changes, or climate variations over time. Additionally, the distribution of magnetic minerals can help trace water movement in the soil, providing insights into past and current moisture regimes (Kader et al. 2022; Kehl et al. 2021). The present study aims to: 1. characterize the pedogenetic process and assess the degree of pedogenesis in various soil profiles sampled from diverse lithological formations under different land uses and slopes, 2. employ χ_{fd} measurements, to demonstrate that this property can serve as a sensitive and reliable indicator of soil pedogenesis

status, whether it is stability or degradation, 3. explore the use of magnetic susceptibility to assess the magnetic grain size of soils and identify specific markers of pedogenesis, 4. significantly contribute to the rapid and precise characterization of soil pedogenesis status and sustainable soil resource management while highlighting its potential to guide soil preservation and restoration strategies.

This study is valuable from both a scientific and practical aspect since it applies magnetic susceptibility data to provide a more thorough understanding of soil pedogenetic processes. This study provides important new information in identifying mineralogical changes and evaluating soil stability. Using magnetic susceptibility to quickly and reliably describe soil parameters has important practical applications in land use planning, agriculture, and environmental management. By providing accurate data on soil composition and condition, it facilitates the identification of regions at risk of degradation, informs methods for soil conservation, and directs sustainable land use practices.

Material and methods

Study area and sampling

The study area is situated in northwest Morocco, on the border between the provinces of Tetouan and Assilah (Fig. 1). The choice of the study area is based on the results of models RUSLE (revised universal soil loss equation), SWAT (soil and water assessment tools), and EPM (erosion potential method), which are a few of the empirical and hydrological models, which have been used in the recent years to investigate soil erosion and degradation (Ouallali et al. 2016, 2020a, b). The sampled sites present different characteristics regarding lithology, land use, and slope (Table 1). These investigations have shown that the areas with the highest erosion rates are mostly found on lower Eocene marl deposits. While Villafranchian sandy deposits are the most stable and least eroded, quaternary fluvial terrace soils typically have moderate erosion rates.

Sampling of 1-m to 1.20-m soil cores was carried out using a cylindrical soil auger with a diameter of 5 cm and a length of 70 cm. The lower end of this auger is sharpened to facilitate soil penetration, while the upper end is reinforced to withstand the impact of hammer blows. A 5 kg hammer is used to aid in the cylinder's penetration into the soil. Once a depth of 50 cm is reached, the auger is extracted from the soil using an iron rod inserted into holes located at its upper part. This is facilitated by digging the sides of the cylinder with a pickaxe until the lower level of the auger is reached. Subsequently, with the assistance of a wooden piece, the soil core is gently pushed out onto a half PVC cylinder, and then it is sliced into several 5 cm sections, each labeled and

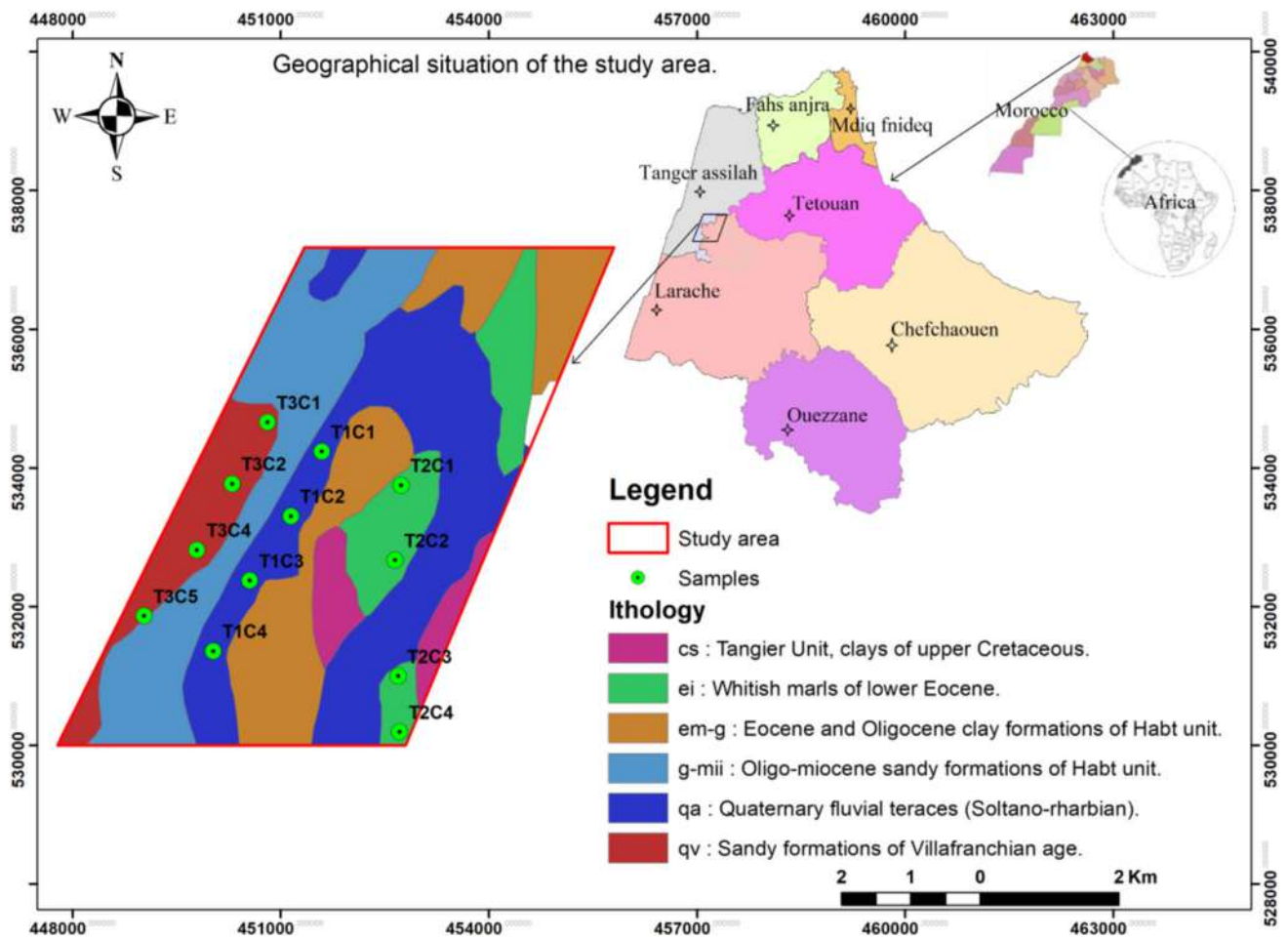


Fig. 1 Geographical location of the study area and positions of the sampled sites

Table 1 Characteristics of the profiles sampled in the study area

TranSect. "Introduction." (T1)			
<i>Cores</i>	<i>Lithology</i>	<i>Land use</i>	<i>Slope class (%)</i>
C1	Quaternary fluvial terraces	Cultivated lands	0–2
C2			5–10
C3			2–5
C4			2–5
TranSect. "Material and methods" (T2)			
C1	Lower Eocene marl formation	Bare land	5–10
C2			30–40
C3			10–15
C4			20–30
TranSect. "Results and discussion" (T3)			
C1	Villafranchian sand formation	White pine reforestation	2–5
C2			5–10
C3		Degraded scrubland	5–10
C4			10–15

placed in plastic bags. The auger is then reinserted to extract the remaining portion of the soil profile, reaching the desired

depths, and the same process is repeated to uncover the second half of the profile (Fig. 2).



Fig. 2 An example of a core sample obtained from sandy formations and within the Quaternary fluvial terraces under white pine reforestation in the study area

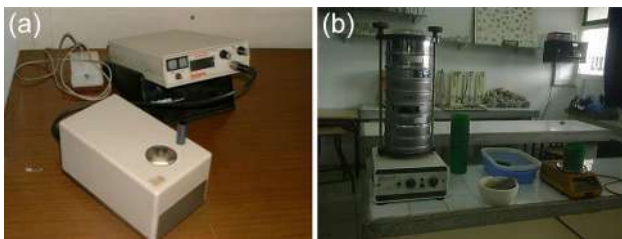


Fig. 3 Bartington MS2 type susceptibility meter (a). Laboratory equipment used for sample pretreatment (b)

Before commencing magnetic measurements, subjecting the samples to the pre-processing stages required by the method is essential. Indeed, each 1-m to 1.20-m core is divided into several 5-cm samples. Each sample is first weighed, then dried in an oven at 40 °C for 24 h, and reweighed to determine the moisture content and to facilitate subsequent grinding. The grinding is done by manually disaggregating each sample in a granite or agate mortar. Subsequently, all samples are sieved through meshes with diameters of 2 mm and 5 mm, and the residues obtained are used to fill plastic containers for magnetic susceptibility measurements (Fig. 3).

Measurement of χ_{lf} magnetic susceptibility

Two forms of magnetic susceptibility can be used to categorize the ease with which a material can get magnetized when exposed to a magnetic field. These are volumetric susceptibility, denoted as κ , which is dimensionless and represents susceptibility per unit volume, and mass susceptibility, denoted as χ , expressed in $\text{m}^3 \text{kg}^{-1}$ (as of Eq. 1), representing susceptibility per unit mass (Aguilera et al. 2020; Alekseev et al. 2023). According to Thompson and Oldfield (1986), at low magnetic field strengths ($H < 1 \text{ mT}$),

susceptibility is virtually independent of the field intensity and depends on the nature and size of the minerals.

$$M = \kappa \cdot H \text{ or } J = \chi \cdot H \quad (1)$$

M and J represent the magnetizations induced per unit volume (Am^{-1}) and per unit mass ($\text{Am}^2 \text{Kg}^{-1}$).

The magnetic susceptibility is simply defined as the ratio of the magnetization M within the material to the applied magnetic field strength H . The Bartington MS2 susceptibility meter enables the measurement of magnetic susceptibility in grains at both low and high frequencies when subjected to a magnetic field (Fig. 3). At low frequency (0.47 kHz), the induced magnetization is in phase with the field, and the 'in-phase' susceptibility equals the effective susceptibility. This allows superparamagnetic (SP) crystals near the boundary with stable single-domain (SSD) grains to contribute fully to the susceptibility (Yang et al. 2020). However, this is not the case at high frequency (4.7 kHz). Relaxation effects at high frequency cause the in-phase susceptibility to decrease and the out-of-phase susceptibility to increase, decreasing the measured susceptibility (Bouhlassa & Bouhsane 2023). The higher frequency shifts the domain boundary between SP and SSD grains toward smaller grain sizes. Consequently, SP grains near the boundary behave like SSD grains, exhibiting lower susceptibility values. The obtained volumetric and mass magnetic susceptibilities are denoted as κ_{lf} , κ_{hf} , χ_{lf} , and χ_{hf} , with lf and hf referring to low and high-frequency measurement successively.

Calculation of frequency-dependent susceptibility χ_{fd} % and assessment of magnetic mineralogy and grain size

Frequent-dependent susceptibility is measured by taking two measurements of a sample at two different magnetization frequencies, low and high (Owliaie 2014; Li et al. 2020). This parameter is handy for detecting the presence of small magnetic grains ($< 0.03 \mu\text{m}$) exhibiting superparamagnetic behavior (Djerrab et al. 2012). There are two possible calculations for this susceptibility: the percentage of frequency-dependent susceptibility ($\chi_{fd}\%$) and the frequency-dependent susceptibility specific to mass ($\chi_{fd} 10^{-8} \text{ m}^3 \text{ kg}^{-1}$). The relationships are illustrated by Eq. 2 and Eq. 3.

$$\chi_{fd}\% = 100 (\chi_{lf} - \chi_{hf}) / \chi_{lf} \quad (2)$$

$$\chi_{fd} = \frac{\chi_{hf} - \chi_{lf}}{\rho \cdot \Delta f \cdot V} \cdot 10^8 \quad (3)$$

Where:

χ_{fd} is the frequency-dependent susceptibility specific to mass, $\chi_{fd}\%$ is the percentage of frequency-dependent susceptibility, χ_{hf} is the magnetic susceptibility at the high

magnetization frequency, χ_{lf} is the magnetic susceptibility at the low magnetization frequency, ρ is the density of the sample, Δf is the difference in frequencies between high and low measurements, and V is the volume of the sample.

χ_{fd} is a parameter used to determine the potential presence of a superparamagnetic (SP) mineral fraction (Dearing 1999). The concentration of SP grains is typically linked to the strength of pedogenic processes (Blundell et al. 2009; Liu et al. 2015; Grison et al. 2023), the pedogenic processes are stronger when the SP concentration is higher. Based on a semi-quantitative index for interpreting frequency-dependent magnetic susceptibility values, environmental magnetic samples can be divided into four classes: samples with $\chi_{fd}\% < 2\%$, which contain virtually no SP grains; samples with $2\% < \chi_{fd}\% < 10\%$, indicating a mixture of SP and larger non-SP grains; samples with $10\% < \chi_{fd}\% < 14\%$, representing an approximate 75% SP concentration; and samples with $\chi_{fd}\% > 14\%$, which are rare values, potentially erroneous measurements, weak samples, or indicative of magnetic anisotropy or contamination (Dearing et al. 1996) (Table 2). The maximum values of $\chi_{fd}\%$ are similar in theoretical calculations and synthetic grain data, reaching 14.5–16.9% for magnetite and 11.6–14.3% for maghemite, with values around 10–12% for a broad and equal distribution of SP grains (Dearing et al. 1996). In nature, it is unlikely that grains exist independently of each other or in narrow size ranges of discrete grains; they are likely to aggregate and form clusters. For example, low-frequency-dependent values in relatively large crystals are probably caused by a small number of SP crystals attached to their surfaces. There is insufficient experimental data to confidently construct a quantitative model to interpret χ_{fd} and $\chi_{fd}\%$ in terms of absolute proportions of different grain sizes, as shown in Table 2.

Physicochemical analysis of soil profiles

Physico-chemical soil analysis plays a crucial role in understanding the regional soil environment. Data on parameters such as texture, organic matter, nutrients, pH, total and free iron content, are taken from an in-depth study by *Institut*

Table 2 Semi-quantitative interpretation of frequency-dependent susceptibility (Dearing et al. 1996; Liu et al. 2015)

Faible $\chi_{fd}\%$	< 2.0	Practically no SP grains (< 10%)
Moderate $\chi_{fd}\%$	2.0–10.0	A mixture of SP grains and coarse non-SP grains, or SP grains < 0.005 μm
High $\chi_{fd}\%$	10.0–14.0	Nearly all SP grains (> 75%)
Very high $\chi_{fd}\%$	> 14.0	Rare values, measurement error, anisotropy, small sample size, or contamination

National de la Recherche Agronomique (INRA) in the Tangier-Tetouan region. Tables 3, 4, and 5 reflect these results, enabling us to assess soil composition, evolution, and pedogenesis. The main aim of these analyses is to understand the detailed composition of soils, to accurately assess their fertility and agricultural potential. These results will be used as a basis for comparison with frequency-dependent magnetic susceptibility values ($\chi_{fd}\%$), a sensitive indicator of pedogenesis. The association between physico-chemical parameters and $\chi_{fd}\%$ values will enrich the understanding of geochemical processes and mineral alteration. These joint analyses aim to shed light on local environmental dynamics, offering practical perspectives for land management, agriculture, and ecosystem sustainability in the study area.

Results and discussion

Statistical analysis of the results ($\chi_{fd}\%$)

The frequency of magnetic susceptibility dependence, $\chi_{fd}\%$, exhibits values ranging between 0 and 14, with an average of 4.71 for samples from tran Sect. "Introduction.". For T2, $\chi_{fd}\%$ varies from 0 to 15, with an average of 5.95, while

Table 3 Results of physico-chemical tranSect. "Introduction." analysis

Depth (cm)	T1				
	0–30	30–50	50–80	80–100	100–160
Clay %			77.7	57.2	65.7
Silt %			3.8	18	18
Fine sand %			12.8	16.3	8.7
Coarse sand %			2.1	3.3	2.3
OM %	4.11	2.33	1.84	1.57	1.24
Carbon %	2.39	1.35	1.07	0.91	0.72
Nitrogen %	0.205	0.135	0.1	0.09	0.07
C/N	11.7	10.0	10.7	10.1	10.3
P ₂ O ₅ % (Total)	1.363	1.028	0.835	0.825	0.761
P ₂ O ₅ % (Assimilable)	0	0	0	0	0
K ₂ O % (Total)	5.175	5.848	5.022	6.004	5.354
K ₂ O % (Assimilable)	0.282	0.174	0.157	0.149	0.115
Calcium ech. meq/100g	44.87	46.6	39.87	31.88	19.16
Magnesium ech	6.61	6.88	10.87	16.08	13.72
Potassium ech	0.59	0.37	0.33	0.31	0.24
Sodium ech	0.85	0.59	1.47	2.11	1.92
pH (H ₂ O)	6.6	7.15	7.85	8.3	8.45
pH (KCl)	5.7	6.1	6.55	7	7.4
Free iron (Fi) %	3.232	3.142	3.107	3.057	3.229
Total iron (Ti) %	7.635	7.944	7.958	7.929	8.005
Fi/Ti	0.42	0.40	0.39	0.39	0.40

Table 4 Results of physico-chemical tranSect. "Material and methods" analyses

Depth (cm)	T2		
	0–40	40–100	100–160
Clay %	57	65.8	44
Silt %	20	12.8	18.5
Fine sand %	2.1	2.6	2.8
Coarse sand %	2.7	0.5	2.8
OM %	1.02	1.22	0.78
Carbon %	0.59	0.607	0.319
Nitrogen %
C/N
P2O5% (Total)	0.008	0	0
P2O5% (Assimilable)	0.051	0.025	0.025
Calcium ech. meq/100g	55.83	49.6	45.36
Magnesium ech	7.87	16.78	17.15
Potassium ech	1.1	0.54	0.53
Sodium ech	0.32	0.75	0.78
PH H2O	7.8	7.95	8.05
PH KcL	7	7.1	7.2
Free iron (Fi) %	2.46	2.84	2.86
Total iron (Ti) %	6.96	7.1	7
Fi/Ti	0.35	0.40	0.41

Table 5 Results of physico-chemical tranSect. "Results and discussion" analyses

Depth (cm)	T3			
	0–25	25–40	40–90	90–120
Clay %	5	10.5	45.5	11.7
Silt %	7.2	6.6	7.8	7.7
Fine sand %	72.4	67.6	33.8	51.8
Coarse sand %	12.1	12.1	7	29
OM %	1.25	0.5	0.92	0.87
Carbon %	0.72	0.29	0.53	0.51
Nitrogen %	0.05	0.03	0.06	0.05
C/N	14.4	9.7	8.8	10.2
P2O5% (Total)	0.487	0.126
P2O5% (Assimilable)	0.002	0
PH	5.5	5.6	4.75	4.9
Free iron (Fi) %	0.5	1.15	6.95	6.06
Total iron (Ti) %	0.72	1.55	9.3	8.01
Fi/Ti	0.69	0.74	0.75	0.76

for T3, $\chi_{fd}\%$ displays susceptibilities ranging from 0.13 to 15.09 with an average of 9.77 (Table 6).

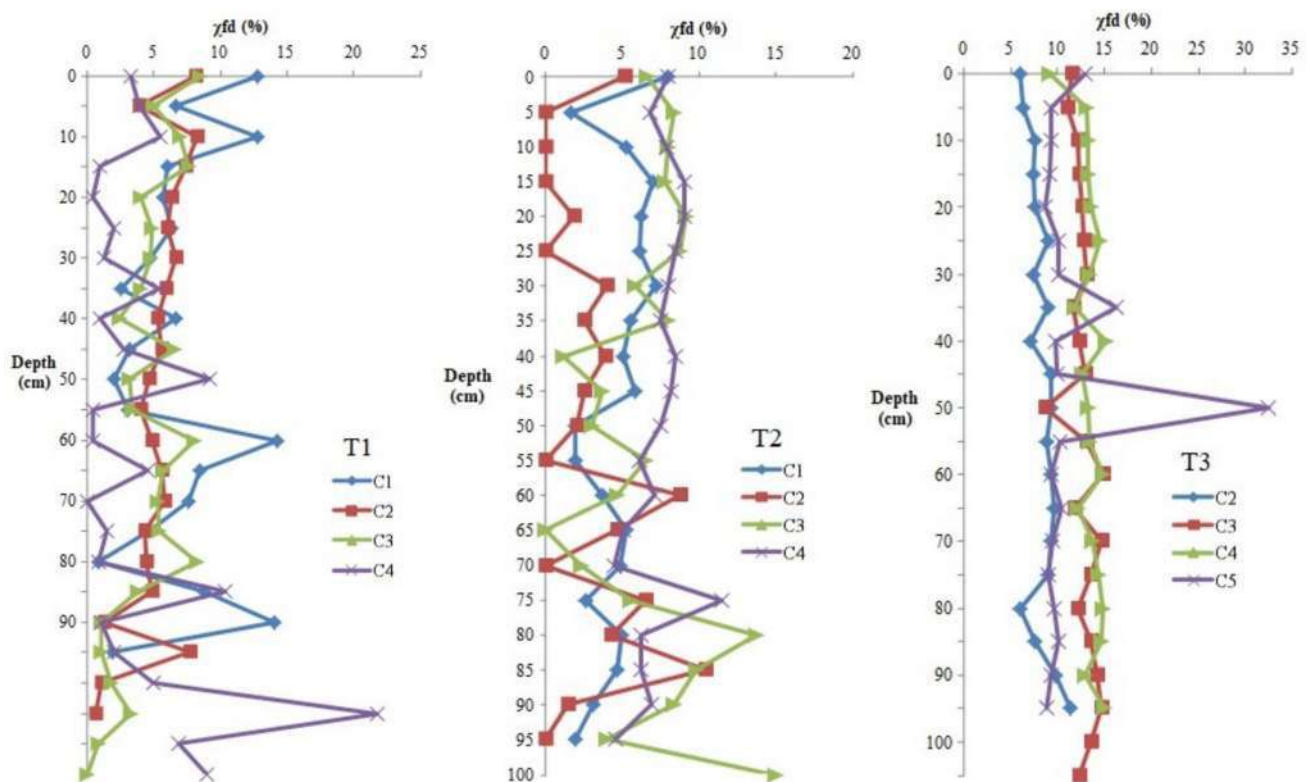
Variation of $\chi_{fd}\%$ with depth

The substrate of transect T1 is primarily composed of fragments of limestone rocks, sandstone fragments, gravel, and pebbles. These elements are occasionally bound together by a relatively weak and easily disintegrated carbonate cement. Some levels of sand appear at different depths with intercalations of silt-sand mixtures. These rock fragments make soil cultivation somewhat challenging, and the soil horizons in these areas are less developed. In the C1 and C2 cores sampled from a wheat cultivation area, there is noticeable irregularity in the evolution of magnetism along the profile, typically resembling a sawtooth pattern. This irregularity is particularly pronounced in the surface layer and is attributed to the effect of soil cultivation (Fig. 4). It also extends to lower bedrock levels, which can be explained by the dilution of magnetic minerals towards deeper horizons. The calculated values of the frequency-dependent magnetic susceptibility, $\chi_{fd}\%$, for these profiles, are generally low (Fig. 4). This parameter is handy for indicating the presence of magnetic grains located at the boundary between single domain (SSD) and superparamagnetic (SP) grains. It is also used as an indirect indicator of relative variations in the concentration of fine-grained magnetic particles defined by pedogenesis (Liu et al., 2005). The calculated averages of this parameter for each core are at most 6%. They, therefore, fall within the 2–10% range, which suggests the presence of a mixture of coarse superparamagnetic and non-SP grains (Djerrab, 2012). Most $\chi_{fd}\%$ values for cores C3 and C4, taken from uncultivated areas, range from 2 to 10%, indicating a mixture of coarse SP and non-SP grains. Pedogenesis is less frequent compared to C1 and C2 due to the absence of soil cultivation through plowing.

The average values of magnetic susceptibility were obtained for the cores from transect. "Material and methods" are weak. These low values indicate intense erosive activity in these formations, high sediment mobilization, and significant soil degradation (Ouallali et al. 2023). In other Rif regions, marls consistently show weak magnetic behavior (Faleh et al. 2005; Ouallali et al. 2020b, 2024), which aligns with the study's findings. In cores C1 and C2, sampled from an unvegetated area, susceptibility values remain consistently low across different profile horizons, showing little variation with depth. This low content of magnetic minerals is due to the marly nature of the substrate and the lack of dense vegetation cover. Consequently, there is almost no pedogenesis due to increased erosion (Rahimi et al. 2013). The calculated $\chi_{fd}\%$ values for this profile are also low, with the majority being less than 2%, indicating a complete absence of superparamagnetic minerals in certain levels (Dearing et al. 1996). However, some levels reach 8.69%, showing a relatively low mixture of SP and non-SP minerals. As for C3 and C4, sampled in cultivated

Table 6 Statistical studies of the results obtained from frequency-dependent susceptibility measurements for all samples

$\chi_{fd}\%$ (T1)		$\chi_{fd}\%$ (T2)		$\chi_{fd}\%$ (T3)	
Median	4.72	Median	6.45	Median	9.51
Min	0	Min	0	Min	0.13
Max	14	Max	15	Max	15.09
Mean	4.71	Mean	5.95	Mean	9.77
Range	14	Range	15	Range	14.96
Standard Deviation (S.D)	2.95	Standard Deviation (S.D)	3.36	Standard Deviation (S.D)	2.81
Coefficient of Variation (CV)	62.54%	Coefficient of Variation (CV)	56.49%	Coefficient of Variation (CV)	28.75%
Skewness	0.58	Skewness	-0.15	Skewness	-0.25
Kurtosis	0.18	Kurtosis	-0.55	Kurtosis	0.12
Depth (cm)	120 cm	Depth (cm)	100 cm	Depth (cm)	120 cm
Total number of samples	96	Total number of samples	80	Total number of samples	96

**Fig. 4** Variation of $\chi_{fd}\%$ values as a function of depth in the profiles of the three sampled sites (T1: TranSect. "Introduction.", T2: TranSect. "Material and methods" and T3: TranSect. "Results and discussion")

areas, the calculation of frequency-dependent susceptibility, $\chi_{fd}\%$, mainly falls within the (2–10%) range. These values suggest a mixture of coarse SP or non-SP minerals, or SP grains $< 0.005 \mu\text{m}$, except for the 100–105 cm level of core C3, where $\chi_{fd}\%$ exceeds 14%. This latter value can be attributed to either a measurement error or contamination of the deeper profile levels (Zong et al. 2017; Kanu et al. 2023). The upper portions of both profiles, composed of soil, contain higher levels of ferromagnetic minerals than the lower

part. On the one hand, this is due to the development of a thin layer of humiferous soil at the surface, accompanied by pedogenesis, which promotes the formation of iron minerals and iron oxides. On the other hand, the lower profile levels consist entirely of marls, which have a lithological nature poor in magnetic minerals (Qian et al. 2020).

At transect T3, two C3 and C4 cores were collected from a degraded shrubland area, each showing a slight altitudinal variation relative to the other. The magnetic susceptibilities

assessed in these two profiles are relatively low compared to C2 and C5 collected from a reforested area with white pine. These low values indicate soil degradation under the degraded shrublands compared to soils under reforestation. This is reflected in the low concentration of magnetic minerals along the profiles (Ayoubi et al. 2012), except for one level (50–55 cm) in core C3, which exhibits a high value reaching $48.91 \times 10^{-8} \text{ m}^3 \text{ kg}^{-1}$. Based on the classification of magnetic minerals developed by Djerrab et al. (2013), this level likely contains a small accumulation of magnetite. A slight decrease in these levels in core C4 is primarily due to the slope effect, as C4 has a higher slope (10–15%) compared to core C3 (5–10%). The variation curve of χ_{lf} with depth does not show significant variations, except for the top 20 cm, which has slightly higher values than the basal part. This is due to the shrubland effect, which promotes soil pedogenesis and retains a small portion of ferromagnetic minerals (Zhang et al. 2023; Bashir, Bangroo, Shafai, Shah, et al., 2024). The profiles' calculated frequency-dependent magnetic susceptibility, $\chi_{fd\%}$, shows values ranging between 10 and 14% for all soil and sand levels (Fig. 4). Therefore, the materials in these profiles consist mainly of superparamagnetic minerals. Uncontaminated soils are generally characterized by a significant superparamagnetic fraction produced by pedogenesis (Lu et al. 2007). Some levels exhibit values exceeding 14%, which may be attributed to either measurement error or sediment contamination by other elements.

The high magnetic susceptibilities in cores C2 and C5 indicate significant formation stability, reduced erosion, and minimal soil degradation. The influence of old pine reforestation prevents particle movement and promotes soil formation (Gennadiev et al. 2002). Magnetic mineralogy in these formations is diverse, showing a mixture of coarse superparamagnetic and non-SP grains belonging to single domain and multi-domain. This is evident in the values of the frequency-dependent magnetic susceptibility, $\chi_{fd\%}$, which belong to the 2–10% class for most horizons in these cores, except for some levels showing values below 2%, confirming the absence of superparamagnetic minerals.

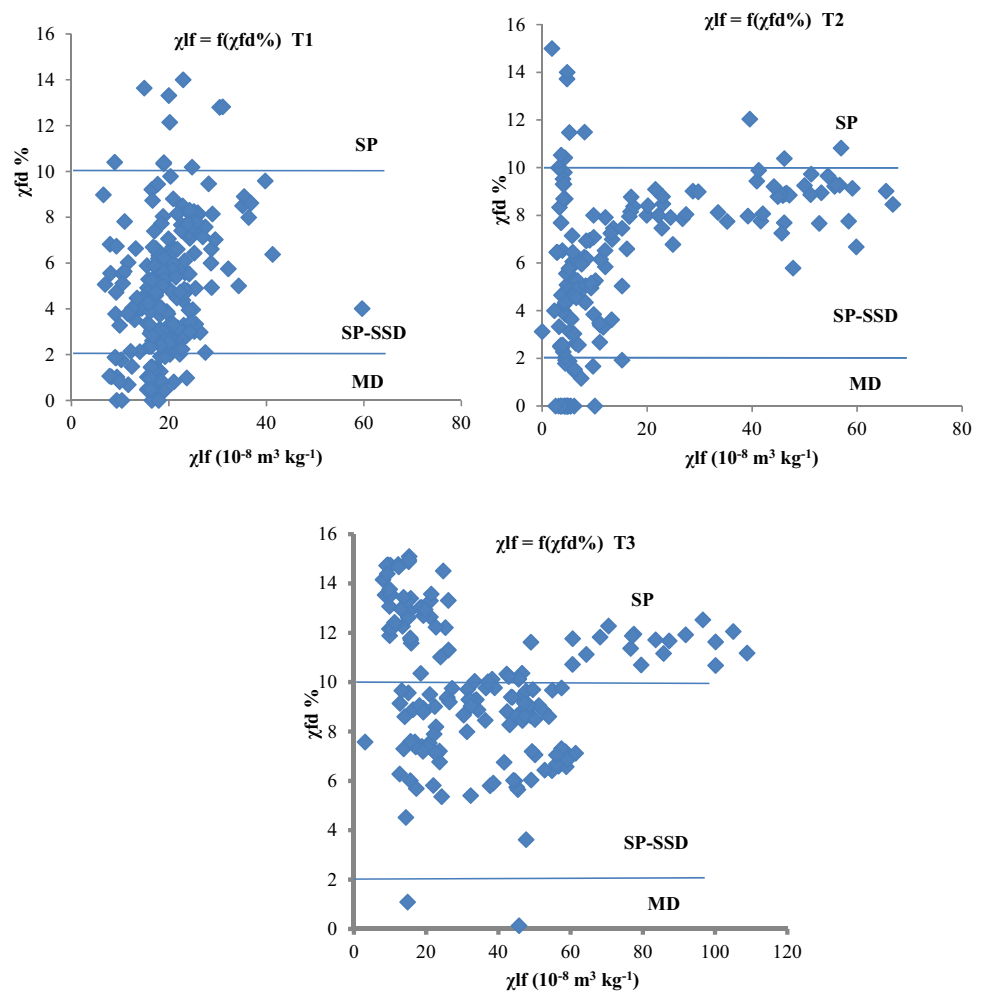
Magnetic particle size analysis and evaluation of pedogenic processes

The measurements of low-frequency magnetic susceptibility (χ_{lf}) and high-frequency magnetic susceptibility (χ_{hf}) are commonly employed to detect the presence of ultrafine ferromagnetic minerals, also referred to as the superparamagnetic fraction measuring less than $0.03 \mu\text{m}$ (Warrier et al. 2021; Kanu et al. 2023). Measurements at higher frequencies do not allow superparamagnetic grains to respond to the magnetic field, as they change more rapidly than their relaxation time (Bouhlassa, & Bouhsane 2019). Consequently, lower

magnetic susceptibility values are encountered at higher frequencies, and this difference is used to estimate ferromagnetic and superparamagnetic particles (Bouhlassa, & Bouhsane 2023). When superparamagnetic (SP) minerals are present in a soil sample, the high-frequency magnetic susceptibility values are slightly lower than those at low frequency. If no SP minerals exist, both measurements are identical (Dearing 1999). The magnetic grain size, evaluated for the three transects using the magnetic susceptibility dependent on frequency ($\chi_{fd\%}$), has allowed us to highlight the soil condition and, most importantly, determine the source of magnetic minerals in the various formations. Based on the semi-quantitative model proposed by Dearing (1999), the results obtained for the different horizons of the transects have shown that most samples contain a mixture of SP (superparamagnetic) grains and coarser grains or grains with SP $< 0.005 \mu\text{m}$. In the samples from transect T1, approximately 10% of the samples exhibit predominantly superparamagnetic (SP) grains, as they have a $\chi_{fd\%}$ proportion ranging from 12 to 14%. In comparison, the remaining samples have values ranging from 2 to 10% (60% of the samples). This indicates the presence of a mixture of SP, multidomain (MD), and Single Stable Domain (SSD) magnetic grains. The remaining samples (30%) correspond to coarser MD grains (Fig. 5).

In the samples from T2, approximately 70% of the samples fall within the middle range of 2 to 10% and may contain a mixture of SP and coarser MD grains. Over 20% of the samples have a low $\chi_{fd\%}$ value ($< 2\%$), implying the absence of SP grains. In comparison, less than 10% have a high $\chi_{fd\%}$ (> 10.04), indicating that the dominant magnetic component of this soil consists of ferrimagnetic SP grains. For the samples from T3, around 50% of the samples have $\chi_{fd\%}$ values exceeding 10%, which can be interpreted as the soil where virtually all iron components are SP grains. This suggests that the magnetic susceptibilities of these samples originate purely from pedogenic sources. The remaining half of the samples have a mixture of SP grains and non-coarser grains or grains $< 0.005 \mu\text{m}$. Therefore, a combination of pedogenic and anthropogenic sources contributes to the magnetic minerals in these samples, while only two samples contain no SP grains (Fig. 5). Generally, transect T3 contains significantly higher levels of SP minerals compared to T1, with T1, in turn, exhibiting higher SP mineral levels compared to T2. Consequently, pedogenesis is much more advanced in T3 compared to T1 and T2. These findings align with the conclusions drawn from the analysis of magnetic susceptibility variation with depth in all sampled soils. Most samples in the studied area contain a mixture of SP and MD magnetic grains, indicating a dual influence of pedogenesis and anthropogenic activities (such as agriculture and construction) on the magnetic behavior of materials. Several authors (Grison et al. 2021; Delbecque et al. 2022; Maity

Fig. 5 Magnetic grain size of soil profiles from the three lithological formations of the study area



et al. 2022) have also reported the combination of anthropogenic and pedogenic contributions to enhance magnetic susceptibility.

The results align with the conclusions of previous soil erosion studies conducted in the same region. Given the intrinsic connection between pedogenetic processes and soil erosion, findings of this research shed light on pedogenesis assessment, provide a basis for discussion and comparison with observations regarding soil degradation. The use of empirical models such as the RUSLE model (Ouallali et al. 2016; Bammou et al. 2024a) and the EPM (Erosion Potential Model) (Ouallali et al. 2020a; Bammou et al. 2024b) has demonstrated that the highest rates of erosion and degradation were associated with soils and areas occupying the lower Eocene marly lithological formations. Concurrently, soil profiles sampled from these same lithologies were subjected to two magnetic susceptibility-based models, T-H and PS. These models also revealed that the highest erosion rates, expressed in centimeters, were present in marly soils. In contrast, the lowest rates were recorded in sandy soils across the entire study area (Ouallali et al. 2023).

Pedogenetic processes play a crucial role in soil formation and transformation, involving forming clay minerals, migrating chemical elements, and structuring aggregates (Benzougagh et al. 2024). However, these evolutionary processes are often inherently linked to soil erosion rates, which can remove organic-rich topsoils and nutrients, directly impacting soil fertility (Ljavić et al. 2023). In the context of these soil profiles sampled from marly lithological formations, a fundamental measurement was the frequency-dependent magnetic susceptibility ($\chi_{fd}\%$). Approximately 70% of the samples exhibited $\chi_{fd}\%$ values falling within the middle range of 2 to 10%, suggesting a potential mixture of superparamagnetic and coarse mono-domain grains. Conversely, over 20% of the samples displayed low $\chi_{fd}\%$ values below 2%, indicating less active and effective pedogenesis in soils associated with this specific lithology. Similarly, a correlation is established for soil profiles sampled from the Villafranchian sandy formation. Approximately 50% of these samples exhibited $\chi_{fd}\%$ values exceeding 10%, indicating a predominance of superparamagnetic (SP) grains, which could imply a predominantly pedogenic origin. The other

half of the samples showed a mixture of SP and non-superparamagnetic grains, potentially resulting from a combination of pedogenic and anthropogenic factors. In summary, soil profiles from the sandy formation exhibited significantly higher SP mineral contents than those from marly formations. Consequently, pedogenetic processes appear to be more advanced in soil profiles derived from sandy formations, highlighting the link between soil mineralogical characteristics and pedogenetic processes. The study findings are in line with the research conducted by Sardoo et al. (2023), which emphasizes the important impact that soil formation and lithology have on magnetic susceptibility. This study confirmed that lithology has a major influence on the magnetic properties of the soil by showing that magnetic susceptibility varies significantly depending on the different parent materials and pedogenic processes, with low values in soils produced on marls and limestones (Sardoo et al. 2023). This provides more evidence in favor of using magnetic susceptibility as an accurate tool to deduce the processes involved in soil formation and the influence of parent material on soil development.

Comparison with results of physico-chemical analysis of soil profiles

Profiles T1, T2, and T3 show distinct characteristics reflecting the diversity of soils in the area. T1 is characterized by a high clay content in the upper layers, indicating a clayey soil, with high organic matter initially, then decreasing with depth, suggesting initial organic input followed by decomposition. High levels of assimilable phosphorus and potassium in T1 indicate adequate nutrient availability for plants, while the slightly acidic to neutral pH may influence nutrient availability (Bashir et al. 2024a, b, c). The presence of iron-rich minerals is also noted in this profile. This is compatible with the high values of the magnetic susceptibility. T2, although rich in clay, has lower levels of organic matter, phosphorus, and assimilable potassium than T1, suggesting limited nutrient availability for plants. The slightly alkaline pH may influence nutrient availability, and iron-rich minerals are also observed (Bashir et al. 2024a, b, c). As for T3, soil texture varies, showing a transition from a sandy texture in the upper layers to a significant increase in clay at depth. Organic matter is lower than in profiles T1 and T2, with variable levels of assimilable phosphorus and potassium. The slightly acidic to neutral pH and the increasing presence of iron-rich minerals at depth indicate soil weathering and formation processes. These variations in profile characteristics suggest differences in soil evolution, pedogenesis, and the potential presence of superparamagnetic particles.

Comparison of the T1, T2, and T3 profiles reveals significant differences in several aspects, offering valuable insights into the soil dynamics in each profile. Regarding

pedogenesis, profiles T1 and T3 show signs of advanced evolution with high clay and organic matter levels, suggesting more pronounced weathering and transformation processes. Conversely, profile T2 appears at an intermediate stage of pedogenesis, showing characteristics between profiles T1 and T3. Regarding nutrients, profiles T1 and T2 show higher levels of assimilable phosphorus and potassium than profile T3, indicating a more limited availability of these nutrients in the latter. Nutrient variability is potentially linked to soil texture and organic matter. Soil response (pH) varies slightly between profiles, keeping all in the neutral to slightly acid range. Regarding iron, free and total iron levels vary, indicating oxidation–reduction processes. The T3 profile is distinguished by a significant increase in iron levels at depth. Magnetic susceptibility ($\chi_{fd}\%$) underlines the advanced pedogenesis of T3 with high values, while T1 and T2 profiles show intermediate levels. Finally, the decrease in organic matter with depth in all profiles suggests implications for the stability of soil aggregates, underlining the importance of considering these variations for a holistic understanding of soil quality and its evolution.

Conclusion

The distinct characteristics observed in Profiles T1, T2, and T3 through physicochemical soil analyses align with the $\chi_{fd}\%$ values, highlighting intricate relationships between soil properties and magnetic susceptibility. T1, with high clay content and organic matter, exhibits elevated magnetic susceptibility, indicating advanced pedogenesis. In contrast, T2, despite clay richness, shows lower nutrient levels, influencing $\chi_{fd}\%$ values and suggesting an intermediate stage of pedogenesis. T3, marked by varying textures and lower organic matter, corresponds to heightened $\chi_{fd}\%$, affirming significant pedogenic advancement. The comparison underscores the utility of $\chi_{fd}\%$ as a proxy for altered horizons, with T3 showcasing increased superparamagnetic grains, emphasizing the role of authigenic magnetic minerals in pedogenesis. Despite $\chi_{fd}\%$'s limitations in capturing all soil development nuances, its association with pedogenic processes enhances the understanding, particularly when considering the broader context of soil evolution.

This research contributes to a global perspective on the applicability of magnetic susceptibility, guiding future studies across diverse regions and soil conditions. Exploring multiple proxies and factors influencing soil development remains crucial for refining the comprehension of pedogenesis and its environmental implications. However, to better understand the processes involved in soil formation, it would be beneficial to carry out more thorough research on how various types of rocks affect $\chi_{fd}\%$ and integrate this measurement with other soil parameters. Indeed, in-depth

characterization of the magnetic mineralogy and identification of the domain state within the samples, requires various methods used for this purpose, including thermomagnetic measurements, analysis of hysteresis loop parameters, and the interpretation of the Day diagram and the first-order inversion curve. These techniques can offer additional insights into the magnetic properties of the samples, allowing a comprehensive understanding of their magnetic behavior. Standardized techniques for measuring $\chi_{fd}\%$ can also improve comparisons across different regions and soil conditions. Ultimately, this study paves the way for a comprehensive assessment of soil development beyond its original scope, offering valuable insights for worldwide soil science and environmental studies.

Authors contributions Conceived and designed the studies—Ouallali Abdessalam, Bouhsane Naima, Saidati Bouhlassa, Velibor Spalevic and Shuraik Kader. Performed the analysis—Ouallali Abdessalam, Bouhsane Naima and Saidati Bouhlassa. Analysed and interpreted the data—Ouallali Abdessalam, Bouhsane Naima, Saidati Bouhlassa, Velibor Spalevic, Shuraik Kader, Ruby Michael and Paul Sestras. Contributed materials, analysis tools or data—Ouallali Abdessalam, Bouhsane Naima, Saidati Bouhlassa, Velibor Spalevic and Paul Sestras. Authored the paper—Ouallali Abdessalam, Bouhsane Naima, Saidati Bouhlassa, Velibor Spalevic, Shuraik Kader, Ruby Michael and Paul Sestras. Internal reviewers – Saidati Bouhlassa, Naima Bouhsane and Velibor Spalevic. Project administration – Ouallali Abdessalam, Bouhlassa Saidati and Bouhsane Naima. All authors have read and agreed to the published version of the manuscript.

Funding Open Access funding enabled and organized by CAUL and its Member Institutions.

Data availability Data will be made available on request.

Code availability "No code or software has been developed for this research."

Declarations

Conflict of interests The authors have no relevant financial or non-financial interests to disclose.

Ethical approval Not Applicable.

Consent to participate Not Applicable.

Consent to publish Not Applicable.

Open Access This article is licensed under a Creative Commons Attribution 4.0 International License, which permits use, sharing, adaptation, distribution and reproduction in any medium or format, as long as you give appropriate credit to the original author(s) and the source, provide a link to the Creative Commons licence, and indicate if changes were made. The images or other third party material in this article are included in the article's Creative Commons licence, unless indicated otherwise in a credit line to the material. If material is not included in the article's Creative Commons licence and your intended use is not permitted by statutory regulation or exceeds the permitted use, you will need to obtain permission directly from the copyright holder. To view a copy of this licence, visit <http://creativecommons.org/licenses/by/4.0/>.

References

- Aguilera A, Morales JJ, Goguitchaichvili A, García-Oliva F, Armandariz-Arnez C, Quintana P, Bautista F (2020) Spatial distribution of magnetic material in urban road dust classified by land use and type of road in San Luis Potosí, Mexico. *Air Qual Atmos Health* 13:951–963. <https://doi.org/10.1007/s11869-020-00851-5>
- Alekseev AO, Shary PA, Malyshev VV (2023) Magnetic susceptibility of soils as an ambiguous climate proxy for paleoclimate reconstructions. *Quatern Int* 661:10–21. <https://doi.org/10.1016/j.quaint.2023.04.002>
- Ayoubi S, Ahmadi M, Abdi MR, Afshar FA (2012) Relationships of ^{137}Cs inventory with magnetic measures of calcareous soils of hilly region in Iran. *J Environ Radioact* 112:45–51. <https://doi.org/10.1016/j.jenvrad.2012.03.012>
- Balsam WL, Ellwood BB, Ji J, Williams ER, Long X, El Hassani A (2011) Magnetic susceptibility as a proxy for rainfall: worldwide data from tropical and temperate climate. *Quatern Sci Rev* 30(19–20):2732–2744. <https://doi.org/10.1016/j.quascirev.2011.06.002>
- Bammou Y, Benzougagh B, Abdessalam O, Brahim I, Kader S, Spalevic V, Erçişli S (2024a) Machine learning models for gully erosion susceptibility assessment in the Tensift catchment, Haouz Plain, Morocco for sustainable development. *J African Earth Sci* 213:105229
- Bammou Y, Benzougagh B, Igmoullan B, Ouallali A, Kader S, Spalevic V, Marković SB (2024b) Optimizing flood susceptibility assessment in semi-arid regions using ensemble algorithms: a case study of Moroccan High Atlas. *Nat Hazards* 120(8):7787–7816
- Bashir O, Bangroo SA, Shafai SS, Senesi N, Kader S, Alamri S (2024a) Geostatistical modeling approach for studying total soil nitrogen and phosphorus under various land uses of North-Western Himalayas. *Eco Inform* 80:102520. <https://doi.org/10.1016/j.ecoinf.2024.102520>
- Bashir O, Bangroo SA, Shafai SS, Senesi N, Naikoo NB, Kader S, Jaufer L (2024b) Unlocking the potential of soil potassium: Geostatistical approaches for understanding spatial variations in Northwestern Himalayas. *Eco Inform* 81:102592. <https://doi.org/10.1016/j.ecoinf.2024.102592>
- Bashir O, Bangroo SA, Shafai SS, Shah TI, Kader S, Jaufer L, Hysa A (2024c) Mathematical vs. machine learning models for particle size distribution in fragile soils of North-Western Himalayas. *J Soils Sediments*. <https://doi.org/10.1007/s11368-024-03820-y>
- Benzougagh B, Al-Quraishi AMF, Bammou Y, Kader S, El Brahim M, Sadkaoui D, Ladel L (2024) Spectral Angle Mapper Approach (SAM) for Land Degradation Mapping: A Case Study of the Oued Lahdar Watershed in the Pre-Rif Region (Morocco). In: Al-Quraishi AMF, Mustafa YT (eds) *Natural Resources Deterioration in MENA Region: Land Degradation, Soil Erosion, and Desertification*. Springer International Publishing, Cham, pp 15–35
- Blundell A, Hannam JA, Dearing JA, Boyle JF (2009) Detecting atmospheric pollution in surface soils using magnetic measurements: a reappraisal using an England and Wales database. *Environ Pollut* 157(10):2878–2890. <https://doi.org/10.1016/j.envpol.2009.02.031>
- Bouhlassa S, Bouhsane N (2019) Assessment of areal water and tillage erosion using magnetic susceptibility: the approach and its application in Moroccan watershed. *Environ Sci Pollut Res* 26:25452–25466. <https://doi.org/10.1007/s11356-019-05510-6>
- Bouhlassa S, Bouhsane N (2023) Assessment of the impacts of land-use change and slope position on soil loss by magnetic susceptibility-based models. *Int J Sedim Res* 38(3):455–468. <https://doi.org/10.1016/j.ijsrc.2022.11.006>
- Brito WBM, Campos MCC, de Souza FG, Silva LS, da Cunha JM, de Lima AFL, de Oliveira IA (2022) Spatial patterns of magnetic susceptibility optimized by anisotropic correction in different Alisols in southern Amazonas, Brazil. *Precision Agric* 23(2):419–449

- Cai W, Bora MJ, Pekkat S, Bordoloi S, Garg A, Sekharan S (2023) A new and simple model for predicting soil erosion based on hole erosion tests. *Acta Geophys* 71(2):823–836. <https://doi.org/10.1007/s11600-022-00904-6>
- Cao Z, Zhang K, He J, Yang Z, Zhou Z (2021) Linking rocky desertification to soil erosion by investigating changes in soil magnetic susceptibility profiles on karst slopes. *Geoderma* 389:114949. <https://doi.org/10.1016/j.geoderma.2021.114949>
- Dakir I, Benamara A, Aassoumi H, Ouallali A, Ait Bahammou Y (2020) Contribution of geophysics to the study of barite mineralization in the Paleozoic formations of Asdaf Tinejdad (Eastern Anti Atlas Morocco). *Econom Environ Geol* 53(3):259e269
- De Mello DC, Demattê JA, Silvero NE, Di Raimo LA, Poppiel RR, Mello FA, Rizzo R (2020) Soil magnetic susceptibility and its relationship with naturally occurring processes and soil attributes in pedosphere, in a tropical environment. *Geoderma* 372:114364
- Dearing JA, Dann RJL, Hay K, Lees JA, Loveland PJ, Maher BA, O'grady, K. (1996) Frequency-dependent susceptibility measurements of environmental materials. *Geophys J Int* 124(1):228–240. <https://doi.org/10.1111/j.1365-246X.1996.tb06366.x>
- Dearing, J. A. (1994). *Environmental magnetic susceptibility: using the Bartington MS2 system*. Chi Pub. <https://gmw.com/wp-content/uploads/2019/03/JDearing-Handbook-OM0409.pdf>
- Dearing J. A. (1999) Magnetic susceptibility. *Environmental magnetism: A practical guide*, 35–62
- Debebe Y, Otterpohl R, Islam Z (2023) Remote sensing and multicriterion analysis for identifying suitable rainwater harvesting areas. *Acta Geophys* 71(2):855–872. <https://doi.org/10.1007/s11600-022-00910-8>
- Delbecque N, Van Ranst E, Dondeyne S, Mouazen AM, Vermeir P, Verdoodt A (2022) Geochemical fingerprinting and magnetic susceptibility to unravel the heterogeneous composition of urban soils. *Sci Total Environ* 847:157502. <https://doi.org/10.1016/j.scitotenv.2022.157502>
- Ding Z, Zhang Z, Li Y, Zhang L, Zhang K (2020) Characteristics of magnetic susceptibility on cropland and pastureland slopes in an area influenced by both wind and water erosion and implications for soil redistribution patterns. *Soil Tillage Res* 199:104568. <https://doi.org/10.1016/j.still.2019.104568>
- Djerrab A, Hedley I, Camps P, Abdessadok S, Ruiz CB, Ortega DB (2013) Contribution des paramètres magnétiques à l'identification des niveaux stratigraphiques et de la pédogenèse (Grotte del Angel, Espagne). *Estud Geol* 69(1):71–84. <https://doi.org/10.1016/10.3989/egol.40946.222>
- Djerrab, A., Zedam, R., Camps, P., Defaffia, N., Abdessadok, S., Triki, D. & Bahra, N. (2012). Etude sédimentologique et magnétique d'une séquence alluviale du pléistocène supérieur-holocène de l'Oued Adaila (El Ma Labiod, Tébessa, Algérie) et indications paléoenvironnementales. *Quaternaire. Revue de l'Association française pour l'étude du Quaternaire*, 23(3):227–240
- Faleh A, Navas A, Sadiki A (2005) Erosion and dam siltation in a Rif catchment (Morocco). *Sediment Budg* 2:58–64
- Gennadiev AN, Olson KR, Chernyanskii SS, Jones RL, Woods WI (2002) Quantification of soil erosion rates within the Indian mounds area in Illinois, the United States. *Eurasian Soil Sci* 35(SUPPL. 1):S8–S17
- Grison H, Petrovsky E, Hanzlikova H (2021) Assessing anthropogenic contribution in highly magnetic forest soils developed on basalts using magnetic susceptibility and concentration of elements. *CATENA* 206:105480. <https://doi.org/10.1016/j.catena.2021.105480>
- Grison H, Janovský MP, Lisá L, Hasil J, Štefan I, Hron K, Hejzman M (2023) Magnetic and geochemical record of soil impacted by 300 years of Early medieval settlement. *CATENA* 231:107368. <https://doi.org/10.1016/j.catena.2023.107368>
- Hanesch M, Rantitsch G, Hemetsberger S, Scholger R (2007) Lithological and pedological influences on the magnetic susceptibility of soil: Their consideration in magnetic pollution mapping. *Sci Total Environ* 382(2–3):351–363. <https://doi.org/10.1016/j.scitotenv.2007.04.007>
- Hannam JA, Dearing JA (2008) Mapping soil magnetic properties in Bosnia and Herzegovina for landmine clearance operations. *Earth Planet Sci Lett* 274(3–4):285–294. <https://doi.org/10.1016/j.epsl.2008.05.006>
- Kader S, Novicevic R, Jaufer L (2022) Soil management in sustainable agriculture: analytical approach for the ammonia removal from the diary manure. *The J Agric Forestry* 68(4):69–78
- Kanu MO, Meludu OC, Basavaiah N, Joseph G (2023) The use of environmental magnetic properties, elemental analysis and geostatistical tools for soil pollution assessment, a lesson from Takum, Nigeria. *Physics Chem Earth, Parts a/b/c* 130:103377. <https://doi.org/10.1016/j.pce.2023.103377>
- Kehl M, Vlaminck S, Köhler T, Laag C, Rolf C, Tsukamoto S, Khorrami F (2021) Pleistocene dynamics of dust accumulation and soil formation in the southern Caspian Lowlands-New insights from the loess-paleosol sequence at Neka-Abelou, northern Iran. *Quaternary Sci Rev* 253:106774
- Kletetschka G, Wasilewski PJ, Taylor PT (2000) Hematite vs magnetite as the signature for planetary magnetic anomalies? *Physics Earth Planetary Interiors* 119(3–4):259–267
- Lal R, Bouma J, Brevik E, Dawson L, Field DJ, Glaser B, Zhang J (2021) Soils and sustainable development goals of the United Nations: An International Union of Soil Sciences perspective. *Geoderma Reg* 25:e00398
- Li G, Xia D, Lu H, Wang Y, Jia J, Liu X, Yang X (2020) Magnetic, granulometric and geochemical characterizations of loess sections in the eastern Arid Central Asia: Implication for paleoenvironmental interpretations. *Quatern Int* 552:135–147. <https://doi.org/10.1016/j.quaint.2020.01.003>
- Liliwirianis N, Isa NNM, Suratman MN (2023) Land Resources and Its Degradation in Asia: Its Control and Management. *Land Environ Manage through Forestry*. <https://doi.org/10.1002/9781119910527.ch2>
- Linford, N. (2005). Archaeological applications of naturally occurring nanomagnets. In *Journal of Physics: Conference Series* (Vol. 17, No. 1, p. 127). IOP Publishing. <https://doi.org/10.1088/1742-6596/17/1/019>
- Liu L, Zhang K, Zhang Z, Qiu Q (2015) Identifying soil redistribution patterns by magnetic susceptibility on the black soil farmland in Northeast China. *CATENA* 129:103–111. <https://doi.org/10.1016/j.catena.2015.03.003>
- Ljavić D, Radović M, Kulina M, Zejak D, Spalević V, Kader S, Jaufer L (2023) Influence of cultivar and fertilization treatment on the yield and leaf nutrients content of apple (*Malus domestica* Borkh.). *Heliyon* 9(6):e16321
- Lu SG, Bai SQ, Xue QF (2007) Magnetic properties as indicators of heavy metals pollution in urban topsoils: a case study from the city of Luoyang. *China Geophys J Int* 171(2):568–580. <https://doi.org/10.1111/j.1365-246X.2007.03545.x>
- Ma Y, Minasny B, Malone BP, Mcbratney AB (2019) Pedology and digital soil mapping (DSM). *Eur J Soil Sci* 70(2):216–235. <https://doi.org/10.1111/ejss.12790>
- Maity R, Mondal S, Venkateshwarlu M, Kapawar M, Gain D (2022) Characterization of anthropogenic contaminants in urban soils around Budgebudge current generating station of West Bengal. *India Arabian J Geosci* 15(17):1428. <https://doi.org/10.1007/s12517-022-10724-z>
- Moukchane M, Bouhiassa S, Chalouan A (1998) Approche cartographique et magnétique pour l'identification des sources de sédiments: cas du bassin versant Nakhla (Rif, Maroc). *Sci Et Changements Planétaires/sécheresse* 9(3):227–232

- Ouallali A, Moukhchane M, Aassoumi H, Berrad F, Dakir I (2016) Evaluation et cartographie des taux d'érosion hydrique dans le bassin versant de l'Oued Arbaa Ayacha (Rif occidental, Nord Maroc). *Bulletin de l'Institut Scientifique, Rabat* (38):65–79
- Ouallali A, Aassoumi H, Moukhchane M, Moumou A, Houssni M, Spalevic V, Keesstra S (2020a) Sediment mobilization study on Cretaceous, Tertiary and Quaternary lithological formations of an external Rif catchment. *Morocco Hydrological Sci J* 65(9):1568–1582. <https://doi.org/10.1080/02626667.2020.1755435>
- Ouallali A, Briak H, Aassoumi H, Beroho M, Bouhsane N, Moukhchane M (2020b) Hydrological foretelling uncertainty evaluation of water balance components and sediments yield using a multi-variable optimization approach in an external Rif's catchment. *Morocco. Alex Eng J* 59(2):775–789. <https://doi.org/10.1016/j.aej.2020.02.017>
- Ouallali A, Bouhsane N, Bouhlassa S, Moukhchane M, Ayoubi S, Aassoumi H (2023) Rapid magnetic susceptibility measurement as a tracer to assess the erosion–deposition process using tillage homogenization and simple proportional models: A case study in northern of Morocco. *Int J Sedim Res* 38(5):739–753. <https://doi.org/10.1016/j.ijsrc.2023.06.002>
- Ouallali A, Kader S, Bammou Y, Aqnouy M, Courba S, Beroho M, Briak H, Spalevic V, Kuriqi A, Hysa A (2024) Assessment of the erosion and outflow intensity in the Rif region under different land use and land cover Scenarios. *Land* 13(2):141. <https://doi.org/10.3390/land13020141>
- Owliaie H (2014) A magnetic investigation along a NE–SW transect of the Yasouj Plain, southwestern Iran. *Archiv Agronomy Soil Sci* 60(7):1015–1027. <https://doi.org/10.1080/03650340.2013.855724>
- Qian Y, Roberts AP, Liu Y, Hu P, Zhao X, Heslop D, Li J (2020) Assessment and integration of bulk and component-specific methods for identifying mineral magnetic assemblages in environmental magnetism. *J Geophys Res: Solid Earth* 125(8):e20190JB19024
- Rahimi MR, Ayoubi S, Abdi MR (2013) Magnetic susceptibility and Cs-137 inventory variability as influenced by land use change and slope positions in a hilly, semiarid region of west-central Iran. *J Appl Geophys* 89:68–75. <https://doi.org/10.1016/j.jappgeo.2012.11.009>
- Sabri E., Spalevic V., Boukadir A., Karaoui I., Ouallali A., Mincato R. L., & Sestras P. (2022) Estimation of soil losses and reservoir sedimentation: a case study in Tillouguite sub-basin (high Atlas-Morocco). *Agriculture & Forestry/Poljoprivreda i Sumarstvo*, 68(2). <https://doi.org/10.17707/AgricultForest.68.2.15>
- Sardoo ES, Farpoor MH, Mahmoodabadi M, Jafari A (2023) Magnetic susceptibility in soil pedons developed on different parent rocks in Kerman province (Iran). *Stud Geophys Geod* 67(1):83–106. <https://doi.org/10.1007/s11200-021-0771-8>
- Shirzaditabar F, Heck RJ (2021) Characterization of soil magnetic susceptibility: a review of fundamental concepts, instrumentation, and applications. *Can J Soil Sci* 102(2):231–251. <https://doi.org/10.1139/cjss-2021-0040>
- Silva SHG, Poggere GC, Menezes MDD, Carvalho GS, Guilherme LRG, Curi N (2016) Proximal sensing and digital terrain models applied to digital soil mapping and modeling of Brazilian Latosols (Oxisols). *Remote Sensing* 8(8):614. <https://doi.org/10.3390/rs8080614>
- Singer MJ, Verosub KL, Fine P, TenPas J (1996) A conceptual model for the enhancement of magnetic susceptibility in soils. *Quatern Int* 34:243–248. [https://doi.org/10.1016/1040-6182\(95\)00089-5](https://doi.org/10.1016/1040-6182(95)00089-5)
- Stefanidis S., Alexandridis V., Spalevic V., & Mincato R. L. (2022) WILDFIRE EFFECTS ON SOIL EROSION DYNAMICS: THE CASE OF 2021 MEGAFIRES IN GREECE. *Agriculture & Forestry/Poljoprivreda i Sumarstvo*, 68(2). <https://doi.org/10.17707/AgricultForest.68.2.04>
- Wang F, Zhang W, Huang T, Xu Y, Lai Z (2022) Particle-size dependent magnetic property variations in the Yangtze delta sediments of late Holocene: Effects of pedogenesis and diagenesis. *CATENA* 209:105832. <https://doi.org/10.1016/j.catena.2021.105832>
- Wang J, Zhen J, Hu W, Chen S, Lizaga I, Zeraatpisheh M, Yang X (2023) Remote sensing of soil degradation: Progress and perspective. *Int Soil Water Conservation Res*. <https://doi.org/10.1016/j.iswcr.2023.03.002>
- Warrier AK, Sebastian JG, Amrutha K, Yamuna Sali AS, Mahesh BS, Mohan R (2021) Magnetic properties of surface sediments in Schirmacher Oasis, East Antarctica: spatial distribution and controlling factors. *J Soils Sediments* 21:1206–1221. <https://doi.org/10.1007/s11368-020-02824-8>
- Yang T, Chou YM, Ferré EC, Dekkers MJ, Chen J, Yeh EC, Tanikawa W (2020) Faulting processes unveiled by magnetic properties of fault rocks. *Rev Geophys* 58(4):e2019RG000690
- Zhang M, Zhang W, Zhang K, Yu Y, Liu L (2023) Centennial scale temporal responses of soil magnetic susceptibility and spatial variation to human cultivation on hillslopes in Northeast China. *Soil Tillage Res* 234:105865. <https://doi.org/10.1016/j.still.2023.105865>
- Zong Y, Xiao Q, Lu S (2017) Magnetic signature and source identification of heavy metal contamination in urban soils of steel industrial city, Northeast China. *J Soils Sediments* 17:190–203. <https://doi.org/10.1007/s11368-016-1522-2>

Authors and Affiliations

Abdessalam Ouallali¹  · Naima Bouhsane²  · Saidati Bouhlassa²  · Velibor Spalevic³  · Shuraik Kader⁴  · Ruby Michael⁴  · Paul Sestras^{5,6} 

✉ Shuraik Kader
s.mohamedabdulkader@griffith.edu.au; shuraik10@gmail.com;
shuraik.mohamedabdulkader@griffithuni.edu.au

Abdessalam Ouallali
abdessalam.ouallali@gmail.com;
abdessalam.ouallali@univh2c.ma

Naima Bouhsane
naimabouhsane@gmail.com

Saidati Bouhlassa
bouhlass@fsr.ac.ma

Velibor Spalevic
velibor.spalevic@gmail.com; velibor.spalevic@ucg.ac.me

Ruby Michael
ruby.michael@griffith.edu.au

Paul Sestras
psestras@yahoo.com

¹ Process Engineering and Environment Laboratory, Faculty of Sciences and Techniques of Mohammedia, Hassan II University of Casablanca, BP 146, 28806 Mohammedia, Morocco

² Department of Chemistry Center of Materials
Science Laboratory of Applied Materials Chemistry, Faculty
of Sciences Rabat, Mohammed V University, 4 Av. Ibn
Battouta, B.P, 1014 Rabat, RP, Morocco

³ Biotechnical Faculty, University of Montenegro,
Podgorica 81000, Montenegro

⁴ School of Engineering and Built Environment, Griffith
University, 170 Kessels Road, Nathan, QLD 4111, Australia

⁵ Faculty of Civil Engineering, Technical University
of Cluj-Napoca, 400020 Cluj-Napoca-Napoca, Romania

⁶ Academy of Romanian Scientists, Ilfov 3, 050044 Bucharest,
Romania